

SEPTEMBER 2022

AJNR

VOLUME 43 • PP 1229–1375

AJNR

AMERICAN JOURNAL OF NEURORADIOLOGY

SEPTEMBER 2022
VOLUME 43
NUMBER 9
WWW.AJNR.ORG

THE JOURNAL OF DIAGNOSTIC AND
INTERVENTIONAL NEURORADIOLOGY

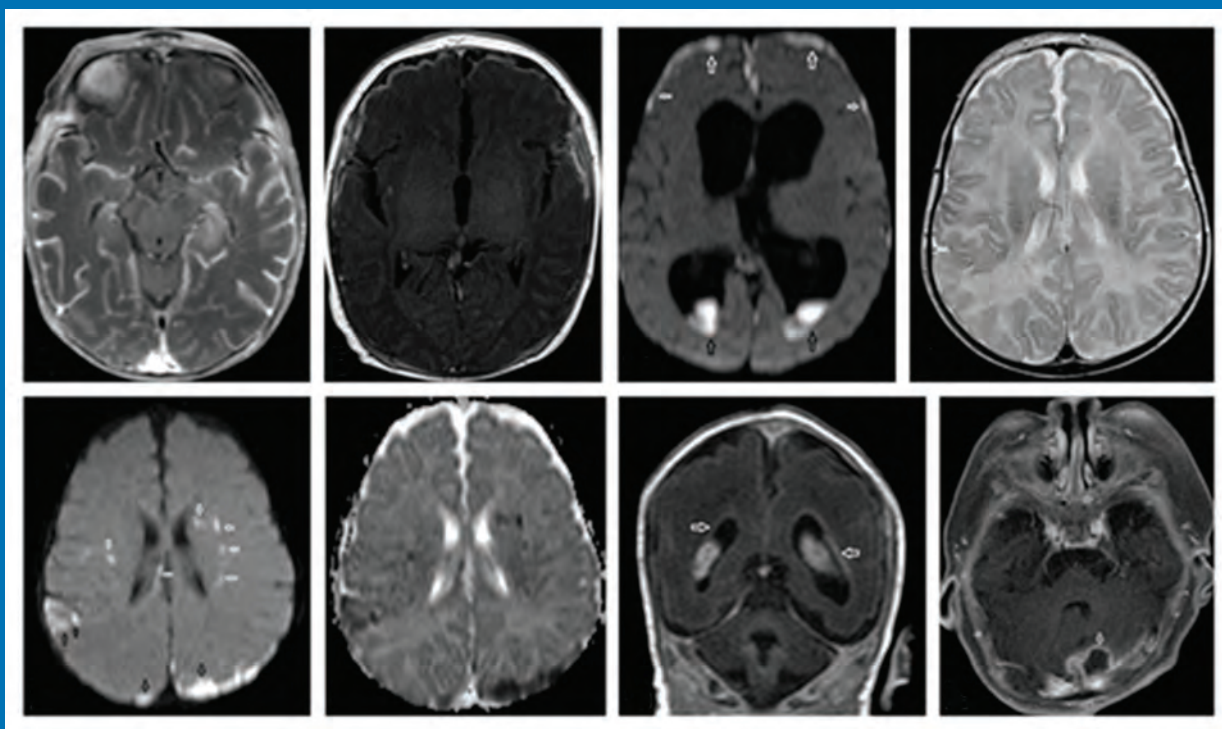
Flow diversion in the treatment of intracranial aneurysms

Detection of meningitis in infants

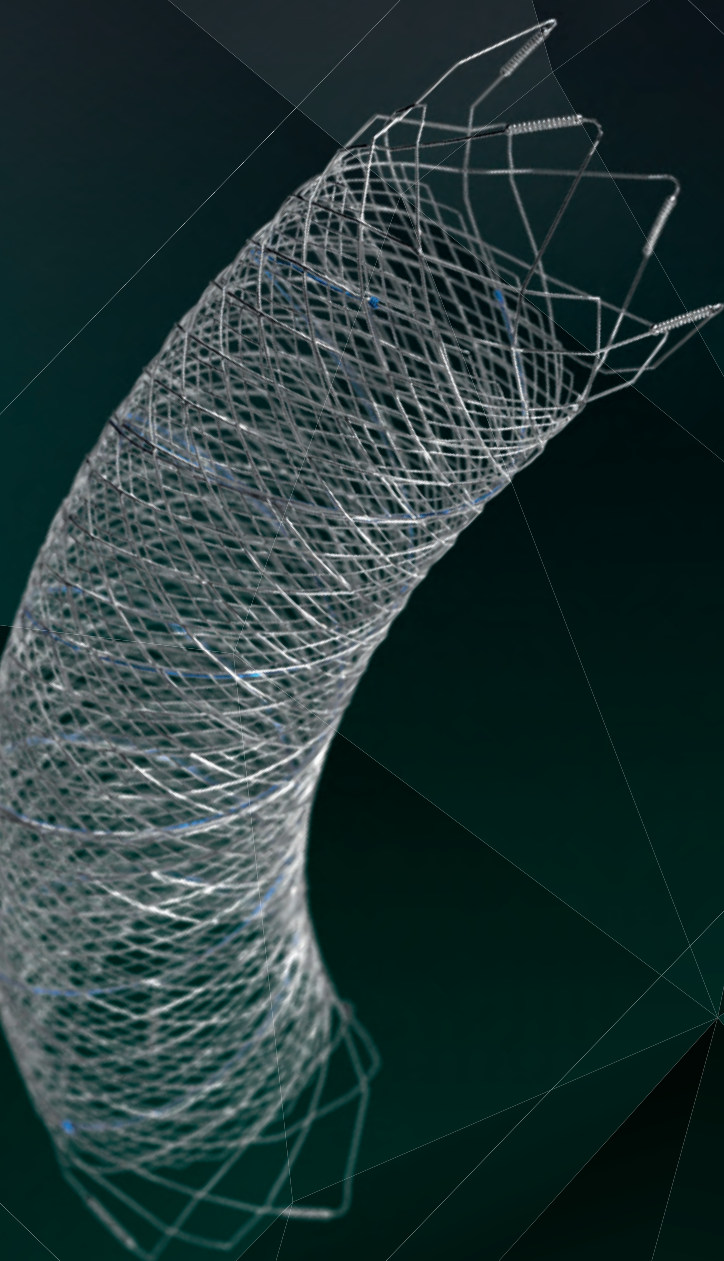
Diagnostic errors in cerebrovascular pathology

Endarterectomy, stenting, or medical treatment for symptomatic
carotid near-occlusion

Official Journal ASNR • ASFNR • ASHNR • ASPNR • ASSR



Introducing FRED™



THE NEXT ADVANCEMENT IN FLOW DIVERSION TECHNOLOGY

The FRED™ X Flow Diverter features the same precise placement and immediate opening of the FRED™ Device, now with X Technology. X Technology is a covalently bonded, nanoscale surface treatment, designed to:

- » **Reduce material thrombogenicity¹**
- » **Maintain natural vessel healing response^{2,3,4}**
- » **Improve device deliverability and resheathing¹**

The only FDA PMA approved portfolio with a 0.021" delivery system for smaller device sizes, and no distal lead wire.



For more information, contact your local MicroVention sales representative or visit our website. www.microvention.com



^{*} Data is derived from in vivo and ex vitro testing and may not be representative of clinical performance.

¹ Data on file

² Tanaka M et al. Design of biocompatible and biodegradable polymers based on intermediate water concept. *Polymer Journal*. 2015;47:114-121.

³ Tanaka M et al. Blood compatible aspects of poly(2-methoxyethylacrylate) (PMEA) – relationship between protein adsorption and platelet adhesion on PMEA surface. *Biomaterials*. 2000;21:1471-1481.

⁴ Schiel L et al. X Coating™: A new biopassive polymer coating. *Canadian Perfusion Canadienne*. June 2001;11(2):9.

Indications for Use: The FRED X System is indicated for use in the internal carotid artery from the petrous segment to the terminus for the endovascular treatment of adult patients (22 years of age or older) with wide-necked (neck width 4 mm or dome-to-neck ratio <2) saccular or fusiform intracranial aneurysms arising from a parent vessel with a diameter 2.0 mm and 5.0 mm.

Rx Only: Federal (United States) law restricts this device to sale by or on the order of a physician.

MICROVENTION, FRED and HEADWAY are registered trademarks of MicroVention, Inc. in the United States and other jurisdictions. Stylized X is a trademark of MicroVention, Inc. © 2022 MicroVention, Inc. MM1222 US 02/22

WEB™ 17

Aneurysm Embolization System

LOWER PROFILE



NEW SIZES



MORE ACCESS OPTIONS



INDICATIONS FOR USE:

The WEB Aneurysm Embolization System is intended for the endovascular embolization of ruptured and unruptured intracranial aneurysms and other neurovascular abnormalities such as arteriovenous fistulae (AVF). The WEB Aneurysm Embolization System is also intended for vascular occlusion of blood vessels within the neurovascular system to permanently obstruct blood flow to an aneurysm or other vascular malformation.

POTENTIAL COMPLICATIONS:

Potential complications include but are not limited to the following: hematoma at the site of entry, aneurysm rupture, emboli, vessel perforation, parent artery occlusion, hemorrhage, ischemia, vasospasm, clot formation, device migration or misplacement, premature or difficult device detachment, non-detachment, incomplete aneurysm filling, revascularization, post-embolization syndrome, and neurological deficits including stroke and death. For complete indications, potential complications, warnings, precautions, and instructions, see instructions for use (IFU provided with the device).

VIA 21, 27, 33 - The VIA Microcatheter is intended for the introduction of interventional devices (such as the WEB device/stents/flow diverters) and infusion of diagnostic agents (such as contrast media) into the neuro, peripheral, and coronary vasculature.

VIA 17, 17 Preshaped - The VIA Microcatheter is intended for the introduction of interventional devices (such as the WEB device/stents/flow diverters) and infusion of diagnostic agents (such as contrast media) into the neuro, peripheral, and coronary vasculature.

The VIA Microcatheter is contraindicated for use with liquid embolic materials, such as n-butyl 2-cyanoacrylate or ethylene vinyl alcohol & DMSO (dimethyl sulfoxide).

The device should only be used by physicians who have undergone training in all aspects of the WEB Aneurysm Embolization System procedure as prescribed by the manufacturer.

RX Only: Federal law restricts this device to sale by or on the order of a physician.

For healthcare professional intended use only.



MicroVention Worldwide
Innovation Center

PH +1.714.247.8000

35 Enterprise
Aliso Viejo, CA 92656 USA
MicroVention UK Limited
MicroVention Europe, S.A.R.L.
MicroVention Deutschland GmbH
Website

PH +44 (0) 191 258 6777
PH +33 (1) 39 21 77 46
PH +49 211 210 798-0
microvention.com



WEB™ and VIA™ are registered trademarks
of Sequent Medical, Inc. in the United States.

©2021 MicroVention, Inc. MM1184 WW 11/2021



TRUST EARNED

What does seeing better with MultiHance® mean?^{1-4*}

MultiHance® demonstrated significantly improved visualization and contrast enhancement of CNS lesions when compared with Gadavist® at 0.1 mmol/kg.^{1†}

- The 0.1 mmol/kg dose of MultiHance demonstrated consistently better lesion visualization for all readers compared to all tested MR contrast agents.¹⁻⁴
- 3 blinded independent readers reported superiority for MultiHance in significantly ($P=.0001$) more patients for all evaluated end points. The opinions of the 3 readers were identical for 61.9%–73.5% of the patients, resulting in values of 0.414–0.629 for inter-reader agreement.

The individuals who appear are for illustrative purposes. All persons depicted are models and not real patients.

Please see Brief Summary of Prescribing Information including Boxed Warning on adjacent page.

*MRI imaging of the CNS in adult and pediatric patients to visualize lesions with abnormal BBB or abnormal vascularity of the brain, spine and associated tissues or to evaluate adults with known or suspected renal or aorto-ilio-femoral occlusive vascular disease.

MultiHance® (gadobenate dimeglumine) injection, 529 mg/mL and MultiHance® Multipack™ (gadobenate dimeglumine) injection, 529 mg/mL

Indications and Usage:

MultiHance® (gadobenate dimeglumine) injection, 529 mg/mL is a gadolinium-based contrast agent indicated for intravenous use in:

- Magnetic resonance imaging (MRI) of the central nervous system (CNS) in adults and pediatric patients (including term neonates) to visualize lesions with abnormal blood-brain barrier or abnormal vascularity of the brain, spine, and associated tissues and
- Magnetic resonance angiography (MRA) to evaluate adults with known or suspected renal or aorto-ilio-femoral occlusive vascular disease

IMPORTANT SAFETY INFORMATION:

WARNING: NEPHROGENIC SYSTEMIC FIBROSIS

Gadolinium-based contrast agents (GBCAs) increase the risk for NSF among patients with impaired elimination of the drugs. Avoid use of GBCAs in these patients unless the diagnostic information is essential and not available with non-contrasted MRI or other modalities. NSF may result in fatal or debilitating systemic fibrosis affecting the skin, muscle and internal organs.

- The risk for NSF appears highest among patients with:
 - chronic, severe kidney disease ($\text{GFR} < 30 \text{ mL/min/1.73m}^2$), or
 - acute kidney injury.
- Screen patients for acute kidney injury and other conditions that may reduce renal function. For patients at risk for chronically reduced renal function (e.g. age > 60 years, hypertension or diabetes), estimate the glomerular filtration rate (GFR) through laboratory testing.
- For patients at highest risk for NSF, do not exceed the recommended MultiHance dose and allow a sufficient period of time for elimination of the drug from the body prior to re-administration.

CONTRAINDICATIONS

MultiHance is contraindicated in patients with known allergic or hypersensitivity reactions to gadolinium-based contrast agents.

WARNINGS AND PRECAUTIONS

Nephrogenic Systemic Fibrosis: NSF has occurred in patients with impaired elimination of GBCAs. Higher than recommended dosing or repeated dosing appears to increase risk.

Hypersensitivity Reactions: Anaphylactic and anaphylactoid reactions have been reported, involving cardiovascular, respiratory, and/or cutaneous manifestations. Some patients experienced circulatory collapse and died. In most cases, initial symptoms occurred within minutes of MultiHance administration and resolved with prompt emergency treatment. Consider the risk for hypersensitivity reactions, especially in patients with a history of hypersensitivity reactions or a history of asthma or other allergic disorders.

Gadolinium Retention: Gadolinium is retained for months or years in several organs. The highest concentrations have been identified in the bone, followed by brain, skin, kidney, liver, and spleen. At equivalent doses, retention varies among the linear agents. Retention is lowest and similar among the macrocyclic GBCAs. Consequences of gadolinium retention in the brain have not been established, but they have been established in the skin and other organs in patients with impaired renal function. Minimize repetitive GBCA imaging studies, particularly closely spaced studies when possible.

Acute Renal Failure: In patients with renal insufficiency, acute renal failure requiring dialysis or worsening renal function have occurred with the use of GBCAs. The risk of renal failure may increase with increasing dose of the contrast agent. Screen all patients for renal dysfunction by obtaining a history and/or laboratory tests.

Extravasation and Injection Site Reactions: Extravasation of MultiHance may lead to injection site reactions, characterized by local pain or burning sensation, swelling, blistering, and necrosis. Exercise caution to avoid local extravasation during intravenous administration of MultiHance.

Cardiac Arrhythmias: Cardiac arrhythmias have been observed in patients receiving MultiHance in clinical trials. Assess patients for underlying conditions



MR Suite



LIFE FROM INSIDE

or medications that predispose to arrhythmias. The effects on QTc by MultiHance dose, other drugs, and medical conditions were not systematically studied.

Interference with Visualization of Certain Lesions: Certain lesions seen on non-contrast images may not be seen on contrast images. Exercise caution when interpreting contrast MR images in the absence of companion non-contrast MR images.

ADVERSE REACTIONS

The most commonly reported adverse reactions are nausea (1.3%) and headache (1.2%).

USE IN SPECIFIC POPULATIONS

Pregnancy: GBCAs cross the human placenta and result in fetal exposure and gadolinium retention. Use only if imaging is essential during pregnancy and cannot be delayed.

Lactation: There is no information on the effects of the drug on the breastfed infant or the effects of the drug on milk production. However, limited literature reports that breastfeeding after MultiHance administration to the mother would result in the infant receiving an oral dose of 0.001%-0.04% of the maternal dose.

Pediatric Use: MultiHance is approved for intravenous use for MRI of the CNS to visualize lesions with abnormal blood brain barrier or abnormal vascularity of the brain, spine, and associated tissues in pediatric patients from birth, including term neonates, to less than 17 years of age. Adverse reactions in pediatric patients were similar to those reported in adults. No dose adjustment according to age is necessary in pediatric patients two years of age and older. For pediatric patients, less than 2 years of age, the recommended dosage range is 0.1 to 0.2 mL/kg. The safety of MultiHance has not been established in preterm neonates.

Please see full Prescribing Information and Patient Medication Guide for additional important safety information for/regarding MultiHance (gadobenate dimeglumine) injection, 529 mg/mL at <https://www.braccoimaging.com/us-en/products/magnetic-resonance-imaging/multihance>

You are encouraged to report negative side effects of prescription drugs to the FDA. Visit www.fda.gov/medwatch or call 1-800-FDA-1088.

MultiHance is manufactured for Bracco Diagnostics Inc. by BIPSO GmbH – 78224 Singen (Germany) and by Patheon Italia S.p.A., Ferentino, Italy. MultiHance is a registered trademark of Bracco International B.V. MultiHance Multipack is a trademark of Bracco International B.V. All other trademarks and registered trademarks are the property of their respective owners.

References: 1. Seidl Z, Vymazal J, Mechi M, et al. Does higher gadolinium concentration play a role in the morphologic assessment of brain tumors? Results of a multicenter intraindividual crossover comparison of gadobutrol versus gadobenate dimeglumine (the MERIT Study). *AJNR Am J Neuroradiol.* 2012;33(6):1050-1058. 2. Maravilla KR, Maldjian JA, Schmalfuss IM, et al. Contrast enhancement of central nervous system lesions: multicenter intraindividual crossover comparative study of two MR contrast agents. *Radiology.* 2006;240(2):389-400. 3. Rowley HA, Scialfa G, Gao PY, et al. Contrast-enhanced MR imaging of brain lesions: a large-scale intraindividual crossover comparison of gadobenate dimeglumine versus gadodiamide. *AJNR Am J Neuroradiol.* 2008;29(9):1684-1691. 4. Vaneckova M, Herman M, Smith MP, et al. The benefits of high relaxivity for brain tumor imaging: results of a multicenter intraindividual crossover comparison of gadobenate dimeglumine with gadoterate meglumine (The BENEFIT Study). *AJNR Am J Neuroradiol.* 2015 Sep;36(9):1589-1598.

Bracco Diagnostics Inc.
259 Prospect Plains Road, Building H
Monroe Township, NJ 08831 USA
Phone: 609-514-2200
Toll Free: 1-877-272-2269 (U.S. only)
Fax: 609-514-2446

© 2022 Bracco Diagnostics Inc. All Rights Reserved. US-MH-2100019 02/22

WARNING: NEPHROGENIC SYSTEMIC FIBROSIS

Gadolinium-based contrast agents (GBCAs) increase the risk for NSF among patients with impaired elimination of the drugs. Avoid use of GBCAs in these patients unless the diagnostic information is essential and not available with non-contrast MRI or other modalities. NSF may result in fatal or debilitating systemic fibrosis affecting the skin, muscle and internal organs.

- The risk for NSF appears highest among patients with:
 - chronic, severe kidney disease (GFR <30 mL/min/1.73m²), or
 - acute kidney injury.
- Screen patients for acute kidney injury and other conditions that may reduce renal function. For patients at risk for chronically reduced renal function (e.g. age > 60 years, hypertension or diabetes), estimate the glomerular filtration rate (GFR) through laboratory testing.
- For patients at highest risk for NSF, do not exceed the recommended Multihance dose and allow a sufficient period of time for elimination of the drug from the body prior to re-administration. [see **Warnings and Precautions (5.1)**]

1 INDICATIONS AND USAGE

1.1 MRI of the Central Nervous System (CNS)

Multihance is indicated for intravenous use in magnetic resonance imaging (MRI) of the central nervous system (CNS) in adults and pediatric patients (including term neonates), to visualize lesions with abnormal blood-brain barrier or abnormal vascularity of the brain, spine, and associated tissues.

1.2 MRA of Renal and Aorta-Iliofemoral Vessels

Multihance is indicated for use in magnetic resonance angiography (MRA) to evaluate adults with known or suspected renal or aorta-iliofemoral occlusive vascular disease.

4 CONTRAINDICATIONS Multihance is contraindicated in patients with known allergic or hypersensitivity reactions to gadolinium-based contrast agents [see **Warnings and Precautions (5.2)**].

5 WARNINGS AND PRECAUTIONS

5.1 Nephrogenic Systemic Fibrosis (NSF) Gadolinium-based contrast agents (GBCAs) increase the risk for nephrogenic systemic fibrosis (NSF) among patients with impaired elimination of the drugs. Avoid use of GBCAs among these patients unless the diagnostic information is essential and not available with non-contrast MRI or other modalities. The GBCA associated NSF risk appears highest for patients with chronic, severe kidney disease (GFR <30 mL/min/1.73m²) as well as patients with acute kidney injury. The risk appears lower for patients with chronic, moderate kidney disease (GFR 30-59 mL/min/1.73m²) and little, if any, for patients with chronic, mild kidney disease (GFR 60-89 mL/min/1.73m²). NSF may result in fatal or debilitating fibrosis affecting the skin, muscle and internal organs. Report any diagnosis of NSF following Multihance administration to Bracco Diagnostics (1-800-257-5181) or FDA (1-800-FDA-1088 or www.fda.gov/medwatch).

Screen patients for acute kidney injury and other conditions that may reduce renal function. Features of acute kidney injury consist of rapid (over hours to days) and usually reversible decrease in kidney function, commonly in the setting of surgery, severe infection, injury or drug-induced kidney toxicity. Serum creatinine levels and estimated GFR may not reliably assess renal function in the setting of acute kidney injury. For patients at risk for chronically reduced renal function (e.g., age > 60 years, diabetes mellitus or chronic hypertension), estimate the GFR through laboratory testing.

Among the factors that may increase the risk for NSF are repeated or higher than recommended doses of a GBCA and the degree of renal impairment at the time of exposure. Record the specific GBCA and the dose administered to a patient. For patients at highest risk for NSF, do not exceed the recommended Multihance dose and allow a sufficient period of time for elimination of the drug prior to re-administration. For patients receiving hemodialysis, physicians may consider prompt initiation of hemodialysis following the administration of a GBCA in order to enhance the contrast agent's elimination. The usefulness of hemodialysis in the prevention of NSF is unknown [see **Dosage and Administration (2)** and **Clinical Pharmacology (12)**].

5.2 Hypersensitivity Reactions Anaphylactic and anaphylactoid reactions have been reported, involving cardiovascular, respiratory, and/or cutaneous manifestations. Some patients experienced circulatory collapse and died. In most cases, initial symptoms occurred within minutes of Multihance administration and resolved with prompt emergency treatment. Prior to Multihance administration, ensure the availability of personnel trained and medications to treat hypersensitivity reactions. If such a reaction occurs stop Multihance and immediately begin appropriate therapy. Additionally, consider the risk for hypersensitivity reactions, especially in patients with a history of hypersensitivity reactions or a history of asthma or other allergic disorders. Observe patients for signs and symptoms of a hypersensitivity reaction during and for up to 2 hours after Multihance administration.

5.3 Gadolinium Retention Gadolinium is retained for months or years in several organs. The highest concentrations (nanomoles per gram of tissue) have been identified in the bone, followed by other organs (e.g., brain, skin, kidney, liver, and spleen). The duration of retention also varies by tissue and is longest in bone. Linear GBCAs cause more retention than macrocyclic GBCAs. At equivalent doses, gadolinium retention varies among the linear agents with Omniscan (gadodiamide) and Optcontrast (gadovimeium) causing greater retention than other linear agents (Eovist (gadoterate dimeglumine), Magnevist (gadopentate dimeglumine), Multihance (gadobenate dimeglumine)). Retention is lowest and similar among the macrocyclic GBCAs (Dotarem (gadotermeium), Gadavist (gadobutrol), ProHance (gadobutrol)).

Consequences of gadolinium retention in the brain have not been established. Pathologic and clinical consequences of GBCA administration and retention in skin and other organs have been established in patients with impaired renal function [see **Warnings and Precautions (5.1)**]. There are reports of pathologic skin changes in patients with normal renal function. Adverse events involving multiple organ systems have been reported in patients with normal renal function without an established causal link to gadolinium retention [see **Adverse Reactions (6.2)**]. While clinical consequences of gadolinium retention have not been established in patients with normal renal function, certain patients might be at higher risk. These include patients requiring multiple lifetime doses, pregnant or pediatric patients, and patients with inflammatory conditions. Consider the retention characteristics of the agent when choosing a GBCA for these patients. Minimize repetitive GBCA imaging studies, particularly closely spaced studies when possible.

5.4 Acute Renal Failure In patients with renal insufficiency, acute renal failure requiring dialysis or worsening renal function have occurred with the use of gadolinium-based contrast agents. The risk of renal failure may increase with increasing dose of the contrast agent. Screen all patients for renal dysfunction by obtaining a history and/or laboratory tests. Consider follow-up renal function assessments for patients with a history of renal dysfunction.

5.5 Extravasation and Injection Site Reactions Extravasation of Multihance may lead to injection site reactions, characterized by local pain or burning, sensation, swelling, blistering, and necrosis. In animal experiments, local reactions including eschar and necrosis were noted even on Day 8 post peritoneal injection of Multihance. Exercise caution to avoid local extravasation during intravenous administration of Multihance. If extravasation occurs, evaluate and treat as necessary if local reactions develop.

5.6 Cardiac Arrhythmias Cardiac arrhythmias have been observed in patients receiving Multihance in clinical trials [see **Adverse Reactions (6.1)**]. Assess patients for underlying conditions or medications that predispose to arrhythmias.

A double-blind, placebo-controlled, 24-hour post dose continuous monitoring, crossover study in 47 subjects evaluated the effect of 0.2 mmol/kg Multihance on ECG intervals, including QTc. The average changes in QTc values compared with placebo were minimal (<5 msec). QTc prolongation between 10 and 50 msec was noted in 20 subjects who received Multihance vs. 11 subjects who received placebo. Prolongations ≥ 61 msec were noted in 6 subjects who received Multihance and in 3 subjects who received placebo. None of these subjects had associated malignant arrhythmias. The effects on QTc by Multihance dose, other drugs, and medical conditions were not systematically studied.

5.7 Interference with Visualization of Certain Lesions Certain lesions seen on non-contrast images may not be seen on contrast images. Exercise caution when interpreting contrast MR images in the absence of companion non-contrast MR images.

6 ADVERSE REACTIONS

The following adverse reactions are discussed in greater detail in other sections of the label:

- Nephrogenic systemic fibrosis [see **Warnings and Precautions (5.1)**]

- Hypersensitivity reactions [see **Warnings and Precautions (5.2)**]

6.1 Clinical Trials Experience

Because clinical trials are conducted under widely varying conditions, adverse reaction rates observed in the clinical trials of a drug cannot be directly compared to rates in the clinical trials of another drug and may not reflect the rates observed in practice.

Adult In clinical trials with Multihance, a total of 4967 adult subjects (137 healthy volunteers and 4830 patients) received Multihance at doses ranging from 0.005 to 0.4 mmol/kg. There were 2538 (57%) men and 2129 (43%) women with a mean age of 56.5 years (range 18 to 90 years). A total of 4403 (89%) subjects were Caucasian, 134 (3%) Black, 275 (6%) Asian, 40 (1%) Hispanic, 70 (1%) in other racial groups, and for 45 (1%) subjects, race was not reported.

The most commonly reported adverse reactions in adult subjects who received Multihance were nausea (1.3%) and headache (1.2%). Most adverse reactions were mild to moderate in intensity. One subject experienced a serious anaphylactoid reaction with laryngeal spasm and dyspnea [see **Warnings and Precautions (5.2)**]. Serious adverse reactions consisting of convulsions, pulmonary edema, acute necrotizing pancreatitis, and anaphylactoid reactions were reported in 0.1% of subjects in clinical trials.

Adverse reactions that occurred in at least 0.5% of 4967 adult subjects who received Multihance are listed below (Table 2), in decreasing order of occurrence within each system.

System	Number of subjects dosed	Number of subjects with any adverse reaction	%
Gastrointestinal Disorders	4967	517 (10.4%)	
Nausea		67 (1.3%)	
Headache		62 (1.2%)	
General Disorders and Administration Site Disorders			
Injection Site Reaction	54 (1.1%)		
Feeling Hot	49 (1.0%)		
Nervous System Disorders			
Dizziness	60 (1.2%)		
Dysgeusia	33 (0.7%)		
Paresthesia	24 (0.5%)		
Dizziness	24 (0.5%)		

The following adverse reactions occurred in less than 0.5% of the 4967 adult subjects who received Multihance. Serious adverse reactions described above are not repeated below.

Blood and Lymphatic System Disorders: Basophilia; **Cardiac Disorders:** Atrioventricular block first degree; **Eye Disorders:** Eye pruritus, eye swelling, ocular hyperemia, visual disturbance; **Gastrointestinal Disorders:** Abdominal pain or discomfort, diarrhea, dry mouth, lip swelling, parosmia oral, tongue edema, vomiting; **General Disorders and Administration Site Conditions:** Chest pain or discomfort, chills, malaise; **Immune System Disorders:** Hypersensitivity; **Investigations:** Non-specific changes in laboratory tests (including hematology, blood chemistry, liver enzymes and urinalysis), blood pressure and electrocardiogram parameters (including PR, QRS and QT intervals and ST-T segment changes); **Musculoskeletal and Connective Tissue Disorders:** Myalgia; **Nervous System Disorders:** Parosmia, tremor; **Respiratory, Thoracic and Mediastinal Disorders:** Dyspnea, laryngospasm, nasal congestion, sneezing, wheezing; **Skin and Subcutaneous Tissue Disorders:** Hyperhidrosis, pruritus, rash, swelling face, urticaria.

Pediatric In clinical trials of Multihance in MRI of the CNS, 217 pediatric subjects received Multihance at a dose of 0.1 mmol/kg. A total of 112 (52%) subjects were male and the overall mean age was 6.3 years (range 4 days to 17 years). A total of 168 (79%) subjects were Caucasian, 12 (6%) Black, 12 (6%) Asian, 24 (11%) Hispanic, and 1 (<1%) in other racial groups.

Adverse reactions were reported for 14 (6.5%) of the subjects. The frequency and the nature of the adverse reactions were similar to those seen in the adult patients. The most commonly reported adverse reactions were vomiting (1.4%), pyrexia (0.9%), and hyperhidrosis (0.9%). No subject died during study participation. A serious adverse reaction of worsening of vomiting was reported for one (0.5%) patient with a brain tumor (glioma) for which a causal relationship to Multihance could not be excluded.

Pediatric Patients In clinical trials of Multihance in MRI of the CNS, 307 pediatric subjects received Multihance at a dose of 0.1 mmol/kg. A total of 160 (52%) subjects were male and the overall mean age was 6.0 years (range, 2 days to 17 years). A total of 211 (69%) subjects were Caucasian, 24 (8%) Black, 15 (5%) Asian, 30 (13%) Hispanic, 2 (<1%) in other racial groups, and for 16 (5%), race was not reported. Adverse reactions were reported for 14 (4.6%) of the subjects. The frequency and the nature of the adverse reactions were similar to those seen in the adult patients. The most commonly reported adverse reactions were vomiting (1.0%), pyrexia (0.7%), and hyperhidrosis (0.7%). No subject died during study participation.

6.2 Post-marketing Experience

The following adverse reactions have been identified during post approval use of Multihance. Because these reactions are reported voluntarily from a population of uncertain size, it is not always possible to reliably estimate their frequency or establish a causal relationship to drug exposure.

Immune System Disorders: Anaphylactic, anaphylactoid and hypersensitivity reactions manifested with various degrees of severity up to anaphylactic shock, loss of consciousness and death. The reactions generally involved signs or symptoms of respiratory, cardiovascular, and/or mucocutaneous abnormalities.

General Disorders and Administration Site Conditions: Extravasation of Multihance may lead to injection site reactions, characterized by local pain or burning sensation, swelling, blistering, and necrosis [see **Warnings and Precautions (5.4)**]. Adverse events with variable onset and duration have been reported after GBCA administration [see **Warnings and Precautions (5.3)**]. These include fatigue, asthenia, pain syndromes, and heterogeneous clusters of symptoms in the neurological, cutaneous, and musculoskeletal systems. Skin: Gadolinium associated plaques.

7 DRUG INTERACTIONS

7.1 Transporter-Based Drug-Drug Interactions Multihance and other drugs may compete for the canalicular multispecific organic anion transporter (MOAT) also referred to as MRP2 or ABCG2. Therefore, Multihance may prolong the systemic exposure of drugs such as cisplatin, anticholinergics (e.g., donepezil, darunavir), anti-alcoholics (e.g., vincristine), methotrexate, etoposide, tamoxifen, and paliperidone. In particular, consider the potential for prolonged drug exposure in patients with decreased MOAT activity (e.g., Dubin Johnson syndrome).

8 USE IN SPECIFIC POPULATIONS

8.1 Pregnancy Risk Summary GBCAs cross the placenta and result in fetal exposure and placental retention. The human data on the association between GBCAs and adverse fetal outcomes are limited and inconclusive [see Data]. In animal reproduction studies, gadobenate dimeglumine has been shown to be teratogenic in rabbits following repeated intravenous administration during organogenesis at doses up to 6 times the recommended human dose. There were no adverse developmental effects observed in rats with intravenous administration of gadobenate dimeglumine during organogenesis at doses up to three times the recommended human dose [see Data]. Because of the potential for gadolinium to the fetus, use Multihance only if imaging is essential during pregnancy and cannot be delayed. The estimated background risk of major birth defects and miscarriage for the indicated population is unknown. All pregnancies have a background risk of birth defect, loss, or other adverse outcomes.

In the U.S. general population, the estimated background risk of major birth defects and miscarriage in clinically recognized pregnancies is 2 to 4% and is 15 to 20%, respectively. **Data Human Data** Contrast enhancement is visualized in the human placenta and fetal tissues after maternal GBCA administration. Cohort studies and case reports on exposure to GBCAs during pregnancy have not reported a clear association between GBCAs and adverse effects in the exposed neonates. However, a retrospective cohort study, comparing pregnant women who had a GBCA MRI to pregnant women who did not have an MRI, reported a higher occurrence of stillbirths and neonatal deaths in the group receiving GBCA MRI. Limitations of this study include a lack of comparison with non-contrast MRI and lack of information about the maternal indication for MRI. Overall, these data preclude a reliable evaluation of the potential risk of adverse fetal outcomes with the use of GBCAs in pregnancy. **Animal Data** Gadolinium Retention GBCAs administered to pregnant non-human primates (0.1 mmol/kg on gestational days 85 and 135) result in measurable gadolinium concentration in the offspring in bone, brain, skin, liver, kidney, and spleen for at least 7 months.

GBCAs administered to pregnant mice (2 mmol/kg daily on gestational days 16 through 19) result in measurable gadolinium concentration in the pups in bone, brain, kidney, liver, blood, muscle, and spleen at one month postnatal age.

Reproductive Toxicology Gadobenate dimeglumine has been shown to be teratogenic in rabbits when administered intravenously at 2 mmol/kg/day (6 times the recommended human dose based on body surface area) during organogenesis (day 6 to 18) inducing microphthalmia/small eye and/or local retinal fold in 3 fetuses from 3 separate litters. In addition, Multihance intravenously administered at 3 mmol/kg/day (10 times the

recommended human dose based on body surface area) has been shown to increase intrauterine deaths in rabbits. There was no evidence that Multihance induced teratogenic effects in rats at doses up to 2 mmol/kg/day (3 times the recommended human dose based on body surface area), however, rats dams exhibited no systemic toxicity at this dose. There were no adverse effects on the birth, survival, growth, development and fertility of the F1 generation at doses up to 2 mmol/kg in a rat peri- and post-natal (Segment III) study.

10 OVERDOSAGE

Clinical consequences of overdose with Multihance have not been reported. Treatment of an overdose should be directed toward support of vital functions and prompt institution of symptomatic therapy. In a Phase I clinical study doses up to 0.4 mmol/kg were administered to patients. Multihance has been shown to be dialyzable [see **Clinical Pharmacology (12.3)**].

12 CLINICAL PHARMACOLOGY

12.1 Mechanism of Action Gadobenate dimeglumine is a paramagnetic agent and, as such, develops a magnetic moment when placed in a magnetic field. The large magnetic moment produced by the paramagnetic agent results in a large local magnetic field, which can enhance the relaxation rates of water protons in its vicinity leading to an increase of signal intensity (brightness) of tissue.

In magnetic resonance imaging (MRI), visualization of normal and pathological tissue depends in part on variations in the radiofrequency signal intensity that occur with 1) differences in proton density, 2) differences of the spin-lattice or longitudinal relaxation times (T1), and 3) differences in the spin-spin or transverse relaxation time (T2). When placed in a magnetic field, gadobenate dimeglumine decreases the T1 and T2 relaxation time in target tissues. At recommended doses, the effect is observed with greatest sensitivity in the T1-weighted sequences.

12.2 Pharmacokinetics Unlike other tested paramagnetic contrast agents (See Table 3), Multihance demonstrates weak and transient interactions with serum proteins that causes slowing in the molecular tumbling dynamics, resulting in strong increases in relaxivity in solutions containing serum proteins. The improved relaxation effect can contribute to increased contrast-to-noise ratio and lesion-to-brain ratio, which may improve visualization.

	Human plasma	
	r ₁	r ₂ ¹
Gadobenate	9.7 ¹	12.5 ¹
Gadopentate	4.9 ¹	6.3 ¹
Gadoterate	5.4 ¹	—
Gadoteridol	4.4 ¹	—

r₁ and r₂ relaxivities indicate the efficiency in shortening T1 and T2 relaxation times, respectively.

¹ In heparinized human plasma, at 37°C.

² In citrated human plasma, at 37°C.

— Not available.

Disruption of the blood-brain barrier or abnormal vascularity allows enhancement by Multihance of lesions such as neoplasms, abscesses, and infarcts. Uptake of Multihance into hepatocytes has been demonstrated.

12.3 Pharmacokinetics Three single-dose intravenous studies were conducted in 32 healthy male subjects to assess the pharmacokinetics of gadobenate dimeglumine. The doses administered in these studies ranged from 0.005 to 0.4 mmol/kg. Upon injection, the meglumine salt is completely dissociated from the gadobenate dimeglumine complex. Staying in the molecular tumbling dynamics, resulting in strong increases in relaxivity in solutions containing serum proteins. The improved relaxation effect can contribute to increased contrast-to-noise ratio and lesion-to-brain ratio, which may improve visualization.

Distribution Gadobenate ion has a rapid distribution half-life (reported as mean ± SD) of 0.084 ± 0.012 to 0.605 ± 0.072 hours. Volume of distribution of the central compartment ranged from 0.074 ± 0.097 to 0.158 ± 0.038 L/kg, and estimates of volume of distribution by area ranged from 0.170 ± 0.016 to 0.282 ± 0.079 L/kg. These latter estimates are approximately equivalent to the average volume of extracellular body water in man. *In vitro* studies showed no appreciable binding of gadobenate ion to human serum proteins.

Elimination Gadobenate ion is eliminated predominantly via the kidneys, with 78% to 96% of an administered dose recovered in the urine. Total plasma clearance and renal clearance estimates of gadobenate ion were similar, ranging from 0.93 ± 0.010 to 1.133 ± 0.270 L/hr/kg and 0.982 ± 0.098 to 1.04 ± 0.039 L/hr/kg, respectively. The clearance is similar to that of substances that are subject to glomerular filtration. The mean elimination half-life ranged from 1.27 ± 0.26 to 2.02 ± 0.60 hours. A small percentage of the administered dose (0.6% to 4%) is eliminated via the biliary route and recovered in feces.

Metabolism There was no detectable biotransformation of gadobenate ion. Dissociation of gadobenate ion *in vivo* has been shown to be minimal, with less than 1% of the free chelating agent being recovered alone in feces.

Pharmacokinetics in Special Populations

Renal Impairment A single intravenous dose of 0.2 mmol/kg of Multihance was administered to 20 subjects with impaired renal function (6 men and 3 women with moderate renal impairment [urine creatinine clearance >30 to <60 mL/min] and 5 men and 6 women with severe renal impairment [urine creatinine clearance >10 to <30 mL/min]). Mean estimates of the elimination half-life were 6.1 ± 3.0 and 9.5 ± 3.1 hours for the moderate and severe renal impairment groups, respectively as compared with 1.0 to 2.0 hours in healthy volunteers.

Hemodialysis A single intravenous dose of 0.2 mmol/kg of Multihance was administered to 11 subjects (5 males and 6 females) with end-stage renal disease requiring hemodialysis to determine the pharmacokinetics and dialyzability of gadobenate. Approximately 72% of the dose was recovered by hemodialysis over a 4-hour period. The mean elimination half-life on dialysis was 1.21 ± 0.29 hours as compared with 4.24 ± 2.4 hours when off dialysis.

Hepatic Impairment A single intravenous dose of 0.1 mmol/kg of Multihance was administered to 11 subjects (8 males and 3 females) with impaired liver function (Class B or C modified Child-Pugh Classification). Hepatic impairment had little effect on the pharmacokinetics of Multihance with the parameters being similar to those calculated for healthy subjects.

Gender, Age, Race A multiple regression analysis performed using pooled data from several pharmacokinetic studies found no significant effect of sex upon the pharmacokinetics of gadobenate. Clearance appeared to decrease slightly with increasing age. Since variations due to age appear minimal, dosage adjustment for geriatric population is not recommended. Pharmacokinetic differences due to race have not been systematically studied.

Pediatric A population pharmacokinetic analysis incorporated data from 25 healthy subjects (14 males and 11 females) and 15 subjects undergoing MRI imaging of the central nervous system (7 males and 8 females) between ages of 2 and 16 years. The subjects received a single intravenous dose of 0.1 mmol/kg of Multihance. The geometric mean C_{max} was 62.3 µg/mL (n=16) in children 2 to 5 years of age, and 64.2 µg/mL (n=24) in children older than 5 years. The geometric mean AUC_{0-∞} was 77.9 µg·h/mL in children 2 to 5 years of age (n=16) and 82.6 µg·h/mL in children older than 5 years (n=24). The geometric mean half-life was 1.2 hours in children 2 to 5 years of age and 0.93 hours in children older than 5 years. There was no significant gender-related difference in the pharmacokinetic parameters in the pediatric patients. Over 80% of the dose was recovered in urine after 24 hours. Pharmacokinetic simulations indicate similar AUC and C_{max} values for Multihance in pediatric subjects less than 2 years when compared to those reported for adults; no age-based dose adjustment is necessary for this pediatric population.

17 PATIENT COUNSELING INFORMATION

17.1 Nephrogenic Systemic Fibrosis Instruct patients to inform their physician if they:

- have a history of kidney and/or liver disease, or a have recently received a GBCA.

GBCAs increase the risk for NSF among patients with impaired elimination of the drugs. To counsel patients at risk for NSF: • Describe the clinical manifestations of NSF • Describe procedures to screen for the detection of renal impairment.

Instruct the patients to contact their physician if they develop signs or symptoms of NSF following Multihance administration, such as burning, itching, swelling, scaling, hardening and tightening of the skin; red or dark patches on the skin; stiffness in joints with trouble moving, bending or straightening the arms, hands, legs or feet; pain in the hip bones or ribs; or muscle weakness.

17.2 Common Adverse Reactions

Inform patients that they may experience:

- reactions along the venous injection site, such as mild and transient burning or pain or feeling of warmth or coldness at the injection site • side effects of feeling hot, nausea, and headache.

17.3 General Precautions

Instruct patients scheduled to receive Multihance to inform their physician if they:

- are pregnant or breast feeding • have a history of seizure, heart disease, seizure, asthma or allergic respiratory diseases • are taking any medications • have any allergies to any of the ingredients of Multihance.

*Multicenter double-blind randomized individual crossover study design of 123 patients with known or suspected brain tumors. Each patient received 0.1-mmol/kg doses of Multihance and Gadavist in 2 identical MRI imaging examinations. Contrast agents were administered by IV using manual bolus injection (n=118) or a power injector (n=4). Both agents were administered at 0.1 mmol/kg of body weight, corresponding to 0.2 mL/kg for Multihance and 0.1 mL/kg for Gadavist. The interval between the 2 MR imaging examinations was >48 hours to avoid carryover effects but <14 days to minimize the chance of measurable disease progression or lesion evolution. All images were evaluated by 3 blinded, independent experienced radiologists who were unaffiliated with the study centers. Each reader evaluated the patient images separately and independently. Images were evaluated qualitatively for diagnostic information and scored for: 1) lesion border delineation, 2) disease extent, 3) visualization of lesion internal morphology, and 4) lesion contrast enhancement compared with surrounding normal tissue. All assessments used a 3-point scales from 1 (examination 1 superior) through 0 (examinations equal) to 1 (examination 2 superior).

Gadavist[®] (gadobutrol) is a registered trademark of Bayer Healthcare. **Reference:** Seidl Z, Vymazal J, Mechl M, et al. Does higher gadolinium concentration play a role in the morphologic assessment of brain tumors? Results of a multicenter intraindividual crossover comparison of gadobutrol versus gadobenate dimeglumine (the MERIT study). *AJNR Am J Neuroradiol*. 2012 Jun-Jul;33(6):1050-1058.

AJNR *go green*

***AJNR* urges American Society of Neuroradiology members to reduce their environmental footprint by voluntarily suspending their print subscription.**

The savings in paper, printing, transportation, and postage directly fund new electronic enhancements and expanded content.

The digital edition of *AJNR* presents the print version in its entirety, along with extra features including:

- Publication Preview
- Case Collection
- Podcasts
- The *AJNR* News Digest
- The *AJNR* Blog

It also reaches subscribers much faster than print. An electronic table of contents will be sent directly to your mailbox to notify you as soon as it publishes.

Readers can search, reference, and bookmark current and archived content 24 hours a day on www.ajnr.org.

ASNR members who wish to opt out of print can do so by using the *AJNR* Go Green link on the *AJNR* Website (<http://www.ajnr.org/content/subscriber-help-and-services>). Just type your name in the email form to stop print and spare our ecosystem.

EDITOR-IN-CHIEF

Jeffrey S. Ross, MD

Professor of Radiology, Department of Radiology,
Mayo Clinic College of Medicine, Phoenix, AZ

SENIOR EDITORS

Harry J. Cloft, MD, PhD

Professor of Radiology and Neurosurgery,
Department of Radiology, Mayo Clinic College of
Medicine, Rochester, MN

Christopher G. Filippi, MD

Professor and Alice Ettinger-Jack R. Dreyfuss
Chair of Radiology,
Tufts University School of Medicine,
Radiologist-in-Chief
Tufts University Medical Center, Boston, MA

Thierry A.G.M. Huisman, MD, PD, FICIS, FACR

Radiologist-in-Chief and Chair of Radiology, Texas
Children's Hospital,
Professor of Radiology, Pediatrics, Neurosurgery,
and OBGYN, Baylor College of Medicine,
Houston, TX

Yvonne W. Lui, MD

Associate Professor of Radiology,
Chief of Neuroradiology,
New York University School of Medicine,
New York, NY

C.D. Phillips, MD, FACR

Professor of Radiology, Weill Cornell Medical
College, Director of Head and Neck Imaging,
New York-Presbyterian Hospital, New York, NY

Lubdhra M. Shah, MD, MS

Professor of Radiology and Director of Spine
Imaging, University of Utah Department of
Radiology and Imaging Sciences, Salt Lake City, UT

STATISTICAL SENIOR EDITOR

Bryan A. Comstock, MS

Senior Biostatistician,
Department of Biostatistics,
University of Washington, Seattle, WA

ARTIFICIAL INTELLIGENCE DEPUTY EDITOR

Peter D. Chang, MD

Assistant Professor-in-Residence,
Departments of Radiological Sciences,
Computer Sciences, and Pathology,
Director, Center for Artificial Intelligence in
Diagnostic Medicine (CAIDM),
University of California, Irvine, Irvine, CA

EDITORIAL BOARD

Ashley H. Aiken, Atlanta, GA

Matthew D. Alexander, Salt Lake City, UT

Lea M. Alhilali, Phoenix, AZ

Jason W. Allen, Atlanta, GA

Mohammed A. Almekhlafi, Calgary, Alberta,
Canada

Niranjan Balu, Seattle, WA

Matthew J. Barkovich, San Francisco, CA

Joachim Berkefeld, Frankfurt, Germany

Karen Buch, Boston, MA

Judah Burns, New York, NY

Danielle Byrne, Dublin, Ireland

Federico Cagnazzo, Montpellier, France

Gloria C. Chiang, New York, NY

Daniel Chow, Irvine, CA

Kars C.J. Compagne, Rotterdam, The Netherlands

Yonghong Ding, Rochester, MN

Birgit Ertl-Wagner, Toronto, Ontario, Canada

Aaron Field, Madison, WI

Nils D. Forkert, Calgary, Alberta, Canada

Frank Gaillard, Melbourne, Australia

Joseph J. Gemmete, Ann Arbor, Michigan

Brent Griffith, Detroit, MI

Michael J. Hoch, Philadelphia, PA

Joseph M. Hoxworth, Phoenix, AZ

Raymond Y. Huang, Boston, MA

Susie Y. Huang, Boston, MA

Ferdinand K. Hui, Honolulu, HI

Christof Karmonik, Houston, TX

Gregor Kasprian, Vienna, Austria

Timothy J. Kaufmann, Rochester, MN

Hillary R. Kelly, Boston, MA

Toshibumi Kinoshita, Akita, Japan

Ioannis Koktzoğlu, Evanston, IL

Stephen F. Kralik, Houston, TX

Luke Ledbetter, Los Angeles, CA

Franklin A. Marden, Chicago, IL

Markus A. Möhlenbruch, Heidelberg, Germany

Mahmud Mossa-Basha, Morrisville, NC

Renato Hoffmann Nunes, Sao Paulo, Brazil

Sam Payabvash, New Haven, CT

Johannes A.R. Pfaff, Salzburg, Austria

Eike I. Piechowiak, Bern, Switzerland

Laurent Pierot, Reims, France

Alexander R. Podgorsak, Chicago, IL

Eytan Raz, New York, NY

Jeff Rudie, San Diego, CA

Paul M. Ruggieri, Cleveland, OH

Fatih Seker, Heidelberg, Germany

Maksim Shapiro, New York, NY

Timothy Shepherd, New York, NY

Mark S. Shiroishi, Los Angeles, CA

Neetu Soni, Rochester, NY

Ashok Srinivasan, Ann Arbor, MI

Jason F. Talbott, San Francisco, CA

Anderanik Tomasian, Los Angeles, CA

Fabio Triulzi, Milan, Italy

Arastoo Vossough, Philadelphia, PA

Richard Watts, New Haven, CT

Elysa Widjaja, Toronto, Ontario, Canada

Ronald Wolf, Philadelphia, Pennsylvania

Shuang Xia, Tianjin, China

Leonard Yeo, Singapore

Woong Yoon, Gwangju, South Korea

David M. Yousem, Evergreen, CO

Carlos Zamora, Chapel Hill, NC

Chengcheng Zhu, Seattle, WA

EDITORIAL FELLOW

Alexandre Boutet, Toronto, Ontario, Canada

SPECIAL CONSULTANTS TO THE EDITOR

AJNR Blog Editor

Neil Lall, Denver, CO

Case of the Month Editor

Nicholas Stence, Aurora, CO

Case of the Week Editors

Matylda Machnowska, Toronto, Ontario, Canada

Anvita Pauranik, Calgary, Alberta, Canada

Vinil Shah, San Francisco, CA

Classic Case Editor

Sandy Cheng-Yu Chen, Taipei, Taiwan

Health Care and Socioeconomics Editor

Pina C. Sanelli, New York, NY

Physics Editor

Greg Zaharchuk, Stanford, CA

Podcast Editor

Kevin Hiatt, Winston-Salem, NC

Twitter Editor

Jacob Ormsby, Albuquerque, NM

Official Journal:

American Society of Neuroradiology

American Society of Functional Neuroradiology

American Society of Head and Neck Radiology

American Society of Pediatric Neuroradiology

American Society of Spine Radiology

Founding Editor
Juan M. Taveras

Editors Emeriti
Mauricio Castillo, Robert I. Grossman,
Michael S. Huckman, Robert M. Quencer

Managing Editor
Karen Halm

Assistant Managing Editor
Laura Wilhelm

Executive Director, ASNR
Mary Beth Hepp

AJNR

AMERICAN JOURNAL OF NEURORADIOLOGY

SEPTEMBER 2022
VOLUME 43
NUMBER 9
WWW.AJNR.ORG





Publication Preview at www.ajnr.org features articles released in advance of print.
Visit www.ajnrblog.org to comment on AJNR content and chat with colleagues
and AJNR's News Digest at <http://ajnrndigest.org> to read the stories behind the
latest research in neuroimaging.

1229 **PERSPECTIVES** *M. Hauben*

REVIEW ARTICLE


 1230 **Multimodality Imaging in Primary Progressive Aphasia** *M. Roytman, et al.* **ADULT BRAIN**

LEVEL 1 EBM EXPEDITED PUBLICATION

    1244 **Flow Diversion in the Treatment of Intracranial Aneurysms: A Pragmatic Randomized Care Trial** *J. Raymond, et al.* **INTERVENTIONAL**

GENERAL CONTENTS


  1252 **3D Enhancement Color Maps in the Characterization of Intracranial Atherosclerotic Plaques** *S. Sanchez, et al.* **ADULT BRAIN**

 1259 **Detection of Early Ischemic Changes with Virtual Noncontrast Dual-Energy CT in Acute Ischemic Stroke: A Noninferiority Analysis** *F. Kauw, et al.* **ADULT BRAIN**

  1265 **Optimizing the Definition of Ischemic Core in CT Perfusion: Influence of Infarct Growth and Tissue-Specific Thresholds** *A. Rodríguez-Vázquez, et al.* **ADULT BRAIN**


 1271 **Diagnostic Errors in Cerebrovascular Pathology: Retrospective Analysis of a Neuroradiology Database at a Large Tertiary Academic Medical Center** *G. Biddle, et al.* **ADULT BRAIN**

  1279 **Larger Posterior Revascularization Associated with Reduction of Choroidal Anastomosis in Moyamoya Disease: A Quantitative Angiographic Analysis** *T. Funaki, et al.* **ADULT BRAIN**

 1286 **Correlation of Call Burden and Sleep Deprivation with Physician Burnout, Driving Crashes, and Medical Errors among US Neurointerventionalists** *R.N. Abdalla, et al.* **INTERVENTIONAL**

  1292 **Predictors and Impact of Sulcal SAH after Mechanical Thrombectomy in Patients with Isolated M2 Occlusion** *D.Y. Kim, et al.* **INTERVENTIONAL**

 1299 **Causes of Death in Endovascularly Treated Patients with Acute Stroke** *H. Nagel, et al.* **INTERVENTIONAL**

 1304 **Endarterectomy, Stenting, or Medical Treatment for Symptomatic Carotid Near-Occlusion: Results from CAOS, a Multicenter Registry Study** *A. Garcia-Pastor, et al., on behalf of the Stroke Project of the Spanish Cerebrovascular Diseases Study Group* **EXTRACRANIAL VASCULAR**

AJNR (Am J Neuroradiol ISSN 0195–6108) is a journal published monthly, owned and published by the American Society of Neuroradiology (ASNR), 820 Jorie Boulevard, Oak Brook, IL 60523. Annual dues for the ASNR include approximately 21% for a journal subscription. The journal is printed by Intellicor Communications, 330 Eden Road, Lancaster, PA 17601; Periodicals postage paid at Oak Brook, IL and additional mailing offices. Printed in the U.S.A. POSTMASTER: Please send address changes to American Journal of Neuroradiology, P.O. Box 3000, Denville, NJ 07834, U.S.A. Subscription rates: nonmember \$430 (\$505 foreign) print and online, \$320 online only; institutions \$495 (\$565 foreign) print and basic online, \$980 (\$1050 foreign) print and extended online, \$380 online only (basic), \$825 online only (extended); single copies are \$35 each (\$40 foreign). Indexed by PubMed/MEDLINE, BIOSIS Previews, Current Contents (Clinical Medicine and Life Sciences), EMBASE, Google Scholar, HighWire Press, Q-Sensei, RefSeek, Science Citation Index, SCI Expanded, ReadCube, and Semantic Scholar. Copyright © American Society of Neuroradiology.

- 1311 **Comparison of 30-Day Outcomes after Carotid Artery Stenting in Patients with Near-Occlusion and Severe Stenosis: A Propensity Score Matching Analysis** *C. Štěchovský, et al.* **EXTRACRANIAL VASCULAR**
- 1318 **Clinical Validation and Extension of an Automated, Deep Learning–Based Algorithm for Quantitative Sinus CT Analysis** *C.J. Massey, et al.* **HEAD & NECK FUNCTIONAL**
- 1325 **Differentiation of Skull Base Chondrosarcomas, Chordomas, and Metastases: Utility of DWI and Dynamic Contrast-Enhanced Perfusion MR Imaging** *Y. Ota, et al.* **HEAD & NECK FUNCTIONAL**
- 1333 **Duct-like Recess in the Infundibular Portion of Third Ventricle Craniopharyngiomas: An MRI Sign Identifying the Papillary Type** *J.M. Pascual, et al.* **HEAD & NECK**
- 1341 **Diffuse Basisphenoid Enhancement: Possible Differentiating Feature for Granulomatous Hypophysitis** *I.T. Mark, et al.* **HEAD & NECK**
- 1346 **Normal Enhancement within the Vestibular Aqueduct: An Anatomic Review with High-Resolution MRI** *G. Liu, et al.* **HEAD & NECK**
- 1350 **Diagnostic Accuracy of MRI for Detection of Meningitis in Infants** *S.F. Kralik, et al.* **PEDIATRICS**
- 1356 **MR Imaging Characteristics and ADC Histogram Metrics for Differentiating Molecular Subgroups of Pediatric Low-Grade Gliomas** *S. Shrot, et al.* **PEDIATRICS FUNCTIONAL**
- 1363 **Noninvasive Follow-up Imaging of Ruptured Pediatric Brain AVMs Using Arterial Spin-Labeling** *J.F. Hak, et al.* **PEDIATRICS FUNCTIONAL**
- 1369 **Effect of Normal Breathing on the Movement of CSF in the Spinal Subarachnoid Space** *C. Gutiérrez-Montes, et al.* **SPINE**
- 1375 **35 YEARS AGO IN AJNR**

ONLINE FEATURES

WHITE PAPER

- E19 **Amyloid-Related Imaging Abnormalities with Emerging Alzheimer Disease Therapeutics: Detection and Reporting Recommendations for Clinical Practice** *P.M. Cogswell, et al.*

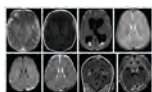
LETTERS

- E36 **Regarding “Brain Perfusion Alterations on 3D Pseudocontinuous Arterial Spin-Labeling MR Imaging in Patients with Autoimmune Encephalitis: A Case Series and Literature Review”** *X. Zhang, et al.*
- E38 **Reply** *R. Li, et al.*

BOOK REVIEWS

R.M. Quencer, Section Editor

Please visit www.ajnrblog.org to read and comment on Book Reviews.



Representative examples of direct MR imaging findings of meningitis from Kralik SF, et al, in this issue.



Indicates Editor's Choices selection



Indicates Fellows' Journal Club selection



Indicates open access to non-subscribers at www.ajnr.org



Indicates article with supplemental online data



Indicates article with supplemental online video



Evidence-Based Medicine Level 1



Evidence-Based Medicine Level 2

Explore the New ASNR Career Center



Your Premier Resource for Professional Development

- Access to jobs in the National Healthcare Career Network
- Confidential resume posting
- One-time free resume review
- Professional online profile
- Saved jobs capability

Start here: careers.asnr.org

ASNR
American Society of Neuroradiology

In Planning for Brain Metastases Treatment, Imaging may be the Missing Link in Cost Containment¹

When faced with a patient presenting with metastatic brain cancer, determining whether to use up-front stereotactic radiosurgery (SRS) vs. first treating with whole brain radiotherapy (WBRT) is a significant clinical decision.

WBRT: The whole story on cognitive impairment

While whole brain radiotherapy (WBRT) has been the main treatment option for many years, experts agree that it often results in cognitive deterioration and a negative impact on quality of life. This mental decline has a devastating impact on patients and their families and adds ongoing costs for the healthcare systems managing these symptoms.

Using WBRT instead of SRS in some patients is estimated to decrease the total costs of brain metastasis management, though with increased toxicity.

SRS: Fewer side effects but greater risk of missed tumors

The cost of upfront SRS is the greatest contributor to cost of brain metastasis management.¹ SRS is often more expensive than WBRT. What's more, multiple applications of SRS can increase the cost of treatment greatly.

Stereotactic radiosurgery (SRS) has far fewer side effects, but upfront use of SRS is expensive and can carry the risk of missed tumors, requiring repeat procedures such as salvage SRS.¹

Number of lesions and lesion size are key factors to be considered when determining the treatment plan for these patients. It follows that increased diagnostic information and accuracy could be beneficial in directing the proper therapy and improving overall long-term patient outcomes and containing costs. Getting the diagnosis right the first time is crucial to ensure proper treatment begins quickly, and high cost/high stakes procedures such as SRS need precise surgical planning.

What does optimal visualization mean for outcomes and cost?

For surgical planning with SRS, radiologists need the best visualization achievable to accurately count the number and size of the lesions. These metrics are the key predictors of the need for SRS,¹ WBRT, or a combination of both.

By selecting the ideal contrast agent and equipment protocols, neuroradiologists can identify the proximate numbers of metastases for upfront treatment and reduced salvage treatment occurrences.

The role of radiology

As medical care for oncology patients continues to evolve, it will be increasingly important to assess the cost of various interventions given the often-limited life expectancy of cancer patients, the rising costs of cancer therapy, and the increasing prevalence of cancer in an aging population.

Through seeing all the tumors and tumor borders as clearly as technology allows, radiology can play a part in ensuring that proper treatment can begin quickly,

while containing costs through optimized patient care. Efforts to carefully manage treatment approaches require improvements in protocol design, contrast administration in imaging, and utilizing multimodal imaging approaches.

In this era of precision medicine, radiology departments' contribution to this improved standard of care will have significant short and long-term implications by reducing cost of care, providing a more proximate diagnosis, and ensuring optimal patient outcomes. ■



Getting the diagnosis right the first time is crucial to ensure proper treatment begins quickly.

Reference: 1. Shenker, R. F., McTyre, E. R., Taksler, D et al. Analysis of the drivers of cost of management when patients with brain metastases are treated with upfront radiosurgery. *Clin Neurol Neurosurg.* 2019 Jan;176:10-14.



For more information on MRI contrast agents, precision medicine, and reducing cost of care please visit bracco.com

© 2022 Bracco Diagnostics Inc.

ASNR 61st Annual Meeting and 2023 Foundation of the ASNR Symposium

Call for Abstracts

Join us April 29-May 3, 2023, to present the best scientific research in neuroradiology.

ASNR is looking for abstract submissions on the topics of Adult Brain, Spine, Head and Neck, Pediatrics, Functional/Advanced Imaging, Interventional, Health Policy, and AI/Informatics.

ABSTRACT SUBMISSION DEADLINE

Tuesday, November 1, 2022 (11:59 PM ET)

Submit online at <https://bit.ly/3PsTO19>

Acceptance notifications will be sent on or before January 17, 2023, upon conclusion of peer review.

ABSTRACT SUBMISSION CATEGORIES

Scientific Oral Presentation: *in person presenter attendance required*

Electronic Scientific Poster: *in person OR virtual presenter attendance required*

Electronic Excerpta Poster: *in person OR virtual presenter attendance required*

Electronic Educational Exhibit: *in person OR virtual presenter attendance required*

ABSTRACT SUBMISSION INFORMATION AND CRITERIA

- **By submitting an abstract, you agree that the presenting author will register for the meeting at their own expense.** Oral abstract presenters must register and attend in-person. ePosters/ Educational Exhibits presenters may register for the virtual or in-person meeting format.
- ASNR requires disclosure from all persons in control of content, including all authors on abstracts. When added to an abstract, all co-authors on your submission will be notified to log-in and complete their own disclosure form. Once all co-authors have submitted disclosure, you will be able to finalize your submission. You will not be able to finalize your submission until all authors and co-authors have completed their disclosure forms. If any disclosures cannot be submitted by the deadline, remove authors with missing disclosures and submit the abstract. Authors may be added after submission if disclosure is completed. Email education@asnr.org to add authors after the submission deadline.
- Maximum length, not including spaces, title, authors, or image: 2,500 characters (combined from all text fields).
- The submission site allows uploading of a **single JPG file** with each submission. Only one graphic file may be submitted with each abstract. This single JPG can contain multiple images, graphics, and tables.
- At least one reference is required, and up to five references may be included. References should be formatted according to *AJNR* author instructions.
- **DO NOT SUBMIT DUPLICATE ABSTRACTS IN MULTIPLE CATEGORIES OR SUBMISSION TYPES.**
- Changes can be made to submitted abstracts until the deadline.
- ASNR encourages presenters to submit manuscripts based on their work to the *American Journal of Neuroradiology* or *Neurographics* before considering other journals.
- Available ASNR awards include the David M. Yousem Research Fellow Award, Cornelius Dyke Memorial Award, Outstanding Presentation Awards, and Educational Exhibit Awards.

Questions? Contact the ASNR Education Department at education@asnr.org.

ASNR23: TRANSFORMING THE FUTURE OF NEURORADIOLOGY



Title: Midtown East. Looking out at the East River in New York City, on the left across the river in the borough of Queens, are two of the red-and-white striped stacks of the Ravensport generating station, a.k.a. Big Allis, for the Allis-Chalmers industrial machinery corporation. One of its units was the world's first 100-million kilowatt generator in the world in 1965. On the right is the Ed Koch Queensboro Bridge. In between are Roosevelt Island and the Roosevelt Island tram, the latter providing the only direct passage to/from Manhattan besides by boat, though the bridge used to have a vehicular elevator down to the island from 1934–1955. Currently a residential area, it was the site of several hospitals serving incarcerated, indigent, psychiatric, long-term, and smallpox patients. Coler Specialty Hospital remains active. This image is dedicated to the memory of my father Richard S. Hauben, MD, who completed a rotating internship and internal medicine residency on Roosevelt Island a very long time ago.

Manfred Hauben, MD, MPH, Pfizer Inc and NYU Langone Health, New York City

Multimodality Imaging in Primary Progressive Aphasia

 M. Roytman,  G.C. Chiang,  M.L. Gordon, and  A.M. Franceschi



ABSTRACT

SUMMARY: Primary progressive aphasia is a clinically and neuropathologically heterogeneous group of progressive neurodegenerative disorders, characterized by language-predominant impairment and commonly associated with atrophy of the dominant language hemisphere. While this clinical entity has been recognized dating back to the 19th century, important advances have been made in defining our current understanding of primary progressive aphasia, with 3 recognized subtypes to date: logopenic variant, semantic variant, and nonfluent/agrammatic variant. Given the ongoing progress in our understanding of the neurobiology and genomics of these rare neurodegenerative conditions, accurate imaging diagnoses are of the utmost importance and carry implications for future therapeutic triaging. This review covers the diverse spectrum of primary progressive aphasia and its multimodal imaging features, including structural, functional, and molecular neuroimaging findings; it also highlights currently recognized diagnostic criteria, clinical presentations, histopathologic biomarkers, and treatment options of these 3 primary progressive aphasia subtypes.

ABBREVIATIONS: AD = Alzheimer disease; ASL = arterial spin-labeling; FTLT = frontotemporal lobar degeneration; lvPPA = logopenic variant PPA; nfvPPA = nonfluent/agrammatic variant PPA; PPA = primary progressive aphasia; 3R = 3-repeat; 4R = 4-repeat; svPPA = semantic variant PPA; TDP-43 = transactive-response DNA-binding protein 43; TSPO = translocator protein 18 kDa

Neurodegenerative disorders encompass an assortment of clinically and histopathologically diverse conditions, typically slowly progressive and associated with gradual neurologic dysfunction. While precise mechanisms leading to their development continue to be elucidated, these disorders can be broadly grouped into categories based on similar histopathology, including tauopathies (eg, some cases of frontotemporal lobar degeneration [FTLD], corticobasal degeneration, progressive supranuclear palsy), transactive-response DNA-binding protein 43 (TDP-43) accumulation (eg, other cases of FTLD, amyotrophic lateral sclerosis), β -amyloid accumulation (eg, Alzheimer disease [AD]), and α -synucleinopathies (eg, Parkinson

disease, dementia with Lewy bodies, multiple system atrophy), noting mixed pathologies in some cases.¹ Primary progressive aphasia (PPA), clinically characterized by language-predominant impairment, has been histopathologically linked to both underlying FTLD (eg, semantic variant PPA [svPPA] and nonfluent/agrammatic variant PPA [nfvPPA]) and AD-type pathology² (eg, logopenic variant PPA [lvPPA]) (Fig 1). The microtubule-associated protein τ , encoded by the *MAPT* gene, has been shown to pathologically aggregate when in an abnormal hyperphosphorylated form (p- τ) and result in extracellular neurofibrillary tangles that contribute to neurodegeneration. Tauopathies are characterized by the predominance of abnormally deposited alternatively spliced τ isoforms (eg, 3-repeat [3R] versus 4-repeat [4R]-tauopathies), which may be seen in some cases of PPA.³ Deposits of TDP-43, a cellular protein encoded by the *TARDBP* gene and with 4 described subtypes (A, B, C, D), is an additional frequently identified pathologic substrate seen in cases of PPA.⁴ While trends have been reported between these histopathologic entities and PPA subtypes (lvPPA: AD pathology; svPPA: TDP-43; nfvPPA: 4R- τ), no absolute association exists and inconsistencies regarding the frequency of molecular alterations for each variant have been described across studies, likely related to varied diagnostic approaches.⁵


While a progressive neurodegenerative disorder characterized by language-predominant impairment has been a recognized entity dating back to the 19th century, inconsistencies regarding its

Received October 24, 2021; accepted after revision November 30.

From the Neuroradiology Division (M.R., G.C.C.), Department of Radiology, Weill Cornell Medical College, New York-Presbyterian Hospital, New York, New York; Departments of Neurology and Psychiatry (M.L.G.), Donald and Barbara Zucker School of Medicine at Hofstra/Northwell, The Litwin-Zucker Research Center, Feinstein Institutes for Medical Research, Manhasset, New York; and Neuroradiology Division (A.M.F.), Department of Radiology, Donald and Barbara Zucker School of Medicine at Hofstra/Northwell, Lenox Hill Hospital, New York, New York.

This work was supported by the Foundation of the American Society of Neuroradiology Boerger Research Fund for Alzheimer's Disease and Neurocognitive Disorders (2021); "18F PI-2620 in Primary Progressive Aphasia" (Principal Investigator: Ana Franceschi).

Please address correspondence to Ana M. Franceschi, MD, Department of Radiology, Lenox Hill Hospital, 100 East 77th St, 3rd Floor, New York, NY 10075; e-mail: afranceschi@northwell.edu

 Indicates open access to non-subscribers at www.ajnr.org

<http://dx.doi.org/10.3174/ajnr.A7613>

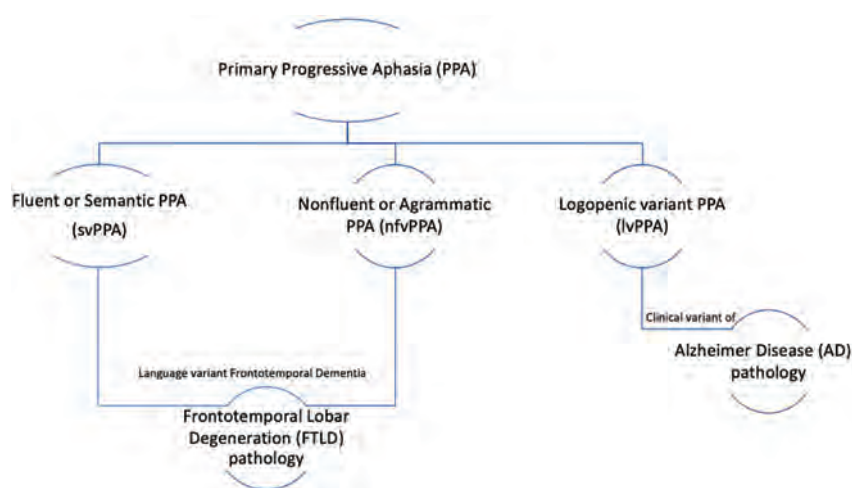


FIG 1. PPA is divided into 3 recognized variants: svPPA, nfvPPA, and lvPPA. svPPA and nfvPPA exhibit FTLD pathology; svPPA and nfvPPA are considered to be language-variant frontotemporal dementias. lvPPA is a clinical variant of AD.

Table 1: Inclusion and exclusion criteria for PPA diagnosis

Criteria
Inclusion
Most prominent clinical feature is language difficulty
These deficits are the principal cause of impaired daily living activities
Aphasia should be the most prominent deficit at symptom onset and for the initial phases of the disease
Exclusion
Pattern of deficits is better accounted for by other nondegenerative nervous system or medical disorders
Prominent initial episodic memory, visual memory, and visuosperceptual impairments
Prominent initial behavioral disturbance

terminology and nomenclature exist in the literature. In an effort to improve diagnostic uniformity and the reliability of research results, Gorno-Tempini et al⁶ published a 2011 framework for PPA diagnosis and classification using a 2-step process. Initially, patients must meet the criteria of Mesulam^{7,8} for the overarching diagnosis of PPA, requiring a language-predominant deficit in the absence of significant episodic memory, behavioral, or visuospatial disturbances,⁶ and are subsequently subdivided into the clinical variant that best corresponds to their specific language disturbance. Inclusion and exclusion criteria for the diagnosis of PPA, as well as the specific diagnostic criteria for each PPA subtype, are outlined in Tables 1 and 2. In addition to clinical features, a PPA diagnosis can be further supported by pathology (eg, FTLD- versus AD-type pathology) if such pathologic or genetic data are available as well as imaging if a typical pattern of atrophy and/or hypometabolism is identified. Therefore, an accurate diagnosis of PPA requires a multidisciplinary approach, inclusive of clinical, pathologic, and radiologic evaluation. Early in the disease course, some patients may be referred to as “PPA unclassifiable,” with further elucidation of their specific subtype as the disease progresses.⁶ While most patients do not have abnormalities on a general neurologic examination at diagnosis, features such as parkinsonism, apraxia, and upper motor neuron involvement have been reported as PPA progresses.⁹

Advances in the understanding of PPA, particularly the recognition of variant-specific patterns of atrophy and/or hypometabolism,

have reinforced the role of structural, functional, and molecular neuroimaging in supporting the diagnosis, when clinically suspected. This review highlights available imaging modalities in the identification of PPA as well as characteristic variant-specific features with which neuroradiologists should be familiar to aid in a prompt and accurate diagnosis.

Logopenic Variant PPA

lvPPA is the most recently described of the 3 PPA variants, first reported in 2004 by Gorno-Tempini et al.¹⁰ Clinically characterized by word-finding difficulties and lapses in conversation, lvPPA has been reported to exhibit histopathologic findings and biomarkers that overlap with AD pathology (eg, β -amyloid [A β] and neurofibrillary tangles)² and, therefore, is considered a clinical variant of AD.

Classically, patients with lvPPA present with word-finding difficulties and lapses in conversation, giving rise to its “logopenic” name (Greek, “lack of words”).¹¹ Early in the disease, patients exhibit “tip-of-the-tongue” hesitation with pauses in word retrieval as well as anomia.⁴ Spelling or speech-sounding errors are also frequently described, and patients may struggle to understand complex sentences or retain verbal information. The diagnostic feature that distinguishes lvPPA from svPPA and nfvPPA is an early and disproportionate difficulty in repeating heard phrases and sentences, corresponding to an impairment of phonologic or verbal working memory.¹² While language is the dominant issue, extralinguistic difficulties related to memory, praxis, and visuospatial awareness have been reported.¹³ Patients often exhibit generalized anxiety, irritability, and dependence on their primary caregivers, behavioral features that may also occur with typical AD or other AD variants.

As a whole, PPA is a rare entity with an estimated prevalence of 3–7 cases per 100,000, often occurring in late middle life (mean age of disease onset, 62.34 years) with an average delay between first symptoms and diagnosis of 3.21 years in 1 study.¹⁴ Given the novelty of lvPPA as a clinical entity, its precise prevalence is not definitively known. However, a 2016 retrospective analysis of a cohort from a tertiary center ($n = 97$) in patients with language deficits and CSF biomarkers from the French AD databank, performed to better understand PPA demographics, revealed lvPPA as the most common variant of PPA (51%, 49/97) with a slight female predominance (57%, 28:21, female/male). Within this group, lvPPA was more frequently associated with an AD CSF profile (85%) than nfvPPA (35%) or svPPA (20%), contributing to the present day notion of lvPPA as a clinical variant of AD.¹⁴

Table 2: Diagnostic criteria for PPA variants

	lvPPA	svPPA	nvPPA
Clinical diagnosis	1. Impaired single-word retrieval in spontaneous speech and naming AND 2. Impaired repetition of sentences and phrases At least 3 of the following: 1. Speech (phonologic) errors in spontaneous speech and naming 2. Spared single-word comprehension and object knowledge 3. Spared motor speech 4. Absence of frank agrammatism	1. Impaired confrontation naming 2. Impaired single-word comprehension AND At least 3 of the following: 1. Impaired object knowledge, particularly for low-frequency or low-familiarity items 2. Surface dyslexia or dysgraphia 3. Spared repetition 4. Spared speech production (grammar and motor speech)	1. Agrammatism in language production AND/OR 2. Effortful, halting speech with inconsistent speech sound errors and distortions (apraxia of speech) At least 2 of the following: 1. Impaired comprehension of syntactically complex sentences 2. Spared single-word comprehension 3. Spared object knowledge
Imaging-supported diagnosis	Predominant left-posterior periSylvian or temporoparietal atrophy and/or hypoperfusion or hypometabolism	Predominant anterior temporal lobe atrophy and/or hypoperfusion or hypometabolism	Predominant left posterior frontoinsula atrophy and/or hypoperfusion or hypometabolism
Pathology-supported diagnosis (or presence of known pathogenic mutation)	AD ^a	TDP-43 ^a	4R- τ ^a

^a Histopathologic evidence of a specific neurodegenerative pathology (eg, FTLD- τ , FTLD-TDP, AD, other), particularly if most characteristic pathology.

In a study investigating CSF fluid biomarkers (including A β 42, τ , p- τ) in 13 patients with lvPPA, 62% (8 of 13) demonstrated a profile indicative of AD pathology (lvPPA+), while 38% (5 of 13) had a non-AD profile (lvPPA-).¹⁵ Subsequent analyses demonstrated that those in the lvPPA+ group exhibited more advanced imaging findings compared with those in the lvPPA-group, including more extensive hypometabolism and larger regions of involvement throughout the inferior parietal and superior and middle temporal cortices. Such heterogeneity of pathologies identified in this study may reflect a “logopenic aphasia complex,” with at least 2 existing lvPPA subvariants.¹⁵

PPA may be inherited in an autosomal dominant manner, most commonly associated with mutations in the progranulin (*GRN*) gene on chromosome 17.⁶ While the presence of a *GRN* mutation does not necessarily lead to PPA, a language disorder often emerges in many patients with this mutation.¹² The clinical symptoms of this language disorder can vary widely, with heterogeneity even among family members with the same *GRN* mutation. However, among patients with nonamyloid PPA with *GRN* mutations, lvPPA was found to be the most frequent linguistic variant.¹⁶ In 1 study, 42% of patients with lvPPA were found to carry the *apolipoprotein E* ϵ 4 allele, known to confer an increased risk of sporadic AD and in keeping with our understanding of lvPPA as a clinical variant of AD, compared with 26% of patients with svPPA and 20% of patients with nvPPA.¹⁷ Other predisposing gene variants or mutations found to be associated with lvPPA include *TREM2*, *TOMM40*, *APP*, *PS1* and *PS2*, and *MAPT*.¹⁸

While the aforementioned evidence supports underlying AD pathology in most patients with lvPPA, not all cases of lvPPA are attributed to AD pathology. In 1 postmortem analysis of 99 patients with lvPPA, 76% had primary AD pathology, while FTLD-TAR DNA-binding protein (FTLD-TDP) and FTLD- τ pathologies were identified in 14% and 5% of patients, respectively.¹⁷

To date, no pharmacologic options have been shown to improve or protect against declining function in lvPPA. However, supportive care measures such as speech-language therapy have demonstrated efficacy in improving communication.¹⁹ Given that underlying AD pathology is associated with most lvPPA cases, use of emerging anti-amyloid therapies in lvPPA may be investigated.

Structural Imaging. The presence of specific regional patterns of atrophy or metabolic impairment is the key neuroimaging diagnostic feature for each of the 3 PPA variants (Table 2). Structural imaging, including CT and MR imaging, can be used to identify these classic patterns of focal atrophy. Included in the 2011 Gorno-Tempini et al⁶ diagnostic criteria, MR imaging can be used to identify asymmetric, classically left-sided widening of the Sylvian fissure, indicative of the posterior peri-Sylvian and temporoparietal atrophy seen in lvPPA. The posterior aspect of the left superior temporal gyrus, corresponding to the expected Wernicke area, is typically involved. This finding, particularly when progressive over multiple examinations and in conjunction with a clinical history of progressive word-finding difficulty, should raise the possibility of underlying lvPPA (Fig 2). Notably,

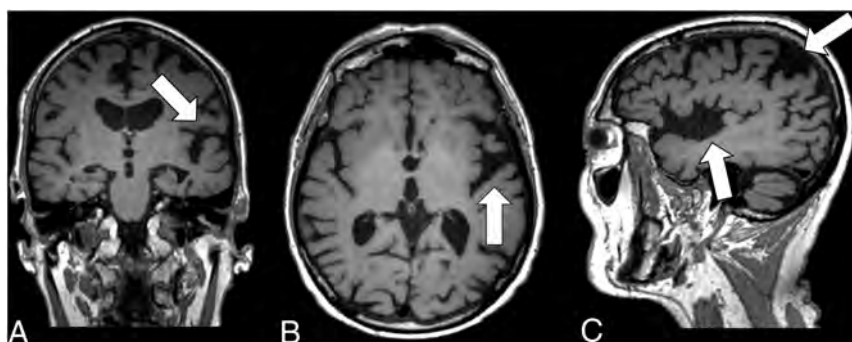


FIG 2. Coronal T1-weighted MR imaging (A), axial T1-weighted MR imaging (B), and sagittal T1-weighted MR imaging (C) in a right-handed individual with impaired repetition of phrases demonstrate asymmetric widening of the left Sylvian fissure with left posterior peri-Sylvian and temporoparietal atrophy (white arrows, A–C), suspicious for lvPPA.

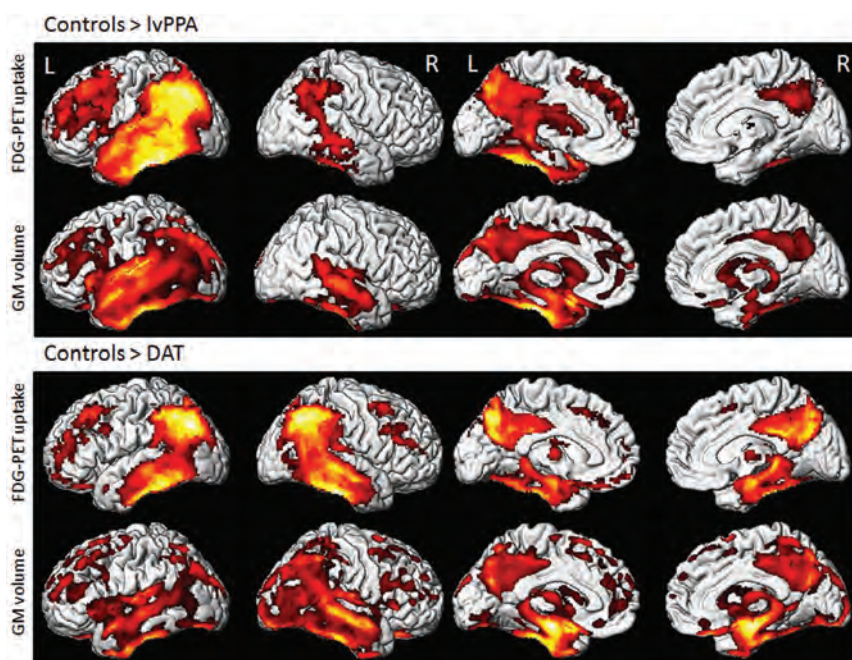


FIG 3. Voxel-level imaging findings in lvPPA and dementia of the Alzheimer type (DAT) compared with controls. 3D renderings show regions of reduced FDG metabolism and GM volume in lvPPA compared with controls and in DAT compared with controls. Note, lvPPA demonstrates hypometabolism and focal atrophy primarily in the left lateral temporal and inferior parietal lobes (including the left angular and supramarginal gyri) and left precuneus and left posterior cingulate gyrus. Adapted with permission from Madhavan et al.⁸⁴ R indicates right; L, left.

while most patients are left-hemispheric language dominant, involvement of the right hemisphere has been reported and hypothesized to occur in left-handed individuals or those with a history of developmental learning disabilities (eg, dyslexia).²⁰

The preferred structural imaging technique for the diagnosis of PPA is MR imaging, due to its superior soft-tissue resolution and ability to precisely localize anatomic atrophy. Advanced MR imaging techniques, such as voxel-based morphometry analysis and DTI, may be used to demonstrate focal GM atrophy (Fig 3) and WM alterations, respectively.²¹ In particular, cortical volumetric software such as the FDA-approved NeuroQuant (<https://www.cortechs.ai/products/neuroquant-ct/>) and Icometrix (<https://www.icometrix.com/>) are increasingly being used in routine

clinical assessment of various neurodegenerative disorders. In a study investigating the utility of MR imaging in differentiating PPA variants, MR imaging demonstrated a high specificity for the characteristic atrophy patterns of lvPPA (95%) and nvPPA (91%), noting a low sensitivity for both (43% for lvPPA; 21% for nvPPA).²² Therefore, while the presence of left posterior peri-Sylvian or temporoparietal region atrophy is highly suggestive of lvPPA, its absence does not exclude the diagnosis. In a prospective study investigating 130 patients with neurodegenerative aphasia, of whom 52 had lvPPA, GM loss was identified in patients with lvPPA, more commonly on the left and greatest in the posterior temporal lobe extending to the frontal and parietal regions.²³ Fractional anisotropy and mean diffusivity analyses within this cohort revealed left-greater-than-right bilateral WM involvement, greatest in the posterior left temporal WM and extending into the anterior temporal, frontal, parietal, and occipital WM, as well as involving the bilateral superior and inferior longitudinal fasciculi and inferior occipitofrontal fasciculus. The posterior superior temporal and inferior parietal cortices have been shown to play a role in phonologic loop functions.²¹ Therefore, involvement of these regions and WM tracts in the superior and inferior longitudinal fasciculi likely account for the poor repetition, naming, and comprehension seen in patients with lvPPA.^{23,24}

Atrophy may also be identified anteriorly with involvement of the hippocampi, among other structures, with the overall extent and pattern of atrophy varying widely among individual patients. Most important, the presence

of progressive atrophy with time supports the diagnosis of PPA, a critical observation worthy of mention when interpreting such structural imaging examinations.

Functional Imaging. fMRI, which can be performed with task-based paradigms or in a resting state, uses blood oxygen level-dependent contrast to identify areas of brain activation on the basis of oxygen extraction.²⁵ While fMRI is not in routine clinical use for the diagnosis of PPA and limited literature exists regarding its specific findings in lvPPA, fMRI has been reported to demonstrate functional changes in patients with svPPA (formerly referred to as semantic dementia),²⁶ to be discussed later in this review. Such advanced imaging techniques could be useful in

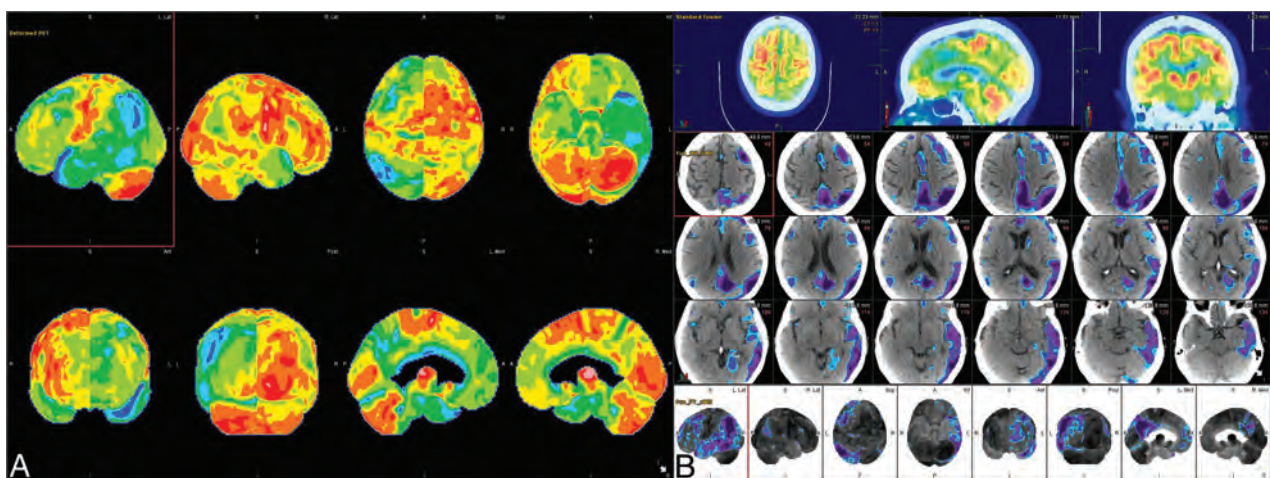


FIG 4. [^{18}F] FDG-PET cortical surface maps demonstrate an abnormal FDG distribution pattern with moderate-to-severe hypometabolism in the left, lateral temporoparietal lobes including in the left precuneus and posterior cingulate gyrus (A), with corresponding disproportionate cortical atrophy in the lateral left temporoparietal region visualized on brain CT (B), findings are further supported by a semiquantitative FDG-PET analysis using z scores calculated in comparison with age-matched cognitively healthy controls, demonstrating markedly decreased values in the left parietal and left lateral temporal regions, including in the precuneus and posterior cingulate gyrus (B).

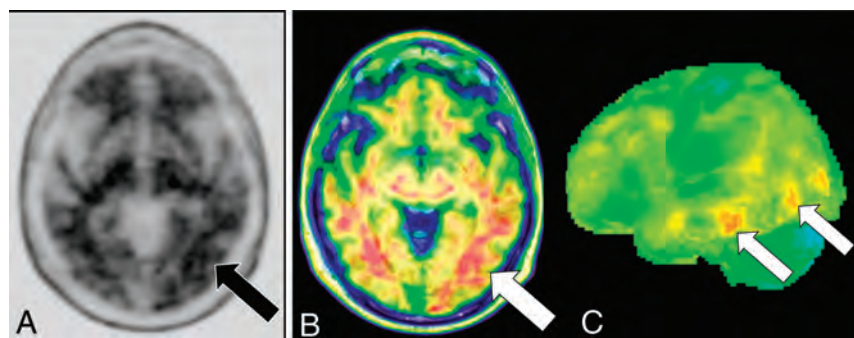


FIG 5. [^{18}F] florbetaben PET axial gray-scale (A), axial color map fused to a T1-weighted MR image (B), and left lateral 3D stereotactic surface projection (C) demonstrate focal areas of increased cortical β -amyloid deposition in the left temporal lobe (arrows).

identifying aberrant and compensatory language network changes and may prove useful in guiding future therapeutic trials.¹¹

Cerebral perfusion, which has been linked to cognition and neuronal activity, can be measured with MR imaging using the noncontrast arterial spin-labeling (ASL) technique.²⁷ While limited data exist regarding use of ASL for lvPPA specifically, ASL has been shown to identify hypoperfusion patterns in other dementia subtypes before symptom onset and also correspond to disease-specific regions of hypometabolism identified on [^{18}F] FDG-PET. However, limitations of the ASL technique for clinical use include its low SNR on conventional 1.5T field strength MR imaging, with 3T field strength MR imaging preferred for use in the ASL technique, as well as technical issues with quantification. Further studies assessing the potential role of ASL for patients with lvPPA as well as its performance compared with [^{18}F] FDG-PET are warranted.

Molecular Imaging Molecular imaging allows in vivo identification and quantification of cerebral metabolism, abnormal

deposition of β -amyloid and τ , and the presence of brain inflammation, important neuroimaging biomarkers that may improve early diagnosis and assist in assessing neurodegenerative disease progression.²⁷⁻²⁹ Currently available molecular imaging modalities include SPECT and PET, with a number of investigational radiotracers on the horizon.³⁰ Advantages of PET imaging include superior spatial and contrast resolution compared with SPECT, though it is a more expensive examination and less widely available. Limitations include attenuation correction and motion artifacts, which may cause inaccurate

anatomic coregistration. Molecular neuroimaging has been shown to be useful in the diagnosis of PPA.³¹⁻³³

[^{18}F] FDG-PET assesses cerebral glucose metabolism, which is abnormally reduced in neurodegeneration due to synaptic dysfunction and neuronal loss.² The characteristic pattern of hypometabolism in lvPPA includes asymmetric involvement of the left posterior peri-Sylvian and left lateral temporoparietal regions, mirroring previously described regions of atrophy, specifically involving the left inferior parietal lobule and left posterior superior and middle temporal gyri, including the expected Wernicke area (Brodmann area 22) (Figs 3 and 4). SPECT, which demonstrates regional hypoperfusion similar to the metabolic alterations on [^{18}F] FDG-PET is infrequently used in clinical practice due to technical disadvantages and poorer accuracy.²⁹

Amyloid PET is a valuable examination for the diagnosis of AD and other neurodegenerative disorders demonstrating A β -pathology.¹⁶ In a meta-analysis of 1251 patients from 36 dementia centers, A β -positivity was identified in 86% of patients with lvPPA with evidence of AD pathology identified in 76% of those who

underwent a postmortem examination (Fig 5).¹⁷ A β -positivity was also seen in a minority of those with nvPPA (20%) and svPPA (16%); however, A β -positivity was thought to represent a concomitant age-related process in these patients rather than being attributable to their PPA syndrome. In another study, 88% (46 of 52 patients) meeting the criteria for lvPPA demonstrated A β -positivity, with low A β -positivity rates in patients not meeting criteria for lvPPA (10%, 13 of 130 patients).¹⁸ In a study evaluating amyloid metabolism in PPA, 100% (4/4) of patients with lvPPA demonstrated elevated cortical Pittsburgh compound B uptake versus 16% (1/6) of patients with nvPPA and 20% (1/5) of those with svPPA.¹⁹ Thus, amyloid PET imaging can be useful in distinguishing lvPPA from nvPPA and svPPA, noting that comorbid age-related A β pathology may occur in each of these entities and an amyloid PET scan with positive findings does not equate to a diagnosis of lvPPA.

In addition to β -amyloid plaques, τ neurofibrillary tangles are a hallmark pathologic finding in AD.²⁰ τ -targeting PET tracers have been used for molecular imaging in PPA, most commonly [¹⁸F] flortaucipir (AV-1451), an FDA-approved, first-generation τ PET ligand.^{21,22} In a study investigating use of [¹⁸F] AV-1451 in PPA, patients with lvPPA exhibited striking uptake throughout the neocortex, most notably in the left temporoparietal region, compared with controls and subjects with other PPA variants, confirming the use of this radiotracer in distinguishing PPA subtypes.²⁰ In a case series of patients with typical amnesic AD and atypical variants (posterior cortical atrophy, lvPPA, and corticobasal syndrome), all patients demonstrated region-specific distribution of [¹⁸F] AV-1451, indicating that τ PET can serve as a key biomarker linking molecular AD neuropathologic conditions with clinically significant neurodegenerative syndromes.²³

The use of PET tracers that target the translocator protein 18 kDa (TSPO) have also been explored in PPA, with the goal of characterizing the role of microglial activation and associated neuroinflammation in the pathogenesis of PPA. TSPO, originally named the peripheral benzodiazepine receptor, is an 18-kDa outer mitochondrial membrane protein, which has been found in disease-relevant areas across a broad spectrum of neurodegenerative diseases.²⁴ Histopathologic studies have demonstrated asymmetric distribution of activated microglia in PPA, including high microglial densities in the superior temporal and inferior frontal gyri of the language-dominant hemisphere, consistent with postmortem and/or in vivo atrophy distribution.²⁵ Patterns of microglial activation revealed variation favoring areas of increased atrophy in regions associated with language function, demonstrating concordance among patterns of microglial activation, atrophy, and clinical PPA phenotype.²⁵ These findings support the potential use of TSPO PET in the evaluation of PPA subtypes.

Semantic Variant PPA

svPPA, previously referred to as “semantic dementia” in case reports throughout the 20th century, is a heterogeneous clinical syndrome characterized by progressive loss of knowledge about words and objects, including a fluent dysphasia with severe anomia, reduced vocabulary, and prominent impairment of single-word

comprehension, which progresses to a stage of virtually complete dissolution of the semantic components of language.²⁶ The criteria for the clinical diagnosis of svPPA are detailed in Table 2. Notably, a right temporal lobe–predominant variant of svPPA featuring impaired facial recognition (ie, prosopagnosia) and changes in affect and social behavior, in addition to semantic memory impairment, has also been described.³⁴

SvPPA is currently recognized within the clinical spectrum of FTLD (Fig 1), with underlying histopathology most often attributable to TDP-43 type C, characterized by long dystrophic neurites and identified in >80% of patients with svPPA.^{5,35,36} Some cases have been associated with other histopathologic findings, including FTLD-TDP types A and B, FTLD- τ (particularly 3R- τ [Pick bodies] and 4R globular glial tauopathy), as well as AD pathology.^{5,35,36} SvPPA is almost always sporadic, rather than familial, and is the least heritable compared with other FTLD syndromes, with only 2%–4% of cases demonstrating an autosomal dominant pattern and suspected family history identified in 2%–17% of patients.^{26,37,38} Genetic disorders linked to familial FTLD-TDP include those associated with mutations in the *GRN* gene (FTLD-TDP type A), expansions in the chromosome 9 open reading frame 72 (*C9orf72*) gene (FTLD-TDP types A or B), and mutations in the valosin-containing protein (*VCP*) gene (FTLD-type D).³⁹ In the absence of a strong family history of svPPA, an underlying genetic abnormality is considered unlikely.³⁵

The precise prevalence of svPPA is not definitively known because diagnosis requires extensive clinical expertise and available data has largely been derived from tertiary care research center referrals, likely not representative of the general population. However, the 2016 retrospective analysis from the French AD databank identified 26% (25 of 97) of PPA cases with CSF biomarkers to be svPPA, with a mean age of disease onset at 59.5 years and an average delay of 4.5 years between first symptom and diagnosis, a male predominance (68%; 18/27, female/male), and underlying AD pathology in only 20% of cases.¹⁴ The estimated svPPA prevalence based on the French AD databank cohort was 0.8 per 100,000 individuals, increasing with patient age. With regard to FTLD, its overall prevalence varies widely across studies, ranging from 2 to 31 per 100,000 individuals with an estimated true point prevalence of 15 to 22 per 100,000 and an incidence of 2.7 to 4.1 per 100,000 in those younger than 70 years of age.⁴⁰ One series assessing 353 consecutive patients with FTLD identified 18.7% as having svPPA.⁴¹ An epidemiologic study investigating FTLD syndromes in 2 UK counties with a population of 1.69 million yielded an estimated svPPA prevalence of 1.2 per 100,000.⁴²

No disease-modifying medications are currently available for the treatment of svPPA. A variety of psychotropic medications have been used to manage associated behavioral symptoms, though evidence of efficacy from randomized clinical trials is lacking. Speech-language therapy has been shown to slow progression of anomia and may even offer a protective benefit to lexical items not yet lost, noting that treatment is suspected to be most beneficial at early stages of disease, supporting the advantage of an early diagnosis.⁴³ A double-blind, sham-controlled, randomized clinical trial of transcranial direct current stimulation in patients with svPPA is ongoing.⁴⁴

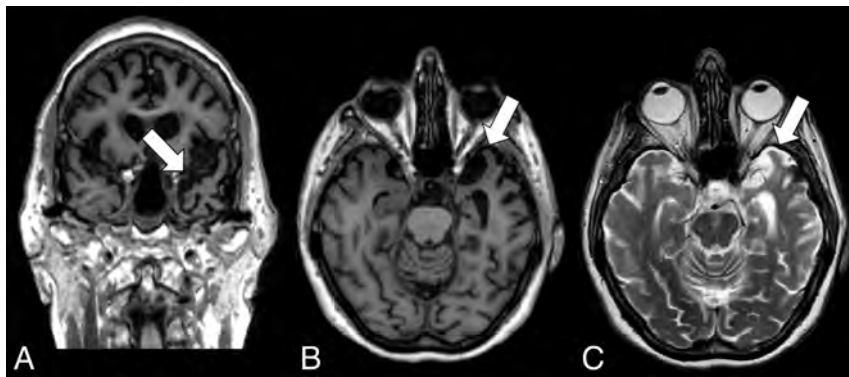


FIG 6. Coronal T1-weighted MR imaging (A), axial T1-weighted MR imaging (B), and axial T2-weighted MR imaging (C) in a right-handed individual with impaired single-word comprehension demonstrate marked asymmetric atrophy of the anterior left temporal lobe (white arrows, A–C), suspicious for svPPA.

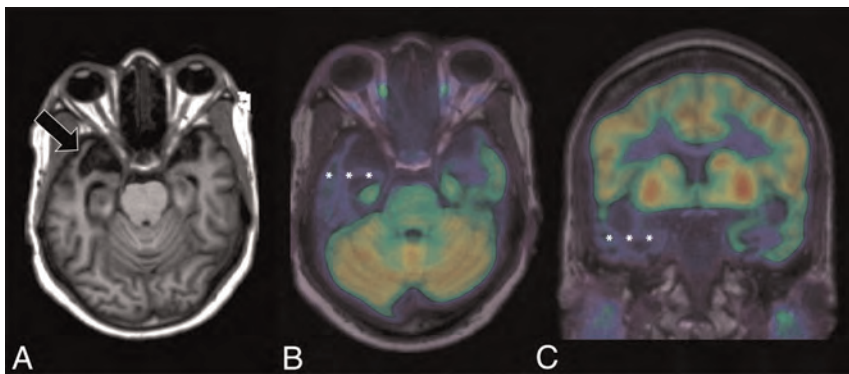


FIG 7. Axial T1-weighted MR imaging (A) and axial and coronal T1-weighted MR imaging fused with [^{18}F] FDG-PET (B and C) in a left-handed individual with impaired single-word comprehension demonstrate marked asymmetric atrophy of the anterior right temporal lobe (black arrow, A) with corresponding marked hypometabolism (white asterisks, B and C) due to svPPA.

Structural Imaging. The most common imaging features associated with svPPA include regional atrophy predominantly involving the left temporal lobe, most marked anteriorly involving the temporal pole (Fig 6).⁴⁵ While focal atrophy is typically more pronounced on the left side, patients presenting with right-dominant temporal atrophy have been described in the literature (Fig 7).^{34,46} A study involving voxel-based morphometry in patients with svPPA reported that those with prosopagnosia had bilateral temporal lobe GM volume loss with greater involvement on the right, while those without prosopagnosia had predominantly left anterior temporal lobe volume loss.⁴⁷

A meta-analysis of voxel-based morphometry studies investigating svPPA identified reduced GM volume in the bilateral fusiform and inferior temporal gyri, extending to the medial portion of the temporal lobes with involvement of the amygdala and parahippocampal gyri, as well as the left temporal pole, middle temporal gyrus, and caudate nucleus.⁴⁸ Surface-based analysis of patients with svPPA identified marked cortical thinning in the left temporal lobe, particularly at the temporal pole; entorhinal cortex; and parahippocampal, fusiform, and inferior temporal gyri, with similar-yet-less extensive involvement of the contralateral cortex.⁴⁹ Similarly, a longitudinal investigation mapping the progression of GM atrophy in

predominantly left-versus-predominantly right temporal lobe variants of svPPA identified significant progression of GM atrophy in both the affected and contralateral temporal regions.⁵⁰ Voxel-based morphometry has also identified asymmetric regional reduction in the temporal, periventricular, and callosal WM in patients with svPPA.⁵¹

DTI has been used to study structural connectivity changes on the whole-brain level in patients with svPPA, with reports of reduced fractional anisotropy and increased diffusivity in the anterior temporal lobe extending dorsally and posteriorly into the ventral frontal regions.⁵² Tractography has similarly been implemented in svPPA, identifying disruptions of structural connectivity related to GM atrophy, most severely affecting the WM tracts connecting the temporal regions with the frontal, parietal, and occipital regions (ie, uncinate fasciculus, arcuate fasciculus, superior longitudinal fasciculus, and inferior longitudinal fasciculus).⁵²

Functional Imaging. Task-based fMRI studies have reported that patients with svPPA compared with healthy controls demonstrate decreased activation in the mid-fusiform and superior temporal gyri; increased activation in the intraparietal sulcus, inferior frontal gyrus, and left superior temporal gyrus/sulcus; and

a lack of activation in the anterior temporal lobe.^{35,52} Similarly, resting-state fMRI studies in patients with svPPA have demonstrated reduced functional connectivity in the language and executive networks, with extensive disruptions between the anterior temporal lobe and a broad range of brain regions across the temporal, frontal, parietal, and occipital lobes.^{35,52,53} Magnetoencephalographic imaging has also been implemented to investigate whole-brain resting-state functional connectivity, identifying significant hyposynchrony of α and β frequencies within the left temporoparietal junction in patients with svPPA.⁵⁴

Regarding ASL MR imaging, a study investigating the prognostic value of regional CBF as measured by ASL MR imaging in patients with svPPA reported that ASL MR imaging may be sensitive to functional changes not identified on structural MR imaging, potentially serving as a prognostic biomarker marker of disease progression.⁵⁵ Further studies assessing the potential role of ASL in patients with svPPA as well as its performance compared with [^{18}F] FDG-PET are warranted.

Molecular Imaging. [^{18}F] FDG-PET and SPECT can be performed to demonstrate characteristic asymmetric hypometabolism/hypoperfusion predominantly affecting the anterior temporal regions, most

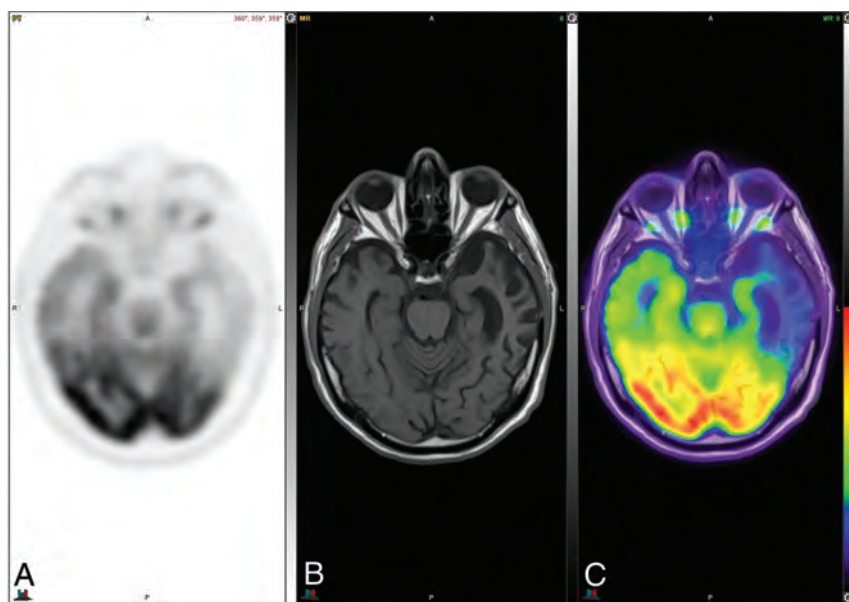


FIG 8. [^{18}F] FDG-PET (A), axial T1 (B), and PET MR imaging (C) views demonstrate an abnormal FDG distribution pattern with markedly decreased tracer uptake in the temporal lobes, particularly in the left temporal pole. There is corresponding advanced cortical atrophy with a “knife-blade” appearance in the left anterior temporal lobe on the axial T1 sequence.

a pattern consistent with the expected distribution of TDP-43 pathology, hypothesized to reflect off-target binding to monoamine oxidase as a consequence of inflammation in the affected regions.^{21,56-58} A study investigating the novel τ PET tracer [^{18}F] PI-2620, which has a low affinity for monoamine oxidase, demonstrated slightly elevated uptake involving the anterior and lateral temporal lobes in 1 of 2 subjects with svPPA, without elevated uptake in the other subject [Fig 10].⁵⁹ There are no studies to date of PET ligands with an affinity for inflammatory biomarkers (eg, monoamine oxidase B, TSPO/peripheral benzodiazepine receptor, or cyclooxygenase) in svPPA.⁶⁰

Nonfluent/Agrammatic PPA

nvPPA, previously referred to as “progressive nonfluent aphasia” in a series by Grossman et al⁶¹ and “PPA with agrammatism” by Mesulam,⁶² is the most

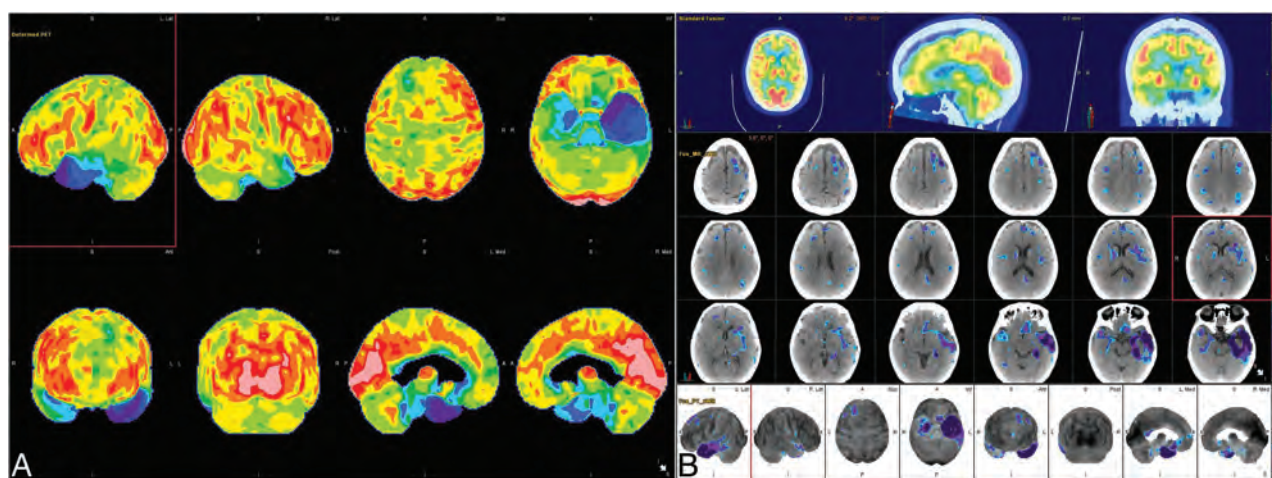


FIG 9. [^{18}F] FDG-PET cortical surface maps demonstrate an abnormal FDG distribution pattern with severe left and moderate right hypometabolism in the anterior temporal lobes (A), with corresponding disproportionate cortical atrophy, particularly pronounced in the left temporal pole visualized on brain CT images (B), findings further supported by semiquantitative FDG-PET analysis using z scores calculated in comparison with findings in age-matched cognitively healthy controls, semiquantitative FDG-PET analysis demonstrate markedly decreased values in the temporal lobes including the temporal poles (left > right) (B).

commonly involving the left temporal pole (Figs 8 and 9). While svPPA is often associated with TDP-43 pathology, no available PET radioligand for TDP-43 exists to date.

Given the presence of AD pathology in some cases of svPPA, reported in up to 20% of cases within the 2016 French AD data-bank retrospective cohort,¹⁴ amyloid PET may result in an amyloid-positive examination in a minority of svPPA patients.

While τ pathology is infrequently reported in patients with svPPA, studies with radioligands that demonstrate an affinity for τ , including [^{18}F] THK-5351 and flortaucipir ([^{18}F] AV-1451), have demonstrated asymmetric retention in the temporal lobes in

diverse of the 3 PPA subtypes. Classically, patients present with a progressive language-predominant disturbance characterized by agrammatism in language production and apraxia of speech, with abnormally short (ie, telegraphic) phrases that tend to lack function words.⁶² Patients with nvPPA have reduced verb production and diminished complexity in terms of grammar use,⁶³ as well as difficulty with complex coordination of muscle groups involved in articulation of speech sounds (ie, apraxia of speech) and distortion of prosody (ie, rhythm, stress, and intonation of speech).⁶⁴ The rate of word production in patients with nvPPA has been reported to be less than one-third of the rate in healthy adults.⁶³ Single-word

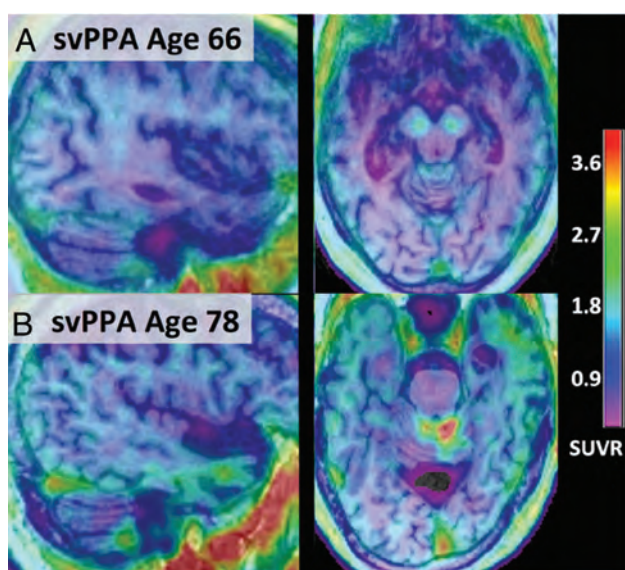


FIG 10. Fused [^{18}F] PI-2620 τ -PET and T1 MPRAGE MR imaging from subjects 66 (A) and 78 years of age (B) with semantic PPA. Notably, [^{18}F] PI-2620 has a low affinity for monoamine oxidase, and subject A demonstrates no focal increased tracer uptake. However, subject B shows binding spanning the anterior and lateral temporal lobes (left greater than right) with corresponding atrophy on MR imaging. Adapted with permission from Mormino et al.⁵⁹

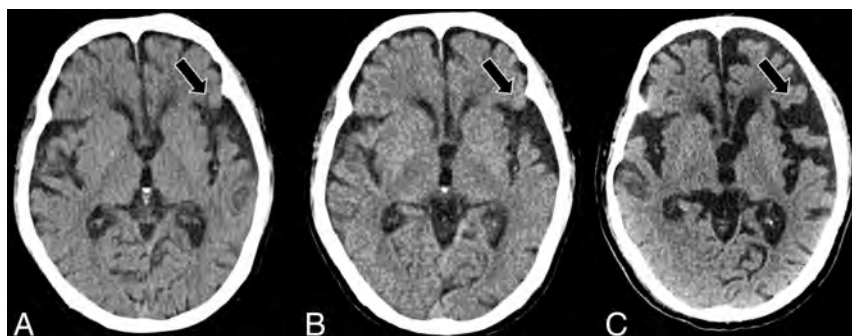


FIG 11. Serial axial CT scans at presentation (A), 2 years post-initial presentation (B), and 4 years post-initial presentation (C) in a right-handed individual with progressive language deficits demonstrate progressive widening of the left-greater-than-right Sylvian fissures (black arrows, A–C), suspicious for nfvPPA.

comprehension is notably preserved, though patients with nfvPPA may experience difficulty understanding sentences with complex syntax, such as those with relative clauses (eg, “he met a man who knew his brother”) or those with passive voice (eg, “the snake was bitten by the mongoose”).^{62,64} Complete criteria for a clinical diagnosis of nfvPPA, as defined by Gorno-Tempini et al,⁶ are described in Table 2.

Although typically considered a tauopathy, nfvPPA is the most heterogeneous of the PPAs, with a variety of other associated underlying pathologies. While 4R- τ is the most commonly reported underlying pathology, 1 postmortem series identified 23% of patients with nfvPPA exhibiting 3R- τ pathology (Pick bodies) and a minority with underlying TDP-43 or AD-type pathology.⁶⁵ Patients with apraxia of speech and parkinsonism are

more often associated with having a tauopathy than TDP-43 pathology.^{5,66} Similar to its pathologic heterogeneity, the clinical spectrum of nfvPPA has been described as the most diverse of the PPA subtypes, with a number of variant nfvPPA subsyndromes reported.¹¹

NfvPPA is also the most heritable of the PPAs, with approximately 30% of patients reporting a positive family history.⁶⁷ Mutations in all of the major genes associated with FTLD (eg, *GRN*, *MAPT*, *C9orf72*) have been identified in nfvPPA. Therefore, genetic screening should be considered in patients with a relevant family history.¹¹ Additional detailed phenotyping of the genetic forms of nfvPPA will be required to improve on the continuously evolving understanding of PPA variants within the spectrum of FTLD.

The precise prevalence of nfvPPA is not definitively known because diagnosis requires extensive clinical expertise and available data have largely been derived from tertiary care research center referrals, likely not representative of the general population. However, the 2016 retrospective analysis from the French AD data-bank identified 24% (23 of 97) of PPA cases with available CSF biomarkers as nfvPPA, with a mean age of disease onset at 60.9 years, an average delay of 2.3 years between first symptom and diagnosis, slight male predominance (52%; 11:12, female/male), and underlying AD pathology in 35% of cases.¹⁴ In 2 series of 353 patients with FTLD, 24.6% of cases were identified as nfvPPA.⁴¹ An epidemiologic study investigating FTLD syndromes in 2 UK counties with a population of 1.69 million yielded an estimated nfvPPA prevalence of 1.5 per 100,000.⁴²

No pharmacologic option exists to improve or protect against declining function for patients with nfvPPA. However, speech-language treatment has demonstrated efficacy and structured oral reading has been proposed as a treatment method for apraxia of speech in nfvPPA.⁶⁸ Additionally, transcranial direct current stimulation over the left posterior peri-Sylvian region and the Broca area has also been investigated as a potential treatment technique for nfvPPA.⁶⁹ Supportive care remains the

Structural Imaging. The most common imaging feature associated with nfvPPA is regional atrophy predominantly involving the inferior frontal, opercular, and insular regions of the dominant hemisphere (Brodmann area 44/45; Broca area), most commonly on

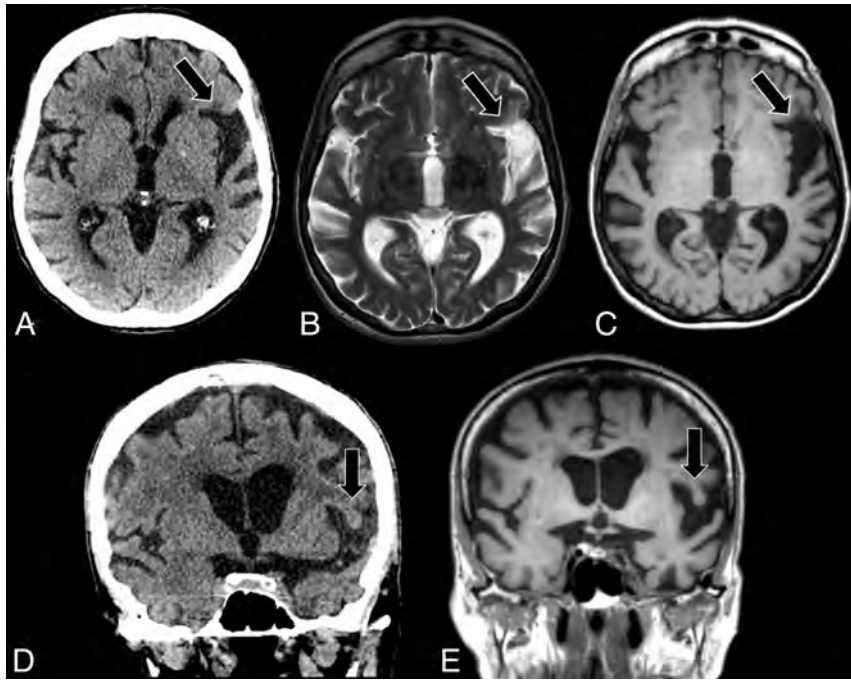


FIG 12. Axial CT (A), axial T2-weighted MR imaging (B), axial T1-weighted MR imaging (C), coronal CT (D), and coronal T1-weighted MR imaging (E) in a right-handed individual with apraxia of speech demonstrate asymmetric widening of the left Sylvian fissure with predominant left posterior frontoinsular atrophy (black arrows, A–E), suspicious for nvfPPA.

the left, with associated widening of the left Sylvian fissure (Fig 11). Notably, the left inferior frontal gyrus and pars opercularis and triangularis of the left frontal operculum are considered the syndrome-specific epicenters of disease in nvfPPA (Fig 12).^{70,71} Similar to other PPA variants, while the presence of left, posterior, frontoinsular atrophy is highly suggestive of nvfPPA, its absence does not exclude the diagnosis. A wide variety of nvfPPA imaging patterns has been reported, ranging from no specific pattern of atrophy to left-hemispheric, left-frontotemporal, bifrontal, or even generalized patterns of atrophy, with imaging inconsistencies largely attributable to the clinical and histopathologic heterogeneity of nvfPPA syndromes.⁷² Given the progressive nature of all PPA subtypes, comparison with prior imaging and serial examinations may reveal subtle region-specific progressive atrophy and should be pursued in the appropriate clinical setting.

DTI techniques have demonstrated involvement of the dorsal language pathway of long-range WM fibers connecting the frontal, subcortical, and parietal areas, a unique finding in nvfPPA that has not been described in other PPA subtypes,^{73,74} as well as WM damage in the dorsal pathway (superior longitudinal fasciculus).⁶⁴ GM atrophy has also been described in the premotor regions, the supplementary motor area, and striatum.^{10,70} Syntactic processing deficits in patients with nvfPPA have been associated with structural and functional abnormalities involving the posterior part of the inferior frontal gyrus.⁷⁵ Although most cases affect the left hemisphere, right-hemispheric involvement has also been reported, hypothesized to occur in left-handed individuals or those with a history of developmental learning disabilities, such as dyslexia.⁷⁶

Longitudinal progression of atrophy in nvfPPA has been reported to involve the posterior frontal regions, supplementary motor area, insula, striatum, inferior parietal regions, and underlying WM.⁷⁰ Furthermore, atrophy typically progresses from the frontal operculum to the supplementary motor complex through the frontal aslant tract, which plays a role in the initiation and execution of movements, particularly articulation, and ultimately to the basal ganglia and supramarginal gyrus.⁷³ The loss of integrity of the frontal aslant tract in nvfPPA is associated with distortion errors made by patients in spontaneous speech, as well as verbal fluency task performance. Therefore, nvfPPA is an example of a network disorder involving the circuit of regions and connections involved in speech production.⁷⁷

Functional Imaging. A resting-state fMRI study demonstrated decreased functional connectivity between the left inferior frontal gyrus and posterior middle temporal gyrus in nvfPPA, even in patients without advanced atrophy.⁷⁸

Such results suggest the possibility of fMRI serving as a useful imaging technique for the early detection of PPA, particularly nvfPPA, which may ultimately improve patient outcomes as disease-modifying therapies emerge in the clinical setting.

There are limited data regarding the use of ASL for nvfPPA specifically. Further studies assessing the potential role of ASL for patients with nvfPPA as well as its performance compared with [¹⁸F] FDG-PET are needed.

Molecular Imaging. [¹⁸F] FDG-PET and SPECT can be performed to demonstrate characteristic asymmetric hypometabolism-hypoperfusion predominantly affecting the left posterior frontal and peri-insular regions, including the left frontal operculum (Fig 13). Specifically, metabolic reduction in the left posterior frontoinsular region, including the inferior frontal gyrus, insula, and premotor and supplementary motor areas, is necessary to make an imaging-supported diagnosis of nvfPPA.⁶

Regarding the cortical amyloid burden in nvfPPA, a study investigating [¹¹C]-Pittsburgh compound B in PPA subtypes demonstrated increased binding in only a few subjects with nvfPPA, in an uptake pattern similar to that of AD, including elevated tracer binding throughout the neocortex and striatum.⁷⁹ A recent study investigating patients with PPA with discordant amyloid status (eg, nvfPPA with AD pathology) found that most cases exhibited FTLD- τ as the primary pathologic diagnosis with AD as an incidental age-related contributor.⁸⁰ Specifically, 24 of 28 patients (86%) with svPPA and 28 of 31 patients (90%) with nvfPPA had negative amyloid PET findings, whereas 25 of 26 patients (96%) with logopenic PPA had scans with positive findings. The

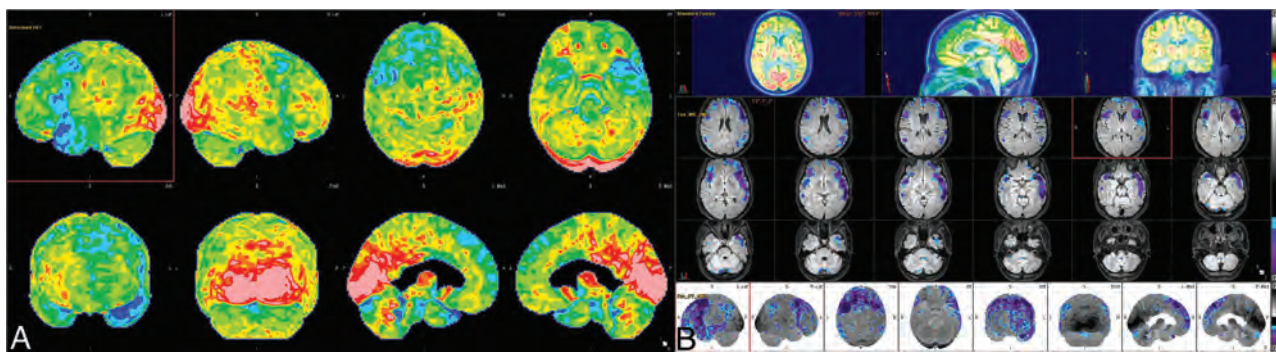


FIG 13. [^{18}F] FDG-PET cortical surface maps demonstrate an abnormal FDG distribution pattern with severe left-greater-than-right hypometabolism, most pronounced in the dorsal frontal lobes and left peri-insular region (A), with corresponding disproportionate cortical atrophy particularly pronounced in the left insular region visualized on brain MR views (B), findings further supported by semiquantitative FDG-PET analysis using z scores calculated in comparison with age-matched cognitively healthy controls, demonstrating markedly decreased values in the left > right peri-insular region, including in the pars opercularis and pars triangularis of the left inferior frontal gyrus, corresponding to the expected Broca area (B).

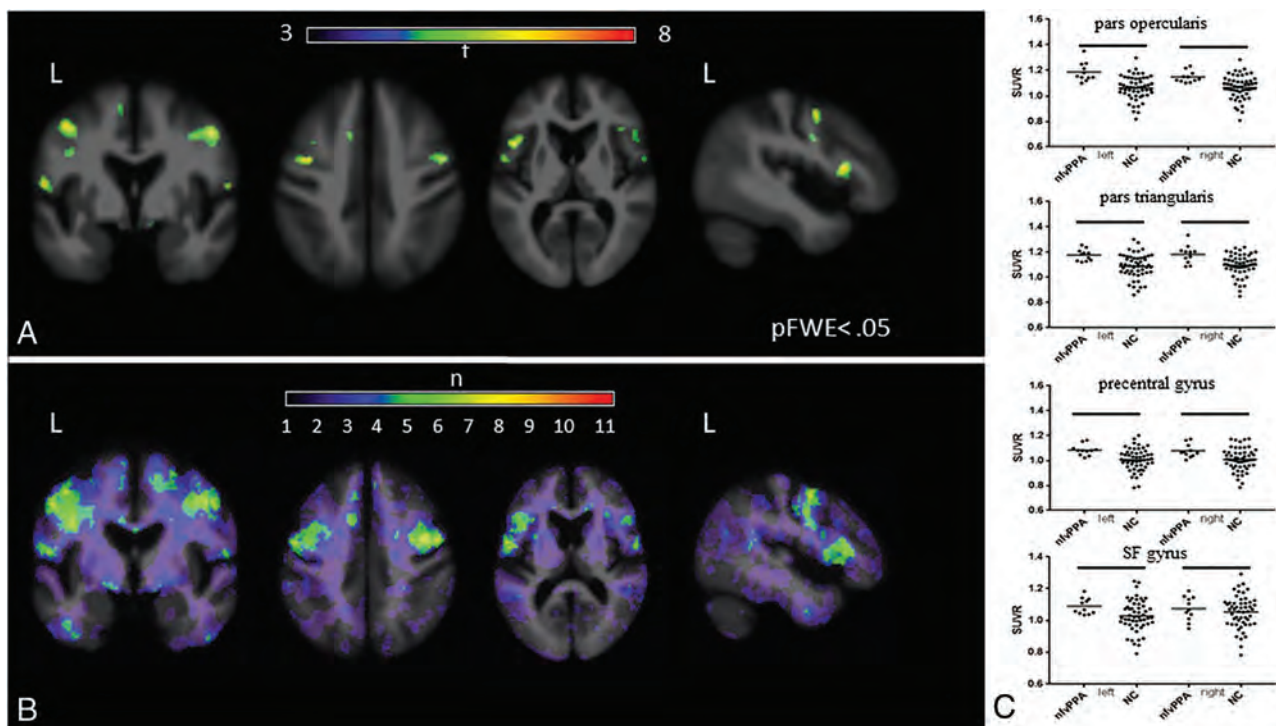


FIG 14. [^{18}F] flortaucipir in nvPPA. A, On voxelwise comparison with healthy controls, agPPA demonstrates increased uptake in the left-greater-than-right frontal operculum; middle and inferior frontal gyri; and left superior frontal gyrus ($p\text{FWE} < .05$). B, The W score frequency map demonstrates elevated W scores above 1.65 in the bilateral middle frontal gyri and frontal operculum in approximately two-thirds of patients scanned, with voxels above 1.65 in 8 of 11 patients in peak areas. C, ROI analyses reveals group differences in those with in nvPPA compared with controls in the bilateral pars opercularis (left, $P = .0001$; right, $P = .0018$), pars triangularis (left, $P = .0016$; right, $P = .0029$), precentral gyrus (left, $P = .003$; right, $P = .0112$), and superior frontal gyrus (left, $P = .03$; right, $P = .045$). Adapted with permission from Tsai et al.⁸¹

amyloid-positive svPPA and nvPPA cases with available postmortem data (2 of 4 and 2 of 3, respectively) all had a primary FTLD and secondary AD pathology diagnoses. Therefore, some patients with nvPPA may have a PET examination positive for amyloid, and the presence of amyloid-positivity is not pathognomonic for any 1 PPA variant.

τ -targeting PET tracers have been used in nvPPA, most commonly [^{18}F] flortaucipir (AV-1451), a first-generation τ PET ligand, which exhibits increased uptake in the left-greater-than-

right frontal operculum and left middle and inferior frontal gyri (Fig 14).¹⁹ nvPPA has also been shown to demonstrate less robust-but-focal uptake in the frontal WM and subcortical structures (Fig 15), regions known to be functionally impaired in nvPPA, suggesting disease-specific binding to FTLD-4R τ .⁸¹ In nvPPA, AV-1451 has been used to study τ propagation in the left-hemispheric syntactic network, which comprises anterior frontal and posterior temporal nodes connected by the left arcuate fasciculus, with deposition greatest in the 2 nodes of the

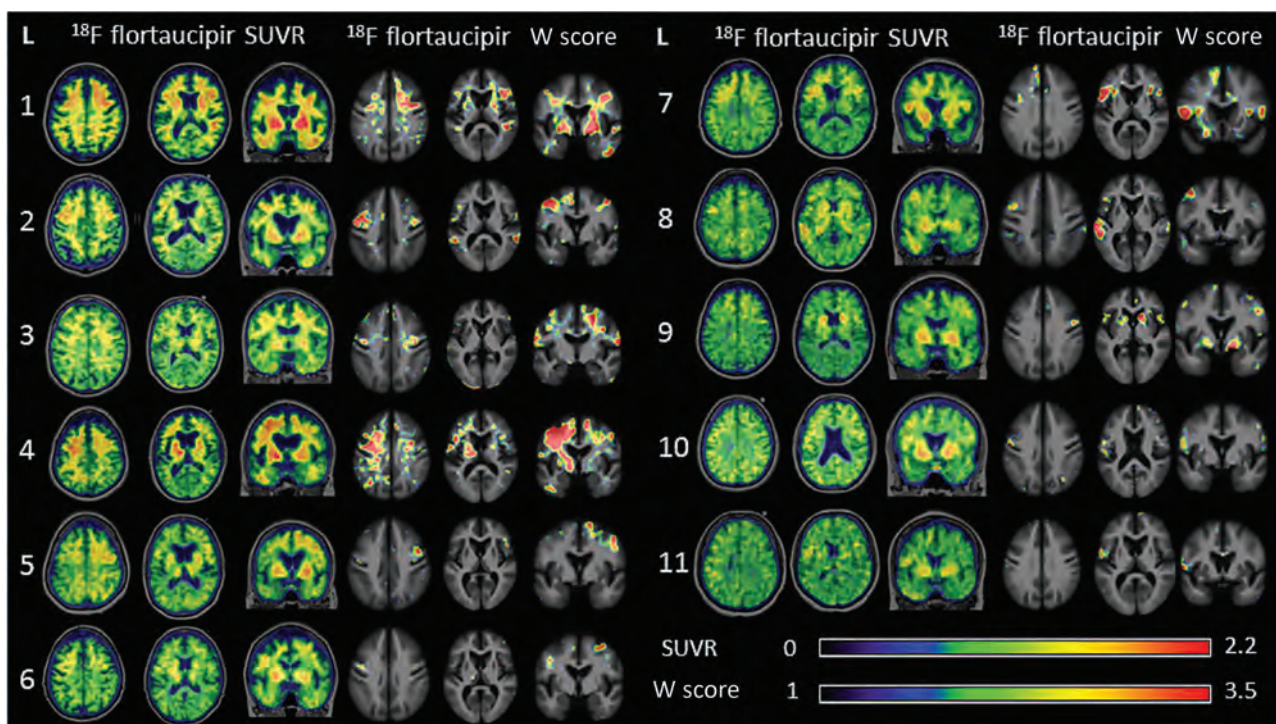


FIG 15. Representative [^{18}F] flortaucipir images from 11 patients with nvPPA and corresponding single-subject W score maps. Tracer retention in the frontal operculum and inferior or middle frontal gyrus is seen in all scans to varying degrees and is more pronounced on the left side. Patients 1–7 show additional bilateral-but-asymmetric frontal WM binding, while patients 8–11 demonstrate mild uptake in the prefrontal cortex. All scans show varying degrees of uptake in the bilateral basal ganglia. Adapted with permission from Tsai et al.⁸¹

syntactic network.⁸² The left arcuate fasciculus also demonstrated decreased fractional anisotropy in nvPPA, particularly near the anterior node, suggesting τ propagation from node to connected node in human brain networks in the setting of neurodegenerative diseases, including PPA.⁸²

TSPO-targeting tracers have been explored in PPA, with the goal of characterizing the role of microglial activation and associated neuroinflammation in the pathogenesis of PPA. One study identified significantly increased mean [^{11}C] PK-11195 binding in FTLTD ($n = 5$, including 4 patients with nvPPA and 1 patient with behavioral-variant frontotemporal dementia) in regions such as the left dorsolateral prefrontal cortex, right hippocampus, and parahippocampus.⁸³

CONCLUSIONS

PPA is a unique and complex spectrum of neurodegenerative disorders that requires a multidisciplinary approach to diagnosis, relying on the aggregate findings of clinical presentation, histopathologic biomarkers, and imaging features. A number of structural, functional, and molecular imaging modalities can support an accurate diagnosis, and neuroradiologists should be familiar with the classic imaging features of each PPA subtype, because prompt and accurate diagnosis may allow improved outcomes and intervention, particularly as disease-modifying therapies enter clinical practice.

Disclosure forms provided by the authors are available with the full text and PDF of this article at www.ajnr.org.



















REFERENCES

- Patel KP, Wymer DT, Bhatia VK, et al. **Multimodality imaging of dementia: clinical importance and role of integrated anatomic and molecular imaging.** *Radiographics* 2020;40:200–22 CrossRef Medline
- Brown RKJ, Bohnen NI, Wong KK, et al. **Brain PET in suspected dementia: patterns of altered FDG metabolism.** *Radiographics* 2014;34:684–701 CrossRef Medline
- Irwin DJ. **Tauopathies as clinicopathological entities.** *Parkinsonism Relat Disord* 2016;22:S29–33 CrossRef Medline
- Montembeault M, Brambati SM, Gorno-Tempini ML, et al. **Clinical, anatomical, and pathological features in the three variants of primary progressive aphasia: a review.** *Front Neurol* 2018;9:692 CrossRef Medline
- Spinelli EG, Mandelli ML, Miller ZA, et al. **Typical and atypical pathology in primary progressive aphasia variants.** *Ann Neurol* 2017;81:430–43 CrossRef Medline
- Gorno-Tempini ML, Hillis AE, Weintraub S, et al. **Classification of primary progressive aphasia and its variants.** *Neurology* 2011;76:1006–14 CrossRef Medline
- Mesulam MM. **Primary progressive aphasia: a language-based dementia.** *N Engl J Med* 2003;349:1535–42 CrossRef Medline
- Mesulam M, Wieneke C, Rogalski E, et al. **Quantitative template for subtyping primary progressive aphasia.** *Arch Neurol* 2009;66:1545–51 CrossRef Medline
- Sitek EJ, Narożńska E, Brockhuis B, et al. **Neuroimaging in the differential diagnosis of primary progressive aphasia: illustrative case series in the light of new diagnostic criteria.** *Polish J Radiol* 2014;79:251–58 CrossRef Medline
- Gorno-Tempini ML, Dronkers NF, Rankin KP, et al. **Cognition and anatomy in three variants of primary progressive aphasia.** *Ann Neurol* 2004;55:335–46 CrossRef Medline
- Marshall CR, Hardy CJ, Volkmer A, et al. **Primary progressive aphasia: a clinical approach.** *J Neurol* 2018;265:1474–90 CrossRef Medline

12. Grossman M. **Primary progressive aphasia: clinicopathological correlations.** *Nat Rev Neurol* 2010;6:88–97 CrossRef Medline
13. Butts AM, Machulda MM, Duffy JR, et al. **Neuropsychological profiles differ among the three variants of primary progressive aphasia.** *J Int Neuropsychol Soc* 2015;21:429–35 CrossRef Medline
14. Magnin E, Démonet JF, Wallon D, et al; on behalf of ePLM orators. **Primary progressive aphasia in the Network of French Alzheimer Plan Memory Centers.** *J Alzheimers Dis* 2016;54:1459–71 CrossRef Medline
15. Teichmann M, Kas A, Boutet C, et al. **Deciphering logopenic primary progressive aphasia: a clinical, imaging and biomarker investigation.** *Brain* 2013;136:3474–88 CrossRef Medline
16. Lundeen TF, Seibyl JP, Covington MF, et al. **Signs and artifacts in amyloid PET.** *Radiographics* 2018;38:2123–33 CrossRef Medline
17. Bergeron D, Gorno-Tempini ML, Rabinovici G, et al. **Prevalence of amyloid- β pathology in distinct variants of primary progressive aphasia.** *Ann Neurol* 2018;84:729–40 CrossRef Medline
18. Botha H, Duffy JR, Whitwell JL, et al. **Classification and clinicoradiologic features of primary progressive aphasia (PPA) and apraxia of speech.** *Cortex* 2015;69:220–36 CrossRef Medline
19. Rabinovici GD, Jagust WJ, Furst AJ, et al. **AB amyloid and glucose metabolism in three variants of primary progressive aphasia.** *Ann Neurol* 2008;64:388–401 CrossRef Medline
20. Beyer L, Brendel M. **Imaging of tau pathology in neurodegenerative diseases: an update.** *Semin Nucl Med* 2021;51:253–63 CrossRef Medline
21. Josephs KA, Martin PR, Botha H, et al. **[18 F]AV-1451 tau-PET and primary progressive aphasia.** *Ann Neurol* 2018;83:599–611 CrossRef Medline
22. Mueller A, Bullich S, Barret O, et al. **Tau PET imaging with 18F-PI-2620 in patients with Alzheimer disease and healthy controls: a first-in-humans study.** *J Nucl Med* 2020;61:911–19 CrossRef Medline
23. Xia C, Makaretz SJ, Caso C, et al. **Association of in vivo [18F]AV-1451 tau PET imaging results with cortical atrophy and symptoms in typical and atypical Alzheimer disease.** *JAMA Neurol* 2017;74:427–36 CrossRef Medline
24. Werry EL, Bright FM, Piguet O, et al. **Recent developments in TSPO PET imaging as a biomarker of neuroinflammation in neurodegenerative disorders.** *Int J Mol Sci* 2019;20:1–21 CrossRef Medline
25. Kim G, Bolbolan K, Gefen T, et al. **Atrophy and microglial distribution in primary progressive aphasia with transactive response DNA-binding protein-43 kDa.** *Ann Neurol* 2018;83:1096–104 CrossRef Medline
26. Hodges J, Patterson K, Oxbury S, et al. **Semantic dementia: progressive fluent aphasia with temporal lobe atrophy.** *Brain* 1992;115:1783–806 CrossRef
27. Mahalingam S, Chen MK. **Neuroimaging in dementias.** *Semin Neurol* 2019;39:188–99 CrossRef Medline
28. Masdeu JC. **Neuroimaging of diseases causing dementia.** *Neurol Clin* 2020;38:65–94 CrossRef Medline
29. Nasrallah IM, Wolk DA. **Multimodality imaging of Alzheimer disease and other neurodegenerative dementias.** *J Nucl Med* 2014;55:2003–11 CrossRef Medline
30. Villemagne VL, Barkhof F, Garibotto V, et al. **Molecular imaging approaches in dementia.** *Radiology* 2021;298:517–30 CrossRef Medline
31. Clark DG, Charuvastra A, Miller BL, et al. **Fluent versus nonfluent primary progressive aphasia: a comparison of clinical and functional neuroimaging features.** *Brain Lang* 2005;94:54–60 CrossRef Medline
32. Collins JA, Montal V, Hochberg D, et al. **Focal temporal pole atrophy and network degeneration in semantic variant primary progressive aphasia.** *Brain* 2017;140:457–71 CrossRef Medline
33. Panegyres PK, McCarthy M, Campbell A, et al. **Correlative studies of structural and functional imaging in primary progressive aphasia.** *Am J Alzheimers Dis Other Demen* 2008;23:184–91 CrossRef Medline
34. Thompson SA, Patterson K, Hodges JR. **Left/right asymmetry of atrophy in semantic dementia: behavioral-cognitive implications.** *Neurology* 2003;61:1196–203 CrossRef Medline
35. Landin-Romero R, Tan R, Hodges JR. **An update on semantic dementia: genetics, imaging, and pathology.** *Alzheimers Res Ther* 2016;8:1–9 CrossRef Medline
36. Rohrer JD, Geser F, Zhou J, et al. **TDP-43 subtypes are associated with distinct atrophy patterns in frontotemporal dementia.** *Neurology* 2010;75:2204–11 CrossRef Medline
37. Seelaar H, Kamphorst W, Rosso SM, et al. **Distinct genetic forms of frontotemporal dementia.** *Neurology* 2008;71:1220–26 CrossRef Medline
38. Goldman J, Farmer J, Wood E, et al. **Comparison of family histories in FTL D subtypes and related tauopathies.** *Neurology* 2005;65:1817–19 CrossRef Medline
39. Pottier C, Ravenscroft TA, Sanchez-Contreras M, et al. **Genetics of FTL D: overview and what else we can expect from genetic studies.** *J Neurochem* 2016;138:32–53 CrossRef Medline
40. Onyike CU, Diehl-Schmid J. **The epidemiology of frontotemporal dementia.** *Int Rev Psychiatry* 2013;25:130–37 CrossRef Medline
41. Clerc MT, Gunten A. **Frontotemporal lobar degeneration.** *Dement Prevalence, Risk Factors Manag Strateg* 2014;62:87–114
42. Coyle-Gilchrist ITS, Dick KM, Patterson K, et al. **Prevalence, characteristics, and survival of frontotemporal lobar degeneration syndromes.** *Neurology* 2016;86:1736–43 CrossRef Medline
43. Henry ML, Beeson PM, Rapcsak SZ. **Treatment for anomia in semantic dementia.** *Semin Speech Lang* 2008;29:60–70 CrossRef Medline
44. Sanches C, Levy R, Benisty S, et al. **Testing the therapeutic effects of transcranial direct current stimulation (tDCS) in semantic dementia: a double blind, sham controlled, randomized clinical trial.** *Trials* 2019;20:1–15 CrossRef Medline
45. Chan D, Fox NC, Scahill RI, et al. **Patterns of temporal lobe atrophy in semantic dementia and Alzheimer's disease.** *Ann Neurol* 2001;49:433–42 CrossRef Medline
46. Edwards-Lee T, Miller B, Benson D, et al. **The temporal variant of frontotemporal dementia.** *Brain* 1997;120:1027–40 CrossRef Medline
47. Josephs KA, Whitwell JL, Vemuri P, et al. **The anatomic correlate of prosopagnosia in semantic dementia.** *Neurology* 2008;71:1628–33 CrossRef Medline
48. Yang J, Pan P, Song W, et al. **Quantitative meta-analysis of gray matter abnormalities in semantic dementia.** *J Alzheimers Dis* 2012;31:827–33 CrossRef Medline
49. Rohrer JD, Warren JD, Modat M, et al. **Patterns of cortical thinning in the language variants of frontotemporal lobar degeneration.** *Neurology* 2009;72:1562–69 CrossRef Medline
50. Brambati SM, Rankin KP, Narvid J, et al. **Atrophy progression in semantic dementia with asymmetric temporal involvement: a tensor-based morphometry study.** *Neurobiol Aging* 2009;30:103–11 CrossRef Medline
51. Good CD, Scahill RI, Fox NC, et al. **Automatic differentiation of anatomical patterns in the human brain: Validation with studies of degenerative dementias.** *Neuroimage* 2002;17:29–46 CrossRef Medline
52. Yang Q, Guo QH, Bi YC. **The brain connectivity basis of semantic dementia: a selective review.** *CNS Neurosci Ther* 2015;21:784–92 CrossRef Medline
53. Guo CC, Gorno-Tempini ML, Gesierich B, et al. **Anterior temporal lobe degeneration produces widespread network-driven dysfunction.** *Brain* 2013;136:2979–91 CrossRef Medline
54. Ranasinghe KG, Hinkley LB, Beagle AJ, et al. **Distinct spatiotemporal patterns of neuronal functional connectivity in primary progressive aphasia variants.** *Brain* 2017;140:2737–51 CrossRef Medline
55. Olm CA, Kandel BM, Avants BB, et al. **Arterial spin labeling perfusion predicts longitudinal decline in semantic variant primary progressive aphasia.** *J Neurol* 2016;263:1927–38 CrossRef Medline
56. Kobayashi R, Hayashi H, Kawakatsu S, et al. **[18F]THK-5351 PET imaging in early-stage semantic variant primary progressive aphasia: a report of two cases and a literature review.** *BMC Neurol* 2018;18:109 CrossRef Medline
57. Bevan-Jones WR, Cope TE, Simon Jones P, et al. **AV-1451 binding in vivo mirrors the expected distribution of TDP-43 pathology in the**

- semantic variant of primary progressive aphasia.** *J Neurol Neurosurg Psychiatry* 2018;89:1032–37 CrossRef Medline
58. Smith R, Santillo AF, Waldö ML, et al. **18 F-Flortaucipir in TDP-43 associated frontotemporal dementia.** *Sci Rep* 2019;9:1–10 CrossRef Medline
 59. Mormino EC, Toueg TN, Azevedo C, et al. **Tau PET imaging with 18F-Pi-2620 in aging and neurodegenerative diseases.** *Eur J Nucl Med Mol Imaging* 2021;48:2233–44 CrossRef Medline
 60. Schain M, Kreisl WC. **Neuroinflammation in neurodegenerative disorders: a review.** *Curr Neurol Neurosci Rep* 2017;17:1–11 CrossRef Medline
 61. Grossman M, Mickanin J, Onishi K, et al. **Progressive nonfluent aphasia: language, cognitive, and PET measures contrasted with probable Alzheimer's disease.** *J Cogn Neurosci* 1996;8:135–54 CrossRef Medline
 62. Mesulam MM. **Primary progressive aphasia.** *Ann Neurol* 2001;49:425–32 CrossRef Medline
 63. Ash S, Moore P, Vesely L, et al. **Non-fluent speech in frontotemporal lobar degeneration.** *J Neurolinguistics* 2009;22:370–83 CrossRef Medline
 64. Grossman M. **The non-fluent/agrammatic variant of primary progressive aphasia.** *Lancet Neurol* 2012;11:545–55 CrossRef Medline
 65. Olney NT, Spina S, Miller BL. **Frontotemporal dementia.** *Neurol Clin* 2017;35:339–74 CrossRef Medline
 66. Xiong L, Xuereb JH, Spillantini MG, et al. **Clinical comparison of progressive aphasia associated with Alzheimer versus FTD-spectrum pathology.** *J Neurol Neurosurg Psychiatry* 2011;82:254–60 CrossRef Medline
 67. Rohrer J, Guerreiro R, Vandrovcsa J, et al. **The heritability and genetics of frontotemporal lobar degeneration.** *Neurology* 2009;73:1451–56 CrossRef Medline
 68. Henry ML, Meese MV, Truong S, et al. **Treatment for apraxia of speech in nonfluent variant primary progressive aphasia.** *Behav Neurol* 2013;26:77–88 CrossRef Medline
 69. Wang J, Wu D, Chen Y, et al. **Effects of transcranial direct current stimulation on language improvement and cortical activation in non-fluent variant primary progressive aphasia.** *Neurosci Lett* 2013;549:29–33 CrossRef Medline
 70. Mandelli ML, Vilaplana E, Brown JA, et al. **Healthy brain connectivity predicts atrophy progression in non-fluent variant of primary progressive aphasia.** *Brain* 2016;139:2778–91 CrossRef Medline
 71. Mandelli ML, Vitali P, Santos M, et al. **Two insular regions are differentially involved in behavioral variant FTD and nonfluent/agrammatic variant PPA.** *Cortex* 2016;74:149–57 CrossRef Medline
 72. Sajjadi SA, Sheikh-Bahaei N, Cross J, et al. **Can MRI visual assessment differentiate the variants of primary-progressive aphasia?** *AJNR Am J Neuroradiol* 2017;38:954–60 CrossRef Medline
 73. Mandelli ML, Caverzasi E, Binney RJ, et al. **Frontal white matter tracts sustaining speech production in primary progressive aphasia.** *J Neurosci* 2014;34:9754–67 CrossRef Medline
 74. Wilson SM, Galantucci S, Tartaglia MC, et al. **Syntactic processing depends on dorsal language tracts.** *Neuron* 2011;72:397–403 CrossRef Medline
 75. Wilson SM, Dronkers NF, Ogar JM, et al. **Neural correlates of syntactic processing in the nonfluent variant of primary progressive aphasia.** *J Neurosci* 2010;30:16845–54 CrossRef Medline
 76. Miller ZA, Mandelli ML, Rankin KP, et al. **Handedness and language learning disability differentially distribute in progressive aphasia variants.** *Brain* 2013;136:3461–73 CrossRef Medline
 77. Dick AS, Garic D, Graziano P, et al. **The frontal aslant tract (FAT) and its role in speech, language and executive function.** *Cortex* 2019;111:148–63 CrossRef Medline
 78. Bonakdarpour B, Rogalski EJ, Wang A, et al. **Functional connectivity is reduced in early-stage primary progressive aphasia when atrophy is not prominent.** *Alzheimer Dis Assoc Disord* 2017;31:101–16 CrossRef Medline
 79. Minoshima S, Drzezga AE, Barthel H, et al. **SNMMI procedure standard/EANM practice guideline for amyloid PET imaging of the brain 1.0.** *J Nucl Med* 2016;57:1316–22 CrossRef Medline
 80. Santos-Santos MA, Rabinovici GD, Iaccarino L, et al. **Rates of amyloid imaging positivity in patients with primary progressive aphasia.** *JAMA Neurol* 2018;75:342–52 CrossRef Medline
 81. Tsai RM, Bejanin A, Lesman-Segev O, et al. **¹⁸F-flortaucipir (AV-1451) tau PET in frontotemporal dementia syndromes.** *Alzheimers Res Ther* 2019;11:1–18 CrossRef Medline
 82. Pascual B, Funk Q, Zanotti-Fregonara P, et al. **Multimodal 18F-AV-1451 and MRI findings in nonfluent variant of primary progressive aphasia: possible insights on nodal propagation of tau protein across the syntactic network.** *J Nucl Med* 2020;61:263–69 CrossRef Medline
 83. Cagnin A, Rossor M, Sampson EL, et al. **In vivo detection of microglial activation in frontotemporal dementia.** *Ann Neurol* 2004;56:894–97 CrossRef Medline
 84. Madhavan A, Whitwell JL, Weigand SD, et al. **FDG PET and MR imaging in logopenic primary progressive aphasia versus dementia of the Alzheimer's type.** *PLoS One* 2013;8:e62471 CrossRef Medline

Flow Diversion in the Treatment of Intracranial Aneurysms: A Pragmatic Randomized Care Trial

 J. Raymond,  D. Iancu,  W. Boisseau,  J.D.B. Diestro,  R. Klink,  M. Chagnon,  J. Zehr,  B. Drake,  H. Lesiuk,  A. Weill,  D. Roy,  M.W. Bojanowski,  C. Chaalala,  J.L. Rempel,  C. O'Kelly,  M.M. Chow,  S. Bracard, and  T.E. Darsaut



ABSTRACT

BACKGROUND AND PURPOSE: Flow diversion is a recent endovascular treatment for intracranial aneurysms. We compared the safety and efficacy of flow diversion with the alternative standard management options.

MATERIALS AND METHODS: A parallel group, prerandomized, controlled, open-label pragmatic trial was conducted in 3 Canadian centers. The trial included all patients considered for flow diversion. A Web-based platform 1:1 randomly allocated patients to flow diversion or 1 of 4 alternative standard management options (coiling with/without stent placement, parent vessel occlusion, surgical clipping, or observation) as prespecified by clinical judgment. Patients ineligible for alternative standard management options were treated with flow diversion in a registry. The primary safety outcome was death or dependency (mRS > 2) at 3 months. The composite primary efficacy outcome included the core lab–determined angiographic presence of a residual aneurysm, aneurysm rupture, progressive mass effect during follow-up, or death or dependency (mRS > 2) at 3–12 months.

RESULTS: Between May 2011 and November 2020, three hundred twenty-three patients were recruited: Two hundred seventy-eight patients (86%) had treatment randomly allocated (139 to flow diversion and 139 to alternative standard management options), and 45 (14%) received flow diversion in the registry. Patients in the randomized trial frequently had unruptured (83%), large (52% ≥ 10 mm) carotid (64%) aneurysms. Death or dependency at 3 months occurred in 16/138 patients who underwent flow diversion and 12/137 patients receiving alternative standard management options (relative risk, 1.33; 95% CI, 0.65–2.69; $P = .439$). A poor primary efficacy outcome was found in 30.9% (43/139) with flow diversion and 45.6% (62/136) of patients receiving alternative standard management options, with an absolute risk difference of 14.7% (95% CI, 3.3%–26.0%; relative risk, 0.68; 95% CI, 0.50–0.92; $P = .014$).

CONCLUSIONS: For patients with mostly unruptured, large, anterior circulation (carotid) aneurysms, flow diversion was more effective than the alternative standard management option in terms of angiographic outcome.

ABBREVIATIONS: ASMO = alternative standard management option; DSMC = Data Safety and Monitoring Committee; FD = flow diversion; FIAT = Flow Diversion in Intracranial Aneurysm Treatment; PVO = parent vessel occlusion; RCT = randomized controlled trial

Flow diversion (FD) is an innovative treatment of intracranial aneurysms.^{1–3} Flow diverters are low-porosity, braided endovascular stent devices designed to normalize flow in a vessel with an aneurysm and occlude the aneurysm by thrombosis of the sac.⁴ FD can often accomplish what other interventions cannot, such as reconstructing a cerebral vessel having a giant aneurysm and occluding the aneurysm while preserving normal parent and branching vessels.⁵ Yet FD has also been associated with unexpected


delayed complications, such as aneurysm ruptures, parenchymal hematomas at a distance from the aneurysm, and strokes from stent thrombosis.^{6,7} First approved in 2011 in the United States for the treatment of unruptured, large and giant aneurysms of the proximal segments of the carotid artery,² clinical usage has since expanded to aneurysms of all sizes, locations, and presentations. More than 22 systematic reviews of case series have shown aneurysm occlusion rates exceeding 75%, with treatment-related morbidity and mortality


Received May 30, 2022; accepted after revision June 28.

From the Department of Radiology (J.R., D.I., W.B., J.D.B.D., R.K., A.W., D.R.), Centre Hospitalier de l'Université de Montréal, Quebec, Canada; Departments of Radiology (D.I.) and Surgery (B.D., H.L.), Ottawa Hospital, Civic Campus, Ottawa, Ontario, Canada; Department of Mathematics and Statistics (M.C., J.Z.), Université de Montréal, Montreal, Canada; Department of Neurosurgery (M.W.B., C.C.), Centre Hospitalier de l'Université de Montréal, Notre-Dame Hospital, Montreal, Quebec, Canada; Departments of Radiology (J.L.R.) and Surgery (C.O., M.M.C., T.E.D.), Division of Neurosurgery, University of Alberta Hospital, Mackenzie Health Sciences Centre, Edmonton, Alberta, Canada; and Neuroradiology (S.B.), CHRU de Nancy, Nancy, Lorraine, France.

Please address correspondence to Jean Raymond, MD, Centre Hospitalier de l'Université de Montréal (CHUM), Department of Radiology, Room D03.5462b, Montreal, PQ, Canada H2X 0C1; e-mail: jean.raymond@umontreal.ca; @RaymondJeanMD1

 Indicates open access to non-subscribers at www.ajnr.org

 Indicates article with online supplemental data.

 Evidence-Based Medicine Level 1.

<http://dx.doi.org/10.3174/ajnr.A7597>

in the range of 2%–10%.^{1,3,8,9} The role that FD should play in clinical practice still remains unclear because opinions and practices vary widely¹⁰ and randomized comparisons with standard management options are few. Two randomized trials were published in 2018; both restricted inclusion to large or complex anterior circulation aneurysms treatable by only 1 specific comparator intervention. One comparison of FD with stent-assisted coiling in 144 patients raised safety concerns but showed increased rates of complete angiographic occlusions with FD.¹¹ Another trial in 80 patients showed FD to be safer but less effective than surgical bypass and parent vessel occlusion (PVO).¹²

The Flow Diversion in Intracranial Aneurysm Treatment (FIAT) trial was launched in 2011 to introduce to endovascular practice a promising-but-unvalidated innovation for patients with difficult intracranial aneurysms.^{13,14} FIAT was pragmatic, all-inclusive, and proposed a 1:1 randomized allocation for the treatment by FD or alternative standard management options (ASMOs) (defined as any other prespecified alternative management option), along with a registry of patients treated with FD considered ineligible for ASMO.¹⁴ The main hypothesis of the trial was that treatment with FD would increase the percentage of patients with a good outcome by 15%, a composite that included occlusion or near-occlusion of the aneurysm combined with an independent clinical outcome (mRS < 3) at 3–12 months. The aim of this article was to present the final results of the FIAT randomized trial.

MATERIALS AND METHODS

FIAT was an investigator-led, pragmatic, multicenter, randomized controlled care trial integrated into clinical practice.¹³ FIAT compared a policy of using either FD (any flow diverter device with or without coiling) or ASMO to manage patients with difficult intracranial aneurysms. The ASMO was selected according to clinical judgment at the time of enrollment but before randomized allocation. Patients deemed ineligible for other management alternatives were included in a parallel FD registry. There were 3 participating Canadian centers (Montreal, Edmonton, Ottawa). All sites received institutional review board approval. The protocol was published,¹⁴ and the trial was registered at ClinicalTrials.gov No. NCT01349582. The trial was temporarily interrupted in June 2014 for safety concerns, mainly driven by registry results, but the Data Safety and Monitoring Committee (DSMC) recommended trial continuation because treatment-related morbidity between randomized groups was similar.¹⁵

Patients

All patients with an aneurysm for which FD was considered a promising treatment were eligible to participate. Exclusion criteria were few: 1) severe allergy, intolerance, or bleeding disorder that precluded dual antiplatelet agents; 2) absolute contraindication to endovascular treatment or anesthesia; and 3) inability to provide consent. All patients or designees signed an informed consent form to participate in the study.

Randomization and Masking

Concealment of randomized allocation was assured through a Web-based platform. Treating physicians first had to choose, for

each patient, 1 of 4 alternatives to permit computer-generated randomized allocation (1, coiling [with or without high-porosity stent placement], 2, PVO, 3, surgical clipping, and 4, conservative management). Patients ineligible for ASMO were treated with FD in a registry. The randomized allocation was stratified according to comparator intervention and center. In February 2015, the protocol was modified to allow the use of prerandomization. With prerandomization, treatment allocation (and that the planned treatment was randomly allocated) is revealed to the patient at the time of consent.^{16,17} Patients who disagreed with the allocated management were still offered study participation.

Patients, interventionalists, and outcome assessors were not masked to treatment assignment, which was deemed unfeasible.

Interventions

There were no selection criteria for centers. Standard local procedures were followed. Any flow-diverting devices implanted in the parent vessel were permitted, but intra-aneurysmal flow diverters (such as the Woven EndoBridge [WEB; Microvention]) were excluded. Antiplatelet and anticoagulation regimens and testing for platelet inhibition were according to routine practice at each site. Case report forms were simple, and data were collected parsimoniously, to facilitate completion by normal care personnel.

Hypotheses, Outcomes, and Number of Patients

The safety of FD was defined in terms of the mRS scale at 3 months for all patients in the randomized controlled trial (RCT) or registry who received FD at any time: Two hundred patients could suffice to show that if the observed number of patients with mRS > 2 is 10%, the 95% CI of the percentage is from 7.0% to 14.9%.¹⁴ The randomized trial was powered (80%) to show a 15% increase (from 75% to 90%, α error = .05; 224 patients plus losses and crossovers, for a total of 250 patients) in the percentage of patients reaching the composite primary efficacy outcome, including complete or near-complete (residual neck) angiographic occlusion of the aneurysm (3–12 months) and an independent functional outcome (mRS < 3). Clinical outcome was determined by clinicians not blinded to the treatment allocation according to a simplified, standardized mRS questionnaire.¹⁸ The target number of patients was reached in July 2020 ($n = 250$), and a blinded report was sent to the DSMC. The DSMC recommended trial continuation to account for crossovers and patients lost to follow-up. The steering committee decided to stop inclusions on December 1, 2020, when 278 patients had been recruited to the RCT (a 24% increase over the initial estimate of 224, to account for 10% dilution of effect because of prerandomization).¹⁹ Data entry was locked on June 1, 2021, without knowledge of outcome results.

The primary safety outcome was death or dependency (mRS > 2) at 3 months. The primary efficacy outcome was a composite of clinical and angiographic results observed at least 3–12 months after treatment. One primary poor efficacy outcome was allocated per patient; when a patient had >1 outcome, the following hierarchic order was used to classify each patient: death > mRS 3–5 (from any cause, including aneurysm rupture or progressing mass effect with the mRS assessment being made at the time of follow-up imaging) > aneurysm rupture during follow-up > retreatment during follow-up > initial treatment failure > residual aneurysm at

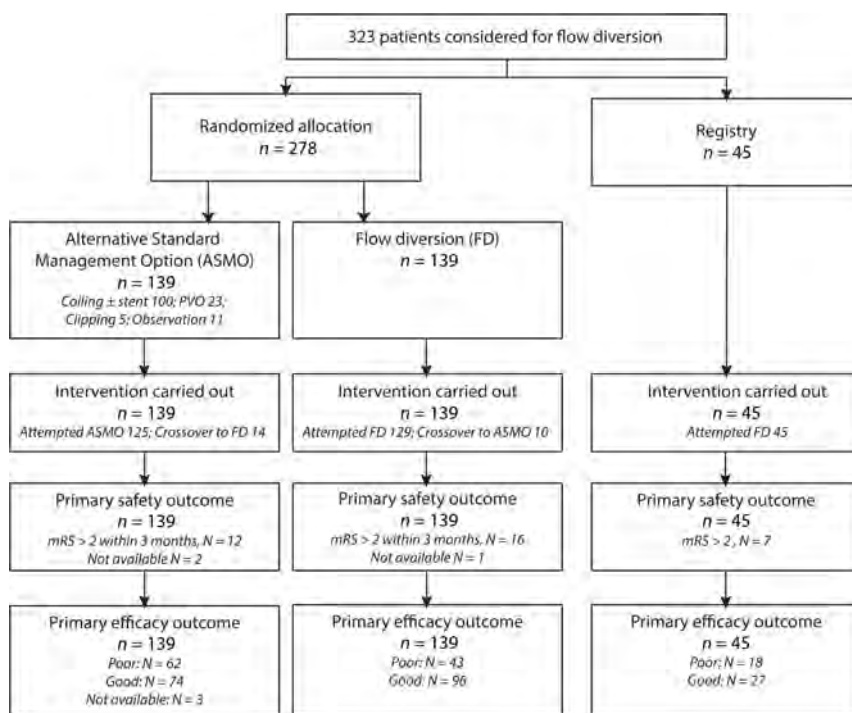


FIG 1. FIAT trial profile.

imaging follow-up (12 months) as adjudicated by an independent core lab according to a previously validated classification system.^{20,21} This system includes 3 ordinal categories (complete occlusion, residual neck, residual aneurysm). The residual aneurysm category was used to adjudicate treatment failure for primary outcome analyses, and the complete occlusion category was used for exploratory analyses. The presence of various endovascular or surgical devices on imaging precluded blinding of core lab assessors.

Secondary outcomes included the individual components of the composite primary outcome as well as the mRS score at discharge and 3 and 12 months posttreatment; success in occluding the aneurysm at the end of the procedure (when appropriate); perioperative complications (ischemic strokes and intracranial hemorrhages within 1 month of the intervention); angiographic results at 12 months; length of hospital stay (number of days); discharge disposition (home, other hospital, rehabilitation facility, death); any new stroke, neurologic symptom, or sign during follow-up; and retreatment of the index aneurysm at any time.

Analyses and Statistics

Blinded data were examined at prespecified intervals by an independent DSMC, composed of an interventional neuroradiologist, a statistician, and an ethicist, but no statistical tests were performed. Three subgroups of patients were analyzed as registered: ASMO (randomly allocated), FD (randomly allocated), and registry. According to protocol, the safety analyses included all patients who were allocated to or received FD at any time. Primary analyses are intent-to-treat. The primary safety outcome was adjudicated when the mRS was >2 within 3 months of the intervention, regardless of the cause. Failure to reach the primary efficacy end point was adjudicated per patient. Primary safety and efficacy

outcomes are described using percentages and 95% confidence intervals. The impact of missing data on the conclusions was studied using sensitivity analyses in which missing data were replaced by either a good or a bad outcome. The risk difference and relative risks were estimated using a generalized estimating equation with a binomial distribution and a log- or identity-link function. The 95% confidence intervals are reported. The groups were not different with respect to risk factors for poor outcomes, and no adjustments for residual confounding factors were made.

The analyses of interactions between prespecified subgroups of interest and treatment were made by adding subgroup variables and interaction in the generalized estimating equation models. Treatment and aneurysm subgroups were examined as prespecified in 2010, regardless of the results of tests for interactions. Subgroup results according to aneurysm size (<10 mm or ≥ 10 mm), location (the proximal carotid artery,

including the cavernous-to-superior hypophyseal segment [the initial FDA-approved FD indications], other anterior circulation, and posterior circulation aneurysms), and according to selected ASMOs before stratified randomized allocation¹⁴ are reported. Per-protocol exploratory analyses were defined in 2 ways: “As-attempted” analyses included patients in whom FD or ASMO was attempted (regardless of randomized allocation), and “as-treated” analyses included only patients in whom FD or ASMO was actually performed at the time of the initial treatment. We also explored what results would have been if complete occlusion (rather than the combination of complete and near-complete occlusion) had been used as the criterion for a good angiographic end point, to comply with a recent FDA definition and to permit comparisons with published case series and meta-analyses. The number of adverse events within the ASMO and FD groups was compared using the χ^2 test with exact *P* values. Analyses were performed using SAS software, Version 9.4 (SAS Institute) and SPSS, Version 26 (IBM) with a significance level of 5%. There was no correction of *P* values to account for the multiplicity of exploratory analyses.

Roles of the Sponsor and Funding Source

The trial was sponsored by the Centre Hospitalier de l'Université de Montréal. The sponsor had no part in study design, conduct, or reporting, and no access to the data. There was no funding source for this study.

RESULTS

The number of patients who were registered or randomly assigned received the intended treatment and were analyzed for the safety and efficacy outcomes are shown in the trial profile (Fig 1). Of 323

Table 1: Patient and aneurysm characteristics for the randomized groups

Characteristics	Randomization	
	ASMO (n = 139)	FD (n = 139)
Age (mean) (SD)	57 (12)	58 (12)
Female (No.) (%)	108 (77.7%)	110 (79.1%)
Presentation (No.) (%)		
Asymptomatic	72 (51.8%)	78 (56.1%)
Mass effect	41 (29.5%)	40 (28.8%)
SAH	26 (18.7%)	21 (15.1%)
Aneurysm size (mm)		
Mean (SD)	13 (9)	13 (10)
Median (range)	10 (2–51)	10 (1–56)
0–9 (No.) (%)	66 (47.5%)	68 (48.9%)
10–25 (No.) (%)	59 (42.4%)	54 (38.8%)
>25 (No.) (%)	14 (10.1%)	17 (12.2%)
Aneurysm neck (mm)		
Mean (SD)	5 (3)	5 (3)
Median (min–max)	5 (2–15)	5 (1–16)
Undefined (No.) (%)	22 (15.8%)	21 (15.1%)
Location (No.) (%)		
Anterior circulation	108 (77.7%)	109 (78.4%)
Proximal carotid	71 (51.1%)	74 (53.2%)
Extradural	14 (10.1%)	21 (15.1%)
Ophthalmic	57 (41.0%)	53 (38.1%)
Other carotid	20 (14.4%)	12 (8.6%)
Other anterior	17 (12.2%)	23 (16.5%)
Posterior circulation	31 (22.3%)	30 (21.6%)

Note:—min indicates minimum; max. maximum.

recruited patients between May 2011 and November 2020, two hundred seventy-eight patients (86%) were randomly allocated to receive FD (n = 139) or ASMO (n = 139), and 45 (14%) received FD in the registry because they were deemed ineligible for standard options.

Patients and aneurysms compared in the randomized trial are described in Table 1. The characteristics of registry patients are described in the Online Supplemental Data. Registry patients more frequently had fusiform aneurysms with undefined necks (22/45 or 49%) than patients included in the RCT (43/278 or 16%). Randomized groups were similar. More than 80% of patients had unruptured aneurysms. Aneurysms were ≥ 10 mm in 52% and symptomatic in 46% of patients. The ASMO selected before randomization was coiling (with or without stent placement) in 199 patients (72%), PVO in 45 (16%), surgical clipping in 11 (4%), and observation in 23 patients (8%). The specific comparator intervention of patients actually randomized to ASMO is detailed in Fig 1.

Details of the interventions actually carried out are provided in the Online Supplemental Data. High-porosity stents were used in 36/87 patients (41%) treated by coiling \pm stent placement in the ASMO group. PVO was performed using endovascular means without surgical bypass in all patients treated by PVO.

Ten patients randomly allocated to FD initially received ASMO, while 14 patients allocated to ASMO initially received FD (Fig 1 and Online Supplemental Data).

The safety of FD, predefined by protocol as mRS > 2 at 3 months in any patient treated with FD at any time (n = 209), is detailed in the Online Supplemental Data.

The primary safety outcome, death or dependency at 3 months from any cause, occurred in 16 of 138 (11.5%; 95% CI, 6.9%–

Table 2: Primary efficacy outcome

	Randomization	
	ASMO (n = 139) (No.) (%)	FD (n = 139) (No.) (%)
Poor outcome	62 (44.6%) ^a	43 (30.9%)
Clinical	13 (9.4%)	12 (8.6%)
mRS > 2 ^b	13 (9.4%)	10 (7.2%)
Aneurysm rupture	0	2 (1.4%)
Angiographic	49 (35.3%)	31 (22.3%)
Retreatment	7 (5.0%)	5 (3.6%)
Immediate failure ^c	8 (5.8%)	7 (5.0%)
Residual aneurysm	34 (24.5%)	19 (13.7%)
Good outcome	74 (53.2%)	96 (69.1%)
Angiographic	74 (53.2%)	96 (69.1%)
Complete occlusion	60 (43.2%)	85 (61.2%)
Residual neck	14 (10.1%)	11 (7.9%)
Not available	3 (2.2%)	0

^a It is 45.6% (62/136) when adjusting for missing data.

^b Comprises 14 deaths (ASMO = 9/FD = 5).

^c Immediate treatment failures are treatments that were attempted but failed, with no further angiographic follow-up.

18.3%) patients randomly allocated to FD and in 12 of 137 (8.6%; 95% CI, 4.7%–14.9%) patients allocated to ASMO (relative risk, 1.33; 95% CI, 0.65–2.69; $P = 0.439$) (Fig 1; details in the Online Supplemental Data). The most frequent causes of death or dependency at 3 months were thromboembolic (n = 14; ASMO = 7/FD = 7), followed by hemorrhagic complications (n = 7; ASMO = 3/FD = 4) and progressive mass effect from giant aneurysms (n = 7; ASMO = 2/FD = 5).

The composite primary efficacy outcome was available for 275 of 278 patients in the RCT (98.9%). A poor primary efficacy outcome was found in 30.9% (43/139; 95% CI, 23.5%–39.4%) of patients with FD and 45.6% (62/136; 95% CI, 37.1%–54.3%) with ASMO, an absolute risk difference of 14.7%, (95% CI, 3.3%–26.0%) (relative risk, 0.68; 95% CI, 0.50–0.92; $P = .014$). Details of each component of the primary outcome are provided in Table 2. Attributing a good or a bad outcome when data were missing did not significantly modify the results. The primary outcome for per-protocol analyses is detailed in the Online Supplemental Data. As-attempted and as-treated analyses yielded similar results compared with intent-to-treat analyses, with patients undergoing FD having better primary efficacy outcomes than those undergoing ASMO ($P < .001$ for both).

The mean time of follow-up mRS recorded for the primary efficacy outcome was at 12.7 (SD, 7.4) months for ASMO and 12.2 (SD, 8.0) months for FD. The mean time of angiographic follow-up included in the primary efficacy outcome measure was 11.0 (SD, 5.3) months for patients randomly allocated to ASMO and 11.6 (SD, 5.7) months for patients randomly allocated to FD.

Prespecified subgroups of interest are shown in Fig 2, even though none of the interaction tests were significant. On the basis of this description, we observed that patients preselected for coiling with or without stent placement (n = 199) who were randomly allocated to FD had better outcomes, as did patients preselected for conservative treatment who randomly underwent

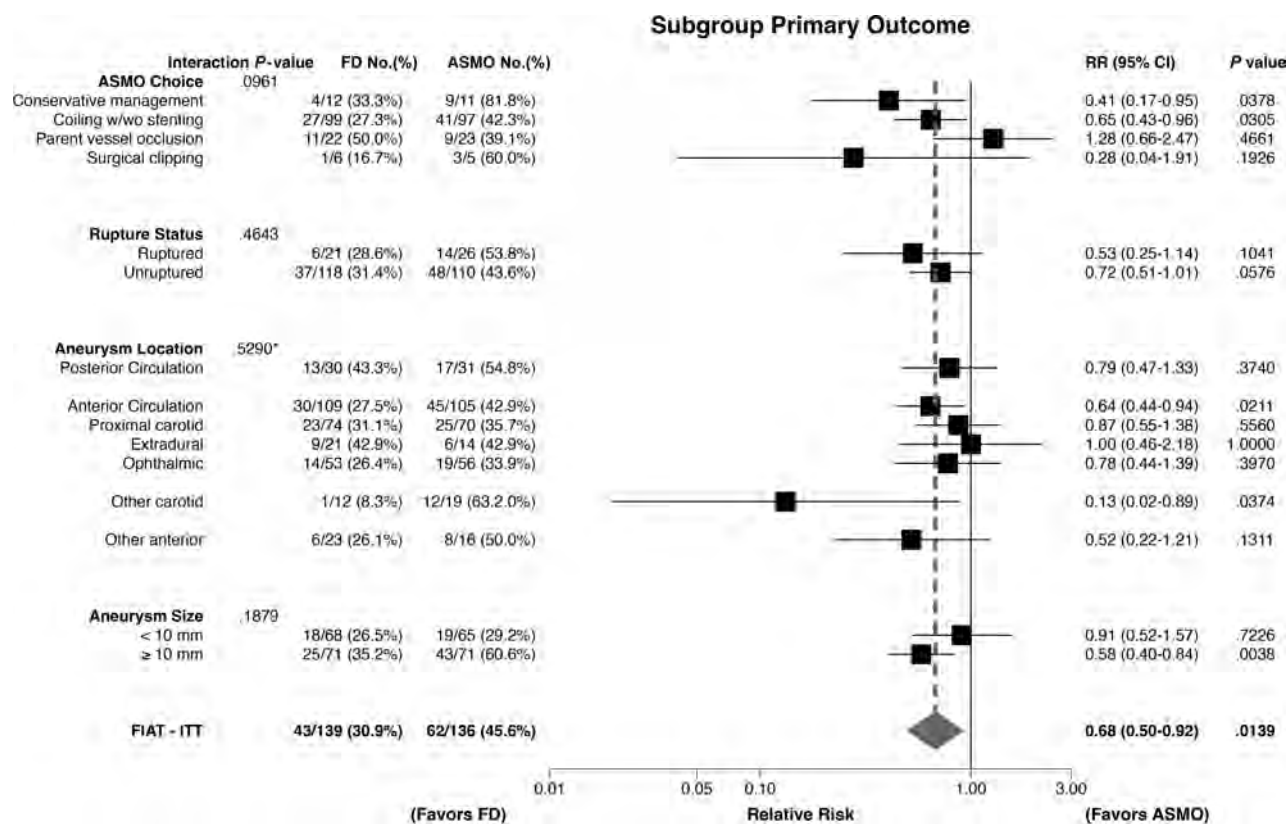


FIG 2. Subgroup analysis. Statistical analysis performed with data considered missing when the primary outcome was not available ($n = 3$). The asterisk indicates that the interaction P value for aneurysm location was calculated for the main division into anterior/posterior. w/w/o indicates with or without; ITT, intention-to-treat; RR, relative risk.

FD ($n = 23$). The comparison of FD with PVO ($n = 45$) appeared to favor PVO, but it was inconclusive. Predefined subgroup analyses according to rupture status, size, and location showed better outcomes for unruptured, anterior circulation, and large (≥ 10 mm) aneurysms, while results were similar for < 10 -mm aneurysms and inconclusive for ruptured and posterior circulation aneurysms (Fig 2).

The primary efficacy outcome, modified to restrict the definition of a good angiographic outcome to complete occlusions, also showed the superiority of FD ($P = .006$) for all patients and for the same subgroups (Online Supplemental Data).

Secondary outcomes (successful intervention, perioperative complications, days of hospitalization, discharge disposition, mRS at discharge, and retreatment of the index aneurysm during follow-up) were similar in both groups (Online Supplemental Data). Details of angiographic results are also provided in the Online Supplemental Data. Complete occlusion of the aneurysm was more frequent with FD ($P = .028$) than with ASMO. When the definition of a good angiographic outcome included residual neck in addition to complete occlusion, the difference did not reach statistical significance ($P = .09$) (Online Supplemental Data).

Serious adverse events occurred in 28 patients with FD and 27 with ASMO. The distribution of serious and nonserious adverse events was not different between groups ($P = .110$). The only differences between groups were a nonsignificantly larger number of delayed (> 1 month) serious events that occurred after FD (9 versus 3 events). Nonserious adverse events were more frequent with FD

(22 versus 9). Details are provided in the Online Supplemental Data. Details of poor clinical outcome at any time point are given for all patients in the Online Supplemental Data. The mRS scores for all patients in the RCT at 3 months and at the time of the primary efficacy outcome are detailed in the Online Supplemental Data.

DISCUSSION

FIAT is the first pragmatic trial showing improved efficacy outcomes with FD compared with other common management options. FIAT is also unique in showing that an endovascular innovation can be assessed in a randomized trial at the same time that it is introduced in clinical practice.^{13,22} This change is an important breakthrough, for neurovascular devices have so far been approved on the basis of industry-led single-arm case series of ~ 100 patients selected for regulatory approval purposes.^{2,23,24} This is problematic, for clinical usage typically expands beyond the initial regulatory indications without reliable evidence that the innovation improves patient outcomes.²⁵

FIAT successfully addressed the multiple challenges that confront trials that assess the safe introduction of promising-but-potentially risky surgical innovations. One challenge is the diversity of patients, aneurysms, and clinical presentations. Before the availability of FD, these patients were treated using various ASMOs selected according to clinical presentation, individual patient anatomy, aneurysm location and morphology, local practice patterns, and individual preferences.¹⁰ The goal of treatment also varies, from relief of symptoms of

mass effect to the prevention of life-threatening aneurysm ruptures in asymptomatic individuals. An explanatory attitude, looking for a signal that the innovation can work, fearing to lose that signal due to the noise associated with heterogeneity, might have called for multiple trials, each comparing FD in homogeneous patients eligible for only a single alternative treatment. However, this approach would not have addressed our main concern, which is whether FD actually improves patient outcomes in routine practice.²⁶

FIAT is also the prototype care trial.¹³ The guiding principle of the design is that patients are better protected when promising-but-unproven innovations are offered within a carefully controlled research context. This principle means that each item of the trial protocol must be reviewed to best protect the medical interest of participants.^{13,22} Care trials are as inclusive as possible; protocols are flexible and allow the use of the treatment the patient would have otherwise received. The comparator intervention was prespecified before stratified randomized allocation, allowing valid comparisons within subgroups.

Care trials are fully integrated into clinical practice, and involve no extra risks, tests, visits, or cost compared with routine care. Although this design allowed us to conduct the trial without the support of industry or research agencies, the lack of funding discouraged many centers from participating. The data were collected by normal care personnel at the time of routine clinical follow-up visits. The main drawback of the approach, when rigorously applied, is that blinding becomes almost impossible. To mitigate that problem, we used a standardized, simplified mRS questionnaire¹⁸ and dichotomized results for a more difficult end point, death or dependency, which is more resistant to bias. This approach has been shown to be reliable.²⁷

The primary end point of the trial was a composite that attempted to capture in 1 judgment the comparative value of treatment in terms of safety and efficacy. This outcome combined clinical results (an independent functional score [mRS <3], which is the scale most frequently used in stroke trials) and the absence of clinical events signaling treatment failure during follow-up (such as aneurysm rupture, progressive mass effect, or retreatment of the index aneurysm). To account for the relatively short follow-up compared with lifetime protection against ruptures, which is the goal of treatment in many patients, the primary outcome included an angiographic result: complete or near-complete occlusion of the aneurysm. Angiographic outcomes are routinely used in practice to judge the success of therapy.²⁸ They are also the most common primary outcome of aneurysm trials.^{20,28-33} Residual aneurysm was used to judge treatment failure because this category has been shown to be repeatable and its clinical significance is more constant across various raters, imaging modalities, and treatments.^{20,21} The exploratory analyses we performed showed that using complete or near-complete occlusion as the angiographic outcome did not change the conclusions.

The overall morbidity and mortality of patients treated in FIAT are relatively high compared with these outcomes in other endovascular trials.³⁴⁻³⁶ However, those comparisons are not valid because aneurysms considered for FD in FIAT were typically larger, more frequently had symptoms of mass effect, and many were difficult to treat by any and all methods. The primary safety outcome for all patients who received FD (26/209 or 12%;

Online Supplemental Data) was at the upper limit of our initial estimate (10%) but similar that in to another randomized trial that compared FD with stent-assisted coiling.¹¹ In the Parent Artery Reconstruction for Large or Giant Cerebral Aneurysms Using a Tubridge Flow Diverter (PARAT) trial, the rates of death or stroke related to target vessels at 1-year follow-up were 14% and 17% in the stent-assisted coiling and FD groups, respectively.¹¹ Delayed complications, such as aneurysm ruptures, parenchymal hematomas at a distance from the aneurysm, and strokes from stent thrombosis were infrequent (10/209 or 4.8% of all patients having undergone FD in FIAT; Online Supplemental Data), but they remain a concern if FD is to be widely used.

The trial was all-inclusive, but not all patients with aneurysms were considered for FD, and results may not apply to all patients. To examine how study results could apply in clinical decision-making, one must examine prespecified subgroups of patients, even if the interaction tests were not statistically significant. The interaction test examines the potential influence of a variable on a single relative treatment effect, an implausible assumption in this trial comparing FD with as widely different options as conservative management and PVO. Nevertheless, subgroup results should always be interpreted with caution.

Examining the prespecified subgroups defined according to the comparator ASMO showed that FD was more effective than coiling with or without stent placement, but comparisons with PVO or surgical clipping were too few to draw firm conclusions.

Because of the pragmatic nature of the trial, conservative management was a potential prespecified ASMO (actually selected in 23 or 8% of patients in the RCT). This design choice may seem to unfairly favor FD. However, the alternative, to exclude these patients from the RCT, would have deprived the trial of the capacity to show this important advance provided by FD, ie, the ability to treat patients who otherwise could not be treated.

For prespecified aneurysm characteristics, FD was shown to be superior in the treatment of large, unruptured intradural carotid aneurysms (>10 mm), confirming the results of a previous trial.¹¹ For the initially approved regulatory indications for the use of FD (proximal carotid aneurysms), results were neutral, for they pull in opposite directions. Many large or giant extradural carotid aneurysms were treated with PVO, a treatment subgroup that was superior to FD (but not significantly) (Fig 2). Another trial showed FD to be less effective (but safer) than surgical occlusion and bypass in the treatment of complex anterior circulation aneurysms.¹² Surgical bypass was not used in FIAT, even in combination with PVO, and the RCT included only those patients with a circle of Willis that allowed safe carotid occlusion without bypass. PVO remains a good option for these selected patients.³⁷

Posterior circulation aneurysms have been shown in observational studies to have worse outcomes after FD than anterior circulation aneurysms, but FIAT randomized results show that ASMOs did not perform better for these difficult lesions (Fig 2).²⁵

There are a priori concerns with the use of antiplatelet regimens that come with the use of FD in patients with SAH from a recently ruptured aneurysm.³⁸ Too few patients with SAH were included in FIAT for conclusions to be drawn about FD use in these patients.

For the most frequently encountered small (<10 mm), unruptured, asymptomatic, intradural aneurysms, the primary efficacy

outcome was similar for patients treated with FD or ASMO. Only by looking at the rate of complete occlusion in exploratory analyses can a signal possibly favoring FD be detected (Online Supplemental Data). FIAT results are in accordance with performance goals for FD of small and medium aneurysms that have recently been proposed (morbidity/mortality in 7.8% of patients [4.8%–11.4%]).³⁹ Subgroup safety data for coiling with or without stent placement (3%; 95% CI, 0%–8.5%) and for the corresponding stratified patients with FD (5%; 95% CI, 1.6%–11.4%) were comparable in FIAT, but a larger RCT would be needed for the ongoing concern of delayed complications with FD related to antiplatelet regimens and delayed stent thrombosis. Some believe that a 5%–8% risk may already be too high to justify the preventive treatment of small unruptured aneurysms.⁹ The pertinent question regarding small asymptomatic aneurysms is whether they should even be treated at all.⁴⁰ A pragmatic RCT has recently been launched to address this question.⁴¹

There are limitations to this study: Only 3 Canadian centers participated, limiting the generalizability of results. The recruitment period had to be increased to nearly 10 years, during which the indications for FD are likely to have changed. FIAT is the largest RCT on FD so far, but the number of patients remains small. On final analysis, safety results include the possibility of harm or benefit compared with other management options. Prerandomization resulted in 24 crossovers (8.6%) that dilute the contrast between groups. An aneurysm for which FD is considered a promising treatment is a vague definition that may be differently interpreted from one clinician to another and that may also change with time and experience. Clinical outcome assessment and core lab adjudications could not be masked to treatment allocation. Trial results were mainly driven by angiographic results, and the hard clinical outcome (death or dependency) accounted for a relatively small number of poor outcomes in both groups (13 versus 10 patients, including 9 versus 5 deaths). Potential bias from lack of blinding of mRS clinical assessors should not have significantly affected the results. The 12-month follow-up period was relatively short; too short to evaluate the effects of treatment on aneurysm rupture. In addition, this follow-up may not have given enough time for some FD-treated aneurysms to become occluded or for some recurrences after coiling to become apparent.⁴²

CONCLUSIONS

For patients with mostly unruptured, large, anterior circulation (carotid) aneurysms, FD was more effective than ASMO in terms of angiographic outcome. More randomized trials are needed to assess safety.







Disclosure forms provided by the authors are available with the full text and PDF of this article at www.ajnr.org.

REFERENCES

- Arrese I, Sarabia R, Pintado R, et al. **Flow-diverter devices for intracranial aneurysms: systematic review and meta-analysis.** *Neurosurgery* 2013;73:193–99; discussion 199–200 CrossRef Medline
- Becske T, Kallmes DF, Saatci I, et al. **Pipeline for uncoilable or failed aneurysms: results from a multicenter clinical trial.** *Radiology* 2013;267:858–68 CrossRef Medline
- Brinjikji W, Murad MH, Lanzino G, et al. **Endovascular treatment of intracranial aneurysms with flow diverters: a meta-analysis.** *Stroke* 2013;44:442–47 CrossRef Medline
- Wakhloo AK, Schellhammer F, de Vries J, et al. **Self-expanding and balloon-expandable stents in the treatment of carotid aneurysms: an experimental study in a canine model.** *AJNR Am J Neuroradiol* 1994;15:493–502 Medline
- Darsaut TE, Bing F, Salazkin I, et al. **Flow diverters can occlude aneurysms and preserve arterial branches: a new experimental model.** *AJNR Am J Neuroradiol* 2012;33:2004–09 CrossRef Medline
- Kulcsar Z, Houdart E, Bonafe A, et al. **Intra-aneurysmal thrombosis as a possible cause of delayed aneurysm rupture after flow-diversion treatment.** *AJNR Am J Neuroradiol* 2011;32:20–25 CrossRef Medline
- Park MS, Albuquerque FC, Nanaszko M, et al. **Critical assessment of complications associated with use of the Pipeline Embolization Device.** *J Neurointerv Surg* 2015;7:652–59 CrossRef Medline
- Houdart E. **Meta-analysis as a symptom: the example of flow diverters.** *AJNR Am J Neuroradiol* 2020;41:E51 CrossRef Medline
- Houdart E. **Commentary about a 20th meta-analysis.** *J Neurointerv Surg* 2021;13:e19 CrossRef Medline
- Darsaut TE, Gentric JC, McDougall CM, et al. **Uncertainty and agreement regarding the role of flow diversion in the management of difficult aneurysms.** *AJNR Am J Neuroradiol* 2015;36:930–36 CrossRef Medline
- Liu JM, Zhou Y, Li Y, et al. **Parent Artery Reconstruction for Large or Giant Cerebral Aneurysms Using the Tubridge Flow Diverter: a multicenter, randomized, controlled clinical trial (PARAT).** *AJNR Am J Neuroradiol* 2018;39:807–16 CrossRef Medline
- Kiselev R, Orlov K, Dubovoy A, et al. **Flow diversion versus parent artery occlusion with bypass in the treatment of complex intracranial aneurysms: immediate and short-term outcomes of the randomized trial.** *Clin Neurol Neurosurg* 2018;172:183–89 CrossRef Medline
- Raymond J, Darsaut TE, Altman DG. **Pragmatic trials can be designed as optimal medical care: principles and methods of care trials.** *J Clin Epidemiol* 2014;67:1150–56 CrossRef Medline
- Raymond J, Darsaut TE, Guilbert F, et al. **Flow diversion in aneurysms trial: the design of the FIAT study.** *Interv Neuroradiol* 2011;17:147–53 CrossRef Medline
- Raymond J, Gentric JC, Darsaut TE, et al. **Flow diversion in the treatment of aneurysms: a randomized care trial and registry.** *J Neurosurg* 2017;127:454–62 CrossRef Medline
- Zelen M. **Randomized consent designs for clinical trials: an update.** *Stat Med* 1990;9:645–66 CrossRef Medline
- Raymond J, Darsaut TE, Roy DJ. **Recruitment in clinical trials: the use of Zelen's prerandomization in recent neurovascular studies.** *World Neurosurg* 2017;98:403–10 CrossRef Medline
- Bruno A, Shah N, Lin C, et al. **Improving modified Rankin Scale assessment with a simplified questionnaire.** *Stroke* 2010;41:1048–50 CrossRef Medline
- Altman DG, Whitehead J, Parmar MK, et al. **Randomised consent designs in cancer clinical trials.** *Eur J Cancer* 1995;31A:1934–44 CrossRef Medline
- Benomar A, Farzin B, Volders D, et al. **Angiographic results of surgical or endovascular treatment of intracranial aneurysms: a systematic review and inter-observer reliability study.** *Neuroradiology* 2021;63:1511–19 CrossRef Medline
- Benomar A, Farzin B, Gevry G, et al. **Noninvasive angiographic results of clipped or coiled intracranial aneurysms: an inter- and intraobserver reliability study.** *AJNR Am J Neuroradiol* 2021;42:1615–20 CrossRef Medline
- Darsaut TE, Raymond J. **Ethical care requires pragmatic care research to guide medical practice under uncertainty.** *Trials* 2021;22:143 CrossRef Medline
- Raymond J, Fahed R, Roy D, et al. **The 2018 ter Brugge Lecture: problems with the Introduction of Innovations in Neurovascular Care.** *Can J Neurol Sci* 2019;46:151–58 CrossRef Medline

24. Fahed R, Darsaut TE, Raymond J. **The Introduction of Innovations in Neurovascular Care: patient selection and randomized allocation.** *World Neurosurg* 2018;118:e99–104 CrossRef Medline
25. Kallmes DF, Hanel R, Lopes D, et al. **International retrospective study of the Pipeline Embolization Device: a multicenter aneurysm treatment study.** *AJNR Am J Neuroradiol* 2015;36:108–15 CrossRef Medline
26. Kallmes DF, Brinjikji W, Rabinstein AA. **Letter to the editor: flow diversion in the treatment of intracranial aneurysm trial.** *J Neurosurg* 2017;127:703–07 CrossRef Medline
27. Bacchus E, Kate MP, Benomar A, et al. **Inter-rater reliability of the simplified Modified Rankin Scale as an outcome measure for treated cerebral aneurysm patients.** *Neurochirurgie* 2022 June 5. [Epub ahead of print] CrossRef Medline
28. Darsaut TE, Chapot R, Raymond J. **Changing the rules of the game: the problem of surrogate angiographic outcomes in the evaluation of aneurysm treatments.** *AJNR Am J Neuroradiol* 2020;41:2174–75 CrossRef Medline
29. White PM, Lewis SC, Gholkar A, et al; HELPS Trial Orators. **Hydrogel-coated coils versus bare platinum coils for the endovascular treatment of intracranial aneurysms (HELPS): a randomised controlled trial.** *Lancet* 2011;377:1655–62 CrossRef Medline
30. Raymond J, Roy D, White PM, et al; the ICONA Collaborative Group. **A randomized trial comparing platinum and hydrogel-coated coils in Patients Prone to Recurrence after Endovascular Treatment (the PRET Trial).** *Interv Neuroradiol* 2008;14:73–83 CrossRef Medline
31. Darsaut TE, Findlay JM, Raymond J; CURES Collaborative Group. **The design of the Canadian UnRuptured Endovascular versus Surgery (CURES) trial.** *Can J Neurol Sci* 2011;38:236–41 CrossRef Medline
32. Darsaut TE, Raymond J. **STAT Collaborative Group. The design of the STenting in Aneurysm Treatments (STAT) trial.** *J Neurointerv Surg* 2012;4:178–81 CrossRef Medline
33. Raymond J, Januel AC, Iancu D, et al. **The RISE trial: A Randomized Trial on Intra-Saccular Endobridge devices.** *Interv Neuroradiol* 2020;26:61–67 CrossRef Medline
34. McDougall CG, Johnston SC, Gholkar A, et al; MAPS Investigators. **Bioactive versus bare platinum coils in the treatment of intracranial aneurysms: the MAPS (Matrix and Platinum Science) trial.** *AJNR Am J Neuroradiol* 2014;35:935–42 CrossRef Medline
35. Molyneux AJ, Clarke A, Sneade M, et al. **Cerecyte coil trial: angiographic outcomes of a prospective randomized trial comparing endovascular coiling of cerebral aneurysms with either Cerecyte or bare platinum coils.** *Stroke* 2012;43:2544–50 CrossRef Medline
36. Raymond J, Klink R, Chagnon M, et al; PRET Collaborative Group. **Patients prone to recurrence after endovascular treatment: periprocedural results of the PRET randomized trial on large and recurrent aneurysms.** *AJNR Am J Neuroradiol* 2014;35:1667–76 CrossRef Medline
37. Cagnazzo F, Mantilla D, Rouchaud A, et al. **Endovascular treatment of very large and giant intracranial aneurysms: comparison between reconstructive and deconstructive techniques-a meta-analysis.** *AJNR Am J Neuroradiol* 2018;39:852–58 CrossRef Medline
38. Madaelil TP, Moran CJ, Cross DT 3rd, et al. **Flow diversion in ruptured intracranial aneurysms: a meta-analysis.** *AJNR Am J Neuroradiol* 2017;38:590–95 CrossRef Medline
39. Fiorella D, Gache L, Frame D, et al. **How safe and effective are flow diverters for the treatment of unruptured small/medium intracranial aneurysms of the internal carotid artery? Meta-analysis for evidence-based performance goals.** *J Neurointerv Surg* 2020;12:869–73 CrossRef Medline
40. Raymond J, Darsaut TE, Molyneux AJ; TEAM Collaborative Group. **A trial on unruptured intracranial aneurysms (the TEAM trial): results, lessons from a failure and the necessity for clinical care trials.** *Trials* 2011;12:64 CrossRef Medline
41. Darsaut TE, Desal H, Cognard C, et al. **Comprehensive Aneurysm Management (CAM): an all-inclusive care trial for unruptured intracranial aneurysms.** *World Neurosurg* 2020;141:e770–77 CrossRef Medline
42. Lecler A, Raymond J, Rodriguez-Regent C, et al. **Intracranial aneurysms: recurrences more than 10 years after endovascular treatment: a prospective cohort study, systematic review, and meta-analysis.** *Radiology* 2015;277:173–80 CrossRef Medline

3D Enhancement Color Maps in the Characterization of Intracranial Atherosclerotic Plaques

 S. Sanchez,  A. Raghuram,  R. Fakhri,  L. Wendt,  G. Bathla,  M. Hickerson,  S. Ortega-Gutierrez,  E. Leira, and  E.A. Samaniego



ABSTRACT

BACKGROUND AND PURPOSE: High-resolution MR imaging allows the identification of culprit symptomatic plaques after the administration of gadolinium. Current high-resolution MR imaging methods are limited by 2D multiplanar views and manual sampling of ROIs. We analyzed a new 3D method to objectively quantify gadolinium plaque enhancement.

MATERIALS AND METHODS: Patients with stroke due to intracranial atherosclerotic disease underwent 7T high-resolution MR imaging. 3D segmentations of the plaque and its parent vessel were generated. Signal intensity probes were automatically extended from the lumen into the plaque and the vessel wall to generate 3D enhancement color maps. Plaque gadolinium (Gd) uptake was quantified from 3D color maps as gadolinium uptake = $(\mu_{\text{Plaque TI}} + \text{Gd} - \mu_{\text{Plaque TI}}) / \text{SD}_{\text{Plaque TI}}$. Additional metrics of enhancement such as enhancement ratio, variance, and plaque-versus-parent vessel enhancement were also calculated. Conventional 2D measures of enhancement were collected for comparison.

RESULTS: Thirty-six culprit and 44 nonculprit plaques from 36 patients were analyzed. Culprit plaques had higher gadolinium uptake than nonculprit plaques ($P < .001$). Gadolinium uptake was the most accurate metric for identifying culprit plaques (OR, 3.9; 95% CI 2.1–8.3). Gadolinium uptake was more sensitive (86% versus 70%) and specific (71% versus 68%) in identifying culprit plaques than conventional 2D measurements. A multivariate model, including gadolinium uptake and plaque burden, identified culprit plaques with an 83% sensitivity and 86% specificity.

CONCLUSIONS: The new 3D color map method of plaque-enhancement analysis is more accurate for identifying culprit plaques than conventional 2D methods. This new method generates a new set of metrics that could potentially be used to assess disease progression.

ABBREVIATIONS: Gd = gadolinium; HR = high-resolution; ICAD = intracranial atherosclerotic disease; IPH = intraplaque hemorrhage; PB = plaque burden; RI = remodeling index; SI = signal intensity

Intracranial atherosclerotic disease (ICAD) can account for 10% of TIAs and 30%–50% of ischemic strokes.¹ The main criterion for diagnosing and monitoring ICAD relies on luminal stenosis. More

accurate methods of detecting the presence of atherosclerotic plaques and monitoring disease progression are needed. There is growing evidence that high-resolution MR imaging (HR-MR imaging) can be used to better characterize atherosclerotic plaques than current luminal imaging modalities. HR-MR imaging can be used to determine plaque burden (PB) and the remodeling index (RI) and detect plaque enhancement after the administration of gadolinium (Gd) contrast. Two meta-analyses of biomarkers of symptomatic ICAD have shown that plaque enhancement has the strongest association with the presence of culprit symptomatic plaques.^{2,3}

Different biologic processes lead to plaque enhancement, including neovascularization, inflammation, and endothelial dysfunction. The analysis of atherosclerotic carotid plaques has shown a correlation between these histopathologic changes and plaque enhancement.⁴ Plaque enhancement is highly suggestive of an “active” plaque that might be symptomatic.⁵ Moreover, strong plaque enhancement suggests greater neovascularization and increased

Received January 27, 2022; accepted after revision June 24.

From the Departments of Neurology (S.S., A.R., R.F., M.H., S.O.-G., E.L., E.A.S.), Radiology (G.B., S.O.-G., E.A.S.), and Neurosurgery (S.O.-G., E.A.S.), University of Iowa Hospitals and Clinics, Iowa City, Iowa; and Institute for Clinical and Translational Science (L.W.), University of Iowa, Iowa City, Iowa.

This study was funded by a Pilot Research Grant from the Society of Vascular and Interventional Neurology granted to Dr Edgar Samaniego. Statistical analysis for this study was supported by the Clinical and Translational Science Award Grant funded from the National Institutes of Health (UL1TR002537). Image and data acquisition was performed using an MR imaging instrument funded by 1S10RR028821-01.

Please address correspondence to Edgar A. Samaniego, MD, MS, Departments of Neurology, Neurosurgery and Radiology, University of Iowa Hospitals and Clinics, 200 Hawkins Dr, Iowa City, IA 52246; e-mail: edgarsama@gmail.com; @esamaniego

 Indicates open access to non-subscribers at www.ajnr.org

 Indicates article with online supplemental data.

<http://dx.doi.org/10.3174/ajnr.A7605>

endothelial permeability. Hence, the exact quantification of plaque enhancement could potentially provide an insight into the biology of intracranial atherosclerosis, by detecting changes such as wall thickening and hemorrhage.⁶ Accurately quantifying plaque enhancement also has the potential of identifying ICAD mimics such as venous plexus contamination and thrombus recanalization, among others.⁷

Current analyses of plaque enhancement are based on 2D imaging sampling and manual determination of ROIs.^{8,9} This approach is limited by sampling errors and the plane of view chosen to draw the ROIs. We describe a new 3D method of plaque sampling that captures the entire plaque and parent artery. This method generates hundreds of data points to determine the level of plaque enhancement, overcoming the limitation of restricting the analysis to a specific plane of view that might not represent the enhancement of the entire plaque. We hypothesize that this new method of 3D plaque enhancement color mapping will lead to better identification of symptomatic atherosclerotic plaques.

MATERIALS AND METHODS

Image Acquisition

After approval from the institutional review board (University of Iowa) and obtaining informed consent, patients with stroke attributable to ICAD underwent 7T MR imaging. The ICAD stroke etiology was adjudicated on the basis of Trial of Org 10172 in Acute Stroke Treatment (TOAST) and ASCOD (A, atherosclerosis; S, small-vessel disease; C, cardiac pathology; O, other causes; and D, dissection) criteria.^{10,11} Patients were excluded if they had any contraindication to 7T MR imaging, were medically unstable, or had a glomerular filtration rate of <45 mL/min per 1.73 m². Images were obtained between August 2018 and July 2021.

HR-MR imaging was acquired with a MR950 7T scanner (GE Healthcare) using an 8-channel head coil. 3D T1-weighted FSE (Cube; GE Healthcare) images were acquired both before and 5 minutes after the administration of Gd. Technical parameters for acquisition are described in the Online Supplemental Data. Images were analyzed in at least 3 planes to identify the presence of atherosclerotic plaques using the PACS. Plaque presence was defined as wall thickening of a vessel segment compared with the proximal and/or normal vessel segment.⁹ A senior investigator analyzed the following arterial segments in each subject to identify the presence of plaques: supraclinoid internal carotid arteries, MCAs, anterior cerebral arteries, V4 segments of the vertebral arteries, basilar artery, and posterior cerebral arteries. The specific stroke mechanism due to ICAD was also adjudicated by the senior investigator on the basis of previously described criteria.¹² The Warfarin-Aspirin Symptomatic Intracranial Disease (WASID)-based degree of stenosis, RI, and the area degree of stenosis were manually calculated in several planes, as previously described.¹³⁻¹⁵ PB was calculated with the following formula: [(Area of the Vessel Wall at Maximal Stenosis – Area of the Lumen at Maximal Stenosis)/Area of the Vessel Wall at Maximal Stenosis] × 100].¹⁵

Plaque Characterization

Plaques were detected by a senior investigator, and culprit status was adjudicated by 2 investigators with extensive experience in the analysis of plaques using HR-MR imaging. If there was disagreement, the

senior investigator adjudicated the culprit status. Generally, a culprit plaque was defined as a lesion in the ipsilateral vascular territory of an area of infarction accompanied by clinical symptoms. If >1 plaque was present in the same vascular territory, the most stenotic lesion was selected for analysis. Areas of cerebral infarction related to the presence of culprit plaques were identified in DWI. Other plaques in the same vascular territory of culprit plaques were excluded from the analysis. Plaques located in other vascular territories were considered asymptomatic or nonculprit. Disagreements were resolved by consensus and after reviewing additional images and clinical data. The morphologic characteristics and enhancement patterns of culprit plaques were compared with those of nonculprit plaques. Additionally, the presence of intraplaque hemorrhage (IPH) was assessed by 2 investigators (S.S. and E.A.S.) by identifying T1 hyperintensity within the plaque.¹⁶

3D Plaque Analysis

We modified a previously described semiautomated method of analyzing Gd enhancement in the wall of brain aneurysms to study plaques and their parent arteries.¹⁷ Luminal segmentations in the vascular territory of the plaque were created manually using 3D Slicer (<http://www.slicer.org>) on T1 and T1 + Gd images.¹⁸ The diseased arterial segment containing the plaque was segmented at the plaque and extended approximately 5 mm beyond the plaque boundaries so that the plaque and the contiguous parent artery were included. Segmentations were performed by 2 investigators with at least 1 year of experience (S.S. and A.R.). In case of disagreement, the senior investigator adjudicated the proper parent vessel and plaque boundaries.

Signal intensity (SI) probes were orthogonally extended from the lumen into the plaque and arterial wall (Fig 1). The high spatial resolution of 7T imaging made it possible to accurately estimate the arterial wall and plaque thickness. For parent vessel analysis, SI probes were extended 0.5 mm into the arterial wall of the parent vessel, which is the average wall thickness used in our analysis and has been reported by others in ex vivo samples.¹⁹ For plaque analysis, the length of the probe was customized on the basis of detailed measurements of plaque thickness obtained on 7T MR images (Fig 2). SI color maps were generated through an automated process using image-processing tools and custom scripts in Matlab 2020b (MathWorks). The SI of the plaque and arterial wall was mapped from T1 and T1 + Gd images separately (Fig 3). The SI of the genu of the corpus callosum was used to obtain a normalized mean enhancement ratio. In addition, conventional 2D CR_{Stalk} was calculated for comparison.⁹

3D Analysis of Plaque Enhancement

The highest SI of each probe on the T1 and T1 + Gd images was obtained for the analysis. The mean (μ) SI and SD of each plaque and parent artery were calculated. These values were then divided by the SI of the corpus callosum to obtain a normalized ratio that could be used to compare among subjects. We studied the following enhancement metrics:

1) Mean enhancement ratio = mean SI on T1 + Gd images normalized to the corpus callosum. This is the standard measurement of contrast enhancement.

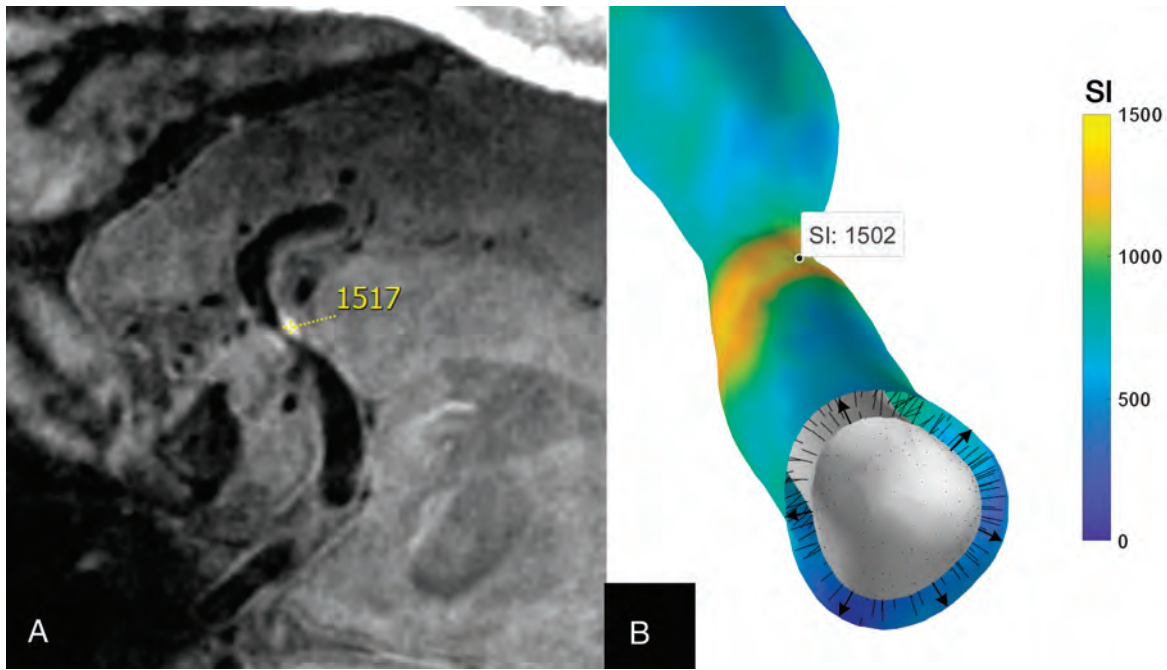


FIG 1. Generation of 3D enhancement maps. *A*, The SI sampled in high-resolution 7T MR imaging is almost the same as that generated with 3D mapping: 1517 and 1502, respectively. *B*, SI probes (arrows) extend from the arterial lumen to the plaque and contiguous vessel wall. An average of 125 probes or data points were generated per plaque, and 858, per arterial segment. This technique makes it possible to generate a detailed color map of Gd enhancement.

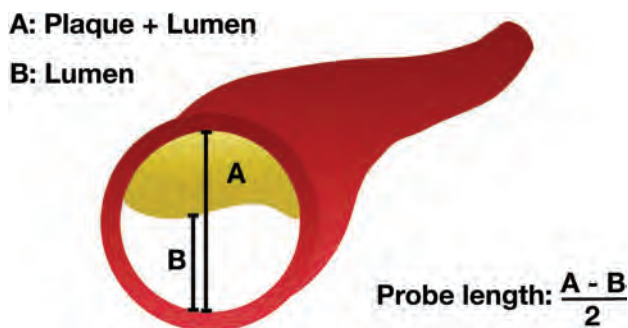


FIG 2. Schematic representation of how the SI probe length was determined. The plaque thickness was estimated using the sum of the diameter of the plaque and the lumen minus the diameter of the lumen, divided by 2. Measurements were obtained at the most stenotic segment. Thus, the probe did not extend beyond the plaque.

2) Plaque enhancement variance = SD^2 of the SI values measured by the probes on T1 + Gd images. This measurement was used to analyze the dispersion of enhancement within the plaque.

3) Gd-uptake, which measured the amount of Gd absorbed by the plaque compared with T1, using the following equation:

$$\text{Gd Uptake} = \frac{\mu_{\text{PlaqueT1+ Gd}} - \mu_{\text{PlaqueT1}}}{SD_{\text{PlaqueT1}}}.$$

Previous studies have shown that culprit plaques had higher SDs in T1 images compared with nonculprit plaques.²⁰ To account for this baseline variation, we decided to include SD as a normalization factor in our analysis.

4) Plaque versus arterial enhancement, which measured the difference in the mean enhancement of the plaque compared with the parent artery.

$$\text{Plaque vs Arterial Enhancement} = \frac{\mu_{\text{PlaqueT1+ Gd}} - \mu_{\text{VesselT1+ Gd}}}{SD_{\text{VesselT1+ Gd}}}.$$

Because we analyzed plaques in different arteries, the SD of the arterial SI was used for normalization and to perform standardized comparisons of plaques in different territories.²⁰

Statistical Analysis

Various statistical analyses were conducted using SPSS Statistics 27.0 (IBM). Interrater reliability in the identification of culprit plaques was calculated with a Cohen κ coefficient. Categorical variables are presented as frequency and percentage, and continuous variables are described as mean (SD). Shapiro-Wilk tests were used to evaluate normality for variables of interest within our sample, with P values of $<.05$ considered non-normally distributed variables. A Student t test was used to compare the means between normally distributed variables, and a Mann-Whitney U test was used to compare the distributions between non-normally distributed variables. χ^2 tests were used to compare categorical variables. Univariate logistic regressions were performed to analyze relevant demographic, morphologic, and SI variables. An α threshold of .05 was used to assess significance for all hypothesis tests.

The multivariate model in this analysis was constructed through an Akaike information criterion-based forward selection procedure. All variables of interest in the data set were initially

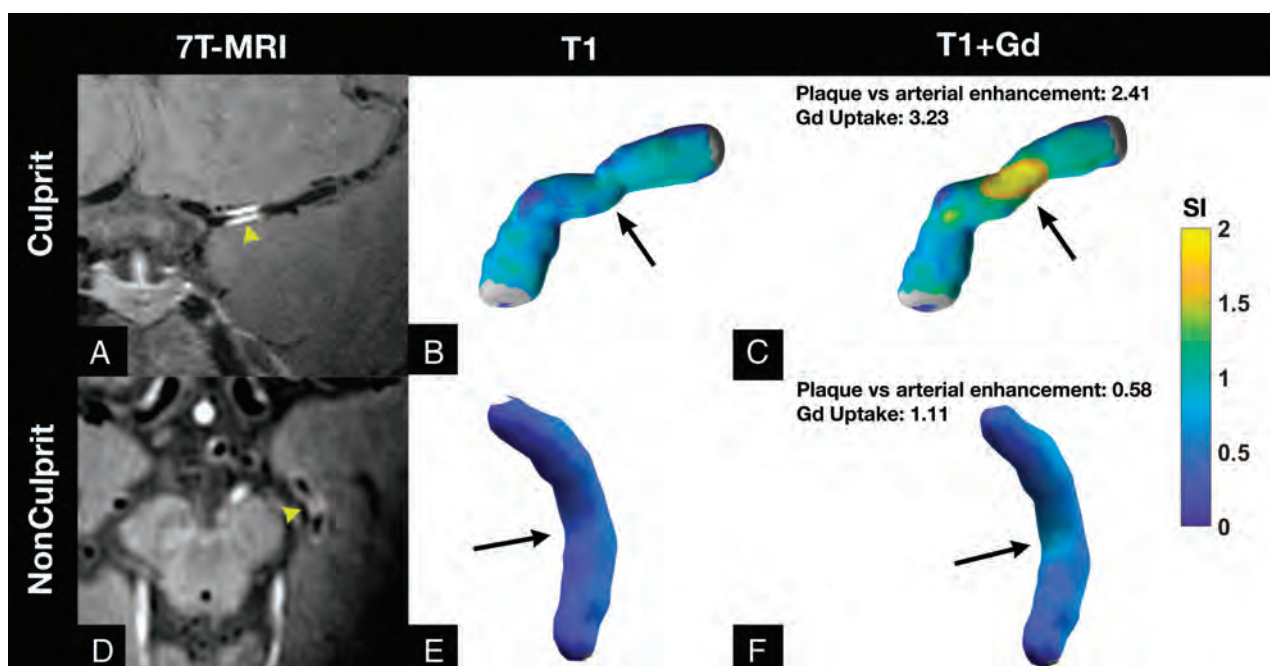


FIG 3. 3D enhancement maps of culprit and nonculprit plaques. *Upper row:* A, A left MCA culprit plaque is seen in a 7T MR imaging coronal view (yellow arrowhead). The 3D reconstruction color maps of this MCA plaque in T1 (B) and T1 + Gd images (C) show a high concentration of plaque enhancement (black arrow). *Lower row:* D, A nonculprit area of enhancement is seen in the left posterior cerebral artery on 7T MR imaging (yellow arrowhead). The 3D color map is depicted in T1 (E) and T1 + Gd (F) images. D, On 7T MR imaging, this arterial segment appears highly enhancing (yellow arrowhead). F, However, the 3D color map does not show avid enhancement (black arrow). Moreover, this arterial segment has lower Gd uptake and plaque versus arterial enhancement than the culprit plaque.

Table 1: Plaque characteristics

	Culprit (n = 36)	Nonculprit (n = 44)	P Values
Plaques (%) (No.)			
MCA	50 (18)	40.9 (18)	
ICA	13.9 (5)	20.5 (9)	
ACA	0	13.6 (6)	
Basilar artery	19.4 (7)	4.5 (2)	
PCA	2.8 (1)	20.5 (9)	
VA	13.9 (5)	0 (0)	
Morphology			
Concentric (%) (No.)	72 (26)	20 (9)	<.001 ^a
Stenosis (%) (mean)	46 (SD, 21)	31 (SD, 15)	.001 ^a
PB (%) (mean)	85 (SD, 13)	65 (SD, 14)	<.001 ^a
RI (mean)	0.37 (SD, 0.27)	0.65 (SD, 0.22)	<.001 ^a
Area of stenosis (%) (mean)	64 (SD, 24)	35 (SD, 22)	<.001 ^a
IPH (%) (No.)	11 (4)	0 (0)	.025 ^a
Enhancement			
Mean enhancement ratio plaque ^b	0.80 (SD, 0.30)	0.61 (SD, 0.17)	.004 ^a
Plaque enhancement variance	0.33 (SD, 0.13)	0.26 (SD, 0.08)	.041 ^a
Gd uptake	2.01 (SD, 0.91)	1.06 (SD, 0.76)	<.001 ^a
Mean enhancement ratio parent vessel ^b	0.59 (SD, 0.20)	0.62 (SD, 0.14)	.62
Plaque vs arterial enhancement	0.99 (SD, 0.94)	−0.02 (SD, 0.48)	<.001 ^a

Note:—ACA indicates anterior cerebral artery; PCA, posterior cerebral artery; VA, vertebral artery.

^a P < .05.

^b Reported as mean SI.

considered candidates for the multivariate model. The variable that reduced the Akaike information criterion of the model the most when added was included in the model. Other variables were included in the model only if they had a correlation of <0.5 with

each variable that was already added to the model. Once there were no remaining variables that reduced the Akaike information criterion value of the multivariate model or had correlations of <0.5 with each variable present in the multivariate model, the algorithm was terminated, and the resulting model was selected.

Receiver operator characteristic metrics, including sensitivity and specificity, were calculated for each variable of interest (including the predictions output from the multivariable model) at its optimal threshold value, as determined by the Youden J statistic. Area under the curve values for each variable were also computed.

RESULTS

Patients and Plaque Characteristics

Thirty-six patients with a total of 80 plaques were included in the analysis.

Approximately 47.2% were men, and the mean age was 59 (SD, 12) years. The mean NIHSS score at admission was 2.5 (SD, 3). Additional demographics are described in the Online Supplemental Data. Areas of cerebral infarction with DWI findings are reported

Table 2: Univariate and multivariate logistic regression

Characteristic	Univariate Logistic Regression			Multivariate Analysis		
	OR ^a	95% CI	P Value	OR ^a	95% CI	P Value
Mean enhancement ratio plaque	2.3	1.4–4.1	.002			
Plaque enhancement variance	1.9	1.2–3.2	.013			
Plaque vs vessel enhancement	7.4	3.2–22	<.001 ^a			
Location ^b	1.5	0.6–4	.4			
Morphology	10.1	3.7–30	<.001 ^c			
Area of stenosis	4	2.3–8	<.001 ^c			
Stenosis	2.4	1.5–4.3	.001 ^c	1.3	0.7–2.7	.4
Gd uptake	3.9	2.1–8.3	<.001 ^c	2.3	1.1–5.3	.033 ^c
PB	6.1	3–14.9	<.001 ^c	3.7	1.6–10	.004 ^c

^a One SD increase in each variable.

^b Anterior-versus-posterior circulation.

^c $P < .05$.

in the Online Supplemental Data. The agreement in the identification of culprit plaques was high ($\kappa = 0.8$). Culprit plaques had a higher degree of stenosis, PB, and RI than nonculprit plaques. In addition, culprit plaques more frequently had a concentric morphology than nonculprit plaques (Table 1).

3D Enhancement Characterization

A mean of 125 (SD, 79) probes per plaque were generated. Culprit plaques had a higher mean enhancement ratio than nonculprit plaques ($\mu = 0.80$ [SD, 0.30] versus 0.61 [SD, 0.17]; $P = .004$). This enhancement was more heterogeneous in culprit plaques than in nonculprit plaques ($SD^2 = 0.33$ [SD, 0.13] versus 0.26 [SD, 0.08]; $P = .041$). Culprit plaques with IPH were also more heterogeneous in T1 than culprit plaques without IPH ($SD_{\text{Plaque T1}} = 0.20 \pm 0.03$ versus 0.15 ± 0.04 ; $P = .03$). Culprit plaques took up significantly more Gd than nonculprit plaques (2.01 [SD, 0.91] versus 1.06 [SD, 0.76]; $P < .001$) (Fig 3).

In univariate logistic regressions, several metrics were used to identify culprit plaques (Table 2). We used the following variables to generate a multivariate logistic regression model of culprit plaque identification: PB (OR, 3.7, 95% CI, 1.6–10; $P = .004$); Gd-uptake (OR, 2.3; 95% CI, 1.1–5.3; $P = .033$); and stenosis (OR, 1.3; 95% CI, 0.7–2.7; $P = .4$). The combined receiver operating characteristic analysis of this model had a sensitivity of 83% and a specificity of 86% (area under the curve = 0.87).

The conventional 2D method to quantify plaque enhancement with a CR_{stalk} of ≥ 0.56 had a sensitivity of 70% and a specificity of 68% in detecting culprit plaques (area under the curve = 0.68). In contrast, a Gd-uptake threshold of ≥ 1.23 had a sensitivity of 86% and a specificity of 71% (area under the curve = 0.81) in detecting culprit plaques with the new 3D method (Online Supplemental Data).

Parent Arteries of Culprit and Nonculprit Plaques

A mean of 858 (SD, 564) probes per arterial segment were generated. There was no statistical difference of enhancement between parent arteries of culprit and nonculprit plaques ($\mu = 0.59$ [SD, 0.20] versus 0.62 [SD, 0.14]; $P = .62$).

DISCUSSION

Identifying symptomatic plaques will improve the diagnosis of ICAD as a stroke etiology and may guide targeted endovascular interventions such as angioplasty and stent placement.²¹ In this

report, we describe a new method to quantify plaque enhancement, which generates 3D enhancement maps from hundreds of data points. Several enhancement metrics generated through this method enable detailed analysis of plaque and its parent artery enhancement. This new method was more accurate in detecting and quantifying plaque enhancement than the conventional 2D multiplanar method.

Gd uptake was the most accurate enhancement metric in detecting culprit plaques (OR, 3.9; 95% CI, 2.1–8.3). This metric quantifies the difference of enhancement between T1 and T1 + Gd images. It is similar to the “enhancement ratio,” which has been shown in other studies to be an independent identifier of stroke in patients with ICAD.²² One key difference is that Gd uptake accounts for the inherent heterogeneity of enhancement on T1 images. This metric analyzes plaques individually. Other metrics such as mean plaque enhancement ratio, plaque versus arterial enhancement, and plaque enhancement variance were also significant in detecting culprit plaques. This last parameter was also described by Shi et al²⁰ as a strong identifier of culprit plaques. The signal dispersion detected in the analysis of histograms in their study was confirmed in our study. This heterogeneity in the distribution of enhancement can be seen in the 3D color maps of the plaque and parent vessel (Figs 1 and 3). Subtle color differences along the diseased arterial segment reflect different enhancement patterns, which ultimately suggest different biologic processes and stages of disease progression.⁶ IPH is a strong identifier of culprit plaques.^{16,20} The new method of plaque-enhancement analysis captured an increased SI dispersion in T1 due to IPH. Detailed quantification of plaque enhancement has the potential of identifying IPH and, in some instances, even determining the response to medical therapy.²³

3D methods of vessel analysis have been used previously to visualize morphologic features such as vessel caliber and angulation.¹⁴ The analysis of vessel wall geometries has been shown to influence the effectiveness of endovascular interventions.²¹ Volumetric 3D maps of ICAD provide a more detailed characterization of PB, RI, and subtle differences in plaque morphology within different vascular territories. Qiao et al¹⁴ showed that posterior circulation arteries have a greater capacity for positive remodeling than anterior circulation arteries. Their 3D volumetric map made it possible to quantify the wall thickness and lumen area of the entire vessel segment. Similarly, our 3D analysis provides an objective survey of enhancement of the target arterial segment. Although our analysis

is not focused on plaque geometry, it has the potential to generate vessel wall metrics that are not limited to plaque enhancement. Quantifying enhancement through 3D analysis allows easier identification of potential culprit plaques.

Identifying symptomatic plaques through HR-MR imaging could lead to the diagnosis of stroke etiology. Fakhri et al⁹ reported that an analysis of a cryptogenic stroke cohort showed that approximately 73% of patients had an underlying atherosclerotic plaque that most likely was the cause of the stroke. A recent review showed that more than half of patients without significant luminal stenosis might have a culprit intracranial plaque identified on HR-MR imaging.²⁴ Generating 3D enhancement color maps for detailed analysis of vessel segments could increase the detection of atherosclerotic changes in patients with cryptogenic stroke. In this study, we found that objectively quantifying Gd uptake combined with PB achieved a sensitivity of 83% and specificity of 86% in detecting culprit plaques. Moreover, when the new 3D method was compared with previous work that used 2D measurements of enhancement,⁹ it proved to be more sensitive and specific.

This was an exploratory pilot study testing a new method to quantify plaque enhancement; therefore, it has several limitations. First, a total of 80 plaques were analyzed, which is standard for 7T MR imaging studies. However, a larger study would be optimal for defining better thresholds of culprit plaque detection. Generating precise segmentations can be time-consuming and requires several quality checkpoints. Each plaque and vessel segmentation requires approximately 60 minutes. Future studies should focus on accurate automated segmentation to reduce the processing time. In some cases, our registration pipeline did not coregister T1 and T1 + Gd sequences well due to image distortion. T1 and T1 + Gd images were segmented individually, increasing the overall analysis time to limit this artifact. Processing time could be shortened if one segmentation is performed in coregistered T1 and T1 + Gd reconstructions. Co-registration may be better implemented using 3T HR-MR imaging, which has fewer challenges for image registration than 7T HR-MR imaging. Once segmentation processing has been completed, generating 3D color maps is automatic and the quantification of plaque enhancement is highly reliable (Fig 1). A second limitation is that although the software was engineered for plaque-enhancement quantification, other metrics such as PB, RI, and area of stenosis were obtained manually from source images.

CONCLUSIONS

Detecting and quantifying plaque enhancement through 3D color maps are promising for characterizing ICAD. This new method is more accurate than current methods that rely on 2D multiplanar analysis.

Disclosure forms provided by the authors are available with the full text and PDF of this article at www.ajnr.org.

REFERENCES

1. Thijs VN, Albers GW. Symptomatic intracranial atherosclerosis: outcome of patients who fail antithrombotic therapy. *Neurology* 2000;55:490–97 CrossRef Medline
2. Song JW, Pavlou A, Xiao J, et al. Vessel wall magnetic resonance imaging biomarkers of symptomatic intracranial atherosclerosis: a meta-analysis. *Stroke* 2021;52:193–202 CrossRef Medline
3. Gupta A, Baradaran H, Al-Dasuqi K, et al. Gadolinium enhancement in intracranial atherosclerotic plaque and ischemic stroke: a systematic review and meta-analysis. *J Am Heart Assoc* 2016;5:e003816 CrossRef Medline
4. Millon A, Boussel L, Brevet M, et al. Clinical and histological significance of gadolinium enhancement in carotid atherosclerotic plaque. *Stroke* 2012;43:3023–28 CrossRef Medline
5. Qiao Y, Zeiler SR, Mirbagheri S, et al. Intracranial plaque enhancement in patients with cerebrovascular events on high-spatial-resolution MR images. *Radiology* 2014;271:534–42 CrossRef Medline
6. Gutierrez J, Elkind MS, Virmani R, et al. A pathological perspective on the natural history of cerebral atherosclerosis. *Int J Stroke* 2015;10:1074–80 CrossRef Medline
7. Kang N, Qiao Y, Wasserman BA. Essentials for interpreting intracranial vessel wall MRI results: state of the art. *Radiology* 2021;300:492–505 CrossRef Medline
8. Xiao J, Song SS, Schlick KH, et al. Disparate trends of atherosclerotic plaque evolution in stroke patients under 18-month follow-up: a 3D whole-brain magnetic resonance vessel wall imaging study. *Neuroradiol J* 2022;35:42–52 CrossRef Medline
9. Fakhri R, Roa JA, Bathla G, et al. Detection and quantification of symptomatic atherosclerotic plaques with high-resolution imaging in cryptogenic stroke. *Stroke* 2020;51:3623–31 CrossRef Medline
10. Adams HP Jr, Bendixen BH, Kappelle LJ, et al. Classification of subtype of acute ischemic stroke: definitions for use in a multicenter clinical trial—TOAST. Trial of Org 10172 in Acute Stroke Treatment. *Stroke* 1993;24:35–41 CrossRef Medline
11. Amarenco P, Bogousslavsky J, Caplan LR, et al. The ASCOD phenotyping of ischemic stroke (Updated ASCO Phenotyping). *Cerebrovasc Dis* 2013;36:1–5 CrossRef Medline
12. Samaniego EA, Shaban A, Ortega-Gutierrez S, et al. Stroke mechanisms and outcomes of isolated symptomatic basilar artery stenosis. *Stroke Vasc Neurol* 2019;4:189–97 CrossRef Medline
13. Chimowitz MI, Kokkinos J, Strong J, et al. The Warfarin-Aspirin Symptomatic Intracranial Disease Study. *Neurology* 1995;45:1488–93 CrossRef Medline
14. Qiao Y, Anwar Z, Intrapromkul J, et al. Patterns and implications of intracranial arterial remodeling in stroke patients. *Stroke* 2016;47:434–40 CrossRef Medline
15. Teng ZZ, Peng WJ, Zhan Q, et al. An assessment on the incremental value of high-resolution magnetic resonance imaging to identify culprit plaques in atherosclerotic disease of the middle cerebral artery. *Eur Radiol* 2016;26:2206–14 CrossRef Medline
16. Turan TN, Bonilha L, Morgan PS, et al. Intraplaque hemorrhage in symptomatic intracranial atherosclerotic disease. *J Neuroimaging* 2011;21:e159–61 CrossRef Medline
17. Raghuram A, Varon A, Roa JA, et al. Semiautomated 3D mapping of aneurysmal wall enhancement with 7T-MRI. *Sci Rep* 2021;11:18344 CrossRef Medline
18. Fedorov A, Beichel R, Kalpathy-Cramer J, et al. 3D Slicer as an image computing platform for the Quantitative Imaging Network. *Magn Reson Imaging* 2012;30:1323–41 CrossRef Medline
19. Harteveld AA, Denswil NP, Van Hecke W, et al. Ex vivo vessel wall thickness measurements of the human circle of Willis using 7T MRI. *Atherosclerosis* 2018;273:106–14 CrossRef Medline
20. Shi Z, Li J, Zhao M, et al. Quantitative histogram analysis on intracranial atherosclerotic plaques: a high-resolution magnetic resonance imaging study. *Stroke* 2020;51:2161–69 CrossRef Medline
21. Hou Z, Zhang Z, Yan L, et al. Association of residual stenosis after balloon angioplasty with vessel wall geometries in intracranial atherosclerosis. *J Neurointerv Surg* 2021;14:762–66 CrossRef Medline
22. Shi Z, Zhao M, Li J, et al. Association of hypertension with both occurrence and outcome of symptomatic patients with mild

- intracranial atherosclerotic stenosis: a prospective higher resolution magnetic resonance imaging study.** *J Magn Reson Imaging* 2021;54:76–88 CrossRef Medline
23. Chung JW, Cha J, Lee MJ, et al. **Intensive statin treatment in acute ischaemic stroke patients with intracranial atherosclerosis: a high-resolution magnetic resonance imaging study (STAMINA-MRI Study).** *J Neurol Neurosurg Psychiatry* 2020;91:204–11 CrossRef Medline
24. Wang Y, Liu X, Wu X, et al. **Culprit intracranial plaque without substantial stenosis in acute ischemic stroke on vessel wall MRI: a systematic review.** *Atherosclerosis* 2019;287:112–21 CrossRef Medline

Detection of Early Ischemic Changes with Virtual Noncontrast Dual-Energy CT in Acute Ischemic Stroke: A Noninferiority Analysis

 F. Kauw,  V.Y. Ding,  J.W. Dankbaar,  F. van Ommen,  G. Zhu,  D.B. Boothroyd,  D.N. Wolman,  L. Molvin,  H.W.A.M. de Jong,  L.J. Kappelle,  B.K. Velthuis,  J.J. Heit, and  M. Wintermark



ABSTRACT

BACKGROUND AND PURPOSE: Dual-energy virtual NCCT has the potential to replace conventional NCCT to detect early ischemic changes in acute ischemic stroke. In this study, we evaluated whether virtual NCCT is noninferior compared with standard linearly blended NCCT, a surrogate of conventional NCCT, regarding the detection of early ischemic changes with ASPECTS.

MATERIALS AND METHODS: Adult patients who presented with suspected acute ischemic stroke and who underwent dual-energy NCCT and CTA and brain MR imaging within 48 hours were included. Standard linearly blended images were reconstructed to match a conventional NCCT. Virtual NCCT images were reconstructed from CTA. ASPECTS was evaluated on conventional NCCT, virtual NCCT, and DWI, which served as the reference standard. Agreement between CT assessments and the reference standard was evaluated with the Lin concordance correlation coefficient. Noninferiority was assessed with bootstrapped estimates of the differences in ASPECTS between conventional and virtual NCCT with 95% CIs.

RESULTS: Of the 193 included patients, 100 patients (52%) had ischemia on DWI. Compared with the reference standard, the ASPECTS concordance correlation coefficient for conventional and virtual NCCT was 0.23 (95% CI, 0.15–0.32) and 0.44 (95% CI, 0.33–0.53), respectively. The difference in the concordance correlation coefficient between virtual and conventional NCCT was 0.20 (95% CI, 0.01–0.39) and did not cross the prespecified noninferiority margin of -0.10 .

CONCLUSIONS: Dual-energy virtual NCCT is noninferior compared with conventional NCCT for the detection of early ischemic changes with ASPECTS.

ABBREVIATION: CCC = concordance correlation coefficient

CT of the head is the most commonly used technique in the evaluation of stroke.¹ Initial NCCT is the first-line study in the evaluation of suspected stroke to exclude intracranial hemorrhage or an alternative explanation for the patient's symptoms. While early ischemic changes can be detected with NCCT, sensitivity is limited relative to DWI, which remains the reference standard for the detection of cerebral ischemia. However, MR imaging has limited

availability.² Early ischemic changes can be evaluated with ASPECTS on CT and are prognostic for functional outcome after IV thrombolysis and endovascular thrombectomy.^{3–5} ASPECTS is used for thrombectomy decision-making, because the large thrombectomy trials excluded patients with a low ASPECTS.^{6,7}

Dual-energy CT enables acquisition of CT images at 2 different tube voltages instead of one and has several applications in neurointervention and neuroradiology.⁸ For instance, iodine contrast can be separated from blood components in patients with large-vessel occlusion who underwent endovascular thrombectomy.^{9,10} Similarly, it is also possible to subtract iodine maps from the CTA images, resulting in virtual NCCT images.


It is unknown whether virtual NCCT is noninferior to conventional NCCT for the detection of early ischemic changes. If virtual NCCT is noninferior compared with conventional NCCT, then the latter may be omitted from the stroke imaging protocol, reducing the radiation exposure to the patient. We performed a noninferiority analysis comparing virtual NCCT with standard linearly blended NCCT, a surrogate of conventional NCCT, for the

Received January 21, 2022; accepted after revision June 17.

From the Departments of Radiology (F.K., F.v.O., G.Z., D.N.W., L.M., J.J.H., M.W.) and Medicine (V.Y.D., D.B.B.), Stanford University, Stanford, California; and Departments of Radiology (F.K., J.W.D., F.v.O., H.W.A.M.d.J., B.K.V.) and Neurology (F.K., L.J.K.), University Medical Center Utrecht, Utrecht University, Utrecht, the Netherlands.

This research has been made possible by the Dutch Heart Foundation, the Netherlands Organisation for Scientific Research, and the Domain Applied and Engineering Sciences, as part of their joint strategic research program: "Earlier Recognition of Cardiovascular Diseases" (grant No. 14732).

Please address correspondence to Frans Kauw, MD, Department of Radiology, Room Q.01.4.46, University Medical Center Utrecht, Heidelberglaan 100, 3584 CX Utrecht, the Netherlands; e-mail: f.kauw-3@umcutrecht.nl

 Indicates open access to non-subscribers at www.ajnr.org

<http://dx.doi.org/10.3174/ajnr.A7600>

detection of early ischemic changes with ASPECTS in patients with acute ischemic stroke.

MATERIALS AND METHODS

Patient Selection

Adult (18 years of age or older) patients who presented with suspected acute ischemic stroke and who underwent dual-energy CT (Somatom Force; Siemens) between February 2018 and February 2019 were selected for this study. The inclusion criteria were the availability of dual-energy NCCT and CTA scans and brain MR imaging within 48 hours after CT. Imaging was routinely performed as part of our standard-of-care stroke protocol. This study was approved by the Stanford University Institutional Review Board and complied with the Health Insurance Portability and Accountability Act. The need for informed consent was waived.

Image Acquisition and Preparation

NCCT and CTA were acquired helically using tube voltages of 80 and 140 kV (peak) with a tin filter and tube currents of 640 and 320 mAs, respectively. The images were acquired in dual-energy mode. The conventional NCCT was a standard linearly blended reconstruction to match a conventional 120-kVp NCCT. The virtual NCCT was reconstructed from CTA. The dual-energy data sets were routinely postprocessed using available dedicated software (syngo; Siemens) that was provided by the vendor to reconstruct virtual NCCT images. Section thicknesses of conventional and virtual NCCT were 3 mm.

DWI parameters were the following: TR = 6000 ms, TE = 78.2 ms, b-values = 0 and 1000, flip angle = 90°, and section thickness = 5 mm.

Interobserver Study

CT data were saved and presented in a random order to 2 experienced neuroradiologists (M.W. and J.W.D.) in the form of videos with fixed window settings (window width = 50 HU and window level = 40 HU). The reviewers evaluated the presence of early ischemic changes (yes or no) and rated ASPECTS, which is a prognostic score and allows quantification of the extensiveness of anterior circulation ischemic stroke.³ ASPECTS ranges from 0 to 10, with 0 indicating involvement of all the ASPECTS areas and 10 indicating involvement of none of the ASPECTS areas. One point is subtracted for every involved area. The areas include the caudate, internal capsule, lentiform nucleus, insular ribbon, anterior MCA cortex (M1), MCA cortex lateral to the insular ribbon (M2), posterior MCA cortex (M3), anterior cortex immediately rostral to M1 (M4), lateral cortex immediately rostral to M3 (M5), and posterior cortex immediately rostral to M3 (M6). Two separate scoring rounds were organized per reviewer, and the presentations contained a mix of virtual and conventional NCCT images. In case of disagreement, a third reviewer (G.Z.) was consulted to reach adjudicated assessments.

The DWIs were anonymized and presented to 1 neurointerventional radiologist with 7 years of experience (J.J.H.) who was blinded to the clinical and other imaging data. The reviewer was able to adjust the window settings and evaluated the presence of ischemia with ASPECTS, which can also be rated on DWI.¹¹

We assessed interobserver agreement of early ischemic changes and ASPECTS, as well as the agreement between adjudicated CT assessments and MR imaging assessments.

Statistical Analysis

We reported frequencies and percentages for categorical characteristics and medians with first (Q1) and third (Q3) quartiles for continuous characteristics. These included symptom laterality (left/right/both/unknown), image assessability (yes/no), as well as MR imaging–assessed early ischemic change (presence/absence)—overall and for each of the 10 brain regions (M1–M6, caudate, lentiform nucleus, internal capsule, and insular cortex). Proportions of the involved brain regions were visualized as barplots.

The agreement between the 2 reviewers was quantified by calculating the Cohen κ , with disagreements weighted according to their squared distance from perfect agreement.¹² The level of agreement was interpreted on the basis of the following intervals for κ : poor, <0.20; fair, 0.21–0.40; moderate, 0.41–0.60; good, 0.61–0.80; and very good, 0.81–1.00. Confidence intervals for κ statistics were based on 5000 bootstrap resamples.

Measures of sensitivity and specificity were calculated for virtual and conventional NCCT. We used a global test to compare the sensitivity and specificity.¹³

For feasibility, we concluded that the maximum study size was 200 patients. Our a priori power calculation determined that this would provide 77% power to show noninferiority, given a noninferiority margin of -0.10 . Concordance between adjudicated CT assessments and the MR imaging criterion standard was quantified using the Lin concordance correlation coefficient (CCC),^{14,15} which is also a measure of accuracy against the criterion standard. Bootstrapped estimates were obtained of the differences between virtual and conventional NCCT with 2-sided 95% CIs. Noninferiority of virtual NCCT to conventional NCCT was prespecified as the lower boundary greater than -0.10 for the 95% CI of their difference in the CCC. In case the 95% CI of the difference in the CCC was greater than 0, superiority could be inferred.

All analyses were performed in the R statistical computing framework, Version 4.0 (<http://www.r-project.org/>), and the CCC was estimated using the epiR R package.

RESULTS

Imaging assessment was not possible in 3 of the 196 included patients. As a result, 193 patients remained for the final analysis (Table 1). In 100 patients (52%), ischemia was detected with MR imaging in different ASPECTS regions.

Some differences were observed between the observations of reviewers 1 and 2 (Fig 1). Interobserver agreement regarding the presence of early ischemic changes was moderate for conventional (weighted $\kappa = 0.42$; 95% CI, 0.27–0.56) and virtual NCCT (weighted $\kappa = 0.48$; 95% CI, 0.36–0.6) (Fig 2). Interobserver agreement regarding ASPECTS was fair for conventional NCCT (weighted $\kappa = 0.38$; 95% CI, 0.23–0.54) and virtual NCCT (weighted $\kappa = 0.27$; 95% CI, 0.14–0.4).

The sensitivity of virtual and conventional NCCT for the detection of early ischemic changes was 0.37 (95% CI, 0.28–0.47) and 0.27 (95% CI, 0.19–0.37), respectively ($P = .078$). Specificity was

Table 1: Baseline characteristics

Characteristic	No. (%)
No. of patients	193
Age (mean) (yr)	67 (SD, 16)
Male sex	103 (53%)
Side of symptoms	
Bilateral	11 (5.7)
Left	59 (30.6)
Right	53 (27.5)
Unknown	70 (36.3)
Presence of early ischemic changes, as determined by DWI	
Overall	100 (51.8)
M1	8 (4.1)
M2	13 (6.7)
M3	18 (9.3)
M4	26 (13.5)
M5	33 (17.1)
M6	29 (15.0)
Caudate	16 (8.3)
Lentiform nucleus	21 (10.9)
Internal capsule	12 (6.2)
Insular cortex	20 (10.4)

0.91 (95% CI, 0.83–0.96) and 0.94 (95% CI, 0.86–0.98), respectively (Table 2). The global test finding was not significant ($P = .111$).

The forest plots (Fig 2) for the CCC showed overlapping intervals for early ischemic changes and nonoverlapping 95% CIs for ASPECTS. The difference in the CCC between virtual and conventional NCCT was 0.201 (95% CI, 0.014–0.389) regarding ASPECTS and 0.077 (95% CI, –0.041–0.191) regarding early ischemic changes. Neither 95% CI for the difference in the CCC crossed the prespecified noninferiority margin of –0.10, thereby establishing noninferiority of virtual NCCT compared with conventional NCCT with respect to both ASPECTS and early ischemic changes. Furthermore, virtual NCCT was demonstrated to be superior to conventional NCCT with respect to ASPECTS. Sample acquisitions of conventional NCCT, virtual NCCT, and DWI MR imaging are shown in Fig 3.

DISCUSSION

This study shows that detection of early ischemic changes with dual-energy virtual NCCT in patients with suspected stroke is

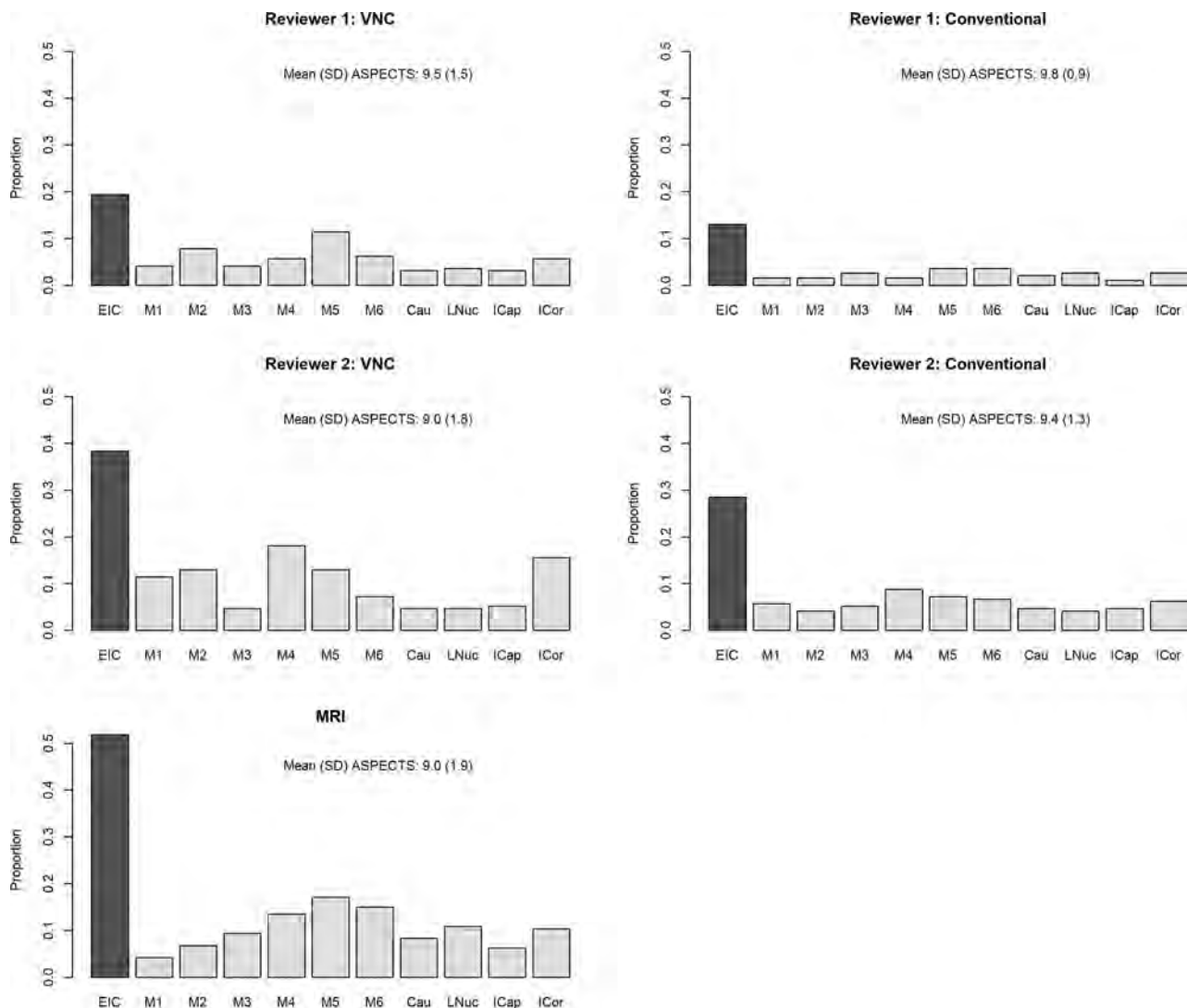


FIG 1. The proportion of CT scans showing early ischemic changes by reviewer and technique. VNC indicates virtual noncontrast; EIC, early ischemic changes; Cau, caudate nucleus; LNuc, lentiform nucleus; ICap, internal capsule; ICor, insular cortex.

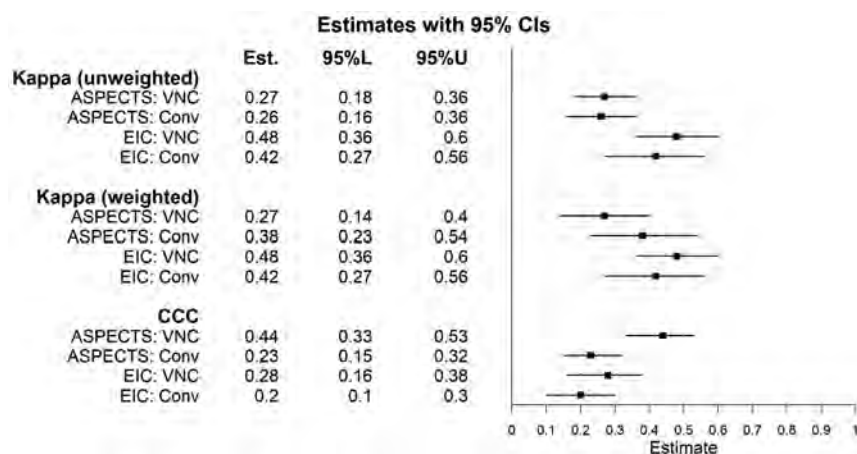


FIG 2. Estimates of interobserver agreement between CT and the reference standard and accuracy with 95% confidence intervals. VNC indicates virtual noncontrast; EIC, early ischemic changes; Conv, conventional; 95%L, lower bound of the 95% confidence interval; 95%U, upper bound of the 95% confidence interval.

Table 2: Adjudicated-versus-criterion standard assessments

DWI		
VNC		
Adjudicated	No EIC	Has EIC
No EIC	83	63
Has EIC	8	37
Conventional		
Adjudicated		
No EIC	87	73
Has EIC	6	27

Note:—VNC indicates virtual noncontrast; EIC, early ischemic changes.

noninferior compared with standard linearly blended NCCT. Furthermore, virtual NCCT was demonstrated to be superior to conventional NCCT with respect to ASPECTS.

To the best of our knowledge, no studies have evaluated early ischemic changes on virtual NCCT images reconstructed from CTA. Studies in fields other than neuroradiology have shown contradictory results, and the reliability of the virtual NCCT maps seems to be influenced by the clinical indication.^{16,17} Excluding intracranial hemorrhage is an important application of NCCT in the acute stroke setting and can also be done with dual-energy virtual NCCT images.^{18–20} Dual-energy CT can also be used to distinguish intracranial hemorrhage and extravasation of iodine contrast after endovascular treatment of stroke.^{21–23} In addition, 1 study showed high sensitivity and specificity for detecting the hyperdense artery sign on dual-energy virtual NCCT.²⁴ Previous studies showed that the detection of the ischemic core with dual-energy virtual NCCT images derived from NCCT was superior compared with conventional NCCT.^{22,25,26} It is difficult to compare these studies with our study because the reconstructions were acquired from different CT images (NCCT versus CTA). However, all studies indicated that dual-energy virtual NCCT has the potential to replace conventional NCCT with respect to the detection of early ischemic changes.

The observed interobserver variability with regard to the detection of early ischemic changes and ASPECTS was moderate and fair, respectively, and similar for virtual NCCT and

conventional NCCT in this study. ASPECTS is known to have relatively poor intraobserver and interobserver agreement, as was the case in this study.²⁷ Recently, this finding was supported by a study that demonstrated a relatively poor interobserver agreement in a large group of 100 readers.²⁸ The agreement, based on the CCC, between the dual-energy virtual NCCT assessments and MR imaging assessments regarding the presence of early ischemic changes was slightly better than the agreement between conventional NCCT assessments and MR imaging assessments. With regard to ASPECTS, the CCC showed fair agreement between both CT modalities and MR imaging, which is in line with findings in a previous study.²⁹

The applications of dual-energy CT are becoming increasingly apparent. If dual-energy virtual NCCT of the brain can replace conventional NCCT, this would result in less radiation exposure for the patient. Whether dual-energy virtual NCCT saves time in the acute stroke work-up needs to be elucidated because dual-energy reconstructions also take time. Automated dual-energy reconstructions do not add extra time to the imaging protocol, unless manual processing is required. The disadvantages of replacing conventional NCCT with virtual NCCT include the necessity of acquiring CTA, turning on the dual-energy mode, and the requirements of added storage and bandwidth. Besides replacing conventional NCCT, future applications of virtual NCCT may include improvement of the conventional NCCT in case of severe movement artifacts and reduction of the radiation dose in a nonacute setting.

Most dual-energy CT scanners, using a dual source with a dual detector or a monosource with rapid kilovolt (peak) switching, require that the dual-energy setting be switched on beforehand to acquire dual-energy data.³⁰ Other detector-based spectral CT scanners have a single source and a single dual-layered detector that is always switched on. In the acute stroke imaging work-up, NCCT needs to be acquired first to exclude intracranial hemorrhage. Because the dual-energy virtual NCCT images need to be reconstructed from the CTA, which is often only performed if an NCCT has ruled out an intracranial hemorrhage, it is difficult to omit the conventional NCCT in clinical practice. On the other hand, even in patients who have intracranial hemorrhage, CTA is often performed to look for cerebral aneurysms, cerebral arteriovenous malformations, or other vascular malformations as the cause of the bleed. Taken together, the role of dual-energy virtual NCCT seems dependent on the indication and on whether CTA is performed regardless of the findings on NCCT.

Several strengths can be noted in this study. To prevent observation bias, the observers who assessed the CT were blinded to clinical information and MR images; vice versa, the observer who assessed the MR images was blinded to the CT images. Another strength was the power calculation, which helped to achieve a reliable noninferiority analysis.

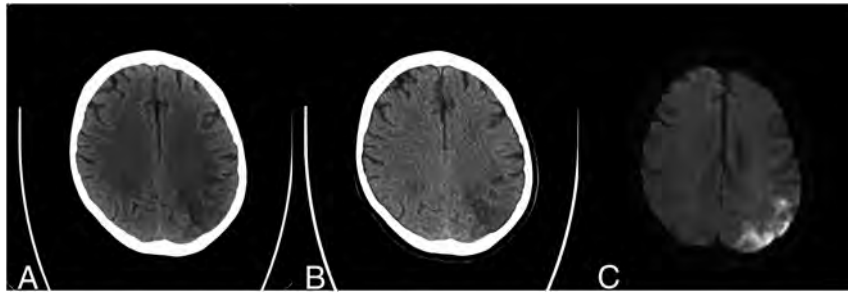


FIG 3. A sample case of a 66-year-old male patient who presented with right-sided weakness and numbness (NIHSS 7). His medical history included diabetes mellitus, hypertension, hyperlipidemia, prior smoking, and prior ischemic stroke, for which the patient used dual-antiplatelet therapy. The time between last seen well and CT was 14 hours. The time between CT and DWI was 12 hours. Conventional NCCT (A) and virtual NCCT (B) show early ischemic changes in the left parietal lobe (ASPECTS region M6). In the same region, DWI (C) shows hyperintensity, indicating diffusion restriction compatible with ischemia.

A limitation of this study was the potential risk of selection bias because patients were selected who underwent dual-energy CT and diffusion-weighted MR imaging. However, besides the imaging criteria, we used wide inclusion criteria (adult patients with a suspicion of acute ischemic stroke). Nevertheless, the results of this study need to be validated, preferably in a large prospective study. Due to missing data, extensive patient characteristics were not reported in this study. Although we did not use conventional single-source NCCT in this study, standard linearly blended images closely resemble conventional NCCT.³¹ Another limitation is the time interval between the acquired CT scan and the DWI. Although the time window was within 48 hours, this theoretically could have resulted in larger or additional infarcts on MR imaging compared with CT. This possibility may also partially explain the fair agreement between CT and MR imaging in this study. In addition, MR imaging is more sensitive for detecting ischemia; therefore, ASPECTS may differ between CT and MR imaging assessments, which are acquired simultaneously because small infarcts may be visible on MR imaging but not on CT. In this study, the dual-energy CT scanner and the software of 1 vendor were used, limiting the ability to generalize these findings. Future studies should include a broader range of CT vendors and software to increase generalizability.

CONCLUSIONS

Dual-energy virtual NCCT is noninferior compared with NCCT for the detection of early ischemic changes with ASPECTS.

Disclosure forms provided by the authors are available with the full text and PDF of this article at www.ajnr.org.

REFERENCES

- Wintermark M, Luby M, Bornstein NM, et al. International survey of acute stroke imaging used to make revascularization treatment decisions. *Int J Stroke* 2015;10:759–62 CrossRef Medline
- Wardlaw JM, Mielke O. Early signs of brain infarction at CT: observer reliability and outcome after thrombolytic treatment—systematic review. *Radiology* 2005;235:444–53 CrossRef Medline
- Barber PA, Demchuk AM, Zhang J, et al. Validity and reliability of a quantitative computed tomography score in predicting outcome of

hyperacute stroke before thrombolytic therapy: ASPECTS Study Group—Alberta Stroke Programme. *Lancet* 2000;355:1670–74 CrossRef Medline

- Jovin TG, Chamorro A, Cobo E, et al; REVASCAT Trial Investigators. Thrombectomy within 8 hours after symptom onset in ischemic stroke. *N Engl J Med* 2015;372:2296–2306 CrossRef Medline
- Goyal M, Demchuk AM, Menon BK, et al. Randomized assessment of rapid endovascular treatment of ischemic stroke. *N Engl J Med* 2015;372:1019–30 CrossRef Medline
- Goyal M, Menon BK, van Zwam WH, et al; HERMES Collaborators. Endovascular thrombectomy after large-vessel ischemic stroke: a meta-analysis of individual patient data from five randomised trials. *Lancet* 2016;387:1723–31 CrossRef Medline

- Jovin TG, Nogueira RG, Lansberg MG, et al. Thrombectomy for anterior circulation stroke beyond 6 h from time last known well (AURORA): a systematic review and individual patient data meta-analysis. *Lancet* 2021;399:249–58 CrossRef Medline
- Wolman DN, Patel BP, Wintermark M, et al. Dual-energy computed tomography applications in neurointervention. *J Comput Assist Tomogr* 2018;42:31–38 CrossRef Medline
- Almqvist H, Holmin S, Mazya MV. Dual energy CT after stroke thrombectomy alters assessment of hemorrhagic complications. *Neurology* 2019;93:e1068–75 CrossRef Medline
- Liu K, Jiang L, Ruan J, et al. The role of dual energy CT in evaluating hemorrhagic complications at different stages after thrombectomy. *Front Neurol* 2020;11:583411 CrossRef Medline
- Barber PA, Hill MD, Eliasziw M, et al. Imaging of the brain in acute ischaemic stroke: comparison of computed tomography and magnetic resonance diffusion-weighted imaging. *J Neurol Neurosurg Psychiatry* 2005;76:1528–33 CrossRef Medline
- Cohen J. Weighted kappa: nominal scale agreement with provision for scaled disagreement or partial credit. *Psychol Bull* 1968;70:213–20 CrossRef Medline
- Roldán-Nofuentes JA. Compbdt: an R program to compare two binary diagnostic tests subject to a paired design. *BMC Med Res Methodol* 2020;20:143 CrossRef Medline
- Lin LI. A concordance correlation coefficient to evaluate reproducibility. *Biometrics* 1989;45:255–68 Medline
- Morgan CJ, Aban I. Methods for evaluating the agreement between diagnostic tests. *J Nucl Cardiol* 2016;23:511–13 CrossRef Medline
- Lehti L, Söderberg M, Höglund P, et al. Reliability of virtual non-contrast computed tomography angiography: comparing it with the real deal. *Acta Radiol Open* 2018;7:2058460118790115 CrossRef Medline
- Noid G, Schott D, Paulson E, et al. Technical note: using virtual non-contrast images from dual-energy CT to eliminate the need of pre-contrast CT for x-ray radiation treatment planning of abdominal tumors. *Med Phys* 2021;48:1365–71 CrossRef Medline
- Ferda J, Novák M, Mírka H, et al. The assessment of intracranial bleeding with virtual unenhanced imaging by means of dual-energy CT angiography. *Eur Radiol* 2009;19:2518–22 CrossRef Medline
- Jiang XY, Zhang SH, Xie QZ, et al. Evaluation of virtual noncontrast images obtained from dual-energy CTA for diagnosing subarachnoid hemorrhage. *AJNR Am J Neuroradiol* 2015;36:855–60 CrossRef Medline
- Bonatti M, Lombardo F, Zamboni GA, et al. Dual-energy CT of the brain: comparison between DECT angiography-derived virtual unenhanced images and true unenhanced images in the detection of intracranial haemorrhage. *Eur Radiol* 2017;27:2690–97 CrossRef Medline
- Tijssen MP, Hofman PA, Stadler AA, et al. The role of dual energy CT in differentiating between brain haemorrhage and contrast

- medium after mechanical revascularisation in acute ischaemic stroke. *Eur Radiol* 2014;24:834–40 CrossRef Medline
22. Gariani J, Cuvinciuc V, Courvoisier D, et al. **Diagnosis of acute ischemia using dual energy CT after mechanical thrombectomy.** *J Neurointerv Surg* 2016;8:996–1000 CrossRef Medline
 23. Ebashi R, Ogata A, Nishihara M, et al. **Significance of simulated conventional images on dual energy CT after endovascular treatment for ischemic stroke.** *J Neurointerv Surg* 2019;11:898–902 CrossRef Medline
 24. Winklhofer S, Vittoria De Martini I, Nern C, et al. **Dual-energy computed tomography in stroke imaging: technical and clinical considerations of virtual noncontrast images for detection of the hyperdense artery sign.** *J Comput Assist Tomogr* 2017;41:843–48 CrossRef Medline
 25. Mohammed MF, Marais O, Min A, et al. **Unenhanced dual-energy computed tomography: visualization of brain edema.** *Invest Radiol* 2018;53:63–69 CrossRef Medline
 26. Wolman DN, van Ommen F, Tong E, et al. **Non-contrast dual-energy CT virtual ischemia maps accurately estimate ischemic core size in large-vessel occlusive stroke.** *Sci Rep* 2021;11:6745 CrossRef Medline
 27. Gupta AC, Schaefer PW, Chaudhry ZA, et al. **Interobserver reliability of baseline noncontrast CT Alberta Stroke Program Early CT Score for intra-arterial stroke treatment selection.** *AJNR Am J Neuroradiol* 2012;33:1046–49 CrossRef Medline
 28. van Horn N, Knierp H, Broocks G, et al. **ASPECTS interobserver agreement of 100 investigators from the TENSION study.** *Clin Neuroradiol* 2021;31:1093–1100 CrossRef Medline
 29. Lansberg MG, Albers GW, Beaulieu C, et al. **Comparison of diffusion-weighted MRI and CT in acute stroke.** *Neurology* 2000;54:1557–61 CrossRef Medline
 30. McCollough CH, Leng S, Yu L, et al. **Dual- and multi-energy CT: principles, technical approaches, and clinical applications.** *Radiology* 2015;276:637–53 CrossRef Medline
 31. Yu L, Primak AN, Liu X, et al. **Image quality optimization and evaluation of linearly mixed images in dual-source, dual-energy CT.** *Med Phys* 2009;36:1019–24 CrossRef Medline

Optimizing the Definition of Ischemic Core in CT Perfusion: Influence of Infarct Growth and Tissue-Specific Thresholds

✉ A. Rodríguez-Vázquez, ✉ C. Laredo, ✉ A. Renú, ✉ S. Rudilosso, ✉ L. Llull, ✉ S. Amaro, ✉ V. Obach, ✉ V. Vera, ✉ A. Páez, ✉ L. Oleaga, ✉ X. Urra, and ✉ Á. Chamorro



ABSTRACT

BACKGROUND AND PURPOSE: CTP allows estimating ischemic core in patients with acute stroke. However, these estimations have limited accuracy compared with MR imaging. We studied the effect of applying WM- and GM-specific thresholds and analyzed the infarct growth from baseline imaging to reperfusion.

MATERIALS AND METHODS: This was a single-center cohort of consecutive patients ($n = 113$) with witnessed strokes due to proximal carotid territory occlusions with baseline CT perfusion, complete reperfusion, and follow-up DWI. We segmented GM and WM, coregistered CTP with DWI, and compared the accuracy of the different predictions for each voxel on DWI through receiver operating characteristic analysis. We assessed the yield of different relative CBF thresholds to predict the final infarct volume and an estimated infarct growth-corrected volume (subtracting the infarct growth from baseline imaging to complete reperfusion) for a single relative CBF threshold and GM- and WM-specific thresholds.

RESULTS: The fixed threshold underestimated lesions in GM and overestimated them in WM. Double GM- and WM-specific thresholds of relative CBF were superior to fixed thresholds in predicting infarcted voxels. The closest estimations of the infarct on DWI were based on a relative CBF of 25% for a single threshold, 35% for GM, and 20% for WM, and they decreased when correcting for infarct growth: 20% for a single threshold, 25% for GM, and 15% for WM. The combination of 25% for GM and 15% for WM yielded the best prediction.

CONCLUSIONS: GM- and WM-specific thresholds result in different estimations of ischemic core in CTP and increase the global accuracy. More restrictive thresholds better estimate the actual extent of the infarcted tissue.

ABBREVIATIONS: ICC = intraclass correlation coefficient; IG = infarct growth; IQR = interquartile range; rCBF = relative CBF

CTP is a widely available technique that allows measuring hypoperfused brain tissue and estimating ischemic core in patients with acute stroke.¹⁻³ The ischemic core is often defined

by CBF thresholds.⁴ However, despite their clinical usefulness, the most often used CBF-based definitions of ischemic core may not be accurate for research purposes.⁵ They often overestimate the true infarct⁶ (example in the Online Supplemental Data) and have limited accuracy compared with MR imaging.⁷ In addition, differences in the neurochemical response to ischemia in GM and WM lead to a varied vulnerability to ischemia.⁸ Applying homogeneous CBF thresholds in the whole brain may result in under- or overestimating the lesion in brain areas with different susceptibility to ischemia.⁹ Also, ischemic core volumes estimated by CTP, especially those affecting WM, are often smaller than in follow-up MR imaging.¹⁰ This overestimation, applied to routine clinical practice, could lead to not offering reperfusion treatment to patients who could benefit from it. These findings can be explained by the delay between baseline imaging and the follow-up imaging used to measure final infarct volume. The baseline-to-follow-up imaging delay may be a source of error because stroke is a dynamic process that results in progressive brain damage, mainly if successful reperfusion is not achieved. In addition,

Received March 28, 2022; accepted after revision June 20.

From the Comprehensive Stroke Center (A.R.-V., C.L., A.R., S.R., L.L., S.A., V.O., V.V., X.U., A.C.), Functional Unit of Cerebrovascular Diseases, and Radiology Department (A.P., L.O.), Hospital Clinic, Barcelona, Spain; Institut d'Investigacions Biomèdiques August Pi i Sunyer (A.R., S.R., L.L., S.A., V.O., X.U., A.C.), Barcelona, Spain; and University of Barcelona (A.R., L.L., S.A., V.O., X.U., A.C.), Barcelona, Spain.

Alejandro Rodríguez-Vázquez and Carlos Laredo contributed equally to this work.

This study was supported by grants of the ISCIII-Subdirección General de Evaluación (FIS PI18/00444 and PI21/00966 to A. Chamorro and X. Urra) cofinanced by the Fondo Europeo de Desarrollo Regional. X.U. was sponsored by ISCIII (INT19/00020) and the European Social Fund "The ESF-Investing in your future." A.R.-V. is funded by the "Emili Letang-Josep Font" research grant from the Hospital Clinic de Barcelona.

Please address correspondence to Xabier Urra, MD, PhD, Functional Unit of Cerebrovascular Diseases, Hospital Clinic, 170 Villarroel, 08036 Barcelona, Spain; e-mail: xurra@clinic.cat; @IctusClinic; @xabierurra

✉ Indicates open access to non-subscribers at www.ajnr.org

☰ Indicates article with online supplemental data.

<http://dx.doi.org/10.3174/ajnr.A7601>

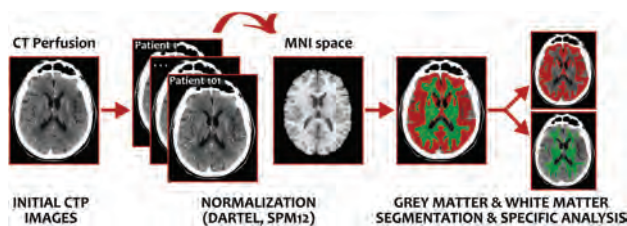


FIG 1. Segmentation methodology for calculating WM- and WM-specific rCBF thresholds. MNI indicates Montreal Neurological Institute.

cerebral ischemia is a dynamic process, and it is difficult to accurately establish the evolution of the infarction. Some studies have assumed both linear¹¹ and logarithmic¹² infarct growth (IG), but it is currently under discussion.¹³

All these factors highlight the need for further research to improve tissue-outcome predictions in patients with stroke.¹⁴ Here, we studied the best thresholds for defining ischemic core using global- versus GM- and WM-specific CBF thresholds and accounting for IG in a cohort of patients with baseline CTP, complete reperfusion, and follow-up MR imaging.

MATERIALS AND METHODS

Study Population

The study population ($n = 101$, Online Supplemental Data) was part of a prospectively collected clinical registry of patients with acute ischemic stroke admitted in to a Comprehensive Stroke Center between March 2010 and December 2017. We included all consecutive patients with proximal occlusions in the carotid territory with a pretreatment whole-brain CTP <6 hours from symptom onset to neuroimaging, complete endovascular reperfusion defined as modified TICI 3, and a follow-up MR imaging. Proximal arterial occlusions included those located at the terminal intracranial carotid artery, the M1–M2 segments of the MCA, and the A1 segment of the anterior cerebral artery. There were no vascular re-occlusions in our cohort. We prospectively collected baseline characteristics, demographics, clinical course, and reperfusion therapy–related variables.

Standard Protocol Approvals, Registrations, and Patient Consent

The local Ethics Committee at Hospital Clinic approved the study (registration code, HCB/2018/0680).

Neuroimaging

The imaging protocol included a baseline multimodal whole-brain CT scan (total acquisition time, 83 seconds), which included NCCT (140 kV, 127 mAs, FOV = 225 mm, matrix = 512×512 , section thickness = 5 mm); CTA (120 kV, 663 mAs, FOV = 261 mm, matrix = 512×512 , section thickness = 0.6 mm); and CTP (80 kV[peak], 250 mAs, 1.5-second rotation, FOV = 18 mm, matrix = 512×512 , and forty-nine 2-mm-thickness slices). Patients were scanned within a median (interquartile range [IQR]) of 129 minutes (72–211 minutes) from stroke onset using a Somatom Definition Flash 128-section dual-source multidetector scanner (Siemens), with a 98-mm z-coverage and 26 time points

acquired each 1.5 seconds and 4 last time points each 5 seconds (total acquisition time, 59 seconds). Fifty milliliters of nonionic iodinated contrast were administered intravenously at 5 mL/s using a power injector, followed by a saline flush of 20 mL at an injection rate of 2 mL/s. To ensure complete filling of the collateral circulation, we acquired CTA after the CTP.

The ASPECTS was assessed on the baseline NCCT. CTP maps were calculated by the commercial software MISTar (Apollo Medical Imaging Technology) using a model-free singular-value decomposition algorithm with a delay and dispersion correction. The software automatically performs motion correction and selects an arterial input function from an unaffected artery (usually the anterior cerebral artery) and a venous output function from a large draining vein (the sagittal sinus). The software generates CBF, CBV, MTT, and delay time maps. Of note, the delay-corrected deconvolution method produces delay time maps rather than the more extensively used time-to-maximum maps.¹⁵ A threshold of 3 seconds on the delay time maps was used to define the hypoperfusion,³ and “ischemic core” was defined within the hypoperfused area with a series of relative CBF thresholds as a percentage of the mean perfusion values from the entire unaffected, contralateral hemisphere.¹⁶ The final vessel patency was graded on DSA at the end of mechanical thrombectomy according to the modified TICI classification.¹⁷ The follow-up MR imaging (total acquisition time, 24 minutes and 18 seconds) was performed on a 1.5T Magnetom Aera unit (Siemens) at a median of 43 hours (IQR, 22–69 hours) after the CTP.

DWI lesion volumes were calculated using Amira software (Visage Imaging) through a semiautomated thresholding method to identify ROIs with a signal intensity exceeding the values in the contralateral hemisphere by >3 SDs.¹⁸ T1WIs were transferred into stereotaxic space using the diffeomorphic anatomical registration through exponentiated lie algebra (DARTEL) normalization algorithm in Statistical Parametric Mapping (SPM12; <http://www.fil.ion.ucl.ac.uk/spm/>), and the resulting GM and WM probabilistic maps obtained in the native space were used to obtain GM and WM segmentations (Fig 1). T1WI, DWI, GM, WM, and lesion masks were coregistered to the baseline CTP for posterior analysis. Moreover, due to the clinical practice nature of our MR imaging protocol, DWI could not be corrected for distortions before applying the normalization.

The increase in infarct volume was calculated by subtracting the baseline CTP ischemic core from the final infarct volume measured on DWI. We calculated a theoretic IG-corrected volume for CTP-based estimations by subtracting the IG from baseline imaging to complete reperfusion. Assuming a linear IG, we estimated the infarct progression rate by dividing the nonviable tissue volume by the time delay to imaging.¹⁹ Finally, the estimated IG was calculated by multiplying the estimated infarct progression rate by the time from baseline imaging to complete reperfusion (Online Supplemental Data).

Statistical Analysis and Outcome Measures

We assessed the yield of different relative CBF (rCBF) thresholds to predict the following: 1) infarcted voxels in coregistered DWI through receiver operating characteristic analysis, and 2) final DWI lesion volume (net difference of the estimation and intra-class correlation coefficient [ICC]). We used the ICC (2-way

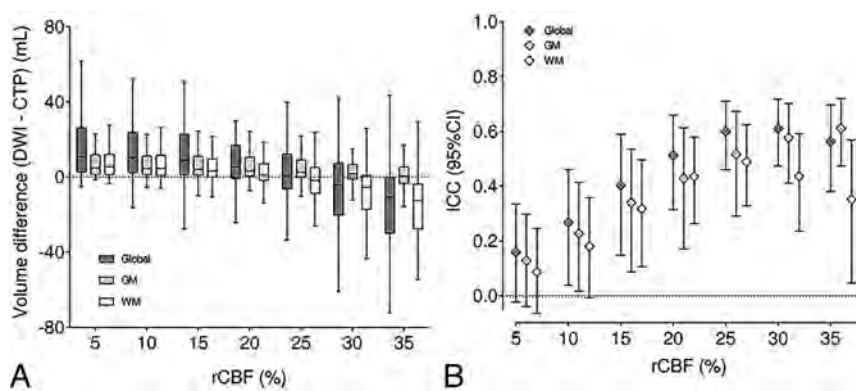


FIG 2. Distribution of rCBF thresholds for the infarct core prediction in the whole brain (dark gray), GM (light gray), and WM (white). The left image (A) represents the net infarct volume difference, and the right image (B) shows the ICC. Boxplots represent median (horizontal line in the inner box) 25% and 75% IQRs.

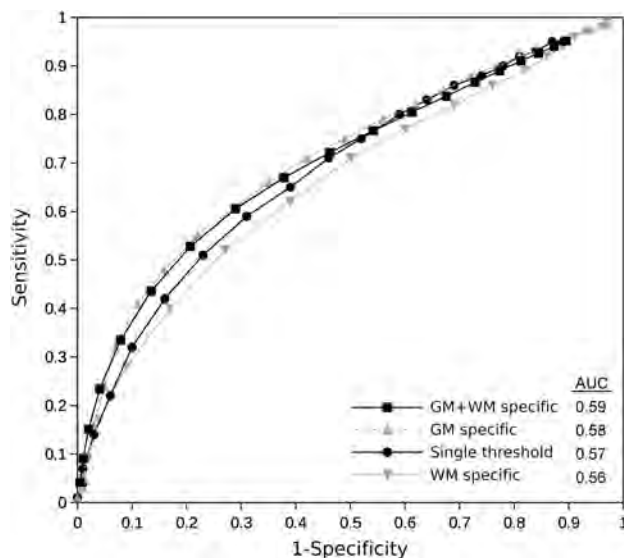


FIG 3. Receiver operating characteristic curves showing the performance of the application of different global GM- and WM-specific and combined rCBF thresholds in the voxel-based analysis to predict tissue fate. The area under the curve (AUC) is for the single best threshold, best GM-specific, best WM-specific, and best GM- and WM-specific thresholds combined. No significant differences in the AUC values were found among the different thresholds applied.

mixed model, absolute agreement for single measures) to study the association between the 2 repeat measurements of ischemic core (acute CTP and follow-up DWI) because the ICC measure reflects both the degree of correlation and agreement between measurements of continuous data. Reliability was considered good when the ICC was ≥ 0.80 . When 2 different thresholds had similar performances according to the ICC and volume prediction, we chose the threshold that caused the least overestimation of the lesion compared with DWI. All these analyses were performed for the entire brain parenchyma and GM and WM separately. The theoretic IG correction was applied only in volume difference and ICC analyses. Continuous variables were reported as mean (SD) or median (IQR) as appropriate, and categorical variables, as proportions. Differences

in proportions were studied with the χ^2 or Fisher exact test. All analyses were performed using SPSS, Version 26.0 (IBM), and the level of significance was set at $P < .05$, 2-sided.

Data Availability

The data sets generated and analyzed during the current study are available from the corresponding author on reasonable request.

RESULTS

From 113 patients with full data available, we excluded 12 patients due to inaccurate WM and GM segmentation or poor CTP/MR imaging coregistration (see the flow diagram in the Online Supplemental Data). The main characteristics of the final cohort of 101 patients are summarized in the Online Supplemental Data.

Whole-Brain versus GM- and WM-Specific Thresholds

In the analysis of the final volume, the best single threshold was rCBF 25%. The best thresholds were different for GM (rCBF 35%) and WM (rCBF 20%). Furthermore, estimates in GM were more constant with less variations when changing the thresholds (Fig 2). A double GM- and WM-specific threshold of rCBF 45% and 30% was superior to a fixed threshold (rCBF 35%) in predicting infarcted voxels (Youden index, 0.32 versus 0.30). The fixed threshold underestimated lesions in GM and overestimated them in WM. The different thresholds between the volume prediction and the individual voxel prediction could be partially explained by the IG from CTP to MR imaging, which cannot be controlled in the voxel-based study (Fig 3). Subgroup analysis of patients with rapid (< 60 minutes after CTP acquisition) complete endovascular reperfusion showed no differences in the results compared with the whole cohort.

Accounting for IG

By means of standard rCBF 30% thresholds, the median time from CTP to complete reperfusion was 95 minutes (IQR, 80–122 minutes), and the median IG was 5.2 mL (IQR, 1.5–10.8 mL). Considering the estimated IG velocity and the time to complete reperfusion, we calculated the theoretic ischemic core in CTP for each case. The closest estimations of this IG-corrected core were based on the rCBF 20% threshold (Figs 4A, -B). The effect of accounting for IG occurred both on WM- and GM-specific thresholds. For GM, the best IG-corrected core was based on the rCBF 25% threshold, while for WM, it was the rCBF 15% threshold (Fig 4C). The combination of 25% for GM and 15% for WM yielded the most accurate representation of IG-corrected ischemic core.

Spatial Distribution Analysis

According to the results obtained by applying the standard rCBF 30% threshold, most false-positives (predicted infarcted tissue in

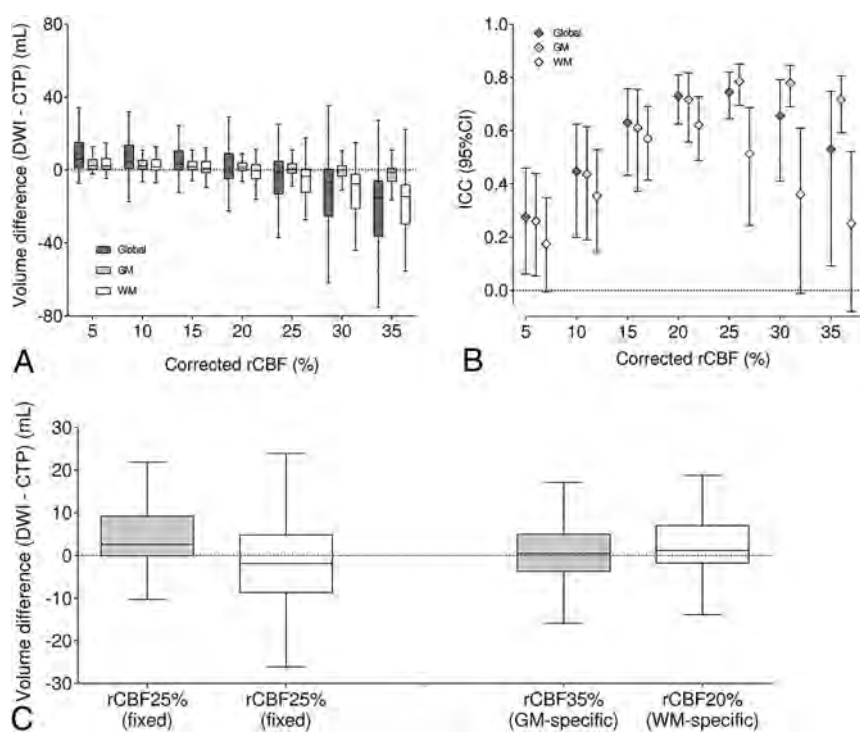


FIG 4. IG-corrected rCBF thresholds for defining infarct core in the whole brain (dark gray), GM (light gray), and WM (white). The left image represents the net infarct volume difference, and the right image shows the ICC (A and B). Accounting for the estimated IG from baseline imaging to complete reperfusion changes the optimal rCBF threshold for defining infarct core (C).

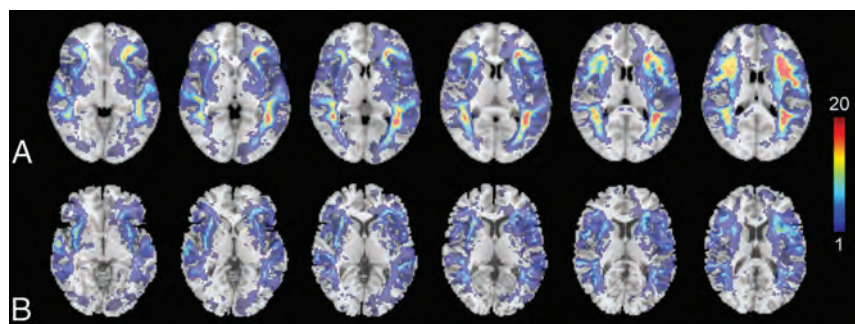


FIG 5. Heat map of the distribution of false-positives according to the following: the single rCBF 30% threshold most used in clinical practice (A) and a variable threshold in WM (rCBF 20%) and GM (rCBF 35%) (B). Warmer colors indicate a greater absolute accumulation of cases, while colder colors mean a lower absolute number of cases.

CTP without an ischemic lesion in DWI) were limited to the subcortical WM, while true-positives (predicted infarcted tissue in CTP with an ischemic lesion in DWI) were more common in the GM of the basal ganglia (Fig 5A). However, by means of a dual GM-WM threshold based on the best performing values in the previous analysis (rCBF 20% for WM and 35% for GM; Fig 5B), the number of false-positives in the subcortical WM was notably lower.

DISCUSSION

Establishing the extent of the ischemic core in the onset of an acute stroke is critical when considering reperfusion therapy.

Although in routine clinical practice, an NCCT is sufficient to decide on treatment in patients with <6 hours from symptom onset, CTP-based definitions have often been used due to the availability of the technique and the fair correlations between the initial ischemic area predicted on CBF or CBV maps and the final lesion on DWI.^{20,21} However, some reports have challenged the value of CTP-based definitions.²² Core overestimation in WM has been highlighted as a focus of future effort to improve CTP accuracy.¹⁰ Here, we addressed 2 physiologically relevant simple issues that can be easily implemented in clinical practice. Advanced computing methods may further help in defining critically hypoperfused areas that predict the irreversible injury of the tissue,²³ but the methodology described here may be enough to avoid overestimations of infarct volumes and undertreating patients who may benefit from reperfusion.

In agreement with previous studies,²⁴ we found that GM showed more vulnerability to ischemia than WM, so applying a common, more traditional threshold for both tissues resulted in overestimating the infarcted area in WM while underestimating the ischemia effects on GM. In that same way, a specific threshold of rCBF 35% in GM and 25% in WM was better correlated with the final infarct on DWI. The greater stability of the GM estimations may be because perfusion is more constant in this tissue or because the final infarct volumes are smaller. The higher estimations of optimal thresholds in the prediction of the fate of individual voxels (a double GM-WM threshold of CBF 45% and 30%) could be due to the limitations of the latter analysis, favoring less specific thresholds.

In accordance with this issue, establishing stricter thresholds in the voxel-based study is related to a greater error when coregistering. However, using a postprocessing program based on density differences between GM and WM entails less inherent error than in previous studies, which were based on probabilistic maps.²⁵ Nevertheless, these results reflect the physiologic aspects of greater ischemia susceptibility on GM compared with WM,^{25,26} which is especially remarkable when optimal reperfusion is achieved and can be neutralized using tissue-specific CTP thresholds.

The reperfusion grade could be a crucial factor confounding the correct estimation of the final ischemic area due to variable IG from baseline to follow-up imaging. Although the rCBF 30% threshold was originally derived using a contemporaneous CTP-

DWI model, in which the potential effect of reperfusion is less relevant,⁴ CTP is especially useful to predict the final infarct with a good correlation between ischemic cores estimated by rCBF 30% and DWI findings when no reperfusion therapies are administered.²⁷ On the other hand, fixed rCBF thresholds may overestimate final infarct volume in the case of recanalization,²⁸ and the overestimation is more relevant when the time from symptom onset to neuroimaging is shorter. It is unclear whether these findings are secondary to the actual reversibility of CBF and CBV lesions after reperfusion or only due to technical limitations. When complete reperfusion occurs, mainly when the time to reperfusion is short as it is in our cohort, it is common for the ischemic lesion to be mostly limited to GM. Collaterality, although not specifically analyzed in this study, also plays an important role in brain tissue viability and IG rate.^{18,29} For example, the hypoperfusion intensity ratio in a biomarker based on CTP reflects the presence of collateral flow and the eligibility of patients for reperfusion treatment in the acute phase.^{30,31} Using more specific CTP thresholds could be especially beneficial for avoiding overestimating infarct size in patients with good collaterals. Our study based on patients with a complete and short time to reperfusion showed a substantial overestimation of the final infarct on WM using a fixed threshold. Applying variable GM-WM thresholds offered a more precise estimation of the final ischemic core, with rCBF thresholds of 25% for GM and rCBF 15% for WM yielding the closest estimate of the IG-corrected core.

IG is also directly related to the time taken to complete the treatment. Theoretically, the penumbra region would become entirely ischemic core if there is no reperfusion, which is not expected to vary its volume time-wise. Ischemic core, however, is likely to expand with time each second the CBF is impaired. It is unclear whether the IG rate threshold varies according to the symptom-onset time to reperfusion,³² but it could change on the basis of the time from imaging to recanalization.³³ Considering that the GM is less resistant to ischemia, a greater IG is expected at lower thresholds than in WM, as shown in our analysis. However, the IG correction is an approximation to a complex phenomenon, and results derived from it should be interpreted with caution.

The quality of the metrics used in the study (IG, volume differences, and so forth) rely on a good coregistration of the CTP and MR imaging techniques. Due to the inherent changes in tissue viability and, therefore, imaging quality and contrast, the coregistration (and segmentation) methodologies used in acute ischemic stroke studies are subject to technical errors. On the other hand, there is no established model of rapid tissue segmentation in routine clinical practice. In this work, as a proof of concept, we have used a more time-consuming postprocessing methodology (the DARTEL toolbox) to normalize coregistered T1WIs to obtain improved GM-WM segmentation compared with those obtained with NCCT. This segmentation, although better than that of NCCT, is not free of potential inaccuracies because the Montreal Neurological Institute templates are derived from much younger, healthier brains. Moreover, due to the clinical practice nature of our MR imaging protocol, DWIs could not be corrected for distortions before applying the normalization. Nevertheless, following the proof-of-concept nature of this work, we included only patients with final optimal CTP-MR imaging coregistration and WM-GM

segmentation. If our approach is replicated in other cohorts and proved useful, future effort should focus on developing a system to improve CTP tissue segmentation fast enough to be used in clinical practice, for example, an atlas-based approach to obtain a rapid WM-GM segmentation in the CTP native space. CTP methods for the definition of ischemic core are an approximation to a dynamic and complex process. CTP acquisition parameters and postprocessing are a source of variability in the values obtained from perfusion maps. The CTP analysis was performed with the commercial software MISTar; therefore, our results may not be generalizable to other methodologies, and further studies with other available commercial software are warranted to confirm these results.

This study has some limitations, mainly related to its retrospective, observational design and the modest population size due to the strict inclusion criteria. However, it accurately represents the actual population and the decision-making issues tested in real-life clinical situations. In addition, its results tally with those obtained in previous studies and current knowledge about the effects of ischemia on the human brain. Also, only patients with complete recanalization were studied, so the generalizability of these results to other clinical contexts has to be analyzed in follow-up studies. An external validation would also reinforce these results. Establishing different thresholds in GM and WM based on their susceptibility to ischemia could enhance the precision of CTP to determine whether it is salvageable tissue, thus helping make therapeutic decisions. However, there is no established model of rapid segmentation in routine clinical practice, so future effort should focus on developing a system to improve CTP accuracy using these pathophysiologic principles adapted to daily practice.

CONCLUSIONS

GM- and WM-specific thresholds result in different thresholds for predicting infarcted tissue in CTP and increase the accuracy of the estimations regarding the tissue fate and total infarct volume of each voxel. IG from baseline to follow-up imaging can substantially alter the predictive value of different CTP-based definitions of ischemic core. Compared with the often-used threshold of rCBF 30%, more restrictive thresholds such as rCBF 20%, mainly referring to WM, may better estimate the actual extent of the infarcted tissue.

ACKNOWLEDGMENTS

The authors thank the staff and participants of Hospital Clínic for their relevant contributions. This work was partially developed at the Centro Esther Koplowitz, Barcelona, Centres de Recerca de Catalunya Programme/Generalitat de Catalunya.

Disclosure forms provided by the authors are available with the full text and PDF of this article at www.ajnr.org.

REFERENCES

1. Vagal A, Wintermark M, Nael K, et al. **Automated CT perfusion imaging for acute ischemic stroke: Pearls and pitfalls for real-world use.** *Neurology* 2019;93:888–98 CrossRef Medline
2. Bivard A, Spratt N, Levi C, et al. **Perfusion computed tomography: imaging and clinical validation in acute ischaemic stroke.** *Brain* 2011;134:3408–16 CrossRef Medline

3. Lin L, Bivard A, Krishnamurthy V, et al. **Whole-brain CT perfusion to quantify acute ischemic penumbra and core.** *Radiology* 2016;279:876–87 CrossRef Medline
4. Campbell BC, Christensen S, Levi CR, et al. **Cerebral blood flow is the optimal CT perfusion parameter for assessing infarct core.** *Stroke* 2011;42:3435–40 CrossRef Medline
5. Copen WA, Yoo AJ, Rost NS, et al. **In patients with suspected acute stroke, CT perfusion-based cerebral blood flow maps cannot substitute for DWI in measuring the ischemic core.** *PLoS One* 2017;12:e0188891 CrossRef Medline
6. Boned S, Padroni M, Rubiera M, et al. **Admission CT perfusion may overestimate initial infarct core: the ghost infarct core concept.** *J Neurointerv Surg* 2017;9:66–69 CrossRef Medline
7. Cereda CW, Christensen S, Campbell BC, et al. **A benchmarking tool to evaluate computer tomography perfusion infarct core predictions against a DWI standard.** *J Cereb Blood Flow Metab* 2016;36:1780–89 CrossRef Medline
8. Dohmen C, Kumura E, Rosner G, et al. **Adenosine in relation to calcium homeostasis: comparison between gray and white matter ischemia.** *J Cereb Blood Flow Metab* 2001;21:503–10 CrossRef Medline
9. Payabvash S, Souza LC, Wang Y, et al. **Regional ischemic vulnerability of the brain to hypoperfusion: the need for location specific computed tomography perfusion thresholds in acute stroke patients.** *Stroke* 2011;42:1255–60 CrossRef Medline
10. Hoving JW, Marquering HA, Majoie CB, et al. **Volumetric and spatial accuracy of computed tomography perfusion estimated ischemic core volume in patients with acute ischemic stroke.** *Stroke* 2018;49:2368–75 CrossRef Medline
11. Saver JL. **Time is brain—quantified.** *Stroke* 2006;37:263–66 CrossRef Medline
12. González RG, Hakimelahi R, Schaefer PW, et al. **Stability of large diffusion/perfusion mismatch in anterior circulation strokes for 4 or more hours.** *BMC Neurol* 2010;10:10:13 CrossRef Medline
13. Suomalainen OP, Elseoud Abou A, Martinez-Majander N, et al. **Is infarct core growth linear? Infarct volume estimation by computed tomography perfusion imaging.** *Acta Neurol Scand* 2022;145:684–91 CrossRef Medline
14. Psychogios MN, Schregel K. **Relativity of ischemic core volume estimation.** *Stroke* 2018;49:2283–84 CrossRef Medline
15. Bivard A, Levi C, Spratt N, et al. **Perfusion CT in acute stroke: a comprehensive analysis of infarct and penumbra.** *Radiology* 2013;267:543–50 CrossRef Medline
16. Laredo C, Renú A, Tudela R, et al. **The accuracy of ischemic core perfusion thresholds varies according to time to recanalization in stroke patients treated with mechanical thrombectomy: a comprehensive whole-brain computed tomography perfusion study.** *J Cereb Blood Flow Metab* 2020;40:966–77 CrossRef Medline
17. Noser EA, Shaltoni HM, Hall CE, et al. **Aggressive mechanical clot disruption: a safe adjunct to thrombolytic therapy in acute stroke?** *Stroke* 2005;36:292–96 CrossRef Medline
18. Renú A, Laredo C, Montejo C, et al. **Greater infarct growth limiting effect of mechanical thrombectomy in stroke patients with poor collaterals.** *J Neurointerv Surg* 2019;11:989–93 CrossRef Medline
19. Renú A, Urrea X, Laredo C, et al. **Benefit from mechanical thrombectomy in acute ischemic stroke with fast and slow progression.** *J Neurointerv Surg* 2020;12:132–35 CrossRef Medline
20. Campbell BC, Yassi N, Ma H, et al. **Imaging selection in ischemic stroke: feasibility of automated CT-perfusion analysis.** *Int J Stroke* 2015;10:51–54 CrossRef Medline
21. Benson J, Payabvash S, Salazar P, et al. **Comparison of CT perfusion summary maps to early diffusion-weighted images in suspected acute middle cerebral artery stroke.** *Eur J Radiol* 2015;84:682–89 CrossRef Medline
22. Bousslama M, Ravindran K, Harston G, et al. **Noncontrast computed tomography e-stroke infarct volume is similar to RAPID computed tomography perfusion in estimating postperfusion infarct volumes.** *Stroke* 2021;52:634–41 CrossRef Medline
23. Kasasbeh AS, Christensen S, Parsons MW, et al. **Artificial neural network computer tomography perfusion prediction of ischemic core.** *Stroke* 2019;50:1578–81 CrossRef Medline
24. Chen C, Bivard A, Lin L, et al. **Thresholds for infarction vary between gray matter and white matter in acute ischemic stroke: a CT perfusion study.** *J Cereb Blood Flow Metab* 2019;39:536–46 CrossRef Medline
25. Arakawa S, Wright PM, Koga M, et al. **Ischemic thresholds for gray and white matter: a diffusion and perfusion magnetic resonance study.** *Stroke* 2006;37:1211–16 CrossRef Medline
26. Bristow MS, Simon JE, Brown RA, et al. **MR perfusion and diffusion in acute ischemic stroke: human gray and white matter have different thresholds for infarction.** *J Cereb Blood Flow Metab* 2005;25:1280–87 CrossRef Medline
27. Demeestere J, García-Espérón C, García-Bermejo P, et al. **Evaluation of hyperacute infarct volume using ASPECTS and brain CT perfusion core volume.** *Neurology* 2017;88:2248–53 CrossRef Medline
28. Angermaier A, Khaw AV, Kirsch M, et al. **Influence of recanalization and time of cerebral ischemia on tissue outcome after endovascular stroke treatment on computed tomography perfusion.** *J Stroke Cerebrovasc Dis* 2015;24:2306–12 CrossRef Medline
29. Rao VL, Mlynash M, Christensen S, et al. **Collateral status contributes to differences between observed and predicted 24-h infarct volumes in DEFUSE 3.** *J Cereb Blood Flow Metab* 2020;40:1966–74 CrossRef Medline
30. Guenego A, Marcellus DG, Martin BW, et al. **Hypoperfusion intensity ratio is correlated with patient eligibility for thrombectomy.** *Stroke* 2019;50:917–22 CrossRef Medline
31. Guenego A, Mlynash M, Christensen S, et al. **Hypoperfusion ratio predicts infarct growth during transfer for thrombectomy.** *Ann Neurol* 2018;84:616–20 CrossRef Medline
32. Qiao Y, Zhu G, Patrie J, et al. **Optimal perfusion computed tomographic thresholds for ischemic core and penumbra are not time dependent in the clinically relevant time window.** *Stroke* 2014;45:1355–62 CrossRef Medline
33. d'Esterre CD, Boesen ME, Ahn SH, et al. **Time-dependent computed tomographic perfusion thresholds for patients with acute ischemic stroke.** *Stroke* 2015;46:3390–97 CrossRef Medline

Diagnostic Errors in Cerebrovascular Pathology: Retrospective Analysis of a Neuroradiology Database at a Large Tertiary Academic Medical Center

G. Biddle, R. Assadsangabi, K. Broadhead, L. Hacein-Bey, and V. Ivanovic



ABSTRACT

BACKGROUND AND PURPOSE: Diagnostic errors affect 2%–8% of neuroradiology studies, resulting in significant potential morbidity and mortality. This retrospective analysis of a large database at a single tertiary academic institution focuses on diagnostic misses in cerebrovascular pathology and suggests error-reduction strategies.

MATERIALS AND METHODS: CT and MR imaging reports from a consecutive database spanning 2015–2020 were searched for errors of attending physicians in cerebrovascular pathology. Data were collected on missed findings, study types, and interpretation settings. Errors were categorized as ischemic, arterial, venous, hemorrhagic, and “other.”

RESULTS: A total of 245,762 CT and MR imaging neuroradiology examinations were interpreted during the study period. Vascular diagnostic errors were present in 165 reports, with a mean of 49.6 (SD, 23.3) studies on the shifts when an error was made, compared with 34.9 (SD, 19.2) on shifts without detected errors ($P < .0001$). Seventy percent of examinations occurred in the hospital setting; 93.3% of errors were perceptual; 6.7% were interpretive; and 93.9% ($n = 155$) were clinically significant (RADPEER 2B or 3B). The distribution of errors was arterial and ischemic each with 33.3%, hemorrhagic with 21.8%, and venous with 7.5%. Most errors involved brain MR imaging (30.3%) followed by head CTA (27.9%) and noncontrast head CT (26.1%). The most common misses were acute/subacute infarcts (25.1%), followed by aneurysms (13.7%) and subdural hematomas (9.7%).

CONCLUSIONS: Most cerebrovascular diagnostic errors were perceptual and clinically significant, occurred in the emergency/inpatient setting, and were associated with higher-volume shifts. Diagnostic errors could be minimized by adjusting search patterns to ensure vigilance on the sites of the frequently missed pathologies.

ABBREVIATIONS: ACA = anterior cerebral artery; PCA = posterior cerebral artery; QA = quality assurance

Diagnostic errors are associated with significant morbidity and mortality.^{1,2} In the United States alone, it is estimated that each year, 10% of deaths and \$29 billion dollars in wasteful medical spending can be directly attributed to diagnostic errors in medicine; furthermore, postmortem studies have suggested that up to 20% of deaths result from a different diagnosis than that made pre-mortem.^{3,4} Diagnostic errors in radiology have been defined as major discrepancies between an interpreting radiologist's findings or impressions on a particular study versus the consensus opinion

of radiologist peers.⁵ Factors that predispose to diagnostic errors in radiology are overall categorized as radiologist-related errors and system-related errors;⁶ of the former, perceptual errors are the most important (60%–80%), while interpretation errors constitute the remainder.^{7,8} System-related errors involve the reading room environment, workload, communication issues, and technical and equipment problems.⁹ Current reported errors pertaining to the neuroradiology subspecialty range between 1.7% and 7.7% overall error rates per study.^{10–17} While there are qualitative articles discussing common blind spots in neurology imaging in general,¹⁸ clinical research on the quantification of diagnostic errors in neurovascular imaging is currently lacking. Increased awareness of factors that promote errors in diagnosing vascular problems on neuroradiology studies may direct more targeted search patterns, potentially leading to reduced error rates, including perceptual errors. The purpose of our study was to quantify vascular errors made by neuroradiology attending physicians at a single tertiary academic center (University of California, Davis Medical Center)

Received December 12, 2021; accepted after revision June 16, 2022.

From the Neuroradiology Division (G.B., L.H.-B.), Department of Radiology, University of California Davis School of Medicine, Sacramento, California; Neuroradiology Division (R.A.), Department of Radiology, University of Southern California, Los Angeles, California; Department of Statistics (K.B.), University of California Davis, Davis, California; and Neuroradiology division (V.I.), Department of Radiology, Medical College of Wisconsin, Milwaukee, Wisconsin.

Please address correspondence to Lotfi Hacein-Bey, MD, Radiology Department, University of California Davis School of Medicine, 4860 Y St, Sacramento, CA, 95817; e-mail: lhaceinbey@ucdavis.edu

<http://dx.doi.org/10.3174/ajnr.A7596>

and to offer potential strategies to decrease error rates, particularly by identifying common blind spots.

MATERIALS AND METHODS

Institutional review board approval was obtained for this retrospective study with a waiver of informed consent. The neuroradiology quality assurance (QA) database of diagnostic errors made by attending neuroradiologists at our institution was searched from January 2015 through March 2020 (63 months). The database was searched for vascular diagnostic errors by the 16 current and recently employed full-time diagnostic neuroradiologists (see below for details regarding the QA process). Vascular diagnostic errors were categorized as follows: ischemic (acute/subacute infarcts, chronic infarcts, multiple infarcts, hypoxic-ischemic encephalopathy), hemorrhagic (subdural, epidural, subarachnoid, contusion, intraventricular, retroclival, quantitative expanding hemorrhage), arterial (aneurysm, large-vessel occlusion, significant stenosis [$>70\%$ narrowing], dissection, AVM-AVF, vasospasm, subclavian steal), venous (abnormalities of the dural sinuses, cortical veins, or deep veins), and other (overcalls, posterior reversible encephalopathy syndrome). A broad definition of large-vessel occlusions was used including the intracranial ICA, M1, and M2 of the MCA, anterior cerebral artery (ACA), intracranial vertebral artery, basilar artery, and proximal posterior cerebral artery (PCA).¹⁹

The primary radiologic peer-review method used in the United States is the American College of Radiology RADPEER (<https://www.acr.org/Clinical-Resources/RADPEER>) scoring system.²⁰ Revised most recently in 2016, RADPEER uses a 3-point scoring scale (1, concur with interpretation; 2, discrepancy in interpretation not ordinarily expected to be made; and 3, discrepancy in an interpretation that should be made most of the time) with the option to designate a discrepancy as likely to be clinically insignificant (option A) or likely to be clinically significant (option B).²¹ Clinically significant errors are defined in this article as findings that were erroneously characterized or not observed that affected the patient's treatment or follow-up if the findings had been accurately reported. Thus, we collected data on the following variables associated with the studies: clinically significant errors (RADPEER 2B, 3B) determined at the time of the peer-review process, interpretation setting (inpatient/emergency versus outpatient), mean number of CT and MR imaging scans read during the shift when the diagnostic error was made, study type, error type (perceptual, interpretive), and mean patient age.

The mean volume of interpreted studies per shift was extracted electronically from the department of radiology database, limiting the search to the shifts that were staffed by a neuroradiologist and MR imaging/CT examinations in neuroradiology. The total volume and mean number of interpreted neuroradiologic studies during the 2015–2020 study period were collected. A shift was defined as daily output of interpreted CT or MR imaging studies by an attending neuroradiologist. Shifts with ≤ 10 interpreted studies per day were excluded as outliers, as many of those likely pertain to reports generated on days off, administrative or other, in order to catch up with overflow work from the day before. The mean volume of interpreted studies per shift for

studies containing a vascular diagnostic error was compared with the mean number of interpreted studies per shift for studies that did not have a documented error, using the Welch t test.

Neuroradiology Division and the QA Process

Our neuroradiology QA database includes only CT and MR imaging examinations that are collected from several sources. As part of the QA process, each radiologist in our department is required to evaluate 3 random (software-generated) studies on the days they are assigned to the clinical service and assign a RADPEER score (1, 2A, 2B, 3A, or 3B) to each reviewed study. RADPEER scores 2 and 3 are flagged for further review. Also, in an effort to capture as many diagnostic errors as possible, all addended neuroradiology reports (approximately 1000 addenda per year) are reviewed. Most reports are addended for technical reasons (ie, documentation of contrast or radiation dose, comparison with outside studies not available at the time of the original interpretation) and, therefore, automatically eliminated from the review process. Reports that contain potential diagnostic errors are flagged for further review. Most (approximately 90%) flagged cases are screened through 2 mechanisms: reviews of random, and addended studies. In addition, reports that are submitted by clinicians or radiologists because of disagreement with the original interpretation are flagged for further review. All flagged studies are either reviewed by 2 attending neuroradiologists, or, during our quarterly QA conference, assigned a consensus RADPEER score and entered in our QA database. Study findings are correlated against histologic findings or clinical follow-up, when available. Our neuroradiology division does not currently support subspecialized rotations such as vascular, head and neck, skull base, brain, or pediatric subdivisions, but rather functions as a general neuroradiology practice wherein every subspecialist reads all types of studies. All neuroradiologists included in this study are attending radiologists, full-time employees, and have similar yearly productivity relative value unit rates per full-time employee effort.

RESULTS

During the study period, a total of 245,762 CT and MR imaging studies were interpreted by our neuroradiology section, with a mean volume of 35.2 interpreted studies per shift. Vascular errors made up 25.8% of documented errors in this data set, with a total of 175 errors seen in 165 studies that contained a vascular diagnostic error, with a mean of 49.6 (SD, 23.3) interpreted CT and MR imaging studies on shifts when errors were made, totaling 158 shifts. Shifts in which no errors were documented had a mean volume of 34.9 (SD, 19.2) interpreted CT and MR imaging studies, totaling 7231 shifts. The Welch t test was used to look for significant differences between the mean volume of interpreted studies per shift for the 2 groups. The results suggest a highly significant difference ($t_{162} = 7.9, P < .0001$), with studies containing an error interpreted during higher-volume shifts.

The mean patient age in this study was 54.9 (SD, 23.8) years; 96 patients (58.2%) were men and 69 (41.8%) were women. Of the 165 studies with an error, 116 (70%) involved patients in the hospital setting (emergency department or inpatient), while the remaining occurred in the ambulatory setting. Table 1 shows the breakdown of errors relative to the examination type, with MR

Table 1: Diagnostic error versus imaging technique

Study	Total Examinations (<i>n</i> = 165)	Percentage (%)
MR imaging brain	50	30.3%
CTA head	46	27.9%
Noncontrast head CT	43	26.1%
CTA neck	7	4.2%
MRA brain	5	3.0%
CT neck	4	2.4%
CT cervical spine	4	2.4%
MR imaging cervical spine	2	1.2%
MRA neck	1	0.6%
MR imaging lumbar spine	1	0.6%
MR imaging total spine	1	0.6%
CT sinus	1	0.6%

Table 2: Error type based on pathology

Pathology	Total Errors (<i>n</i> = 175)	Percentage (%)
Acute/subacute infarct	44	25.1%
Aneurysm	24	13.7%
Subdural hematoma	17	9.7%
Significant arterial stenosis	11	6.3%
Dural sinus occlusion	11	6.3%
Epidural hematoma	8	4.6%
Large-vessel occlusion	8	4.6%
Overcall	7	4.0%
Arterial dissection	7	4.0%
Hypoxic-ischemic encephalopathy	7	4.0%
Chronic infarct	5	2.9%
AVM-AVF	5	2.9%
Subarachnoid hemorrhage	5	2.9%
Hemorrhagic contusion	3	1.7%
Embolic infarct	2	1.1%
Intraventricular hemorrhage	2	1.1%
Retroclival bleed	2	1.1%
Vasospasm	2	1.1%
Subclavian steal	1	0.6%
Sinus pericranii	1	0.6%
Deep neck vein occlusion	1	0.6%
Growing hemorrhage	1	0.6%
PRES	1	0.6%

Note:—PRES indicates posterior reversible encephalopathy syndrome.

imaging of the brain being the most common with 30.3% (*n* = 50), followed by CTA of the head (27.9%, *n* = 46) and noncontrast head CT (26.1%, *n* = 43). The remaining study types for which an error was detected had ≤7 cases each. Errors were considered perceptual in 154 (93.3%) and interpretive in the remaining 11 (6.7%) cases. Clinically significant errors were found in 155 (93.9%) cases (RADPEER score of 2B or 3B). All non-clinically significant errors were found to be perceptual.

The total distribution of errors in this study is given in Table 2. Figure 1 shows that ischemic and arterial errors were equally prevalent with 58 errors each (33.3%), followed by hemorrhage (21.8%, *n* = 38) and venous abnormalities (7.5%, *n* = 13). Eight errors categorized as “other” (4.6%) included a single case of a posterior reversible encephalopathy syndrome as well as 7 overcalls consisting of 2 aneurysms, a pseudoaneurysm, a carotid injury, a vertebral

artery occlusion, an epidural bleed, and a penumbra called an infarct. The breakdown of 58 missed ischemic injuries included 44 that were acute/subacute, 7 attributed to hypoxic-ischemic encephalopathy, 5 chronic ischemic insults, as well as 2 multiple, thought to be embolic. Figure 2 demonstrates the specific locations of acute infarcts, with MCA territory being the most common, followed by thalamic and cerebellar territories. The average size of infarct errors was: MCA (1.6 cm; range, 0.5–3.5 cm); cerebellar (2.0 cm; range, 0.4–3.9 cm); thalamic (1.4 cm; range, 0.6–2.4 cm), while the less frequently seen errors involved the ACA at 2.6 cm (range, 0.7–4.5 cm), brainstem at 0.8 cm (range 0.4–1.1 cm), and embolic at 0.6 cm (range, 0.4–0.8 cm).

Figure 3 shows that of 58 cases of arterial pathology, 24 were attributed to cerebral aneurysms; 11, to significant stenoses; 8, to large-vessel occlusion (5 located at the M2 segment, as well as 1 each in the M1, PCA, and basilar artery, respectively); 7, to arterial dissection; 5, to AVM/AVF; 2, to vasospasm, and 1, to subclavian steal. With the exception of a 5.3-cm abdominal aortic aneurysm that was not discussed on MR imaging of the lumbar spine, the average size of aneurysms was 0.5 cm (range, 0.2–0.7 cm). Table 3 shows the location of missed aneurysms: 14 of the 25 aneurysmal errors (56.0%) involved the ICA, with 5 in the cavernous segment, 4 in the clinoid and supraclinoid segments, 3 in the terminus, and 2 paraophthalmic aneurysms. There were 4 MCA aneurysms as well as 2 aneurysms seen in the ACA and posterior communicating artery, while the abdominal aorta and PCA had 1 aneurysm. Figure 4 demonstrates the location of the combined 27 cases of significant stenosis, large-vessel occlusion, and arterial dissection, with the ICA and MCA, specifically the distal M2 segment, being the most common. Of the 8 large-vessel occlusions, 5 were of the M2 segment of the MCA, with single cases involving the M1 segment of the MCA, the PCA, and the basilar artery respectively.

The most common missed hemorrhagic lesions were subdural hematomas (*n* = 17), followed by epidural hematomas (*n* = 8) and subarachnoid hemorrhage (*n* = 5). We found ≤3 errors of the following conditions: hemorrhagic contusion (*n* = 3), intraventricular hemorrhage (*n* = 2), retroclival bleed (*n* = 2), and expanding parenchymal hemorrhage (*n* = 1) using a standard 3-orthogonal-plane measurement and comparison per routine interpretation determined at the time of the RADPEER process (Fig 5). The average size of hemorrhagic lesions included 0.5 cm for subdural hematoma (range, 0.3–1.0 cm), 0.4 cm for epidural hematomas (range, 0.3–0.5 cm), 0.6 cm for contusions (range, 0.2–0.9 cm), and 0.3 cm for retroclival bleed (range, 0.2–0.4 cm). The growing hemorrhage on the follow-up CT 12 hours later increased to a volume of 10.9 mL from an initial 5.7 mL, which was not reported. The most common error involving the venous system was dural sinus occlusion, which was seen in 11 cases; the remaining 2 cases were sinus pericranii and a deep neck vein thrombosis.

The imaging technique with errors was further categorized for the top 3 most common pathologies. For the 44 acute/subacute ischemic strokes, 21 were on MR imaging of the brain, 12 were on CTA of the head, and 11 were on noncontrast head CT. Of the 24 aneurysms (seen on 23 examinations; 1 CTA study contained bilateral missed aneurysms), 14 were on CTA of the head, 5 were on MR imaging of the brain, 3 were on MRA of the brain, and 1 abdominal aortic aneurysm was seen on MR imaging of

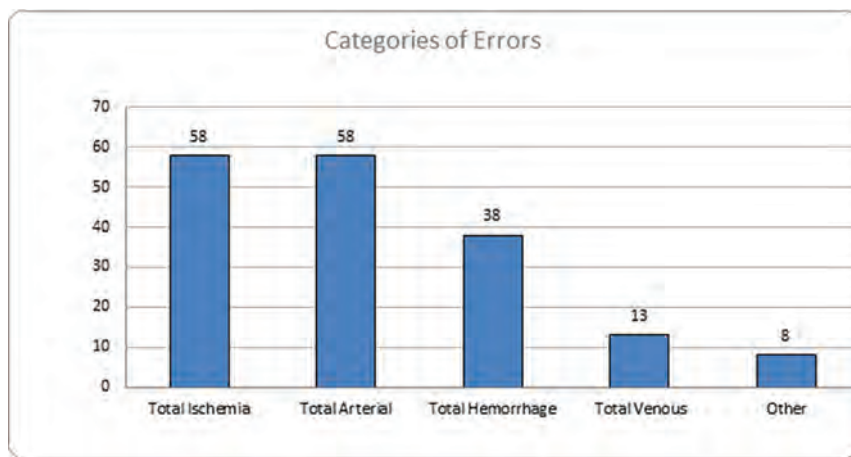


FIG 1. Categories of errors.

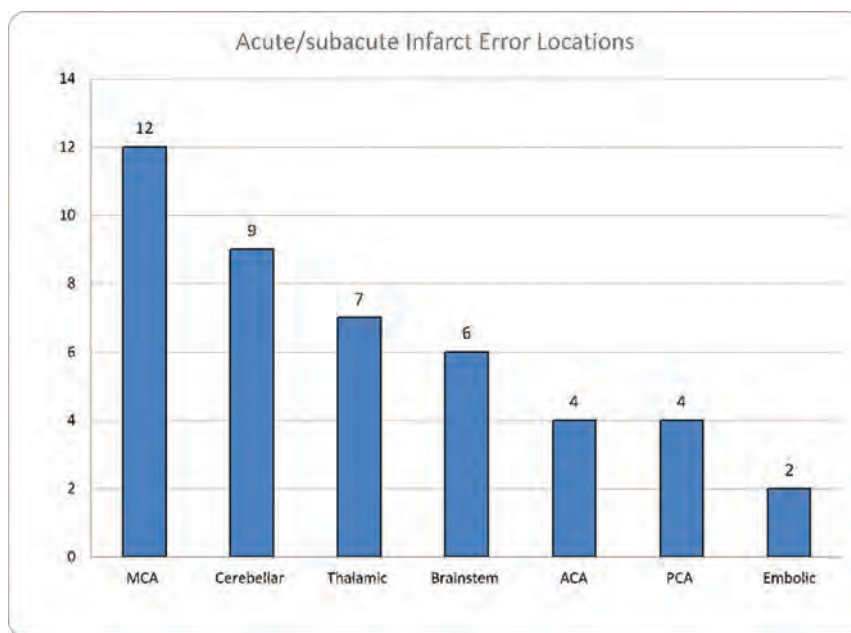


FIG 2. Errors in acute/subacute infarct location.

the lumbar spine. Seventeen subdural hematomas were on 15 noncontrast head CTs, 1 on MR imaging of the brain, and 1 on CT of the sinus and face.

Although random, our method of collecting cases has yielded a very narrow and consistent range of total diagnostic neuroradiology error rates shown to range between 0.20% and 0.25% (2014–2020, internal records), which may be interpreted as indicative of reproducibility and reliability.

DISCUSSION

In this series, most cerebrovascular diagnostic errors were perceptual and clinically significant and occurred in the emergency/inpatient setting and were associated with higher-volume shifts. Although uncommon, cerebrovascular diagnostic errors had a significant clinical impact on most patients because 54.8% of errors

involved acute/subacute ischemic injuries, cerebral aneurysms, subdural hematomas, and significant arterial stenosis. Every year in the United States, >215,000 deaths are thought to result from medical errors, third in prevalence only after cancer and heart disease,²² for which the impact of radiologic diagnostic errors is considered major.^{5,23} The current standard used to define errors in radiology interpretation is a discrepancy in interpretation that differs substantially from the consensus of peers, for which the current evaluation mechanism in the United States is the aforementioned RADPEER process.^{20,21} In that sense, a criterion standard is lacking; objective reference standards such as postmortem-proved or surgically confirmed diagnoses are, indeed, very uncommonly available.²⁴

Because most cerebrovascular conditions have a poor natural history, particularly severe consequences can be expected to result from an erroneous or delayed diagnosis.²⁵ Therefore, diagnostic errors in this organ system have relatively heightened relevance in comparison with other, more forgiving anatomic areas and disease processes.^{26,27} For instance, the reported prognosis of untreated acute ischemic stroke from large-vessel occlusion is consistent with high rates (up to 64%) of severe functional dependence or death (measured by the 90-day mRS, with scores of >2); for non-large-vessel occlusion strokes, the reported average expected rates of functional dependence or death are around 24%.^{19,28} Our study contained 44 missed, acute/subacute ischemic injuries.

The natural history of intracranial aneurysms suggests annual rupture rates around 1.1%–1.3%.^{29,30} Although the prevalence of intracranial aneurysms worldwide may be far larger than previously thought, possibly ranging between 5% and 8%,^{31,32} hemorrhagic rates may be high in certain populations with specific risk factors.^{33–35} A cumulative hemorrhagic rate of 10.5% at 10 years has been estimated for previously unruptured aneurysms,³⁰ and the 10-year mortality rate for ruptured, untreated aneurysms was reported at around 76%.³⁶ Our study contained 24 missed aneurysms.

Subdural and epidural hematomas can have devastating morbidity and mortality if not recognized and acted on in a timely manner.³⁷ Subdural hematomas may often be treated conservatively on the basis of objective criteria such as the Glasgow Coma Scale score, the width of the hematoma, or the amount of midline shift.^{38,39} A study by Ryan et al⁴⁰ published in 2012 in the *Journal of Trauma and Acute Care Surgery* explored mortality and functional outcomes

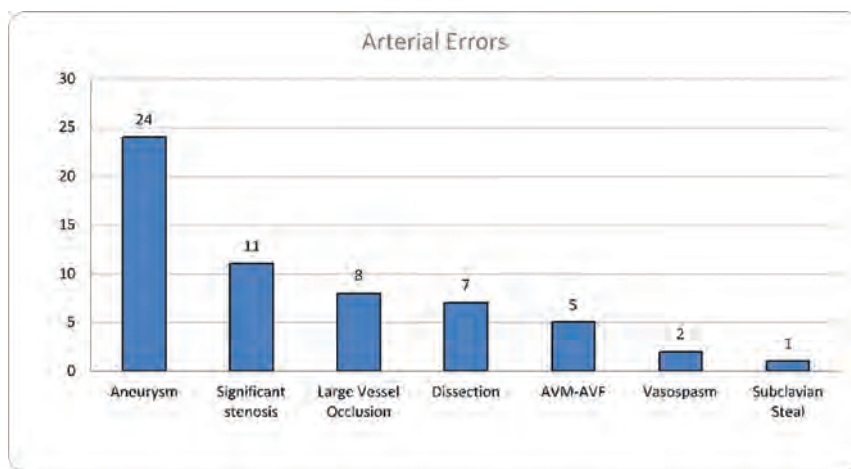


FIG 3. Errors in overall vascular pathology.

Table 3: Location of missed aneurysm

Aneurysm Location	Total (n = 24)	Percentage
ICA, cavernous	5	20.8%
MCA	4	16.7%
ICA, clinoid	4	16.7%
ICA, terminus	3	12.50%
ICA, paraophthalmic	2	8.3%
AcomA	2	8.3%
PcomA	2	8.3%
Abdominal aorta	1	4.2%
PCA	1	4.2%

Note:—AcomA indicates anterior communicating artery; PcomA, posterior communicating artery.

in adult patients at a Level 1 Trauma Center. That study demonstrated that inpatient mortality was 16% (15% for surgical patients, 17% for the nonsurgical group), lower than that in previous studies from the 1970s to 2000s, which reported 22%–57% mortality ranges.^{37,41,42} The authors credited the widespread and liberal use of CT, which allows detecting patients with less severe hematomas, and recent advances in surgical techniques as the main reasons for improved outcomes. Our study contained 17 missed subdural hematomas. Epidural hematomas may have better prognoses compared with subdural hemorrhage with prompt surgical evacuation, with a 17% reported mortality; however, that figure rises to 65% if surgery is performed >2 hours from the onset of coma.³⁷ Our study contained 8 missed epidural hematomas.

The prognosis of large intracranial artery stenotic disease was evaluated in multiple trials,⁴³ which have found an annual risk of death around 11.2% and an annual risk of stroke of 12.5%–17.1%.^{44,45} Our study contained 11 missed large-artery stenoses.

Cerebral venous thrombosis, which encompasses both dural sinus and cortical vein thrombosis, accounts for 0.5% of all strokes.⁴⁶ Common predisposing factors are hypercoagulable disorders (known or cryptic), trauma, and infection, though rare occurrences have recently been shown to be linked to some coronavirus disease 2019 (COVID-19) vaccines.⁴⁶ Despite being uncommon, cerebral venous thrombosis is potentially fatal if diagnosis and treatment are delayed,⁴⁷ with median reported mortality rates of 5.6% (range, 0%–15.2%).⁴⁸ Our study contained 11 missed venous thromboses.

Although relatively benign compared with other causes of stroke, possibly due to the younger age of patients, the natural history of cervical artery dissection includes neurologic injury and severe hemodynamic compromise.⁴⁹ Recurrent TIA, stroke, or death may be seen in up to 15% within 2 weeks following intimal injury,⁵⁰ and recurrence of dissection is seen in roughly 1%–8% of patients.^{51,52} Our study contained 7 cases of missed dissections.

The mean number of interpreted studies per shift was a factor that reached statistical significance, because more errors were made on busier shifts, showing a higher propensity for diagnostic errors with higher-volume reads, as suggested by the literature.^{5,7,10,11,25–27}

Again, most errors in our series were perceptual errors, ie, radiologists did not identify the abnormality. Causes of errors may include type I heuristic thinking (rapid problem-solving based on presumptions and previous experiences), cognitive biases (satisfaction of search, availability, anchoring and framing biases), as well as systemic causes such as increased workload, understaffing, workplace interruptions, software failure, and insufficient clinical information.^{1,6,8,9} Therefore, our response to the study findings included heightened attention paid to identifying the perceptual errors in structured radiology reports to quantify anatomic blind spots in vascular pathology to help create a checklist and minimize future errors. This checklist of anatomic regions requiring hypervigilance included areas susceptible to ischemic injury, locations of commonly missed cerebral aneurysms, and stenosis, as well as the large and small extra-axial spaces to look for extra-axial hematomas (subdural and epidural). The MCA and distal branches, ICA, thalamus, as well as the cerebellum made up the location of 57 (32.6%) errors in this article. Adding these areas to a checklist of items for which additional scrutiny is required would have a significant impact on reducing errors. Having such systems in place for error identification and reduction/elimination is not just important for patient care but also serves to decrease medicolegal exposure.

Potential avenues toward error reduction indeed include reporting template adjustments to include areas affected by frequent errors, additional educational initiatives, multidisciplinary/multispecialty conferences, subspecialty morbidity and mortality conferences, and occasionally double reading.^{8,25} Although recent evidence exists that double reading of CTA might reduce error rates,¹⁷ as suggested by Garland⁵³ as far back as 1949, there is generally strong structural resistance to double reading in the United States because the second read is not reimbursed and for concern about the additional time commitment in a productivity-based system.⁵⁴

Limitations to our study include those inherent to a retrospective design and a relatively low rate of detected misses, given the volume of interpreted examinations. No standardized methodology is currently available for the recording of errors in QA databases, which has to be taken into account when interpreting our findings. Our neuroradiology section reads a large number of studies (>240,000

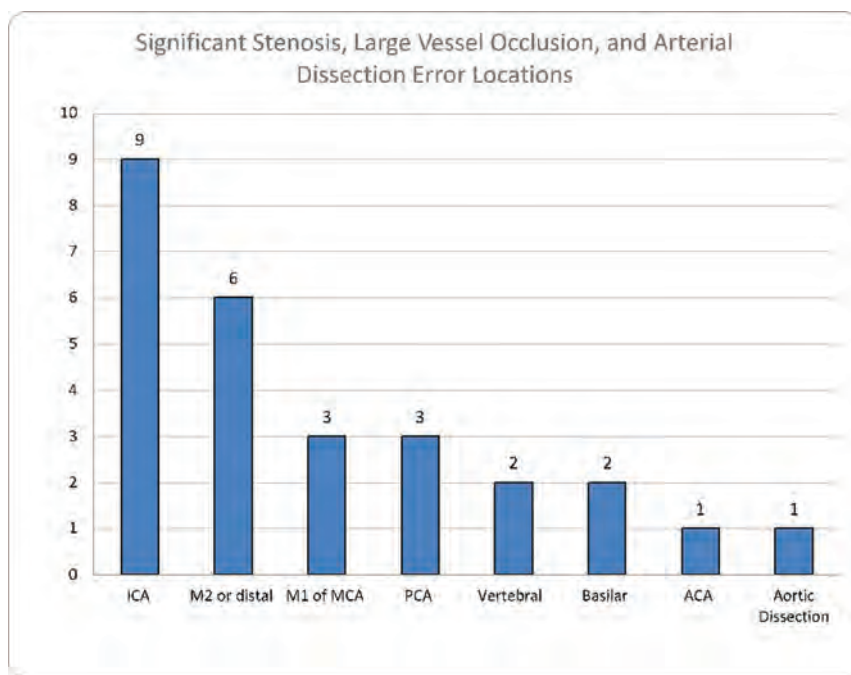


FIG 4. Errors in arterial pathology.

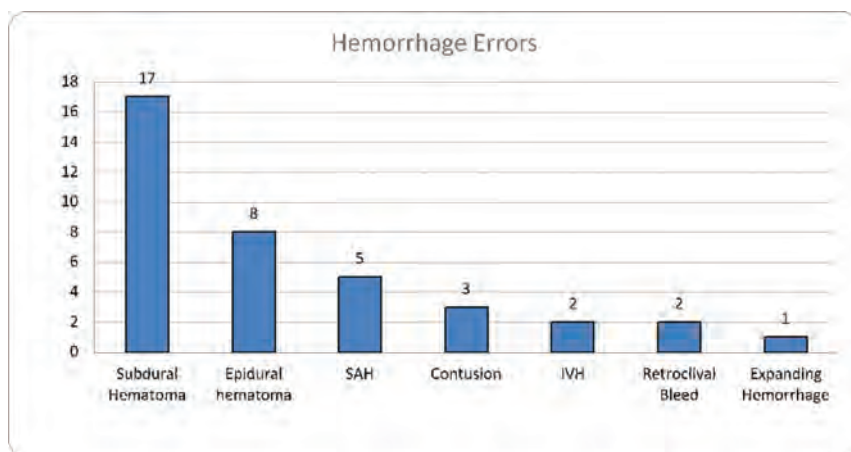


FIG 5. Errors in hemorrhage detection.

studies in this article), so a second reading cannot be reasonably used widely; however, we used the double-reading method in collecting cases for our QA database and when assessing addended reports, which has proved efficient in uncovering a large number of diagnostic errors that could then be further analyzed. Our robust quality-improvement program methods used to identify errors uncovered approximately 10% of our total errors (internal data), and any strategy aimed at reducing errors based on the findings in our sample of discovered errors is expected to be applicable to our studies. Although our QA methods may be biased toward detecting clinically significant errors, we believe that such methodology does the following: 1) serves to collect as many cases as feasible in a random manner, 2) allows root-cause analysis, and 3) provides an opportunity for the design of interventional strategies aimed at reducing diagnostic errors.

A direct comparison of our neurovascular error rates with those of other practices is not possible because no relevant literature exists that discusses vascular error rates. Why our perceptual error rates are at the high end of the spectrum of published literature is currently being evaluated, with possible factors including technical issues in vascular imaging, volumes of interpreted examinations per shift, significant underappreciation of neuroradiology error rates in the literature, and, possibly, our unique methodology of collecting cases for the QA database. Error identification and implementation of corrective systems significantly impact patient care and medicolegal exposure. We are also actively investigating other variables that may show potential correlations with diagnostic errors. For example, there is evidence that high participation rates at multidisciplinary tumor boards is strongly correlated with low attending errors.⁵⁵ These data may offer additional guidance on future interventions toward error reduction.

CONCLUSIONS

Most vascular errors noted in our series were perceptual and clinically significant, occurring in the emergency/inpatient setting and associated with higher-volume shifts. Acute/subacute ischemia, aneurysms, and subdural hematomas represent more than half of all errors. Hopefully, errors in vascular neuroradiology could be minimized if search patterns were altered to include hypervigilance of the sites most frequently affected by disease.

ACKNOWLEDGMENT

We would like to acknowledge Michelle Wilkins for data mining and data analysis support.

Disclosure forms provided by the authors are available with the full text and PDF of this article at www.ajnr.org.

REFERENCES

1. Itri JN, Tappouni RR, McEachern RO, et al. **Fundamentals of diagnostic error in imaging.** *Radiographics* 2018;38:1845–65 CrossRef Medline
2. Balogh EP, Miller BT, Ball JR, eds; Committee on Diagnostic Error in Health Care, Board on Health Care Services, Institute of Medicine, and National Academies of Sciences, Engineering, and Medicine.

Improving Diagnosis in Health Care. National Academies Press (US) 2015

3. Kohn LT, Corrigan JM, Donaldson MS, eds; Institute of Medicine Committee on Quality of Health Care in America. *To Err is Human: Building a Safer Health System*. National Academies Press (US) 2000
4. Singh H, Meyer AN, Thomas EJ. **The frequency of diagnostic errors in outpatient care: estimations from three large observational studies involving US adult populations.** *BMJ Qual Saf* 2014;23:727–31 CrossRef Medline
5. Waite S, Scott J, Gale B, et al. **Interpretive error in radiology.** *AJR Am J Roentgenol* 2017;208:739–49 CrossRef Medline
6. Itri JN, Patel SH. **Heuristics and cognitive error in medical imaging.** *AJR Am J Roentgenol* 2018;210:1097–1105 CrossRef Medline
7. Berlin L. **Radiologic errors, past, present and future.** *Diagnosis (Berl)* 2014;1:79–84 CrossRef Medline
8. Busby LP, Courtier JL, Glastonbury CM. **Bias in radiology: the how and why of misses and misinterpretations.** *Radiographics* 2018;38:236–47 CrossRef Medline
9. Hanna TN, Lamoureux C, Krupinski EA, et al. **Effect of shift, schedule, and volume on interpretive accuracy: a retrospective analysis of 2.9 million radiologic examinations.** *Radiology* 2018;287:205–12 CrossRef Medline
10. Donald JJ, Barnard SA. **Common patterns in 558 diagnostic radiology errors.** *J Med Imaging Radiat Oncol* 2012;56:173–78 CrossRef Medline
11. Kim YW, Mansfield LT. **Fool me twice: delayed diagnoses in radiology with emphasis on perpetuated errors.** *AJR Am J Roentgenol* 2014;202:465–70 CrossRef Medline
12. Wu MZ, McInnes MD, Macdonald DB, et al. **CT in adults: systematic review and meta-analysis of interpretation discrepancy rates.** *Radiology* 2014;270:717–35 CrossRef Medline
13. Babiarz LS, Yousem DM. **Quality control in neuroradiology: discrepancies in image interpretation among academic neuroradiologists.** *AJNR Am J Neuroradiol* 2012;33:37–42 CrossRef Medline
14. Soffa DJ, Lewis RS, Sunshine JH, et al. **Disagreement in interpretation: a method for the development of benchmarks for quality assurance in imaging.** *J Am Coll Radiol* 2004;1:212–17 CrossRef Medline
15. Borgstede JP, Lewis RS, Bhargavan M, et al. **RADPEER quality assurance program: a multifacility study of interpretive disagreement rates.** *J Am Coll Radiol* 2004;1:59–65 CrossRef Medline
16. Viertel VG, Babiarz LS, Carone M, et al. **Quality control in neuroradiology: impact of trainees on discrepancy rates.** *AJNR Am J Neuroradiol* 2012;33:1032–36 CrossRef Medline
17. Lian K, Bharatha A, Aviv RI, et al. **Interpretation errors in CT angiography of the head and neck and the benefit of double reading.** *AJNR Am J Neuroradiol* 2011;32:2132–35 CrossRef Medline
18. Bahrami S, Yim CM. **Quality initiatives: blind spots at brain imaging.** *Radiographics* 2009;29:1877–96 CrossRef Medline
19. Rennert RC, Wali AR, Steinberg JA, et al. **Epidemiology, natural history, and clinical presentation of large vessel ischemic stroke.** *Neurosurgery* 2019;85:S4–S8 CrossRef Medline
20. Abujudeh H, Pyatt RS Jr, Bruno MA, et al. **RADPEER peer review: relevance, use, concerns, challenges, and direction forward.** *J Am Coll Radiol* 2014;11:899–904 CrossRef Medline
21. Goldberg-Stein S, Frigini LA, Long S, et al. **ACR RADPEER Committee White Paper with 2016 Updates: Revised Scoring System, New Classifications, Self-Review, and Subspecialized Reports.** *J Am Coll Radiol* 2017;14:1080–86 CrossRef Medline
22. Makary MA, Daniel M. **Medical error—the third leading cause of death in the US.** *BMJ* 2016;353:i2139 CrossRef Medline
23. Sabih DE, Sabih A, Sabih Q, et al. **Image perception and interpretation of abnormalities; can we believe our eyes? Can we do something about it?** *Insights Imaging* 2011;2:47–55 CrossRef Medline
24. Bruno MA, Walker EA, Abujudeh HH. **Understanding and confronting our mistakes: the epidemiology of error in radiology and strategies for error reduction.** *Radiographics* 2015;35:1668–76 CrossRef Medline
25. Patel SH, Stanton CL, Miller SG, et al. **Risk factors for perceptual-versus-interpretative errors in diagnostic neuroradiology.** *AJNR Am J Neuroradiol* 2019;40:1252–56 CrossRef Medline
26. Renfrew DL, Franken EA Jr, Berbaum KS, et al. **Error in radiology: classification and lessons in 182 cases presented at a problem case conference.** *Radiology* 1992;183:145–50 CrossRef Medline
27. Waite S, Farooq Z, Grigorian A, et al. **A review of perceptual expertise in radiology: how it develops, how we can test it, and why humans still matter in the era of artificial intelligence.** *Acad Radiol* 2020;27:26–38 CrossRef Medline
28. Malhotra K, Gornbein J, Saver JL. **Ischemic strokes due to large-vessel occlusions contribute disproportionately to stroke-related dependence and death: a review.** *Front Neurol* 2017;8:651 CrossRef Medline
29. Juvela S, Porras M, Poussa K. **Natural history of unruptured intracranial aneurysms: probability of and risk factors for aneurysm rupture.** *J Neurosurg* 2000;93:379–87 CrossRef Medline
30. Juvela S, Poussa K, Lehto H, et al. **Natural history of unruptured intracranial aneurysms: a long-term follow-up study.** *Stroke* 2013;44:2414–21 CrossRef Medline
31. Vlak MH, Algra A, Brandenburg R, et al. **Prevalence of unruptured intracranial aneurysms, with emphasis on sex, age, comorbidity, country, and time period: a systematic review and meta-analysis.** *Lancet Neurol* 2011;10:626–36 CrossRef Medline
32. Li MH, Chen SW, Li YD, et al. **Prevalence of unruptured cerebral aneurysms in Chinese adults aged 35 to 75 years: a cross-sectional study.** *Ann Intern Med* 2013;159:514–21 CrossRef Medline
33. Greving JP, Wermer MJ, Brown RD, Jr, et al. **Development of the PHASES score for prediction of risk of rupture of intracranial aneurysms: a pooled analysis of six prospective cohort studies.** *Lancet Neurol* 2014;13:59–66 CrossRef Medline
34. Backes D, Rinkel GJ, Greving JP, et al. **ELAPSS score for prediction of risk of growth of unruptured intracranial aneurysms.** *Neurology* 2017;88:1600–06 CrossRef Medline
35. Etminan N, Brown RD Jr, Beseoglu K, et al. **The unruptured intracranial aneurysm treatment score: a multidisciplinary consensus.** *Neurology* 2015;85:881–89 CrossRef Medline
36. Korja M, Kivisaari R, Rezai Jahromi B, et al. **Natural history of ruptured but untreated intracranial aneurysms.** *Stroke* 2017;48:1081–84 CrossRef Medline
37. Haselsberger K, Pucher R, Auer LM. **Prognosis after acute subdural or epidural haemorrhage.** *Acta Neurochir (Wien)* 1988;90:111–16 CrossRef Medline
38. Bullock MR, Chesnut R, Ghajar J, et al. **Surgical management of acute subdural hematomas.** *Neurosurgery* 2006;58:S2–16–24 CrossRef Medline
39. Vega RA, Valadka AB. **Natural history of acute subdural hematoma.** *Neurosurg Clin N Am* 2017;28:247–55 CrossRef Medline
40. Ryan CG, Thompson RE, Temkin NR, et al. **Acute traumatic subdural hematoma: current mortality and functional outcomes in adult patients at a level I trauma center.** *J Trauma Acute Care Surg* 2012;73:1348–54 CrossRef Medline
41. Tian HL, Chen SW, Xu T, et al. **Risk factors related to hospital mortality in patients with isolated traumatic acute subdural haematoma: analysis of 308 patients undergone surgery.** *Chin Med J (Engl)* 2008;121:1080–84 Medline
42. Tallon JM, Ackroyd-Stolarz S, Karim SA, et al. **The epidemiology of surgically treated acute subdural and epidural hematomas in patients with head injuries: a population-based study.** *Can J Surg* 2008;51:339–45 Medline
43. Pu Y, Dou X, Liu L. **Natural history of intracranial atherosclerotic disease.** *Front Neurol* 2014;5:125 CrossRef Medline
44. Wong KS, Li H. **Long-term mortality and recurrent stroke risk among Chinese stroke patients with predominant intracranial atherosclerosis.** *Stroke* 2003;34:2361–66 CrossRef Medline
45. Kern R, Steinke W, Daffertshofer M, et al. **Stroke recurrences in patients with symptomatic vs asymptomatic middle cerebral artery disease.** *Neurology* 2005;65:859–64 CrossRef Medline
46. Ropper AH, Klein JP. **Cerebral venous thrombosis.** *N Engl J Med* 2021;385:59–64 CrossRef Medline

47. Idiculla PS, Gurala D, Palanisamy M, et al. **Cerebral venous thrombosis: a comprehensive review.** *Eur Neurol* 2020;83:369–79 CrossRef Medline
48. Dentali F, Gianni M, Crowther MA, et al. **Natural history of cerebral vein thrombosis: a systematic review.** *Blood* 2006;108:1129–34 CrossRef Medline
49. Schwartz NE, Vertinsky AT, Hirsch KG, et al. **Clinical and radiographic natural history of cervical artery dissections.** *J Stroke Cerebrovasc Dis* 2009;18:416–23 CrossRef Medline
50. Beletsky V, Nadareishvili Z, Lynch J, et al; Canadian Stroke Consortium. **Cervical arterial dissection: time for a therapeutic trial?** *Stroke* 2003;34:2856–60 CrossRef Medline
51. Touzé E, Gauvrit JY, Moulin T, et al; Multicenter Survey on Natural History of Cervical Artery Dissection. **Risk of stroke and recurrent dissection after a cervical artery dissection: a multicenter study.** *Neurology* 2003;61:1347–51 CrossRef Medline
52. Schievink WI, Mokri B, O'Fallon WM. **Recurrent spontaneous cervical-artery dissection.** *N Engl J Med* 1994;330:393–97 CrossRef Medline
53. Garland LH. **On the scientific evaluation of diagnostic procedures.** *Radiology* 1949;52:309–28 CrossRef Medline
54. Onega T, Aiello Bowles EJ, Miglioretti DL, et al. **Radiologists' perceptions of computer aided detection versus double reading for mammography interpretation.** *Acad Radiol* 2010;17:1217–26 CrossRef Medline
55. Ivanovic V, Assadsangabi R, Hacein-Bey L, et al. **Neuroradiology diagnostic errors at a tertiary academic centre: effect of participation in tumour boards and physician experience.** *Clin Radiol* 2022 May 16. [Epub ahead of print] CrossRef Medline

Larger Posterior Revascularization Associated with Reduction of Choroidal Anastomosis in Moyamoya Disease: A Quantitative Angiographic Analysis

T. Funaki, A. Miyakoshi, H. Kataoka, J.C. Takahashi, Y. Takagi, K. Yoshida, T. Kikuchi, Y. Mineharu, M. Okawa, Y. Yamao, Y. Fushimi, and S. Miyamoto



ABSTRACT

BACKGROUND AND PURPOSE: Choroidal anastomosis, a hemorrhage-prone periventricular collateral manifestation in Moyamoya disease, outflows to the cortex posterior to the central sulcus. The objective of the present study was to test whether the angiographic extent of revascularization posterior to the central sulcus contributes to the postoperative reduction of choroidal anastomosis.

MATERIALS AND METHODS: This retrospective cohort study included choroidal anastomosis-positive hemispheres before direct bypass surgery. The postoperative reduction of choroidal anastomosis was determined by a consensus of 2 raters according to the previous research. An imaging software automatically traced the angiographic revascularization area, which was subsequently divided into anterior and posterior parts by an anatomic line corresponding to the central sulcus. Each area was quantitatively measured as a percentage relative to the whole supratentorial area.

RESULTS: Postoperative reduction of choroidal anastomosis was achieved in 68 (85.0%) of the 80 included hemispheres. The revascularization area posterior to the central sulcus was significantly larger in the hemispheres with reduction than in those with no reduction (mean, 15.2% [SD, 7.1%] versus 4.2% [SD, 3.4%], $P < .001$), whereas no significant difference was observed in the revascularization area anterior to the central sulcus. Multivariate analysis revealed that the revascularization area posterior to the central sulcus was the only significant factor associated with reduction (OR, 1.57; 95% CI, 1.21–2.03, for every 1% increase).

CONCLUSIONS: The results suggest that a larger revascularization posterior to the central sulcus is associated with postoperative reduction of choroidal anastomosis regardless of the extent of anterior revascularization. It might facilitate optimal selection of the revascularization site for preventing hemorrhage.

ABBREVIATIONS: CS = central sulcus; PCA = posterior cerebral artery; STA = superficial temporal artery

Choroidal anastomosis is one of the abnormal periventricular collaterals in Moyamoya disease.^{1–5} The collateral is characterized by a connection between the choroidal and medullary arteries, which outflows to the cortex via retrograde flow in the medullary artery (Fig 1).^{2,3,6} Choroidal anastomosis is commonly observed in

hemorrhagic Moyamoya disease^{7–9} and is associated with an extremely high risk of bleeding.^{4,5,10} After bypass surgery, the normalized direction of flow in the medullary artery can induce angiographic reduction of choroidal anastomosis.^{6,11} This change might explain the effectiveness of direct bypass in preventing bleeding.^{12–14} However, only a few studies have focused on the factors contributing to this change.¹⁵ A recent study revealed that choroidal anastomosis outflows to the cortex posterior to the central sulcus (CS).¹⁶ We hypothesized that a larger angiographic extent of revascularization posterior to the CS is associated with the reduction of choroidal anastomosis. Testing this hypothesis might help to determine the optimal revascularization site for preventing hemorrhage.

MATERIALS AND METHODS

The present retrospective cohort study was approved by Kyoto University Hospital institutional ethics committee (R1600). The Strengthening the Reporting of Observational Studies in Epidemiology was followed. All participants gave opt-out

Received April 21, 2022; accepted after revision June 28.

From the Departments of Neurosurgery (T.F., A.M., K.Y., T.K., Y.M., M.O., Y.Y., S.M.) and Diagnostic Imaging and Nuclear Medicine (Y.F.), Kyoto University Graduate School of Medicine, Kyoto, Japan; Department of Neurosurgery (H.K.), National Cerebral and Cardiovascular Center, Osaka, Japan; Department of Neurosurgery (J.C.T.), Kindai University Faculty of Medicine, Osaka, Japan; and Department of Neurosurgery (Y.T.), Tokushima University Graduate School of Biomedical Sciences, Tokushima, Japan.

This work was partly supported by a Grants-in-Aid for Scientific Research from the Japan Society for the Promotion of Science (JP21K16628).

Please address correspondence to Takeshi Funaki, MD, PhD, Graduate School of Medicine, Kyoto University, 54 Kawahara-cho, Shogoin, Sakyo-ku, Kyoto 606-8507, Japan; e-mail: tfunaki@kuhp.kyoto-u.ac.jp

Indicates open access to non-subscribers at www.ajnr.org

Indicates article with online supplemental data.

<http://dx.doi.org/10.3174/ajnr.A7609>

consent in accordance with the ethical standards of the institutional and national research committees.

Patients and Setting

The present study included patients who had been diagnosed with Moyamoya disease according to the guidelines,¹⁷ who had presented with ischemic and hemorrhagic symptoms, who had undergone superficial temporal artery (STA)-MCA anastomosis at our hospital in the past 5 years, and who had been deemed positive for choroidal anastomosis before the operation.

Our original surgical procedures for STA-MCA anastomosis have been described in detail elsewhere.¹⁸ The addition of encephalomyosynangiosis was considered in pediatric patients.

Assessment of Choroidal Anastomosis

Patients routinely underwent MR imaging and conventional angiography before and after the operation. Postoperative

angiographies were acquired at 3–6 months after completion of bilateral operations.

Two raters (T.F. and A.M.), blinded to other clinical information to avoid biases, viewed conventional angiograms and the sliding-thin-slab MIP coronal MRA² to grade the development of choroidal anastomosis by hemisphere. The presence or absence of the anastomosis was determined by a consensus of 2 raters. The determinants for the presence of choroidal anastomosis were defined in the previous studies.^{1,2} In brief, choroidal anastomosis is defined as an anastomosis between the choroidal artery, either anterior or posterior, and the medial end of the medullary artery. The positive angiographic indicator of choroidal anastomosis is dilation and extension of the choroidal artery beyond the level of the lateral ventricle.^{1,5,9} This indicator corresponded to that of grade 2 choroidal anastomosis defined by Fujimura et al.⁹

According to previous research,⁶ reduction of choroidal anastomosis was defined as no apparent anastomosis on a postoperative image, which corresponded to grade 0 or 1 defined by Fujimura et al.⁹ Reduction was recorded as a dichotomous variable (yes/no). The study population partly overlapped with that of our previous study.⁶ Recording of this variable had been completed for all hemispheres before the measurement of the revascularization area, to avoid making arbitrary decisions on the reduction of choroidal anastomosis.

Measurement of Revascularization Area

According to the method of Bang et al,¹⁹ we quantitatively measured the revascularization area relative to the whole supratentorial area on the lateral views of postoperative external carotid angiography. To ensure objectivity, we used imaging software (ImageJ, Version 1.52a; National Institutes of Health), which facilitated binary image conversion and automatic tracing of the revascularization area (Fig 2). The threshold for binary image conversion was set as the “default.” An unsubtracted angiographic image was also imported into the software for measuring the supratentorial area and determining the CS. We adopted the Rhoton method²⁰ to determine the location of the CS. In brief, the extended line of the CS was approximated to the line connecting the midportion of the zygomatic arch and the point located

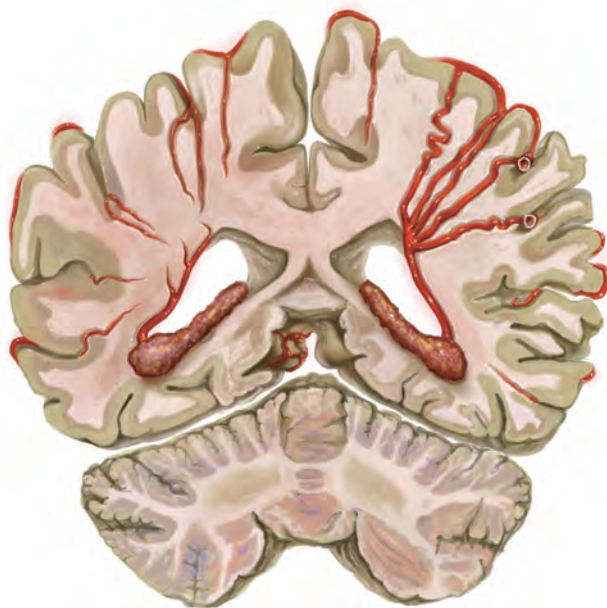


FIG 1. Schematic illustration showing choroidal anastomosis (left hemisphere) in the coronal plane.

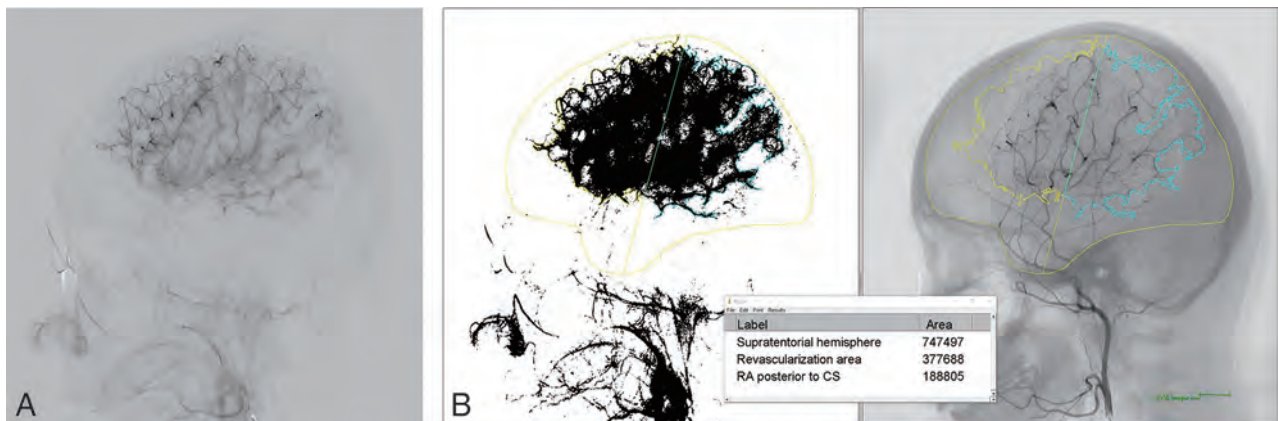


FIG 2. Quantitative measurement of revascularization areas. A, Original image of the postoperative external carotid angiography in the capillary phase. B, Images imported into the software (ImageJ, Version 1.52a). The revascularization area (RA) posterior to the CS (blue line) is 188805/747497 = 25.3%.

2 cm behind the midpoint between the nasion and inion. The accuracy of this topographic method has been confirmed in several studies.^{21,22} The extended line of the CS divided the revascularization area into 2 areas, those anterior and posterior to the CS, and each pixel area was measured. Anterior and posterior revascularization areas were calculated as a percentage relative to the whole supratentorial area through setting each revascularization pixel area and whole supratentorial pixel area as the numerator and denominator, respectively (Fig 2). Revascularization areas were regarded as a continuous variable.

Other Variables

We measured 7 other variables as potential confounders: age at the operation, sex, symptom at onset, Suzuki stage,²³ the presence or absence of posterior cerebral artery (PCA) involvement,²⁴ the addition of encephalomyosynangiosis,²⁵ and the preoperative hemodynamic state assessed with SPECT.²⁶ According to Takahashi et al,²⁶ the hemodynamic state in the MCA territory was classified into 1 of the following 3 stages: stage 0, normal baseline with normal acetazolamide-challenged CBF; stage 1, normal baseline with reduced acetazolamide-challenged CBF; and stage 2, reduced baseline with reduced acetazolamide-challenged CBF. We also assessed the hemodynamic status in the posterior half of the MCA territory

because this area might be more closely associated with choroidal anastomosis. A commercially available software (NEURO FLEXER; <https://neuro-flexer.software.informer.com/>) with the functions of NEUROSTAT (<http://128.95.65.28/~Download/>) developed by Ogura et al²⁷ was used to set the ROIs. The latest version of this software can automatically set ROIs including the anterior cerebral artery, MCA, anterior MCA, posterior MCA, PCA, basal ganglia, thalamus, pons, vermis, and cerebellar hemisphere. The hemodynamic status in the posterior MCA territory was classified into 1 of the 3 stages in the same manner as described above. All variables were recorded separately by hemisphere.

Statistical Analysis

The sample size was determined by the number of cases treated during the study period. All statistical analyses were performed for single hemispheres. For comparison of baseline characteristics (univariate analysis), the *t* test, Wilcoxon rank-sum test, χ^2 test, or Fisher exact test was used as appropriate. To identify independent factors associated with the reduction of choroidal anastomosis, we used a multiple logistic regression analysis. Variables with a *P* value < .1 in univariate analyses were incorporated into the multiple logistic regression analysis. *P* values < .05 were considered significant. Neither loss to follow-up nor missing data occurred. All analyses were performed using JMP software (Version 15; SAS Institute).

RESULTS

Of a total of 121 patients (184 hemispheres) who underwent STA-MCA anastomosis in the study period, 88 hemispheres were identified as positive for choroidal anastomosis with preoperative MR imaging and conventional angiography. Postoperative angiography was not performed in 8 hemispheres for the following reasons: allergic reaction to the contrast medium occurring after the first angiography (3 hemispheres) and patients not providing informed consent for the second angiography (5 hemispheres). The remaining 80 hemispheres were included in the analysis (Fig 3). Baseline characteristics of the 80 hemispheres, including 43 left and 37 right hemispheres, are summarized in Table 1.

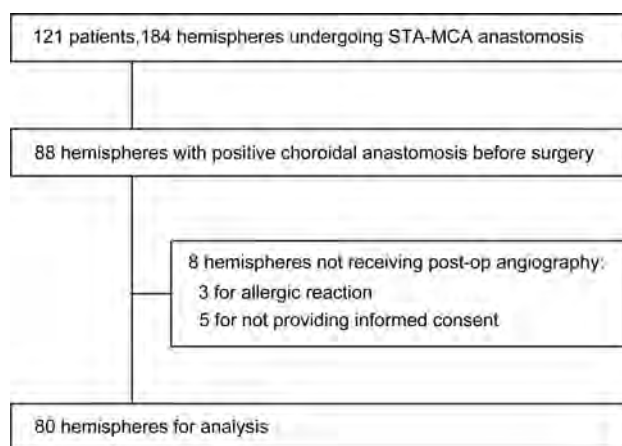


FIG 3. Flow chart for patient inclusion.

Table 1: Baseline variables

	Total	Reduction of Choroidal Anastomosis		P Value
		Yes	No	
No. of hemispheres	80	68	12	NA
Revascularization area (mean) (%) ^a				
Posterior to CS	13.6 (SD, 7.7)	15.2 (SD, 7.1)	4.2 (SD, 3.4)	<.001
Anterior to CS	12.6 (SD, 7.0)	12.5 (SD, 6.7)	13.2 (SD, 8.9)	.74
Median age (yr) (IQR)	12 (8–36)	11 (8–33)	19.5 (5.25–47.5)	.57
Female (%)	47 (58.8)	43 (63.2)	4 (33.3)	.05
Hemorrhagic presentation (%)	17 (21.3)	12 (17.7)	5 (41.7)	.06
Median Suzuki stage (IQR)	3 (3–3)	3 (3–3)	3 (2–3)	.33
PCA involvement (%)	10 (12.5)	10 (14.7)	0	.34
SPECT stage 2				
MCA territory (%)	37 (46.3)	32 (47.1)	5 (41.7)	.73
Posterior MCA territory (%)	27 (33.8)	25 (36.8)	2 (16.7)	.17
Addition of EMS (%)	21 (26.3)	16 (23.5)	5 (41.7)	.19

Note:—EMS indicates encephalomyosynangiosis; IQR, interquartile range; NA, not applicable.

^a Percentage relative to whole supratentorial area.

Reduction of choroidal anastomosis after the operation was confirmed in 68 (85.0%) of the 80 hemispheres with postoperative conventional and MR angiographies. Conventional and MR angiographies were performed an average of 148.7 and 129.3 days after ipsilateral surgery, respectively.

Revascularization Area and Choroidal Anastomosis Reduction

The relationship between each revascularization area and reduction of choroidal anastomosis is shown in Table 1 and Fig 4. The revascularization area posterior to the CS was significantly larger in the hemispheres exhibiting reduction than in those exhibiting no reduction (mean, 15.2% [SD, 7.1%] versus 4.2% [SD, 3.4%]; $P < .001$), whereas no significant difference was observed in the revascularization area anterior to the CS ($P = .74$). The cutoff value of the revascularization area posterior to the CS for predicting

reduction was 10.7% according to the analysis of the receiver operating characteristic curve (Fig 4, dotted line). All 52 hemispheres in which the area exceeded 10.7% showed reduction, whereas only 16 of the 28 hemispheres (57.1%) with the area below 10.7% showed reduction.

Figure 5 shows a representative case in which choroidal anastomosis responsible for hemorrhage has been markedly reduced after bypass surgery. The revascularization area posterior to the CS was relatively large (16.1%), whereas that anterior to the CS was small (3.4%).

Factors Associated with Choroidal Anastomosis Reduction

In the univariate analysis, the revascularization area posterior to the CS was the only significant factor associated with reduction of choroidal anastomosis (Table 1). Although the proportion of the hemisphere with stage 2 hemodynamic compromise in the posterior MCA territory was larger in the reduction group than in the no-reduction group (36.8% versus 16.7%), the difference was not statistically significant ($P = .17$). Three variables with a P value $< .1$ (the revascularization area posterior to the CS, sex, and hemorrhagic presentation) were incorporated in the multiple logistic regression analysis, revealing that the revascularization area posterior to the CS remained statistically significant (OR, 1.57; 95% CI, 1.21–2.03, for every 1% increase; Table 2).

We performed a sensitivity analysis in which we incorporated SPECT stage 2 in the posterior MCA territory in the multivariate analysis together with the above 3 variables. This analysis also revealed that the revascularization area posterior to the CS remained statistically significant (Online Supplemental Data).

Outcome

No subsequent intracranial hemorrhage associated with choroidal anastomosis occurred after the operation in the study population. However, there was a patient in whom de novo bleeding from the remaining choroidal anastomosis occurred 13 years after the operation (Fig 6). In this case, the revascularization area anterior to the CS was relatively large (12.3%), but that posterior to the CS was very small (1.5%). This patient's data were not included in the statistical analyses because the patient did not fulfil the inclusion criteria in terms of the operation date.

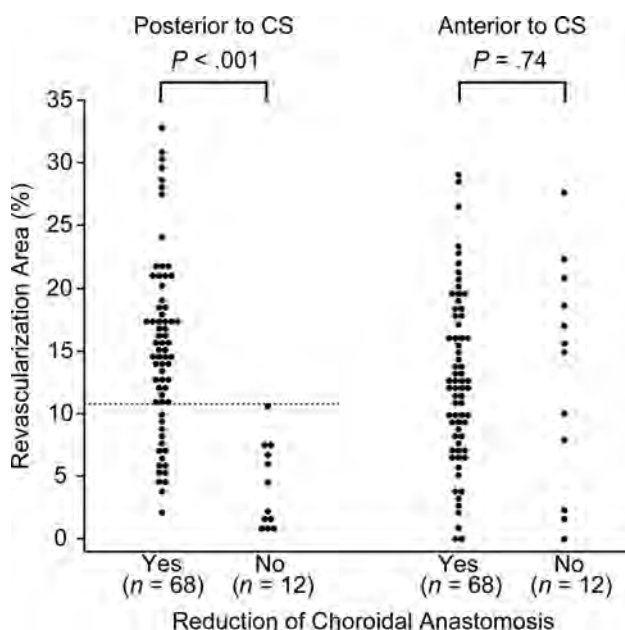


FIG 4. Comparison of each revascularization area between hemispheres exhibiting reduction of choroidal anastomosis and those exhibiting no reduction. The dotted line indicates the cutoff value (10.7%).

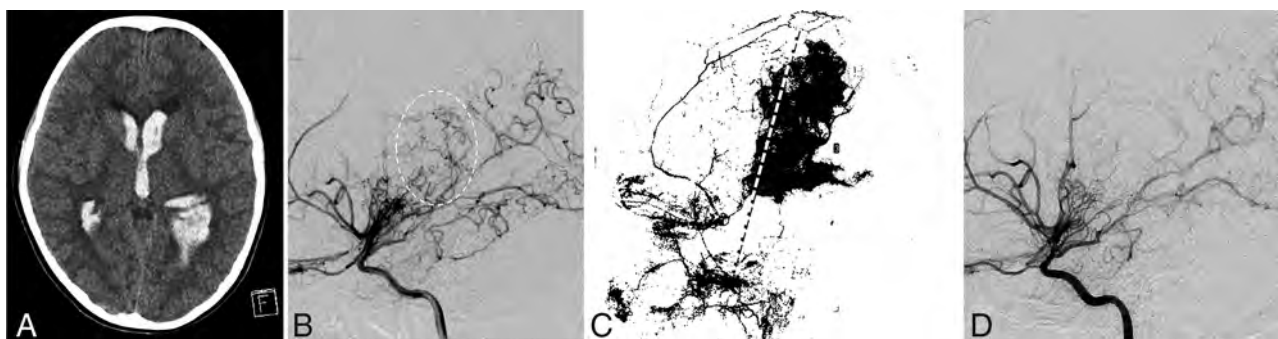


FIG 5. Case 1 (a 9-year-old girl). A, CT at onset shows intraventricular hemorrhage. B, Preoperative left internal carotid angiography shows choroidal anastomosis (dotted circle), which corresponds to the hemorrhage site. C, Quantitative measurement of the revascularization area in the left hemisphere. The revascularization areas anterior and posterior to the CS are 3.4% and 16.1%, respectively. The dotted line indicates the CS. D, Postoperative left internal carotid angiography shows reduction of choroidal anastomosis.

Table 2: Multiple adjusted ORs for reduction of choroidal anastomosis

	Crude		Multivariate Adjustment	
	OR	(95% CI)	OR	(95% CI)
Revascularization area posterior to CS ^a	1.53	(1.20–1.95)	1.57	(1.21–2.03)
Female	3.44	(0.94–12.59)	3.96	(0.66–23.86)
Hemorrhagic presentation	0.3	(0.08–1.11)	0.97	(0.16–6.07)

^a Every 1% increase.

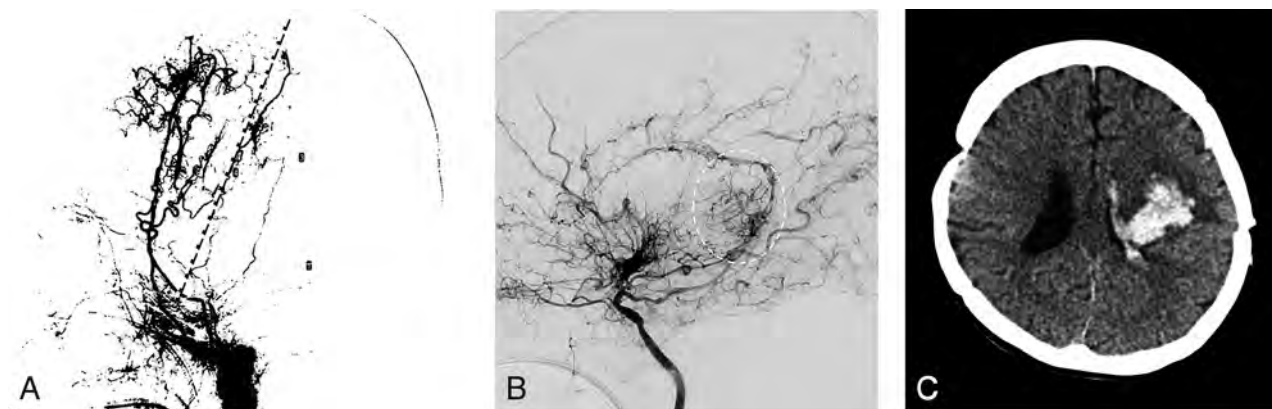


FIG 6. Case 2. The patient had initially manifested seizure at 43 years of age and had undergone direct bypass. *A*, Quantitative measurement of the revascularization area in the left hemisphere. The revascularization areas anterior and posterior to the CS were 12.3% and 1.5%, respectively. The dotted line indicates the CS. *B*, Postoperative left ICA shows persistence of choroidal anastomosis (dotted circle). *C*, CT obtained at the onset of de novo intracranial hemorrhage, which occurred 13 years after the operation.

Supplemental Data

We performed a supplemental analysis to identify factors associated with the overall revascularization area (the area comprising both anterior and posterior revascularization areas). As shown in the Online Supplemental Data, female sex ($P = .02$), PCA involvement ($P < .001$), and SPECT stage 2 in the MCA territory ($P < .001$) were univariate factors positively associated with the overall revascularization area.

DISCUSSION

There were 3 major observations from our study: First, 85% of the patients had reduction of choroidal anastomosis after bypass surgery. Second, the revascularization area posterior to the CS was significantly associated with the reduction, whereas that anterior to the CS was not. Third, a posterior revascularization area of $<10.7\%$ increased the risk of choroidal anastomosis persistence.

The reduction rate of choroidal anastomosis in our series seems comparable with that in the literature (62%–70%).^{15,28,29} Our results are also in line with the seminal work by Yamamoto et al,¹⁵ one of the first to identify the factors associated with this change. They revealed that a revascularized area exceeding two-thirds of the MCA territory was associated with reduction of choroidal anastomosis. Our study might add novel information to theirs because the posterior extent of revascularization might be an underlying mechanism for the reduction.

Our results are highly consistent with those of recent studies focusing on the posterior half of the brain in hemorrhagic Moyamoya disease. The prespecified analysis of the Japan Adult Moyamoya Trial has revealed that patients with posterior

hemorrhage, who are at higher risk of rebleeding, accrue greater benefit in preventing rebleeding from an operation.³⁰ The angiographic analysis of the trial has also revealed that choroidal anastomosis, which is most likely to be distributed posteriorly, is responsible for posterior hemorrhage.¹ PCA involvement is another significant factor associated with posterior hemorrhage.¹ All these findings, together with ours, suggest the significance of the revascularization site for preventing hemorrhage.

The periventricular vascular morphology typical of Moyamoya disease might explain the reduction of choroidal anastomosis depending on the revascularization site. Periventricular anastomosis is a term defining anastomotic collaterals between the perforating or choroidal artery and the medullary artery in the periventricular area.^{2,3} It is classified into 3 types: lenticulostriate, thalamic, and choroidal anastomosis. Choroidal anastomosis outflows to the cortex posterior to the CS, whereas lenticulostriate anastomosis outflows anterior to the CS.¹⁶ Because a revascularization overlapping the outflow is more likely to normalize the medullary artery flow and promote successful reduction of the anastomosis,^{6,31} a larger revascularization area posterior to the CS might increase the probability of the reduction of choroidal anastomosis.

We identified, however, some hemispheres exhibiting reduction of choroidal anastomosis despite relatively small posterior revascularization. This finding might be explained by 2 possible reasons: First, some of the choroidal anastomoses might outflow exactly into the CS¹⁶; in such cases, the revascularization could overlap the outflow even with a limited revascularization area posterior to the CS. Second, augmentation of CBF in the cortex posterior to the CS, which could not be assessed with angiography alone, might account for the reduction of choroidal anastomosis.

Our results do not conflict with various excellent modifications of direct bypass,^{32–39} most of which target the frontal lobe. Targeting the frontal lobe, including the motor cortex, seems a reasonable approach for ischemic Moyamoya disease. However, our results suggest that hemorrhagic Moyamoya disease requires a different strategy in terms of the revascularization site, especially for those with both choroidal anastomosis and mild hemodynamic failure. According to a recent study, a substantial number of patients with hemorrhagic Moyamoya disease have only mild hemodynamic failure.²⁶ Given that the overall width of revascularization depends on the preoperative hemodynamic status as suggested in our Online Supplemental Data, bypass directly targeting the outflow might be reasonable for those with mild hemodynamic failure.³¹

Our results suggest that severe hemodynamic compromise in the posterior half of the MCA territory, which might partly lead to a larger posterior revascularization area, is not a direct factor for reducing choroidal anastomosis. This finding is supported by the previous report, in which development of choroidal anastomosis showed no relation to the hemodynamic stage.²⁶ Reduction of choroidal anastomosis might depend more directly on the surgical procedure, including selection of the recipient artery, than on the hemodynamic status in the parietal lobe. This speculation, however, should be validated in further studies.

The present study has several limitations. First, the study excluded 8 hemispheres in which postoperative angiography was not performed. The possible selection bias caused by this exclusion seems minimal, however, because exclusions should occur randomly according to the reasons for not performing postoperative angiography. Second, the present results were obtained at a single institution, and this might limit generalization, especially to indirect bypass. Third, it remains unknown whether reduction of periventricular anastomosis, including choroidal anastomosis, is associated with subsequent bleeding. Answering this question might require long-term follow-up, considering late-onset hemorrhage shown in Fig 6. Further prospective studies are required.

CONCLUSIONS

The present results support our hypothesis that a larger angiographic extent of revascularization posterior to the CS is associated with postoperative reduction of choroidal anastomosis. A small revascularization in this area might result in persistence of choroidal anastomosis regardless of the revascularization extent anterior to the CS. The present study might facilitate optimization of a direct bypass strategy focusing on hemorrhage prevention through selection of the revascularization site. Further studies are required.

ACKNOWLEDGMENT

We are grateful to Ms Mayu Masuko and Dr Makiko Haragi for providing the beautiful illustration (Fig 1).

Disclosure forms provided by the authors are available with the full text and PDF of this article at www.ajnr.org.

REFERENCES

- Funaki T, Takahashi JC, Houkin K, et al. **Angiographic features of hemorrhagic Moyamoya disease with high recurrence risk: a supplementary analysis of the Japan Adult Moyamoya Trial.** *J Neurosurg* 2018;128:777–84 CrossRef Medline
- Funaki T, Takahashi JC, Yoshida K, et al. **Periventricular anastomosis in Moyamoya disease: detecting fragile collateral vessels with MR angiography.** *J Neurosurg* 2016;124:1766–72 CrossRef Medline
- Funaki T, Fushimi Y, Takahashi JC, et al. **Visualization of periventricular collaterals in Moyamoya disease with flow-sensitive black-blood magnetic resonance angiography: preliminary experience.** *Neurol Med Chir (Tokyo)* 2015;55:204–09 CrossRef Medline
- Funaki T, Takahashi JC, Houkin K, et al. **Effect of choroidal collateral vessels on de novo hemorrhage in Moyamoya disease: analysis of nonhemorrhagic hemispheres in the Japan Adult Moyamoya Trial.** *J Neurosurg* 2019;132:408–14 CrossRef Medline
- Funaki T, Takahashi JC, Houkin K, et al. **High rebleeding risk associated with choroidal collateral vessels in hemorrhagic Moyamoya disease: analysis of a nonsurgical cohort in the Japan Adult Moyamoya Trial.** *J Neurosurg* 2019;130:525–30 CrossRef Medline
- Miyakoshi A, Funaki T, Takahashi JC, et al. **Restoration of periventricular vasculature after direct bypass for Moyamoya disease: intra-individual comparison.** *Acta Neurochir (Wien)* 2019;161:947–54 CrossRef Medline
- Irikura K, Miyasaka Y, Kurata A, et al. **A source of haemorrhage in adult patients with Moyamoya disease: the significance of tributaries from the choroidal artery.** *Acta Neurochir (Wien)* 1996;138:1282–86 CrossRef Medline
- Morioka M, Hamada J, Kawano T, et al. **Angiographic dilatation and branch extension of the anterior choroidal and posterior communicating arteries are predictors of hemorrhage in adult Moyamoya patients.** *Stroke* 2003;34:90–95 CrossRef Medline
- Fujimura M, Funaki T, Houkin K, et al. **Intrinsic development of choroidal and thalamic collaterals in hemorrhagic-onset Moyamoya disease: case-control study of the Japan Adult Moyamoya Trial.** *J Neurosurg* 2019;130:1453–59 CrossRef Medline
- Wang J, Yang Y, Li X, et al. **Lateral posterior choroidal collateral anastomosis predicts recurrent ipsilateral hemorrhage in adult patients with Moyamoya disease.** *AJNR Am J Neuroradiol* 2019;40:1665–71 CrossRef Medline
- Jang DK, Lee KS, Rha HK, et al. **Bypass surgery versus medical treatment for symptomatic Moyamoya disease in adults.** *J Neurosurg* 2017;127:492–502 CrossRef Medline
- Miyamoto S, Yoshimoto T, Hashimoto N, et al; JAM Trial Investigators. **Effects of extracranial-intracranial bypass for patients with hemorrhagic Moyamoya disease: results of the Japan Adult Moyamoya Trial.** *Stroke* 2014;45:1415–21 CrossRef Medline
- Jeon JP, Kim JE, Cho WS, et al. **Meta-analysis of the surgical outcomes of symptomatic Moyamoya disease in adults.** *J Neurosurg* 2018;128:793–99 CrossRef Medline
- Ding J, Zhou D, Paul Cosky EE, et al. **Hemorrhagic Moyamoya disease treatment: a network meta-analysis.** *World Neurosurg* 2018;117:e557–62 CrossRef Medline
- Yamamoto S, Kashiwazaki D, Uchino H, et al. **Ameliorative effects of combined revascularization surgery on abnormal collateral channels in Moyamoya disease.** *J Stroke Cerebrovasc Dis* 2021;30:105624 CrossRef Medline
- Miyakoshi A, Funaki T, Fushimi Y, et al. **Cortical distribution of fragile periventricular anastomotic collateral vessels in Moyamoya disease: an exploratory cross-sectional study of Japanese patients with Moyamoya disease.** *AJNR Am J Neuroradiol* 2020;41:2243–49 CrossRef Medline
- Research Committee on the Pathology and Treatment of Spontaneous Occlusion of the Circle of Willis; Health Labour Sciences Research Grant for Research on Measures for Intractable Diseases. **Guidelines for diagnosis and treatment of Moyamoya disease (spontaneous occlusion of the Circle of Willis).** *Neurol Med Chir (Tokyo)* 2012;52:245–66 CrossRef Medline
- Karasawa J, Touho H, Ohnishi H, et al. **Long-term follow-up study after extracranial-intracranial bypass surgery for anterior circulation**

- ischemia in childhood Moyamoya disease. *J Neurosurg* 1992;77:84–89 CrossRef Medline
19. Bang JS, Kwon OK, Kim JE, et al. Quantitative angiographic comparison with the OSIRIS program between the direct and indirect revascularization modalities in adult Moyamoya disease. *Neurosurgery* 2012;70:625–32 CrossRef Medline
 20. Rhoton AL Jr. The cerebrum. *Neurosurgery* 2002;51:S1–51 CrossRef Medline
 21. Sun A, Hou L, Cheshier S, et al. The accuracy of topographical methods in determining central sulcus: a statistical correlation between modern imaging data and these historical predications. *Cureus* 2014;6:e186 CrossRef
 22. Reis CV, Sankar T, Crusius M, et al. Comparative study of cranial topographic procedures: Broca's legacy toward practical brain surgery. *Neurosurgery* 2008;62:294–310 CrossRef Medline
 23. Suzuki J, Kodama N. Moyamoya disease: a review. *Stroke* 1983;14:104–09 CrossRef Medline
 24. Funaki T, Takahashi JC, Takagi Y, et al. Impact of posterior cerebral artery involvement on long-term clinical and social outcome of pediatric Moyamoya disease. *J Neurosurg Pediatr* 2013;12:626–32 CrossRef Medline
 25. Karasawa J, Kikuchi H, Furuse S, et al. A surgical treatment of "Moyamoya" disease "encephalo-myo synangiosis." *Neurol Med Chir (Tokyo)* 1977;17(1 Pt 1):29–37 CrossRef Medline
 26. Takahashi JC, Funaki T, Houkin K, et al. Impact of cortical hemodynamic failure on both subsequent hemorrhagic stroke and effect of bypass surgery in hemorrhagic Moyamoya disease: a supplementary analysis of the Japan Adult Moyamoya Trial. *J Neurosurg* 2021;134:940–45 CrossRef Medline
 27. Ogura T, Hida K, Masuzuka T, et al. An automated ROI setting method using NEUROSTAT on cerebral blood flow SPECT images. *Ann Nucl Med* 2009;23:33–41 CrossRef Medline
 28. Jiang H, Ni W, Xu B, et al. Outcome in adult patients with hemorrhagic Moyamoya disease after combined extracranial-intracranial bypass. *J Neurosurg* 2014;121:1048–55 CrossRef Medline
 29. Irikura K, Miyasaka Y, Kurata A, et al. The effect of encephalo-myo-synangiosis on abnormal collateral vessels in childhood Moyamoya disease. *Neurol Res* 2000;22:341–46 CrossRef Medline
 30. Takahashi JC, Funaki T, Houkin K, et al; JAM Trial Investigators. Significance of the hemorrhagic site for recurrent bleeding: prespecified analysis in the Japan Adult Moyamoya Trial. *Stroke* 2016;47:37–43 CrossRef Medline
 31. Funaki T, Kataoka H, Yoshida K, et al. The targeted bypass strategy for preventing hemorrhage in Moyamoya disease: technical note. *Neurol Med Chir (Tokyo)* 2019;59:517–22 CrossRef Medline
 32. Kuroda S, Houkin K, Ishikawa T, et al. Novel bypass surgery for Moyamoya disease using pericranial flap: its impacts on cerebral hemodynamics and long-term outcome. *Neurosurgery* 2010;66:1093–101 CrossRef Medline
 33. Houkin K, Kamiyama H, Takahashi A, et al. Combined revascularization surgery for childhood Moyamoya disease: STA-MCA and encephalo-duro-arterio-myo-synangiosis. *Childs Nerv Syst* 1997;13:24–29 CrossRef Medline
 34. Matsushima T, Inoue T, Suzuki SO, et al. Surgical treatment of Moyamoya disease in pediatric patients: comparison between the results of indirect and direct revascularization procedures. *Neurosurgery* 1992;31:401–05 CrossRef Medline
 35. Kim DS, Yoo DS, Huh PW, et al. Combined direct anastomosis and encephaloduroarteriogaleosynangiosis using inverted superficial temporal artery-galeal flap and superficial temporal artery-galeal pedicle in adult Moyamoya disease. *Surg Neurol* 2006;66:389–94 CrossRef Medline
 36. Acker G, Fekonja L, Vajkoczy P. Surgical management of Moyamoya disease. *Stroke* 2018;49:476–82 CrossRef Medline
 37. Guzman R, Steinberg GK. Direct bypass techniques for the treatment of pediatric Moyamoya disease. *Neurosurg Clin N Am* 2010;21:565–73 CrossRef Medline
 38. Fujimura M, Tominaga T. Lessons learned from Moyamoya disease: outcome of direct/indirect revascularization surgery for 150 affected hemispheres. *Neurol Med Chir (Tokyo)* 2012;52:327–32 CrossRef Medline
 39. Wanebo JE, Zabramski JM, Spetzler RF. Superficial temporal artery-to-middle cerebral artery bypass grafting for cerebral revascularization. *Neurosurgery* 2004;55:395–98 CrossRef Medline

Correlation of Call Burden and Sleep Deprivation with Physician Burnout, Driving Crashes, and Medical Errors among US Neurointerventionalists

R.N. Abdalla, S.A. Ansari, M.C. Hurley, H. Attarian, K.M. Fargen, J.A. Hirsch, D.R. Cantrell, P.K. Curl, P.R. Daves, and A. Shaibani



ABSTRACT

BACKGROUND AND PURPOSE: High call frequency can lead to inadequate sleep, fatigue, and burnout, resulting in detrimental effects on physicians and patients. We aimed to assess the correlation between the frequency and burden of neurointerventional surgery calls and sleep deprivation with physician burnout, physical and driving safety, and fatigue-related medical errors.

MATERIALS AND METHODS: We sent an online questionnaire to the members of the 2 neurointerventional surgery societies comprising 50 questions and spanning 3 main topics: 1) overnight/weekend call burden, 2) sleeping patterns, and 3) Copenhagen Burnout Inventory.

RESULTS: One hundred sixty-four surveys were completed. Most (54%) neurointerventional surgeons reported burnout. Call burden of ≥ 1 every 3 days and being in practice >10 years were independent predictors of burnout. Thirty-nine percent reported falling asleep at the wheel, 23% reported a motor vehicle crash/near-crash, and 34% reported medical errors they considered related to call/work fatigue. On multivariate logistic regression, high call burden (called-in >3 times/week) was an independent predictor of sleeping at the wheel and motor vehicle crashes. Reporting <4 hours of uninterrupted sleep was an independent predictor of motor vehicle crashes and medical errors. Most neurointerventional surgeons recommended a maximum call frequency of once every 3 days.

CONCLUSIONS: Call frequency and burden, number of years in practice, and sleep deprivation are associated with burnout of neurointerventional surgeons, sleeping at the wheel, motor vehicle crashes, and fatigue-related medical errors. These findings contribute to the increasing literature on physician burnout and may guide future societal recommendations related to call burden in neurointerventional surgery.

ABBREVIATIONS: CBI = Copenhagen Burnout Inventory; NIS = neurointerventional surgeons; RVU = Relative Value Unit; SNIS = Society of Neurointerventional Surgery; SVIN = Society of Vascular and Interventional Neurology

Physician burnout is a major health care concern and is very common among health care workers compared with the general population.¹ More than 45% of US physicians reported at least 1 symptom of burnout with a prevalence approaching 50%.^{2,3}

Work-related burnout has been defined as a combination of emotional exhaustion, depersonalization, and job dissatisfaction.⁴

Physicians experiencing burnout syndrome feel emotional exhaustion with a loss of enthusiasm for work, depersonalization and cynicism, and a low sense of personal accomplishment.^{5,6} Burnout is associated with alcohol and substance abuse, broken relationships, early retirement, and suicidal ideation in cross-sectional studies.⁷⁻¹⁰ Not only does burnout correlate with adverse personal effects, but it is also associated with professionalism, quality of patient care, and increased medical errors.^{11,12} Variable rates of physician burnout are noted among different subspecialties but range from approximately 40% to 75% in certain specialties such as emergency medicine. Nearly 60% of radiologists and neurologists as well as 50% of neurosurgeons have reported burnout.¹³

Neurointerventional surgeons (NIS) may be at high risk for burnout given the call frequency, overnight calls, the relatively high proportion of urgent/emergent cases, and, in particular, the

Received April 6, 2022; accepted after revision June 27.

From the Departments of Radiology (R.N.A., S.A.A., D.R.C., A.S.), Neurology (S.A.A.), Neurological Surgery (R.N.A., S.A.A., A.S.), and Sleep Medicine (H.A.), Northwestern University, Feinberg School of Medicine, Chicago, Illinois; Department of Radiology (R.N.A.), Ain Shams University, Cairo, Egypt; Department of Radiology (M.C.H.), University of Chicago, Chicago, Illinois; Department of Neurosurgery (K.M.F.), Wake Forest University, Winston-Salem, North Carolina; Department of Radiology (J.A.H.), Massachusetts General Hospital and Harvard Medical School, Boston, Massachusetts; Department of Radiology (P.K.C.), University of Washington, Seattle, Washington; and Department of Finance (P.R.D.), University of Tennessee, Knoxville, Tennessee.

Please address correspondence to Ali Shaibani, MD, Departments of Radiology and Neurological Surgery, Northwestern University, Feinberg School of Medicine, 676 N St Clair St, Suite 800, Chicago, IL 60611-2927; e-mail: Ali.shaibani@nm.org



Indicates article with online supplemental data.

<http://dx.doi.org/10.3174/ajnr.A7606>

considerable increase since 2015 in the number of acute stroke thrombectomy cases, frequently occurring outside regular hours. NIS often commute emergently from home with interrupted sleep, raising their risk of sleeping at the wheel, being involved in motor vehicle crashes, and committing fatigue-related medical errors. Work-related interruption of sleep has been strongly correlated with physician burnout.^{14,15}

The American College of Graduate Medical Education has recently increased its focus on promoting well-being and avoiding burnout in trainees by increasing education on wellness, exercise, healthy diet, sleeping habits, and work-life balance, in addition to setting limits on weekly and individual shift work hours. However, attending physicians are not subject to these guidelines on call frequency or work hours. Our study aimed to establish more accurate and robust rates of burnout among NIS by using the Copenhagen Burnout Inventory (CBI) survey and to specifically assess the association of call frequency and coverage to rates of burnout, inadequate sleep, daytime fatigue, medical errors, and vehicular crashes/near-crashes. Finally, we polled the NIS community for recommendations on optimum call frequency, organization, and compensation.

MATERIALS AND METHODS

The study protocol was reviewed by Northwestern University, Feinberg School of Medicine institutional review board, which exempted the study as a nonhuman subject design. The study survey was designed by 5 experienced NIS and 1 sleep medicine physician. The study used a 3-part survey (a detailed 3-part questionnaire that can be found in the Online Supplemental Data) and was designed to be completed in 5 minutes. The survey was initially developed in the REDCap electronic data capture tool (<https://catalyst.harvard.edu/redcap/>) and distributed via e-mail to the Society of Neurointerventional Surgery (SNIS) and Society of Vascular and Interventional Neurology (SVIN) boards as a single-click link to be distributed to their membership. In addition, it was then posted to SNIS members using the society's "SNIS Connect" platform, and the remainder was sent by direct e-mail. A reminder e-mail was sent 10–15 days later during the period of the study, which extended from March 1 to May 31, 2018. Because responses were anonymous, REDCap recorded the Internet Protocol addresses of respondents to avoid duplicates.

The study questionnaire comprised 3 parts:

Part 1, Overnight and weekend call: 15 questions that surveyed the existing frequency and model of call, including backup call, number of hospitals covered, following-day adjustment in response to being late on call, division of weeknight and weekend calls, call-compensation systems, and their recommendations on optimal call frequency, model, and compensation.

Part 2, Sleep: surveyed the association of work and call coverage with sleep, daytime fatigue, history of previous call-related motor vehicle crashes/near-crashes, history of previous work-related errors, and the existing prevalence of sleep disorders. We categorized sleeping hours into 3 categories: <4 hours, 4–6 hours, and 6–8 hours.

Part 3, Burnout: CBI used 3 domains: personal burnout (6 questions), work-related burnout (7 questions), and patient-related burnout (6 questions).

There were 5 possible answers to each question, and those answers were converted to a scoring system from 0 to 100 and subcategorized as follows: always, 100; often, 75; sometimes, 50; seldom, 25; and never/almost never, 0. A mean score of >50 points in any domain was positive for burnout.^{16,17} We also collected the demographics of survey respondents, including age, sex, years of practice, practice setting, and location.

Statistical Analysis

All analysis was conducted using SPSS (Version 24.0; IBM) and R statistical and computing software (<http://www.r-project.org/>). Descriptive statistics were reported in percentages, means, medians, and range. Factors affecting our dependent variables (burnout, motor vehicle crashes/near-crashes, sleeping at the wheel, and fatigue-related medical errors) were evaluated in a univariate analysis using the Fisher exact and χ^2 tests. Multivariate logistic regression analysis was performed to evaluate independent predictors of those dependent variables. A *P* value < .05 was considered statistically significant. The Cronbach α coefficient testing was used to assess the reliability of the CBI Likert scale, with values $\geq .9$ considered excellent, .7 to <.9 good, .6 to <.7 acceptable, .5 to <.6 poor, and <.5 unacceptable.

RESULTS

Sample and Demographics

Based on a previously published study in 2019, the number of US NIS in 2 of the largest neurointerventional societies in the United States, SNIS and SVIN, was 898 and 496, respectively with many of those physician-surgeons having dual membership in >1 society. The study estimated the total number of US NIS at that time to be approximately 1200 physicians. After sending surveys to the members of SNIS and SVIN, we had 164 respondents, most of whom were between 40 and 49 years of age (50%), with approximately 20% of respondents between 30 and 39 years, 20% between 50 and 59 years, and 10% between 60 and 69 years of age. Only 1 respondent was older than 69 years of age, and 2 respondents were younger than 30 years of age. Seventy-eight percent of respondents had been in practice for >5 years, with approximately 18% practicing for >20 years. Most respondents practiced in large urban cities with populations of >500,000, with only 11.5% of respondents practicing in small or rural cities. There was a homogeneous distribution among respondents in terms of their practice settings with 41.5% in academic, 33.5% in private practice, and 25% in a mixed practice. The male/female ratio among respondents was approximately 9:1.

Call Burden

Regarding call frequency, 48% of respondents were on call more than once every 3 days; 32%, once every 3 days; 15%, once every 4 days; 4%, once every 5 days; and only 1%, less than once every 5 days. Most respondents (59%) use a one week at a time call coverage model, whereas 28% had fixed weekdays with a rotating weekend, and 13% used miscellaneous arrangements including a night float, sole operator call, or alternating calls on a biweekly or monthly basis. When it came to being "called-in" during nights and weekends, 33% of respondents reported an average ≥ 4 times during a week of calls; 26%, 3 times; 29%, twice; and 12%, once,

Table 1: Baseline characteristic (in scores) of CBI questionnaires

CBI Dimension	Cronbach α	Mean (SD)	Median	Min/Max	% Mean Score > 50
Personal burnout	0.9	49.4 (19.9)	45.8	8.3–100	48.8
Work-related burnout	0.8	47.4 (15.9)	46.4	3.6–92.9	44.5
Patient-related burnout	0.9	29.9 (20.4)	29.2	0–100	16.5

Note:—Min indicates minimum; Max, maximum.

resulting in approximately 60% of respondents being called-in ≥ 3 times during weekends and after-hours. Nearly all (98%) respondents had no built-in mechanism for taking the next day off if they were called-in or worked past midnight, and 86% responded “never or rarely” to how often they rescheduled next-day patients under these circumstances. A third (35%) of respondents covered >1 hospital when on-call, but only 6% were responsible for >3 hospitals. Only 34% of respondents reported having >1 person on call (eg, backup or call tree), while 48% of respondents who covered call at >1 hospital did not have a built-in system for a backup call person. When asked what would constitute optimal call frequency, most NIS recommended once every 3–4 days (39% once every 4 days and 37% once every 3 days) with only 7% suggesting a call frequency greater than every 3 days.

Increased call-in frequency ≥ 3 times a week was significantly associated with falling asleep at the wheel (47.9% versus 26.5%, $P = .006$), and in multivariate logistic regression, it was an independent predictor of falling asleep at the wheel (OR, 3.36; 95% CI, 1.51–7.86; $P = .004$). Even though increased call-in frequency showed a trend only toward motor vehicle crashes/near-crashes in univariate analysis (28.1% versus 16.2%, $P = .09$), when controlling for other variables in a multivariate logistic regression analysis, increased call-in frequency was an independent predictor of motor vehicle crashes/near-crashes (OR, 3.07; 95% CI, 1.17–8.80; $P = .03$).

Call Compensation

When looking at different compensation models, 84% of respondents were salary-based versus only 8% reporting a compensation model that was purely based on Relative Value Units (RVUs) or 9% with alternative compensation models. Greater than half of respondents received bonuses based on RVUs alone (18%) or RVUs combined with other productivity factors (35%), but only 8% of respondents had their RVUs in after-hours multiplied by a factor because most (92%) had fixed RVUs regardless of the day and time of the week. Only half of respondents (51%) received extra compensation for overnight/weekend calls, with 22% having call compensation built into their base salary and the rest having a certain number of calls included in their baseline salary. Only 61 physicians (37%) responded to the question about the number of calls included in the baseline salary, and the mean/median and mode of answers were 10 calls per month, with a range between 1 and 31. When we looked at the monetary value for weeknight call compensation, 50% of respondents were compensated at \$1000–\$2000, 30% were compensated $< \$1000$, and 20% were compensated at $> \$2000$. Call compensation was overall slightly greater on the weekends, with 21% being compensated $< \$1000$ and 28% compensated $> \$2000$.

Physician Burnout

Table 1 demonstrates the mean, SD, median, and range of the CBI scales. The results showed good-to-excellent internal consistency with a Cronbach α coefficient of ≥ 0.8 . The Cronbach α was .91 for personal burnout, .79 for work-related burnout, and .91 for

patient-related burnout. More than half of respondents (54%) reported burnout in at least 1 of the domains: 12.2% in a single domain, 28.7% in 2 domains, and 13.4% in all domains. The highest burnout perceived was in the personal burnout domain with almost half of respondents (48.8%) reporting burnout in this domain and a nearly equivalent number (44.5%) of respondents reporting work-related burnout, but only 16.5% perceived patient-related burnout (for which the cutoff point of CBI scale score was 50 points).

The Online Supplemental Data demonstrate a univariate correlation of potential independent factors for burnout. There was a trend toward increased burnout in respondents who covered calls a week at a time compared with using a split weekday/weekend model (60.4% versus 43.5%; $P = .07$) after removing other less common models. There was a trend toward increased burnout with decreased sleep (61.4% versus 48.9%, $P = .12$, for < 4 hours of uninterrupted sleep and 75% versus 51.4%, $P = .06$, for < 6 total hours of sleep), but this did not reach statistical significance. Even though call frequency did not correlate with burnout in univariate analysis, a call frequency of ≥ 3 times a week was an independent predictor of burnout (OR, 3.24; 95% CI, 1.22–9.19; $P = .02$) when accounting for various factors in a multivariate logistic regression model (Online Supplemental Data). NIS with > 10 years of practice showed a trend toward an increased likelihood of experiencing burnout (59.3% versus 47.9%, $P = .16$), and practicing for > 10 years was an independent predictor of burnout in multivariate logistic regression analysis (OR, 2.78; 95% CI, 1.11–7.69; $P = .03$). However, physicians reporting burnout did not have a statistically increased risk of motor vehicle crashes/near-crashes (28.1% versus 17.3%; $P = .14$), sleeping at the wheel (39.3% versus 38.7%; $P = .99$), and/or reporting fatigue-related medical errors (31.5% versus 37.3%; $P = .51$).

Sleep and Fatigue

The total and uninterrupted hours of sleep while on call and not on call are demonstrated in Table 2. Regarding on-call days and total sleep hours, 65% slept between 4 and 6 hours versus 23% who had 6–8 hours of sleep, but there was also less uninterrupted sleep, with 43% reporting < 4 hours and only 10% achieving 6–8 hours. When off-call, no respondent slept < 4 hours, and 89% reported 6–8 hours of sleep per day, most of which was uninterrupted (80%). When asked to rate the quality of sleep during a call night, only 9% of respondents thought it was average/same as a noncall night, 57% believed they had fair sleep quality, and 34% reported poor sleep quality. Sleep disorders were identified in 16% of respondents, with 9% reporting sleep apnea. Sleep deprivation and call-/work-related fatigue resulted in 39% falling asleep at the wheel at least once, 23% experiencing motor vehicle crashes/near-crashes, and 34% reporting medical errors. Most (75%) respondents related that they needed a daytime nap due to call-related

Table 2: Total and uninterrupted sleep hours—on call versus not on call

	Total Sleep Hours/Call	Total Sleep Hours/Not on Call	Uninterrupted Sleep Hours/Call	Uninterrupted Sleep Hours/Not on Call
Less than 4	20 (12.2%)	0	70 (42.7%)	2 (1.2%)
4–6	106 (64.6%)	19 (11.6%)	77 (47%)	31 (18.9%)
6–8	38 (23.2%)	145 (88.4%)	17 (10.4%)	131 (79.9%)
P value		.01		.05

fatigue, yet only 42% would have the ability/chance to sleep during work hours.

The Online Supplemental Data demonstrate a univariate correlation between multiple independent factors and burnout, sleeping at the wheel, having motor vehicle crashes/near-crashes, and fatigue-related medical errors. Less than 4 hours of total sleep and <4 hours of uninterrupted sleep demonstrated a trend toward burnout (75% versus 51.4%, $P = .06$, and 61.4% versus 48.9%, $P = .12$, respectively). There was a statistically significant association of sleeping <6 hours with falling asleep at the wheel (43.7% versus 23.7%, $P = .04$) and fatigue-related medical errors (38.9% versus 18.4%, $P = .02$). The risk of medical errors showed an even stronger association in respondents reporting <4 hours of uninterrupted sleep (45.7% versus 25.5%, $P = .008$), as well as a significantly increased risk for motor vehicle crashes/near-crashes (34.3% versus 14.9%, $P = .005$). Uninterrupted sleep of <4 hours was an independent predictor of motor vehicle crashes/near-crashes (OR, 3.11; 95% CI, 1.28–7.92; $P = .01$) and medical errors (OR, 2.60; 95% CI, 1.21–5.68; $P = .01$). In terms of demographics, men were more likely to fall asleep at the wheel (OR, 10.90; 95% CI, 1.83–210.90; $P = .03$), and women were more likely to report fatigue-related medical errors (OR, 4.17; 95% CI, 1.10–18.52; $P = .04$).

DISCUSSION

NIS may be at high risk of burnout, in large part due to the high proportion of emergency procedures and the frequency of on-call coverage.^{18,19} Among those who participated in our study, we found that increased years of practice and a call frequency greater than or equal to once every 3 days (increased call frequency) were independently associated with burnout. In addition, an increased call frequency was associated with an increased risk of falling asleep at the wheel, motor vehicle crashes/near-crashes, and medical errors. In addition, sleeping <4 hours, which was more commonly encountered during call days, was an independent predictor of motor vehicle crashes and medical errors. To date, there are no standards for call frequency for NIS; when asked about optimal call frequency, most responding physicians selected a maximum of once every 3 days.

In our survey, 54% of respondents reported burnout in at least 1 domain of the CBI survey, with 13.4% reporting burnout in all domains. We used the CBI survey rather than the more commonly used Maslach Burnout Inventory for several reasons. The validity of the CBI has been supported by prior studies and has been used in multiple health care studies.^{17,20,21} When they are compared directly, the CBI and Maslach Burnout Inventory showed very similar results, but unlike the Maslach Burnout Inventory, the CBI can measure personal burnout as a total score with better psychomotor properties, allowing it to measure the

degree of burnout change across time (rather than assuming a stable individual trait).^{22,23} The CBI is also nonproprietary and open access.

In a previous study of burnout, physician well-being, and the correlation to medical errors in 6695 physicians across different medical specialties, 54.3% of physicians reported burnout; 32.8%, excessive fatigue; and 10.5%, a major medical error within the prior 3 months. The study found that burnout and fatigue were independently associated with medical errors.²⁴ Risks for burnout included long working hours, frequent overnight call duties, sleep deprivation and sleep disturbances, high work intensity, and sub-optimal compensation among other factors.¹⁹ In our study, call burden (being on call once or more every 3 days) was an independent predictor of burnout. This finding aligns with prior studies showing a 3% increased risk for burnout with every extra hour of work per week and a 3%–9% increased risk of burnout for additional nights and weekend call.²⁵

As per the American Heart Association/American Stroke Association guidelines, mechanical thrombectomy is standard-of-care treatment for large-vessel-occlusion acute ischemic strokes with salvageable brain tissue up to 24 hours from symptom onset or time last known well.^{26,27} Stroke call is inherently stressful due to the challenging, emergent nature of the interventions and the often high morbidity of the disease, with increased burnout also demonstrated among noninterventional stroke neurologists.²⁸ Wilson et al²⁹ demonstrated that almost 60% of stroke consults in a 24-hour shift occurred during nonworking hours. The same study showed increasing stroke thrombectomy rates from once every 5 days to once every 3 days,²⁹ which are expected to further increase with expanding indications and place NIS at an even higher risk of burnout. When asked about the optimal maximal neurointerventional call burden in our survey, approximately 80% of respondents selected a call frequency not to exceed once every 3 days, with 39% selecting once every 4 days as the ideal call frequency, yet nearly half (48%) reported a current call frequency of greater than once every 3 days.

Our finding that >10 years of neurointerventional practice experience independently predicts burnout is contrary to prior studies that showed early-to-middle career physicians work more hours and have lower career satisfaction, less work-life balance, and more burnout and are more likely to quit the practice of medicine.³⁰ The discrepancy may be related to the steep learning curve and time required for proficiency as well as the novel, challenging nature of neurointervention being strong motivators in the early years, whereas senior practitioners are liable to experience greater monotony, frustration, and less opportunity for advancement.

As a direct consequence of call burden, sleep deprivation, and burnout, it is important to consider the physical well-being of physicians and the risk of medical errors, patient harm, and litigation. Most studies find that a majority of emergent stroke

thrombectomy calls occur outside standard daytime work hours. Combined with stricter guidelines for earlier access and reperfusion times, this timing means that the NIS will often transition from sleeping to driving within minutes, potentially putting them at risk for motor vehicle crashes. Although the frequency of call coverage did not directly correlate with sleeping at the wheel or motor vehicle crashes, increased call-in frequency or being called-in >3 times per week was an independent predictor of sleeping at the wheel or being involved in motor vehicle crashes/near-crashes. This finding is alarming and raises an important question of who should be responsible for ensuring good backup coverage from partners when the interventionalist has been up all night treating patients. Should there be a societal guideline by the SNIS/SVIN to restrict the number of call days per week, number of call days taken back-to-back, and the number of hours worked continuously? Does the frequency of call coverage need to be tailored to practice volumes, the number of hospitals covered on call, and the likelihood of being called-in multiple times during call periods?

The relationship between sleep and cognitive and psychomotor function has been well-established, as well as the impact on medical errors, motor vehicle crashes, and health, such as obesity and heart disease. Sleep is a very complex process and varies significantly from one night to another. Frequent call coverage is likely to cause disturbed sleep. In our survey, 65% of respondents reported <6 hours of total sleep when on call, and 43% reported <4 hours of uninterrupted sleep. While the American College of Graduate Medical Education has regulated minimum hours of protected sleep among trainees, no such rules exist for attending physicians.^{31,32} The American Academy of Sleep Medicine recently published a position statement on sleep, fatigue, and burnout, estimating that maladaptive sleep techniques led to a burnout prevalence of 50%, with sleep deprivation being one of the main culprits.³² A previous study demonstrated that the risk of procedural complication rates significantly increased if physicians experienced <6 hours of sleep (3.4% versus 6.2% with an OR of 1.72).³³ In our study, having <4 hours of uninterrupted sleep while on call was an independent predictor of motor vehicle crashes/near-crashes and medical errors, whereas we found a nonsignificant trend toward increased burnout.

Again, this sounds an alarm on what needs to be done to provide call coverage for emergency stroke cases, without affecting the patients' outcomes or putting the providers at considerable risk. Should we train more neurointerventionalists to have adequate coverage, and if so, how would that affect the volume for other neurovascular pathologies treated by those physicians and would that eventually reduce individual expertise for treating those pathologies? On the other hand, should there be an alternative training pathway in which physicians are given the opportunity to do either 1 year of training to only perform stroke thrombectomies versus 2 years of training for all neurovascular pathologies, to ensure adequate stroke coverage without affecting the expertise in treatment of other neurovascular pathologies? Should there be a minimum number of emergent large-vessel occlusions in a hospital to allow the hospital to offer stroke thrombectomy service while having enough physicians to cover/backup the call? Should there be a minimum number of neurointerventionalists/stroke interventionalists employed by the hospital to provide thrombectomy service?

With regard to compensation models that use productivity/RVU as a basis, other specialties such as Emergency Medicine have developed formulas that assign a positive multiplication factor to RVUs generated during evening/night shifts. Should this model be applied to NIS as well? Given the tremendous societal burden of stroke, should productivity models be used at all for NIS compensation? These are all important questions that need to be addressed on a societal level to ensure continued provision of thrombectomy coverage without putting physicians at significant life-threatening risk or increasing medical errors that would affect patients' outcomes.

Our study has several limitations. First, the survey results may be distorted by recall and selection bias in that a physician experiencing burnout may be more inclined to respond and lead to an overestimation of the burnout problem. However, the rates of burnout in our survey aligned with previously published data in the neurointerventional surgery field¹⁸ and other studies analyzing burnout in radiology, neurology, and neurosurgery.¹³ Second, the small proportion of responses limited the power of our study to find statistically significant associations. Due to the relatively small number of NIS compared with other specialties, we suggest conducting a repeat survey designed by a collaboration of the major neurointerventional societies, distributed more efficiently through conferences and e-mail lists, with emphasis on specific issues identified in these previous studies. Finally, we assessed burnout, accidents, and medical errors as a function of call burden, compensation, and sleep deprivation but did not include other, more difficult-to-categorize personal factors. Controlling for this myriad of influences will always pose a challenge to surveys addressing the complex causes of burnout, fatigue, and sleep disturbances.

CONCLUSIONS

Call frequency/burden, the number of years in practice, and sleep deprivation are associated with NIS burnout, falling asleep at the wheel, motor vehicle crashes/near-crashes, and fatigue-related medical errors. Our findings add to the increasing literature on physician burnout and point out the increased risk of medical errors in patient care and significant life-threatening risks for physicians, and hopefully, they will guide future society-led surveys and practice-improvement guidelines related to call burden for NIS.

Disclosure forms provided by the authors are available with the full text and PDF of this article at www.ajnr.org.

REFERENCES

1. Dyrbye LN, West CP, Satele D, et al. **Burnout among U.S. medical students, residents, and early career physicians relative to the general U.S. population.** *Acad Med* 2014;89:443–51 CrossRef Medline
2. Rotenstein LS, Torre M, Ramos MA, et al. **Prevalence of burnout among physicians: a systematic review.** *JAMA* 2018;320:1131–50 CrossRef Medline
3. Shanafelt TD, Boone S, Tan L, et al. **Burnout and satisfaction with work-life balance among US physicians relative to the general US population.** *Arch Intern Med* 2012;172:1377–85 CrossRef Medline
4. Maslach C, Jackson SE. **The measurement of experienced burnout.** *J Organiz Behav* 1981;2:99–113 CrossRef
5. Spickard A Jr, Gabbe SG, Christensen JF. **Mid-career burnout in generalist and specialist physicians.** *JAMA* 2002;288:1447–50 CrossRef Medline

6. Shanafelt TD, Balch CM, Bechamps GJ, et al. **Burnout and career satisfaction among American surgeons.** *Ann Surg* 2009;250:463–71 CrossRef Medline
7. Shanafelt T, Sloan J, Satele D, et al. **Why do surgeons consider leaving practice?** *J Am Coll Surg* 2011;212:421–22 CrossRef Medline
8. Shanafelt TD, Sloan JA, Habermann TM. **The well-being of physicians.** *Am J Med* 2003;114:513–19 CrossRef Medline
9. Oreskovich MR, Kaups KL, Balch CM, et al. **Prevalence of alcohol use disorders among American surgeons.** *Arch Surg* 2012;147:168–74 CrossRef Medline
10. Shanafelt TD, Balch CM, Dyrbye L, et al. **Special report: suicidal ideation among American surgeons.** *Arch Surg* 2011;146:54–62 CrossRef Medline
11. Dyrbye LN, Massie FS Jr, Eacker A, et al. **Relationship between burnout and professional conduct and attitudes among US medical students.** *JAMA* 2010;304:1173–80 CrossRef Medline
12. Shanafelt TD, Balch CM, Bechamps G, et al. **Burnout and medical errors among American surgeons.** *Ann Surg* 2010;251:995–1000 CrossRef Medline
13. Shanafelt TD, Hasan O, Dyrbye LN, et al. **Changes in burnout and satisfaction with work-life balance in physicians and the general US working population between 2011 and 2014.** *Mayo Clin Proc* 2015;90:1600–13 CrossRef Medline
14. Vela-Bueno A, Moreno-Jiménez B, Rodríguez-Muñoz A, et al. **Insomnia and sleep quality among primary care physicians with low and high burnout levels.** *J Psychosom Res* 2008;64:435–42 CrossRef Medline
15. Stewart NH, Arora VM. **The impact of sleep and circadian disorders on physician burnout.** *Chest* 2019;156:1022–30 CrossRef Medline
16. Creedy DK, Sidebotham M, Gamble J, et al. **Prevalence of burnout, depression, anxiety and stress in Australian midwives: a cross-sectional survey.** *BMC Pregnancy Childbirth* 2017;17:13 CrossRef Medline
17. Kristensen TS, Borritz M, Villadsen E, et al. **The Copenhagen Burnout Inventory: a new tool for the assessment of burnout.** *Work & Stress* 2005;19:192–207 CrossRef
18. Fargen KM, Arthur AS, Leslie-Mazwi T, et al. **A survey of burnout and professional satisfaction among United States neurointerventionalists.** *J Neurointerv Surg* 2019;11:1100–04 CrossRef Medline
19. Fargen KM, Hirsch JA. **Neurointerventionalists, stroke and burnout.** *J Neurointerv Surg* 2018;10:811–12 CrossRef Medline
20. Bourbonnais R, Brisson C, Vinet A, et al. **Development and implementation of a participative intervention to improve the psychosocial work environment and mental health in an acute care hospital.** *Occup Environ Med* 2006;63:326–34 CrossRef Medline
21. Bourbonnais R, Brisson C, Vinet A, et al. **Effectiveness of a participative intervention on psychosocial work factors to prevent mental health problems in a hospital setting.** *Occup Environ Med* 2006;63:335–42 CrossRef Medline
22. Maslach C, Schaufeli WB, Leiter MP. **Job burnout.** *Annu Rev Psychol* 2001;52:397–422 CrossRef Medline
23. Winwood PC, Winefield AH. **Comparing two measures of burnout among dentists in Australia.** *Int J Stress Manag* 2004;11:282–89 CrossRef Medline
24. Tawfik DS, Profit J, Morgenthaler TI, et al. **Physician burnout, well-being, and work unit safety grades in relationship to reported medical errors.** *Mayo Clin Proc* 2018;93:1571–80 CrossRef Medline
25. West CP, Dyrbye LN, Shanafelt TD. **Physician burnout: contributors, consequences and solutions.** *J Intern Med* 2018;283:516–29 CrossRef Medline
26. Goyal M, Menon BK, van Zwam WH, et al; HERMES collaborators. **Endovascular thrombectomy after large-vessel ischaemic stroke: a meta-analysis of individual patient data from five randomised trials.** *Lancet* 2016;387:1723–31 CrossRef Medline
27. Powers WJ, Rabinstein AA, Ackerson T, et al. **Guidelines for the Early Management of Patients with Acute Ischemic Stroke: 2019 Update to the 2018 Guidelines for the Early Management of Acute Ischemic Stroke: A Guideline for Healthcare Professionals From the American Heart Association/American Stroke Association.** *Stroke* 2019;50:e344–418 CrossRef Medline
28. Kenton EJ, Culebras A, Fayad PB, et al; AAN Vascular Neurology Stroke Practice Resources Workgroup. **Impact of stroke call on the stroke neurology workforce in the United States: possible challenges and opportunities.** *J Stroke Cerebrovasc Dis* 2018;27:2019–25 CrossRef Medline
29. Wilson TA, Leslie-Mazwi T, Hirsch JA, et al. **A multicenter study evaluating the frequency and time requirement of mechanical thrombectomy.** *J Neurointerv Surg* 2018;10:235–39 CrossRef Medline
30. Dyrbye LN, Varkey P, Boone SL, et al. **Physician satisfaction and burnout at different career stages.** *Mayo Clin Proc* 2013;88:1358–67 CrossRef Medline
31. McHill AW, Czeisler CA, Shea SA. **Resident physician extended work hours and burnout.** *Sleep* 2018;41:zsy112 CrossRef Medline
32. Kancherla BS, Upender R, Collen JF, et al. **Sleep, fatigue and burnout among physicians: an American Academy of Sleep Medicine position statement.** *J Clin Sleep Med* 2020;16:803–05 CrossRef Medline
33. Rothschild JM, Keohane CA, Rogers S, et al. **Risks of complications by attending physicians after performing nighttime procedures.** *JAMA* 2009;302:1565–72 CrossRef Medline

Predictors and Impact of Sulcal SAH after Mechanical Thrombectomy in Patients with Isolated M2 Occlusion

 D.Y. Kim,  S.H. Baik,  C. Jung,  J.Y. Kim,  S.-G. Han,  B.J. Kim,  J. Kang,  H.-J. Bae, and  J.H. Kim



ABSTRACT

BACKGROUND AND PURPOSE: Data on SAH after M2 mechanical thrombectomy are limited. We aimed to determine the prevalence of sulcal SAH after mechanical thrombectomy for M2 occlusion, its associated predictors, and the resulting clinical outcome.

MATERIALS AND METHODS: The study retrospectively reviewed the data of patients with acute ischemic stroke who underwent mechanical thrombectomy for isolated M2 occlusion. The patients were divided into 2 groups according to the presence of sulcal SAH after M2 mechanical thrombectomy. Angiographic and clinical outcomes were compared. Multivariable analysis was performed to identify independent predictors of sulcal SAH and unfavorable outcome (90-day mRS, 3–6).

RESULTS: Of the 209 enrolled patients, sulcal SAH was observed in 33 (15.8%) patients. The sulcal SAH group showed a higher rate of distal M2 occlusion (69.7% versus 22.7%), a higher rate of superior division occlusion (63.6% versus 43.8%), and a higher M2 angulation (median, 128° versus 106°) than the non-sulcal SAH group. Of the 33 sulcal SAH cases, 23 (66.7%) were covert without visible intraprocedural contrast extravasation. Distal M2 occlusion (OR, 12.04; 95% CI, 4.56–35.67; $P < .001$), superior division (OR, 3.83; 95% CI, 1.43–11.26; $P = .010$), M2 angulation (OR, 1.02; 95% CI, 1.01–1.04; $P < .001$), and the number of passes (OR, 1.58; 95% CI, 1.22–2.09; $P < .001$) were independent predictors of sulcal SAH. However, covert sulcal SAH was not associated with an unfavorable outcome ($P = .830$).

CONCLUSIONS: After mechanical thrombectomy for M2 occlusion, sulcal SAH was not uncommon and occurred more frequently with distal M2 occlusion, superior division, acute M2 angulation, and multiple thrombectomy passes (≥ 3). The impact of covert sulcal SAH was mostly benign and was not associated with an unfavorable outcome.

ABBREVIATIONS: AIS = acute ischemic stroke; CA = contact aspiration; EVT = endovascular treatment; GRE = gradient recalled-echo; ICH = intracerebral hemorrhage; MT = mechanical thrombectomy; mTICI = modified TICI; SR = stent retriever; SS = sulcal SAH

Since the publication of a recent endovascular treatment (EVT) trial in 2015,¹ many studies have demonstrated the feasibility and safety of mechanical thrombectomy (MT) for treating patients with MCA M2 occlusion, which is a medium-vessel occlusion.^{2–6} Accordingly, acute ischemic stroke (AIS) due to M2 occlusion has been increasingly treated with EVT despite the lack of clear guideline-based recommendations.⁷ However, the anatomic features of M2, including smaller diameters, tortuous vessels, and thinner vessel walls could be

linked to poor accessibility and high periprocedural complication rates.⁸


SAH is one of the most concerning periprocedural complications after MT for AIS according to neurointerventionalists.^{9–11} More distal and narrower M2 vessels could particularly lead to iatrogenic SAH; however, to date, its related procedural factors have not been fully elucidated. In our preliminary experience, sulcal SAH (SS), which was undetected during M2 MT, was observed on postprocedural imaging. Given the technical challenges and lesser severity of M2 stroke, balancing the potentially increased risk of periprocedural complications and the clinical benefit of MT for M2 occlusion is essential.¹² However, the clinical impact of SS after M2 MT remains largely unknown.

This study aimed to investigate the frequency and angiographic predictors of SS. We also investigated the clinical impact of SS, focusing on covert SS, which is angiographically occult but is detected by postprocedural imaging in patients who undergo MT for isolated M2 occlusion.

Received April 7, 2022; accepted after revision June 17.

From the Departments of Radiology (D.Y.K., S.H.B., C.J., J.H.K.) and Neurology (D.Y.K., J.Y.K., S.-G.H., B.J.K., J.K., H.-J.B.), Seoul National University Bundang Hospital, Seongnam, South Korea.

Please address correspondence to Sung Hyun Baik, MD, Department of Radiology, Seoul National University Bundang Hospital, 82, Gumi-ro 173beon-gil, Bundang-gu, Seongnam, 13620, South Korea; e-mail: mdshbaik@gmail.com

 Indicates article with online supplemental data.
<http://dx.doi.org/10.3174/ajnr.A7594>

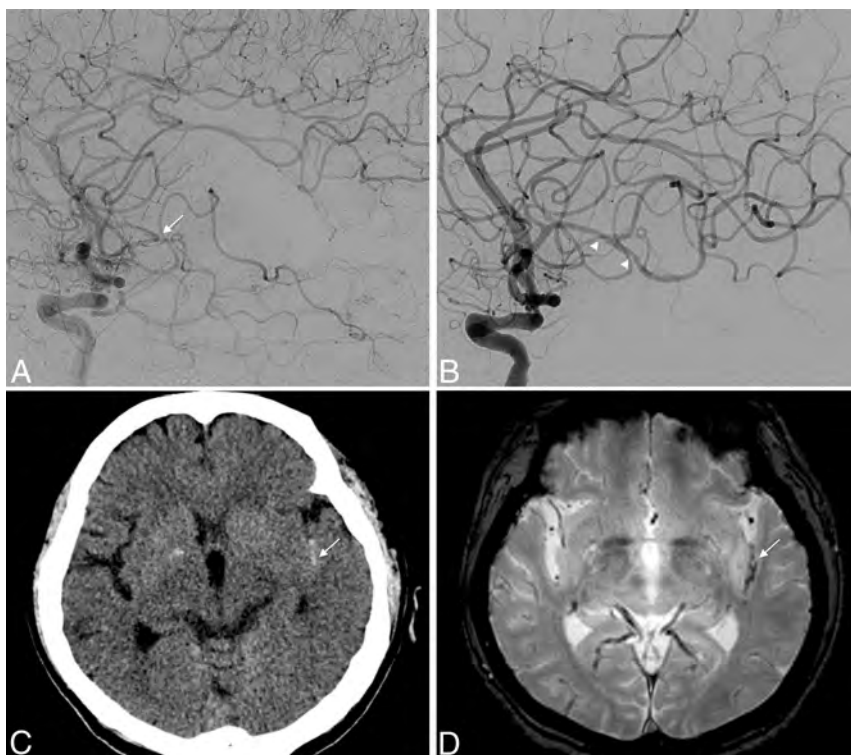


FIGURE. Illustrative case showing covert SS. A patient in her 60s presented with aphasia and right-sided weakness. A, A left ICA lateral angiogram shows occlusion of distal M2 segment (arrow). B, After 3 attempts of thrombectomy using a Trevo 3 × 20 mm (not shown), successful reperfusion was achieved. Note that vasospasm is revealed (arrowheads) without definite contrast extravasation. M2 angulation is measured as 130° on the final angiogram. C, A noncontrast CT scan obtained 1 day after thrombectomy shows a small amount of hyperdense lesions (arrow) in the left Sylvian fissure. D, Axial GRE MR imaging performed 3 days after thrombectomy reveals an apparent hypointense signal lesion in the left Sylvian fissure (arrow), consistent with SAH.

MATERIALS AND METHODS

Patients

This study was approved by the local institutional review board of the Seoul National University Bundang Hospital, and the requirement for written informed consent was waived because of the retrospective nature of this study.

This retrospective analysis included all consecutive patients with AIS who underwent EVT between January 2013 and July 2021 at our stroke center. The inclusion criteria for the study were as follows: 1) time from symptom onset to groin puncture ≤24 hours; 2) primary isolated MCA M2 segment occlusion visible on CT or MR angiography; 3) baseline NIHSS score, ≥2 points; 4) history of immediate postprocedural and follow-up CT or MR imaging; and 5) stent retriever (SR), contact aspiration (CA), or CA with an SR as the primary treatment. The exclusion criteria of this study were as follows: 1) tandem or multiple occlusions, 2) prestroke mRS score >2, and 3) insufficient data or poor image quality. This study defined the M2 segment as the MCA segment from the genu to the circular sulcus of the insula; early MCA branches arising from the M1 segment before the genu were not considered.^{2,3}

Endovascular Treatment

All procedures were performed by 3 experienced neurointerventionalists (C.J., S.H.B., and J.Y.K.) using the femoral artery

approach with the patient under local anesthesia or conscious sedation. Unless technically infeasible, a balloon-guide catheter was routinely used. The choice of the first-line technique was left to the discretion of the treating operator. All included patients were treated with an SR alone, CA alone, or CA combined with an SR. If successful reperfusion was not achieved with the initially selected first-line MT despite multiple attempts, rescue therapy was performed by switching to the other strategy.

Thrombectomy with SR was performed using an SR device (Solitaire 4 × 20 mm, Covidien; Trevo 3 × 20/4 × 20 mm, Stryker; or Aperio 3.5 × 28 mm, Acandis). CA thrombectomy was performed using an aspiration catheter (3MAX or 4MAX; Penumbra) or an intermediate catheter (Sofia 5F; MicroVention; or AXS Catalyst 6, Stryker) alone or in combination with an SR. The details of the conventional MT technique have been described previously.^{9,13}

Data Collection and Outcome Measures

The primary outcome was the occurrence of SS after M2 mechanical thrombectomy. Patients were divided into SS and non-SS groups according to the presence of SS after M2 MT. SS was diagnosed by a hypointense and hyperintense lesion in the subarachnoid space, which was located in the Sylvian fissure or cerebral sulci on gradient recalled-echo (GRE) T2* and FLAIR sequences or via a persistent hyperdense lesion on serial noncontrast CT.^{9,14} The interpretation of SAH with a GRE sequence took precedence over the CT scan because the former can distinguish true SAH from contrast leakage.¹⁴ The diagnosis of SS with CT was performed if there was persistent sulcal hyperdensity on serial CT scans to exclude the contrast leakage. Regarding the institutional protocol, immediate postprocedural MR imaging or CT was performed, and follow-up MR imaging was routinely performed at our center 3–5 days after EVT. Additionally, secondary SAH that was not detected in the immediate postprocedural CT or MR imaging but was accompanied by hemorrhagic transformation was not included in the SS group.

Patients with SS were further classified into overt or covert SS subgroups according to the presence of intraprocedural contrast extravasation. Overt SS was defined as diffuse or confluent SAH with apparent intraprocedural contrast extravasation during EVT on DSA. Conversely, covert SS was defined as minimal, isolated SAH identified only on postprocedural MR imaging or CT, without intraprocedural contrast extravasation (Figure). All angiographic and imaging findings were independently checked by 2 neurointerventionalists (D.Y.K. and S.H.B.) in consensus.

M2 angulation was defined as a total calculated vessel angle that was the sum of the calculated M1–M2 and M2–M2' angles.¹⁵ The M1–M2 angle was defined as the angle from the M1 segment as it turns superiorly (at the M1–M2 junction) to become the M2 segment into which the thrombectomy device is positioned as the vessel courses toward the circular sulcus. M2–M2' was defined as the angle between the just proximal and distal M2 segment of clot. Each calculated M1–M2 and M2–M2' angle was obtained by subtracting the measured angle from 180°. Thus, a higher number of M2 angulations indicates greater vessel curvature. For the assessment of vessel angle, the best vessel contrast was selected from the final angiogram without a thrombectomy device in situ to avoid straightening the vessel anatomy. We measured the angles on the frontal projection of 2D DSA from the final angiogram using a PACS tools for angle measurement (Online Supplemental Data).

The demographic information included age, sex, and vascular risk factors (hypertension, diabetes, dyslipidemia, current smoking, coronary artery disease, atrial fibrillation, and previous stroke history). Stroke and treatment information, such as occlusion site mechanism (thromboembolic, in situ thrombosis, or unknown), IV tPA use, admission NIHSS score, baseline ASPECTS, M2 divisions (superior, inferior, or both), and proximal/distal M2 location, were collected. The proximal and distal M2 segments were distinguished by the line delineating the midheight of the insula.

According to the modified TICI (mTICI) scale, we reported successful and complete reperfusion rates (defined as mTICI 2b–3 and mTICI 3, respectively). The number of thrombectomy passes was counted, and the outcomes and complications were analyzed. The first-pass effect was defined as achieving complete reperfusion with a single thrombectomy device pass. A favorable clinical outcome was defined as a 90-day mRS score of 0–2.

Safety outcomes included procedural (perforation, dissection, vasospasm, and distal embolism) and hemorrhagic complications. Vessel perforation was defined as frank angiographic contrast extravasation that occurred during the procedure. Distal embolism was defined as fragmentation of a primary clot downstream of the primary occlusion and embolization into a new territory. Intracerebral hemorrhage (ICH) was classified according to the European-Australasian Acute Stroke Study classification, and symptomatic intracerebral hemorrhage was defined as any hemorrhage associated with an NIHSS score increase of ≥ 4 points within 24 hours.¹⁶ Neurologic deterioration associated with SAH was defined as a ≥ 4 -point increase in the NIHSS score assessed 24 hours after MT that was not attributable to any other cause.^{10,17}

Statistical Analysis

The differences in the baseline characteristics as well as the procedural and clinical outcomes were compared between patients with and without SS. The Pearson χ^2 test or the Fisher exact test was used for categorical variables, and the Student *t* test or Mann-Whitney *U* test was used for continuous variables. A binary logistic regression analysis was performed to determine the predictors of SS. Finally, the association between covert SS and 90-day clinical outcomes was investigated only in patients without intraprocedural contrast extravasation (overt SS). Variables with a *P* value $< .10$ from univariate analysis and those considered clinically relevant

were included in a multivariate model. All statistical analyses were performed using R version 3.5.1 (<http://www.r-project.org/>). Statistical significance was set at *P* $< .05$.

RESULTS

A total of 1502 patients with AIS underwent EVT between January 2013 and July 2021. Among these, 236 patients who met the inclusion criteria were initially enrolled. Of these, 27 patients were excluded for the following reasons: 1) tandem or multiple occlusions (*n* = 11); 2) prestroke mRS score of > 2 (*n* = 6); and 3) insufficient data or poor image quality (*n* = 10). Finally, 209 patients (mean age, 69 [SD, 12.4] years; 110 men [56.9%]) with primary isolated M2 occlusions qualified for the final analysis. Of the enrolled 209 patients, SS was observed in 33 (15.8%) patients; the remaining 176 patients (84.2%) were assigned to the non-SS group.

Baseline and Procedural Characteristics

The baseline characteristics of the SS and non-SS groups are presented in Table 1. The median NIHSS score at admission was 10 (interquartile range, 7–15). The involved sites were the proximal M2 (69.9%) and the superior division (46.9%). The SS group more frequently had distal M2 (69.7% versus 22.7%, *P* $< .001$) and superior division (63.6% versus 43.8%, *P* = .036) occlusion compared with the non-SS group. Age, vascular risk factors, etiology of the occlusion, intravenous tPA, and admission ASPECTS were comparable between the 2 groups.

The treatment and clinical outcomes are summarized in the Online Supplemental Data. Thrombectomy with an SR was most often used as the first-line treatment (71.8%). Overall, successful recanalization was achieved in 85.2% of the patients. The SS group showed a lower rate of CA thrombectomy (0% versus 11.9%, *P* $< .001$), higher M2 angulation (median 128° versus 106°, *P* $< .001$), and a larger number of passes (median, 3 versus 1; *P* $< .001$) than the non-SS group. Additionally, the SS group showed a longer procedural time (median, 48 versus 28 minutes; *P* $< .001$), a lower rate of successful reperfusion (57.6% versus 90.3%, *P* $< .001$), and a lower first-pass effect (0% versus 29.0%, *P* = .001). There were no significant differences in the rates of favorable clinical outcome or mortality between the 2 groups. The incidence of hemorrhagic complications was not significantly different between the 2 groups.

Characteristics of Sulcal SAH

Thirty-three patients had SS, of whom 10 (30.3%) had overt SS with intraprocedural contrast extravasation, whereas the remaining 23 (69.7%) patients had covert SS with angiographically occult SAH detected on postprocedural imaging (Table 2). Seven of the 10 patients with overt SS underwent emergent coil embolization, whereas contrast extravasation spontaneously ceased in the remaining 3 patients during the procedure. Covert SS was observed only in the ipsilateral Sylvian fissure (*n* = 14, 60.9%) and in the Sylvian fissure with other sulci (*n* = 9, 39.1%) (Fig 1). Of the 23 patients with covert SS, only one (4.3%) was symptomatic with neurologic deterioration, resulting in a prevalence of 0.48%. Conversely, patients with overt SS showed a higher rate of neurologic deterioration (40% versus 4.3%; *P* = .021) and unfavorable outcome (70% versus 47.8%; *P* = .283) than those with covert SS.

Table 1: Baseline characteristics between sulcal SAH versus non-sulcal SAH^a

	Total (n = 209)	Sulcal SAH (n = 33)	Non-Sulcal SAH (n = 176)	P Value
Age (mean) (yr)	69.9 (SD, 12.4)	73.1 (SD, 11.2)	69.3 (SD, 12.6)	.104
Male	110 (56.9)	16 (48.5)	103 (58.5)	.38
Risk factor				
Hypertension	139 (66.5)	21 (63.6)	118 (67.0)	.857
Diabetes	71 (34.0)	13 (39.4)	58 (33.0)	.606
Dyslipidemia	53 (25.4)	11 (33.3)	42 (23.9)	.353
Smoking	43 (20.6)	10 (30.3)	33 (18.8)	.203
Coronary artery disease	21 (10.0)	3 (9.1)	18 (10.2)	1.0
Atrial fibrillation	97 (46.4)	13 (39.4)	84 (47.7)	.49
Previous stroke	30 (14.4)	4 (12.1)	26 (14.8)	.898
Etiology of occlusion				
Thromboembolic	180 (86.1)	29 (87.9)	151 (85.8)	.999
In-situ thrombosis	27 (12.9)	3 (9.1)	24 (13.6)	.583
Intravenous tPA	44 (21.1)	6 (18.2)	38 (21.6)	.835
Prestroke mRS	0 (0–1)	0 (0–0)	0 (0–1)	.85
Admission NIHSS ^b	10 (7–15)	11 (7–15)	10 (7–15)	.953
ASPECTS ^b	9 (8–10)	9 (8–9)	9 (8–10)	.764
Occlusion site				<.001
Proximal	146 (69.9)	10 (30.3)	136 (77.3)	
Distal	63 (30.1)	23 (69.7)	40 (22.7)	
Division				.064
Superior	98 (46.9)	21 (63.6)	77 (43.8)	
Inferior	106 (50.7)	11 (33.3)	95 (54.0)	
Middle	5 (2.4)	1 (3.0)	4 (2.3)	

^a Data are presented as number (%) except where otherwise noted.

^b Data are median, and numbers in parentheses are interquartile range.

Table 2: Characteristics of SS^a

Characteristics	Sulcal SAH (n = 33)	
	Overt SAH (with Intraprocedural Contrast Extravasation) (n = 10) (30.3%)	Covert SAH (without Intraprocedural Contrast Extravasation) (n = 23) (69.7%)
Management		
Coil embolization	7 (70.0)	
Observation	3 (30.0)	
Imaging findings		
SAH detected solely by serial CT	5 (50.0)	2 (8.7)
SAH detected by GRE/FLAIR	5 (50.0)	21 (91.3)
Location of SAH		
Only Sylvian fissure	0 (0)	14 (60.9)
Sylvian fissure + 1 sulcus	0 (0)	9 (39.1)
Sylvian fissure + ≥2 sulci	5 (50.0)	0 (0)
Diffuse, bilateral	5 (50.0)	0 (0)
Clinical outcomes		
Neurologic deterioration	4 (40.0)	1 (4.3)
mRS at 90 days ^b	4 (4–5)	2 (1–5)
mRS 0–2 at 90 days	3 (30.0)	12 (52.2)
Mortality at 90 days	1 (10.0)	3 (13.0)

^a Data are presented as number (%) except where otherwise noted.

^b Data are median, and numbers in parentheses are interquartile range.

Predictors of Sulcal SAH

In the univariate analysis, procedural time, distal M2, superior division, M2 angulation, and number of passes were associated with SS (Table 3). In the multivariable analysis, distal M2 occlusion (OR, 12.04; 95% CI, 4.56–35.67; $P < .001$), superior division (OR, 3.83; 95% CI, 1.43–11.26; $P = .010$), M2 angulation (OR, 1.02; 95% CI, 1.01–1.04; $P < .001$), and number of passes (OR,

1.58; 95% CI, 1.22–2.09; $P < .001$) were independent predictors of SS. Additionally, distal M2 occlusion (OR, 8.53; 95% CI, 2.98–27.33; $P < .001$), superior division (OR, 3.86; 95% CI, 1.30–13.00; $P = .020$), M2 angulation (OR, 1.02; 95% CI, 1.01–1.03; $P = .005$), and number of passes (OR, 1.60; 95% CI, 1.21–2.13; $P < .001$) were also significantly associated with covert SS (Online Supplemental Data).

Table 3: Multivariable analysis for predictors of SS

Variable	Crude OR (95% CI)	P Value	Adjusted OR (95% CI)	P Value
Age	1.02 (0.99–1.06)	.105		
Female	1.49 (0.70–3.18)	.287		
Hypertension	0.86 (0.40–1.91)	.704		
History of stroke	0.79 (0.22–2.23)	.691		
Prestroke mRS	0.88 (0.58–1.22)	.749		
Admission NIHSS	1.01 (0.92–1.09)	.854		
Baseline ASPECTS	0.96 (0.71–1.31)	.805		
Procedural time (min)	1.02 (1.01–1.03)	<.001		
Distal (vs proximal)	7.82 (3.52–18.50)	<.001	12.04 (4.56–35.67)	<.001
Superior division	2.25 (1.06–4.99)	.039	3.83 (1.43–11.26)	.010
SR use (vs aspiration)	1.56 (0.67–4.09)	.332		
M2 angulation ^a	1.02 (1.01–1.03)	<.001	1.02 (1.01–1.04)	<.001
No. of passes	1.51 (1.22–1.89)	<.001	1.58 (1.22–2.09)	<.001

^a Continuous variable. Higher M2 angulation indicates greater vessel curvature.

Impact of Covert SS on Clinical Outcomes

In the subgroup analysis excluding 10 patients with overt SS, age (OR, 1.11; 95% CI, 1.05–1.18; $P < .001$), atrial fibrillation (OR, 0.33; 95% CI, 0.11–0.90; $P = .037$), admission NIHSS score (OR, 1.15; 95% CI, 1.05–1.26; $P = .002$), baseline ASPECTS (OR, 0.53; 95% CI, 0.32–0.83; $P = .009$), and parenchymal hematoma (OR, 21.93; 95% CI, 2.31–50.77; $P = .015$) were predictors of unfavorable outcome in the multivariate logistic regression analysis. However, covert SS was not significantly associated with unfavorable outcome ($P = .830$) (Online Supplemental Data).

DISCUSSION

In the current study, SS after MT for M2 occlusion was not uncommon, and two-thirds of SS cases were covert SS, which were angiographically occult but revealed by postprocedural imaging. In addition, several procedural factors including distal location, superior division, acute vessel angulation, and multiple passes (≥ 3) were independently associated with the occurrence of SS. Although common, SS has a non-notable impact and is not associated with unfavorable clinical outcome.

To the best of our knowledge, this is the first study to show the prevalence of SAH as well as related procedural factors and clinical impact in patients undergoing M2 thrombectomy. Although there have been several studies on MT for M2 occlusion, they merely reported either the rate of symptomatic ICH or safety outcomes that focused on intraprocedural SAH or perforation.^{2,4,5,12,18–21} However, the present study attempted to assess not only overt SS but also covert SS and investigated procedural predictors of SS. The current study indicates that SS following M2 thrombectomy is relatively common, and distally located, superior division, acute-angle M2 occlusion with multiple thrombectomies is likely to result in SS.

The incidence of SAH after MT ranges from 0.5% to 24% according to previous reports,^{9–11,15,22–25} and in our cohort, the observed incidence was 15.8%. In previous M2 studies, SAH after M2 thrombectomy ranged from 0.9% to 7.7%,^{1–5,8,18,19,23} which was still lower than our data (15.8%). However, if the definition of SAH is restricted to the procedural angiographic findings, intraprocedural SAH was 4.8% in this study, showing similar or lower rates of SAH than in other studies. In addition, the incidence of SAH in previous studies might have been under-reported because of the lack of MR

imaging or follow-up CT. According to the protocol at our center, most patients with AIS who underwent MT also underwent MR imaging within 3 days after EVT. Therefore, postprocedural MR imaging was available for 184 (88.0%) of the enrolled patients. As described in Table 2, in addition, 71% of angiographically occult SAH cases were found by MR imaging; thus, a higher proportion of SAH might be attributable to the application of the GRE sequence, which offers higher sensitivity than CT alone in diagnosing SAH.

The clinical consequences of SAH differ according to the type of SAH and the co-occurrence of ICH.^{24,25} While isolated SAH after MT does not influence long-term clinical outcomes, the presence of diffuse SAH, including that associated with concomitant parenchymal hematoma, reduces the chances of clinical recovery. Qureshi et al²⁵ showed that the rates of independent functional outcome were lower among subjects with SAH with intraparenchymal hemorrhage or other ICH but not in subjects with isolated SAH. Renú et al²⁴ recently reported that the post-MT diffuse subarachnoid hyperattenuation pattern was mostly composed of blood extravasation and emerged as a biomarker of an increased risk of poor outcome and death. In line with these studies, covert SS was not associated with unfavorable outcome, whereas overt SS showed a trend toward unfavorable outcome.

The elevated SAH risk due to distal location and acute M2 angulation in the current study might be explained by several possible mechanisms: First, a more curved, distal location with thinner vessel walls causes difficulties in procedural accessibility and a higher risk of microguidewire perforation and tearing of tiny arterioles. Second, in the distally located M2 segment, because these vessels have a small normal diameter, any reduction in vessel caliber would result in greater friction and traction forces during MT than in larger proximal vessels. Third, acute M2 angulation increases friction between the vessel wall and the device, with increased vessel stretching during stent retrieval.²⁶ As noted in our study, Ng et al¹⁵ found a trend toward postprocedural SAH occlusion in patients with extreme MCA angulation and distal device positioning. Lee et al¹¹ also reported that the distal location of vessel occlusion was associated with a higher probability of SAH.

A higher number of MT passes was associated with SS in this study. Previous studies have shown that a greater number of thrombectomy device passes increases the prevalence of SAH, supporting our results.^{10,11,15} This outcome may occur because additional passes of the SR cause repeat traction injury to small perforating branches or venules. In addition, multiple passes of MT necessitate repeat guidewire probing of the occluded vessel, which increases the potential for unrecognized microguidewire perforation or dissection. Microperforation may not result in overt contrast extravasation on DSA or immediate bleeding if the vessel remains occluded or if the vessel immediately develops vasospasm. Subsequent recanalization of an occluded vessel with occult microperforation or dissection may lead to delayed occult SAH.¹⁵

Most interesting, there was no occurrence of SS in patients treated with CA alone as the primary MT method for M2 occlusion. In contrast, 78.8% of patients in the SS group were treated with an SR alone. Similar to our findings, Renieri et al²¹ recently reported that SR and combined techniques were associated with higher rates of intraprocedural SAH. Theoretically, SRs result in more extensive endothelial injury than aspiration catheters during stent retrieval because they exert a continuous radial action against the vessel wall.^{27,28} Additionally, it has been suggested that an SR exerts traction forces applied to the vessel, and deformation of the adjacent anatomy causes stretching and rupture of small arterioles or venules.²⁹ Because distal M2 branches typically have a small diameter (≤ 2.0 mm), a higher traction force might be required during SR thrombectomy, which increases the likelihood of stretch injury to M2 perforating arterioles, and this phenomenon might be exacerbated by the greater M2 angulation compared with a proximal and smaller M2 angulation.^{15,27}

In our study, although clinical consequences were different between overt and covert SS, distal M2 occlusion and acute M2 angulation were associated with both overt and covert SS. Therefore, when planning a procedural strategy, identifying these angiographic findings is important, and when the performing M2 thrombectomy under these anatomic conditions, a tailored thrombectomy technique as well as delicate microguidewire navigation is required to reduce SS occurrence.

This study has several limitations. First, inherent selection bias was inevitable because of the nonrandomized and retrospective study design. In particular, it is challenging to deliver a thromboaspiration catheter to the face proximal to the clot, especially in the distally located or curved M2, and this issue may influence the selection of first-line MT devices. Thus, careful interpretation of the results is required. Second, the sample size may not have been large enough to show statistical differences between the subgroups of this cohort from a single center. Most important, the sample size of the SS subgroups was very small, thus hampering appropriate analysis of their association with clinical outcome variables. Additionally, the application rate of CA was low (10.0%), and the differential effect derived from the use of the device on SS was not sufficient for assessment. Third, the wide range of the study period, including the potential effect of advancements in endovascular techniques and operator skill on treatment outcomes, is another potential limitation of this study.

CONCLUSIONS

After MT for M2 occlusion, SS was not uncommon and occurred more frequently with distal M2 occlusion, superior division, acute M2 angulation, and a higher number of thrombectomy passes. The clinical course of SS was different according to the type of SS. The impact of covert SS was mostly benign and was not associated with unfavorable outcome, whereas overt SS was symptomatic.

Disclosure forms provided by the authors are available with the full text and PDF of this article at www.ajnr.org.

REFERENCES

- Goyal M, Menon BK, van Zwam WH, et al. **Endovascular thrombectomy after large-vessel ischaemic stroke: a meta-analysis of individual patient data from five randomised trials.** *Lancet* 2016;387:1723–31 CrossRef Medline
- Coutinho JM, Liebeskind DS, Slater LA, et al. **Mechanical thrombectomy for isolated M2 occlusions: a post hoc analysis of the STAR, SWIFT, and SWIFT PRIME studies.** *AJNR Am J Neuroradiol* 2016;37:667–72 CrossRef Medline
- Sarraj A, Sangha N, Hussain MS, et al. **Endovascular therapy for acute ischemic stroke with occlusion of the middle cerebral artery M2 segment.** *JAMA Neurol* 2016;73:1291–96 CrossRef Medline
- Menon BK, Hill MD, Davalos A, et al. **Efficacy of endovascular thrombectomy in patients with M2 segment middle cerebral artery occlusions: meta-analysis of data from the HERMES Collaboration.** *J Neurointerv Surg* 2019;11:1065–69 CrossRef Medline
- Miura M, Yoshimura S, Sakai N, et al. **Endovascular therapy for middle cerebral artery M2 segment occlusion: subanalyses of RESCUE-Japan Registry 2.** *J Neurointerv Surg* 2019;11:964–69 CrossRef Medline
- Dobrocky T, Piechowiak EI, Volbers B, et al. **Treatment and outcome in stroke patients with acute M2 occlusion and minor neurological deficits.** *Stroke* 2021;52:802–10 CrossRef Medline
- Almekhlafi M, Ospel JM, Saposnik G, et al. **Endovascular treatment decisions in patients with M2 segment MCA occlusions.** *AJNR Am J Neuroradiol* 2020;41:280–85 CrossRef Medline
- Tomsick TA, Carrozzella J, Foster L, et al; IMS III Investigators. **Endovascular therapy of M2 occlusion in IMS III: role of M2 segment definition and location on clinical and revascularization outcomes.** *AJNR Am J Neuroradiol* 2017;38:84–89 CrossRef Medline
- Yoon W, Jung MY, Jung SH, et al. **Subarachnoid hemorrhage in a multimodal approach heavily weighted toward mechanical thrombectomy with Solitaire stent in acute stroke.** *Stroke* 2013;44:414–19 CrossRef Medline
- Nikoubashman O, Reich A, Pjontek R, et al. **Postinterventional subarachnoid haemorrhage after endovascular stroke treatment with stent retrievers.** *Neuroradiology* 2014;56:1087–96 CrossRef Medline
- Lee H, Qureshi AM, Mueller-Kronast NH, et al. **Subarachnoid hemorrhage in mechanical thrombectomy for acute ischemic stroke: analysis of the STRATIS Registry, systematic review, and meta-analysis.** *Front Neurol* 2021;12:663058 CrossRef Medline
- Dobrocky T, Bellwald S, Kurmann R, et al. **Stent retriever thrombectomy with mindframe capture LP in isolated M2 occlusions.** *Clin Neuroradiol* 2020;30:51–58 CrossRef Medline
- Turk AS, Frei D, Fiorella D, et al. **ADAPT FAST study: a direct aspiration first pass technique for acute stroke thrombectomy.** *J Neurointerv Surg* 2014;6:260–64 CrossRef Medline
- Mitchell P, Wilkinson ID, Hoggard N, et al. **Detection of subarachnoid haemorrhage with magnetic resonance imaging.** *J Neurol Neurosurg Psychiatry* 2001;70:205–11 CrossRef Medline
- Ng PP, Larson TC, Nichols CW, et al. **Intraprocedural predictors of post-stent retriever thrombectomy subarachnoid hemorrhage in middle cerebral artery stroke.** *J Neurointerv Surg* 2019;11:127–32 CrossRef Medline
- Hacke W, Kaste M, Fieschi C, et al. **Randomised double-blind placebo-controlled trial of thrombolytic therapy with intravenous alteplase in acute ischaemic stroke (ECASS II): Second European-Australasian Acute Stroke Study Investigators.** *Lancet* 1998;352:1245–51 CrossRef Medline
- Noser EA, Shaltoni HM, Hall CE, et al. **Aggressive mechanical clot disruption: a safe adjunct to thrombolytic therapy in acute stroke?** *Stroke* 2005;36:292–96 CrossRef Medline
- Saber H, Narayanan S, Palla M, et al. **Mechanical thrombectomy for acute ischemic stroke with occlusion of the M2 segment of the middle cerebral artery: a meta-analysis.** *J Neurointerv Surg* 2018;10:620–24 CrossRef Medline
- de Havenon A, Narata AP, Amelot A, et al; ARISE II investigators. **Benefit of endovascular thrombectomy for M2 middle cerebral artery occlusion in the ARISE II study.** *J Neurointerv Surg* 2021;13:779–83 CrossRef Medline
- Pérez-García C, Rosati S, Gómez-Escalonilla C, et al. **Stent-retriever alone versus combined use of stent-retriever and contact aspiration**

- technique for middle cerebral artery M2 occlusions: a propensity score analysis. *J Neurointerv Surg* 2021 Nov 8. [Epub ahead of print]
21. Renieri L, Valente I, Dmytriw AA, et al. **Mechanical thrombectomy beyond the circle of Willis: efficacy and safety of different techniques for M2 occlusions.** *J Neurointerv Surg* 202 ;14:546–50 CrossRef Medline
 22. Raychev R, Jahan R, Liebeskind D, SWIFT Trial Investigators, et al. **Determinants of intracranial hemorrhage occurrence and outcome after neurothrombectomy therapy: insights from the Solitaire FR with Intention for Thrombectomy Randomized Trial.** *AJNR Am J Neuroradiol* 2015;36:2303–07 CrossRef Medline
 23. Mokin M, Fargen KM, Primiani CT, et al. **Vessel perforation during stent retriever thrombectomy for acute ischemic stroke: technical details and clinical outcomes.** *J Neurointerv Surg* 2017;9:922–28 CrossRef Medline
 24. Renú A, Laredo C, Rodríguez-Vázquez A, et al. **Characterization of subarachnoid hyperdensities after thrombectomy for acute stroke using dual-energy CT.** *Neurology* 2022;98:e601–11 CrossRef Medline
 25. Qureshi AI, Saleem MA, Aytac E. **Postprocedure subarachnoid hemorrhage after endovascular treatment for acute ischemic stroke.** *J Neuroimaging* 2017;27:493–98 CrossRef Medline
 26. Schwaiger BJ, Gersing AS, Zimmer C, et al. **The curved MCA: influence of vessel anatomy on recanalization results of mechanical thrombectomy after acute ischemic stroke.** *AJNR Am J Neuroradiol* 2015;36:971–76 CrossRef Medline
 27. Kurre W, Aguilar-Pérez M, Martínez-Moreno R, et al. **Stent retriever thrombectomy of small caliber intracranial vessels using pREset LITE: safety and efficacy.** *Clin Neuroradiol* 2017;27:351–60 CrossRef Medline
 28. Peschillo S, Diana F, Berge J, et al. **A comparison of acute vascular damage caused by ADAPT versus a stent retriever device after thrombectomy in acute ischemic stroke: a histological and ultrastructural study in an animal model.** *J Neurointerv Surg* 2017;9:743–49 CrossRef Medline
 29. Teng D, Pannell JS, Rennert RC, et al. **Endothelial trauma from mechanical thrombectomy in acute stroke: in vitro live-cell platform with animal validation.** *Stroke* 2015;46:1099–106 CrossRef Medline

Causes of Death in Endovascularly Treated Patients with Acute Stroke

 H. Nagel,  J. Pinho,  D. Hasan,  H. Ridwan,  P. Habib,  J.B. Schulz,  M. Wiesmann,  A. Reich, and  O. Nikoubashman



ABSTRACT

BACKGROUND AND PURPOSE: Because stroke therapy has changed with the introduction of endovascular stroke treatment as a standard approach, studies on intrahospital causes of death from stroke are no longer up-to-date. The purpose of this observational study was to present the causes of death during hospitalization of patients with ischemic stroke who received endovascular stroke treatment, with the focus on a differentiation of curative and secondary palliative treatment.

MATERIALS AND METHODS: We studied a total cohort of 1342 patients who received endovascular stroke treatment in a tertiary stroke center (Aachen, Germany) between 2010 and 2020 and analyzed the causes of death in all 326 consecutive deceased patients. We distinguished between curative treatment and a secondary palliative approach and analyzed causes of death and treatment numbers across the years.

RESULTS: In the entire cohort of 326 deceased patients, the most common cause of death was of a cerebrovascular nature (51.5%), followed by pneumonia and sepsis (25.8%) and cardiovascular causes (8.3%). Neurovascular causes constituted 75.8% of reasons for palliation. In the group with a secondary palliative approach, causes of death were neurovascular in 54.0% of patients and pneumonia and sepsis in 26.0% of patients.

CONCLUSIONS: Cerebrovascular causes in patients with stroke play a major role in the intrahospital causes of death and reasons for palliation. Considering the large proportion of secondarily palliative-treated patients, reasons for palliation should be considered instead of causes of death to avoid concealment by, for example, life-terminating measures.

ABBREVIATION: IQR = interquartile range

Stroke is ranked by the World Health Organization as the second leading cause of death worldwide in 2019 and forms the third most common cause of death in Germany.^{1,2} Feigin et al³ confirmed the increasing burden of stroke on patients globally, but especially in low-income and middle-income countries. Depending on the type of stroke and the therapy administered, the mortality in untreated patients can be as high as 80%.⁴

It has been shown that there is an increased risk of death in the acute phase after stroke and a long-term risk of poststroke death that is twice as high as in the healthy population.⁵⁻⁷ Before endovascular stroke treatment was established, various studies showed that the most common cause of death in the first 7 days was due to


cerebrovascular issues, and most deaths within the first 30 days can be attributed to the initial infarction.^{8,9} The profile of the causes of death after ischemic stroke is reported to change with time: In the first 5 years after stroke, cardiovascular causes of death were shown to be most prominent, whereas nonvascular events accounted for most causes of death during the poststroke period of 5–10 years.¹⁰ Equally large but more recent studies are rare: D'Alton et al¹¹ reported pneumonia as the most common cause of death in patients with both hemorrhagic and ischemic stroke; in contrast Ake et al¹² reported a majority of cerebrovascular causes of death after 3 years, followed by cardiovascular deaths.

However, the standards in the treatment of patients with ischemic stroke have changed across the years, and there are few records with more recent and larger data sets that would allow an analysis of changes in causes of death resulting from the increasing use of endovascular stroke treatment. In patients with emergent, large-vessel-occlusion stroke, thrombectomy results in a better functional outcome and shows no increased mortality rates compared with intravenous thrombolysis or standard therapy only.¹³⁻¹⁵ Hence, it is equally conceivable that causes of death vary depending on

Received March 13, 2022; accepted after revision June 17.

From the Departments of Neuroradiology (H.N., D.H., H.R., M.W., O.N.) and Neurology (J.P., P.H., J.B.S., A.R.), University Hospital RWTH, Aachen, Germany.

Please address correspondence to Omid Nikoubashman, MD, Klinik für Neuroradiologie, Uniklinik RWTH Aachen, Pauwelsstr 30, 52074 Aachen, Germany; e-mail: onikoubashman@ukaachen.de; @o_nikoubashman

 Indicates article with online supplemental data.

<http://dx.doi.org/10.3174/ajnr.A7599>

treatment type: while thrombolytic therapies carry a risk of intracranial bleeding, endovascular stroke treatment is additionally associated with technical complications such as vascular dissection, vasospasm, embolus formation, bleeding, and device failure.¹⁶⁻¹⁸ The objective of this study was to determine intrahospital causes of death in patients receiving endovascular stroke treatment in a tertiary stroke center during 10 years.

MATERIALS AND METHODS

This study is based on a prospective registry of consecutive patients with acute ischemic stroke admitted to a tertiary stroke center of the University Hospital RWTH Aachen (Aachen, Germany). The study was approved by our local ethics committee. A need for written consent for this analysis was waived by this committee.

Our university hospital is a tertiary stroke center that serves an area of approximately 1 million inhabitants. In our regional stroke network of 4 hospitals, only 2 hospitals provide endovascular stroke therapy, with our university hospital being the only hospital that provides endovascular stroke therapy 24 hours a day and 7 days a week. Most patients eligible for endovascular stroke therapy are either directly admitted to our institution or transferred. Our standard is to continue treatment in our hospital and not to transfer patients back to their referring hospital.

We included all consecutive patients with acute ischemic stroke submitted to endovascular stroke treatment (including mechanical thrombectomy and/or intra-arterial thrombolysis, in combination or not with intravenous thrombolysis) between January 2010 and September 2020. The applied diagnostic methods and indicators for therapeutic measures used have already been described in a previous publication.¹⁹

We collected the following variables from the prospective registry and from the patients' clinical records when needed: demographic information, comorbidities, initial NIHSS score, ASPECTS, large-vessel occlusion site, established concept of treatment after endovascular stroke treatment, poststroke mRS, length of stay, intrahospital mortality, and causes of intrahospital death. Missing data were marked as "missing/unknown," whenever retrospective analysis did not allow completion of data. The concept of treatment and causes of intrahospital death were retrieved from the patient's clinical records and independently reviewed by 2 senior neurologists. Disagreements were settled in a consensus reading. We specifically focused on the spectrum of causes of death during approximately 1 decade rather than analyzing risk factors leading to death in endovascularly treated patients with stroke. We assessed baseline clinical characteristics and treatment modalities.

The established concept of clinical treatment after endovascular stroke treatment was classified into the following categories: curative care (maximal therapy during hospital stay) and secondary palliative care (palliative care decided by the treating physicians together with the patient or with the patient's legal representatives or care partners, taking into consideration the patient's will and expected outcome). The decision to establish a secondary palliative care concept in our institution is multidisciplinary and is always documented in the patient's clinical record. Palliative care was performed in-hospital and based on generally accepted recommendations; patients were not transferred to external facilities for secondary palliative care.²⁰

Causes of death were classified into the following categories: cerebrovascular, pneumonia and/or sepsis, cardiovascular, other (eg, renal failure), and a combination of multiple causes. This classification was based on previous studies and adapted to the intrahospital setting of our study.¹¹ For the secondary palliative care group, reasons for palliation were collected and the same categories were used.

Statistics

We analyzed the baseline data of the overall collective of endovascularly treated patients with stroke and compared the baseline characteristics of curative and secondary palliative care groups using χ^2 tests or Mann-Whitney *U* tests as appropriate. All values are indicated as frequencies or as median with interquartile range (IQR) due to the nonparametric nature of our data. We characterized causes of death in the overall study population but also separately for the curative care group and the secondary palliative group. Additionally, we characterized reasons for establishing a secondary palliative care concept. To assess changes across time, we analyzed the causes of death and reasons for secondary palliative care during the years of the study using trend analyses for proportions. Likewise, changes of continuous baseline variables across the study period were tested using the Cuzick nonparametric test. The Wilcoxon signed-rank test was used to compare the reasons for palliation with the actual causes of death in the secondary palliative group. We also compared the extreme ends of our observation period, namely patients in 2010–2011, when we established thrombectomy as a standard of care in our department, and patients in 2019, a more recent time period.

Statistical analyses were performed with SPSS Statistics 26 (IBM) and Stata Statistical Software, Release 16.1 (StataCorp). Statistical significance was set at an α value $< .05$.

RESULTS

During the study period, 2846 patients with acute ischemic stroke underwent acute reperfusion treatment, of whom 1342 received endovascular treatment and were included in our study. Among the latter, 597 patients (44.5%) received isolated mechanical thrombectomy, 722 patients (53.8%) received mechanical thrombectomy in combination with IV thrombolysis, and 23 patients (1.7%) received isolated intra-arterial thrombolysis. The distribution of treatment modalities was similar among patients who died in the curative care group and in the secondary palliative care group ($P = .840$).

The median age of all patients was 75 years (IQR, 64–82 years); 667 patients (49.7%) were women (median NIHSS score, 16; IQR, 10–20). We focused our analysis on all 326 patients (24.3%) who died during hospitalization in our institution. Among patients who died in the hospital, a curative care concept had been pursued in 37 patients (11.3%) and a secondary palliative care concept had been established in 289 patients (88.7%). Baseline characteristics of the study population are presented in the Table. Patients who died under curative care were significantly younger (median age, 72 versus 80 years; $P < .001$) than patients for whom secondary palliative care was established and had a shorter median length of stay (3 versus 5 days, $P = .005$). A detailed analysis of the time period from stroke onset to death is found in the Online Supplemental Data. In summary, cerebrovascular causes were the earliest to

Baseline data

Characteristic	Overall Collective (n = 1342) All Treatment Groups	Deceased Patients (n = 326)			P Value ^a
		Overall (n = 326)	Secondary Palliative (n = 289)	Curative (n = 37)	
Age (median) (IQR) (yr)	75 (64–82)	80 (71–86)	80 (72–87)	72 (62–82)	.001 ^b
Female sex (No.)	667 (49.7%)	163 (50.0%)	147 (50.9%)	16 (43.2%)	.383
Hypertension (No.) (n = 2 missing)	1067 (79.5%)	260 (79.8%)	232 (80.3%)	28 (75.7%)	.427
Cardiovascular disease (No.) (n = 4 missing)	657 (49%)	167 (51.2%)	146 (50.5%)	21 (56.8%)	.367
Diabetes mellitus (No.) (n = 3 missing)	342 (25.5%)	97 (29.8%)	78 (27%)	19 (51.4%)	.809
Obesity (No.) (n = 4 missing)	374 (27.9%)	78 (23.9%)	69 (23.9%)	9 (24.3%)	.360
Atrial fibrillation (No.) (n = 3 missing)	640 (47.7%)	168 (51.5%)	153 (52.9%)	15 (40.5%)	.304
Prior stroke (No.) (n = 2 missing)	255 (19%)	79 (24.2%)	72 (24.9%)	7 (18.9%)	.919
NIHSS score (median) (IQR)	16 (10–20)	18 (15–21)	18 (15–21)	20 (16–23)	.381
mRS at discharge (median) (IQR)	4 (2–5)	Noncalculable	Noncalculable	Noncalculable	NA
Length of stay (median) (IQR) (day)	12 (6–22)	5 (3–12)	5 (3–13)	3 (1–8)	.005 ^b

Note:—NA indicates noncalculable.

^a Comparison of secondary palliative and curative groups.

^b Statistically significant.

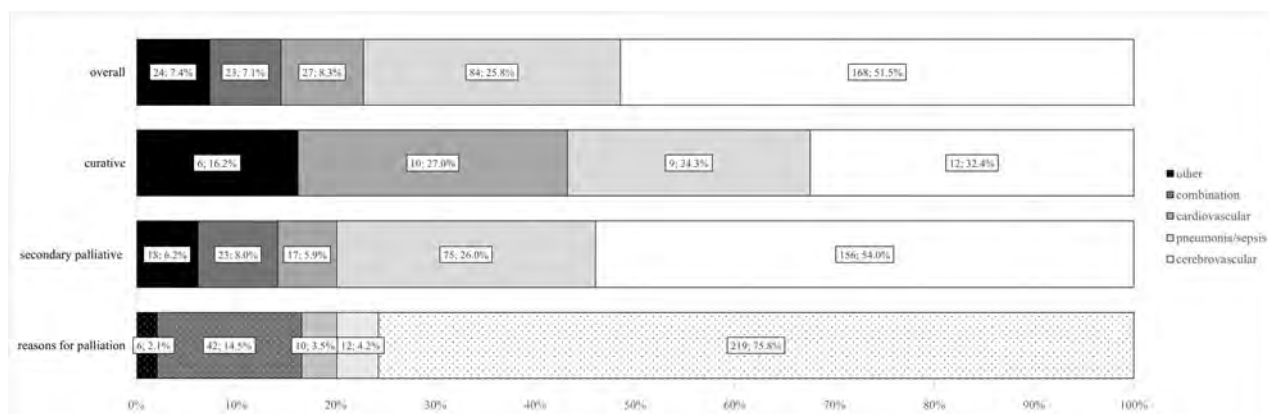


FIGURE. Causes of death in the overall, curative, and secondary palliative groups as well as reasons for palliation (absolute numbers and percentage). The exact reason for palliation was not determinable with sufficient certainty in 1 case.

cause death (median of 4 days), followed by cardiovascular, other, and a combination of causes (median of 7 days each), and pneumonia and sepsis (median of 11 days). The median onset to death was significantly shorter in the curative group compared with the secondary palliative group when the cause of death was cerebrovascular (2.5 days versus 4 days, $P = .016$) or cardiovascular (2 days versus 8 days, $P = .027$).

The Figure shows the causes of death and reasons for establishing a secondary palliative care concept. The most common cause of death in the entire cohort as well as in the curative and the secondary palliative care groups was cerebrovascular. However, the groups differed regarding the subsequent causes of death: In the entire cohort, most patients (51.5%; 168/326) died from cerebrovascular causes, with pneumonia and sepsis (25.8%; 84/326) being the second most frequent cause of death, whereas cardiovascular reasons (8.3%; 27/326) were less common. In the curative group, cerebrovascular deaths (32.4%; 12/37) were also

the most common cause, with cardiovascular events (27.0%; 10/37) being the second most frequent cause of death, closely followed by pneumonia and sepsis (24.3%; 9/37). In the secondary palliative group, cerebrovascular deaths (54.0%; 156/289) were also the most common cause, with pneumonia and sepsis (26.0%; 75/289) being the second most frequent cause of death, whereas cardiovascular reasons (5.9%; 17/289) were markedly less frequent. The most common combination cause of death was pneumonia and sepsis and cardiovascular diseases (57%; 13/23). This was followed by the combination of cerebrovascular causes and pneumonia and sepsis (22%; 5/23). The most common combination cause of palliation was pneumonia and sepsis and cardiovascular causes (26%; 11/42), followed by pneumonia and sepsis and other causes of palliation (19%; 8/42). Causes of death differed significantly ($P = .011$) between the curative and secondary palliative groups. In contrast, cerebrovascular causes (75.4%; 218/289) were the main reason to pursue secondary palliative care in most

patients, with a combination of causes (14.5%; 42/289) being the second most frequent reason for secondary palliative care. The reason for palliation could not be specified with sufficient certainty in 1 patient.

A comparison of reasons for palliation and causes of death in the secondary palliative group showed no significant alteration ($P = .169$).

Trends across the Study Period

An analysis of treatment numbers during 2010–2019 shows an increase in endovascular stroke treatment, ranging from 27 (31.0%) cases in 2010 to a maximum of 210 (61.4%) cases in 2019, with isolated mechanical thrombectomy being the most frequent approach after 2016. During the study period, the median age of patients undergoing endovascular treatment increased significantly ($P < .001$) and the median NIHSS score decreased significantly in the entire cohort ($P < .001$) and in the secondary palliative group ($P < .001$). No time trend was observed for in-hospital mortality for patients who underwent endovascular treatment during the study period ($P = .384$). However, there was a higher proportion of patients receiving palliative care ($P = .045$) and a lower proportion of curative care deaths ($P < .001$) across time. Our trend analysis also revealed that the proportion of cardiovascular deaths among patients who died decreased across the study period ($P = .026$) and that specifically in the curative group, the proportion of cerebrovascular deaths ($P = .003$) and cardiovascular deaths ($P = .002$) also decreased. Detailed information on the trend analyses and comparison of 2010–2011 versus 2019 is found in the Online Supplemental Data.

DISCUSSION

An initial objective of our study was to identify the intrahospital causes of death in endovascularly treated patients with stroke. Our analysis shows that in patients in whom a curative approach was pursued throughout, cerebrovascular causes and cardiovascular causes, and pneumonia and sepsis were the 3 main causes of death (sorted in order). This finding is in accordance with previous studies that demonstrated that cerebrovascular causes constitute most causes of death a short time after stroke.^{7–10,12} This is also in accordance with previous studies that demonstrated the importance of pneumonia as a main cause of death after stroke, which usually occurs due to prolonged ventilation times or dysphagia.^{9,11,21} Some authors report that pneumonia may play a particular role in patients with intracranial hemorrhage, who are reported to be likely to have dysphagia and subsequent pneumonia.^{22,23} The high proportion of cardiovascular deaths in the curative group is rather surprising, considering that previous data revealed an increase of cardiovascular deaths only in the first months poststroke.^{6,7,24} Acknowledging that cardiovascular reasons are less likely in our overall cohort and in our secondary palliative group, a possible explanation for the excess of cardiovascular causes of death in the curative group may be that patients who had previously died from large-vessel stroke now survive their stroke due to endovascular treatment but might die from their concomitant cardiovascular diseases. This finding is supported by our observation that in our curative cohort, cardiovascular disease was the earliest cause of death. However, our cohort is too small to draw definite conclusions. Also, previous studies were based on data from before endovascular stroke treatment was established and

mainly focused on long-term analyses of causes of death and are, therefore, difficult to compare with our study that focuses on intrahospital deaths after endovascular stroke treatment.

Curative versus Secondary Palliative Care

A novel finding of our analysis is that a differentiation must be made between patients receiving secondary palliative therapy and those treated with curative intent throughout because their causes of death differed considerably. Cerebrovascular causes, cardiovascular causes, and pneumonia and sepsis are the 3 main causes of death (sorted in order) in our patients, but these results must be interpreted with great caution because our results show that the reasons for death and palliation differed, albeit not significantly. Our analysis showed that because of the therapeutic switch, the causes of death of patients receiving secondary palliative care could not be equated to those of the curative group. It was interesting to compare the reasons for switching to the palliative approach with the actual causes of death. In line with the palliative concept, minimized therapeutic intervention results in a high number of pulmonary, cardiovascular, and other causes of death. At the same time, the most common reason for palliation appears to be neurovascular. Supporting data can be found in the literature indicating that withdrawal of life-sustaining treatment is the most common cause of death in ventilated patients in the intensive care unit and is primarily associated with a severe neurologic condition.^{25,26} On the basis of these findings, further analyses regarding case fatality and causes of death should pay attention to the large proportion of patients receiving palliative care. In accordance with Singh et al,²⁷ the quality of acute hospital care should not depend solely on the mortality rate, given the varying frequency of palliative concepts used.

Trends across the Study Period

Given a shift toward isolated mechanical thrombectomy across time as well as an increasing median age of patients and a decreasing median NIHSS score on admission, a change in causes of death with time would not have been surprising, especially with regard to the inclusion of elderly patients who are more likely to be treated with a palliative approach.²⁸ In fact, there was a higher proportion of patients receiving palliative care across time in our cohort. Even though the overall mortality did not change with time, there was a trend toward a lower proportion of cardiovascular deaths across time. Additionally, we found a time trend for decreasing cardiovascular and cerebrovascular deaths in the curative group. Higher rates of palliation on the one hand and lower rates of cardiovascular and cerebrovascular deaths in the curative group on the other hand may be explained by the inclusion of a wider spectrum of patients across time, with older patients on the one hand and patients with less severe stroke on the other receiving endovascular stroke therapy. This trend may also be explained by imbalances in the distribution of comorbidities, vascular risk factors, and frailty status, which were not the focus of this analysis. Because subsequent increases of other causes of death do not appear to have had a significant impact in the curative group, a note of caution is due here because the number of patients in each group across the years was very small, especially within the curative cohort.

Limitations

The monocentric approach of our study can be seen as both an advantage and a disadvantage. Systematic bias occurs due to internal standards for inclusion of patients and implementation of therapies, such as general anesthesia for thrombectomies. On the other hand, this bias can be seen as an advantage because the same conditions and criteria apply to the therapy of all patients. Selection and attrition biases are expected to be negligible because most patients eligible for endovascular stroke therapy are admitted to our institution by the regional emergency service or transferring hospitals and only 1 patient was transferred back to their referring hospital immediately after stroke therapy due to capacity reasons. Nonetheless, even though we included a very wide spectrum of patients, the small sample size within the individual groups (especially in our trend analyses) requires a cautious interpretation of our results. Also, causes of death could not be determined in a blinded fashion because the treating clinicians and the reviewing neurologists needed to be aware of the clinical course of patients for their assessment. To develop a full picture of intrahospital mortality, causes of death, and changes due to increased use of endovascular therapy, additional studies will be needed that include additional treatment groups (eg, intravenous thrombolysis) or data of different stroke units.

CONCLUSIONS

The most common intrahospital causes of death in patients with acute stroke who received endovascular therapy are cerebrovascular causes, cardiovascular causes followed by pneumonia and sepsis. One of the most striking findings to emerge from this study is that a large proportion of deceased patients with stroke were treated secondarily with a palliative approach; here, the causes of death should be considered with caution because the reasons for palliation and causes of death differ, albeit not significantly. The reasons for palliation are less vulnerable to bias by life-terminating measures and should be considered when analyzing causes of death.

Disclosure forms provided by the authors are available with the full text and PDF of this article at www.ajnr.org.

REFERENCES

1. World Health Organization. **Global Health Estimates: Life expectancy and leading causes of death and disability**. <https://www.who.int/data/gho/data/themes/mortality-and-global-health-estimates>. Accessed June 28, 2021
2. World Health Organization. **Global health estimates: Leading causes of death—Cause-specific mortality, 2000–2019**. <https://www.who.int/data/gho/data/themes/mortality-and-global-health-estimates>. Accessed June 28, 2021
3. Feigin VL, Forouzanfar MH, Krishnamurthi R, et al. **Global and regional burden of stroke during 1990–2010: findings from the Global Burden of Disease Study 2010**. *Lancet* 2014;383:245–54 CrossRef Medline
4. Huttner HB, Schwab S. **Malignant middle cerebral artery infarction: clinical characteristics, treatment strategies, and future perspectives**. *Lancet Neurol* 2009;8:949–58 CrossRef Medline
5. Brønnum-Hansen H, Davidsen M, Thorvaldsen P; Danish MONICA Study Group. **Long-term survival and causes of death after stroke**. *Stroke* 2001;32:2131–36 CrossRef Medline
6. Hankey GJ, Jamrozik K, Broadhurst RJ, et al. **Five-year survival after first-ever stroke and related prognostic factors in the Perth Community Stroke Study**. *Stroke* 2000;31:2080–86 CrossRef Medline
7. Loor HI, Groenier KH, Limburg M, et al. **Risks and causes of death in a community-based stroke population: 1 month and 3 years after stroke**. *Neuroepidemiology* 1999;18:75–84 CrossRef Medline
8. Kiyohara Y, Kubo M, Kato I, et al. **Ten-year prognosis of stroke and risk factors for death in a Japanese community**. *Stroke* 2003;34:2343–47 CrossRef Medline
9. Vernino S, Brown RD, Sejvar JJ, et al. **Cause-specific mortality after first cerebral infarction**. *Stroke* 2003;34:1828–32 CrossRef Medline
10. Hardie K, Hankey GJ, Jamrozik K, et al. **Ten-year survival after first-ever stroke in the Perth Community Stroke Study**. *Stroke* 2003;34:1842–46 CrossRef Medline
11. D'Alton M, Coughlan T, Cogan N, et al. **Patterns of mortality in modern stroke care**. *Ir Med J* 2018;111:750 Medline
12. Ake J, Delavaran H, Lindgren AG. **Survival, causes of death and recurrence up to 3 years after stroke: a population-based study**. *Eur J Neurol* 2021;28:4060–68 CrossRef Medline
13. Nogueira RG, Jadhav AP, Haussen DC, et al. **Thrombectomy 6 to 24 hours after stroke with a mismatch between deficit and infarct**. *N Engl J Med* 2018;378:11–21 CrossRef Medline
14. Goyal M, Menon BK, van Zwam WH, et al. **Endovascular thrombectomy after large-vessel ischaemic stroke: a meta-analysis of individual patient data from five randomised trials**. *Lancet* 2016;387:1723–31 CrossRef Medline
15. Bhatia R, Hill MD, Shobha N, et al. **Low rates of acute recanalization with intravenous recombinant tissue plasminogen activator in ischemic stroke: real-world experience and a call for action**. *Stroke* 2010;41:2254–58 CrossRef Medline
16. Emberson J, Lees KR, Lyden P, et al. **Effect of treatment delay, age, and stroke severity on the effects of intravenous thrombolysis with alteplase for acute ischaemic stroke: a meta-analysis of individual patient data from randomised trials**. *Lancet* 2014;384:1929–35 CrossRef Medline
17. Elakkad A, Drocton G, Hui F. **Endovascular stroke interventions: procedural complications and management**. *Semin Intervent Radiol* 2020;37:199–200 CrossRef Medline
18. Balami JS, White PM, McMeekin PJ, et al. **Complications of endovascular treatment for acute ischemic stroke: prevention and management**. *Int J Stroke* 2018;13:348–61 CrossRef Medline
19. Nikoubashman O, Dekeyser S, Riabikin A, et al. **True first-pass effect**. *Stroke* 2019;50:2140–46 CrossRef Medline
20. Woerdehoff D, Bredbach GB, Frohnhoefen H, et al. **Palliativversorgung bei Schlaganfall**. *NeuroGeriatr* 2014;11:69–73
21. Nikoubashman O, Schurmann K, Probst T, et al. **Clinical impact of ventilation duration in patients with stroke undergoing interventional treatment under general anesthesia: the shorter the better?** *AJNR Am J Neuroradiol* 2016;37:1074–79 CrossRef Medline
22. Liljeblom J, Christensen T, Christensen KB. **Early prediction of one-year mortality in ischemic and haemorrhagic stroke**. *J Stroke Cerebrovasc Dis* 2020;29:104667 CrossRef Medline
23. Joundi RA, Martino R, Saposnik G, et al. **Dysphagia screening after intracerebral hemorrhage**. *Int J Stroke* 2018;13:503–10 CrossRef Medline
24. Olsen TS. **Stroke recurrence and prognosis after stroke**. *Handb Clin Neurol* 2009;92:407–21 CrossRef Medline
25. Diring MN, Edwards DF, Aiyagari V, et al. **Factors associated with withdrawal of mechanical ventilation in a neurology/neurosurgery intensive care unit**. *Crit Care Med* 2001;29:1792–97 CrossRef Medline
26. Verkade MA, Epker JL, Nieuwenhoff MD, et al. **Withdrawal of life-sustaining treatment in a mixed intensive care unit: most common in patients with catastrophic brain injury**. *Neurocrit Care* 2012;16:130–35 CrossRef Medline
27. Singh T, Peters SR, Tirschwell DL, et al. **Palliative care for hospitalized patients with stroke: results from the 2010 to 2012 National Inpatient Sample**. *Stroke* 2017;48:2534–40 CrossRef Medline
28. Parry-Jones AR, Paley L, Bray BD, et al; on behalf of the SSNAP Collaborative Group. **Care-limiting decisions in acute stroke and association with survival: analyses of UK national quality register data**. *Int J Stroke* 2016;11:321–31 CrossRef Medline

Endarterectomy, Stenting, or Medical Treatment for Symptomatic Carotid Near-Occlusion: Results from CAOS, a Multicenter Registry Study

✉ A. Garcia-Pastor, ✉ A. Gil-Núñez, ✉ J.M. Ramirez-Moreno, ✉ N. González-Nafria, ✉ J. Tejada, ✉ F. Moniche, ✉ J.C. Portilla-Cuenca, ✉ P. Martínez-Sánchez, ✉ B. Fuentes, ✉ M.A. Gamero-García, ✉ M.A. de Leciñana, ✉ J. Masjuan, ✉ D.C. Verge, ✉ Y. Aladro, ✉ V. Parkhutik, ✉ A. Lago, ✉ A.M. de Arce-Borda, ✉ M. Usero-Ruiz, ✉ R. Delgado-Mederos, ✉ A. Pampliega, ✉ Á. Ximenez-Carrillo, ✉ M. Bártulos-Iglesias, and ✉ E. Castro-Reyes, on behalf of the Stroke Project of the Spanish Cerebrovascular Diseases Study Group



ABSTRACT

BACKGROUND AND PURPOSE: The treatment of symptomatic carotid near-occlusion is controversial. Our aim was to analyze the results of carotid endarterectomy and carotid artery stent placement in patients with symptomatic carotid near-occlusion and to identify factors related to technical failure, periprocedural complications, and restenosis.

MATERIALS AND METHODS: We conducted a multicenter, prospective nonrandomized study. Patients with angiography-confirmed carotid near-occlusion were included. We assessed the revascularization rate and periprocedural stroke or death. Twenty-four-month clinical and carotid imaging follow-up was performed, and rates of carotid restenosis or occlusion, ipsilateral stroke, and mortality were analyzed. Carotid artery stent placement, carotid endarterectomy, and medical treatment were compared.

RESULTS: One hundred forty-one patients were included. Forty-four carotid artery stent placement and 23 carotid endarterectomy procedures were performed within 6 months after the event. Complete revascularization was achieved in 83.6%, 81.8% in the carotid artery stent placement group and 87% with carotid endarterectomy ($P = .360$). Periprocedural stroke or death occurred in 6% (carotid artery stent placement = 2.3%; carotid endarterectomy = 13%; $P = .077$) and was not related to revascularization failure. The carotid restenosis or occlusion rate was 8.3% (5% restenosis, 3.3% occlusion); with carotid artery stent placement it was 10.5%; and with carotid endarterectomy it was 4.5% ($P = .419$). The 24-month cumulative rate of ipsilateral stroke was 4.8% in the carotid artery stent placement group, 17.4% for carotid endarterectomy, and 13.1% for medical treatment ($P = .223$). Mortality was 12%, 4.5%, and 5.6%, respectively ($P = .422$). Revascularization failure and restenosis occurred more frequently in patients with full collapse compared with patients without full collapse (33.3% versus 5.6%, $P = .009$; 21.4% versus 2.9%, $P = .032$, respectively).

CONCLUSIONS: Carotid artery stent placement and carotid endarterectomy are associated with high rates of failure and periprocedural stroke. Carotid near-occlusion with full collapse appears to be associated with an increased risk of technical failure and restenosis. Carotid near-occlusion revascularization does not seem to reduce the risk of stroke at follow-up compared with medical treatment.

ABBREVIATIONS: CAS = carotid artery stent placement; CEA = carotid endarterectomy; CHS = cerebral hyperperfusion syndrome; CNO = carotid near-occlusion; IQR = interquartile range

The treatment of symptomatic carotid near-occlusion (CNO) is controversial. Post hoc analyses of the NASCET and the

European Carotid Surgery Trial (ECST) conducted in the 1990s revealed that the risk of recurrent stroke could be lower in

Received March 15, 2022; accepted after revision June 17.

From the Department of Neurology (A.G.-P., A.G.-N., E.C.-R.), Hospital General Universitario Gregorio Marañón, Madrid, Spain; Department of Neurology (J.M.R.-M.), Hospital Universitario Infanta Cristina, Badajoz, Spain; Department of Neurology (N.G.-N., J.T.), Complejo Asistencial Universitario de León, Neurology, León, Spain; Department of Neurology (F.M.), Hospital Universitario Virgen del Rocío, Sevilla, Spain; Department of Neurology (J.C.P.-C.), Hospital San Pedro Alcántara, Cáceres, Spain; Department of Neurology (P.M.-S., B.F.), Hospital Universitario La Paz, Madrid, Spain; Department of Neurology (M.A.G.-G.), Hospital Universitario Virgen Macarena, Sevilla, Spain; Department of Neurology (M.A.d.L., J.M.), Hospital Universitario Ramón y Cajal, Madrid, Spain; Department of Neurology (D.C.V.), Corporació Sanitaria Parc Taulí, Sabadell, Spain; Department of Neurology (Y.A.), Hospital Universitario de Getafe, Getafe, Spain; Department of Neurology (V.P., A.L.),

Hospital Universitari La Fe, Valencia, Spain; Department of Neurology (A.M.d.A.-B.), Hospital Universitario de Donostia, Donostia, Spain; Department of Neurology (M.U.-R.), Hospital Universitario de Valladolid, Valladolid, Spain; Department of Neurology (R.D.-M.), Hospital de la Santa Creu i Sant Pau, Barcelona, Spain; Department of Neurology (A.P.), Hospital General Universitario de Alicante, Alicante, Spain; Department of Neurology (Á.X.-C.), Hospital Universitario de La Princesa, Madrid, Spain; and Department of Neurology (M.B.-I.), Hospital Universitario de Burgos, Burgos, Spain.

Please address correspondence to Andrés García-Pastor, MD, Stroke Center, Vascular Neurology Section, Hospital General Universitario Gregorio Marañón, Madrid, Spain, C/Dr Esquerdo 46, 28007 Madrid, Spain; e-mail: angarpas@yahoo.es; @angarpas1

<http://dx.doi.org/10.3174/ajnr.A7617>

patients with CNO than in patients with conventional severe carotid stenosis and that patients with CNO might not benefit from revascularization.¹⁻³ On the basis of this evidence, the latest guidelines of the European Society for Vascular Surgery do not recommend revascularization in patients with CNO.⁴ However, recent studies have reported a higher recurrence rate in patients with CNO, especially when associated with full collapse,^{5,6} and several meta-analyses have shown the nonsuperiority of best medical treatment over revascularization therapies.⁷⁻⁹

Many case series have shown that both carotid endarterectomy (CEA) and carotid artery stent placement (CAS) are effective and safe in patients with CNO.¹⁰⁻¹⁵ However, most of these studies are retrospective single-center series that do not even compare the 2 techniques. To date, only 2 retrospective studies have directly compared CEA and CAS in patients with CNO with similar rates of periprocedural complications and long-term recurrences.^{16,17} Additionally, recent pooled analyses did not show relevant differences between CEA and CAS in CNO in both periprocedural and long-term follow-up.^{8,9} Unfortunately, we do not have better quality evidence because the latest clinical trials comparing CAS and CEA in the treatment of symptomatic carotid stenosis did not include patients with CNO.^{18,19}

The objectives of this study were to analyze the results obtained with revascularization and medical treatment in patients with symptomatic CNO, to compare periprocedural and follow-up results of CEA and CAS, and to identify factors related to technical failure, periprocedural complications, and restenosis.

MATERIALS AND METHODS

Study Design and Patient Selection

The CAOS study (in Spanish “CASi Oclusión Sintomática”) is a nonrandomized, prospective, observational, multicenter registry study conducted in 17 Spanish university hospitals from January 2010 to May 2016. The CAOS study methodology has been described previously.²⁰ The study population comprised adult patients with an angiography-confirmed diagnosis of atherosclerotic CNO and ipsilateral ischemic stroke, TIA, or retinal ischemia in the previous 6 months. This study was supported by the “Stroke Project” initiative of the Spanish Cerebrovascular Diseases Study Group and obtained ethics approval from “Comité de Ética e investigación Clínica Hospital General Universitario Gregorio Marañón,” with ID number of the approval: 122/09. Participants gave informed consent before taking part in the study.

CNO was diagnosed in all patients using DSA. On the basis of the report by Fox et al,¹ diagnosis of ICA near-occlusion was confirmed when the angiographic findings fulfilled at least 2 of the following 4 criteria: 1) delayed cranial arrival of ICA contrast compared with the external carotid artery, 2) intracranial collaterals seen as cross-filling of contralateral vessels or ipsilateral contrast dilution, 3) frank reduced diameter of the ICA compared with the contralateral ICA, and 4) reduced ICA diameter compared with the ipsilateral external carotid artery. The presence or absence of a full collapse was determined by each participating center using DSA and/or CT angiography and defined as a “threadlike” lumen distal to the stenosis.²¹

The treatment decision (medical therapy versus revascularization) as well as the type of revascularization treatment (CEA or

CAS) was based on the criteria and routine practice of each participating center. Patients who underwent revascularization beyond 6 months were included in the medical treatment group, and their follow-up was censored at the time of the intervention.

Follow-up and Outcome Measures

The immediate result of the revascularization procedure was assessed in the CAS group by performing an angiographic control series after carotid stent implantation. In the surgical group, a non-invasive carotid imaging test (usually CT angiography or carotid sonography) was performed within 48 hours of the procedure. The result of the revascularization procedure was classified as follows: 1) complete revascularization if a complete or almost-complete recovery of the distal caliber of ICA was achieved, 2) incomplete revascularization when the distal ICA collapse persisted after the intervention, and 3) carotid occlusion when the procedure resulted in complete occlusion of the treated ICA. Revascularization failure was defined as incomplete revascularization or a complete occlusion occurring immediately after the procedure.

Carotid imaging follow-up of the near-occlusion using carotid sonography, CT angiography, and/or MR angiography was performed at 6, 12, and 24 months. Restenosis (defined as a stenosis of >50% of the treated ICA) and complete ICA occlusion rates at 24-month follow-up were collected. Any periprocedural (ie, within 30 days after the procedure) stroke or death rate and other complications were recorded. A clinical follow-up was performed at 3, 6, 12, and 24 months after the presenting event.

The 24-month ipsilateral ischemic stroke rate (including periprocedural events) and mortality were also assessed. Disabling stroke was defined as a stroke associated with a 3-month mRS score of 3–5.

Statistical Analysis

Statistical analyses were performed using the SPSS Statistics 23.0 software package for Windows (IBM). The results were expressed as proportions for categorical variables and as mean (SD) or medians and interquartile range (IQR) for continuous variables. Categorical variables were compared using the χ^2 test or 2-tailed Fisher exact test. Continuous variables were compared using a 2-sample *t* test or the Mann-Whitney test. Univariate and age- and revascularization procedure-adjusted multivariate logistic regression analyses were performed to determine factors related to revascularization failure, periprocedural stroke, or death and restenosis. The cumulative incidences were calculated using Kaplan-Meier curves. Differences among treatment groups were determined using the log-rank test. *P* values $\leq .05$ were considered statistically significant.

RESULTS

A total of 141 patients with angiography-confirmed CNO were recruited. Most patients were men (120; 85.1%), with a mean age of 68.71 (SD, 9.05) years.

Seventy patients underwent revascularization. In 3 of them, the procedure was performed beyond 6 months, and patients were assigned to the medical treatment group. Therefore, 74 patients were included in the medical treatment group, and 67, in the revascularization group (44 CAS and 23 CEA procedures). No

Table 1: Baseline characteristics of the patients

	CEA (<i>n</i> = 23)	CAS (<i>n</i> = 44)	Medical Treatment (<i>n</i> = 74)	<i>P</i> Value
Demographics				
Age (mean) (SD) (yr)	68.6 (7.9)	68.4 (10.9)	69.0 (8.3)	.946
Age younger than 65 yr (No.) (%)	7 (30.4)	13 (29.5)	22 (31.1)	.985
Age 65–74 yr (No.) (%)	9 (39.1)	16 (36.4)	30 (40.5)	.904
Age 75 yr or older (No.) (%)	7 (30.4)	15 (34.1)	21 (28.4)	.809
Male sex (No.) (%)	19 (82.6)	39 (88.6)	62 (83.8)	.723
Time to revascularization				
Days to revascularization, (median) (IQR)	22 (11–53)	21 (8–39.5)		.930
Revascularization within 15 days after the presenting event (No.) (%)	8 (34.8)	20 (45.5)		.400
Risk factors				
Hypertension (No.) (%)	15 (65.2)	35 (79.5)	51 (68.9)	.352
Diabetes mellitus (No.) (%)	10 (43.5)	12 (27.3)	29 (39.2)	.311
Dyslipidemia (No.) (%)	13 (56.5)	21 (47.7)	39 (52.7)	.770
Current smoker (No.) (%)	9 (39.1)	17 (38.6)	23 (31.1)	.629
Ischemic heart disease (No.) (%)	2 (8.7)	8 (18.2)	13 (17.6)	.556
Atrial fibrillation (No.) (%)	0	1 (2.3)	6 (8.1)	.180
Previous stroke/TIA (No.) (%) ^a	4 (17.4)	11 (25)	20 (27)	.646
Peripheral artery disease (No.) (%)	3 (13)	5 (11.4)	5 (6.8)	.554
Clinical presentation				
Ipsilateral ischemic stroke or retinal infarct (No.) (%)	17 (73.9)	31 (70.5)	47 (63.5)	.566
Ipsilateral transient symptoms (No.) (%)	6 (26.1)	13 (29.5)	27 (36.5)	.566
Ipsilateral recurrent events (No.) (%)	4 (17.4)	7 (15.9)	13 (17.6)	.972
Full collapse (No.) (%) ^b	5 (23.8)	10 (33.3)	26 (41.3)	.332

^a The history of stroke/TIA before the index event.

^b The presence or absence of full collapse could be determined in 114 patients.

significant differences were observed in the baseline characteristics among CEA, CAS, and medical treatment groups (Table 1).

The median time from the presenting event to the revascularization was 21 days (IQR, 11–43 days), 22 for CEA and 21 for CAS. Ultra-early treatment (ie, within 24 hours) was performed in 4 patients, and 28 patients (41.8%) were treated in the 15 days following the event. One patient had an ipsilateral retinal infarct while awaiting CEA.

Complete revascularization was achieved in 56 patients (83.6%). Revascularization failure was observed in 11 patients (16.4%), incomplete revascularization occurred in 8 patients, and carotid occlusion during the procedure, in 3. No significant differences in the proportion of complete revascularization or failure were observed between CAS and CEA (Table 2).

Six patients (8.9%) had a periprocedural stroke or TIA, all of them ipsilateral to the treated CNO. Three strokes or TIAs occurred in the CAS group (6.8%, 1 disabling stroke and 2 TIAs), and the other 3 cases, in the CEA group (13%, all of them nondisabling strokes). The rate of periprocedural stroke or death was 6% (*n* = 4) and tended to be higher for CEA (13% versus 2.3%, *P* = .077). Revascularization failure was not associated with an increased risk of periprocedural events: Only 1 patient treated with CAS had an ICA occlusion and ipsilateral disabling stroke. None of the patients died within the first 30 days following the procedure, though 1 patient treated with CAS who had a cerebral hyperperfusion syndrome (CHS) died 67 days after the procedure. Twelve other periprocedural complications were registered (Table 2). CHS was recorded in 2 cases (3%), with no differences between surgical and endovascular treatments.

Carotid imaging follow-up was performed in 60 patients. Restenosis or ICA occlusion was detected in 5 patients (8.3%). Restenosis occurred in 3 patients (5%), all of them treated with CAS. In 1 patient, restenosis was symptomatic, presenting as an ipsilateral TIA. Progression to complete ICA occlusion was observed in 2 patients (3.3%), one (4.8%) in the surgical group and another (2.3%) in the CAS group (*P* = .636). The patient who progressed to ICA occlusion after endovascular treatment had a disabling ipsilateral stroke (Table 2).

Revascularization failure occurred more frequently in patients with full collapse: 33.3% compared with 5.6% (*P* = .009). Additionally, restenosis or ICA occlusion was more frequent in patients with CNO with full collapse (21.4% versus 2.9%, *P* = .032). No significant relationship was observed between the presence of full collapse and the risk of periprocedural stroke or death (6.7% in CNO with full collapse and 8.3% in CNO without full collapse, *P* = .840) or with CHS (6.7% and 2.8%, *P* = .514). In the multivariate analysis, the presence of full collapse was the only factor independently related to an increased risk of revascularization failure (OR, 11.6; 95% CI, 1.6–84.6) and restenosis at follow-up (OR, 27.4; 95% CI, 1.3–567.7) (Table 3).

Fifteen patients had an ipsilateral ischemic stroke during the 24-month follow-up, resulting in a cumulative rate of 11.1% (95% CI, 5.8%–16.4%). Two ipsilateral strokes occurred in the CAS group (cumulative rate, 4.8%; 95% CI, 0%–11.3%), 4 in the surgical group (1 before CEA and 3 in the periprocedural period, cumulative rate, 17.4%; 95% CI, 1.9%–32.9%), and 9 in the medical treatment group (13.1%; 95% CI, 5.1%–21.1%; *P* = .223) (Figure). We recorded 6 disabling strokes: 2 in the endovascular

Table 2: Revascularization results, periprocedural complications, carotid imaging follow-up, and clinical follow-up

	CEA (n = 23)	CAS (n = 44)	Medical Treatment (n = 74)	P Value
Immediate results of the procedure				
Complete revascularization	20 (87)	36 (81.8)		.360
Revascularization failure	3 (13)	8 (18.2)		
Incomplete revascularization	2 (8.7)	6 (13.6)		
ICA occlusion	1 (4.3)	2 (4.5)		
Periprocedural complications				
Ipsilateral stroke or TIA	3 (13)	3 (6.8)		.397
Disabling stroke	0	1 (2.3)		
Nondisabling stroke	3 (13)	0		
TIA	0	2 (4.5)		
Death	0	0 ^a		
Periprocedural stroke or death	3 (13)	1 (2.3)		.077
Other complications	5 (21.7)	7 (15.9)		.555
Stent thrombosis	0	1 (2.3)		
Cerebral hyperperfusion syndrome	1 (4.3)	1 (2.3)		
Epileptic seizures	0	1 (2.3)		
Complications in the puncture area	0	2 (4.5)		
Hypoglossal nerve palsy/dysphonia	3 (13.6)	0		
Asystolia/bradycardia	0	2 (4.5)		
Airway compression	1 (4.3)	0		
Carotid-imaging follow-up				
Carotid restenosis or occlusion ^b	1 (4.5)	4 (10.5)		.419
Carotid restenosis	0	3 (6.8)		.200
Symptomatic carotid restenosis	0	1 ^c		
Carotid occlusion	1 (4.8)	1 (2.3)		.636
Symptomatic carotid occlusion	0	1 ^d		
Clinical follow-up				
Ipsilateral ischemic stroke at 24 months' follow-up	4 (17.4)	2 (4.8)	9 (13.1)	.223
Mortality at 24 months' follow-up	1 (4.5)	5 (12)	4 (5.6)	.422

^a One patient had cerebral hyperperfusion syndrome and died 67 days after the procedure.

^b Carotid imaging follow-up was performed in 62 patients (22 in the CEA group and 40 in the CAS group).

^c Carotid restenosis manifested clinically as a TIA.

^d Disabling ipsilateral stroke.

group (cumulative rate, 4.8%), none in the CEA group, and 4 in the medical treatment group (5.8%, $P = .518$).

Ten patients died during follow-up. The 24-month cumulative mortality rate was 7.5% (95% CI, 3.0%–12.0%). Five deaths occurred in the endovascular group (12%; 95% CI, 2.2%–21.8%), 1 patient died in the CEA group (4.5%; 95% CI, 0%–13.1%), and 4, in the group of patients treated medically (5.6%; 95% CI, 0.3%–10.9%) ($P = .422$; Figure).

DISCUSSION

In the present study, a revascularization rate of 84% was obtained with no significant differences between CEA and CAS. Our revascularization results are lower than those observed in previous series with success rates well above 90%.^{10,11,15–17} However, these results come from retrospective single-center studies in which selection biases cannot be ruled out.

Traditionally, CNO revascularization has been associated with a high risk of complications. However, the NASCET and ECST studies showed similar periprocedural stroke and death rates for CNO and conventional ICA stenosis (5.4% and 6.2%, respectively),² and a recent meta-analysis found a perioperative risk of 4.8% for CEA and 5.4% for CAS.⁸ The periprocedural stroke and death rate was 6% in our study and was especially high in the CEA group (13% versus 2.3%). These poor results should be viewed with caution considering the small number of patients

included in each treatment group, which could be overstating some of our results. Furthermore, all 3 perioperative strokes that occurred in the CEA group were nondisabling.

The incidence of CHS after carotid revascularization ranges between 0% and 3%.²² However, a recent meta-analysis described a higher incidence for patients treated with CAS, reaching 4.6%.²³ The incidence of CHS could also be higher in patients with CNO: Cay et al²⁴ reported an 8.6% rate after CAS and observed a significantly higher risk among patients with full collapse (30% compared with 4.2% in CNO without full collapse). A decreased cerebral autoregulation or underlying blood-brain barrier damage has been proposed to explain this finding. In our study, CHS occurred in 3% of cases, and no differences were observed between CAS and CEA or between CNO with or without full collapse.

Restenosis or ICA occlusion at 2-year follow-up was detected in 8.3% of our patients and occurred more frequently with CAS (10.5% versus 4.5%), though the difference did not reach statistical significance. Pooled analyses found a rate of restenosis in patients with CNO that ranged between 4% and 6.4% for CEA and 4.1% and 7.5% for CAS,^{8,9} not very different from the restenosis rate of 4%–5% at 1 year for conventional ICA stenosis described in the Carotid Revascularization Endarterectomy Versus Stenting Trial (CREST).¹⁸ However, Kim et al¹⁷ observed a higher proportion of restenosis in CNO, reaching 20% for CAS and 17.4% for CEA.

Table 3: Factors related to revascularization failure, periprocedural stroke or death, and carotid restenosis

	Revascularization Failure		Periprocedural Stroke or Death		Carotid Restenosis or Occlusion at Follow-up	
	Univariate Analysis	Multivariate Analysis ^a	Univariate Analysis	Multivariate Analysis ^a	Univariate Analysis	Multivariate Analysis ^a
Age 75 yr or older	1.91 (0.51–7.13)		2.15 (0.28–16.38)		3.66 (0.56–24.00)	
Male sex	0.64 (0.12–3.61)		0.44 (0.04–4.72)			
Hypertension	4.00 (0.47–33.86)		1.02 (0.10–10.53)			
Diabetes mellitus	0.40 (0.08–2.03)		2.15 (0.28–16.38)		0.51 (0.05–4.94)	
Dyslipidemia	0.30 (0.07–1.26)		0.97 (0.13–7.31)		1.56 (0.24–10.05)	
Current smoker	0.54 (0.13–2.25)		1.63 (0.22–12.31)		1.00 (0.15–6.48)	
Ischemic heart disease	2.63 (0.56–12.31)		2.00 (0.19–21.41)		1.71 (0.17–17.63)	
Previous stroke/TIA	1.375 (0.32–6.00)		1.17 (0.11–12.11)		0.90 (0.09–8.78)	
Clinical presentation as transient symptoms	0.37 (0.04–3.16)		1.42 (0.14–14.84)		3.41 (0.50–23.39)	
Full collapse	8.50 (1.43–50.66) ^b	11.60 (1.59–84.63) ^c	0.79 (0.08–8.22)		9.27 (0.87–98.51) ^d	27.40 (1.32–567.74) ^e
CEA vs CAS	0.68 (0.16–2.84)		6.45 (0.63–65.93)		0.41 (0.04–3.87)	

^a Age- and revascularization procedure-adjusted multivariate logistic regression analysis.

^b $P = .019$.

^c $P = .016$.

^d $P = .065$.

^e $P = .003$.

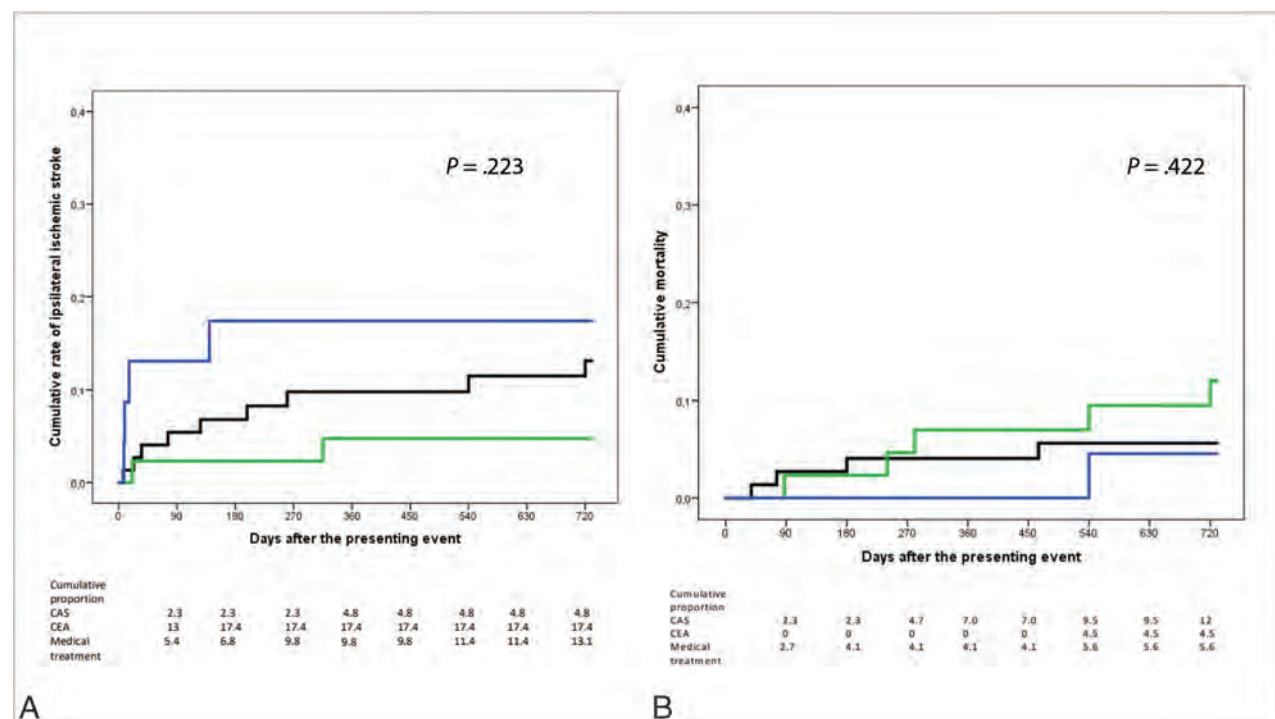


FIGURE. Kaplan-Meier curves comparing the effect of CAS (green line), CEA (blue line), and medical treatment (black line) on the cumulative rate of ipsilateral ischemic stroke (A) and mortality (B).

Recent meta-analyses have described a long-term stroke rate below 5% in patients with CNO who undergo revascularization.^{8,9} The 24-month cumulative stroke rate is strikingly higher in our study, especially for CEA, reaching 17%. These results are clearly related to the high rate of periprocedural stroke observed in proportion to the small number of patients included in this treatment group. On the other hand, if we re-analyze the cumulative recurrence rate in the CEA group and consider the event that occurred before surgery as a recurrence in the medical treatment group, the cumulative rates of both groups would be similar

(13.6% for CEA and 14.3% for medical treatment). In any case, our study has not been able to show clear differences in the risk of recurrent stroke at 2 years among the different treatment groups.

Full collapse has been associated with an increased risk of recurrence in medically treated patients with CNO,^{5,6} though this effect has not been confirmed in all studies.²⁵

On the other hand, the impact of full collapse on the results of the revascularization of CNO has been less often studied. In our study, CNO with full collapse was associated with a greater

probability of revascularization failure (33% versus 6%). This finding may be explained by the technical difficulties involved in fully expanding the stent in a narrow artery or in implanting a shunt in patients treated with CEA. The study by Neves et al²⁶ also showed a high failure rate with CAS (21%) in patients with CNO and full collapse. Other studies do not seem to confirm these findings.^{24,27} We also observed an increased risk of restenosis or ICA occlusion in patients with collapsed CNO. Meershoek et al²⁷ did not record restenosis in their 17 patients with CNO with full collapse treated with CEA, and Neves et al described 2 occlusions during follow-up in their 19 patients treated with CAS. Recently, Johansson et al²⁸ have described a high rate of postprocedural stroke or death in patients with CNO and full collapse (2 of 10 versus 0 of 43 in CNO without full collapse and 5 of 166 in conventional carotid stenosis). Most interesting, the 2 cases described were intracerebral hemorrhages. In our study, no association was observed between the presence of full collapse and the risk of periprocedural stroke or death.

This study has some limitations. First, this is a subanalysis of a previous study, which was not specifically designed to compare CEA, CAS, and medical treatment. Second, the sample size of the study does not have sufficient statistical power for an adequate comparison between CEA and CAS; therefore, the periprocedural stroke rate in the CEA group could have been overestimated. On the other hand, the small number of patients with CNO and full collapse may have affected the precision of the multivariate analysis. Third, patients were not randomized to medical or revascularization treatment and CEA or CAS; treatment decisions were based on the criteria of each participating center. Fourth, the study provides limited information on the technical aspects of the different treatments used. The main strength of this study is its prospective design and the use of predefined diagnostic criteria for CNO.

CONCLUSIONS

Our results suggest that revascularization of CNO is a technically challenging procedure with a high failure rate and an increased risk of periprocedural stroke and other potentially serious complications such as CHS. In addition, revascularization in patients with CNO with full collapse appears to be associated with a higher risk of technical failure and restenosis. On the other hand, CAS or CEA was not associated with a significant reduction of ipsilateral stroke at follow-up compared with medical treatment.

These findings raise new questions about the optimal management of CNO and force us to consider the risk-benefit balance between medical treatment and revascularization in this group of patients.

Future research in CNO should focus on the following:

- A better understanding of the pathophysiology and natural history of CNO
- Elucidating the impact that the presence or absence of full collapse may have in patients with CNO
- Identifying other factors associated with an increased risk of stroke

- Studies specifically designed to allow comparison between medical treatment and revascularization and between CEA and CAS.

Disclosure forms provided by the authors are available with the full text and PDF of this article at www.ajnr.org.

REFERENCES

1. Fox AJ, Eliasziw M, Rothwell PM, et al. **Identification, prognosis, and management of patients with carotid artery near occlusion.** *AJNR Am J Neuroradiol* 2005;26:2086–94 Medline
2. Rothwell PM, Eliasziw M, Gutnikov S. A, et al. **Analysis of pooled data from the randomised controlled trials of endarterectomy for symptomatic carotid stenosis.** *Lancet* 2003;361:107–16 CrossRef Medline
3. Rothwell PM, Gutnikov SA, Warlow CP; European Carotid Surgery Trialists' Collaboration. **Reanalysis of the final results of the European Carotid Surgery Trial.** *Stroke* 2003;34:514–23 CrossRef Medline
4. Naylor AR, Ricco JB, de Borst GJ, et al. **Management of Atherosclerotic Carotid and Vertebral Artery Disease: 2017 Clinical Practice Guidelines of the European Society for Vascular Surgery (ESVS).** *Eur J Vasc Endovasc Surg* 2018;55:3–81 CrossRef Medline
5. Johansson E, Öhman K, Wester P. **Symptomatic carotid near-occlusion with full collapse might cause a very high risk of stroke.** *J Intern Med* 2015;277:615–23 CrossRef Medline
6. Gu T, Aviv RI, Fox AJ, et al. **Symptomatic carotid near-occlusion causes a high risk of recurrent ipsilateral ischemic stroke.** *J Neurol* 2020;267:522–30 CrossRef Medline
7. Antonopoulos CN, Giosdekos A, Mylonas SN, et al. **Management of internal carotid artery near-occlusion: the need for updated evidence.** *Ann Transl Med* 2020;8:1263–63 CrossRef Medline
8. Xue S, Tang X, Zhao G, et al. **A systematic review and updated meta-analysis for carotid near-occlusion.** *Ann Vasc Surg* 2020;66:636–45 CrossRef Medline
9. Meershoek AJ, Vries EE, Veen D, et al; NEON Study Group. **Meta-analysis of the outcomes of treatment of internal carotid artery near occlusion.** *Br J Surg* 2019;106:665–71 CrossRef Medline
10. González A, Gil-Peralta A, Mayol A, et al. **Internal carotid artery stenting in patients with near occlusion: 30-day and long-term outcome.** *AJNR Am J Neuroradiol* 2011;32:252–58 CrossRef Medline
11. Akkan K, Ilgit E, Onal B, et al. **Endovascular treatment for near occlusion of the internal carotid artery.** *Clin Neuroradiol* 2018;28:245–52 CrossRef Medline
12. Kniemeyer HW, Aulich A, Schlachetzki F, et al. **Pseudo- and segmental occlusion of the internal carotid artery: a new classification, surgical treatment and results.** *Eur J Vasc Endovasc Surg* 1996;12:310–20 CrossRef Medline
13. Radak DJ, Tanaskovic S, Ilijevski NS, et al. **Eversion carotid endarterectomy versus best medical treatment in symptomatic patients with near total internal carotid occlusion: a prospective non-randomized trial.** *Ann Vasc Surg* 2010;24:185–89 CrossRef Medline
14. Berman SS, Bernhard VM, Erly WK, et al. **Critical carotid artery stenosis: diagnosis, timing of surgery, and outcome.** *J Vasc Surg* 1994;20:499–508 CrossRef Medline
15. Ruiz-Salmerón RJ, Gamero MA, Carrascosa C, et al. **Carotid artery stenting: clinical and procedural implications for near-occlusion stenosis.** *Neurologia* 2013;28:535–42 CrossRef Medline
16. Yan D, Tang X, Shi Z, et al. **Perioperative and follow-up results of carotid artery stenting and carotid endarterectomy in patients with carotid near-occlusion.** *Ann Vasc Surg* 2019;59:21–27 CrossRef Medline
17. Kim J, Male S, Damania D, et al. **Comparison of carotid endarterectomy and stenting for symptomatic internal carotid artery near-occlusion.** *AJNR Am J Neuroradiol* 2019;40:1207–12 CrossRef Medline
18. Brott TG, Howard G, Roubin GS, et al; CREST Investigators. **Long-term results of stenting versus endarterectomy for carotid-artery stenosis.** *N Engl J Med* 2016;374:1021–31 CrossRef Medline

19. Bonati LH, Dobson J, Featherstone RL, et al. **Long-term outcomes after stenting versus endarterectomy for treatment of symptomatic carotid stenosis: the International Carotid Stenting Study (ICSS) randomised trial.** *Lancet* 2015;385:529–38 CrossRef Medline
20. García-Pastor A, Gil-Núñez A, Ramírez-Moreno JM, et al; Stroke Project of the Spanish Cerebrovascular Diseases Study Group. **The risk of recurrent stroke at 24 months in patients with symptomatic carotid near-occlusion: results from CAOS, a multicentre registry study.** *Eur J Neurol* 2019;26:1391–98 CrossRef Medline
21. Johansson E, Fox A. **Carotid near-occlusion: a comprehensive review, Part 1: definition, terminology, and diagnosis.** *AJNR Am J Neuroradiol* 2016;37:2–10 CrossRef Medline
22. van Mook WN, Rennenberg RJ, Schurink GW, et al. **Cerebral hyperperfusion syndrome.** *Lancet Neurol* 2005;4:877–88 CrossRef Medline
23. Huibers AE, Westerink J, de Vries EE, et al. **Editor's choice: cerebral hyperperfusion syndrome after carotid artery stenting—a systematic review and meta-analysis.** *Eur J Vasc Endovasc Surg* 2018;56:322–33 CrossRef Medline
24. Cay F, Cil BE, Balci S, et al. **Relevance of distal arterial collapse in stenting of atherosclerotic near-occlusion of the carotid artery.** *AJNR Am J Neuroradiol* 2020;41:1054–60 CrossRef Medline
25. García-Pastor A, Gil-Núñez A, Ramírez-Moreno JM, et al; Stroke Project of the Spanish Cerebrovascular Diseases Study Group. **Comment on the article “Symptomatic carotid near-occlusion causes a high risk of recurrent ipsilateral ischemic stroke” by Gu et al.** *J Neurol* 2020;267:849–51 CrossRef Medline
26. Neves CR, Casella IB, da Silva ES, et al. **Medical therapy for asymptomatic patients and stent placement for symptomatic patients presenting with carotid artery near-occlusion with full collapse.** *J Vasc Interv Radiol* 2018;29:998–1005 CrossRef Medline
27. Meershoek AJ, Vonken EP, Nederkoorn PJ, et al. **Carotid endarterectomy in patients with recurrent symptoms associated with an ipsilateral carotid artery near occlusion with full collapse.** *J Neurol* 2018;265:1900–05 CrossRef Medline
28. Johansson E, Gu T, Castillo S, et al. **Intracerebral haemorrhage after revascularisation of carotid near occlusion with full collapse.** *Eur J Vasc Endovasc* 2022;63:523–24 CrossRef Medline

Comparison of 30-Day Outcomes after Carotid Artery Stenting in Patients with Near-Occlusion and Severe Stenosis: A Propensity Score Matching Analysis

C. Štěchovský, K. Hulíková Tesárková, P. Hájek, M. Horváth, E. Hansvenclová, and J. Veselka



ABSTRACT

BACKGROUND AND PURPOSE: Carotid artery near-occlusion is a type of severe stenosis with complete or partial distal luminal collapse and intracranial collaterals. This study aimed to compare 30-day outcomes and 10-year survival in patients undergoing carotid artery stenting for near-occlusion with a control group of patients with severe stenosis.

MATERIALS AND METHODS: We used data from a registry of 639 patients who underwent 789 carotid artery stenting procedures between 2005 and 2021. The primary end point was any stroke or death within 30 days after carotid artery stenting. Patients were matched using propensity scores based on 6 variables.

RESULTS: Propensity score matching yielded 84 subjects in the near-occlusion group matched with 168 subjects in the control group. In the matched cohort, the primary end point occurred in 7 (8.3%) and 11 (6.6%) patients in the near-occlusion and control groups, respectively ($P = .611$). In the unmatched cohort, the primary end point occurred in 7 (8.3%) and 19 (4.1%) patients ($P = .101$). Survival in the near-occlusion group versus the control group in the matched cohort at 5 and 10 years was 69.8% (95% CI, 58.0%–78.8%) versus 77.3% (95% CI, 70.0%–83.1%) and 53.3% (95% CI, 39.9%–65.0%) versus 53.3% (95% CI, 44.5%–61.4%) (log-rank, $P = .798$).

CONCLUSIONS: Carotid stent placement in patients with ICA near-occlusion was not associated with an increased 30-day risk of stroke or death compared with severe stenosis. Survival up to 10 years after carotid artery stenting was similar in both groups.

ABBREVIATIONS: CAS = carotid artery stenting; ECA = external carotid artery; ESC = European Society of Cardiology; ESVS = European Society for Vascular Surgery

Carotid artery near-occlusion is a type of severe stenosis with complete or incomplete distal luminal collapse and intracranial collaterals.¹ Various terms have been used to describe near-occlusion: subtotal stenosis or occlusion, functional occlusion, string sign, slim sign, critical stenosis, and others.² Calculating the percentage stenosis for ICA near-occlusion according to the NASCET criteria^{3,4} is a fallacious approach. Near-occlusion can be confused with complete occlusion or severe stenosis when imaging with CTA or sonography is suboptimal.⁴ The multitude of terms, subtle variation in the definition, and diagnostic ambiguity lead to uncertainty about the true incidence, prognosis, and optimal treatment of ICA near-

occlusion. Some early observational studies^{5,6} suggested that near-occlusion carries a high risk of stroke and should be promptly recognized and treated by endarterectomy. This suggestion was later negated by the re-analysis of the NASCET and the European Carotid Surgery Trial.^{3,7} Patients with near-occlusion were either excluded or not assessed or reported in further randomized clinical trials comparing surgery or conservative treatment of asymptomatic stenosis.² Both current European and American guidelines state that there is no clear evidence that endarterectomy or carotid artery stenting (CAS) prevents stroke in patients with near-occlusion of the ICA.^{8,9} Another position paper admits that the prognoses of asymptomatic near-occlusion and periprocedural risks of CAS or endarterectomy are unknown.¹⁰ A recent meta-analysis showed that the 30-day risk of stroke or death after endarterectomy or CAS for symptomatic ICA near-occlusion was 2%.¹¹

In this study, we report 30-day outcomes after CAS in patients with ICA near-occlusion and compare them with a control group of patients with severe stenosis after CAS using a propensity score matching analysis. Additionally, we report 10-year survival after CAS.

Received March 2, 2022; accepted after revision June 17.

From the Department of Cardiology (C.Š., P.H., M.H., E.H., J.V.), Second Faculty of Medicine, Charles University, Motol University Hospital, Prague, Czech Republic; and Department of Demography and Geodemography (K.H.T.), Faculty of Science, Charles University, Prague, Czech Republic.

Please address correspondence to Cyril Štěchovský, MD, Department of Cardiology, Motol University Hospital, V Uvalu 84, 150 06, Prague, Czech Republic; e-mail: stechovsky@gmail.com

 Indicates article with online supplemental data.

<http://dx.doi.org/10.3174/ajnr.A7598>

Table 1: Patient characteristics

	Unmatched Cohort			Matched Cohort		
	Near-Occlusion (n = 84 Patients)	Control Group (n = 460 Patients)	P Value	Near-Occlusion (n = 84 Patients)	Control Group (n = 168 Patients)	P Value
Age (mean) (yr)	70.3 (SD, 9.7)	68.6 (SD, 8.3)	.091	70.3 (SD, 9.7)	70.2 (SD, 7.7)	.943
Men	68%	65%	.620	68%	64%	.576
Current smokers	43%	40%	.629	43%	37%	.411
Arterial hypertension	88%	88%	1.000	88%	88%	1.000
Total plasma cholesterol level (mean) (mmol/L)	4.4 (SD, 1.1)	4.2 (SD, 1.0)	.126	4.4 (SD, 1.1)	4.4 (SD, 1.1)	.664
LDL cholesterol level (mean) (mmol/L)	2.6 (SD, 0.9)	2.4 (SD, 0.8)	.171	2.6 (SD, 0.9)	2.5 (SD, 0.9)	.629
HDL cholesterol level (mean) (mmol/L)	1.06 (SD, 0.31)	1.09 (SD, 0.33)	.695	1.06 (SD, 0.31)	1.09 (SD, 0.33)	.659
Plasma triglyceride level (mean) (mmol/L)	1.93 (SD, 1.2)	1.8 (SD, 1.1)	.638	1.93 (SD, 1.2)	1.78 (SD, 1.0)	.614
CRP level (median) (IQR) (mg/L)	3.6 (1.1–8.6)	2.3 (0.8–5.5)	.008	3.6 (1.1–8.6)	2.1 (0.9–4.9)	.010
Body mass index (mean)	28.6 (SD, 4.8)	28.1 (SD, 4.4)	.483	28.6 (SD, 4.8)	28.0 (SD, 4.1)	.540
Diabetes	33%	42%	.184	33%	37%	.676
Chronic kidney disease	27%	22%	.324	27%	24%	.644
Chronic bronchopulmonary disease	14%	13%	.723	14%	15%	1.000
Peripheral arterial disease	32%	39%	.271	32%	33%	.888
Heart failure with reduced ejection fraction	15%	11%	.320	15%	11%	.374
Previous coronary artery bypass	20%	18%	.649	20%	17%	.490
Need for heart surgery within 30 days	5%	9%	.281	5%	10%	.224
Previous myocardial infarction	24%	28%	.506	24%	30%	.302
Previous percutaneous coronary artery intervention	23%	32%	.094	23%	24%	.876
Known multivessel coronary artery disease	39%	40%	1.000	39%	35%	.490
Previous stroke	37%	30%	.252	37%	40%	.683
Ipsilateral cerebral ischemic symptoms in the past month	37%	21%	.003	37%	33%	.577
Ipsilateral cerebral ischemic symptoms in the past 6 months (ie, symptomatic stenosis)	45%	29%	.005	45%	46%	.894
Patients with ≥ 1 risk factors for endarterectomy ^a	82%	80%	.766	82%	82%	1.000

Note:—IQR indicates interquartile range; CRP, C-reactive protein.

^a One of the following: left ventricle ejection fraction of $\leq 40\%$, chronic bronchopulmonary disease, prior myocardial infarction, coronary artery bypass grafts, or age 75 years or older.

MATERIALS AND METHODS

We retrospectively analyzed data from a single-center (Motol University Hospital) registry of 639 patients who underwent 789 CAS procedures between 2005 and 2021. Patients who had bilateral CAS or CAS for in-stent restenosis were excluded from the analysis. Some of the patients were included in previous studies.^{12–16}

Patient Assessment, Procedure, and Follow-up

Patients were referred to carotid angiography and CAS by a neurologist, cardiologist, or vascular surgeon on the basis of Doppler sonography and/or CTA. Patient characteristics are listed in Table 1, and their medication before CAS is found in the Online Supplemental Data. Stenosis was quantified angiographically according to the NASCET criteria.³ Inclusion criteria were symptomatic ($\geq 50\%$) or asymptomatic ($\geq 70\%$) stenosis of the ICA in a patient who was considered eligible for CAS. Carotid stenosis was considered symptomatic if the patient had a stroke, TIA, or amaurosis fugax ipsilateral to the stenosis in the previous 6 months. All patients provided written informed consent for the procedure. Procedures were performed via the femoral artery using a 7F or 8F guiding catheter or a long 6F sheath. The antithrombotic regimen included administration of 500 mg of aspirin and 300 mg of clopidogrel before CAS in naïve patients; a bolus of heparin (70 IU/kg) was administered at the beginning of CAS. Types and manufacturers of stents and embolic protection devices

were at the operator's discretion and current availability. Detailed angiographic and procedural characteristics are listed in the Online Supplemental Data. After CAS, patients were examined by a physician, and all symptomatic patients were examined by a neurologist. Postprocedural CTA or MR imaging was performed in all cases of clinically suspected stroke. Patients were discharged with dual antiplatelet therapy for 1 month and single antiplatelet therapy and high-dose statin therapy life-long. Follow-up consisted of a history and review of medical documentation if the patient had neurologic symptoms and Doppler sonography at 1, 6, and 12 months after CAS. Information about vital status was retrieved from the National Death Index. In the deceased patients, cause of death was adjudicated as cardiovascular or noncardiovascular. The study was conducted in accordance with the Declaration of Helsinki principles.

Definitions and End Points

Patients in the registry were divided into near-occlusion and control groups. Angiographic criteria described in the NASCET^{2,3} were used to distinguish near-occlusion from conventional stenosis: 1) partial or complete collapse of the distal lumen (diameter of the ipsilateral distal ICA less than that of the contralateral distal ICA), 2) diameter of ipsilateral distal ICA less than that of the ipsilateral external carotid artery (ECA), 3) delayed filling of the ipsilateral distal ICA, and 4) intracranial collaterals (Fig 1). Two

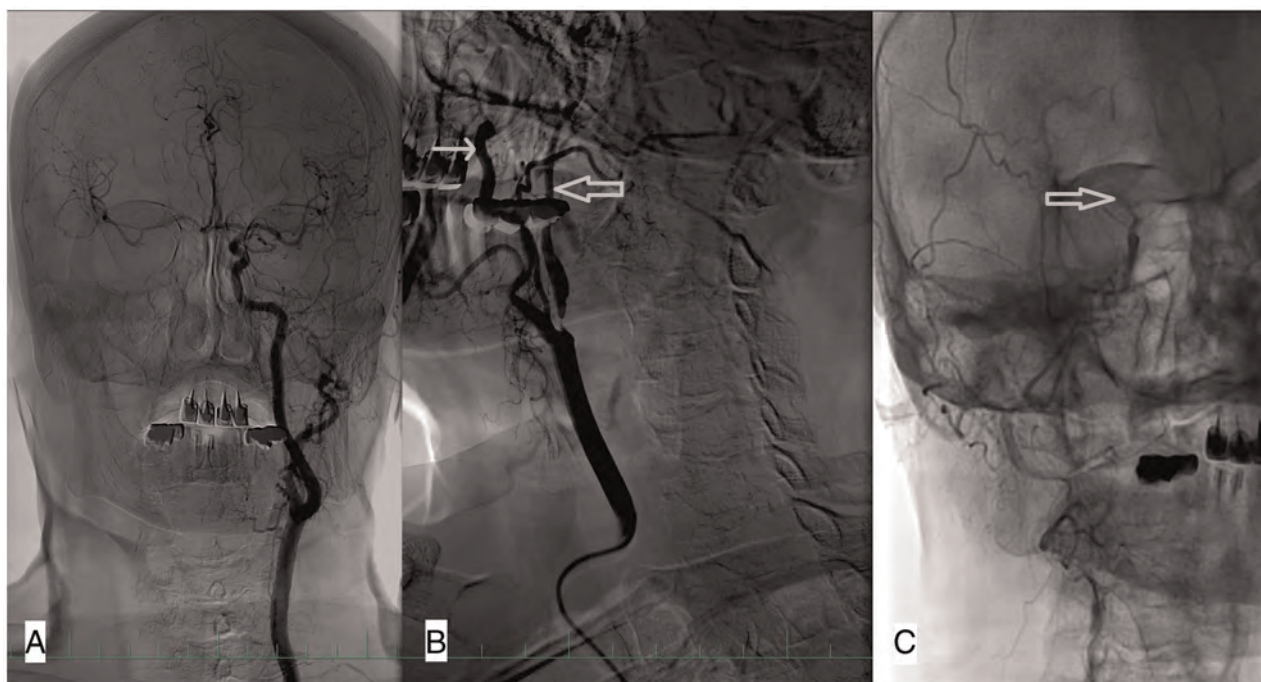


FIG 1. An angiogram in a patient with right ICA near-occlusion. A, In a selective angiogram of the left carotid artery, no stenosis is present; the diameter of the ICA is larger than that of the ECA; and there is rapid filling of the intracranial circulation and intracranial collaterals to the right ACA and MCA. B, Near-occlusion of the right ICA. The diameter of the distal ICA (*thick arrow*) is smaller than that of the ECA (*thin arrow*) and much smaller than that of the contralateral ICA. Late filling of the distal ICA. C, In the late phase of the angiogram, the contrast filling stops at the level of carotid siphon (*thick arrow*). The intracranial circulation is not visualized because the contrast is diluted by collateral flow. ACA indicates anterior cerebral artery.

of the 4 criteria were required for the diagnosis. In patients without acute neurologic symptomatology, intracranial collaterals must always be present in the near-occlusion. The primary end point consisted of any stroke or death within 30 days after CAS. Ischemic stroke was defined as an acute neurologic event with focal symptoms, lasting for ≥ 24 hours. Minor stroke was defined as a new neurologic deficit that resolved within 30 days without any limiting disability (≤ 1 on the mRS) or return to baseline status. Major stroke was defined as a new neurologic deficit with persisting disability (≥ 2 on mRS). TIA was defined as an episode of new neurologic dysfunction attributed to focal cerebral ischemia, with resolution within 24 hours.

Statistical Analysis

Statistical analyses were performed using SAS software, Version 9.4 (SAS Institute). Data are presented as means (SD) or median and interquartile range or counts and proportions. The Student *t* test or Mann-Whitney *U* test was used to evaluate the difference among continuous variables, and the Fisher exact test was used for the evaluation among categorical variables. Kaplan-Meier survival analysis was used to estimate long-term survival in patients after CAS with 95% confidence intervals. Given the inherent differences between patients with near-occlusion and the control group, using the logit model, we calculated propensity scores for the following variables as covariates: age, sex, total plasma cholesterol, diabetes, previous percutaneous coronary intervention, and ipsilateral cerebral ischemic symptoms in the past 6 months. Other potential covariates were confirmed as nonsignificant or

highly correlated to other variables. Matching on the propensity scores was performed using the 1:2 nearest neighbor method without replacement.^{17,18} A 2-sided *P* value $\leq .05$ was considered to indicate statistical significance.

RESULTS

A total of 544 patients were analyzed, 84 (15%) in the near-occlusion group and 460 (85%) in the control group. Propensity score matching yielded 84 subjects in the near-occlusion group matched with 168 subjects in the control group (Table 1 and Online Supplemental Data). Patients in the unmatched cohort with near-occlusion had symptomatic stenosis significantly more often, higher median C-reactive protein levels, used less statin therapy, had longer fluoroscopic times, and more often required predilation ($P < .05$ for all) (Table 1 and Online Supplemental Data). After matching, patients with near-occlusion had significantly higher median C-reactive protein levels and longer fluoroscopy time and more often required predilation ($P < .05$ for all) (Table 1 and Online Supplemental Data).

Data on major adverse in-hospital and 30-day events were available in 544 (100%) and 527 (97%) patients, respectively. Vital status at the end of the follow-up was available in all patients from the National Death Index. In the unmatched cohort, the primary end point occurred in 7 (8.3%) patients in the near-occlusion group and 19 (4.1%) patients in the control group ($P = .101$) and in the matched cohort in 7 (8.3%) and 11 (6.6%) patients ($P = .611$). Individual components of the end point are summarized in Table 2. In the matched subgroup of symptomatic patients, the primary end

Table 2: Thirty-day major adverse events and long-term follow-up

	Unmatched Cohort			Matched Cohort		
	Near-Occlusion (n = 84 Patients)	Control Group (n = 460 Patients)	P	Near-Occlusion (n = 84 Patients)	Control Group (n = 168 Patients)	P
TIA during hospitalization (No.) (%)	6 (7.1)	12 (2.6)	.045	6 (7.1)	7 (4.2)	.368
A, Minor stroke during hospitalization (No.) (%)	3 (3.6)	5 (1.1)	.111	3 (3.6)	3 (1.8)	.404
B, Major stroke during hospitalization (No.) (%)	1 (1.2)	6 (1.3)	1.000	1 (1.2)	4 (2.4)	.668
Hyperperfusion syndrome during hospitalization (No.) (%)	0	2 (0.4)	1.000	0	0	
Myocardial infarction during hospitalization (No.) (%)	1 (1.2)	0	.154	1 (1.2)	0	.333
Death during hospitalization (No.) (%)	2 (2.4)	2 (0.4)	.115	2 (2.4)	0	.110
C, Minor stroke in 30-day hospitalization (No.) (%)	0	4 (0.9)	1.000	0	2 (1.2)	.554
D, Major stroke in 30-day hospitalization (No.) (%)	1 (1.2)	2 (0.4)	.396	1 (1.2)	1 (0.6)	1.000
E, Death in 30 days (including during hospitalization) (No.) (%)	3 (3.6)	3 (0.7)	.050	3 (3.6)	1 (0.6)	.109
Primary end point: A + B + C + D + E (No.) (%)	7 (8.3)	19 (4.1)	.101	7 (8.3)	11 (6.6)	.611
Re-intervention for restenosis during follow-up (No.) (%)	9 (10.7)	19 (4.1)	.026	9 (10.7)	6 (3.6)	.044
All-cause mortality during follow-up (No.) (%)	33 (39.3)	202 (43.9)	.473	33 (39.3)	76 (45.2)	.419
Cardiovascular death (No.) (%)	25 (29.8)	129 (28.0)	.792	25 (29.8)	53 (31.6)	.885
Noncardiovascular death (No.) (%)	6 (7.1)	64 (13.9)	.110	6 (7.1)	19 (11.3)	.374
Unknown death (No.) (%)	2 (2.4)	9 (2.0)	.682	2 (2.4)	4 (2.4)	1.000
Mortality per 100 patient-years	6.6	6.8		6.6	6.5	

Note:—TIA indicates transient ischemic attack.

point occurred in 4 (10.5%) patients in the near-occlusion group and 7 (9%) patients in the control group ($P = .748$). In the asymptomatic patients, the primary end point occurred in 3 (6.5%) patients in the near-occlusion group and 4 (4.4%) patients in the control group ($P = .688$). The results for the symptomatic and asymptomatic patients are summarized in the Online Supplemental Data.

In the unmatched cohort, the mean follow-up was 5.9 (SD, 4.1) years in the near-occlusion group and 6.5 (SD, 4.1) years in the control group, which yielded 499 and 2980 patient-years of follow-up. Thirty-three (39.3%) patients in the near-occlusion group and 202 (43.9%) patients in the control group died ($P = .473$), which translated into 6.6 and 6.8 deaths per 100 patient-years, respectively. In the matched cohort, the mean follow-up was 5.9 (SD, 4.1) years in the near-occlusion group and 7.0 (SD, 4.2) years in the control group, which yielded 499 and 1176 patient-years of follow-up. In the matched cohort, 33 (39.3%) patients in the near-occlusion group and 76 (45.2%) patients in the control group died ($P = .419$), which translated into 6.6 and 6.5 deaths per 100 patient-years, respectively. In the matched cohort, survival in the near-occlusion group versus the control group at 5 and 10 years was 69.8% (95% CI, 58.0%–78.8%) versus 77.3% (95% CI, 70.0%–83.1%) and 53.3% (95% CI, 39.9%–65.0%) versus 53.3% (95% CI, 44.5%–61.4%) (log-rank, $P = .798$) (Fig 2A). In the unmatched cohort, survival at 5 and 10 years was similar (log-rank, $P = .996$) (Fig 2B).

During the follow-up, 9 (10.7%) patients and 19 (4.1%) patients underwent re-intervention for in-stent restenosis in the near-

occlusion and control groups, respectively ($P = .026$) (Fig 3A). After matching, the difference was still statistically significant, 10.7% versus 3.6% ($P = .044$) (Fig 3B).

DISCUSSION

Results of our observational study suggest that patients with near-occlusion had a high incidence of stroke or death within 30 days after CAS (8.3%) and high annual mortality (6.7%). However, the risk was not significantly different from that of severe stenosis after the adjustment using the propensity score matching. Although we observed a trend toward higher periprocedural risk in the near-occlusion group, which was numerically 2-fold, it did not reach statistical significance. The difference in the primary end points was even smaller after the adjustment. We believe that this difference is due to the higher proportion of symptomatic patients in the near-occlusion group. However, it could be related to the number of patients in the registry and confounders. The NASCET and European Carotid Surgery Trial included 262 cases of near-occlusion.^{3,7} The risk of perioperative stroke and death was similar in near-occlusion (5.4%) and 70%–99% stenosis (6.2%),¹⁹ and lower periprocedural risks have been reported since then.¹¹ Later, trials comparing endarterectomy and CAS either excluded patients with near-occlusion or did not assess near-occlusion. The real-world registry might provide valuable information about the early risk of CAS for near-occlusion in a population of patients with high cardiovascular comorbidity that is not typically represented in randomized trials. Given the differences in the population

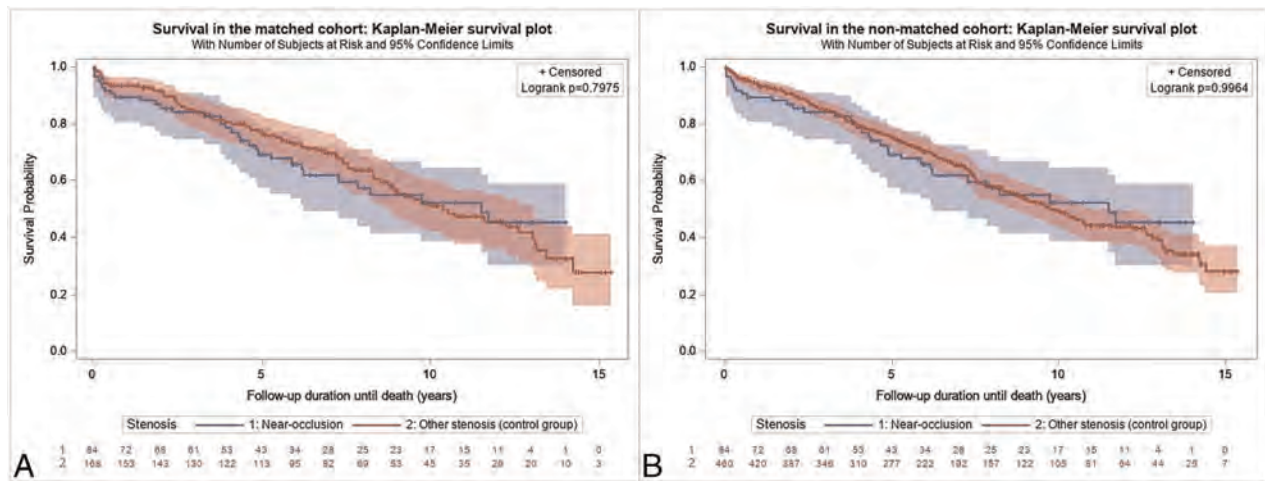


FIG 2. Kaplan-Meier estimate of 10-year survival after carotid stent placement in the near-occlusion-versus-control groups in the matched (A) and unmatched (B) cohorts.

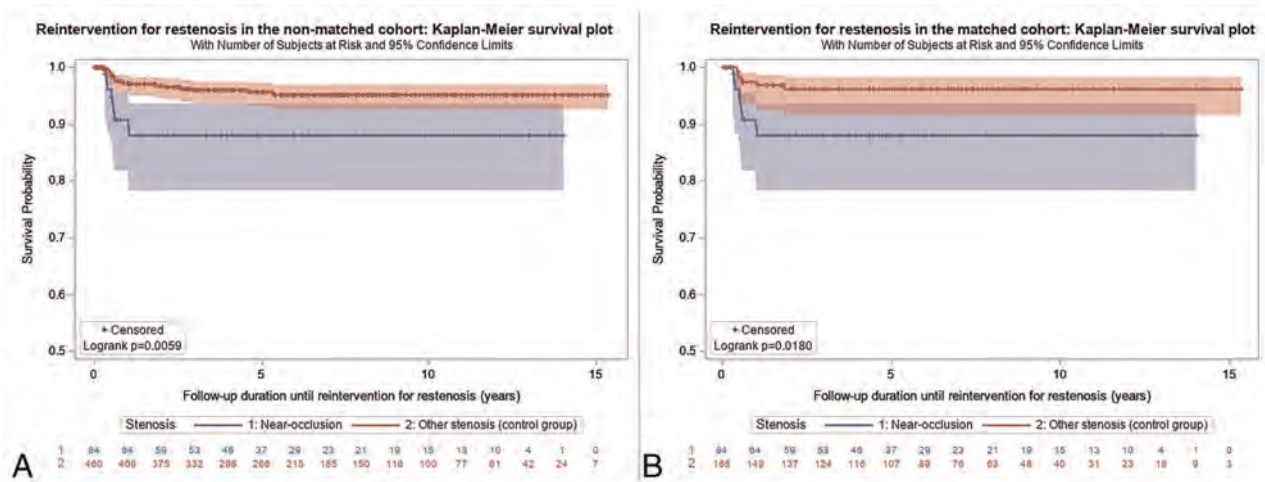


FIG 3. Kaplan-Meier estimate of freedom from re-intervention for in-stent restenosis after carotid stent placement in the near-occlusion-versus-control groups in the unmatched (A) and matched (B) cohorts.

of patients with near-occlusion and conventional severe stenosis and a most notably higher incidence of symptomatic stenosis in the near-occlusion group, we decided to compare the groups with the propensity score matching analysis to balance the baseline characteristics in both groups and lower the risk of selection bias.

The high periprocedural risk of stroke in ICA near-occlusion might be explained by the slow flow of blood distal to the lesion, which promotes in situ thrombosis that is embolized during CAS or protrudes through the stent struts and embolizes in the early postprocedural period. Angiography might not be able to distinguish ruptured atherosclerotic plaque with mural thrombus or mural thrombus in the distal ICA. Some cases of near-occlusion are actually recanalized thrombotic occlusions. Indeed, Hirata et al²⁰ reported that those old, organized thrombi were more frequently found in the endarterectomy specimens from near-occlusions than in high-grade stenoses. In our study, the 30-day stroke or death rate in the near-occlusion group (8.3%) was higher than that in a recent meta-analysis of some 703 patients with near-occlusion (226

underwent CAS; the 30-day stroke or death rate was 2.2%).¹¹ Individual observational studies included in the meta-analysis reported a 30-day stroke or death rate after CAS between 0% and 7%.²¹⁻²⁵ These studies had only 1 arm and did not compare the risk of CAS for near-occlusion with that in a control group. The high variability in the reported periprocedural risks might reflect different baseline characteristics and selection of patients rather than procedural techniques. It is also possible that the periprocedural stroke and death risk reported in the meta-analysis by Meershoek et al¹¹ underestimated the true risk because of bias in the reporting of small observational studies with unfavorable results.

The high all-cause mortality rate in our study is in contrast to the much lower mortality in the long-term follow-up of a recent, large, randomized Second Asymptomatic Carotid Surgery Trial (ACST-2: 330 deaths in 1811 patients randomized to CAS with a mean follow-up of 5 years and an annual mortality of \approx 3.6%).²⁶ On the other hand, a study that analyzed data from Medicare

beneficiaries treated with CAS reported a mortality rate of 8.0% per year after the periprocedural period.²⁷ This study included older patients than in our registry, but other baseline characteristics were similar, with high cardiovascular comorbidity. These differences indicate that clinical trials enroll populations different from high-risk patients in whom the investigated technique is used in clinical practice.

We should carefully consider performing CAS in a patient with ICA near-occlusion, given the substantial periprocedural risk and life expectancy that might be shorter than 5 years reported by the European Society of Cardiology (ESC) and the European Society for Vascular Surgery (ESVS).²⁸ Meershoek et al²⁹ suggested that although the initial approach to symptomatic near-occlusion with full distal luminal collapse should be conservative, patients with recurrent events may be treated with endarterectomy. There is a need for further studies that could be based on large registries like the mandatory German Carotid National Registry.³⁰ We believe that the treatment of patients with ICA near-occlusion is one of the important topics in the field of carotid interventions that will require continued research before more evidence-based recommendations can be made.

The study is not without limitations. First, data were collected from a single center for 16 years. Although operators and procedural techniques remained unchanged, protection devices and stents changed across time. Referral of patients for carotid angiography and the criteria for selection of patients who would benefit from CAS changed during that time, with updated ESC/ESVS guidelines and results of randomized controlled trials.^{26,28} The proportion of patients with near-occlusion and conventional stenosis who were selected for CAS compared with endarterectomy or medical therapy is unknown. Our results cannot be generalized to all patients with ICA near-occlusion. Second, propensity score matching is associated with inherent limitations. Although the matched cohort might seem well-balanced for baseline characteristics, there is always a risk of confounding bias. Third, we did not systematically collect data on major adverse cardiovascular events beyond the 30-day period after CAS; therefore, we reported only data on long-term survival.

CONCLUSIONS

Carotid stent placement in patients with ICA near-occlusion was not associated with an increased 30-day risk of stroke or death compared with severe stenosis. Survival up to 10 years after CAS was similar in both groups.

Disclosure forms provided by the authors are available with the full text and PDF of this article at www.ajnr.org.

REFERENCES

1. Fox AJ, Eliasziw M, Rothwell PM, et al. **Identification, prognosis, and management of patients with carotid artery near occlusion.** *AJNR Am J Neuroradiol* 2005;26:2086–94 Medline
2. Johansson E, Fox AJ. **Carotid near-occlusion: a comprehensive review, Part 1: definition, terminology, and diagnosis.** *AJNR Am J Neuroradiol* 2016;37:2–10 CrossRef Medline
3. Morgenstern LB, Fox AJ, Sharpe BL, et al. **The risks and benefits of carotid endarterectomy in patients with near occlusion of the carotid artery: North American Symptomatic Carotid Endarterectomy Trial (NASCET) group.** *Neurology* 1997;48:911–15 CrossRef Medline
4. Bartlett ES, Walters TD, Symons SP, et al. **Quantification of carotid stenosis on CT angiography.** *AJNR Am J Neuroradiol* 2006;27:13–19 Medline
5. Ringelstein EB, Berg-Dammer E, Zeumer H. **The so-called atheromatous pseudo-occlusion of the internal carotid artery: a diagnostic and therapeutical challenge.** *Neuroradiology* 1983;25:147–55 CrossRef Medline
6. O'Leary DH, Mattle H, Potter JE. **Atheromatous pseudo-occlusion of the internal carotid artery.** *Stroke* 1989;20:1168–73 CrossRef Medline
7. Rothwell PM, Gutnikov SA, Warlow CP. **Reanalysis of the final results of the European Carotid Surgery Trial.** *Stroke* 2003;34:514–23 CrossRef Medline
8. Bonati LH, Kakkos S, Berkefeld J, et al. **European Stroke Organisation guideline on endarterectomy and stenting for carotid artery stenosis.** *Eur Stroke J* 2021;6:1–XLVII CrossRef Medline
9. Kleindorfer DO, Towfighi A, Chaturvedi S, et al. **2021 Guideline for the Prevention of Stroke in Patients with Stroke and Transient Ischemic Attack: a Guideline From the American Heart Association/American Stroke Association.** *Stroke* 2021;52:e364–467 CrossRef Medline
10. Johansson E, Fox AJ. **Carotid near-occlusion: a comprehensive review, Part 2: prognosis and treatment, pathophysiology, confusions, and areas for improvement.** *AJNR Am J Neuroradiol* 2016;37:200–04 CrossRef Medline
11. Meershoek AJ, de Vries EE, Veen D, et al; NEON study group. **Meta-analysis of the outcomes of treatment of internal carotid artery near occlusion.** *Br J Surg* 2019;106:665–71 CrossRef Medline
12. Veselka J, Hajek P, Štěchovský C, et al. **Long-term survival of carotid stenting patients with regard to single- or double-vessel carotid artery disease: a propensity score matching analysis.** *Arch Med Sci* 2021;17:849–55 CrossRef Medline
13. Štěchovský C, Hájek P, Horváth M, et al. **Near-infrared spectroscopy combined with intravascular ultrasound in carotid arteries.** *Int J Cardiovasc Imaging* 2016;32:181–88 CrossRef Medline
14. Štěchovský C, Hájek P, Horváth M, et al. **Effect of stenting on the near-infrared spectroscopy-derived lipid core burden index of carotid artery plaque.** *Eurointervention* 2019;15:e289–96 CrossRef Medline
15. Veselka J, Špacôek M, Horváth M, et al. **Impact of coexisting multi-vessel coronary artery disease on short-term outcomes and long-term survival of patients treated with carotid stenting.** *Arch Med Sci* 2016;12:760–65 CrossRef Medline
16. Veselka J, Cerná D, Zimolová P, et al. **Feasibility, safety, and early outcomes of direct carotid artery stent implantation with use of the FilterWire EZ Embolic Protection System.** *Catheter Cardiovasc Interv* 2009;73:733–38 CrossRef Medline
17. Rosenbaum PR, Rubin DB. **Constructing a control group using multivariate matched sampling methods that incorporate the propensity score.** *The American Statistician* 1985;39:33–38 CrossRef
18. Fraeman KH. **An introduction to implementing propensity score matching with SAS.** NESUG 2010: Applications Development. <https://www.lexjansen.com/nesug/nesug10/ad/ad05.pdf>. Accessed September 07, 2021
19. Rothwell PM, Eliasziw M, Gutnikov SA, et al. **Analysis of pooled data from the randomised controlled trials of endarterectomy for symptomatic carotid stenosis.** *Lancet* 2003;361:107–16 CrossRef Medline
20. Hirata Y, Sakata N, Inoue T, et al. **Histopathological features with angiographic correlates of internal carotid artery pseudo-occlusion: impact of plaque compositions—clinical article.** *J Neurosurg* 2011;115:350–58 CrossRef Medline
21. Oka F, Ishihara H, Kato S, et al. **Cerebral hemodynamic benefits after carotid artery stenting in patients with near occlusion.** *J Vasc Surg* 2013;58:1512–17 CrossRef Medline
22. González A, Gil-Peralta A, Mayol A, et al. **Internal carotid artery stenting in patients with near occlusion: 30-day and long-term outcome.** *AJNR Am J Neuroradiol* 2011;32:252–58 CrossRef Medline

23. Matsuda Y, Terada T, Okada H, et al. **Angiographic characteristics of pseudo-occlusion of the internal carotid artery before and after stenting.** *Neurosurgery* 2016;79:832–38 CrossRef Medline
24. Son S, Choi DS, Kim SK, et al. **Carotid artery stenting in patients with near occlusion: a single-center experience and comparison with recent studies.** *Clin Neurol Neurosurg* 2013;115:1976–81 CrossRef Medline
25. Sakamoto S, Kiura Y, Kajihara Y, et al. **Carotid artery stenting using the proximal or dual protection method for near occlusion of the cervical internal carotid artery.** *Neurosurg Rev* 2013;36:551–58 CrossRef Medline
26. Halliday A, Bulbulia R, Bonati LH, et al; ACST-2 Collaborative Group. **Second asymptomatic carotid surgery trial (ACST-2): a randomised comparison of carotid artery stenting versus carotid endarterectomy.** *Lancet* 2021;398:1065–73 CrossRef Medline
27. Jalbert JJ, Nguyen LL, Gerhard-Herman MD, et al. **Outcomes after carotid artery stenting in Medicare beneficiaries, 2005 to 2009.** *JAMA Neurol* 2015;72:276–86 CrossRef Medline
28. Aboyans V, Ricco JB, Bartelink MEL, ESC Scientific Document Group, et al. **2017 ESC Guidelines on the Diagnosis and Treatment of Peripheral Arterial Diseases, in collaboration with the European Society for Vascular Surgery (ESVS): document covering atherosclerotic disease of extracranial carotid and vertebral, mesenteric, renal, upper and lower extremity arteries endorsed by: the European Stroke Organization (ESO), the Task Force for the Diagnosis and Treatment of Peripheral Arterial Diseases of the European Society of Cardiology (ESC) and of the European Society for Vascular Surgery (ESVS).** *Eur Heart J* 2018;39:763–816 CrossRef Medline
29. Meershoek AJ, Vonken EP, Nederkoorn PJ, et al. **Carotid endarterectomy in patients with recurrent symptoms associated with an ipsilateral carotid artery near occlusion with full collapse.** *J Neurol* 2018;265:1900–05 CrossRef Medline
30. Kallmayer MA, Tsantilas P, Knappich C, et al. **Patient characteristics and outcomes of carotid endarterectomy and carotid artery stenting: analysis of the German mandatory national quality assurance registry - 2003 to 2014.** *J Cardiovasc Surg (Torino)* 2015;56:827–36 Medline

Clinical Validation and Extension of an Automated, Deep Learning–Based Algorithm for Quantitative Sinus CT Analysis

C.J. Massey, L. Ramos, D.M. Beswick, V.R. Ramakrishnan, and S.M. Humphries



ABSTRACT

BACKGROUND AND PURPOSE: Sinus CT is critically important for the diagnosis of chronic rhinosinusitis. While CT is sensitive for detecting mucosal disease, automated methods for objective quantification of sinus opacification are lacking. We describe new measurements and further clinical validation of automated CT analysis using a convolutional neural network in a chronic rhinosinusitis population. This technology produces volumetric segmentations that permit calculation of percentage sinus opacification, mean Hounsfield units of opacities, and percentage of osteitis.

MATERIALS AND METHODS: Demographic and clinical data were collected retrospectively from adult patients with chronic rhinosinusitis, including serum eosinophil count, Lund-Kennedy endoscopic scores, and the SinoNasal Outcomes Test-22. CT scans were scored using the Lund-Mackay score and the Global Osteitis Scoring Scale. CT images were automatically segmented and analyzed for percentage opacification, mean Hounsfield unit of opacities, and percentage osteitis. These readouts were correlated with visual scoring systems and with disease parameters using the Spearman ρ .

RESULTS: Eighty-eight subjects were included. The algorithm successfully segmented 100% of scans and calculated features in a diverse population with CT images obtained on different scanners. A strong correlation existed between percentage opacification and the Lund-Mackay score ($\rho = 0.85$, $P < .001$). Both percentage opacification and the Lund-Mackay score exhibited moderate correlations with the Lund-Kennedy score ($\rho = 0.58$, $P < .001$, and $\rho = 0.58$, $P < .001$, respectively). The percentage osteitis correlated moderately with the Global Osteitis Scoring Scale ($\rho = 0.48$, $P < .001$).

CONCLUSIONS: Our quantitative processing of sinus CT images provides objective measures that correspond well to established visual scoring methods. While automation is a clear benefit here, validation may be needed in a prospective, multi-institutional setting.

ABBREVIATIONS: AI = artificial intelligence; CRS = chronic rhinosinusitis; CNN = convolutional neural network; GOSS = Global Osteitis Scoring Scale; LKS = Lund-Kennedy score; LMS = Lund-Mackay score; mHU = mean Hounsfield Units; %OST = percentage of osteitis; %SO = percentage sinus opacification; SNOT-22 = SinoNasal Outcomes Test-22

CT provides invaluable visualization of sinus anatomy and plays an essential role in the work-up of chronic rhinosinusitis (CRS), with an estimated 713,482 scans ordered in 2010 by otolaryngologists alone.¹ The presence of sinus inflammation on CT is an objective diagnostic criterion for CRS.^{2–4} While CT has

been used for objective sinus evaluation for decades, visual assessment of images is limited by variable interpretations, and results are generally reported in nonstandard or imprecise terms, which may or may not carry particular clinical significance.⁵ There exists a clear need for efficient, quantitative assessment of the degree of paranasal sinus inflammation on CT. Detailed, reproducible, and objective reports could be extremely valuable in

Received February 8, 2022; accepted after revision June 18.

From the Department of Otolaryngology–Head and Neck Surgery (C.J.M., L.R., V.R.R.), University of Colorado School of Medicine, Aurora, Colorado; Department of Otolaryngology–Head and Neck Surgery (D.M.B.), University of California–Los Angeles School of Medicine, Los Angeles, California; and Quantitative Imaging Laboratory (S.M.H.), Department of Radiology, National Jewish Health, Denver, Colorado.

This work was supported by an American Academy of Otolaryngology–Head and Neck Surgery CORE Grant and Xoran Technologies (C.J.M.); and Colorado Advanced Industries Accelerator Program (S.M.H.). V.R.R. and C.J.M. were supported, in part, by a grant from the National Institute on Deafness and Other Communication Disorders, one of the National Institutes of Health, Bethesda, Maryland (K23DC014747 and K23DC014747-04S1).

These funding organizations did not contribute to the design or conduct of this study, preparation, review, approval, or decision to submit this manuscript for publication.

Please address correspondence to Stephen M. Humphries, PhD, National Jewish Health, 1400 Jackson St, Room k012d, Denver, CO 80206; e-mail: humphriess@NJHealth.org

Indicates open access to non-subscribers at www.ajnr.org

Indicates article with online supplemental data.

<http://dx.doi.org/10.3174/ajnr.A7616>

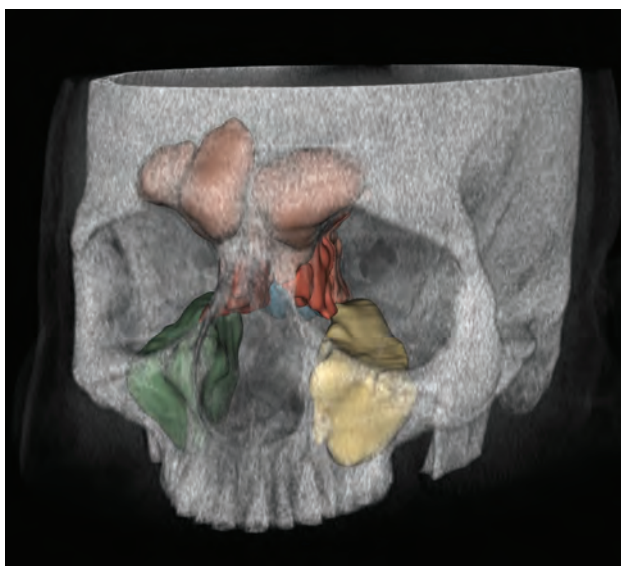


FIG 1. 3D reconstructed sinus CT scan with bony overlay (gray) and segmentation of the paranasal sinuses (colored) produced by the algorithm.

clinical and research settings if performed in a simple, automated, and universal fashion.

Our group has developed a novel approach that uses deep learning, a form of artificial intelligence (AI) whereby a computer algorithm may “learn” to recognize image patterns in exemplar data.^{6,7} Using a convolutional neural network (CNN), one of the primary information-processing models of deep learning, this fully automated system produces precise 3D segmentations of the individual paranasal sinuses and allows quantitation of sinus cavity opacification (Fig 1). Initial validation of this approach was recently published, examining all comers presenting for multidisciplinary airway evaluation at a single tertiary care respiratory institution, and demonstrated very good correlation of the algorithm to the existing criterion standard visual scoring system, the Lund-Mackay score (LMS). However, certain outcome measures were not universally available in that cohort, such as surgical status, disease-specific quality-of-life indices, and endoscopic scores, and images were obtained from only 2 scanners at a single institution.

The objectives of the current investigation expand the initial study in a number of ways. Here, we aimed to test a refinement of the initial algorithm, now capable of segmenting separate sinus cavities, in a strict CRS cohort with an extended set of disease-specific outcomes. Furthermore, segmentation and analysis were applied to images obtained from a variety of scanners and protocols commonly used in clinical practice to ascertain real-world applicability. Finally, we introduced and performed initial clinical validation of algorithmic characterization of 2 potentially important radiologic biomarkers in CRS, sinus osteitis and opacification density.

MATERIALS AND METHODS

Study Population

Subjects were enrolled from an institutional review board–approved (Colorado Multi-Institutional Review Board No.

14–0269) prospective cohort of patients undergoing rhinologic surgery at the University of Colorado Hospital from 2012 to 2018. Subjects who met the diagnostic criteria for CRS⁴ were included in the present study when all the following were available: thin cut (<1.25 mm) sinus CT images, serum eosinophil count within 6 months of surgery, and corresponding surgical pathology specimens stored at the University of Colorado Biorepository. Demographic and clinical data from these subjects were prospectively collected, including preoperative SinoNasal Outcomes Test 22 (SNOT-22) and the Lund-Kennedy score (LKS), performed and documented on the day of surgery by the senior surgeon (V.R.R.).

CT Image Acquisition and Quantitative Analysis

Subjects underwent sinus CT at the University of Colorado Hospital system as well as a number of different institutions in the metropolitan Denver area and beyond, with scans being performed on machines from various manufacturers. Scans were generally completed within 6 months before the date of surgery. Patients with scans obtained using in-office conebeam CT were excluded due to the substantial differences in image characteristics compared with traditional CT and the lack of pixel-intensity standardization to the Hounsfield unit scale.⁸ All CT examinations were downloaded from the PACS at the University of Colorado Hospital, de-identified, and then electronically transferred to the Quantitative Imaging Laboratory at National Jewish Health for analysis.

An initial CNN was developed, trained, tested, and validated as previously described.⁶ Details regarding the development of the current CNN are described in the Online Supplemental Data. The resulting algorithm was used to perform all quantitative analyses on the transferred scans using an Intel Core i9 7980XE CPU, Dual NVIDIA GeForce GTX 1080Ti GPUs, and 64GB RAM. The algorithm segments each sinus cavity individually, combining left and right sides except for the maxillary sinuses, which are segmented separately. A visual, qualitative assessment was performed on each segmentation produced by the algorithm to grossly check for accuracy.

Percentage sinus opacification (%SO) is determined by calculating the percentage of each segmentation cavity volume occupied by CT pixels ranging from −500 to +200 HU, a range corresponding to soft-tissue density; the individual cavity percentage volume opacifications were then averaged to control the effects of volume as follows:

$$\%SO = \frac{[\text{Left Maxillary}] + [\text{Right Maxillary}] + [\text{Anterior Ethmoid}] + [\text{Posterior Ethmoid}] + [\text{Frontal}] + [\text{Sphenoid}]}{6}.$$

We used an averaged sinus volume to calculate %SO as opposed to an overall total opacification percentage, given that the LMS does not factor in cavity size into its scoring system.

mHU is the mean Hounsfield unit value of the opacified regions within the total segmentation cavity, and it was applied to investigate soft-tissue hyperdensity that may be indicative of eosinophilic processes.⁹ The algorithm was also used to assess osteitis by generation of a 7-mm “rind” around the sinus cavity (Fig 2). This was achieved through dilation of the segmented sinus cavities by 5 mm, with subsequent subtraction of a copy of the sinus cavity

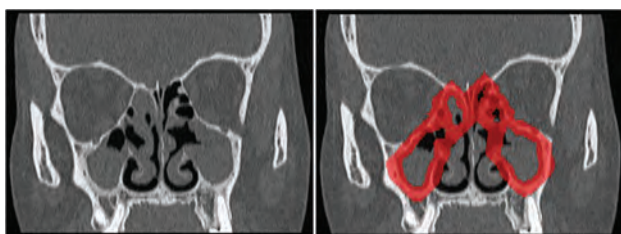


FIG 2. Illustration demonstrating application of osteitis segmentation rind. *Left*, Coronal CT with total GOSS score of 32. *Right*, Segmentation rind overlaid in red. Forty-eight percent of the rind is occupied by CT voxels corresponding to bone.

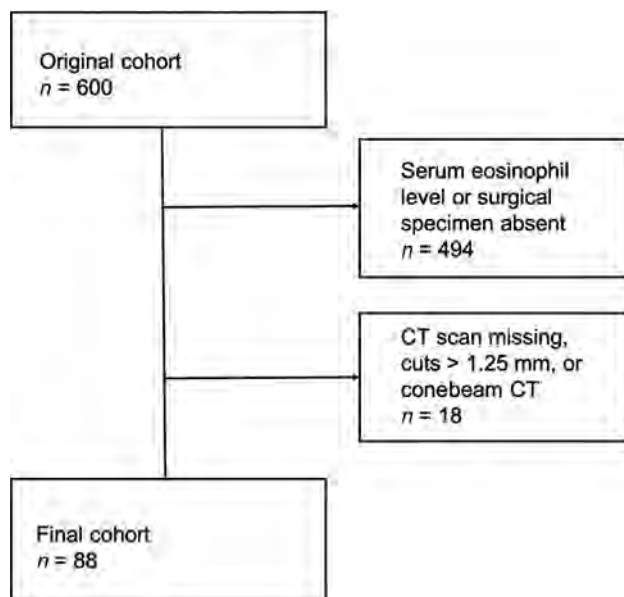


FIG 3. Flow diagram demonstrating the cohort-selection process.

segmentation that had been eroded by 2 mm. The percentage of this space occupied by bone (corresponding to a Hounsfield unit of ≥ 150) was used to calculate the percentage of osteitis (%OST). Additional details, including a schematic of the image-processing operations used to achieve %OST, are found in the Online Supplemental Data. This operation works to capture any bony expansion of the sinus cavity that one would expect in osteitic disease states.¹⁰

Visual Scoring

Lund-Mackay scoring was performed by 2 independent scorers (C.J.M., V.R.R.). Any difference of >1 between scores was resolved by consensus between the 2 parties. Scores differing by 1 point were averaged. If consensus was not achieved, a third party would decide the score (L.R.). Osteitis was assessed using the Global Osteitis Scoring Scale (GOSS).¹⁰ Scoring was also performed by 2 independent assessors (C.J.M., L.R.). A difference of >2 between scores was resolved in a similar fashion to that of the LMS with a third-party evaluator (V.R.R.). Scores differing by ≤ 2 points were averaged. All scorers had considerable experience interpreting sinus CT as senior rhinology faculty (V.R.R.) or otolaryngology resident physicians (C.J.M., L.R.).

Table 1: Demographics of the study population

Cohort Features	n = 88 (% or range)
Female (%)	52 (59)
Avg. age (range) (yr)	48.5 (22–78)
White (%)	70 (80)
Polyps (%)	59 (67)
Asthma (%)	53 (60)
AERD (%)	8 (9)
Never smoker (%)	55 (62)
Prior surgery (%)	48 (55)
Avg. absolute serum eosinophils $\times 10^9/L$	0.31 (0–2.6)
Avg. tissue eosinophils per HPF	80 (0–413)
Avg. SNOT-22	49.6 (15–95)
Avg. LKS	6.8 (1–12)
Avg. LMS	13.5 (2–24)
Avg. GOSS	2.7 (0–35)
Avg. sinus cavity volume (mL)	60.8 (24.8–109.0)
Avg. %SO	60.1 (20.7–99.6)
Avg. mHU	10.5 (–139.2 to +57.4)
Avg. %OST	41.4 (32.1–52.2)

Note:—AERD indicates aspirin-exacerbated respiratory disease; HPF, high-power field; Avg., average.

Quantification of Tissue Eosinophilia

H&E-stained sections of sinus mucosa from surgical pathology specimens were retrieved from the University of Colorado Biorepository. Tissue eosinophil counts were performed as previously described, blinded to patient metadata and CT.¹¹ Counts were performed in areas of densest cellular infiltrate to consistently determine eosinophil levels on the basis of areas of high inflammation. The absolute number of eosinophils per high-power field was recorded. This process was repeated in triplicate for each specimen, and the counts were averaged.

Statistical Analysis

Descriptive statistics on the study population were generated and reviewed. Univariate associations between algorithm-generated readouts, eg, %SO and %OST, and various clinical parameters were analyzed with the Spearman rank correlation. All statistical calculations and data visualization were performed in R, Version 3.6.0 (April 16, 2019; <http://www.r-project.org/>).

RESULTS

Study Population

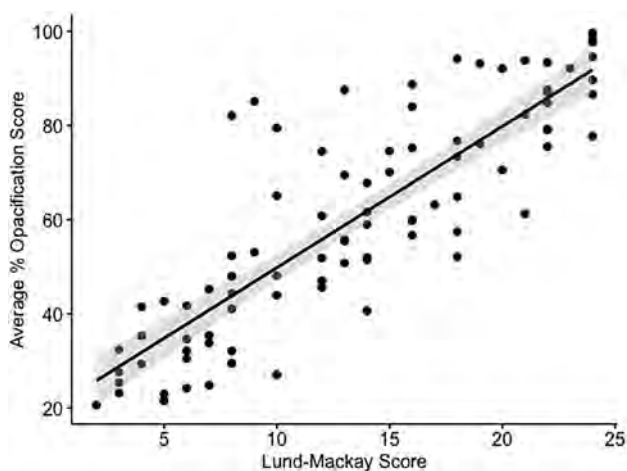
Eighty-eight subjects met the inclusion criteria (Fig 3). Demographic data are summarized in Table 1. The mean age was 48.5 years, and 59% of subjects were women. Sixty-seven percent of subjects had a diagnosis of CRS with nasal polyps; 60% had comorbid asthma. Fifty-five percent of subjects reported a history of prior sinus surgery; validation of algorithmic performance in postsurgical patients has been previously performed.⁶ SNOT-22 and LKSs were incomplete or missing in 7 and 4 subjects, respectively.

Quantitative Percentage Opacification and Correlation with LMS

The CNN-based algorithm successfully segmented all 88 scans, which were acquired on scanners from 4 different manufacturers using 10 different reconstruction kernels (Table 2). The study population average %SO was 60.1% (range, 20.7%–99.6%). %SO

Table 2: CT scanner metrics and acquisition protocols used for the included scans

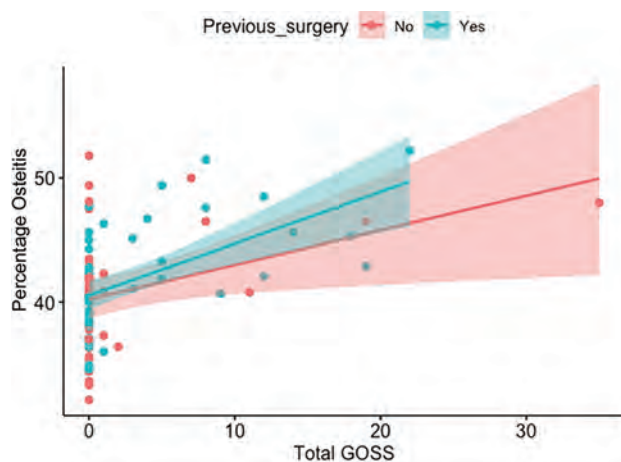
Model (No.)	Reconstruction Kernel (No.)	Tube Potential (No.)	Tube Current (No.)	Pitch (No.)	Axial Section Thickness (No.)	Axial Section Spacing (No.)
Siemens (<i>n</i> = 77)						
Sensation 64 (42)	H31s (2)	100 kVp (2)	Modulated (22)	0.7 (43)	1.0 mm (77)	0.6 mm (2)
Definition (4)	H60f (2)	120 kVp (75)	91 mA (41)	0.8 (19)		0.9 mm (63)
Definition AS (3)	H60s (1)		100 mA (8)	0.9 (14)		1.0 mm (12)
Definition AS+ (4)	H70h (54)		108 mA (6)	1.0 (1)		
Definition Flash (18)	J40s\\2 (1)					
Biograph 40 (6)	J70h\\2 (17)					
GE Healthcare (<i>n</i> = 5)						
LightSpeed Pro 16 (1)	Bone (5)	120 kVp (5)	110 mA (1)	0.50–0.75 (2)	0.625 mm (3)	0.625 mm (3)
LightSpeed VCT (1)			150 mA (1)	0.90–1.0 (3)	1.25 mm (2)	1.0 mm (1)
Optima CT540 (2)			160 mA (1)			1.25 mm (1)
Optima CT660 (1)			>200 mA (2)			
Philips Healthcare (<i>n</i> = 4)						
Brilliance 64 (4)	YC (3)	120 kVp (4)	85 mA (1)	1.0 (4)	1.0 mm (4)	0.8 mm (1)
	YD (1)		119 mA (2)			0.9 mm (3)
			170 mA (1)			
Toshiba/Canon (<i>n</i> = 2)						
Aquilion ONE (1)	FC30 (2)	120 kVp (2)	150 mA (1)	1.0 (2)	1.0 mm (2)	0.8 mm (1)
Aquilion Prime (1)			200 mA (1)			1.0 mm (1)

**FIG 4.** Scatterplot demonstrating algorithm-generated %SO versus LMS. The gray shaded area represents a 95% confidence interval for the regression line ($\rho = 0.85$, $P < .001$).

correlated well with the LMS, as shown in Fig 4 ($\rho = 0.85$, $P < .001$). The intraclass correlation coefficient between LMS scorers demonstrated strong agreement ($\rho = 0.92$, $P < .001$).

Osteitis Quantitation and Correlation with GOSS

The overall average percentage of pixels corresponding to bone contained within the 7-mm segmentation ring (%OST) was 41% (range, 32%–52%). %OST exhibited a moderate-but-significant correlation with GOSS ($\rho = 0.48$, $P < .001$). The surgical status impacted correlation, with a weaker correlation demonstrated in the surgically naïve patients compared with patients with prior surgery, as shown in Fig 5. Linear regression was used to assess the impact of sinus cavity volume on the interaction between GOSS and %OST ($R^2 = 0.20$, and 0.24 when adjusted for volume). The intraclass correlation coefficient between GOSS scorers demonstrated strong agreement ($\rho = 0.83$, $P < .001$).

**FIG 5.** Algorithm-derived %OST versus total GOSS as stratified by surgical status. Overall $\rho = 0.48$ ($P < .05$). For surgically naïve patients, $\rho = 0.29$ ($P = .08$), and for postoperative subjects, $\rho = 0.59$ ($P < .001$).

Associations between Algorithm-Derived Readouts and Clinical Parameters (LKS, SNOT-22, Tissue and Serum Eosinophil Levels)

Moderate associations were seen between algorithm-derived readouts (%SO, mHU) and endoscopic LKS. Weak associations were seen between algorithm-derived readouts and tissue eosinophil levels. Weak correlations were seen across the board with serum eosinophil counts, though statistical significance for mHU was not reached. No correlation was seen between CT-derived measures and SNOT-22. Associations between LMS and clinical parameters were similar to algorithm-generated associations and are presented in Table 3.

Correlation between clinical parameters and percentage sinus opacification was also performed and is shown in Table 4. In general, stronger correlations were seen in the anterior and posterior ethmoid cavities for LKS, absolute serum eosinophil counts, and tissue eosinophil counts. These correlations illustrate that the

Table 3: Correlation (ρ) values for CT-derived metrics and clinical parameters

Clinical Parameter	(%SO)	LMS	mHU of Opacified Regions
LKS	0.58 ^a	0.58 ^a	0.48 ^a
SNOT-22	0.05	−0.02	0.08
Absolute serum eosinophils	0.26 ^b	0.34 ^b	0.14
Tissue eosinophil count	0.31 ^b	0.33 ^b	0.22 ^b

^a $P < .001$.^b $P < .05$.**Table 4: Correlation (ρ) values for percentage sinus opacification stratified by sinus cavity and clinical parameters**

Clinical Parameter	Left Maxillary	Right Maxillary	Anterior Ethmoid	Posterior Ethmoid	Frontal	Sphenoid
LKS	0.43 ^a	0.34 ^b	0.64 ^a	0.56 ^a	0.53 ^a	0.35 ^b
SNOT-22	0.10	0.06	0.06	−0.03	0.10	−0.10
Absolute serum eosinophils	0.03	0.15	0.23 ^b	0.26 ^b	0.21	0.18
Tissue eosinophil count	0.13	0.21	0.37 ^a	0.39 ^a	0.23 ^b	0.11

^a $P < .001$.^b $P < .05$.

bulk of the correlation strength seen in overall %SO is carried by these cavities.

DISCUSSION

Objective quantification of sinus mucosal disease is important for several reasons. From a clinical perspective, detailed quantification would allow a more nuanced understanding of inflammatory burden and response to therapy. For researchers, quantification systems are frequently used to objectively compare disease burden among different patients in cross-sectional analysis or longitudinally within-subject to document the efficacy of therapeutic interventions. Current objective CT scoring measures may not offer the necessary sensitivity for such comparisons.

Semiquantitative visual assessment of radiologic disease severity involves visual estimation of sinus opacification and grading with standardized scoring systems. While dozens of such scoring systems exist, the most widely accepted method used today is the LMS.¹² While the LMS has demonstrated good interrater reliability and relative ease of use, a drawback of the LMS is that a score of 1 for a given cavity encompasses 99% of the radiologic disease spectrum, under which most sinus cavities will likely be classified. In other words, the LMS can distinguish those without disease and those with the most severe disease but has poor discrimination among patients with mild-to-moderate levels of disease for a given sinus cavity. Furthermore, the importance of ostiomeatal complex opacification has been reconsidered, and given the potential subjectivity of the 0-versus-2 score, it is not clear whether this measure is truly meaningful.¹³

Several groups have recognized this shortcoming and have sought to improve the LMS using computer-assisted volumetric analysis of sinus opacification.^{14,15} These methods aim to calculate the percentage of sinus cavity occupied by soft-tissue density, allowing characterization of mucosal inflammation on a continuous scale. While shown to improve the clinical utility of the LMS for the most part, these staging systems have failed to gain wide acceptance due to their unwieldy implementation. These methods rely on an experienced clinician or radiologist with knowledge of complex sinus anatomy to manually segment the sinus cavities for each patient. Even when using semiautomated

computerized techniques, these methods are heavily time-consuming and potentially prone to human error.

Methods that strive to create more objective computer analysis of sinus CT have surfaced only recently. Chowdhury et al¹⁶ used deep learning to classify opacification of the ostiomeatal complex on selected 2D coronal sections. Using a CNN trained on 296 CT scans from patients with CRS, the authors reported that their method was able to correctly detect ostiomeatal complex opacification 85% of the time. To our knowledge, our group was the first to develop, test, and validate a fully automated deep learning-based algorithm capable of 3D volumetric segmentation of the paranasal sinuses on CT.⁶ In this proof-of-principle study, the algorithm was tested on subjects presenting for multidisciplinary respiratory evaluation at a single institution. The results showed that algorithm-derived quantitative assessment of the total percentage sinus opacification correlated well with the current criterion standard visual grading system, the LMS.

The current study expands on this work in several ways, with an overarching goal being further demonstrating the applicability and utility of a fully automated system for disease quantification, while also exploring novel radiologic disease-specific readouts. The current algorithm is capable of individual sinus cavity segmentation, a feature that was not yet developed in our initial report of our technique. Averaging of individual sinus cavities represents an improvement in overall characterization of sinus disease burden, considering that in this work, we demonstrate an overall %SO-versus-LMS correlation of 0.85, which is an increase compared with our initial work in which we reported a correlation of 0.82. While the study cohort in this work is smaller, it is an independent cohort consisting exclusively of patients with well-characterized CRS. We used a number of disease-specific metrics that were not available in the initial study, including polyp status, endoscopic disease assessments, quality-of-life surveys, and serum/tissue eosinophil measurement. Additionally, CT scans in the present study were obtained using several different scanner manufacturers with varied reconstruction kernel protocols, illustrating potential broad applicability of such an algorithm. That this approach was capable of successfully analyzing a diverse set of scans while producing an improved association with LMS to the initial study demonstrates promise in the wide-spread application of this AI technology.

We also explored the clinical significance of novel automated CT metrics that have been proposed in the literature. The significance of Hounsfield unit values of sinus opacities has been investigated previously, with 1 study showing that when the LMS is weighted by certain Hounsfield unit values, correlation of the weighted LMS score to symptom indices increased.¹⁷ Opacification hyperdensity has also been found to be a key radiologic biomarker for certain CRS subtypes, such as allergic fungal rhinosinusitis¹⁸ and eosinophilic mucin rhinosinusitis. Our algorithm is capable of calculating the mHU of opacified regions across all sinus cavities for a given study, a readout that has not been studied before. In the current study, mHU correlations to clinical parameters, in particular tissue and serum eosinophils, were lower than we had expected. While we had hypothesized that radiologic density measures would have correlated with eosinophilic inflammatory markers based on the known relationship between allergic fungal concretions and eosinophilic mucin, there is, in fact, a dearth of published data to support this theory, probably, in part, because an objective radiologic metric examining this issue has not been easily obtainable until now. Furthermore, our study was not powered to examine opacification density characteristics for diseases in which this may be important, such as eosinophilic CRS or allergic fungal rhinosinusitis. More study is needed to examine how this newly available radiologic measure can be used in these conditions.

We also investigated osteitis of bony lamellae in the sinus cavities, an important clinical marker that typically indicates recalcitrant or long-standing CRS disease status and may portend worse outcomes after endoscopic sinus surgery.¹⁹⁻²² This investigation was performed by assessing a 7-mm rind along the perimeter of each sinus cavity and determining what percentage of the rind was occupied by bone. We hypothesized that subjects with a greater degree of bony thickening would correlate to having a higher total GOSS, a currently applied radiologic measure of paranasal sinus osteitis. Our results showed a moderate correlation between the algorithm readout and the visual assessment. Stratifying the correlation by surgical status strengthened the correlation in postoperative subjects, possibly because these patients had more recalcitrant disease or from repeat insults from the surgery itself. Our initial method of assessment may be limited by patients who naturally have thicker bone but lack osteitic change; further refinement of this technique may be needed in the future.

We had hypothesized that an AI-based quantitative algorithm would offer a sensitive method to measure disease severity, and it seems to have performed similar to LMS measurements. Neither LMS nor quantitative %SO demonstrated any meaningful association with SNOT-22 scores in this cohort, supporting prior literature observations that likewise showed no relationship between CT disease burden and symptoms.²³⁻²⁵ As has been proposed in other work, biologic factors may play only a partial role in the determination of symptom burden and expression,²⁶ and we are still a long way from deciphering how certain radiologic findings such as Hounsfield units can be used as biomarkers or as a method of endotyping patients with CRS.

Performing well compared with the criterion standard LMS, our AI-based approach has marked and obvious advantages in that it is rapid and completely automated and eliminates any bias or human error that may be part of a visual assessment. The algorithm, now

demonstrating successful segmentation from scanners from multiple different manufacturers, also allows quantitation or detection of other important radiologic entities for clinical and research purposes, such as osteitis and assessment of opacification density.

Limitations of the current work include the retrospective study design. While use of a diverse set of scans may be argued as a potential drawback for a validation study, we think that this, in fact, represents a strength that showcases algorithm robustness with respect to varied scan-acquisition parameters, especially because initial validation work using a homogeneous cohort of scans has already been published by our group. Further validation and utility assessment will be of interest in a prospective multi-institutional trial setting.

CONCLUSIONS

Our CNN-based approach to sinus CT evaluation is capable of rapid and automated quantitative assessment, as demonstrated in this CRS cohort with images obtained from a diverse set of scanners. This AI technology performs well compared with the current criterion standard visual-assessment system. With further testing and continued refinement, quantitative assessment of sinus CT enabled by AI is poised to become a valuable tool for quantification of radiologic disease burden in both clinical and research applications.

Disclosure forms provided by the authors are available with the full text and PDF of this article at www.ajnr.org.

REFERENCES

1. Bhattacharyya N. Trends in otolaryngologic utilization of computed tomography for sinonasal disorders. *Laryngoscope* 2013;123:1837–39 CrossRef Medline
2. Orlandi RR, Kingdom TT, Smith TL, et al. International consensus statement on allergy and rhinology: rhinosinusitis 2021. *Int Forum Allergy Rhinol* 2021;11:213–739 CrossRef Medline
3. Fokkens WJ, Lund VJ, Hopkins C, et al. European Position Paper on Rhinosinusitis and Nasal Polyps 2020. *Rhinology* 2020;58(Suppl S29):1–464 CrossRef Medline
4. Rosenfeld RM, Piccirillo JF, Chandrasekhar SS, et al. Clinical practice guideline (update): adult sinusitis. *Otolaryngol Head Neck Surg* 2015;152(2 Suppl):S1–39 CrossRef Medline
5. Deutschmann MW, Yeung J, Bosch M, et al. Radiologic reporting for paranasal sinus computed tomography: a multi-institutional review of content and consistency. *Laryngoscope* 2013;123:1100–05 CrossRef Medline
6. Humphries SM, Centeno JP, Notary AM, et al. Volumetric assessment of paranasal sinus opacification on computed tomography can be automated using a convolutional neural network. *Int Forum Allergy Rhinol* 2020;10:1218–25 CrossRef Medline
7. Chartrand G, Cheng PM, Vorontsov E, et al. Deep learning: a primer for radiologists. *Radiographics* 2017;37:2113–31 CrossRef Medline
8. Pauwels R, Jacobs R, Singer SR, et al. CBCT-based bone quality assessment: are Hounsfield units applicable? *Dentomaxillofac Radiol* 2015;44:20140238 CrossRef Medline
9. Park SK, Park KW, Mo JH, et al. Clinicopathological and radiological features of chronic rhinosinusitis with eosinophilic mucin in Chungcheong Province of Korea. *Mycopathologia* 2019;184:423–31 CrossRef Medline
10. Georgalas C, Videler W, Freling N, et al. Global Osteitis Scoring Scale and chronic rhinosinusitis: a marker of revision surgery. *Clin Otolaryngol* 2010;35:455–61 CrossRef Medline
11. Gitomer SA, Fountain CR, Kingdom TT, et al. Clinical examination of tissue eosinophilia in patients with chronic rhinosinusitis and nasal

- polyposis.** *Otolaryngol Head Neck Surg* 2016;155:173–78 CrossRef Medline
12. Lund VJ, Mackay IS. **Staging in rhinosinusitis.** *Rhinology* 1993;31:183–84 Medline
 13. Snidvongs K, Chin D, Sacks R, et al. **Eosinophilic rhinosinusitis is not a disease of ostiomeatal occlusion.** *Laryngoscope* 2013;123:1070–74 CrossRef Medline
 14. Pallanch JF, Yu L, Delone D, et al. **Three-dimensional volumetric computed tomographic scoring as an objective outcome measure for chronic rhinosinusitis: clinical correlations and comparison to Lund-Mackay scoring.** *Int Forum Allergy Rhinol* 2013;3:963–72 CrossRef Medline
 15. Garneau J, Ramirez M, Armato SG 3rd, et al. **Computer-assisted staging of chronic rhinosinusitis correlates with symptoms.** *Int Forum Allergy Rhinol* 2015;5:637–42 CrossRef Medline
 16. Chowdhury NI, Smith TL, Chandra RK, et al. **Automated classification of osteomeatal complex inflammation on computed tomography using convolutional neural networks.** *Int Forum Allergy Rhinol* 2019;9:46–52 CrossRef Medline
 17. Sedaghat AR, Bhattacharyya N. **Chronic rhinosinusitis symptoms and computed tomography staging: improved correlation by incorporating radiographic density.** *Int Forum Allergy Rhinol* 2012;2:386–91 CrossRef Medline
 18. Ponikau JU, Sherris DA, Kern EB, et al. **The diagnosis and incidence of allergic fungal sinusitis.** *Mayo Clin Proc* 1999;74:877–84 CrossRef Medline
 19. Baban MIA, Mirza B, Castelnuovo P. **Radiological and endoscopic findings in patients undergoing revision endoscopic sinus surgery.** *Surg Radiol Anat* 2020;42:1003–12 CrossRef Medline
 20. Sacks PL, Snidvongs K, Rom D, et al. **The impact of neo-osteogenesis on disease control in chronic rhinosinusitis after primary surgery.** *Int Forum Allergy Rhinol* 2013;3:823–27 CrossRef Medline
 21. Bhandarkar ND, Sautter NB, Kennedy DW, et al. **Osteitis in chronic rhinosinusitis: a review of the literature.** *Int Forum Allergy Rhinol* 2013;3:355–63 CrossRef Medline
 22. Lee JT, Kennedy DW, Palmer JN, et al. **The incidence of concurrent osteitis in patients with chronic rhinosinusitis: a clinicopathological study.** *Am J Rhinol* 2006;20:278–82 CrossRef Medline
 23. Ryan WR, Ramachandra T, Hwang PH. **Correlations between symptoms, nasal endoscopy, and in-office computed tomography in post-surgical chronic rhinosinusitis patients.** *Laryngoscope* 2011;121:674–78 CrossRef Medline
 24. Hopkins C, Browne JP, Slack R, et al. **The Lund-Mackay staging system for chronic rhinosinusitis: how is it used and what does it predict?** *Otolaryngol Head Neck Surg* 2007;137:555–61 CrossRef Medline
 25. Basu S, Georgalas C, Kumar BN, et al. **Correlation between symptoms and radiological findings in patients with chronic rhinosinusitis: an evaluation study using the Sinonasal Assessment Questionnaire and Lund-Mackay grading system.** *Eur Arch Otorhinolaryngol* 2005;262:751–54 CrossRef Medline
 26. Wilson IB, Cleary PD. **Linking clinical variables with health-related quality of life: a conceptual model of patient outcomes.** *JAMA* 1995;273:59–65 Medline

Differentiation of Skull Base Chondrosarcomas, Chordomas, and Metastases: Utility of DWI and Dynamic Contrast-Enhanced Perfusion MR Imaging

Y. Ota, E. Liao, A.A. Capizzano, A. Baba, R. Kurokawa, M. Kurokawa, and A. Srinivasan



ABSTRACT

BACKGROUND AND PURPOSE: Differentiation of skull base tumors, including chondrosarcomas, chordomas, and metastases, on conventional imaging remains a challenge. We aimed to test the utility of DWI and dynamic contrast-enhanced MR imaging for skull base tumors.

MATERIALS AND METHODS: Fifty-nine patients with chondrosarcomas, chordomas, or metastases between January 2015 and October 2021 were included in this retrospective study. Pretreatment normalized mean ADC and dynamic contrast-enhanced MR imaging parameters were calculated. The Kruskal-Wallis H test for all tumor types and the Mann-Whitney U test for each pair of tumors were used.

RESULTS: Fifteen chondrosarcomas (9 men; median age, 62 years), 14 chordomas (6 men; median age, 47 years), and 30 metastases (11 men; median age, 61 years) were included in this study. Fractional plasma volume helped distinguish all 3 tumor types ($P = .003$, $<.001$, and $<.001$, respectively), whereas the normalized mean ADC was useful in distinguishing chondrosarcomas from chordomas and metastases ($P < .001$ and $P < .001$, respectively); fractional volume of extracellular space, in distinguishing chondrosarcomas from metastases ($P = .02$); and forward volume transfer constant, in distinguishing metastases from chondrosarcomas/chordoma ($P = .002$ and $.002$, respectively) using the Kruskal-Wallis H test. The diagnostic performances of fractional plasma volume for each pair of tumors showed areas under curve of 0.86–0.99 (95% CI, 0.70–1.0); the forward volume transfer constant differentiated metastases from chondrosarcomas/chordomas with areas under curve of 0.82 and 0.82 (95% CI, 0.67–0.98), respectively; and the normalized mean ADC distinguished chondrosarcomas from chordomas/metastases with areas under curve of 0.96 and 0.95 (95% CI, 0.88–1.0), respectively.

CONCLUSIONS: DWI and dynamic contrast-enhanced MR imaging sequences can be beneficial for differentiating the 3 common skull base tumors.

ABBREVIATIONS: AUC = area under the curve; DCE-MR imaging = dynamic contrast-enhanced perfusion MR imaging; IQR = interquartile range; k^{trans} = forward volume transfer constant; V_e = fractional volume of extracellular space; V_p = fractional plasma volume; $nADC_{mean}$ = normalized mean ADC

The skull base is involved in a wide variety of neoplasms.¹ They include primary bone tumors such as chondrosarcomas and chordomas, both of which show similarities in anatomic location, clinical manifestations, and conventional imaging findings, with a combined annual incidence of approximately 1 per 100,000.²

Chondrosarcomas arise from the embryonic rest of the cartilaginous matrix of the cranium and tend to be centered at the petrous apex or petro-occipital fissure,³ compared with chordomas that arise from remnants of the notochord and are typically centered on the clivus. However, both tumors tend to be locally aggressive, limiting the feasibility and diagnostic utility of establishing the site of origin on conventional CT and MR imaging.⁴ In the skull base, especially in the clivus and petrous regions, skull base metastases are also diagnostic considerations. The prevalence of skull base metastases among patients with cancer remains to be revealed, but it has been suggested that it is underreported.⁵ Breast, lung, prostate, and head and neck cancers, as well as melanomas have been reported.^{6,7} Skull base metastases of unknown origin have been reported as well.⁷ Conventional MR imaging has been reported as a sensitive tool to detect abnormalities in the skull base,⁸ but MR imaging features are not specific and may overlap between chondrosarcomas and chordomas.⁴ The

Received January 2, 2022; accepted after revision June 28.

From the Division of Neuroradiology (Y.O., E.L., A.A.C., A.B., R.K., M.K., A.S.), Department of Radiology, University of Michigan, Ann Arbor, Michigan; Department of Radiology (A.B.), Jikei University School of Medicine Ringgold Standard Institution, Tokyo, Japan; Department of Radiology (R.K.), The University of Tokyo Hospital, Tokyo, Japan; and Department of Radiology (M.K.), Tokyo Metropolitan Cancer and Infectious Diseases Center Komagome Hospital Ringgold Standard Institution, Bunkyo-ku, Japan.

Please address correspondence to Yoshiaki Ota, MD, University of Michigan, Department of Radiology, 1500 E Medical Center Dr, UH B2, Ann Arbor, MI 48109; e-mail: yoshiako@med.umich.edu; @GattsukiRadiol

Indicates open access to non-subscribers at www.ajnr.org

<http://dx.doi.org/10.3174/ajnr.A7607>

treatment strategy and long-term prognosis differ depending on the above-mentioned 3 tumors,^{5,9} making it clinically important to distinguish them, especially in patients in whom an abnormality is detected on MR imaging or CT in the skull base but who do not have confirmed primary cancers elsewhere in the body.

DWI can characterize cellularity and unique microstructures, and dynamic contrast-enhanced MR imaging (DCE-MR imaging) can evaluate permeability patterns and vascularity¹⁰⁻¹⁴ and is increasingly used for tumor differentiation and evaluation of treatment effects.^{15,16} The ADC value has been shown to assist in the differentiation of chondrosarcomas and chordomas,¹⁷ but the differentiation of metastases from chondrosarcomas and chordomas has not been fully explored. Recently, DCE-MR imaging has been used to differentiate bone metastases from benign lesions.^{17,18} However, no studies have explored the differentiation of these 3 tumor types using DCE-MR imaging. The calculated parameters from DCE-MR imaging include fractional plasma volume (Vp), which can reflect tumor vascularity, as well as fractional volume of extracellular space (Ve) and forward volume transfer constant (K^{trans}), which can represent permeability.¹¹ Chondrosarcomas, chordomas, and metastases can show different internal structures, microvascularization, and permeability, suggesting that DWI and DCE-MR imaging can be helpful in the differentiation of the 3 tumor types.

In this study, we aimed to test the ability of DWI and DCE-MR imaging to differentiate chondrosarcomas, chordomas, and metastases in the skull base.

MATERIALS AND METHODS

Study Population

This retrospective single-center study was approved by University of Michigan institutional review board, and the requirement of informed consent was waived. Data were acquired and de-identified before any analysis, in compliance with all applicable Health Insurance Portability and Accountability Act regulations. We reviewed the medical records of 368 patients, including 68 patients diagnosed with chondrosarcomas, 60 patients with chordomas, and 240 patients with skull base metastases from January 2015 to October 2021 in a single center. Patients with chondrosarcomas and classic chordomas were diagnosed pathologically. Skull base metastases were diagnosed by biopsy or on the basis of the clinical evidence of confirmed primary cancers, other biopsied-confirmed metastatic lesions, and skull base lesions detected on conventional CT/MR imaging and FDG-PET/CT. Cases without pretreatment DWI or DCE-MR imaging (including biopsy, surgery, or radiation therapy) ($n = 295$) or poor image quality ($n = 14$) were excluded.

All 30 patients with skull base metastases had confirmed primary cancers. Six of 30 patients underwent a biopsy (3 lung cancers, 2 breast cancers, and 1 renal cell carcinoma), and 24 of 30 patients were clinically diagnosed on the basis of all 24 patients having histories of confirmed primary cancers, biopsy-confirmed metastatic lesions in the other regions, and positive conventional head and neck CT/MR imaging and PET/CT findings in the skull base. For patients diagnosed with skull base metastases, the treatment response of the skull base lesions following chemotherapy or chemotherapy plus radiation therapy was confirmed on follow-up CT or MR imaging. Corresponding treatments such as chemotherapy

($n = 18$) or chemotherapy plus radiation therapy ($n = 12$) were used, and a decrease in size was observed on CT or MR imaging.

In total, 59 patients (20 men, 39 women; median age, 61 years; interquartile range [IQR], 45–70 years) with 15 chondrosarcomas, 14 chordomas, and 30 skull base metastases were included in this study. Patient demographics such as age and sex for all tumor types and primary cancers for skull base metastases were reviewed from medical records.

MR Imaging Protocol

Head and neck MR imaging examinations were performed using a 1.5T or 3T system (Ingenia; Philips Healthcare) with patients in the supine position. The acquired sequences were axial plane T1WI, T2WI, FLAIR, and contrast-enhanced fat-saturated T1WI and coronal plane contrast-enhanced fat-saturated T1WI. DWI was performed using echo-planar imaging with the following DWI parameters: TE range, 58–106 ms; TR range, 5000–9500 ms; number of excitations, 1; section thickness and gap, 3.5–4 and 0–1 mm; FOV, 220–240 mm; matrix size, 128×128 to 200×200 ; and 3 diffusion directions. Sensitizing diffusion gradients were sequentially applied. B values were 0 and 1000 s/mm².

A DCE-MR imaging sequence was performed using a 3D T1-weighted fast-field echo technique with a 16-channel Neurovascular coil. Twenty milliliters of gadobenate dimeglumine (MultiHance; Bracco Diagnostics) was administered through a peripheral arm vein using a power injector at a flow rate of 5.0 mL/s and followed by a 20-mL saline flush. DCE-MR imaging was sequentially acquired with the following parameters of 3D-T1 fast-field echo: TE, 1.86 ms; TR, 4.6 ms; flip angle, 30°; section thickness, 5.0 mm; FOV, 240×240 mm²; voxel size, $1.0 \times 1.0 \times 5.0$ mm³; number of excitations, 1; number of slices per dynamic scan, 48; temporal resolution, 8.4 seconds; dynamic phase, 30 dynamics; total acquisition time, 4 minutes 24 seconds.

Imaging Processing and Analysis

Two board-certified radiologists with 7 and 10 years of experience independently performed DWI and DCE-MR imaging analyses. The same board-certified radiologist with 7 years of experience reviewed conventional MR imaging. The 2 readers were blinded to the histologic results.

Conventional Imaging

The maximum axial diameter was measured using contrast-enhanced axial and coronal fat-saturated T1WI. As conventional MR imaging features, the main skull base location was identified using axial and coronal contrast-enhanced fat-saturated T1WI and recorded as the clivus or petrous bone. In addition, both radiologists evaluated the following imaging characteristics with consensus and recorded them as binary variables:

- 1) Cystic changes, defined as focal areas with nonenhancing, predominantly T2-hyperintense areas and necrotic changes defined as focal areas with nonenhancing, predominantly T1-hypointense and heterogeneously T2-hyperintense areas.
- 2) T2 hyperintensity or iso-/hypointensity in the lesion relative to the brain parenchyma, evaluated on T2WI, excluding the areas of cystic/necrotic changes.

Table 1: Patient demographics^a

	Chondrosarcoma	Chordoma	Metastasis
No. of patients	15	14	30
Sex (male/total)	9/15	6/14	11/30
Age (yr)	62 (46–70)	47 (32–58)	61 (47–70)
Maximum axial diameter (mm)	29.5 (24–36)	33 (24–40)	18.5 (15–23)
Primary cancer type	NA	NA	11 Breast, 6 lung, 6 malignant melanoma, 4 head and neck, 2 sarcoma, 1 kidney

Note:—NA indicates not applicable.

^a Values are presented as the median (IQR).

- Enhancement patterns (homogeneous or heterogeneous), evaluated on postcontrast fat-saturated T1-weighted images.
- Other metastatic lesions in the FOV of the head and neck scan, evaluated on T1WI, T2WI, and postcontrast T1WI.

DWI Analysis

The same 2 board-certified radiologists with 7 and 10 years of experience manually delineated a single freehand ROI on the axial contrast-enhanced fat-saturated T1WI. ADC maps were constructed using commercially available software (Olea Sphere, Version 3.0; Olea Medical). On the ADC maps, the corresponding ROIs were again contoured with reference to the ROIs delineated on axial postcontrast T1WI. The 2 readers adhered to the following procedure:

- ROIs were encompassed in the areas on axial postcontrast fat-saturated T1WI where the tumors showed solid enhancing components, excluding necrotic or cystic regions. When the lesions extended beyond the clivus into surrounding soft tissues, both the bony and soft structures were included in a ROI.
- The peripheral 2 mm of the lesions were excluded from an ROI to avoid volume averaging.
- The ROIs were manually adjusted on the ADC map if geometric artifacts were observed.
- An ROI was placed within the medulla oblongata as an internal control. The mean ADC values of the tumor were divided by the mean ADC values of the medulla oblongata, and the normalized mean ADC (nADCmean) was calculated.

DCE-MR Imaging Analysis

Quantitative analyses were performed using the Olea Sphere 3.0 software. An arterial input function was automatically computed. While this process was automated, the corresponding time-intensity curves that demonstrated a rapid increase in attenuation with sharp peaks were deemed appropriate and accurate for analysis. The permeability module was based on the extended Tofts model, and pixel-based parameter maps were calculated from time-intensity curves. ROIs were placed by means of the method used for the DWI analysis. Quantitative parameters, V_p , V_e , and K^{trans} , were calculated.

Statistical Analysis

nADCmean and V_e , K^{trans} , and V_p were compared among the 3 tumor types using the Kruskal-Wallis H test and the post hoc test with Bonferroni correction and were described as medians (IQR). The conventional MR imaging features were compared between each pair of tumor types by the Fisher exact test. For each pair of tumor type (chondrosarcomas and chordomas, chondrosarcomas

and metastases, and chordomas and metastases), the parameters from DWI and DCE-MR imaging analyses were compared using the Mann-Whitney U test with a Bonferroni correction and described as median (IQR). For statistically significant diagnostic parameters, receiver operating characteristic analysis was performed with the optimal cutoff values, which were determined to maximize the Youden index (sensitivity + specificity-1). The intra-class correlation coefficient was used to assess the interobserver agreement for DWI and DCE-MR imaging parameters. All statistical calculations were conducted using R statistical and computing software (<http://www.r-project.org/>). Variables with P values < .05 were considered statistically significant.

RESULTS

Patient Demographics

There were 15 chondrosarcomas (9 men; median age, 62 years; IQR, 46–70 years), 14 chordomas (6 men; median age, 47 years; IQR, 32–58 years), and 30 metastases (11 men; median age, 61 years; IQR, 47–70 years) in this study. Patient demographic and tumor characteristics are summarized in Table 1. As shown in Table 1, the metastatic cohort was a heterogeneous group of primary cancer types. The 3 most frequently seen primary cancers were breast (37%, 11/30), lung (20%, 6/30), and malignant melanomas (20%, 6/30).

Conventional MR Imaging Features

The results of the comparisons between chondrosarcomas versus chordomas and between chondrosarcomas and chordomas versus metastases are presented in Table 2.

Chondrosarcomas versus Chordomas

There was no significant difference in main locations, the presence of cystic/necrotic changes, signal intensity (T2 hyperintensity or iso-/hypointensity), and enhancement patterns ($P = .08$ – 1.0).

Chondrosarcomas versus Metastases

T2 hyperintensity in the lesion was more often seen in chondrosarcomas than in metastases (10/15 versus 9/30, $P = .027$). Otherwise, there was no significant difference in main locations and the presence of cystic/necrotic changes or enhancement patterns between them ($P = .14$ – $.29$).

Chordomas versus Metastases

T2 hyperintensity in the lesion was more often seen in chordomas than in metastases (9/14 versus 9/30; $P = .049$). Otherwise, there was no significant difference in other conventional imaging features between them ($P = .29$ – $.65$).

Table 2: Conventional imaging characteristics of chondrosarcomas, chordomas, and metastases

	Chondrosarcoma	Chordoma	Metastasis	P Value
Main location (petrous bone:clivus)	9/6	1/13	5/25	$P^a = .08$ $P^b = .14$ $P^c = .65$
Cystic/necrotic changes	8/15	7/14	10/30	$P^a = 1.0$ $P^b = .22$ $P^c = .33$
T2 hyperintensity or iso-/hypointensity relative to the brain parenchyma (T2 hyperintensity/total)	10/15	9/14	9/30	$P^a = 1.0$ $P^b = .027$ $P^c = .049$
Enhancement patterns (heterogeneous/total)	15/15	14/14	26/30	$P^a = 1.0$ $P^b = .29$ $P^c = .29$
Other metastatic lesions in the head and neck	NA	NA	5/30	NA

Note:— P^a is obtained from a comparison between chondrosarcoma and chordoma, P^b is from a comparison between chondrosarcoma and metastasis, and P^c is from a comparison between chordoma versus metastasis.

Table 3: DWI and DCE-MR imaging parameters of chondrosarcoma, chordoma, and metastasis using the Kruskal-Wallis H test and the post hoc test with Bonferroni correction^a

	Chondrosarcoma	Chordoma	Metastasis	P Value ^a	P Value ^b		
					Chondrosarcoma vs Chordoma	Chondrosarcoma vs Metastasis	Chordoma vs Metastasis
nADCmean	2.44 (2.27–2.71)	1.30 (1.07–1.73)	1.39 (1.21–1.70)	<.001	<.001	<.001	1.0
Vp	0.015 (0.01–0.028)	0.045 (0.04–0.068)	0.12 (0.09–0.14)	<.001	.003	<.001	<.001
Ve	0.25 (0.15–0.31)	0.35 (0.30–0.40)	0.48 (0.34–0.63)	.007	.14	.022	.17
K^{trans} (minute ⁻¹)	0.08 (0.06–0.17)	0.16 (0.13–0.20)	0.39 (0.20–0.63)	<.001	.16	.002	.002

Note:— P^a is from Kruskal–Wallis H test. P^b is adjusted for pair-wise comparison by Bonferroni correction.

^a Numbers in parentheses indicate interquartile range.

DWI and DCE-MR Imaging Analysis

The intraclass correlation coefficient for DWI and DCE-MR imaging parameters was excellent (nADCmean, 0.94; Vp, 0.95; K^{trans} , 0.97; Ve, 0.95).

In the Kruskal-Wallis H test and the post hoc test with a Bonferroni correction, there were statistically significant differences in nADCmean, Vp, Ve, and K^{trans} among all tumor types (nADCmean, $P < .001$; Vp, $P < .001$; Ve, $P = .007$; and K^{trans} , $P < .001$). Vp showed significant differences in each pair of tumors (chondrosarcomas versus chordomas, $P = .003$; chondrosarcomas versus metastases, $P < .001$; and chordomas versus metastases, $P < .001$, respectively). Table 3 and Fig 1 summarize the comparisons of DWI and DCE-MR imaging parameters among the 3 tumors.

Chondrosarcomas versus Chordomas

The median nADCmean was significantly higher and the median Vp was significantly lower in chondrosarcomas than in chordomas (nADCmean: 2.4 [IQR, 2.3–2.7] versus 1.30 [IQR, 1.07–1.73]; $P < .001$; Vp: 0.015 [IQR, 0.01–0.028] versus 0.045 [IQR, 0.04–0.068]; $P = .012$), while the median Ve and K^{trans} were insignificantly different (Ve: 0.25 [IQR, 0.15–0.31] versus 0.35 [IQR, 0.30–0.40]; $P = .57$; K^{trans} : 0.08 [IQR, 0.06–0.17] versus 0.16 [IQR, 0.13–0.20]; $P = .64$).

Chondrosarcomas versus Metastases

nADCmeans were significantly higher, and Vp and K^{trans} were significantly lower in chondrosarcomas than in metastases (nADCmean: 2.44 [IQR, 2.27–2.71] versus 1.39 [IQR, 1.21–1.70]; $P < .001$; Vp: 0.015 [IQR, 0.01–0.028] versus 0.12 [IQR, 0.09–0.14]; $P < .001$;

K^{trans} : 0.08 [IQR, 0.06–0.17] versus 0.39 [IQR, 0.20–0.63]; $P = .008$), while Ve was insignificantly different (Ve: 0.25 [IQR, 0.15–0.31] versus 0.48 [IQR, 0.34–0.63]; $P = .09$).

Chordomas versus Metastases

Median Vp and K^{trans} were significantly lower in chordomas than in metastases (Vp: 0.045 [IQR, 0.04–0.068] versus 0.12 [IQR, 0.09–0.14]; $P < .001$; K^{trans} : 0.16 [IQR, 0.13–0.20] versus 0.39 [IQR, 0.20–0.63]; $P = .008$), while nADCmean and Ve were insignificantly different (nADCmean: 1.30 [IQR, 1.07–1.73] versus 1.39 [IQR, 1.21–1.70]; $P = 1.0$; Ve: 0.35 [IQR, 0.30–0.4] versus 0.48 [IQR, 0.34–0.63]; $P = .68$).

Diagnostic Performance of DWI and DCE-MR Imaging

The diagnostic performance of parameters of DWI and DCE-MR imaging analyses, which showed significant differences between chondrosarcomas versus chordomas, chondrosarcomas versus metastases, and chordomas versus metastases is demonstrated in Table 4 and Fig 2.

nADCmean showed areas under the curve (AUCs) of 0.96 and 0.95 (95% CI, 0.88–1.0) between chondrosarcomas and chordomas and between chondrosarcomas and metastases, respectively. Vp showed AUCs of 0.86, 0.99, and 0.92 (95% CI, 0.72–1.0) between chondrosarcomas and chordomas, between chondrosarcomas and metastases, and between chordomas and metastases, respectively. K^{trans} showed AUCs of 0.82 and 0.82 (95% CI, 0.67–0.98) between chondrosarcomas and metastases and between chordomas and metastases, respectively.

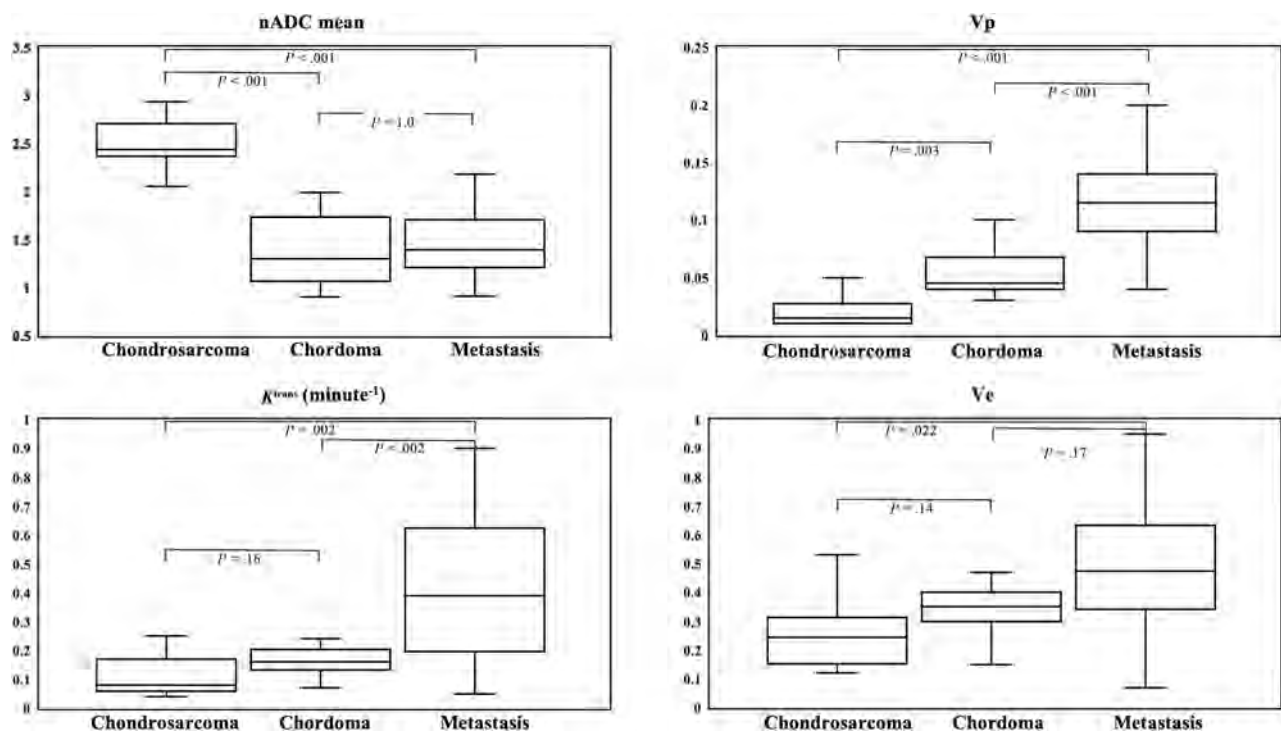


FIG 1. Box-and-whisker plots of DWI and DCE-MR imaging parameters with the Kruskal-Wallis H test and post hoc test with the Bonferroni correction are shown. The *boundaries* of boxes represent 25th and 75th percentiles, and the *lines* in boxes indicate medians.

Table 4: Diagnostic performance of DCE-MR imaging parameters for each tumor comparison^a

Parameters	Chondrosarcoma vs Chordoma		Chondrosarcoma vs Metastasis			Chordoma vs Metastasis	
	nADCmean	Vp	nADCmean	Vp	K^{trans} (minute ⁻¹)	Vp	K^{trans} (minute ⁻¹)
Cutoff	1.99	0.03	2.09	0.06	0.12	0.09	0.30
Sensitivity	1.0 (0.68–1)	0.93 (0.66–0.99)	0.93 (0.76–0.99)	0.93 (0.78–0.99)	0.93 (0.78–0.99)	0.80 (0.61–0.92)	0.60 (0.41–0.77)
Specificity	0.86 (0.57–0.98)	0.71 (0.42–0.92)	0.87 (0.60–0.98)	0.93 (0.66–0.9)	0.71 (0.42–0.92)	0.93 (0.66–1)	1.0 (0.68–1)
PPV	0.88 (0.62–0.98)	0.77 (0.50–0.93)	0.93 (0.76–0.99)	0.97 (0.82–1)	0.88 (0.71–0.97)	0.96 (0.80–1)	1.0 (0.74–1)
NPV	1.0 (0.64–1)	0.91 (0.59–0.99)	0.87 (0.60–0.98)	0.87 (0.60–0.98)	0.83 (0.52–0.98)	0.68 (0.43–0.87)	0.54 (0.33–0.73)
Accuracy	0.93 (0.78–0.99)	0.82 (0.63–0.94)	0.91 (0.77–0.97)	0.93 (0.81–0.99)	0.86 (0.73–0.95)	0.84 (0.70–0.93)	0.73 (0.57–0.85)
AUC	0.96 (0.90–1)	0.86 (0.72–1)	0.95 (0.88–1)	0.99 (0.96–1)	0.82 (0.67–0.98)	0.92 (0.84–1)	0.82 (0.70–0.95)

Note:—PPV indicates positive predictive value; NPV, negative predictive value.

^a Numbers in parentheses represent 95% CIs.

Representative cases of chondrosarcoma, chordoma, and metastasis with DWI and DCE-MR imaging analyses are shown in Figs 3–5.

DISCUSSION

This study aimed to test the utility of DWI and DCE-MR imaging for skull base chondrosarcomas, chordomas, and metastases. nADCmean, Vp, Ve, and K^{trans} showed significant differences among all tumor types, and Vp showed significant differences between each pair of tumor comparisons using the Kruskal-Wallis H test. In the Mann-Whitney U test for each pair of 2 tumors, Vp distinguished all tumor types with AUCs of 0.86–0.99 with cutoffs of 0.03–0.09, K^{trans} distinguished metastases from chondrosarcomas and chordomas with an AUC of 0.82 with cutoffs of 0.12 and 0.30, and nADCmean distinguished chondrosarcomas from chordomas and metastases with AUCs of 0.96 and 0.95 and cutoffs of 1.99 and 2.09, respectively. Ve was not a significant differentiator of tumor types.

Regarding conventional MR imaging features, T2 hyperintensity of the lesion was shown to be significantly higher in chondrosarcomas and chordomas than in metastases, which can be used as a differentiator from metastases between chondrosarcomas and chordomas. Other imaging features such as main locations, cystic/necrotic changes, or enhancement patterns did not identify any significant difference between each pair of tumor type. Also, in patients with metastases, only 5 of 30 patients showed other metastatic lesions in head and neck MR imaging, suggesting that other metastatic lesions may not be a decisive factor for differentiation of these tumors.

Regarding DWI analysis, ADC values were lower in chordomas than in chondrosarcomas in this study, as suggested by a previous study.¹⁷ It has been suggested that the difference in tumoral microstructure, such as cartilaginous stroma with varying degrees of cellularity in chondrosarcomas as well as myxoid stroma arranged through sheets of physaliferous cells in chordoma, contributes to the difference in ADC values.¹⁷ ADC values were also lower in metastases than in chondrosarcomas. Generally, malignant tumors show

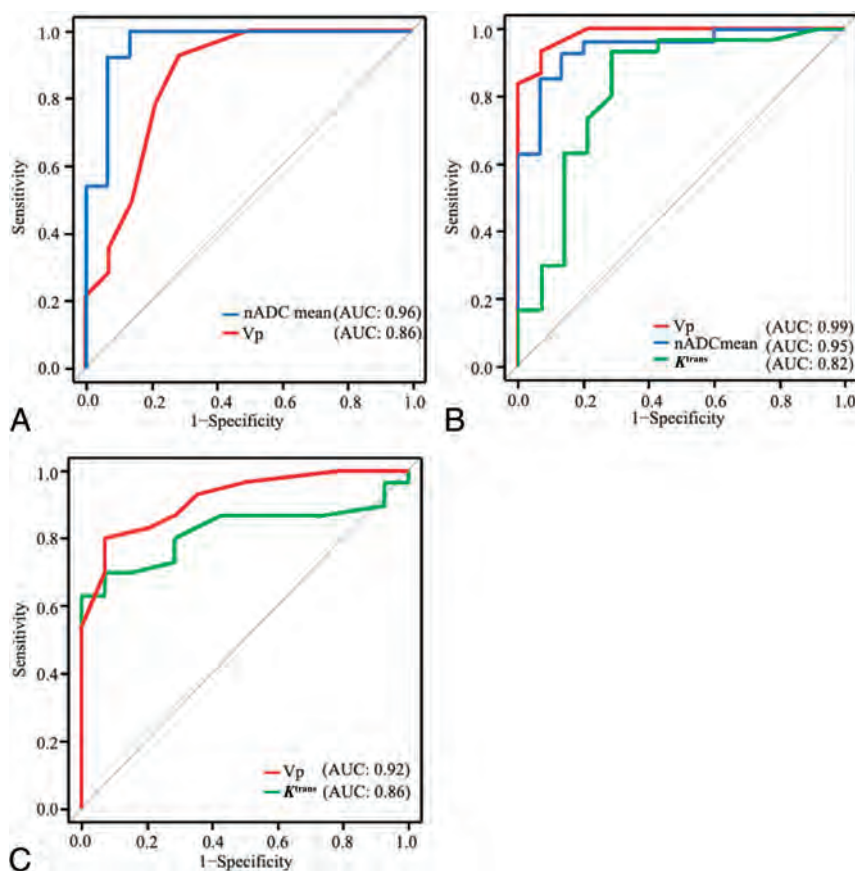


FIG 2. Receiver operating characteristic curves of chondrosarcoma versus chordoma (A), chondrosarcoma versus metastasis (B), and chordoma versus metastasis (C) are shown.

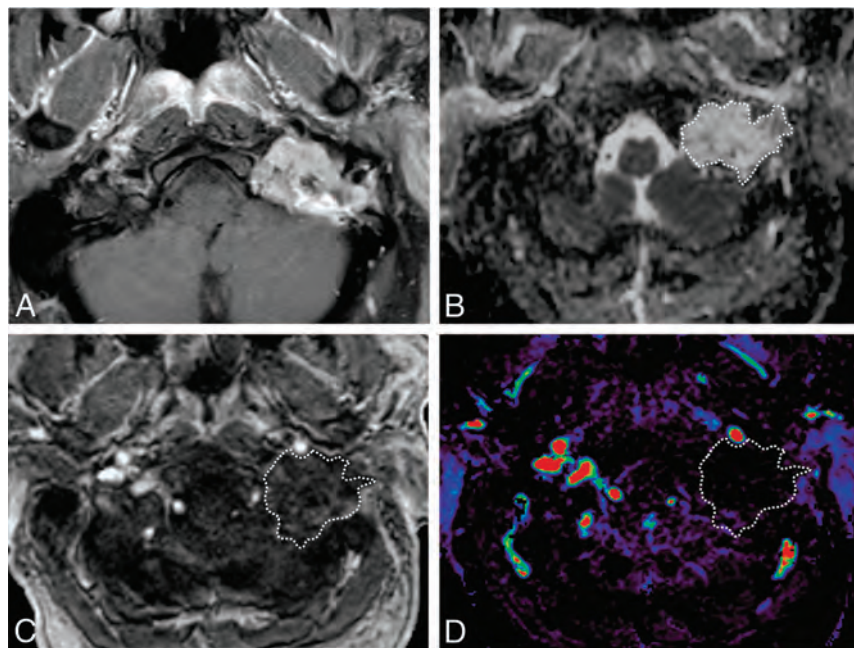


FIG 3. A 56-year-old man with a chondrosarcoma in the left petrous apex. A, Axial fat-saturated postcontrast T1-weighted image shows a heterogeneously enhancing mass in the left petrous apex. B, An ROI was placed on the ADC map, and the nADCmean was calculated. Mean ADC and ADC values in the medulla were 2.05, and $0.80 \times 10^{-3} \text{ mm}^2/\text{s}$, respectively. The nADCmean was 2.56. C, An ROI was placed on the permeability map, and V_p , K^{trans} , and V_e were calculated. D, V_p is 0.01.

high cellularity, which is assumed to result in low ADC values in metastases.¹⁹ In contrast, nADCmean was not a significant differentiator between chordomas and metastases, which is thought to stem from the complexity of internal structures and cellularity of each tumor group or from the heterogeneity of primary cancers of metastases. We divided the ADC values of the tumors by those of the medulla oblongata for normalization to minimize variations due to differences in magnetic field and scanner parameters. The medulla is usually included within the FOV of head and neck protocols and is rarely affected by chronic microvascular diseases,²⁰ offering easy reproducibility of the internal standard reference. This standardization method was thought to make our results robust.

Regarding DCE-MR imaging analysis, V_p , which is a marker of microvascularity, was lowest in chondrosarcomas, intermediate in chordomas, and highest in metastases, with significant differences, and showed promising diagnostic performances in the receiver operating characteristic analysis. Both chondrosarcomas and chordomas are known to have poor vascularity,²¹⁻²³ and DCE-MR imaging has been used to investigate each tumor type separately.^{24,25} However, there have been no studies that compared perfusion characteristics between chondrosarcomas and chordomas using DCE-MR imaging perfusion. On the basis of our study, V_p and ADC values can be significant differentiators between the 2 tumors, with promising diagnostic performance. In addition, clival metastases, which included a variety of primary cancer types such as breast, lung, melanoma, and head and neck cancers, showed significantly higher V_p values than chondrosarcomas and chordomas. Previous studies have shown that there were no significant differences in V_p between vertebral hematologic malignancies and solid malignancy metastases¹⁸ or between breast and lung cancer metastases.²⁶ However, a study showed higher V_p in vertebral metastasis from renal cancer (known as a hypervascular tumor) than from prostate cancer metastases (known as a hypovascular tumor).²⁷ This finding suggests that V_p in bone metastases can vary according to the primary cancer type. Nevertheless, when

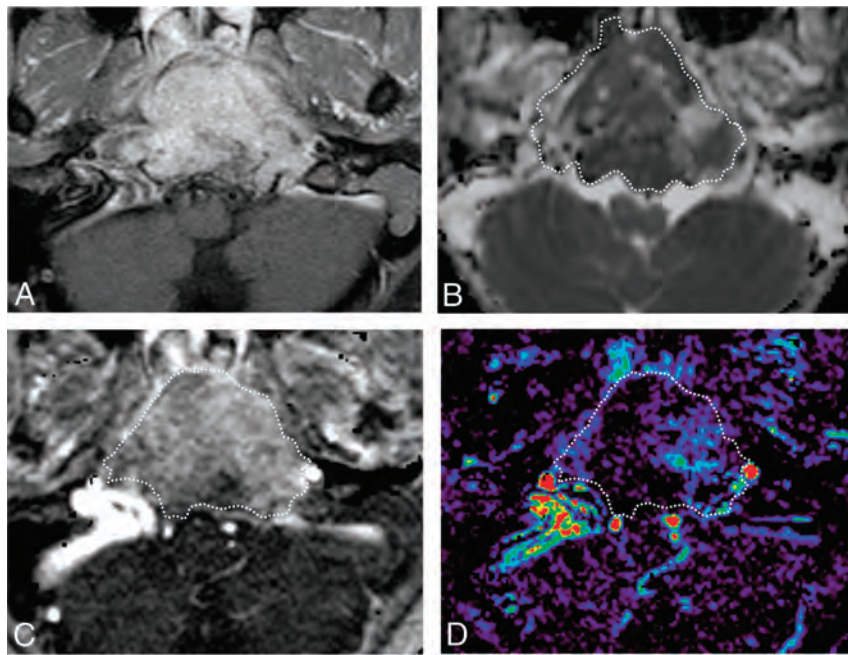


FIG 4. A 16-year-old boy with a chordoma in the clivus. *A*, Axial fat-saturated postcontrast T1-weighted image shows a heterogeneously enhancing mass in the clivus. *B*, An ROI was placed on the ADC map, and the nADCmean was 1.5. *C*, An ROI was placed on the permeability map, and V_p , K^{trans} , and V_e were calculated. *D*, V_p is 0.08.

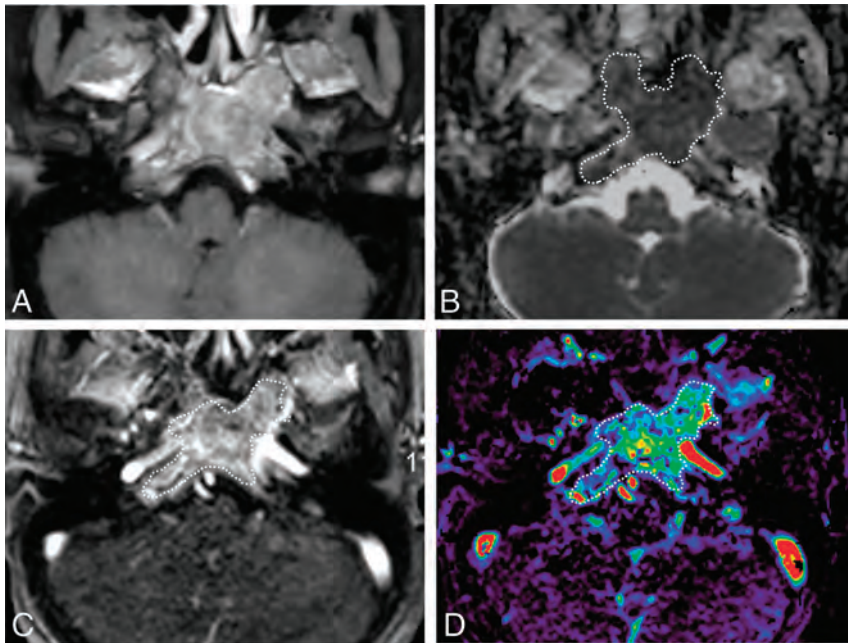


FIG 5. A 39-year-old woman with a metastatic breast cancer lesion in the clivus. *A*, Axial fat-saturated postcontrast T1-weighted image shows a heterogeneously enhancing mass in the clivus. *B*, An ROI was placed on the ADC map, and the nADCmean was 0.97. *C*, An ROI was placed on the permeability map, and V_p , K^{trans} , and V_e were calculated. *D*, V_p showed 0.23.

metastatic lesions are grouped together as a general population, irrespective of the primary cancer type, our results suggest that V_p remains a significant differentiator from primary bone lesions, such as chordomas or chondrosarcomas.

K^{trans} , which is a marker of tumor permeability, was higher in metastases than in the chondrosarcomas and chordomas in our

study. Malignant tumors generally show higher tumor permeability than benign tumors.²⁶ Similar to V_p , K^{trans} within the metastatic cohort can demonstrate variation on the basis of the type of primary malignancy,²⁷ though our overall results suggest that the general population of metastatic lesions will demonstrate significantly higher K^{trans} than primary bone lesions such as chordomas or chondrosarcomas. There were no significant differences in K^{trans} between chondrosarcomas and chordomas; therefore, it was not applicable for the differentiation of the 2 tumors on the basis of our results.

In our study, nADCmean showed the highest diagnostic performance in differentiating chondrosarcomas from chordomas, while V_p distinguished skull base metastases from chondrosarcomas and chordomas with the highest diagnostic performance. A biopsy is typically required for definite diagnosis and management. However, there are some clinical situations in which the invasive diagnostic procedure could be avoided. In fact, avoiding a biopsy in favor of short-term follow-up scans is often recommended at multidisciplinary conferences when the lesions are located close to or involve the vasculature or when the patients tend to have comorbidities that put them at higher risk of hemorrhage. In these clinical settings, adding DWI and DCE-MR imaging can be beneficial for clinical judgment and further management. In addition, when conventional imaging is indeterminate or PET/CT is not available or feasible at the time of diagnosis, DWI and DCE-MR imaging can enhance the confidence in the diagnosis when combined with the conventional imaging findings and can assist in proper clinical management.

There were several limitations to this study. First, it was retrospectively conducted at a single institution and included a relatively small population. In addition, we could not include head and neck CT imaging features because head and neck CT was not performed in all included patients. Second, most metastases ($n = 24$) could not be histologically confirmed owing to the anatomic accessibility of the skull base and risk of complications. However, all cases had confirmed primary cancers with abnormal skull base findings on CT or MR imaging and PET/CT, and other metastatic lesions were detected by biopsy or surgery. Third, this study used 1.5T and 3T scanners, which might result

in heterogeneity of DCE-MR imaging parameters. Forth, we did not conduct out-of-sample validation in statistical analysis, which potentially caused overly optimistic results in the diagnostic performance of DWI and DCE-MR imaging parameters. Finally, we included heterogeneous primary cancer diseases in patients with metastases, though this heterogeneous group can represent general populations of patients with cancer.

CONCLUSIONS

DWI and DCE-MR imaging sequences can help differentiate chondrosarcomas, chordomas, and metastases. When a skull base lesion is indeterminate on conventional imaging and/or a biopsy should be avoided due to the location of the lesion in close proximity to major vasculature or the patient's underlying comorbidities, DWI and DCE-MR imaging sequences can enhance the confidence in arriving at an appropriate diagnosis.

Disclosure forms provided by the authors are available with the full text and PDF of this article at www.ajnr.org.

REFERENCES

- Kelly HR, Curtin HD. **Imaging of skull base lesions.** *Handb Clin Neurol* 2016;135:637–57 CrossRef Medline
- Dolecek TA, Propp JM, Stroup NE, et al. **CBTRUS statistical report: primary brain and central nervous system tumors diagnosed in the United States in 2005–2009.** *Neuro Oncol* 2012;1(Suppl 5):v1–49 CrossRef Medline
- Almefty K, Pravdenkova S, Colli BO, et al. **Chordoma and chondrosarcoma: similar, but quite different, skull base tumors.** *Cancer* 2007;110:2467–67 CrossRef Medline
- Pamir MN, Ozduman K. **Analysis of radiological features relative to histopathology in 42 skull-base chordomas and chondrosarcomas.** *Eur J Radiol* 2006;58:461–70 CrossRef Medline
- Mehta GU, Raza SM. **Management of skull base metastases.** *Neurosurg Clin N Am* 2020;31:659–66 CrossRef Medline
- Chaichana KL, Flores M, Acharya S, et al. **Survival and recurrence for patients undergoing surgery of skull base intracranial metastases.** *J Neurol Surg B Skull Base* 2013;74:228–35 CrossRef Medline
- Laigle-Donadey F, Taillibert S, Martin-Duverneuil N, et al. **Skull-base metastases.** *J Neurooncol* 2005;75:63–69 CrossRef Medline
- Mitsuya K, Nakasu Y, Horiguchi S, et al. **Metastatic skull tumors: MRI features and a new conventional classification.** *J Neurooncol* 2011;104:239–45 CrossRef Medline
- Kremenevski N, Schlaffer SM, Coras R, et al. **Skull base chordomas and chondrosarcomas.** *Neuroendocrinology* 2020;110:836–47 CrossRef Medline
- Surov A, Meyer HJ, Wienke A. **Apparent diffusion coefficient for distinguishing between malignant and benign lesions in the head and neck region: a systematic review and meta-analysis.** *Front Oncol* 2019;9:1362 CrossRef Medline
- Gaddikeri S, Gaddikeri RS, Tailor T, et al. **Dynamic contrast-enhanced MR imaging in head and neck cancer: techniques and clinical applications.** *AJNR Am J Neuroradiol* 2016;37:588–95 CrossRef Medline
- Ota Y, Moore AG, Spector ME, et al. **Prediction of wound failure in patients with head and neck cancer treated with free flap reconstruction: utility of CT perfusion and MR perfusion in the early postoperative period.** *AJNR Am J Neuroradiol* 2022;43:585–91 CrossRef Medline
- Ota Y, Liao E, Capizzano AA, et al. **MR diffusion and dynamic-contrast enhanced imaging to distinguish meningioma, paraganglioma, and schwannoma in the cerebellopontine angle and jugular foramen.** *J Neuroimaging* 2021;32:502–10 CrossRef Medline
- Ota Y, Naganawa S, Kurokawa R, et al. **Assessment of MR imaging and CT in differentiating hereditary and nonhereditary paragangliomas.** *AJNR Am J Neuroradiol* 2021;42:1320–26 CrossRef Medline
- Ota Y, Liao E, Capizzano AA, et al. **Diagnostic role of diffusion-weighted and dynamic contrast-enhanced perfusion MR imaging in paragangliomas and schwannomas in the head and neck.** *AJNR Am J Neuroradiol* 2021;42:1839–46 CrossRef Medline
- Ota Y, Liao E, Kurokawa R, et al. **Diffusion-weighted and dynamic contrast-enhanced MRI to assess radiation therapy response for head and neck paragangliomas.** *J Neuroimaging* 2021;31:1035–43 CrossRef Medline
- Yeom KW, Lober RM, Mobley BC, et al. **Diffusion-weighted MRI: distinction of skull base chordoma from chondrosarcoma.** *AJNR Am J Neuroradiol* 2013;34:1056–61, S1 CrossRef Medline
- Guan Y, Peck KK, Lyo J, et al. **T1-weighted dynamic contrast-enhanced MRI to differentiate nonneoplastic and malignant vertebral body lesions in the spine.** *Radiology* 2020;297:382–89 CrossRef Medline
- Ginat DT, Mangla R, Yeane G, et al. **Diffusion-weighted imaging for differentiating benign from malignant skull lesions and correlation with cell density.** *AJR Am J Roentgenol* 2012;198:W597–601 CrossRef Medline
- Koontz NA, Wiggins RH 3rd. **Differentiation of benign and malignant head and neck lesions with diffusion tensor imaging and DWI.** *AJR Am J Roentgenol* 2017;208:1110–15 CrossRef Medline
- Katonis P, Alpantaki K, Michail K, et al. **Spinal chondrosarcoma: a review.** *Sarcoma* 2011;2011:378957 CrossRef Medline
- Fromm J, Klein A, Baur-Melnyk A, et al. **Survival and prognostic factors in conventional central chondrosarcoma.** *BMC Cancer* 2018;18:849 CrossRef Medline
- Bergh P, Kindblom LG, Gunterberg B, et al. **Prognostic factors in chordoma of the sacrum and mobile spine: a study of 39 patients.** *Cancer* 2000;88:2122–34 CrossRef Medline
- Santos P, Peck KK, Arevalo-Perez J, et al. **T1-weighted dynamic contrast-enhanced MR perfusion imaging characterizes tumor response to radiation therapy in chordoma.** *AJNR Am J Neuroradiol* 2017;38:2210–16 CrossRef Medline
- De Coninck T, Jans L, Sys G, et al. **Dynamic contrast-enhanced MR imaging for differentiation between enchondroma and chondrosarcoma.** *Eur Radiol* 2013;23:3140–52 CrossRef Medline
- Morales KA, Arevalo-Perez J, Peck KK, et al. **Differentiating atypical hemangiomas and metastatic vertebral lesions: the role of T1-weighted dynamic contrast-enhanced MRI.** *AJNR Am J Neuroradiol* 2018;39:968–73 CrossRef Medline
- Saha A, Peck KK, Lis E, et al. **Magnetic resonance perfusion characteristics of hypervascular renal and hypovascular prostate spinal metastases: clinical utilities and implications.** *Spine (Phila Pa 1976)* 2014;39:E1433–40 CrossRef Medline

Duct-like Recess in the Infundibular Portion of Third Ventricle Craniopharyngiomas: An MRI Sign Identifying the Papillary Type

J.M. Pascual, R. Carrasco, L. Barrios, and R. Prieto



ABSTRACT

BACKGROUND AND PURPOSE: Papillary craniopharyngiomas (PCPs) are particularly challenging lesions requiring accurate diagnosis to plan the best therapy. Our aim was to define a narrow duct-like recess identified on MR imaging at the base of papillary craniopharyngiomas with a strict third ventricle location.

MATERIALS AND METHODS: A duct-like recess at the infundibular portion of craniopharyngiomas was observed on conventional T1WI and T2WI in 3 strict third ventricle papillary craniopharyngiomas in our craniopharyngioma series ($n = 125$). We systematically investigated this finding on the MR imaging of 2582 craniopharyngiomas and 10 other categories of third ventricle tumors ($n = 690$) published in the modern era (1986–2020). The diagnostic value and significance of this finding are addressed.

RESULTS: The duct-like recess was recognized in 52 papillary craniopharyngiomas, including 3 of our own cases, as a narrow canal-shaped cavity invaginated at the tumor undersurface, just behind the optic chiasm. This structure largely involves papillary craniopharyngiomas with a strict third ventricle topography (96%), follows the same diagonal trajectory as the pituitary stalk, and finishes at a closed end. The duct-like recess sign identifies the papillary craniopharyngioma type with a specificity of 100% and a sensitivity of 38% in the overall craniopharyngioma population. This finding can also establish the strictly intra-third ventricle location of the lesion with a 90% specificity and 33% sensitivity. These recesses appear as hypointense circular spots on axial/coronal T1WI and T2WI. Their content apparently corresponds to CSF freely flowing within the suprasellar cistern.

CONCLUSIONS: The presence of a duct-like recess at the infundibular portion of a third ventricle tumor represents a distinctive hallmark of papillary craniopharyngiomas that can be used as a simple MR imaging sign to reliably diagnose these lesions.

ABBREVIATIONS: ACP = adamantinomatous craniopharyngioma; CP = craniopharyngioma; CP-DR = CPs with a basal duct-like recess; CP-nDR = CPs without a basal duct-like recess; DR = duct-like recess; PCP = papillary craniopharyngioma; PS = pituitary stalk; 3V = third ventricle; 3VF = third ventricle floor

Papillary craniopharyngiomas (PCPs) comprise >10%–20% of all craniopharyngioma (CP) cases, affect almost exclusively adult patients, and typically grow within the third ventricle (3V) as purely solid masses or unilocular cysts lined with papillomatous excrescences of stratified squamous epithelium.¹ From a surgical viewpoint, PCPs are a particularly challenging group of lesions owing to their intra-3V location and tenacious attachment to the infundibulotuberal region of the hypothalamus.² The discovery of *BRAF* V600E

oncogene mutations specific to this CP type has prompted the use of targeted chemotherapies with preliminary, successful results.³ Therefore, an accurate preoperative diagnosis of PCPs is essential for planning a proper surgical approach, or, alternatively, choosing nonsurgical therapies such as radiosurgery or chemotherapy.

During the past decade, our group has systematically analyzed the most pertinent information from conventional MR imaging to make reliable preoperative diagnoses of the PCP variant and to accurately define the tumor topography and adherence.^{4,5} After thoroughly examining MR images of >3000 CP records, we have identified some specific morphologic features predictive of the papillary type, such as tumor consistency, anatomic appearance of the pituitary stalk (PS), and the position of the hypothalamus relative to the tumor.⁵ In the present work, we describe and characterize an additional specific MR imaging sign identified in a subgroup of PCPs primarily developed within the 3V: a duct-like recess (DR) extending from the undersurface of the lesion toward its center and connected to the suprasellar cistern. This MR imaging finding,

Received April 8, 2022; accepted after revision June 20.

From the Department of Neurosurgery (J.M.P.), La Princesa University Hospital, Madrid, Spain; Department of Neurosurgery (R.C.), Ramón y Cajal University Hospital, Madrid, Spain; Statistics Department (L.B.), Computing Center, Spanish National Research Council, Madrid, Spain; and Department of Neurosurgery (R.P.), Puerta de Hierro University Hospital, Madrid, Spain.

Please address correspondence to José María Pascual, MD, PhD, Department of Neurosurgery, La Princesa University Hospital, C/Diego de León 62, 28006-Madrid, Spain; e-mail: jmpasncj@hotmail.com



Indicates article with online supplemental data.

<http://dx.doi.org/10.3174/ajnr.A7602>

clearly distinguishable on midsagittal and coronal transinfundibular T1WI and T2WI, has never been observed in adamantinomatous CPs (ACPs) or in other pathologic categories of 3V tumors. Consequently, we consider that it constitutes a distinctive sign of the PCP type. The present work morphologically and neuroradiologically characterizes this CP finding and analyzes its potential diagnostic significance.

MATERIALS AND METHODS

DR Sign in Craniopharyngiomas: MR Imaging Definition

The DR is defined as a narrow and hollow duct-like cavity invaginated at the infundibular portion of a 3V tumor that follows a diagonal trajectory toward the center of the lesion through its midsagittal plane. DRs have a variable length, and they are closed at the top end and open at the bottom and show the same homogeneous hypointense signal on T1WI and hyperintensity on T2WI sequences as CSF, which can apparently flow freely between the suprasellar cistern and these tubular structures.

Case Series Generation and Inclusion Criteria

We conducted a systematic review of the well-described CP cases reported in the MR imaging era, from 1984 to June 2020 ($n = 3352$), according to the Preferred Reporting Items for Systematic Reviews and Meta-Analyses (PRISMA) criteria (Online Supplemental Data). This study involved CPs reported in journals from the PubMed and MEDLINE databases ($n = 2036$) and CPs discussed either in specialized monographs ($n = 796$) or in professional Web pages ($n = 520$) focused on the treatment of pituitary/3V tumors. Likewise, an exhaustive search was made for primarily 3V tumors different from CPs published between 1984–2020 ($n = 690$), including 10 major pathologic categories detailed in the Online Supplemental Data. Finally, the medical charts and MR imaging studies of CPs treated from 1994 to 2020 in the authors' departments of neurosurgery ($n = 125$; 106 ACPs/19 PCPs) were retrospectively examined.

From these databases, 2582 well-depicted CPs were deemed eligible for neuroradiologic assessment, among them 2426 ACPs and 156 PCPs, according to the following criteria: 1) Craniopharyngioma diagnosis was confirmed pathologically (CP histology verified in 81% of ACPs and 77% of PCPs, the remaining 23% showing MR imaging macroscopic features typical of the papillary type); 2) Preoperative midsagittal and/or coronal transinfundibular MR images of the lesion obtained with T1WI and/or T2WI sequences were given in the scientific report/Web page/clinical chart showing the presence of a DR at the tumor base; 3) A brief description of epidemiologic/clinical/pathologic and/or surgical findings of the case was provided. On the basis of these criteria, a collection of 52 CPs with a basal duct-like recess reported from 1994 to 2020 was finally included in this cohort, named the CPs with basal duct-like recess cohort (CP-DR).

Assessment of Histologic and Topographic Diagnostic Accuracy of the DR Sign

With the aim of ascertaining the diagnostic accuracy of the DR sign identified on MR imaging to establish the papillary histology and the strict 3V CP topography, we tested the specificity and sensitivity of this finding in the cohort of 200 CPs used by our group in 2017 to analyze the MR imaging reliability for the definition of

the CP topography (CP MR imaging 200 control cohort).⁵ This series, which formed part of the data bank of 2582 CPs examined for the present study, included 14 CP-DR cases and had the advantage of having a balanced distribution of CP histologies (163 ACPs/37 PCPs), patient ages (148 adults/37 pediatric cases), and CP topographies (47% sellar/suprasellar; 32% infundibulotuberal; 21% strict 3V), all of these rates being similar to those observed in the overall CP population.

In addition, the diagnostic reliability of the DR MR imaging sign for establishing the papillary type was evaluated in a cohort of 106 strictly 3V CPs (CP strict 3V 106 control cohort) obtained from our recent review of the CP cases reported with a verified strictly 3V topography.⁶ This cohort, formed of 74 PCPs and 32 ACPs, included 49 CP-DR cases. Similarly, the DR MR imaging sign specificity and sensitivity for accurately classifying the strictly 3V tumor location were tested in a large cohort of 142 papillary CPs (PCP 142 control cohort) diagnosed with MR imaging and obtained from our recent comprehensive research on 350 well-described PCPs from the medical literature, which included 50 CP-DR cases.¹

Comparison Cohort of CPs without Basal DR

To differentiate the clinicopathologic and MR imaging features of the tumors in the CP-DR cohort, formed of only adult patients, from the general population of adult CPs, a comparison cohort of adult CPs without a basal DR was created (CP-nDR). This comparison cohort formed part of the 2582 CP data bank eligible for this study and was gathered from our prior studies analyzing the MR imaging signs defining CP topography and adherence by arbitrarily selecting the consecutive 52 well-described CPs without a DR published in the most recent period (2004–2016).^{4,7} These cases met the same inclusion criteria as those defined for the CP-DR, except for the presence of a DR. Systematic bivariate analyses were then performed for clinicopathologic and MR imaging characteristics differentiating the CP-DR and the CP-nDR cohorts.

RESULTS

DR in Papillary CPs: MR Imaging Characteristics

The Online Supplemental Data present the main clinicopathologic and neuroradiologic features of the 52 CPs with a DR identified on preoperative MR images in the medical literature, including the 3 new cases from our own series. The DR can be observed on routine T1WI and T2WI midsagittal sections as a narrow hollow canal-shaped structure with a diagonal upward course along the midsagittal plane of the CP (Fig 1). All recesses follow the same diagonal trajectory as the PS and are open at the tumor undersurface, just at the area of the third ventricle floor (3VF), where the PS joins the infundibulum, connecting the recess cavity with the suprasellar or chiasmatic cistern. All DRs appear homogeneously hypointense on T1WI (Figs 1) and homogeneously hyperintense on T2WI (Fig 4B), with an intensity identical to that of the CSF, a sign indicating that CSF may flow freely into and out of the DR.

According to their length, DRs can be classified into 2 major types: long DRs (Fig 1A₁), with a length ranging between 10 and 15 mm ($n = 33$, 63.5%) and short DRs (Fig 4C), which invaginate into the tumor ≤ 5 mm ($n = 19$, 36.5%). No DR enhancement

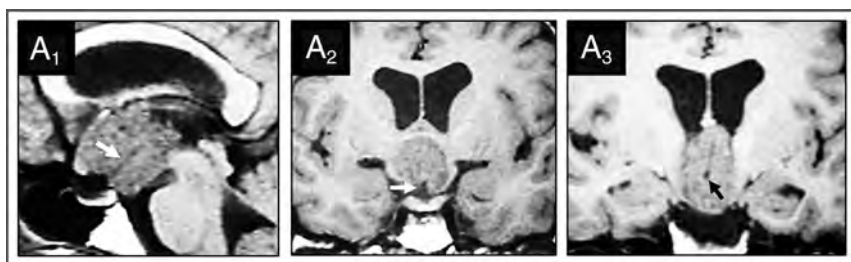


FIG 1. Basal recess in strictly 3V CPs of the papillary type: MR imaging evidence in 1 case identified from our series. Case 1 (Online Supplemental Data): This papillary CP was diagnosed in a 34-year-old woman with headaches, Fröhlich syndrome, poikilothermy, and emotional lability. Preoperative T1WI shows this strictly 3V homogeneously isointense lesion above the intact 3VF, with papillomatous excrescences at its surface. On the midsagittal (A_1) and coronal (A_2 , A_3) scans, a long basal recess can be identified as a tube-like hypointense structure extending from the suprasellar cistern to the center of the tumor (white arrows, A_1 and A_2 ; black arrow, A_3).

after gadolinium administration was observed in any of the cases, nor were any recognizable vascular structures identified, except in 1 case (with gadolinium). On coronal/axial MR imaging sections, all recesses have a circular outline and are engulfed by the central bulk of the tumor (Fig 1A₃). From all these MR imaging data, the recesses seem to represent tubular invaginations of the 3VF infundibular region into the base of 3V CPs.

CP-DR Cohort: MR Imaging Characterization

The Online Supplemental Data show the categorization of the main clinicopathologic, neuroradiologic, and surgical variables analyzed in the CP-DR cohort. Contrary to the balanced sex division and age distribution in pediatric/adult cases in the general CP population, all CP-DR cases occurred in patients older than 20 years of age, affecting mostly men (73%) (Fig 2A). Clinically, headache was the most frequent symptom (75%), and it showed an almost perfect correlation with the presence of obstructive hydrocephalus (71%). Notably, the rates of psychiatric disturbances (58%) and other hypothalamic alterations (20.5%) were markedly high, in accordance with the expansion of these lesions within the 3V, causing mass effect on the hypothalamus. Conversely, visual defects and endocrine deficits due to hypopituitarism were described in a relatively small number of patients, given the preserved anatomic integrity of the optic chiasm and PS in many cases.

Morphologically, we differentiated 2 main tumor patterns: 1) the most common group of pure solid and round lesions, homogeneously isointense on T1WI, showing homogeneous gadolinium enhancement (90%); and 2) the less frequent subgroup of unilocular cystic lesions with a cauliflower-like solid nodule at the base of the cyst (Fig 2C). Both macroscopic architectures markedly differed from the multilocular, solid-cystic consistency usually found in ACPs and were certainly influenced by the papillary histology and the intra-3V development of all CP-DRs (Fig 2B, -D). Histologic confirmation of the papillary type was provided in all except 3 cases, which showed on MR imaging a gross berrylike morphology with papillary protrusions at the tumor surface, identical to all the other counterparts with a verified histology.

Diagnostic Accuracy of the DR Sign to Define the CP Histology and Topography

The DR occurred in 16% of PCPs in our own series ($n = 125$), a rate that increased to 27% when considering only the PCPs with a strict 3V topography. The DR was also present in 33% of the 156 PCPs with available MR imaging examined from the literature for this study. The specificity of the DR sign to define the papillary histology on MR imaging was 100% in both the CP MR imaging 200 and the CP strict 106 control cohorts. This finding validates the DR as a hallmark of PCPs. The sensitivity of this sign was 37.8% when

tested in the CP MR imaging 200 control cohort and 66% in the CP strict 106 control cohort. This means that the finding of the DR alone permits the accurate diagnosis of the papillary histology in about 38% of PCPs spanning all kinds of topographies and in two-thirds of the PCPs with a strict 3V topography.

Concerning the definition of CP topography, the DR sign specificity for establishing the strictly 3V CP location was 100% in the CP MR imaging 200 control cohort and 90% in the CP papillary 142 control cohort, whereas the sensitivity rates for this strict 3V topography were 33.3% and 53%, respectively. This finding means that the DR sign by itself reliably allows the diagnosis of the strict 3V topography in one-third of CPs with such a topography and in more than half of all PCPs.

Pathologic and Topographic Differentiation of CPs with a Basal DR

The Table shows a comparative analysis of the clinical and anatomic features that best differentiate the CP-DR cohort, formed exclusively of adult patients, and the CP-nDR comparison cohort, representative of the adult CP population. The essential pathologic characteristic differentiating both cohorts was the diagnosis of the papillary variant in 100% of the cases in the former (Fig 2B). This papillary architecture definitely influenced the predominant solid tumor consistency (Fig 2C) and lack of calcifications in CP-DR tumors. Second, most CP-DR cases primarily developed within the 3V, above an intact 3VF. This is an exceedingly rare topography among CPs, even among adult patients (Fig 2D). Such a pure intra-3V CP location determines the anatomic intactness of the pituitary-hypothalamic axis structures confirmed on preoperative MR imaging in many patients with CP-DR, in particular an anatomically intact PS in 84.5% of strictly 3V PCPs (Fig 3A). The position of the hypothalamus around the lower portion of the tumor on coronal transinfundibular MR images, observed in 74.5% of strict 3V cases, was also a defining feature of the CP-DR cohort (Fig 3C). However, even though these MR imaging signs strongly point to a strictly 3V CP location, the complete integrity of the 3VF beneath the tumor could only be confirmed in 61% of cases on preoperative MR imaging (Fig 3B). Notably, the identification of a DR yielded better results than all

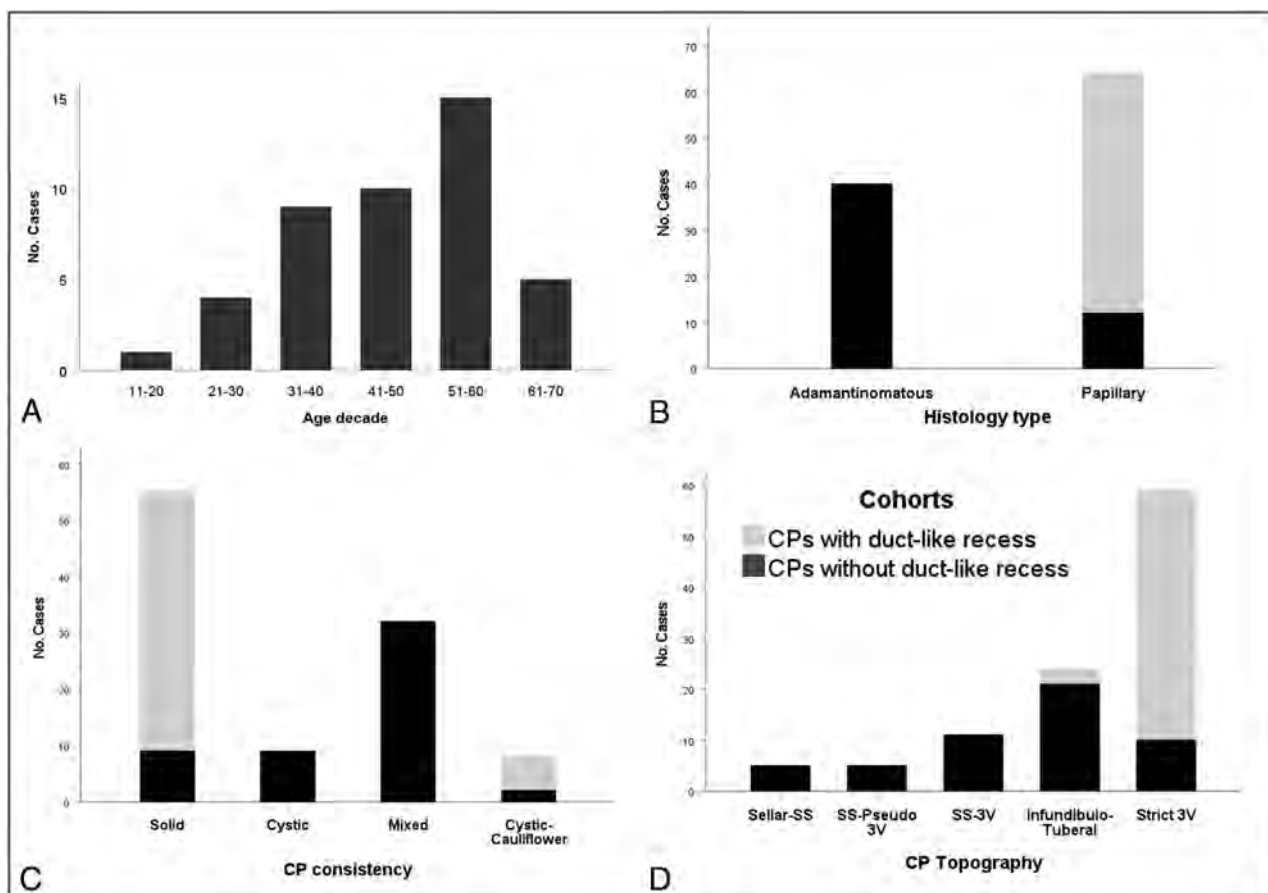


FIG 2. Epidemiologic, pathologic, and topographic characterization of the 52-craniopharyngioma cohort with a basal recess (CP-DR cohort). A, Bar chart shows the age distribution. Observe that no cases were diagnosed in the first decade. About 65% of cases occurred in adults between 30 and 60 years of age. B, Stacked bar chart comparing the distribution of histologic CP types between the CP-DR and the CP-nDR cohorts. All tumors with a DR belonged to the squamous-papillary type, only diagnosed in 23% of CPs without a DR in the adult CP population ($P < .001$). C, Stacked bar graph comparing tumor consistencies. Most CP-DR tumors had a homogeneous solid consistency (90%), whereas a mixed solid-cystic pattern was predominant among ACPs without a DR (61.5%) ($P < .001$). D, Topographic distribution of tumors. More than 80% of papillary CPs with a DR corresponded to strictly 3V tumors located above an anatomically intact 3VF. No CP-DR lesions originated at the sellar or suprasellar compartments below the 3VF ($P < .001$).

these aforementioned MR imaging signs to achieve an accurate topographic diagnosis of a strictly 3V CP in 96% of cases.

DISCUSSION

Basal DR: A Hallmark of Strictly 3V CPs of the Papillary Type

In 1990, Fukushima et al⁸ first noticed a linear hypointense zone on the midsagittal T1WI of an intraventricular PCP (Fig 4A₁ and A₂). A more detailed description of a similar tube-shaped basal hypointensity in a 3V PCP was provided by Urbach et al,⁹ who pointed out that it could represent a diagnostic sign specific to the solid papillary CP variant. No additional insights about the nature or diagnostic significance of this MR imaging sign could be gained from the medical literature. The papillary variant constitutes a minority of CPs (10%–20% of cases), usually developing at the infundibulum or entirely within the 3V.^{1,6} Radical excision of 3V PCPs is commonly associated with a high surgical risk, owing to the mass effect on the hypothalamus and tight tumor attachments to the 3VF.^{2,7} In addition, many PCPs affect elderly patients in poor clinical condition, precluding any complex

neurosurgical procedure. Consequently, achieving a correct preoperative diagnosis of 3V PCPs is essential to plan the most judicious treatment to diminish the risk of surgical hypothalamic injury.¹⁰

A papillary histology can be suspected on preoperative MR imaging mainly by assessing some CP features, such as a spherical shape, a homogeneous solid consistency, and a lack of calcifications within the tumor.^{4,5,10,11} The strictly 3V topography can be even more difficult to ascertain because CP boundaries are usually fused to the 3VF, which can become an unrecognizable structure on preoperative MR imaging.^{4,6,10} Moreover, many other strictly 3V tumors such as chordoid gliomas, astrocytomas, germinomas, and ependymomas are round with a solid consistency similar to features of PCPs.¹² Therefore, verifying a duct-like recess at the base of a 3V tumor represents a novel, valuable diagnostic sign, permitting not only the pathologic diagnosis of a PCP but also a reliable definition of a strictly 3V topography in about 90% of cases.

A DR in a CP represents a morphologic feature 100% specific to the papillary type, with the sensitivity of this finding ranging between 33% in the global PCP population and 66% in the

Differential characteristics between the CP-DR on MR imaging and a cohort of adults with CPs without such a structure

CP Characteristics	Categories	CP-DR (n = 52)	Adult CP-nDR (n = 52)	P Value
Sex	Male	73%	50%	.012
	Female	27%	50%	
Hydrocephalus	Present	71%	25.5%	<.001
Headache	Present	75%	49%	.01
Visual deficits	Present	51%	73.5%	.032
Endocrine deficits	Present	38.5%	39%	NS
Hypothalamus disturbances	Present	20.5%	0%	.001
Mental alterations	Present	58%	12%	<.001
HTIC Sd	Present	72%	41%	.002
Hypothalamic Sd	Present	67.5%	26.5%	<.001
Tumor histology	Squamous-papillary	100%	23%	<.001
	Adamantinomatous	0%	77%	
Tumor topography	Sellar/suprasellar	0%	40%	<.001
	Infundibulo-tuberal	4%	41%	
	Strictly 3V	96%	19%	
	Present nodular	0%	58%	
Tumor consistency	Pure solid	90%	17%	<.001
	Cystic-cauliflower	10%	4%	
	Pure cystic	0%	17.5%	
	Mixed solid-cystic	0%	61.5%	
Sella turcica	Occupied by tumor	0%	31%	<.001
	Intact	84.5%	15.5%	
PS status	Lower portion visible	15.5%	27%	<.001
	Infiltrated/invaded	0%	57.5%	
	Tumor-free	44%	31%	
	Partially occupied	54%	32.5%	
Suprasellar cistern status	Wholly occupied	2%	36.5%	.001
	Around CP lower third	74.5%	13.5%	
	Around CP middle third	26.5%	60%	
	Around CP upper third	0%	26.5%	
3VF status	Visible intact	61%	6%	<.001
	Only MBs visible	27.5%	33%	
	Not visible	11.5%	61%	

Note:—HTIC indicates high intracranial pressure; MBs, mammillary bodies; NS, not significant; Sd, syndrome.

subpopulation of CPs with a strict 3V topography. The papillary variant represents between 10% and 20% of all CP cases, but because this type almost exclusively affects adult patients, the PCP rate can reach a peak of >30% in the age interval between 30 and 80 years, as observed in the recent study by Momin et al.¹³ Given the CP incidence of between 1.3 and 1.6 cases/million people observed in the United States, about 600 new cases/year, the identification of the DR sign alone on a preoperative MR imaging could confirm the certain diagnosis of a PCP in approximately 45 tumors from the pool of around 140 PCPs diagnosed every year in the United States.¹³ Moreover, the DR is an invaluable MR imaging sign to establish the strict 3V location of the lesion, with a 90% specificity and a sensitivity ranging between 33% in the overall CP population and 53% in the subpopulation of PCPs. This topographic information is of the utmost importance for neurosurgeons to plan the proper surgical approach for lesions known to be wholly confined within the 3V.

CP-DR Cohort: Differences from the General Adult CP Population

The unique pathologic characteristics of the CP-DR cohort, formed exclusively of PCPs with a 3V topography, contrasted markedly with those observed in the overall population of adult CP cases,

which largely consist of ACPs developed either beneath the 3V (sellar/suprasellar, 60%) or within the 3VF itself (infundibulo-tuberal, 40%) (Table). These crucial differences definitely influenced the significant morphologic and clinical discrepancies between both cohorts. Symptoms of hypothalamic impairment, including psychiatric and cognitive disturbances, were prominent among CP-DR lesions, which caused severe compression and edema in the hypothalamic region.^{1,2} By contrast, visual disturbances due to optic chiasm stretching, usually caused CPs originating beneath the 3V, predominated in the CP-nDR cohort. The prevailing 3V topography among CP-DR lesions also determined the high rate of obstructive hydrocephalus and the round shape and solid consistency of these PCPs, tumor features that differed from the typical solid-cystic multilobulated morphology observed among ACPs. Finally, PCP-DR tumors affected male patients more frequently, a tendency not present among ACPs, plausibly attributable to genetic causes and deserving further investigation.

DR: A Sign Differentiating PCPs from Other 3V Tumors

The identification on conventional MR imaging of a hollow recess at the infundibular midline region of a solid 3V tumor distinguishes a particular subpopulation of 3V PCPs. We were able to confirm this finding after methodically reviewing the MR images displayed in a total of 2582 CPs. The DR was never observed in

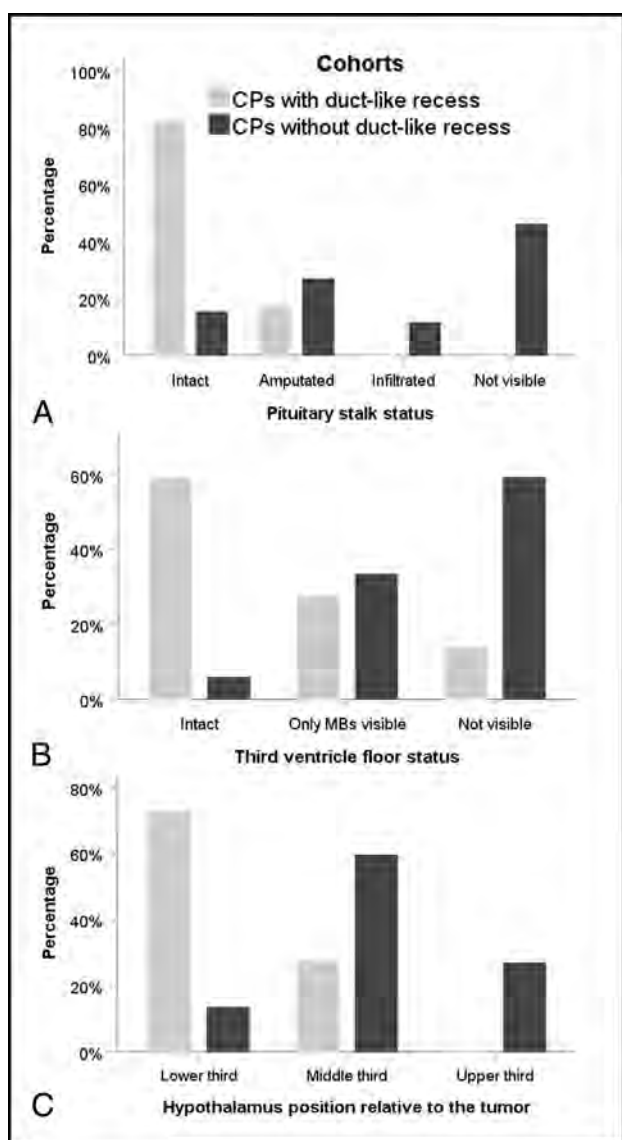


FIG 3. MR imaging characterization of the anatomic relationships between the tumor and the 3V in CPs with or without a DR. **A**, PS status. Among the lesions in the CP-DR cohort, the PS is observed intact under the basal recess (85%), whereas it is wholly or partially engulfed by the tumor in about 85% of adults with CPs without a DR ($P < .001$). **B**, Anatomic status of the 3VF. An intact 3VF was observed in 60% of CPs with a DR, whereas this structure cannot usually be distinguished from the tumor boundaries in CPs without a DR ($P < .001$). **C**, Bar graph shows the distribution of hypothalamus positions relative to the tumor. In almost 75% of papillary CPs with a DR, the hypothalamus is located around the lower third of the lesion. In contrast, it is observed encircling its central portion in 60% of adult CP cases without a DR ($P < .001$). MBs indicates mamillary bodies.

ACPs nor among PCPs growing beneath the 3VF. Very important, after systematically reviewing the MR images of >500 3V tumors of various pathologic diagnoses other than CP, we were unable to find any similar duct-like structures (Fig 1). Among originally developing 3V tumors, neither chordoid gliomas ($n = 128$) nor ependymomas ($n = 116$) showed, in any of the reports examined, a DR structure resembling those observed in the PCPs of the present cohort, nor in any of the secondary 3V tumor categories

investigated, such as germinomas ($n = 73$), lymphomas ($n = 58$), epidermoids ($n = 36$), and teratomas ($n = 66$), could a similar tubular recess be recognized. This finding suggests the existence of a pathogenetic mechanism specific for the presence of a DR in 3V PCPs.

The category of 3V choroid plexus papillomas ($n = 84$), lesions with a macroscopic papillary architecture mimicking PCPs, may show multiple fissures and crevices somewhat resembling the DR.¹⁴ The DR in PCPs could then be interpreted as a large crack or fissure formed by the natural process of dehiscence of the squamous epithelium that gives these lesions a pseudopapillary appearance.¹ However, small cracks and fissures are randomly present all around the tumor surface in both choroid plexus papillomas and PCPs, whereas the DR shows a consistent tubular shape and a constant position at the PCP midline undersurface, following the same course as the PS, evidence that goes against this view. Rather, the morphologic DR characteristics suggest a pathogenetic link between the intra-3V location of CP precursors and the embryogenesis of the pituitary-hypothalamic axis.

DR in 3V PCPs: Anatomic Clues Pointing toward an Embryologic Pathogenesis

The hollow, duct-like cavity identified in 3V PCPs in this study can also be defined as a tumor recess, because it presumably corresponds to the intratumor extension of the suprasellar (subarachnoid) space, filled with CSF. Anatomically, the 3VF is shaped like 2 recesses, the chiasmatic recess, a V-shaped 3V extension above the optic chiasm, and the infundibular recess, the funnel-shaped 3V downward extension into the PS.¹⁵ This anatomy raises the question as to whether the DR may represent a residual, patent portion of the infundibular recess invaginated within the lesion. Such an interpretation seems highly implausible because tumors expanding within the 3V, including CPs, usually compress the 3VF downward and obliterate the 3V recesses rather than filling in these spaces.⁶ Alternatively, the DR could be interpreted as a fibrovascular core providing the blood supply to the tumor. However, the basal stemlike fibrovascular attachment feeding 3V PCPs has a solid structure, not a hollow one.¹ No blood vessels within the DR could be identified on the MR images available in this cohort, with the exception of the case by Sartoretti-Sheffer et al,¹ in which a narrow vessel running along the anterior aspect of the PS penetrates the DR.¹⁶ Instead, the duct-like shape of the CP recess, its variable length, and, above all, its diagonal trajectory following the same course as the PS axis suggest that the DR formation could be linked to the embryologic process of the pituitary axis development from the Rathke pouch.

Most PCPs with a basal recess have a strict 3V location. How a tumor apparently originating from remnants of an extraventricular structure such as the Rathke pouch could develop exclusively within the 3V, a portion of the closed neural tube, has been a source of puzzlement since strictly 3V CPs were first identified at postmortem examination.¹⁷ In the 1980s, Ciric and Cozzens¹⁸ theorized that strictly 3V CPs could originate from the Rathke pouch cells if this embryonic structure merged with the 3VF before the pia mater was formed.¹⁵ Indeed, a close attachment between the ventral neural tube and the roof of an embryo's primitive mouth occurs at the earliest stages of pituitary gland organogenesis, and

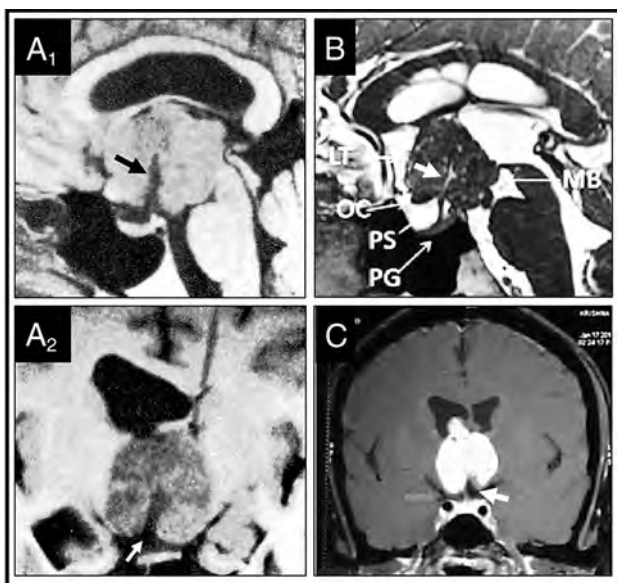


FIG 4. Basal recess at the infundibular portion of 3V papillary craniopharyngiomas. MR imaging characterization in seminal cases from the medical literature (A₁–A₂). Diverticulum-like recess at the base of a strict 3V papillary CP identified on preoperative MR imaging (Online Supplemental Data). On the midsagittal T1WI (A₁), the hypointense recess (black arrowhead) is open at the suprasellar cistern and extends to the tumor center, following the same trajectory as the PS. The coronal-transinfundibular MR image (A₂) shows the hypointense signal of the recess identical to CSF, indicating free passageway of CSF between the suprasellar cistern and the recess and the rounded dead end of the recess at the tumor center. Reproduced with permission from the Fukushima et al.⁸ B, Duct-like long-recess type in a strict papillary CP (Online Supplemental Data). This midsagittal T2WI shows the hyperintense signal of the duct, identical to that in the CSF (white arrow). Reproduced with permission Gu et al.²¹ C, Coronal-transinfundibular T1WI of a short-type basal DR in a strict 3V PCP (Online Supplemental Data). Note the isointense rim of the 3V floor covering the undersurface of this solid homogeneously gadolinium-enhancing tumor and how the 3VF invaginates at the midline of the basal pole of the CP to form the recess (white arrow). Reproduced with permission from Rambarki and Rajesh.²² PG indicates pituitary gland; MB, mammillary body; OC, optic chiasm.

this union could explain the inclusion of CP ectodermal cell precursors within the 3V.¹⁸ The presence of a DR at the base of 3V PCPs supports a dysembryogenetic origin of this histologic variant, linking PCPs with the developing course of stomodeal precursors moving with the Rathke pouch along the migratory pathway followed by the craniopharyngeal canal.¹⁹ The DR extending upward into the 3V can be judged to be an equivalent of the duct-like downward passageway between the 3V and the sella turcica, known as a persisting embryonal infundibular recess, likewise thought to be the result of a failed obliteration of the infundibular recess during pituitary organogenesis.²⁰

CONCLUSIONS

The presence of a DR at the infundibular portion of a solid 3V tumor represents an MR imaging sign diagnostic of the papillary CP type with a specificity of 100% and a sensitivity of 33% in the global population of PCPs. This finding is also a reliable MR imaging sign for establishing the strictly 3V topography, with a

specificity of 90% and a sensitivity of 33% in the overall CP population. The DR can be easily identified on midsagittal and coronal T1WI and T2WI as a hypointense canal-shaped signal of variable length. No similar duct-like structure has ever been observed in any other 3V tumor category. Therefore, the DR represents an invaluable sign for accurately diagnosing strictly 3V papillary CPs.

ACKNOWLEDGMENTS

The authors wish to especially thank Crystal Smith and Liliya Gusakova, Reference Librarians of the National Library of Medicine, National Institutes of Health (Bethesda, Maryland) for their kind assistance during the process of searching and retrieving articles and monographs used in this study. We are also grateful to Melissa Grafe, Librarian for Medical History Library, Yale University (New Haven, Connecticut) and to Lucretia MacLure, Jack Eckert, and the staff at the Francis A. Countway Library of Medicine at Harvard Medical School (Boston, Massachusetts) for their invaluable help in obtaining some of the original research material used for this study. Finally, we are grateful to George Hamilton for his critical review of the language and style of the manuscript.

Disclosure forms provided by the authors are available with the full text and PDF of this article at www.ajnr.org.

REFERENCES

- Prieto R, Barrios L, Pascual JM. **Papillary craniopharyngioma: a type of tumor primarily impairing the hypothalamus: a comprehensive anatomo-clinical characterization of 350 well-described cases.** *Neuroendocrinology* 2021 Dec 28. [Epub ahead of print] CrossRef Medline
- Pascual JM, Prieto R, Rosdolsky M. **Craniopharyngiomas primarily affecting the hypothalamus.** *Handb Clin Neurol* 2021;181:75–115 CrossRef Medline
- Juratli TA, Jones PS, Wang N, et al. **Targeted treatment of papillary craniopharyngiomas harboring BRAF 600 mutations.** *Cancer* 2019;125:2910–14 CrossRef Medline
- Pascual JM, Prieto R, Carrasco R, et al. **Displacement of mammillary bodies by craniopharyngiomas involving the third ventricle: surgical-MRI correlation and use in topographical diagnosis.** *JNS* 2013;119:381–405 CrossRef Medline
- Prieto R, Pascual JM, Barrios L. **Topographic diagnosis of craniopharyngiomas: the accuracy of MRI findings observed on conventional T1 and T2 images.** *AJNR Am J Neuroradiol* 2017;38:2073–80 CrossRef Medline
- Prieto R, Barrios L, Pascual JM. **Strictly third ventricle craniopharyngiomas: pathological verification, anatomo-clinical characterization and surgical results from a comprehensive overview of 245 cases.** *Neurosurg Rev* 2022;45:375–94 CrossRef Medline
- Prieto R, Pascual JM, Rosdolsky M, et al. **Craniopharyngioma adherence: a comprehensive topographical categorization and outcome-related risk stratification model based on the methodical examination of 500 tumors.** *Neurosurg Focus* 2016;41:E13 CrossRef Medline
- Fukushima T, Hirakawa K, Kimura M, et al. **Intraventricular craniopharyngioma: its characteristics in magnetic resonance imaging and successful total removal.** *Surg Neurol* 1990;33:22–27 CrossRef Medline
- Urbach H, Behrens E, von Deimling A, et al. **Solides Kraniopharyngiom im III: Ventrikel-Differential-diagnostische Aspekte [in German].** *Aktuelle Radiol* 1998;8:95–97 Medline
- Pascual JM, Prieto R, Castro-Dufourny I, et al. **Topographic diagnosis of papillary craniopharyngiomas: the need for an accurate MRI-**

- surgical correlation.** *AJNR Am J Neuroradiol* 2015;36:E55–56 CrossRef Medline
11. Yue Q, Yu Y, Shi Z, et al. **Prediction of BRAF mutation status of craniopharyngioma using magnetic resonance imaging features.** *J Neurosurg* 2018;129:27–34 CrossRef Medline
 12. Glastonbury CM, Osborn AG, Salzman KL. **Masses and malformations of the third ventricle: normal anatomic relationships and differential diagnoses.** *Radiographics* 2011;31:1889–1905 CrossRef Medline
 13. Momin AA, Recinos MA, Cioffi G, et al. **Descriptive epidemiology of craniopharyngiomas in the United States.** *Pituitary* 2021;24:517–22 CrossRef Medline
 14. Buckle C, Smith JK. **Choroid plexus papilloma of the third ventricle.** *Pediatr Radiol* 2007;37:725 CrossRef Medline
 15. Tsutsumi S, Hori M, Ono H, et al. **The infundibular recess passes through the entire pituitary stalk.** *Clin Neuroradiol* 2016;26:465–69 CrossRef Medline
 16. Sartoretti-Schefer S, Wichmann W, Aguzzi A, et al. **MR differentiation of adamantinomatous and squamous-papillary craniopharyngiomas.** *AJNR Am J Neuroradiol* 1997;18:77–87 CrossRef Medline
 17. Pascual JM, Rosdolsky M, Prieto R, et al. **Jakob Erdheim (1874–1937): father of hypophyseal-duct tumors (craniopharyngiomas).** *Virchows Arch* 2015;467:459–69 CrossRef Medline
 18. Ciric IS, Cozzens JW. **Craniopharyngiomas: transsphenoidal method of approach: for the virtuoso only?** *Clin Neurosurg* 1980;27:169–87 CrossRef Medline
 19. Kollias SS, Ball WS, Prenger EC. **Review of the embryologic development of the pituitary gland and report of a case with hypophyseal duplication detected by MRI.** *Neuroradiology* 1995;37:3–12 CrossRef Medline
 20. Steno A, Popp AJ, Wolfsberger S, et al. **Persisting embryonal infundibular recess.** *J Neurosurg* 2009;110:359–62 CrossRef Medline
 21. Gu Y, Zhang X, Hu F, et al. **Suprachiasmal translamina terminalis corridor used in endoscopic endonasal approach for resecting third ventricular craniopharyngioma.** *J Neurosurg* 2015;122:1166–72 CrossRef Medline
 22. Rambarki O, Rajesh A. **Third ventricular craniopharyngioma.** *Neurol India* 2016;64:834–35 CrossRef Medline

Diffuse Basisphenoid Enhancement: Possible Differentiating Feature for Granulomatous Hypophysitis

I.T. Mark and C.M. Glastonbury

ABSTRACT

BACKGROUND AND PURPOSE: Granulomatous hypophysitis is a rare inflammatory condition of the pituitary gland with an imaging appearance that can overlap with that of pituitary adenoma. Differentiating the two before surgical resection can have important treatment implications. The purpose of our study was to determine whether it was possible to differentiate between granulomatous hypophysitis and pituitary adenoma on the basis of diffuse enhancing infrasellar basisphenoid bone marrow.

MATERIALS AND METHODS: We present 3 cases, initially thought to be pituitary adenomas, that were pathology-proved granulomatous hypophysitis. The preoperative MR images were reviewed for diffuse, enhancing infrasellar basisphenoid bone marrow. For comparison, we reviewed 100 cases of pathology-proved pituitary adenoma for the same finding. Additionally, imaging findings including the sphenoid sinus pneumatization pattern, clinical history, laboratory values, and pathology results were reviewed.

RESULTS: All 3 cases of granulomatous hypophysitis had diffuse enhancing infrasellar basisphenoid bone marrow. Conversely, this was not seen in any of the 100 pituitary adenomas. The patients with granulomatous hypophysitis were all women. Two patients had idiopathic granulomatous hypophysitis, and 1 had secondary granulomatous hypophysitis with sarcoidosis. Of the 100 patients with pituitary adenomas, 67 were women. The basisphenoid pneumatization patterns was as follows: 15 (type 2), 40 (type 3), and 45 (type 4).

CONCLUSIONS: We present 3 cases of granulomatous hypophysitis with diffuse enhancement of the infrasellar basisphenoid bone marrow that was not seen in our 100 cases of pituitary adenomas. This imaging feature may be valuable for suggesting a diagnosis of granulomatous hypophysitis and avoiding surgical resection of what might otherwise be misdiagnosed as a pituitary adenoma.

ABBREVIATIONS: AH = autoimmune hypophysitis; GH = granulomatous hypophysitis; LH = lymphocytic hypophysitis

Granulomatous hypophysitis (GH) is a rare, inflammatory condition of the pituitary gland characterized by the presence and formation of granulomas throughout or around the pituitary gland. It is most often associated with systemic diseases such as sarcoidosis or tuberculosis (secondary GH) and, less commonly, isolated to the gland (idiopathic GH). GH forms a subset of autoimmune hypophysitis (AH), which also includes lymphocytic hypophysitis (LH) and Langerhans cell histiocytosis in the differential.^{1,2}

The imaging appearance of AH is nonspecific and overlaps with that of pituitary adenomas, with 1 prior study describing a grading scale to distinguish these entities.³ In terms of GH, there are scant case reports on the imaging findings, and they also

overlap with those of pituitary adenomas.⁴⁻¹⁰ The purpose of this study was to test our observation that diffuse enhancement within the basisphenoid marrow below the sella can distinguish GH from a pituitary adenoma, a feature that is important diagnostically because medical and surgical management differs for these conditions.^{11,12}

MATERIALS AND METHODS

We retrospectively reviewed an internal database for pathology-proved GH with preoperative contrast-enhanced MR imaging with a small FOV focused on the sella. T2-weighted, precontrast T1-weighted, and postcontrast T1-weighted images were reviewed for edema and enhancement of the basisphenoid bone marrow. Additionally, the patients' electronic medical records were reviewed for clinical history, surgical pathology, and relevant laboratory results.

Our internal database was also reviewed for 100 consecutive pathology-proved pituitary adenomas with preoperative MR

Received March 25, 2022; accepted after revision June 28.

From the Department of Radiology and Biomedical Imaging, University of California, San Francisco, San Francisco, California.

Please address correspondence to Ian Mark, MD, Mayo Clinic, 200 1st Street SW, Rochester, MN 55905; e-mail: mark.ian@mayo.edu; @iantmark

<http://dx.doi.org/10.3174/ajnr.A7618>

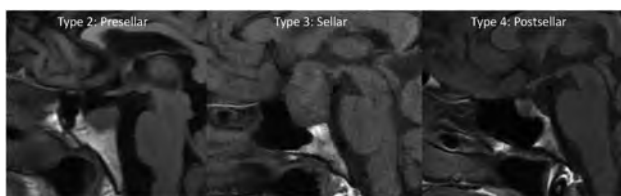


FIG 1. Precontrast T1-weighted sagittal images show the 3 types of sphenoid sinus pneumatization seen in our patients. Type 2 (presellar): the posterior wall of the sphenoid sinus is in front of the anterior wall of the sella turcica; type 3 (sellar): the posterior wall of the sphenoid sinus is between the anterior and posterior wall of the sella turcica; type 4 (postsellar): the posterior wall of the sphenoid sinus is located behind the posterior wall of the sella turcica. An example of type 1 (conchal type, minimal air in the sphenoid sinus) is not shown because this is uncommon and we did not have a patient with this pneumatization pattern.

imaging from January 2021 to January 2022. Images were primarily reviewed for edema and enhancement of the basisphenoid bone marrow. Additionally, the pneumatization pattern of the sphenoid sinus can limit bone marrow evaluation; therefore, the sphenoid sinus pneumatization was evaluated and graded as follows (Fig 1): type 1, conchal; type 2, presellar; type 3, sellar; and type 4, postsellar.¹³ For the adenoma cases, we measured the maximum diameter and recorded their prolactin levels.

All cases were reviewed by a neuroradiology instructor (I.T.M.). Cases with equivocal findings were additionally reviewed by a neuroradiologist with 20 years of experience (C.M.G.). Basic statistical analysis was performed with Excel (Microsoft).

RESULTS

Patients with GH

Three cases of pathology-proved GH are presented below. Each patient had bone marrow enhancement of the basisphenoid below the sella.

Patient 1. A 51-year-old woman presented to an outside institution with headache, dizziness, hyponatremia (113 mEq/L), and emesis with 11 kg of unintentional weight loss (Fig 2). Her laboratory values were consistent with central hypothyroidism, and she was treated with levothyroxine. The contrast-enhanced MRI showed a 1.8-cm sellar mass with type 3 pneumatization of the sphenoid sinus and enhancing bone marrow edema of the basisphenoid. The diffuse enhancement spanned nearly the entire anterior-posterior and transverse dimensions of the bone marrow beneath the sella. She was thought to have a pituitary macroadenoma and underwent endoscopic transsphenoidal resection of the central pituitary gland. The pathology demonstrated GH. Staining for acid-fast Bacillus was negative. She did not have a history of systemic granulomatous disease, and her pituitary lesion was thought to represent primary, idiopathic GH.

Patient 2. A 30-year-old woman presented with right orbital headaches, polydipsia, and polyuria (Fig 3). She was found to have hyperprolactinemia (49.5 μ g/L) and a 1.7-cm sellar mass with type 3 pneumatization of the sphenoid sinus and diffuse enhancing bone marrow of the basisphenoid below the sella on MRI, thought



FIG 2. MR images of patient 1 with idiopathic GH and type 3 (sellar) sphenoid sinus pneumatization. Precontrast T1-weighted sagittal image (A) shows low signal in the infrasellar basisphenoid bone marrow. This low signal corresponds to bone marrow enhancement below the sella (arrows) seen on sagittal (B) and coronal (C) T1-weighted fat-saturated postcontrast images.

to be a pituitary adenoma. She underwent a pituitary biopsy, findings of which were consistent with GH. Following the biopsy, she was treated with dexamethasone and desmopressin. Follow-up MRI 6 months later showed a decrease in the size of the pituitary gland and resolved bone marrow enhancement of the basisphenoid. A cervical lymph node biopsy for work-up of sarcoidosis was negative. She did not have a diagnosis of a granulomatous systemic disease, and her pituitary lesion was thought to represent primary, idiopathic GH. At follow-up 1.5 years after biopsy, the patient did not have symptoms of hypopituitarism, and her diabetes insipidus had resolved.

Patient 3. A 34-year-old woman presented with 3 months of progressive headache, gastrointestinal upset, amenorrhea, fatigue, and blurry vision (Fig 4). She was found to have hyperprolactinemia (78.1 μ g/L) and a 1.6-cm sellar mass with type 3 pneumatization of the sphenoid sinus and diffuse enhancing edema of the basisphenoid below the sella, thought to be a pituitary adenoma. She underwent an endoscopic transsphenoidal exploration with a biopsy that revealed granulomatous inflammation. After treatment with oral dexamethasone, a follow-up MRI 7 months later showed a marked decrease in the size of the pituitary gland with resolved enhancing edema of the basisphenoid. One month after her pituitary biopsy, she had a stomach biopsy that was positive for non-necrotizing granulomas, and her pituitary lesion was thought to represent secondary GH in the setting of sarcoidosis.

Pituitary Adenoma. Of the 100 patients with pathology-proved pituitary adenomas, 67 were women and 33 were men. The average age was 53.3 (SD, 17.3) years (range, 19–84 years). The basisphenoid pneumatization patterns were as follows: 15 (type 2), 40 (type 3), and 45 (type 4). None of the 100 patients had diffuse basisphenoid enhancement (Fig 5). One patient had focal enhancement of the basisphenoid (Fig 6) but did not have the diffuse enhancement seen in the 3 GH cases. The adenomas had an average maximum diameter of 2.6 cm (range, 0.4–4.4 cm). The average prolactin level was 103.4 μ g/L (range, 0.3–1781.0 μ g/L); however, when we excluded 3 outlier patients with markedly high prolactin levels (1189, 1750, and 1781 μ g/L), the average was 54.9 μ g/L.

DISCUSSION

Our study presents 3 cases of pituitary GH with diffuse basisphenoid bone marrow enhancement that was not found in any of our cases

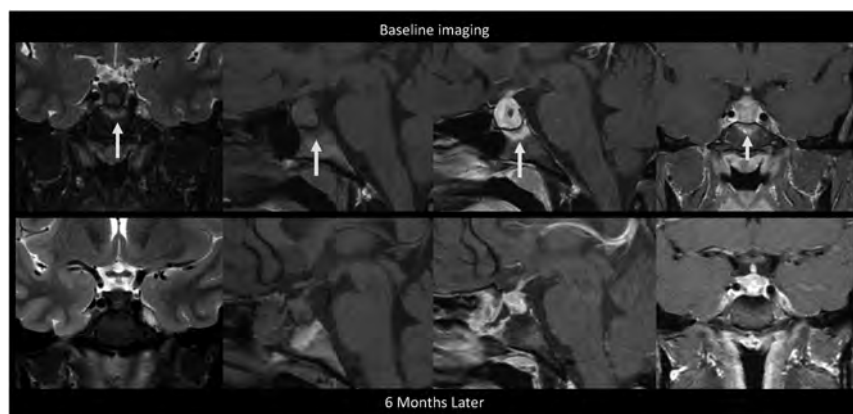


FIG 3. MR images of patient 2 with idiopathic GH and type 3 (sellar) sphenoid sinus pneumatization. This is a collage of images of a single patient at baseline before intervention (*upper row*) followed by postbiopsy and post-steroid treatment. *Left to right*, Coronal T2-weighted, precontrast sagittal T1-weighted, fat-saturated postcontrast sagittal T1-weighted, and fat-saturated postcontrast coronal T1-weighted images show diffuse infrasellar basisphenoid bone marrow-enhancing edema (*arrows*) on baseline that resolved 6 months later after biopsy and steroids.

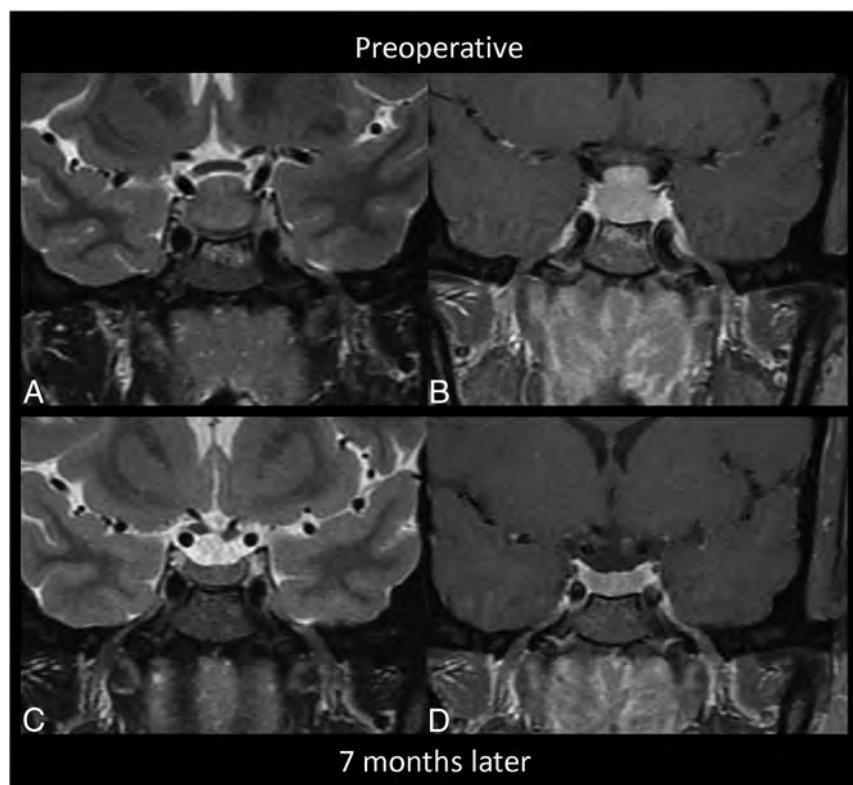


FIG 4. MR images of patient 3 with secondary GH from sarcoidosis. These show preoperative edema (A, coronal T2-weighted image) and enhancement (B, postcontrast coronal T1-weighted image) of the infrasellar basisphenoid bone marrow. After biopsy and oral dexamethasone, follow-up imaging 7 months later shows resolution of the edema (C, coronal T2-weighted image) and enhancement (D, postcontrast coronal T1-weighted image) with a decreased size of the pituitary mass.

of pituitary adenoma. Differentiating pituitary adenoma and GH can have a large impact on patient care. Pituitary adenomas, as in all 100 of our cases, are frequently resected. GH, on the other hand, can be treated with steroids after diagnosis with biopsy and

can potentially spare the pituitary function.¹² We found that the diffuse enhancement of the basisphenoid below the sella can be used to distinguish GH from pituitary adenoma.

GH can be seen primarily in the sella or found in association with systemic disease such as sarcoidosis and tuberculosis. Histologically, GH is an inflammatory process with granulomas and multinucleated giant cells.³ Therefore, it should not be surprising that the adjacent bone of the basisphenoid below the sella had enhancement in the 3 cases that we present. However, this has not been described with LH, which, along with GH, is considered a subtype of AH. The relationship between LH and GH is controversial, with some believing that they represent opposite ends of the spectrum, while others report that they are 2 separate diseases.¹¹ Unlike LH, which has a greater affinity for women and typically involves the late pregnancy or early postpartum periods, GH does not preferentially affect women or have an association with pregnancy.³

The literature contains several case reports of GH, but they largely describe nonspecific imaging findings and do not assist in differentiation from adenomas.^{4-10,14} In a systematic review, Hunn et al¹² examined the MR imaging findings of 51 cases of GH. Their most frequent MR imaging finding was isointense T1 lesion signal in 29.4% of patients. The next most frequent finding was loss of the posterior pituitary bright spot (19.6%), followed by T2-hyperintense signal (15.7%).

Vasile et al¹⁵ presented a case of GH and summarized 7 cases from the literature with MR imaging findings that were nonspecific: T1 isointense to brain (4/7 cases), heterogeneous T2 signal (2/2 cases), and homogeneous enhancement (3/7 cases). This work did state that findings of inflammation including dural enhancement, sphenoid sinus mucosal thickening, and bone marrow abnormality could be seen; however, abnormal bone marrow

was not further explained. Bhansali et al⁶ described pituitary stalk thickening and loss of the posterior pituitary bright spot as clues to the diagnosis of GH, but again, these are nonspecific to this diagnosis.

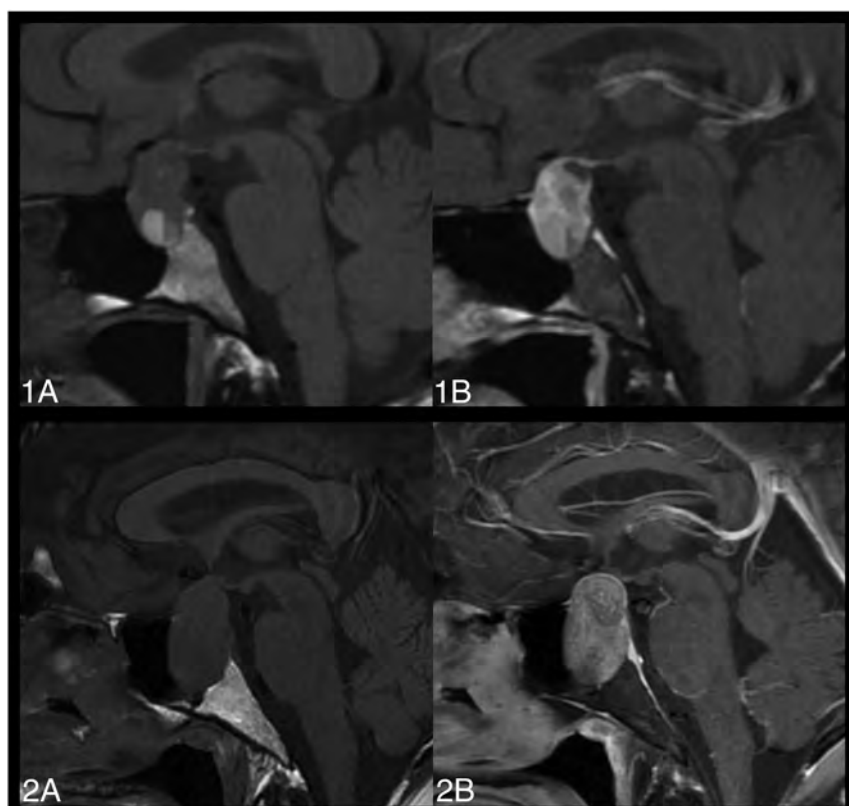


FIG 5. MR images of 2 patients with large pituitary adenomas demonstrate the typical nonenhancing basisphenoid bone marrow. Precontrast (1A/2A) and fat-saturated postcontrast (1B/2B), sagittal T1-weighted images without basisphenoid bone marrow enhancement. Both patients have type 2 pneumatization of the sella.

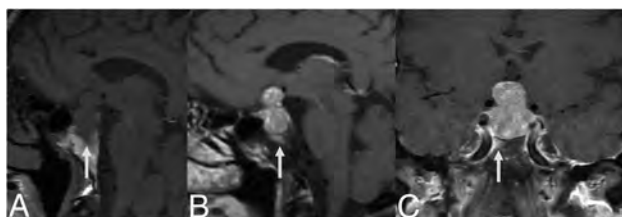


FIG 6. A large pituitary adenoma on precontrast sagittal T1-weighted (A), postcontrast sagittal (B), and coronal (C) T1-weighted images shows focal bone marrow enhancement in the right anterior and lateral aspect of the basisphenoid. This is a distinct pattern from the diffuse enhancement in patients with GH.

Gutenberg et al³ proposed a scoring system to distinguish AH and pituitary adenoma on the basis of an evaluation of 19 clinical and imaging features. However, their study examined all patients with AH, combining a smaller number of patients with GH and a larger number of those with LH. The case-control study included only 46 biopsy-proved cases of GH of 402 patients (11.4%). The most useful clinical feature to distinguish AH and pituitary adenoma was pregnancy; however, this is a key feature that differentiates LH and GH. Unfortunately, enhancing edema of the basisphenoid was not studied. One of their MR imaging features highly indicative of AH was loss of the posterior pituitary bright spot; however, 30% of their large adenomas had the same finding.

Similarly, Saeki et al¹⁶ reported that the posterior pituitary bright spot was nonvisible in 20% of large adenomas, which can also be seen in nonpathologic conditions such as dehydration.¹⁷

A case report by Kartal et al¹⁸ described clival enhancement in a patient with lymphocytic hypophysitis. However, on their fat-saturated postcontrast figure, the enhancement was along the dorsal cortex of the clivus and could very well represent dural thickening and/or venous congestion. In fact, their images clearly demonstrated no basisphenoid bone marrow enhancement. Nakata et al¹⁹ described T2 parasellar dark signal in cases of LH, which we did not see in our cases of GH.

Our study has several limitations, the first being the small sample size. GH is a rare disease and does not necessitate a biopsy if there is known systemic disease; therefore, we were only able to present 3 pathology-proved cases. However, all cases had stark diffuse enhancement of the basisphenoid bone marrow below the sella, which is distinctly different from findings in pituitary adenomas. Additionally, the identification of enhancing bone marrow depends on having bone marrow to evaluate; therefore, type 4 pneumatization patterns are difficult to evaluate in the bone marrow and comprised 45% of our pituitary adenoma cases. Additionally, if the postcontrast images are not fat-saturated, evaluating true enhancement from the T1-hyperintense signal of fatty bone marrow would be extremely limited. While GH is a rare disease, the implication for patient treatment compared with pituitary adenoma suggests that preoperative pituitary MR imaging protocols should contain postcontrast images with fat saturation.

While basisphenoid bone marrow enhancement is not necessarily specific to GH, we could not find studies describing this in other inflammatory pathologies (abscess, LH), and more important, we did not find it any of our cases of pituitary adenoma.

We did not evaluate other pathologies such as Rathke cleft cysts, intrasellar craniopharyngioma, or metastases. Finally, cases of infection, including sphenoid sinusitis and skull base osteomyelitis, could lead to bone marrow edema; however, clinical history as well as the epicenter of bone marrow edema could help to differentiate these cases, because GH primarily involves the bone marrow directly beneath the sella.

CONCLUSIONS

We present 3 cases of GH with diffuse enhancement of the infrasellar basisphenoid bone marrow that was not seen in our review of 100 cases of pituitary adenomas. This imaging feature may be

valuable to suggest a diagnosis of GH and avoid resection of what would otherwise be mistaken for a pituitary adenoma.

Disclosure forms provided by the authors are available with the full text and PDF of this article at www.ajnr.org.

REFERENCES

1. Faje A. **Hypophysitis: evaluation and management.** *Clin Diabetes Endocrinol* 2016;2:15 CrossRef Medline
2. Caturegli P, Newschaffer C, Olivi A, et al. **Autoimmune hypophysitis.** *Endocr Rev* 2005;26:599–614 CrossRef Medline
3. Gutenberg A, Larsen J, Lupi I, et al. **A radiologic score to distinguish autoimmune hypophysitis from nonsecreting pituitary adenoma preoperatively.** *AJNR Am J Neuroradiol* 2009;30:1766–72 CrossRef Medline
4. Gazioğlu N, Tüzgen S, Oz B, et al. **Idiopathic granulomatous hypophysitis: are there reliable, constant radiological and clinical diagnostic criterias?** *Neuroradiology* 2000;42:890–94 CrossRef Medline
5. Çavuş oğlu M, Elverici E, Duran S, et al. **Idiopathic granulomatous hypophysitis: a rare cystic lesion of the pituitary.** *Intern Med* 2015;54:1407–10 CrossRef Medline
6. Bhansali A, Velayutham P, Radotra BD, et al. **Idiopathic granulomatous hypophysitis presenting as non-functioning pituitary adenoma: description of six cases and review of literature.** *Br J Neurosurg* 2004;18:489–94 CrossRef Medline
7. Sharifi G, Mohajeri-Tehrani MR, Navabakhsh B, et al. **Idiopathic granulomatous hypophysitis presenting with galactorrhea, headache, and nausea in a woman: a case report and review of the literature.** *J Med Case Rep* 2019;13:334 CrossRef Medline
8. Park HJ, Park SH, Kim JH, et al. **Idiopathic granulomatous hypophysitis with rapid onset: a case report.** *Brain Tumor Res Treat* 2019;7:57–61 CrossRef Medline
9. Elgamal ME, Mohamed RM, Fiad T, et al. **Granulomatous hypophysitis: rare disease with challenging diagnosis.** *Clin Case Rep* 2017;5:1147–51 CrossRef Medline
10. Su SB, Zhang DJ, Yue SY, et al. **Primary granulomatous hypophysitis: a case report and literature review.** *Endocr J* 2011;58:467–73 CrossRef Medline
11. Kong X, Wang R, Yang Y, et al. **Idiopathic granulomatous hypophysitis mimicking pituitary abscess.** *Medicine (Baltimore)* 2015;94:e1099 CrossRef Medline
12. Hunn BH, Martin WG, Simpson S Jr, et al. **Idiopathic granulomatous hypophysitis: a systematic review of 82 cases in the literature.** *Pituitary* 2014;17:357–65 CrossRef Medline
13. Pirinc B, Fazliogullari Z, Guler I, et al. **Classification and volumetric study of the sphenoid sinus on MDCT images.** *Eur Arch Otorhinolaryngol* 2019;276:2887–94 CrossRef Medline
14. Husain Q, Zouzias A, Kanumuri VV, et al. **Idiopathic granulomatous hypophysitis presenting as pituitary apoplexy.** *J Clin Neurosci* 2014;21:510–12 CrossRef Medline
15. Vasile M, Marsot-Dupuch K, Kujas M, et al. **Idiopathic granulomatous hypophysitis: clinical and imaging features.** *Neuroradiology* 1997;39:7–11 CrossRef Medline
16. Saeki N, Hayasaka M, Murai H, et al. **Posterior pituitary bright spot in large adenomas: MR assessment of its disappearance or relocation along the stalk.** *Radiology* 2003;226:359–65 CrossRef Medline
17. Brooks BS, el Gammal T, Allison JD, et al. **Frequency and variation of the posterior pituitary bright signal on MR images.** *AJNR Am J Neuroradiol* 1989;10:943–48 Medline
18. Kartal I, Yarman S, Tanakol R, et al. **Lymphocytic panhypophysitis in a young man with involvement of the cavernous sinus and clivus.** *Pituitary* 2007;10:75–80 CrossRef Medline
19. Nakata Y, Sato N, Masumoto T, et al. **Parasellar T2 dark sign on MR imaging in patients with lymphocytic hypophysitis.** *AJNR Am J Neuroradiol* 2010;31:1944–50 CrossRef Medline

Normal Enhancement within the Vestibular Aqueduct: An Anatomic Review with High-Resolution MRI

G. Liu, J.C. Benson, C.M. Carr, and J.I. Lane

ABSTRACT

BACKGROUND AND PURPOSE: The normal appearance of the vestibular aqueduct on postcontrast MR images has not been adequately described in the literature. This study set out to characterize the expected appearance of the vestibular aqueduct, with particular emphasis on the enhancement of the structure on both 3D FSE T1 and 3D-FLAIR sequences.

MATERIALS AND METHODS: All MR imaging examinations of the internal auditory canals performed between March 1, 2021, and May 20, 2021, were retrospectively reviewed. All studies included high-resolution (≤ 0.5 -mm section thickness) pre- and postgadolinium 3D FSE T1 with fat-saturated and postgadolinium 3D-FLAIR sequences. Two neuroradiologists independently reviewed the MR images of the vestibular aqueduct for the presence or absence of enhancement on both T1 and FLAIR images and compared the relative intensity of enhancement between sequences. The presence or absence of an enlarged vestibular aqueduct was also noted.

RESULTS: Ninety-five patients made up the patient cohort, of whom 5 did not have postcontrast FLAIR images available (50 women [55.6%]). On both sides, enhancement was significantly more commonly seen on postgadolinium FLAIR (76/180, 42.2%) than on T1 fat-saturated images (41/190, 21.6%) ($P < .001$). The intensity of enhancement was significantly greater on postgadolinium FLAIR images than on T1 fat-saturated images (38.9% versus 3.7%, respectively; $P < .001$).

CONCLUSIONS: Enhancement within the vestibular aqueduct is an expected finding on MR imaging and is both more common and more intense on postgadolinium 3D-FLAIR than on T1 fat-saturated sequences. Such enhancement should not be confused with pathology on MR imaging unless other suspicious findings are present.

ABBREVIATIONS: FS = fat-saturation; IAC = internal auditory canal; postgad = postgadolinium; VA = vestibular aqueduct

The vestibular aqueduct (VA) is a J-shaped bony canal measuring approximately 5–17 mm in length.¹ It extends from the medial side of the vestibule to the petrous portion of the temporal bone and contains the endolymphatic duct, which is lined with cuboidal or low-columnar epithelial cells.¹ Along its course, the duct progressively narrows until it becomes the endolymphatic sac.¹ The endolymphatic duct serves to connect the endolymphatic sac, inner ear vestibule, and cochlea. It functions as 1 of the 3 communication pathways between the intracranial space and inner ear and is thought to provide inner ear pressure equilibrium and fluid homeostasis.¹ The endolymphatic duct also acts as an intracranial pressure buffer via the connection between the cochlea aqueduct and CSF.²

Accurate evaluation of the VA is of utmost importance because abnormalities of the aqueduct can be associated with pathologic

conditions, most notably enlarged VA syndrome and endolymphatic sac tumors. The anatomy of the VA and its appearance on MR cisternogram sequences have been previously described. Multiple studies have demonstrated high sensitivity in diagnosing an enlarged VA on MR imaging. McKinney³ has reported that enhancement within the VA can be a normal finding in 20%–30% of asymptomatic patients on MR imaging. Little, however, is known about the expected appearance of the VA on postcontrast MR imaging T1 and FLAIR sequences. Thus, this study set out to characterize the expected appearance of the VA in a cohort of patients being evaluated for asymmetric sensorineural hearing loss, with particular emphasis on enhancement within the structure on both T1 and FLAIR sequences.

MATERIALS AND METHODS

Patient Selection

Institutional review board approval was obtained for this study. A retrospective review was completed of all internal auditory canal (IAC) protocol MR imaging examinations performed between

Received March 29, 2022; accepted after revision June 28.

From the Department of Radiology, Mayo Clinic, Rochester, Minnesota.

Please address correspondence to Grace Liu, MD, Department of Radiology, Mayo Clinic, Rochester, 200 1st St SW, Rochester, MN 55905; e-mail: liu.grace@mayo.edu
<http://dx.doi.org/10.3174/ajnr.A7615>

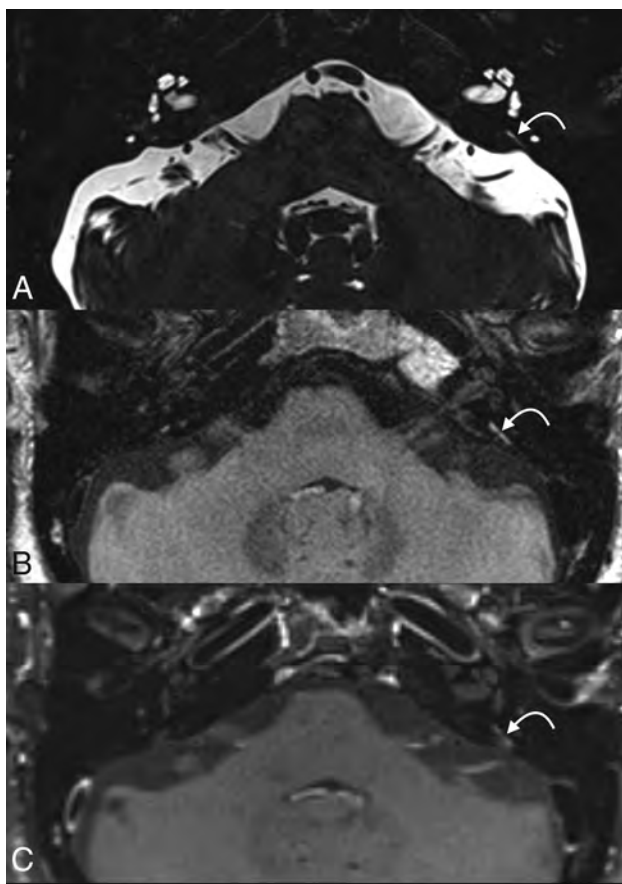


FIG 1. An example of VA enhancement. The VA is visible on thin-section 3D SPACE FSE T2 image (A), which demonstrates a normal-caliber aqueduct. Prominent enhancement is seen on postgad FLAIR image (B), while less prominent enhancement is seen on postgad T1-FS image (C). The curved arrow points to the vestibular aqueduct.

March 1, 2021, and May 20, 2021, in patients being evaluated for asymmetric sensorineural hearing loss. We included MRIs with findings that were considered normal on both the initial interpretation and our subsequent review as part of this study. Included patients had 3T MR examinations (Verio, Skyra, Prisma; Siemens) that included high-resolution (≤ 0.5 -mm section thickness) pre- and postgadolinium (postgad) sequences completed for IAC protocol imaging with 3D sampling perfection with application-optimized contrasts by using different flip angle evolution (SPACE; Siemens) FSE T2, 3D SPACE FSE T1 pre- and postgad (with fat-saturation [FS]), and 3D SPACE FLAIR. As part of the standard IAC MR imaging protocol of our institution, pre- and postgad T1-FS images and postgad FLAIR images are routinely obtained.

Imaging and Clinical Review

Two neuroradiologists independently reviewed MR images of the VA for the following: 1) the presence or absence of T1 postcontrast enhancement, 2) the presence or absence of postgad FLAIR enhancement, 3) comparison of enhancement intensity between T1 postcontrast and postgad FLAIR (ie, whether enhancement was subjectively greater on T1-FS or FLAIR sequences), and 4) the presence or absence of VA enlargement. To ensure that we were observing real enhancement, we coregistered pre- and

postcontrast T1-weight images. All discrepancies were resolved by consensus.

Statistical Analysis

The frequency of enhancement in T1 postcontrast and FLAIR postcontrast images was compared. Two group proportions were compared using 2 group binomial tests. Additionally, the intensity of enhancement of both sequences was compared. Agreement for the left and right sides for both MR imaging sequences was compared using the χ^2 test. The α level of $< .05$ was used as the significance level. All the statistical analyses were performed by BlueSky Statistics (Commercial server edition, Version 7.40; <https://www.blueskystatistics.com/category-s/118.htm>).

RESULTS

Of the 100 patients who met the inclusion criteria for this study, 5 were excluded due to incomplete MR imaging sequences. Five patients did not have postgad FLAIR sequence performed but were included in the remainder of the study. Hence, 95 patients made up the patient cohort, allowing a total of 190 VAs for analysis on postgad T1-FS images and 180 VAs for analysis on postgad FLAIR images. Fifty (55.6%) of the included subjects were women. The average patient age was 58 years, ranging from 18 to 84 years of age.

Enhancement was observed in 76/180 (42.2%) VAs on postgad FLAIR images, and in 41/190 (21.6%) VAs on postgad T1-FS images. VA enhancement was observed in significantly greater frequency on postgad FLAIR than on T1-FS sequences ($P < .0001$). In patients who had enhancement on both sequences, the intensity of enhancement was subjectively greater on a larger proportion of postgad FLAIR than on T1-FS sequences (38.9% versus 3.7%, respectively; $P < .0001$). There was no significant difference in the incidence of VA enhancement between the left and right sides ($P < .0001$). Only 1 VA was noted to be enlarged, which did not demonstrate enhancement on either sequence.

DISCUSSION

This study sought to characterize the prevalence of enhancement within the VA in healthy patients on high-resolution MR imaging. Our findings indicate that VA enhancement is an expected finding and is both more commonly observed and subjectively intense on postcontrast 3D-FLAIR sequences than on T1-FS sequences, as seen in Figure 1. The observed enhancement was present in patients with a normal-appearing VA on MR imaging. Only 1 VA was found to be enlarged on MR imaging, which did not demonstrate enhancement. For example, Figure 2 demonstrates a case of nonenhancing VA. Thus, unless other suspicious findings are present to raise concern for a pathologic process such as associated osseous abnormalities, endolymphatic duct or sac enlargement, or VA enlargement, the results indicate that enhancement of the VA should not be confused with pathology on MR imaging. Like all anatomic descriptions in radiology, this finding should serve as a foundation for many types of imaging interpretations. For example, if an examination is performed to assess leptomeningeal disease, isolated enhancement within the vestibular aqueduct should not be considered pathologic because we have shown that it frequently occurs in healthy patients. Thus, these findings can be used

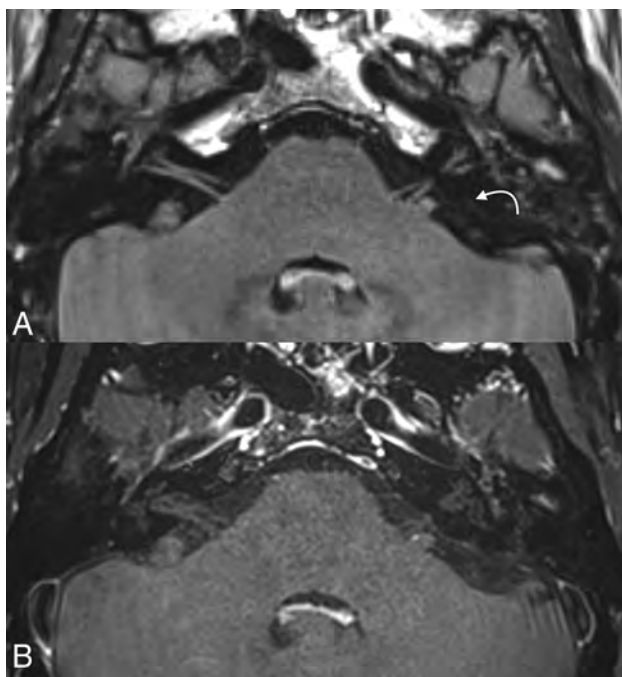


FIG 2. An example of a nonenhancing VA. The VA is faintly visible on axial postgad FLAIR (A) image but does not demonstrate enhancement. The structure cannot convincingly be seen on postgad T1-FS image (B). The curved arrow points to the vestibular aqueduct.

to prevent inaccurate interpretation of enhancement in the VA as a pathologic abnormality.

While CT is better at visualizing the osseous VA, multiple studies have demonstrated that CT is not necessary to exclude a pathologically enlarged VA. In 1 study, MR imaging had a 97% sensitivity in diagnosing an enlarged VA.⁴ Another study demonstrated that there is diagnostic agreement of 93% on CT and MR imaging if applying the Valvassori criterion, which determined that the VA is enlarged when measuring >1.5 mm at the midpoint.⁵ The advantages of using MR imaging include better visualization of the cochlear nerve and lack of radiation,⁴ especially valuable in the pediatric population to reduce exposure.

Although it is uncertain why enhancement within the VA was observed with such frequency, the most likely explanation is that the enhancement is related to normal vasculature within or immediately adjacent to the aqueduct. This hypothesis fits with what is known about the anatomy of the VA. An accessory canal, called the paravestibular canal, runs parallel to the VA, which usually contains 1 or 2 paravestibular veins.^{1,6} A micro-CT study by Nordström et al⁶ demonstrated the proximity of the VA to the vein of the VA. These form a rich vascular plexus containing the vein of the VA, which provides the main venous outflow of the vestibule, endolymphatic walls, and endolymphatic sac.¹

FLAIR is an inversion recovery sequence that is heavily T2-weighted with nulled CSF signals and a component of mild T1-weighted contrast.⁷ Therefore, any enhancement on postcontrast T1-weighted images will also be demonstrated on postcontrast FLAIR imaging.⁷ Many studies have shown contrast-enhanced FLAIR images to be better at detecting enhancement in comparison with T1-weighted imaging, such as identification of inflammatory

leptomeningeal disease,⁸ disruption of blood-CSF barrier,⁹ infectious meningitis,¹⁰ and so forth. A probable explanation for this phenomenon may be that postcontrast FLAIR is more sensitive to the T1-shortening agent in comparison with T1-weighted imaging.⁹ Additionally, suppression of the CSF signal on FLAIR postcontrast imaging could demonstrate better contrast of enhancement.¹¹ Thus, the observations of this study—that contrast was more readily seen on FLAIR than T1-FS—fit with the known sensitivity of the postgad FLAIR sequences to detect subtle enhancement.

To our knowledge, there have been only a few studies on enhancement within the VA on MR imaging in the past. A 2001 study by Naganawa et al¹² using a mixed cohort of patients with hearing loss and Menière disease and age-matched controls found that enhancement of the endolymphatic sac was seen in similar frequency among patients with Menière disease and age-matched controls, though it was noted in higher frequency in patients with sudden hearing loss. A 2003 study by Sugiura et al,¹³ however, found that the frequency of endolymphatic sac enhancement was similar among patients with hearing loss and control subjects. Our study has a much larger sample size and hence more statistical power.

Our study has a few limitations. First, this was a single-institution study, which may limit the generalizability of our results, particularly because differences in MR imaging sequences between institutions may affect the observed findings. Second, this was a retrospective, observational study that cannot provide definite information on cause-and-effect relationships. Further studies will be needed to evaluate any relationships between VA enhancement and pathology.

CONCLUSIONS

Enhancement within the VA is frequently present on high-resolution MR imaging and should be considered a normal finding unless other suspicious findings are present. The observed enhancement is more common and more intense on FLAIR images than on T1-FS sequences.

Disclosure forms provided by the authors are available with the full text and PDF of this article at www.ajnr.org.

REFERENCES

1. Ciuman RR. **Communication routes between intracranial spaces and inner ear: function, pathophysiologic importance and relations with inner ear diseases.** *Am J Otolaryngol* 2009;30:193–202 CrossRef Medline
2. Guan Q, Sun D, Zhao M, et al. **The biomechanical characteristics of human vestibular aqueduct: a numerical-based model construction and simulation.** *Comput Methods Biomech Biomed Engin* 2021;24:905–12 CrossRef Medline
3. McKinney AM. *Atlas of Normal Imaging Variations of the Brain, Skull, and Craniocervical Vasculature.* Springer-Verlag International Publishing; 2017
4. Clarke RL, Isaacson B, Kutz JW, et al. **MRI evaluation of the normal and abnormal endolymphatic duct in the pediatric population: a comparison with high-resolution CT.** *AJNR Am J Neuroradiol* 2021;42:1865–69 CrossRef Medline
5. Connor SE, Dudau C, Pai I, et al. **Is CT or MRI the optimal imaging investigation for the diagnosis of large vestibular aqueduct syndrome and large endolymphatic sac anomaly?** *Eur Arch Otorhinolaryngol* 2019;276:693–702 CrossRef Medline
6. Nordström CK, Li H, Ladak HM, et al. **A micro-CT and synchrotron imaging study of the human endolymphatic duct with special reference**

- to endolymph outflow and Meniere's disease. *Sci Rep* 2020;10:8295 CrossRef Medline
7. Lee EK, Lee EJ, Kim S, et al. **Importance of contrast-enhanced fluid-attenuated inversion recovery magnetic resonance imaging in various intracranial pathologic conditions.** *Korean J Radiol* 2016;17:127–41 CrossRef Medline
 8. Vaswani A, Nizamani WM, Ali M, et al. **Diagnostic accuracy of contrast-enhanced flair magnetic resonance imaging in diagnosis of meningitis correlated with CSF analysis.** *ISRN Radiol* 2014;2014:578986 CrossRef Medline
 9. Davis TS, Nathan JE, Tinoco Martinez AS, et al. **Comparison of T1-post and FLAIR-post MRI for identification of traumatic meningeal enhancement in traumatic brain injury patients.** *PLoS One* 2020;15:e0234881 CrossRef Medline
 10. Mahale A, Choudhary S, Ullal S, et al. **Postcontrast fluid-attenuated inversion recovery (FLAIR) sequence MR imaging in detecting intracranial pathology.** *Radiol Res Pract* 2020;2020:8853597 CrossRef Medline
 11. Bellanger G, Biotti D, Adam G, et al. **Leptomeningeal enhancement on post-contrast FLAIR images for early diagnosis of Susac syndrome.** *Mult Scler* 2022;28:189–97 CrossRef Medline
 12. Naganawa S, Koshikawa T, Fukatsu H, et al. **Contrast-enhanced MR imaging of the endolymphatic sac in patients with sudden hearing loss.** *Eur Radiol* 2002;12:1121–26 CrossRef Medline
 13. Sugiura M, Naganawa S, Nakashima T, et al. **Magnetic resonance imaging of endolymphatic sac in acute low-tone sensorineural hearing loss without vertigo.** *ORL J Otorhinolaryngol Relat Spec* 2003;65:254–60 CrossRef Medline

Diagnostic Accuracy of MRI for Detection of Meningitis in Infants

 S.F. Kralik,  J.G. Vallejo,  M.K. Kukreja,  R. Salman,  G. Orman,  T.A.G.M. Huisman, and  N.K. Desai



ABSTRACT

PURPOSE: To determine the accuracy of MR imaging for diagnosis of meningitis in infants.

MATERIALS AND METHODS: Retrospective review of infants less than 1 year of age who underwent a brain MR imaging for meningitis from 2010–2018. Gold standard for diagnosis of bacterial meningitis was a positive bacterial CSF culture or a positive blood culture with an elevated CSF WBC count, and diagnosis of viral meningitis was a positive CSF PCR result and elevated CSF WBC count. Sensitivity, specificity, PPV, NPV, and accuracy for MR imaging diagnosis of meningitis were calculated.

RESULTS: Two hundred nine infants with mean age 80 days (range 0–347 days) were included. There were 178 true positives with the most common pathogens being: *Group B Streptococcus* (58), *E. coli* (50), *Streptococcus pneumoniae* (21), *H. influenzae* (4); Herpes simplex virus 1 or 2 (18); Enterovirus (4); and other (23). There were 31 true negatives. Range of sensitivity, specificity, PPV, NPV, and accuracy of MR imaging for detection of meningitis was 67.4–83.5%, 92.3–95.7%, 95.0–98.6%, 33.3–76.5%, and 71.3–86.5% respectively. MR imaging sensitivity decreased after 10 days from time of presentation while specificity remained stable. Among individual MR imaging findings, leptomeningeal enhancement was the most sensitive finding, while cerebritis, infarction, ventriculitis, abscess, and intraventricular purulent material were the most specific findings.

CONCLUSIONS: MR imaging of the brain demonstrates high specificity and moderate sensitivity for diagnosis among infants presenting with signs and symptoms of meningitis. The results reflect current standard of care for imaging of infants with meningitis however a selection bias for imaging of more severe meningitis may affect these results.

ABBREVIATIONS: NPV = negative predictive value; PCR = polymerase chain reaction; PPV = positive predictive value; WBC = white blood cell

Bacterial and viral CNS infections are common in infants and can present with various nonspecific signs and symptoms, including fever, hypothermia, irritability, poor feeding, bulging fontanelle, and seizures. Bacterial meningitis is an inflammation of the meninges affecting the pia and arachnoid and subarachnoid spaces in response to bacteria and/or bacterial products and is most common in the first year of life.^{1,2} In infants, bacteria and viruses can enter the body through the skin, mucosa, blood, and respiratory and gastrointestinal tracts. They most commonly enter the CNS by the hematogenous route and, less commonly, by direct spread from adjacent sites such as the sinuses or mastoids. In the modern era, the mortality from bacterial meningitis is approximately 10%, and

survivors remain at high risk for neurologic sequelae.^{3,4} In neonates, the most common pathogens causing bacterial meningitis are *Group B Streptococcus* and *Escherichia coli*, while *Streptococcus pneumoniae* is the most common cause in infants.^{1,5} The most common causes of viral meningitis in neonates and infants are herpes simplex and Enterovirus; however, many viral infections remain undiagnosed due to limitations in laboratory testing.

The diagnosis of bacterial or viral meningitis relies on isolation in a culture or detection by molecular testing of the causative pathogen from the CSF. Patients with potential meningitis will often undergo an MR imaging of the brain to assess imaging findings supportive of a CNS infection and complications that can include abscess, empyema, arterial or venous infarction, and hydrocephalus/CSF circulation disorders. However, the exact diagnostic accuracy of MR imaging for the detection of meningitis in infants remains unknown. In addition, it is unknown which MR imaging findings are the most sensitive or specific for the diagnosis of meningitis and whether the length of time from presentation to MR imaging affects the diagnostic sensitivity of MR imaging.

Received May 2, 2022; accepted after revision June 28.

From the Department of Radiology (S.F.K., M.K.K., R.S., G.O., T.A.G.M.H., N.K.D.), Texas Children's Hospital, Houston, Texas; and Department of Pediatrics (J.G.V.), Baylor College of Medicine, Houston Texas.

Please address correspondence to Stephen F. Kralik, MD, Department of Radiology, Texas Children's Hospital, 6701 Fannin St, Suite 470, Houston, TX, 77030; e-mail: steve.kralik@gmail.com

<http://dx.doi.org/10.3174/ajnr.A7610>

Therefore, the purpose of this study was to determine the diagnostic accuracy of MR imaging for the diagnosis of meningitis among infants and determine which factors affect the diagnostic performance of MR imaging.

MATERIALS AND METHODS

Following institutional review board approval (Texas Children's Hospital), a retrospective review was performed from 2010 to 2018 among infants younger than 1 year of age who presented with signs and symptoms of meningitis, including any combination of fever, seizure, lethargy, respiratory distress, decreased oral intake, or irritability. All patients had a lumbar puncture with CSF laboratory data, CSF culture, anaerobic and aerobic blood cultures, and an MR imaging of the brain performed without and with IV contrast within 30 days of presentation. The timing from when CSF was obtained with respect to administration of IV antibiotics and acyclovir was recorded as either before administration, <24 hours after administration, or >24 hours after administration. The age (including neonate age range defined as age <30 days) and prematurity (defined as <37 gestational weeks) of the patients were extracted from the electronic medical records. Because of the retrospective nature of this study, decision to perform an MR imaging was based on standard clinical care and at our institution this includes routine MR imaging for infants less than 6 weeks and after 6 weeks is based on physician judgment of severity or potential for complications of meningitis.

The criterion standard diagnosis of bacterial meningitis was determined by either a CSF culture positive for meningitis or a blood culture positive for meningitis combined with elevated CSF white blood cell (WBC) count (>20 WBC/ μ L for younger than 30 days of age, >9 WBC/ μ L for 30–90 days of age, and >6 WBC/ μ L for older than 90 days of age).⁶ The criterion standard diagnosis of viral meningitis was a viral polymerase chain reaction (PCR) from CSF with positive findings and an elevated CSF WBC count. Patients with true-negative findings had a normal CSF WBC count and a CSF culture and CSF PCR testing with negative findings. A total of 42 patients with CSF WBC counts above the normal range but without a CSF culture, blood culture, or viral PCR positive for meningitis were excluded from analysis. CSF cultures with coagulase-negative staphylococci or other skin contaminants were excluded. Patients with no CSF sampling, immunodeficiency, malignancy, or presence of an intracranial shunt were also excluded.

MR imaging of the brain was performed in all patients on 1.5T and 3T MR imaging scanners using standard departmental protocols including precontrast axial and sagittal 2D T1-weighted TSE with 3- to 4-mm section thickness, axial 2D FLAIR with 3- to 4-mm section thickness, axial and coronal 2D T2-weighted TSE with 2.5- to 4-mm section thickness, axial gradient-echo or SWI with 2.5- to 4-mm section thickness, axial DWI/DTI with 2.5- to 4-mm section thickness, and postcontrast axial and coronal 2D T1-weighted imaging with 3- to 4-mm section thickness with the axial imaging performed immediately after intravenous contrast administration followed by the coronal imaging. The TE/TR times varied by scanner with T1W MRI TE/TR ranging from 10–12.5 ms/458–533 ms and T2W MRI TE/TR times ranging from 80–120 ms/3074–7000ms. Standard of care at our institution is to perform post contrast imaging in patients with

suspected meningitis unless standard contraindications existed such as renal failure or contrast allergy.

Retrospective independent blinded reviews of initial brain MRIs performed without and with intravenous contrast were performed by 2 board-certified neuroradiologists (S.K., and M.K.) with, respectively, 10 and 13 years of experience in pediatric neuroradiology, for the presence of direct signs of meningitis, including leptomeningeal enhancement, ventriculitis, cerebritis, infarction, abscess/granuloma, and extra-axial (subarachnoid or subdural spaces) or intraventricular purulent material. Representative examples of these findings are shown in Fig 1. These findings are considered most typical for intracranial infection in patients presenting with signs and symptoms of meningitis.^{7–12} The neuroradiologists reviewed the MRIs of the brain with the clinical indication of possible meningitis but were blinded to the CSF analysis results and pathogen diagnosis.

Meningeal enhancement was defined as abnormal/increased contrast enhancement of the leptomeninges on postcontrast T1-weighted imaging. Ventriculitis was defined as contrast enhancement of the ependymal surface of the ventricles on postcontrast T1-weighted imaging. Cerebritis was defined as cortical contrast enhancement on postcontrast T1-weighted imaging or diffusion restriction or edema as indicated by T2/FLAIR hyperintense signal in a nonvascular distribution involving the cortex. Infarction was defined as diffusion restriction in an arterial or venous vascular distribution in either a wedge-shaped cortical distribution or a lacunar infarct pattern. Abscess was defined as a peripherally enhancing intraparenchymal lesion on postcontrast T1-weighted imaging with or without associated diffusion restriction. Granuloma was defined as a homogeneously enhancing parenchymal lesion on postcontrast T1-weighted imaging. Extra-axial purulent material was defined as extra-axial (subarachnoid, subdural, or epidural space) diffusion restriction not caused by hemorrhage as indicated by a lack of susceptibility artifacts or T1-shortening. Intraventricular purulent material was defined as diffusion restriction within the ventricles not caused by hemorrhage as indicated by a lack of susceptibility artifacts or T1-shortening. Additional findings that are considered indirect signs or complications of meningitis were recorded, including hydrocephalus, dural sinus thrombosis, and hemorrhage.

For all patients in whom there was a discordant MR imaging finding, the reviewers reached a consensus on the finding, and this consensus was used as the final diagnosis. Interobserver agreement for individual MR imaging findings was calculated using the κ statistic. A κ value of 0.81–1.0 indicated excellent agreement; 0.61–0.80, good agreement; 0.41–0.60, moderate agreement; 0.21–0.40, fair agreement; and 0–0.20, slight agreement.

An MR imaging diagnosis positive for meningitis was defined as any combination of leptomeningeal enhancement, ventriculitis, extra-axial or intraventricular purulent material, or cerebritis. Subsequently, the sensitivity, specificity, positive predictive value (PPV), negative predictive value (NPV), and accuracy of an MR imaging diagnosis of meningitis was calculated for the initial MRIs of the brain performed within 1, 3, 7, 10, 14, 21, and 30 days of the initial presentation. Following these calculations, the timeframe of brain MRIs performed within 7 days of presentation (the timeframe that demonstrated the greatest accuracy) was chosen to subsequently determine the accuracy of indirect MR imaging findings, the effects of the timing of antibiotic and acyclovir administration,

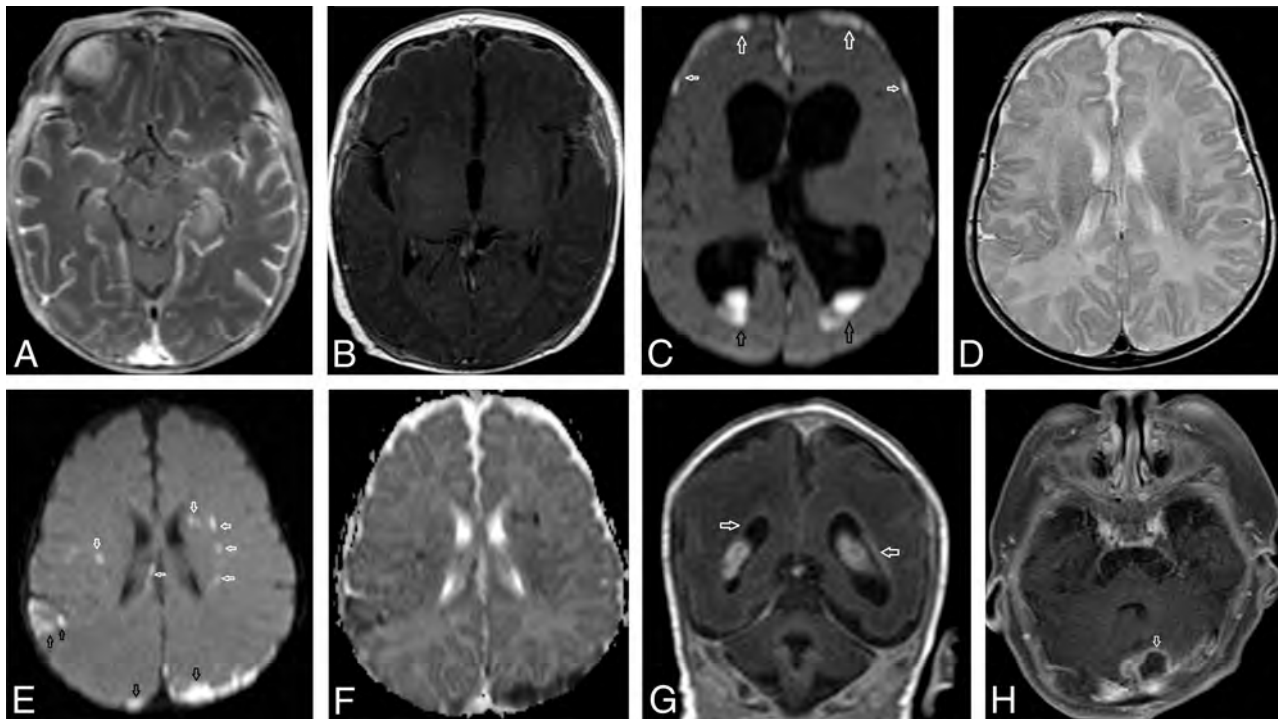


FIG 1. Representative examples of direct MR imaging findings of meningitis. A and B, Axial postcontrast T1-weighted images in 2 separate patients with herpes simplex virus meningitis and Group B streptococcal meningitis, respectively, demonstrating abnormal leptomeningeal enhancement indicative of meningitis. C, Axial DWI demonstrates restricted diffusion (ADC not shown) in the occipital horns of the lateral ventricles indicative of intraventricular purulent material (*black arrows*) and extra-axial diffusion restriction, indicative of extra-axial purulent material (*white arrows*). D–F, Axial T2-weighted imaging, axial DWI, and an axial ADC map demonstrate focal areas of restricted diffusion in the caudate head, periventricular WM, and corona radiata, indicative of acute lacunar infarctions (*white arrows*), and cortical areas of diffusion restriction and T2 hyperintensity, indicative of cerebritis (*black arrows*). G, Coronal postcontrast T1-weighted image demonstrates ependymal enhancement, indicative of ventriculitis (*white arrows*). H, Axial postcontrast T1-weighted image demonstrates a peripherally enhancing fluid (*arrow*) with restricted diffusion (not shown), indicative of an abscess.

Table 1: Patient demographics

Demographics	
Total No. of patients	209
Age	80 days (range, 0–347 days)
Male/female ratio	126:83
Prematurity	19% (39/209)
Most common presenting signs and symptoms	
Fever	75% (156/209)
Vomiting/decreased oral intake	27% (57/209)
Seizure	22% (47/209)
Apnea/respiratory distress	18% (37/209)
Irritability	21% (44/209)
Lethargy	12% (26/209)
Rash	4% (9/209)

prematurity, and age (neonate versus non-neonate age) on the diagnostic performance of MR imaging and to evaluate the diagnostic performance of individual MR imaging findings. Last, a Fisher exact test was used to compare direct MR imaging findings of meningitis found in bacterial-versus-viral meningitis. A *P* value < .05 was considered statistically significant.

RESULTS

Patient demographics are shown in Table 1. Two hundred nine infants with a mean age 80 days (range, 0–347 days) were included.

The mean days from presentation to lumbar puncture were 0.9 (SD, 1.6) days. The mean difference between date of symptom onset and date of presentation was 0.6 days (range 0–3 days). There were a total of 178 cases of meningitis (true-positives). Bacterial meningitis pathogens included the following: *Group B Streptococcus* (*n* = 58); *E coli* (*n* = 50); *S pneumoniae* (*n* = 21); *Haemophilus Influenza* (*n* = 4); *Neisseria meningitidis* (*n* = 3); *Enterobacter* (*n* = 3); *Enterococcus* (*n* = 3); *Streptococcus bovis* (*n* = 2); *Citrobacter* (*n* = 2); *Salmonella* (*n* = 2); *Streptococcus pyogenes* (*n* = 2); *Streptococcus infantarius* (*n* = 1); *Proteus mirabilis* (*n* = 1); *Pseudomonas aeruginosa* (*n* = 1); *Klebsiella* (*n* = 1); *Acinetobacter* (*n* = 1); *Serratia* (*n* = 1). Viral pathogens included herpes simplex 1 or 2 (*n* = 18) and Enterovirus (*n* = 4).

There was excellent interobserver agreement for all direct MR imaging findings of meningitis as follows: leptomeningeal enhancement, 0.85 (95% CI, 0.74–0.95); cerebritis, 0.90 (95% CI, 0.78–1.0); ventriculitis, 0.91 (95% CI, 0.80–1.0); abscess, 1.0 (95% CI, 1.0–1.0); infarction, 0.95 (95% CI, 0.89–1.0); extra-axial purulent material, 0.90 (95% CI, 0.81–0.99); and intraventricular purulent material, 0.96 (95% CI, 0.89–1.0).

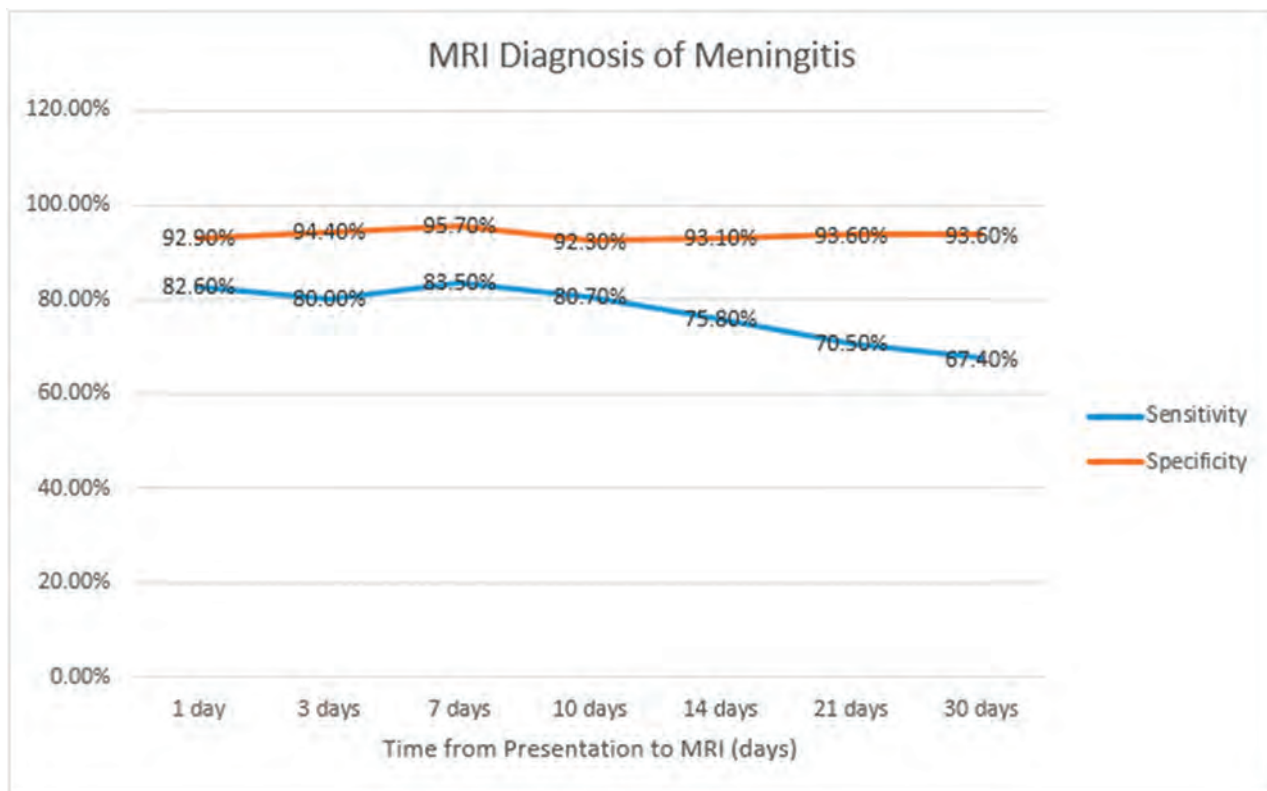
The diagnostic performance of brain MRIs with respect to the time from presentation is shown in Table 2. Overall, brain MRIs demonstrated high specificity and moderate sensitivity. The range of diagnostic performance of MR imaging for the detection of meningitis was the following: sensitivity, 70.5%–83.5%;

Table 2: MR imaging diagnosis of meningitis with respect to time^a

Time from Presentation to MR Imaging	No. of Patients	Sensitivity	Specificity	PPV	NPV	Accuracy
1 day	37	82.6% (61.2%–95.1%)	92.9% (66.1%–99.8%)	95.0% (74.0%–99.2%)	76.5% (56.9%–88.9%)	86.5% (71.2%–95.5%)
3 days	69	80.0% (66.3%–90.0%)	94.4% (72.7%–99.9%)	97.6% (85.6%–99.6%)	63.0% (49.1%–75.0%)	83.8% (72.9%–91.6%)
7 days	108	83.5% (73.9%–90.7%)	95.7% (78.1%–99.9%)	98.6% (91.2%–99.8%)	61.1% (49.0%–72.2%)	86.1% (78.1%–92.0%)
10 days	119	80.7% (71.2%–88.1%)	92.3% (74.9%–99.1%)	97.4% (90.8%–99.3%)	57.1% (46.5%–67.2%)	83.2% (75.2%–89.4%)
14 days	157	75.8% (67.4%–82.9%)	93.1% (77.23%–99.2%)	98.0% (92.7%–99.5%)	46.6% (38.7%–54.6%)	79.0% (71.8%–85.1%)
21 days	197	70.5% (62.9%–77.3%)	93.6% (78.6%–99.2%)	98.3% (93.9%–99.6%)	37.2% (31.5%–43.2%)	74.1% (67.4%–80.1%)
30 days	209	67.4% (60.0%–74.2%)	93.6% (75.6%–99.2%)	98.4% (94.0%–99.6%)	33.3% (28.4%–38.6%)	71.3% (64.7%–77.3%)

Note:—True positives/True negatives for each time frame as follows: 1 day (19/13), 3 days (41/17), 7 days (71/22), 10 days (75/24), 14 days (97/27), 21 days (117/29), 30 days (178/29).

^a Numbers in parentheses are 95% confidence intervals.

**FIG 2.** MR imaging diagnosis of meningitis relative to the time from presentation to MR imaging.

specificity, 92.9%–95.7%; PPV, 95.0%–98.6%; NPV, 33.3%–76.5%; and accuracy, 71.3%–86.5%. Although there was overlap of the 95% confidence intervals, there was a trend toward decreasing sensitivity but consistent specificity as the duration of time increased from clinical presentation to brain MR imaging as seen in Fig 2.

Because MRIs performed within 7 days showed the highest accuracy, this timeframe was chosen to evaluate additional factors. Diagnostic performance of individual MR imaging findings is shown in Table 3. Among individual MR imaging findings, leptomeningeal contrast enhancement was the most sensitive finding (73.3%), while cerebritis, infarction, ventriculitis, abscess, and intraventricular purulent material were the most specific findings (100%). For MRIs performed within 7 days of presentation, the sensitivity and specificity for patients receiving antibiotics before CSF ($n = 39$) versus after CSF ($n = 70$) were 86% (95% CI, 66%–

95%) and 91% (95% CI, 57%–99%) versus 83% (95% CI, 70%–91%) and 92% (95% CI, 62%–100%). For MRIs performed within 7 days of presentation, the sensitivity and specificity for neonates ($n = 37$) versus non-neonates ($n = 72$) was 76% (95% CI, 56%–89%) and 88% (95% CI, 47%–99%) versus 88% (95% CI, 75%–94%) and 94% (95% CI, 68%–100%). For MRIs performed within 7 days of presentation, the sensitivity and specificity for premature infants ($n = 15$) versus full-term infants ($n = 94$) was 81% (95% CI, 48%–97%) and 100% (95% CI, 40%–100%) versus 84% (95% CI, 73%–91%) and 90% (95% CI, 67%–98%). Last, for MRIs within 7 days of presentation, indirect findings and complications of meningitis including hydrocephalus, dural sinus thrombosis, and hemorrhage demonstrated a sensitivity and specificity of 78% and 62%, respectively, for the diagnosis of meningitis, indicating an expected reduced accuracy compared with direct MR imaging findings of meningitis.

Table 3: Diagnostic performance of individual MR imaging findings for the diagnosis of meningitis^a

MR Imaging Findings	Sensitivity	Specificity	PPV	NPV	Accuracy
Leptomeningeal enhancement	73.3% (62.6%–82.2%)	78.1% (78.1%–99.9%)	98.4% (90.2%–99.7%)	48.9% (40.0%–57.8%)	78.0% (69.0%–85.4%)
Ventriculitis	13.8% (7.3%–22.9%)	100% (84.6%–100%)	100% (100%)	22.7% (21.2%–24.2%)	31.2% (22.7%–40.8%)
Cerebritis	28.7% (19.5%–39.4%)	100% (84.6%–100%)	100% (100%)	26.2% (23.7%–28.9%)	43.1% (33.7%–53.0%)
Infarct	43.7% (33.1%–54.7%)	100% (84.6%–100%)	100% (100%)	31.0% (27.2%–35.1%)	55.1% (45.2%–64.6%)
Extra-axial purulent material	32.6% (22.8%–43.5%)	95.7% (78.1%–99.9%)	96.6% (80.1%–99.5%)	27.5% (24.2%–31.0%)	36.3% (36.3%–55.7%)
Intraventricular purulent material	13.8% (7.3%–22.9%)	100% (84.6%–100%)	100% (100%)	22.7% (21.2%–24.2%)	31.2% (22.7%–40.8%)
Abscess/granuloma	2.3% (0.28%–8.1%)	100% (84.6%–100%)	100% (100%)	20.6% (20.0%–21.1%)	22.0% (14.7%–31.0%)

^a Numbers in parentheses are 95% confidence intervals. Data were obtained from brain MRIs within 7 days of presentation.

Table 4: Diagnostic performance of MR imaging findings for the diagnosis of bacterial and viral meningitis^a

MR Imaging Findings	Sensitivity	Specificity	PPV	NPV	Accuracy
Bacterial	87.9% (77.5%–94.6%)	95.7% (78.1%–99.9%)	98.3% (89.5%–99.8%)	73.3% (58.8%–84.1%)	89.9% (81.7%–95.3%)
Viral	73.3% (44.9%–92.2%)	95.7% (78.1%–99.9%)	91.7% (61.2%–98.7%)	84.6% (70.2%–92.8%)	86.8% (71.9%–95.6%)

^a Numbers in parentheses are 95% confidence intervals. Data were obtained from brain MRIs within 7 days of presentation.

The diagnostic performance for the detection of bacterial and viral meningitis is shown in Table 4. Although there is overlap in the 95% confidence intervals between the groups, there was a trend toward higher sensitivity for the detection of bacterial meningitis compared with viral meningitis. Differences in the detection of individual direct MR imaging findings for patients with bacterial meningitis versus viral meningitis are as follows: leptomeningeal enhancement, 54% (84/156) versus 36% (8/22) ($P = .17$); extra-axial purulent material, 38% (60/156) versus 0% (0/22) ($P < .0001$); intraventricular purulent material, 15% (24/156) versus 0% (0/22) ($P = .048$); ventriculitis, 12% (19/156) versus 9% (2/22) ($P = 1.0$); infarction, 28% (43/156) versus 36% (8/22) ($P = .45$); cerebritis, 17% (26/156) versus 36% (8/22) ($P = .13$); and abscess, 1% (2/156) versus 0% (0/22) ($P = 1.0$).

DISCUSSION

In this study, we evaluated the accuracy of MR imaging for the detection of meningitis in infants and evaluated which factors may affect the accuracy of MR imaging. The results of this study demonstrate that MR imaging has a high specificity and PPV but moderate sensitivity for the diagnosis of meningitis in infants. MR imaging retains the high level of specificity, even with an increasing length of time from presentation. Conversely, the sensitivity of MR imaging appears to decrease with time after approximately 10 days. Prematurity, neonatal age, and administration of antibiotics or acyclovir before obtaining CSF do not appear to affect the accuracy of MR imaging; however, the sensitivity of MR imaging may be lower for viral meningitis compared with bacterial meningitis.

Although CSF laboratory and culture remain the criterion standard for diagnosis, these results provide useful clinical information and quantitative data for the long-held clinical notion regarding the utility of MR imaging for the diagnosis of meningitis. These results quantitatively demonstrate the percentage of false-negative MRIs in patients with CSF culture or PCR-confirmed meningitis, supporting the established practice of CSF analysis, culture, and PCR for diagnosis. The results are also useful for other frequent clinical scenarios in which the diagnosis of

meningitis is uncertain. In some patients, CSF can be difficult to obtain at presentation, and in these patients, MR imaging could be performed to assess meningitis and provide information supportive of the diagnosis. Other patients may have a CSF culture with negative findings, a blood culture with positive findings, and a borderline or elevated CSF WBC count. In these patients, an MR imaging with positive findings would support the diagnosis of meningitis because the PPV is $>95\%$, while an MR imaging with negative findings could be better understood as indeterminate because the NPV ranges from 33% to 77%. As both PPV and NPV are dependent on the prevalence of disease, a PPV in the setting of high prevalence generally has less utility but for serious infections from meningitis this would still retain its value. We chose to exclude patients with elevated CSF WBC count but negative culture and PCR results because additional factors including CSF glucose and protein values, and whether the infant was pretreated with antibiotics influences our physicians whether to continue to treat or not treat as meningitis. For this reason and our definition of gold standard diagnosis of meningitis, these patients were excluded.

We evaluated the various factors that may affect an MR imaging diagnosis of meningitis. The duration from presentation to MR imaging affects its accuracy. Sensitivity decreases with time while the specificity remains at a consistently high level. While it is unlikely that MR imaging would be used for diagnosing meningitis at 30 days from presentation, the results form a better understanding of the evolution of imaging findings, but further research is needed for better understanding the expected duration for which MR imaging findings persist. Other factors including antibiotic and acyclovir administration before obtaining CSF, prematurity, and neonatal age were evaluated but did not alter the sensitivity and specificity of MR imaging when performed within 7 days of presentation. Last, we compared MR imaging findings in patients with bacterial and viral pathogens. As expected, extra-axial purulent material, intraventricular purulent material, and abscess were found only with bacterial meningitis and not in viral meningitis. Meanwhile, leptomeningeal enhancement, cerebritis, infarction, and ventriculitis were found with both bacterial and viral meningitis.

There are several limitations of this study. First, this was a single-center, retrospective study, so external validity may be limited. The inclusion criteria create a potential selection bias because patients with less severe disease may not be imaged but reflect the current clinical practice. Another potential limitation of this study is the subjectivity in the determination of individual MR imaging findings. This subjectivity was mitigated by independent imaging reviews by 2 experienced pediatric neuroradiologists, consensus diagnosis in discordance findings, and calculation of interobserver agreement. We observed excellent interobserver agreement for all MR imaging findings. Although some of the MR imaging findings could be seen in diseases other than meningitis such as leptomeningeal enhancement with malignancy, this study was performed among patients with signs and symptoms of meningitis, many of whom will present with fever. This clinical context is necessary, and extrapolation of these results to other clinical scenarios should be avoided.

Another potential limitation is the lack of a postcontrast FLAIR imaging of the brain. Postcontrast FLAIR may increase the sensitivity for the detection of leptomeningeal enhancement, which may improve the sensitivity of MR imaging.¹³⁻¹⁶ Because our institution does not routinely use postcontrast FLAIR imaging, these data were not available in all patients and, therefore, could not be included in this study. Further research assessing the accuracy of MR imaging, including the use of postcontrast FLAIR, would be valuable because this may further increase the sensitivity of MR imaging. Another limitation is the exclusion of patients with a CSF culture and blood culture with negative findings but with an elevated CSF WBC count. These patients represent a substantial number of patients and are a challenge with regard to clinical decision-making about treatment. Because this study required a criterion standard for comparison with MR imaging, we did not evaluate the role of MR imaging in these patients. One could extrapolate, however, that given the high PPV of MR imaging, an MR imaging with positive findings in these patients could be considered evidence of meningitis. Similarly, we used CSF or blood culture and CSF PCR testing as criterion standards; however, these tests may have limitations in the detection of meningitis, and although this represents standard clinical care, it could impact our results. In particular, the detection of viral causes of meningitis is likely to be incomplete so that the accuracy of MR imaging should be reassessed if further advances in laboratory testing occur. Lastly, subgroup analysis for bacterial and viral pathogens was performed to establish an understanding of potential differences, however, the smaller numbers of patients with a viral pathogen is a limitation and future studies with larger numbers of infants with viral meningitis should be performed to better understand the accuracy of MR imaging.

CONCLUSIONS

MR imaging of the brain demonstrates high specificity and moderate sensitivity for diagnosis of meningitis in infants. The accuracy of MR imaging is greatest when performed within 7 days of the time of presentation, but the specificity remains for a much longer

time period. Accuracy does not appear to be affected by pretreatment with antibiotics or acyclovir, prematurity, or neonatal age. Institutional selection bias for imaging may affect the results of the accuracy of MR imaging for diagnosis of meningitis.

Disclosure forms provided by the authors are available with the full text and PDF of this article at www.ajnr.org.

REFERENCES

1. Chávez-Bueno S, McCracken GH Jr. **Bacterial meningitis in children.** *Pediatr Clin North Am* 2005;52:795–810 CrossRef Medline
2. Feigin RD, McCracken GH Jr, Klein JO. **Diagnosis and management of meningitis.** *Pediatr Infect Dis J* 1992;11:785–814 CrossRef Medline
3. Ouchenir L, Renaud C, Khan S, et al. **The epidemiology, management, and outcomes of bacterial meningitis in infants.** *Pediatrics* 2017;140:e20170476 CrossRef Medline
4. Bedford H, de Louvois J, Halket S, et al. **Meningitis in infancy in England and Wales: follow-up at age 5 years.** *BMJ* 2001;323:533–36 CrossRef Medline
5. Oliveira CR, Morriss MC, Mistrot JG, et al. **Brain magnetic resonance imaging of infants with bacterial meningitis.** *J Pediatr* 2014 Jul;165:134–39 CrossRef Medline
6. Kestenbaum LA, Ebberson J, Zorc JJ, et al. **Defining cerebrospinal fluid white blood cell count reference values in neonates and young infants.** *Pediatrics* 2010;125:257–64 CrossRef Medline
7. Chang CJ, Chang WN, Huang LT, et al. **Cerebral infarction in perinatal and childhood bacterial meningitis.** *QJM* 2003;96:755–62 CrossRef Medline
8. Hernández MI, Sandoval CC, Tapia JL, et al. **Stroke patterns in neonatal group B streptococcal meningitis.** *Pediatr Neurol* 2011;44:282–88 CrossRef Medline
9. Ferreira NPI, Otta GM, Faria do Amaral LL, et al. **Imaging aspects of pyogenic infections of the central nervous system.** *Top Magn Reson Imaging* 2005;16:145–54 CrossRef Medline
10. Kanamalla US, Ibarra RA, Jinkins JR. **Imaging of cranial meningitis and ventriculitis.** *Neuroimaging Clin N Am* 2000;10:309–31 Medline
11. Fukui MB, Williams RL, Mudigonda S. **CT and MR imaging features of pyogenic ventriculitis.** *AJNR Am J Neuroradiol* 2001;22:1510–16 Medline
12. Kralik SF, Kukreja MK, Paldino MJ, et al. **Comparison of CSF and MRI findings among neonates and infants with E coli or group B streptococcal meningitis.** *AJNR Am J Neuroradiol* 2019;40:1413–17 CrossRef Medline
13. Taoka T, Yuh WT, White ML, et al. **Sulcal hyperintensity on fluid attenuated inversion recovery MR images in patients without apparent cerebrospinal fluid abnormality.** *AJR Am J Roentgenol* 2001;176:519–24 CrossRef Medline
14. Galassi W, Phuttharak W, Hesselink JR, et al. **Intracranial meningeal disease: comparison of contrast-enhanced MR imaging with fluid attenuated inversion recovery and fat-suppressed T1-weighted sequences.** *AJNR Am J Neuroradiol* 2005;26:553–59 Medline
15. Kamran S, Bener AB, Alper D, et al. **Role of fluid-attenuated inversion recovery in the diagnosis of meningitis: comparison with contrast enhanced magnetic resonance imaging.** *J Comput Assist Tomogr* 2004;28:68–72 CrossRef Medline
16. Singer MB, Atlas SW, Drayer BP. **Subarachnoid space disease: diagnosis with fluid-attenuated inversion-recovery MR imaging and comparison with gadolinium-enhanced spin-echo MR imaging—blinded reader study.** *Radiology* 1998;208:417–22 CrossRef Medline

MR Imaging Characteristics and ADC Histogram Metrics for Differentiating Molecular Subgroups of Pediatric Low-Grade Gliomas

 S. Shrot,  A. Kerpel,  J. Belenky,  M. Lurye,  C. Hoffmann, and  M. Yalon



ABSTRACT

BACKGROUND AND PURPOSE: *BRAF* and type 1 neurofibromatosis status are distinctive features in pediatric low-grade gliomas with prognostic and therapeutic implications. We hypothesized that DWI metrics obtained through volumetric ADC histogram analyses of pediatric low-grade gliomas at baseline would enable early detection of *BRAF* and type 1 neurofibromatosis status.

MATERIALS AND METHODS: We retrospectively evaluated 40 pediatric patients with histologically proved pilocytic astrocytoma ($n = 33$), ganglioglioma ($n = 4$), pleomorphic xanthoastrocytoma ($n = 2$), and diffuse astrocytoma grade 2 ($n = 1$). Apart from 1 patient with type 1 neurofibromatosis who had a biopsy, 11 patients with type 1 neurofibromatosis underwent conventional MR imaging to diagnose a low-grade tumor without a biopsy. *BRAF* molecular analysis was performed for patients without type 1 neurofibromatosis. Eleven patients presented with *BRAF* V600E-mutant, 20 had *BRAF*-*KIAA* rearrangement, and 8 had *BRAF* wild-type tumors. Imaging studies were reviewed for location, margins, hemorrhage or calcifications, cystic components, and contrast enhancement. Histogram analysis of tumoral diffusivity was performed.

RESULTS: Diffusion histogram metrics (mean, median, and 10th and 90th percentiles) but not kurtosis or skewness were different among pediatric low-grade glioma subgroups ($P < .05$). Diffusivity was lowest in *BRAF* V600E-mutant tumors (the 10th percentile reached an area under the curve of 0.9 on receiver operating characteristic analysis). There were significant differences between evaluated pediatric low-grade glioma margins and cystic components ($P = .03$ and $P = .001$, respectively). Well-defined margins were characteristic of *BRAF*-*KIAA* or wild-type *BRAF* rather than *BRAF* V600E-mutant or type 1 neurofibromatosis tumors. None of the type 1 neurofibromatosis tumors showed a cystic component.

CONCLUSIONS: Imaging features of pediatric low-grade gliomas, including quantitative diffusion metrics, may assist in predicting *BRAF* and type 1 neurofibromatosis status, suggesting a radiologic-genetic correlation, and might enable early genetic signature characterization.

ABBREVIATIONS: AUC = area under the curve; GG = ganglioglioma; MAPK = mitogen-activated protein kinase pathway; NFI = type 1 neurofibromatosis; pLGG = pediatric low-grade glioma; rADC = relative ADC; RAS = rat sarcoma virus; ROC = receiver operating characteristic

Pediatric low-grade gliomas (pLGGs) are the most frequent brain tumors in children.¹ pLGGs are defined as World Health Organization grade I or II malignancies and include a wide array of histologies, such as juvenile pilocytic astrocytoma, ganglioglioma (GG), dysembryoplastic neuroepithelial tumor, and pleomorphic xanthoastrocytoma.² The components of treatment for pLGGs

have historically been surgery, radiation, and multiagent chemotherapy. Surgical resection may be curative in the case of gross total resection. However, most children cannot undergo complete resection due to the location of the tumor. Ten-year progression-free survival drops significantly if a radiologically visible residual tumor is evident.³ In such patients, adjuvant focal radiation therapy was performed in the past. However, due to the long-term adverse effects of radiation, adjuvant chemotherapy has been the main treatment technique for patients with pLGG.

BRAF is a serine/threonine-protein kinase that has a key role in growth signal transduction. In the past decade, emerging molecular data have suggested that in pLGGs, there is near-universal up-regulation of the rat sarcoma virus (RAS)-mitogen-activated protein kinase pathway (MAPK),⁴ most commonly due to somatic alterations involving the *BRAF* proto-oncogene or germline type 1

Received February 28, 2022; accepted after revision June 28.

From the Section of Neuroradiology, Division of Diagnostic Imaging (S.S., A.K., J.B., C.H.) and Department of Pediatric Hemato-Oncology (M.L., M.Y.), Sheba Medical Center, Ramat-Gan, Israel; and Sackler School of Medicine (S.S., C.H., M.Y.), Tel Aviv University, Tel Aviv, Israel.

Please address correspondence to Shai Shrot, MD, Section of Neuroradiology, Division of Diagnostic Imaging, Sheba Medical Center, 2 Sheba Rd, Ramat Gan, 52621 Israel; e-mail: shai.shrot@sheba.health.gov.il

 Indicates article with online supplemental data.

<http://dx.doi.org/10.3174/ajnr.A7614>

neurofibromatosis (NF1) alterations.⁵ The 2 major *BRAF* gene alterations in pLGG are *BRAF* rearrangement (duplication of the *BRAF* oncogene, followed by its insertion into 1 of several fusion targets, most often the *KIAA1549* gene) and *BRAF* V600E point mutation (V600E).⁴ These molecular alterations in the *BRAF* gene lead to constitutive activation of the kinase and downstream signaling pathways that drive uncontrolled cell proliferation and tumorigenesis.

NF1 is a common autosomal dominant disorder that results in the most frequent tumor predisposition syndrome. Neurofibromin, the protein product of the *NF1* gene that is mutated in patients with NF1, has been shown to function as a tumor-suppressor gene, acting as a negative regulator of RAS. Loss of neurofibromin increases RAS activity and induces downstream activity of the MAPK pathway as well as the PI3K-Akt-mammalian target of rapamycin (mTOR) pathway.⁵ Approximately 15% of children with NF1 develop low-grade optic pathway gliomas. Therefore, optic pathway gliomas in these patients are primarily diagnosed via germline *NF1* alteration and imaging rather than a biopsy.⁶

Exploring the *BRAF* status of pLGGs improves risk-stratification and tailored targeted therapies in patients with residual disease in whom additional therapy is needed.⁷ Whereas patients with *BRAF* fusion and NF1 have a favorable outcome, those with the *BRAF* V600E mutation, particularly associated with cyclin-dependent kinase inhibitor 2A (*CDKN2A*) deletion, are at increased risk of progression with shorter progression-free survival rates and worse response to chemotherapy.^{7,8} Furthermore, molecularly targeted therapies have been shown to be effective in patients with residual pLGGs; for instance, type I *BRAF* inhibitors for *BRAF* V600E pLGG and mitogen-activated protein kinase inhibitors for pLGGs driven by *NF1*, *BRAF-KIAA* rearrangement, or *BRAF* V600E mutation. Most important, type I *BRAF* inhibitors have been shown to result in paradoxical activation and accelerating growth of pLGGs driven by the *BRAF-KIAA* fusion.⁹ Therefore, identifying the exact molecular alteration is crucial.

Radiogenomic techniques, which have emerged as valuable imaging tools to characterize brain tumors noninvasively, have a pivotal role in making treatment decisions in patients with pLGGs. Recently, a few studies have described imaging features of pLGGs in correlation with their *BRAF* status.^{10,11} Ramaglia et al¹¹ found lower ADC values in V600E-mutant pLGGs, though no morphologic imaging characteristics were found to have discriminative power from wild-type *BRAF*. More advanced ADC metrics (such as histogram analysis) found to be of diagnostic value in pediatric tumors^{12,13} have not been evaluated in the genetic characterization of pLGG (*BRAF* or *NF1* status). We hypothesized that ADC metrics obtained through volumetric ADC histogram analyses of pLGGs at baseline would enable early detection of *BRAF* and *NF1* status.

MATERIALS AND METHODS

The institutional review board of the Sheba Medical Center approved this retrospective study.

Study Design and Population

Patients with pLGG, diagnosed and treated in our tertiary pediatric neuro-oncology clinics, were included. Inclusion criteria were the

following: 1) available baseline presurgical MR imaging, and 2) biopsy and characteristics of *BRAF* status or a diagnosis of germline *NF1*. Exclusion criteria included a markedly degraded MR imaging study, pure optic nerve involvement, and spinal location.

Brain MR Imaging

MR imaging studies were performed in multiple centers on 1.5T or 3T magnets across various vendors. All patients had routine clinical MR imaging scans, including precontrast and postcontrast T1-weighted images, T2-FLAIR, and T2-weighted images. These sequences were performed with variable section thickness ranging from 1 to 5 mm. Heme-sensitive sequences, such as T2* gradient recalled-echo or SWI, were available in 33 patients. On each scanner, the DWI acquisition consisted of a diffusion-sensitized axial 2D spin-echo sequence with an EPI readout, with 2 *b* values of 0 and 1000 s/mm². Section thickness ranged from 3 to 4 mm, with interslice gaps of 0–1 mm.

Image Analysis

We analyzed the following tumoral morphologic imaging features: the presence of well-defined margins, a cystic component, contrast enhancement, and hemorrhagic components or calcifications, which were evaluated only in cases with available heme-sensitive MR imaging sequences (T2* or SWI) or CT scans. These were recorded as binary variables. As for location, classification was according to the epicenter of the tumor (cerebral hemispheres, cerebellum, brainstem, or diencephalon). All images were assessed in consensus by 2 board-certified neuroradiologists (J.B. and S.S.) with 3 and 6 years of experience, respectively, blinded to the pathologic diagnosis.

DWI Measurements

Tumor segmentation was performed by a board-certified radiologist (A.K.) and was confirmed in consensus by a board-certified neuroradiologist with 6 years of neuroradiology experience (S.S.) using 3D Slicer (Version 4.11.2; <http://www.slicer.org>¹⁴). Semiautomated tumor segmentation was performed on T2-FLAIR images in all respective MR imaging sections on noncystic, noncalcified, or hemorrhagic tumor areas using the level tracing effect tool. All ROIs were then copied to the automatically coregistered corresponding ADC maps via 3D Slicer. The transposed volumetric ROI was evaluated and manually corrected on the ADC maps, if necessary, by A.K. and S.S. in consensus. DWI metrics and histogram analysis of the selected volumetric whole-lesion ROIs were performed using the module SlicerRadiomics extension.¹⁵ For normalization of ADC values, a circular ROI was drawn on the right eye and left thalamus. Relative ADC (rADC) ratios were calculated by dividing each ADC metric of the lesion by the mean ADC value of the right eye and the normal-appearing thalamus. This step was performed to adjust ADC values across MR imaging vendors and magnetic field strengths.

Statistical Analysis

Descriptive statistics included mean and SD of continuous parameters; in the case of categorical factors, number and percentage distribution were used. The χ^2 test was used to analyze the differences in the categorical parameters and qualitative features among the various molecular tumor groups. DWI histogram analysis included

10th and 90th percentiles, mean, median, skewness, and kurtosis. The Kruskal-Wallis test with the post hoc Dunn-Bonferroni method was used to compare diffusivity metrics among genetic subgroups. *P* values have been adjusted by the Bonferroni correction for multiple comparisons. Receiver operating characteristic (ROC) curve analysis was performed, and the respective area under the curve (AUC) was calculated to assess the accuracy of ADC histogram features in differentiating various pLGG subgroups. The ROC curve plots the true-positive rate against the false-positive rate at various threshold settings. The DeLong test was used for the comparison of various AUCs. A 2-tailed *P* < .05 was considered statistically significant. Analyses were performed with SPSS (Version 27.0, 2021; IBM).

RESULTS

Study Population

The study cohort (Fig 1) included 51 patients in whom histologically proved tumors included pilocytic astrocytoma (*n* = 33), GG (*n* = 4), pleomorphic xanthoastrocytoma (*n* = 2), and diffuse astrocytoma grade II (*n* = 1). Of patients with NF1, 11 underwent imaging with a diagnosis of a low-grade tumor without a biopsy.

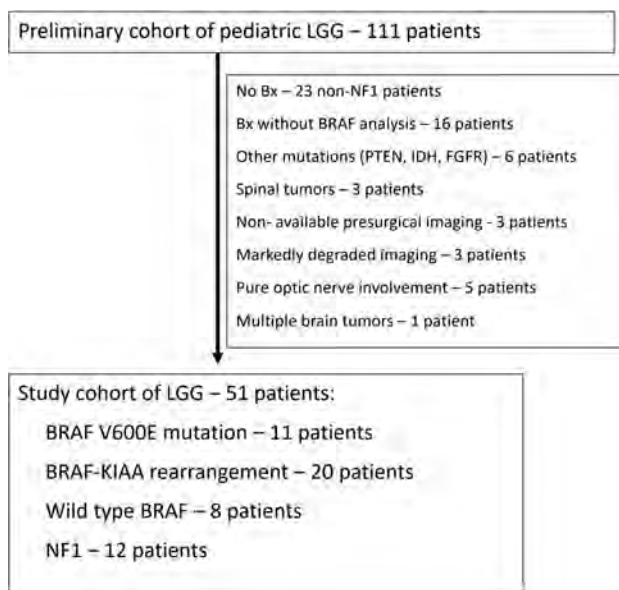


FIG 1. Study flow chart. Bx indicates biopsy.

One patient with NF1 underwent a biopsy with a histology of GG. *BRAF* molecular analysis was performed for patients without NF1. Eleven patients presented with the *BRAF* V600E mutation; 20 patients had *BRAF*-*KIAA* rearrangement, and 8 had *BRAF* wild-type tumors. pLGG was diagnosed at a younger age in patients with *BRAF*-*KIAA* rearrangement and NF1 groups than in *BRAF* V600E-mutant or wild-type *BRAF* groups (*P* = .03). The major demographic data are presented in Table 1.

Morphologic MR Imaging Findings

Ill-defined borders were more characteristic of *BRAF* V600E-mutant tumors rather than in *BRAF*-*KIAA* rearrangement or wild-type *BRAF* pLGGs. Examples of MR images of pLGGs are shown in Fig 2. Hemorrhagic components or calcifications were seen in wild-type *BRAF* tumors compared with *BRAF* alterations of NF1 tumors. Lack of a cystic component characterized NF1 tumors compared with *BRAF* alteration of wild-type *BRAF* tumors. No significant differences were found among study groups in terms of tumor location. A summary of the morphological imaging findings is presented in Table 2.

Diffusion Metrics

Significant differences were found in evaluated diffusion metrics between pLGG subgroups, except for kurtosis and skewness (Online Supplemental Data). These results were similar when ADC measurements were normalized to the thalamus or the eye globe. For most diffusivity metrics, rADC measurements were lower in *BRAF* V600E-mutant tumors than in the *BRAF*-*KIAA* rearrangement subgroup (representative metrics are presented in Fig 3). rADC_{mean} and rADC_{median} (relative to the thalamus) were significantly lower in NF1 tumors compared with *BRAF*-*KIAA* rearrangement or wild-type *BRAF* subgroups (*P* < .001). Differences in diffusion histogram metrics among pLGG subgroups were also significant when excluding NF1 tumors (Online Supplemental Data).

According to ROC curve analyses, the rADC₁₀ values had the highest AUC values for differentiating *BRAF* V600E-mutant from the *BRAF*-*KIAA* rearrangement group (AUC = 0.895 and 0.905, relative to the thalamus or eye globe, respectively). rADC₁₀ values also had high diagnostic performances for differentiating *BRAF* V600E-mutant from *BRAF*-*KIAA* rearrangement or wild-type *BRAF* (AUC = 0.873 and 0.864, relative to the thalamus or eye globe, respectively). However, the high performance of rADC₁₀ did not reach statistical significance compared with other diffusivity metrics. For differentiating NF1 tumors from wild-

Table 1: Major clinical characteristics and tumor histology in various pLGG subgroups

	<i>BRAF</i> V600E-Mut (<i>n</i> = 11)	<i>BRAF</i> - <i>KIAA</i> Rearrangement (<i>n</i> = 20)	Wild-Type <i>BRAF</i> (<i>n</i> = 8)	NF1 (<i>n</i> = 12)	<i>P</i> Value
Sex (male/female)	8/3	7/13	5/3	7/5	.45
Age at diagnosis (mean) (yr)	9.1 (SD, 4.7)	5.4 (SD, 3.9)	14.6 (SD, 8.7)	4.9 (SD, 2.9)	.03
Histology (No.)					
PA	7	19	7		
GG	2		1	1 ^a	
PXA	2				
Diffuse astrocytoma (grade II)		1			

Note:—PA indicates pilocytic astrocytoma; PXA, pleomorphic xanthoastrocytoma; Mut, mutant.

^a In 1 patient with NF1, a ganglioglioma was found at biopsy.

type or altered *BRAF*, the performance of diffusivity metrics was relatively low, except for $rADC_{min}$ (AUC = 0.803 and 0.746, relative to the thalamus or eye globe, respectively). Overall, diagnostic performances were similar when comparing the normalization of ADC values with that of the thalamus or eye globe. In NF1

tumors, except for $rADC_{min}$, there was higher discriminative power for normalization to the globe over the thalamus ($P < .001-.02$), even though absolute AUC values were relatively low. The diagnostic performance of $rADC_{min}$, $rADC_{10}$, $rADC_{90}$, $rADC_{mean}$, and $rADC_{median}$ for differentiating various pLGG subgroups is summarized in the Online Supplemental Data.

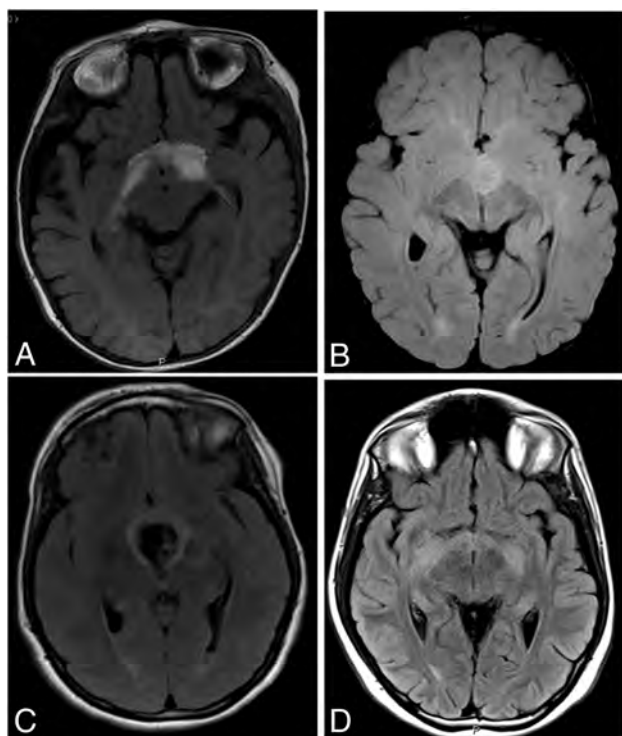


FIG 2. Representative T2-FLAIR images of pLGGs of various molecular subgroups. A, A 5-month-old boy with a diencephalic pLGG infiltrating the optic tracts (*BRAF*-mutant). B, A 15-year-old boy with a well-defined diencephalic pLGG (*BRAF*-KIAA rearrangement). C, A 20-year-old woman with well-defined diencephalic pLGG (wild-type *BRAF*), associated with a large central hemorrhagic area. D, A 16-year-old boy with a typical diencephalic glioma infiltrating the optic tracts (NF1).

DISCUSSION

In the past decade, there has been increasing evidence of the importance of *BRAF* status, which has major therapeutic and prognostic implications in pLGGs, especially if these tumors are unresectable.⁷ Currently, most non-NF1 pLGGs undergo surgical biopsy for genetic analysis, even if curative resection is not possible. Our results suggest that in pLGGs, morphologic MR imaging features show significant differences according to *BRAF* and *NF1* status, which might improve the early prediction of the genetic alterations of pLGGs. Quantitative diffusion metrics from cumulative ADC histograms based on the T2-FLAIR imaging abnormalities were found to be promising for differentiating pLGG subgroups. However, other parameters of histogram distribution, particularly kurtosis and skewness, have limited diagnostic value.

The ill-defined border of the pLGG, radiographically suggesting infiltration, was found in our cohort to be more characteristic for *BRAF* V600E-mutant pLGGs (10/11) compared with wild-type *BRAF* (5/13) or *BRAF*-KIAA rearrangement (11/20). Ho et al¹⁰ have described peritumoral T2 abnormality, suggesting infiltration in half the *BRAF* V600E-mutant pLGGs compared with a minority (~8%) of wild-type *BRAF* tumors. Most interesting, such infiltration is a well-known feature of NF1 tumors, also found in our cohort (10/12). In our cohort, hemorrhagic components or calcifications were characteristic of wild-type *BRAF* pLGG over other *BRAF* alterations or NF1 tumors.

Nevertheless, there is usually an overlap of qualitative imaging characteristics, limiting their use in defining the pLGG subgroup signature. Studies describing quantitative imaging features differentiating pLGG molecular subgroups are even more sparse than

Table 2: Morphologic MR imaging characteristics

	<i>BRAF</i> V600E-Mut (n = 11)	<i>BRAF</i> -KIAA Rearrangement (n = 20)	Wild-Type <i>BRAF</i> (n = 8)	NF1 (n = 12)	P Value
Location (No.) (%)					
Cerebral hemisphere	3 (27.3%)	3 (15%)	1 (12.5%)	1 (8.3%)	.15
Cerebellum	1 (9.1%)	7 (35%)	5 (62.5%)	2 (16.7%)	
Brainstem	2 (18.2%)	6 (30%)	0 (0%)	2 (16.7%)	
Diencephalon	5 (45.5%)	4 (20%)	2 (25%)	7 (58.3%)	
Well-defined margins (yes/no)	9.1% (1/10)	45.0% (9/11)	62.5% (5/3)	16.6% (2/10)	.03 ^{a,b,c}
Hemorrhagic components or calcifications (yes/no)*	0% (0/8)	15.3% (2/11)	62.5% (5/3)	0% (0/6)	.005 ^{b,c,f}
Cystic components (yes/no)	45.4% (5/6)	60% (12/8)	87.5% (7/1)	0% (0/12)	.001 ^{c,d,e}
Contrast enhancement (yes/no)	81.8% (9/2)	85% (17/3)	100% (8/0)	50% (6/6)	.04 ^{c,d}

Note:—Mut indicates mutant. Each superscript letter represents a significant difference between 2 categories.

^a *BRAF* V600E-mutant versus *BRAF*-KIAA rearrangement.

^b *BRAF* V600E-mutant versus *BRAF* wild-type.

^c *BRAF* wild-type versus NF1.

^d *BRAF* V600E-mutant versus NF1.

^e *BRAF*-KIAA rearrangement versus NF1.

^f *BRAF* wild-type versus *BRAF*-KIAA rearrangement.

* Evaluated only when SWI/T2* or CT scans were available (n = 35).

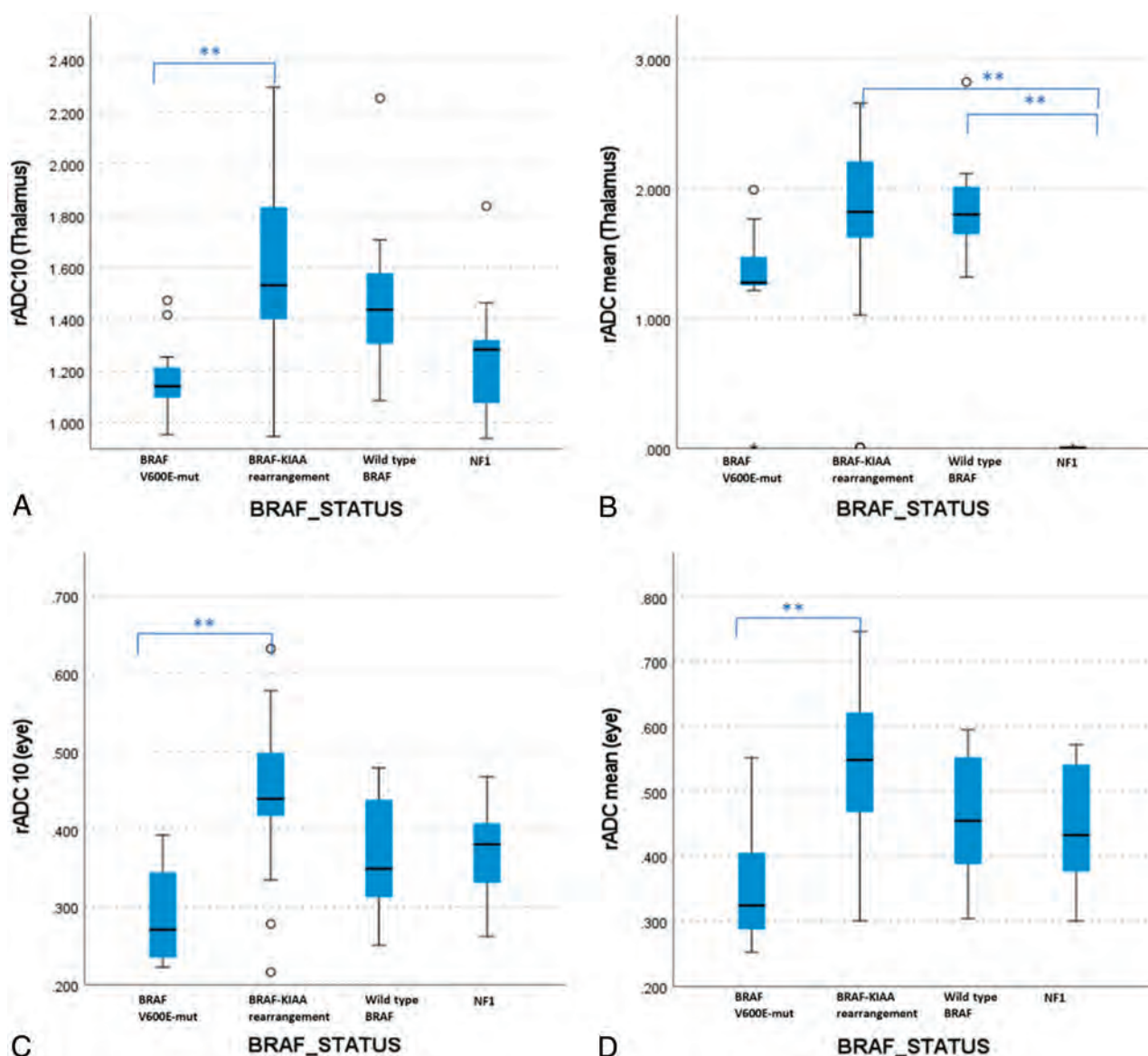


FIG 3. Boxplots comparing rADC₁₀ and rADC_{mean}, relative to the mean ADC values of the right thalamus (A and B, respectively) or the right eye globe (C and D, respectively). Group differences were significant ($P < .001$, Kruskal-Wallis test). Significant pair-wise differences are indicated in the figure (Dunn-Bonferroni post hoc analysis, Double asterisks indicate $P < .005$).

descriptive imaging studies. To our knowledge, there have been only a limited number of reports regarding genetic profiling of pLGG using DWI and no literature reports investigating the usefulness of the ADC histogram for such analysis. In our study, *BRAF* V600E-mutant pLGGs showed decreased diffusivity on various diffusion histogram metrics (ADC₁₀, ADC₉₀, mean and median ADC values) compared with *BRAF*-KIAA rearrangement pLGGs. Similar results were also reported by Ramaglia et al¹¹ for *BRAF* V600E-mutant pLGG, compared with wild-type *BRAF*, though *BRAF*-KIAA rearrangement or NF1 pLGG were not included in their study.

In a small case series, Ishi et al¹⁶ described a lower T2 signal and a larger T2/contrast-enhanced T1 mismatch to be more suggestive of *BRAF* V600E-mutation in optic pathway gliomas. Recently, Wagner et al described using a machine learning scheme to differentiate pLGG genetics subgroups according to their T2-FLAIR features.¹⁷ Although machine learning-based approaches might detect

differences in neuroimaging data that might not be identified with conventional approaches, such as multiple T2-FLAIR features, traditional statistical approaches, such as used in the current study, might improve our understanding of the different radiologic-pathologic correlations in various pLGGs. Although isocitrate dehydrogenase (*IDH*) mutations are rare among pLGGs,¹⁸ diffusion metrics were also found to assist in differentiating *IDH* status in adult LGGs.^{19,20} Most ADC percentiles were found to be lower in *IDH*-negative compared with *IDH*-mutated gliomas.

DWI reflects the free motion of water molecules in biologic tissue.²¹ Highly cellular tumors, ie, with a high nuclear-to-cytoplasmic ratio, typically show diffusion restriction with decreased ADC values.²² Ho et al¹⁰ have described a distinctive histologic pattern in *BRAF* V600E-mutant pLGG of a monophasic dense, compact architecture resembling the compact, fiber-rich regions previously described in pilocytic astrocytomas, which might explain the

decreased diffusivity found in these tumors in our cohort compared with wild-type *BRAF* pLGG. For ADC measurements, most studies used ROI analysis to evaluate brain lesions. Such analysis is based on the representative part of the lesion.^{23,24} However, selecting a representative location is subjective and may be difficult, especially when the lesion is heterogeneous and includes atypical imaging features. ADC histogram analysis was found to be useful for grading gliomas and predicting the treatment response and progression-free survival rates in patients with high-grade gliomas.^{25–27} Given that histogram analysis includes an entire lesion, it may reveal the heterogeneity of lesions and thus ensure more accurate tissue characteristics.

NF1 is a tumor-predisposition genetic disorder, usually diagnosed using a clinical phenotype indicative of a germline *NF1* mutation.⁶ The most common CNS tumors in NF1 are low-grade gliomas, with the optic pathway glioma being the hallmark lesion. Surgery is not the first treatment choice in NF1-associated gliomas, which are commonly nonresectable and have a relatively benign course. However, infiltrative optic pathway pLGG, typical of patients with NF1, might have a *BRAF* alteration rather than an *NF1* mutation, a difference that has major clinical consequences.²⁸ A biopsy is often performed in such cases, especially if NF1 cannot be diagnosed clinically or genetically. Our results might also assist in identifying the imaging signature of NF1 pLGG relative to other *BRAF*-altered gliomas.

The reproducibility of lesional ADC measurements over various field strengths, different vendors, and acquisition parameters is critical for the applicability of our results. Multiple in vivo studies have reported near-identical ADC measurements on 1.5T and 3T scanners.^{29,30} However, other phantoms and in vivo studies have demonstrated a significant ADC difference among different magnet fields.^{31,32} Therefore, Sasaki et al³¹ have suggested using rADC values because they might be more suitable than absolute ADC values for evaluating diffusion abnormalities acquired in different scanners and field strengths. ROIs drawn on the normal-appearing white matter³³ or gray matter¹¹ are commonly used for ADC normalization. We have calculated the rADC values normalized to the normal-appearing thalamus and the eye globe to minimize the differences among absolute ADC values across various platforms. Both references have shown similar reproducible and discriminative results among various pLGG subgroups. Such rADCs are robust across MR imaging vendors and platforms and may be considered reliable.^{11,34} The ADC histogram analysis technique used in the current study is a promising method that can be used on clinically acquired diffusion MR imaging data for subsequent analysis, allowing comparison at different institutions and use in multicenter clinical trials.

There are several limitations to our study. First, our study was a retrospective investigation of a relatively small patient cohort. More pLGGs will be required to strengthen the statistical power and generalize our results in future studies. Due to the small cohort, obtaining ADC thresholds from ROC-AUC, which can be used in clinical settings, is limited. Second, accurately defining the imaging borders of infiltrative lesions is suboptimal, with relatively high interobserver variability. Given the large volumetric data included in the histogram analysis of an entire lesion, the

nonperfect delineation of the lesion boundaries is relatively acceptable compared with ROI analysis. Last, tumor delineation was performed on T2-FLAIR images, and coregistration of T2-FLAIR imaging with the ADC map was required in our study. Although the tumor was carefully delineated, there is still the possibility of misregistration and the inclusion of erroneous ADC values at the tumor boundaries.

In the current study, diffusion metrics have improved radiologic-genetic correlation in pLGGs. Such tumoral quantitative features have the potential for better characterizing tumor structure and evaluating early treatment-related changes. Diffusion metrics have been shown to correlate and even predict the response to radiation or biologic treatment in high-grade gliomas.^{35,36} Moreover, Poussaint et al³⁷ described a significant correlation between diffusion metrics and survival in patients with diffuse intrinsic pontine gliomas. In the current study, due to the small number of patients and heterogeneity of treatment protocols, such correlation between diffusion metrics and response to treatment could not be assessed.

CONCLUSIONS

Our results suggest that ADC histogram analysis based on an entire pLGG could help to discriminate various pLGG genetic subgroups, thus expanding and refining the correlation between clinically acquired imaging, including DWI, and the pLGG genetic signature. Such radiologic-genetic correlation has a critical role in the early detection of molecular subgroups and early clinical stratification of children with pLGGs.

Disclosure forms provided by the authors are available with the full text and PDF of this article at www.ajnr.org.

REFERENCES

- Ostrom QT, de Blank PM, Kruchko C, et al. **Alex's Lemonade Stand Foundation Infant and Childhood Primary Brain and Central Nervous System Tumors Diagnosed in the United States in 2007–2011.** *Neuro Oncol* 2015;16(Suppl 10):x1–36 CrossRef Medline
- Komori T. **The 2016 WHO Classification of Tumours of the Central Nervous System: the major points of revision.** *Neurol Med Chir (Tokyo)* 2017;57:301–11 CrossRef Medline
- Wisoff JH, Sanford RA, Heier LA, et al. **Primary neurosurgery for pediatric low-grade gliomas: a prospective multi-institutional study from the Children's Oncology Group.** *Neurosurgery* 2011;68:1548–54; discussion 1554–55 CrossRef Medline
- AlRayahi J, Zapotocky M, Ramaswamy V, et al. **Pediatric brain tumor genetics: what radiologists need to know.** *Radiographics* 2018;38:2102–22 CrossRef Medline
- Szudek J, Birch P, Riccardi VM, et al. **Associations of clinical features in neurofibromatosis 1 (NF1).** *Genet Epidemiol* 2000;19:429–39 CrossRef Medline
- Helfferich J, Nijmeijer R, Brouwer OF, et al. **Neurofibromatosis type 1 associated low grade gliomas: a comparison with sporadic low grade gliomas.** *Crit Rev Oncol Hematol* 2016;104:30–41 CrossRef Medline
- Vuong HG, Altibi AM, Duong UN, et al. **BRAF mutation is associated with an improved survival in glioma—a systematic review and meta-analysis.** *Mol Neurobiol* 2018;55:3718–24 CrossRef Medline
- Mistry M, Zhukova N, Merico D, et al. **BRAF mutation and CDKN2A deletion define a clinically distinct subgroup of childhood secondary high-grade glioma.** *J Clin Oncol* 2015;33:1015–22 CrossRef Medline

9. Karajannis MA, Legault G, Fisher MJ, et al. **Phase II study of sorafenib in children with recurrent or progressive low-grade astrocytomas.** *Neuro Oncol* 2014;16:1408–16 CrossRef Medline
10. Ho CY, Mobley BC, Gordish-Dressman H, et al. **A clinicopathologic study of diencephalic pediatric low-grade gliomas with BRAF V600 mutation.** *Acta Neuropathol* 2015;130:575–85 CrossRef Medline
11. Ramaglia A, Tortora D, Mankad K, et al. **Role of diffusion weighted imaging for differentiating cerebral pilocytic astrocytoma and ganglioglioma BRAF V600E-mutant from wild type.** *Neuroradiology* 2020;62:71–80 CrossRef Medline
12. Rodriguez Gutierrez D, Awwad A, Meijer L, et al. **Metrics and textural features of MRI diffusion to improve classification of pediatric posterior fossa tumors.** *AJNR Am J Neuroradiol* 2014;35:1009–15 CrossRef Medline
13. Bull JG, Saunders DE, Clark CA. **Discrimination of paediatric brain tumours using apparent diffusion coefficient histograms.** *Eur Radiol* 2012;22:447–57 CrossRef Medline
14. Parmar C, Rios Velazquez E, Leijenaar R, et al. **Robust radiomics feature quantification using semiautomatic volumetric segmentation.** *PLoS One* 2014;9:e102107 CrossRef Medline
15. van Griethuysen JJ, Fedorov A, Parmar C, et al. **Computational radiomics system to decode the radiographic phenotype.** *Cancer Res* 2017;77:e104–07 CrossRef Medline
16. Ishi Y, Yamaguchi S, Yoshida M, et al. **Correlation between magnetic resonance imaging characteristics and BRAF alteration status in individuals with optic pathway/hypothalamic pilocytic astrocytomas.** *J Neuroradiol* 2021;48:266–270 CrossRef Medline
17. Wagner MW, Hain N, Khalvati F, et al. **Radiomics of pediatric low-grade gliomas: toward a pretherapeutic differentiation of BRAF-mutated and BRAF-fused tumors.** *AJNR Am J Neuroradiol* 2021;42:759–765 CrossRef Medline
18. Ryall S, Tabori U, Hawkins C. **Pediatric low-grade glioma in the era of molecular diagnostics.** *Acta Neuropathol Commun* 2020;8:30 CrossRef Medline
19. Lee S, Choi SH, Ryoo I, et al. **Evaluation of the microenvironmental heterogeneity in high-grade gliomas with IDH1/2 gene mutation using histogram analysis of diffusion-weighted imaging and dynamic-susceptibility contrast perfusion imaging.** *J Neurooncol* 2015;121:141–50 CrossRef Medline
20. Lee MK, Park JE, Jo Y, et al. **Advanced imaging parameters improve the prediction of diffuse lower-grade gliomas subtype, IDH mutant with no 1p19q codeletion: added value to the T2/FLAIR mismatch sign.** *Eur Radiol* 2020;30:844–54 CrossRef Medline
21. Koh DM, Collins DJ. **Diffusion-weighted MRI in the body: applications and challenges in oncology.** *AJR Am J Roentgenol* 2007;188:1622–35 CrossRef Medline
22. Guo AC, Cummings TJ, Dash RC, et al. **Lymphomas and high-grade astrocytomas: comparison of water diffusibility and histologic characteristics.** *Radiology* 2002;224:177–83 CrossRef Medline
23. Doskalyev A, Yamasaki F, Ohtaki M, et al. **Lymphomas and glioblastomas: differences in the apparent diffusion coefficient evaluated with high b-value diffusion-weighted magnetic resonance imaging at 3T.** *Eur J Radiol* 2012;81:339–44 CrossRef Medline
24. Calli C, Kitis O, Yuntun N, et al. **Perfusion and diffusion MR imaging in enhancing malignant cerebral tumors.** *Eur J Radiol* 2006;58:394–403 CrossRef Medline
25. Gühr G, Horvath-Rizea D, Hekeler E, et al. **Diffusion weighted imaging in high-grade gliomas: a histogram-based analysis of apparent diffusion coefficient profile.** *PLoS One* 2021;16:e0249878 CrossRef Medline
26. Aboian MS, Tong E, Solomon DA, et al. **Diffusion characteristics of pediatric diffuse midline gliomas with histone H3-K27M mutation using apparent diffusion coefficient histogram analysis.** *AJNR Am J Neuroradiol* 2019;40:1804–10 CrossRef Medline
27. Kang Y, Choi SH, Kim YJ, et al. **Gliomas: histogram analysis of apparent diffusion coefficient maps with standard- or high-b-value diffusion-weighted MR imaging—correlation with tumor grade.** *Radiology* 2011;261:882–90 CrossRef Medline
28. Lobon-Iglesias MJ, Laurendeau I, Guerrini-Rousseau L, et al. **NF1-like optic pathway gliomas in children: clinical and molecular characterization of this specific presentation.** *Neurooncol Adv* 2020;2:i98–106 CrossRef Medline
29. Matsuoka A, Minato M, Harada M, et al. **Comparison of 3.0- and 1.5-Tesla diffusion-weighted imaging in the visibility of breast cancer.** *Radiat Med* 2008;26:15–20 CrossRef Medline
30. Saremi F, Jalili M, Sefidbakht S, et al. **Diffusion-weighted imaging of the abdomen at 3 T: image quality comparison with 1.5-T magnet using 3 different imaging sequences.** *J Comput Assist Tomogr* 2011;35:317–25 CrossRef
31. Sasaki M, Yamada K, Watanabe Y, et al; Acute Stroke Imaging Standardization Group-Japan (ASIST-Japan) Investigators. **Variability in absolute apparent diffusion coefficient values across different platforms may be substantial: a multivendor, multi-institutional comparison study.** *Radiology* 2008;249:624–30 CrossRef Medline
32. Tsujita N, Kai N, Fujita Y, et al. **Interimager variability in ADC measurement of the human brain.** *Magn Reson Med Sci* 2014;13:81–87 CrossRef Medline
33. Wu CC, Jain R, Radmanesh A, et al. **Predicting genotype and survival in glioma using standard clinical MR imaging apparent diffusion coefficient images: a pilot study from the Cancer Genome Atlas.** *AJNR Am J Neuroradiol* 2018;39:1814–20 CrossRef Medline
34. Harreld JH, Hwang SN, Qaddoumi I, et al. **Relative ADC and location differ between posterior fossa pilocytic astrocytomas with and without gangliocytic differentiation.** *AJNR Am J Neuroradiol* 2016;37:2370–75 CrossRef Medline
35. McDonald CR, Delfanti RL, Krishnan AP, et al. **Restriction spectrum imaging predicts response to bevacizumab in patients with high-grade glioma.** *Neuro Oncol* 2016;18:1579–90 CrossRef Medline
36. Rodriguez Gutierrez D, Manita M, Jaspan T, et al. **Serial MR diffusion to predict treatment response in high-grade pediatric brain tumors: a comparison of regional and voxel-based diffusion change metrics.** *Neuro Oncol* 2013;15:981–89 CrossRef Medline
37. Poussaint TY, Vajapeyam S, Ricci KI, et al. **Apparent diffusion coefficient histogram metrics correlate with survival in diffuse intrinsic pontine glioma: a report from the Pediatric Brain Tumor Consortium.** *Neuro Oncol* 2016;18:725–34 CrossRef Medline

Noninvasive Follow-up Imaging of Ruptured Pediatric Brain AVMs Using Arterial Spin-Labeling

J.F. Hak, G. Boulouis, B. Kerleroux, S. Benichi, S. Stricker, F. Gariel, L. Garzelli, P. Meyer, M. Kossorotoff, N. Boddaert, N. Girard, V. Vidal, V. Dangouloff Ros, T. Blauwblomme, and O. Naggara

ABSTRACT

BACKGROUND AND PURPOSE: Brain AVMs represent the main etiology of pediatric intracranial hemorrhage. Noninvasive imaging techniques to monitor the treatment effect of brain AVMs remain an unmet need. In a large cohort of pediatric ruptured brain AVMs, we aimed to investigate the role of arterial spin-labeling for the longitudinal follow-up during treatment and after complete obliteration by analyzing CBF variations across treatment sessions.

MATERIALS AND METHODS: Consecutive patients with ruptured brain AVMs referred to a pediatric quaternary care center were prospectively included in a registry that was retrospectively queried for children treated between 2011 and 2019 with unimodal or multimodal treatment (surgery, radiosurgery, embolization). We included children who underwent an arterial spin-labeling sequence before and after treatment and a follow-up DSA. CBF variations were analyzed in univariable analyses.

RESULTS: Fifty-nine children with 105 distinct treatment sessions were included. The median CBF variation after treatment was -43 mL/100 mg/min (interquartile range, -102 – -5.5), significantly lower after complete nidus surgical resection. Following radiosurgery, patients who were healed on the last DSA follow-up demonstrated a greater CBF decrease on intercurrent MR imaging, compared with patients with a persisting shunt at last follow-up (mean, -62 [SD, 61] mL/100 mg/min versus -17 [SD, 40.1] mL/100 mg/min; $P = .02$). In children with obliterated AVMs, recurrences occurred in 12% and resulted in a constant increase in CBF (mean, $+89$ [SD, 77] mL/100 mg/min).

CONCLUSIONS: Our results contribute data on the role of noninvasive arterial spin-labeling monitoring of the response to treatment or follow-up after obliteration of pediatric AVMs. Future research may help to better delineate how arterial spin-labeling can assist in decisions regarding the optimal timing for DSA.

ABBREVIATIONS: ASL = arterial spin-labeling; EVT = endovascular treatment; IQR = interquartile range; SRS = stereotactic radiosurgery

Pediatric intracerebral hemorrhage accounts for half of strokes in children^{1–3} and has severe long-term medical and psychosocial consequences.⁴ In children, brain AVMs represent the main underlying risk factor for hemorrhage, being responsible for up to

80% of nontraumatic hemorrhages.^{1,3} Treatment strategy includes surgical excision, serial endovascular treatment (EVT), and stereotactic radiosurgery (SRS), alone or in combination, according to the AVM size and location. After the initial work-up and treatment of a ruptured AVM, invasive DSA is the criterion standard to tailor the adequate subsequent therapeutic strategy^{5,6} or to confirm the complete obliteration of the AVM. Nevertheless, repeat DSA exposes children to the long-term risks of ionizing radiation, injection of an exogenous contrast agent, multiple exposures to general anesthesia, and neurologic adverse events. Hence, in children with ruptured AVMs, evaluating noninvasive imaging techniques for the mid and long-term intermediate follow-up and treatment

Received February 2, 2022; accepted after revision June 28.

From the Department of Pediatric Radiology (J.F.H., G.B., B.K., F.G., L.G., N.B., V.D.R., O.N.), Pediatric Neurointensive Care Unit (P.M.), and Department of Pediatric Neurology (M.K.), Assistance Publique–Hôpitaux de Paris, Hôpital Universitaire, Necker Hospital–Sick Children, Paris, France; Department of Neuroradiology (J.F.H., G.B., B.K., O.N.), GHU Paris, Paris, France; L'Institut National de la Santé et de la Recherche Médicale, University Hospital Group Paris, 1266, IMA-BRAIN (J.F.H., G.B., B.K., O.N.), Université de Paris, Paris, France; Department of Pediatric Neurosurgery (S.B., S.S., T.B.), Institut Imagine, L'Institut National de la Santé et de la Recherche Médicale, Unité Mixte de Recherche 1163, Assistance Publique–Hôpitaux de Paris, Necker Hospital–Sick Children, Paris, France; Department of Neuroradiology (F.G.), University Hospital of Bordeaux, Bordeaux, France; INSERM U894, French Center for Pediatric Stroke (M.K., T.B., O.N.), L'Institut National de la Santé et de la Recherche Médicale, Paris, France; Departments of Neuroradiology (N.G.) and Radiology (V.V.), University Hospital La Timone Hospital, Assistance Publique–Hôpitaux de Marseille, Marseille, France; Université de Paris (N.B., V.D.R.), L'Institut National de la Santé et de la Recherche Médicale, ERL, Paris, France; and Institut Imagine (N.B., V.D.R.), Université de Paris, Unité Mixte de Recherche 1163, Paris, France.

J.F. Hak and G. Boulouis contributed equally to this work.

J.F. Hak was supported by a grant provided by the Société Française de Radiologie, French Society of Radiology, together with the Collège des Enseignants en Radiologie de France, French Academic College of Radiology.

Please address correspondence to Jean-Francois Hak, MD, Department of Pediatric Radiology, AP-HP, University Hospital Necker-Enfants-Malades, 75015 Paris, France; e-mail: jeanfrancois.hak@gmail.com; @JFHak

<http://dx.doi.org/10.3174/ajnr.A7612>

planning is an important purpose. In this context, MR imaging possibly represents the best noninvasive technique, and advanced techniques such as arterial spin-labeling (ASL) sequences have shown their role in detecting increased CBF in patients with AVMs⁶ and are useful tools in adults for the follow-up of AVMs after embolization⁷ or SRS.⁸⁻¹¹ Furthermore, accumulating evidence indicates that AVMs in children are more likely to re-appear after DSA-proved complete obliteration,^{12,13} reinforcing the need for prolonged follow-up and the drawbacks of invasive imaging in the setting of a healed shunt. A preliminary analysis from our group¹⁴ evaluated the CBF, computed using ASL after treatment in 21 patients (yet only including 9 patients who had undergone ASL both before and after therapeutic procedures), and demonstrated its potential role in the noninvasive follow-up of AVMs in patients under treatment or after treatment.

In a large cohort of children with an initially ruptured AVM, we aimed to investigate the role of ASL for the longitudinal follow-up of patients under treatment and after complete obliteration by analyzing CBF variations on pseudocontinuous ASL across treatment sessions.

MATERIALS AND METHODS

Study Design and Patient Selection

Consecutive patients referred to our institution, a pediatric quaternary care center and coordinating center for the French Pediatric Stroke Network, were prospectively enrolled in a registry initiated in 2008. The registry has been described elsewhere in detail.⁴ For the purpose of this analysis, the sample was restricted to children (1 month to 18 years of age) meeting the following criteria: 1) ruptured brain AVMs; 2) between January 2011 (date of ASL implementation at our site) and October 2019; 3) with unimodal or multimodal AVM treatment (surgery, SRS, embolization); and 4) an ASL sequence before and after treatment and intercurrent DSA, performed within 24 hours of the ASL sequence. Patients were excluded for the following reasons: 1) no ASL follow-up; 2) no DSA follow-up; 3) a ruptured AVM without treatment; and 4) lost to follow-up.

Imaging Acquisition

MR Imaging Procedure. MR imaging was performed for each patient with a Signa HDxt 1.5T system (GE Healthcare) and a 12-channel head-neck-spine coil. The MR imaging investigation included standard pulse sequences according to local AVM protocol: 3D T1WI, 4D-MRA, gadolinium-enhanced 3D T1WI, T2*WI, DWI, TOF-MRA of the circle of Willis, and unenhanced perfusion imaging with a 3D pseudocontinuous ASL sequence. Acquisition parameters for the ASL pulse sequence were unchanged since the beginning of the protocol:¹⁴ TR/TE, 4428/10.5 ms; postlabeling delay, 1025 ms; label duration, 1500 ms; 80 axial partitions; FOV, 240 × 240 × 4 mm; acquisition matrix, 8 spiral arms in each 3D partition with 512 points per arm; flip angle, 155°; acquisition time, 4 minutes 17 seconds.

Paired DSA and ASL. At our institution, follow-up DSAs are performed 3 years after SRS or after the last treatment to document AVM obliteration, 3 and 5 years thereafter, and at 18 years of age, whichever comes last. DSAs were performed with the patient

under general anesthesia in a dedicated neuroangiography suite. A brain MR imaging including an ASL sequence was performed systematically the day before DSA.

Imaging Analysis

DSA Analysis. Two readers (15 [O.N.] and 7 [G.B.] years of experience) evaluated DSA during a single joint reading session. A residual AVM was defined as the early opacification of a cerebral vein, visible in the vicinity of nidus location, during the arterial phase of angiographic runs.

MR Imaging and ASL Analysis. Image analysis was performed using a PACS, independently, by 2 readers (6 [J.F.H.] and 5 [B.K.] years of experience). Readers were blinded to clinical and follow-up data and reported patient and AVMs characteristics. The CBF map was automatically generated using the 3D-ASL application of the Advantage Windows Workstation Functool (GE Healthcare) postprocessing software. For qualitative analysis, the color scale was set to rainbow with the warmer color representing the highest CBF.

Criteria for the presence of an AVM on MR images were defined with the visualization of an early venous filling at the arterial phase (4D-MRA), enlarged and dilated serpiginous vessels (TOF-MRA, postgadolinium 3D-T1), and/or direct visualization of the fistulous point/nidus (TOF-MRA)¹⁵ and, for ASL, the presence of an intracranial venous hypersignal within the dural sinuses or cortical veins and a focal intravascular warm color ("hot spot") on a CBF map.

The quantitative analysis of ASL was staged as follows:

1. Visual inspection of the ASL-derived CBF maps and identification of the most densely perfused areas of the lesion, if present.
2. 2D ROI placement using a calibrated round 20-mm² ROI on the region where the CBF was visually of the highest value corresponding to the AVM nidus or draining vein. Inside each ROI, the nidus CBF (CBF_{nidus}) mean values were automatically calculated by the software. We analyzed the mean values of the 2 readers for each variable. For each patient, the ROI was placed in the exact same hot spot localization as in the MRIs performed before and after each treatment.
3. The relative lesion CBF, corresponding to the ratio of CBF_{nidus}/CBF_{cortex}, was obtained by normalizing CBF to a 20-mm² ROI in the contralateral normal-appearing cortical gray matter (CBF_{cortex}) in the cerebellum for posterior fossa AVMs and in the frontal and parietal lobes for supratentorial AVMs. Gray matter was chosen as a reference because it has a higher SNR.

If a difference of >10 mL/100 mg/min was realized between the 2 readers, a consensus was reached on CBF maps and other MR imaging sequences to best position the ROIs. In case of negative ASL findings following treatment, the nidus ROI was placed at the exact same localization as the presurgical ASL ROI after manual coregistration of MR imaging sequences.

Statistical Analysis

Baseline characteristics were explored using descriptive statistics as appropriate per variable makeup and are displayed as absolute number (percentage) or mean (SD) or median (interquartile

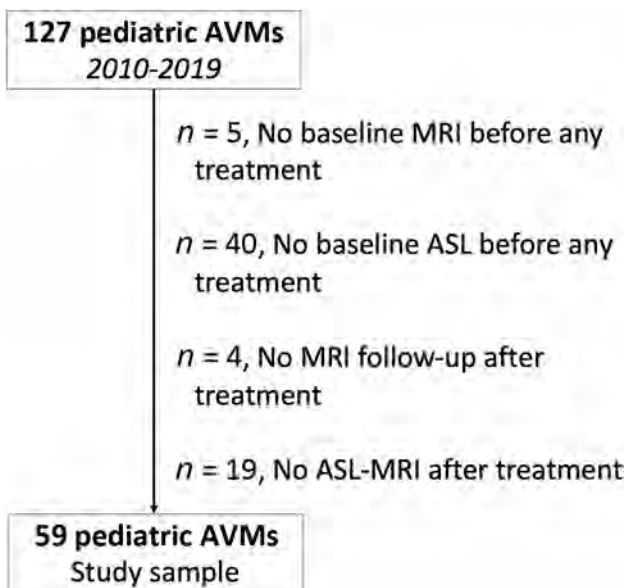


FIG 1. Flow chart of patient selection.

range [IQR], eg, 25th–75th quantiles). Univariable comparisons were performed using appropriate tests per variable makeup, distribution, and central tendency. All analyses were performed using JMP, Version Pro 14 (SAS Institute; 1989–2019), with $P < .05$ as a threshold for statistical significance.

RESULTS

Patients and AVM Characteristics

A total of 127 children were prospectively enrolled after 2011 in the database. After the application of study-specific inclusion and exclusion criteria, 59 patients were analyzed, and 68 patients were excluded. The flow chart in Fig 1 details patient selection. In included patients, AVMs were more frequently superficially located (57.4% versus 29.3%, $P = .02$). There was no difference between included and excluded patients in age at presentation (mean, 9.8 [SD, 3.7] versus 9.8 [SD, 3.8] years), clinical outcomes ($P = .36$), AVM location (supratentorial, 90% versus 83%, $P = .23$), and AVM grades ($P = .12$).

The 59 included patients benefited from 105 distinct treatment sessions with pre- and posttreatment MR imaging including ASL. The initial treatment was partial EVT, SRS, and partial and exhaustive microsurgery for, respectively, 38 (64.4%), 12 (20.3%), 3 (5.1%), and 6 (10.2%) children. Study sample baseline characteristics as well as treatments are detailed in the Table.

On baseline MR imaging performed before any treatment, findings of the visual inspection of the ASL-derived CBF map were considered positive in 56 patients (94.9%). The mean CBF_{nidus} was 192.1 (SD, 106) mL/100 mg/min with a mean ratio of lesion/cortex CBF of 2.2 (SD, 1.2).

AVM Follow-up of Patients under Treatment

General Considerations. We observed high interreader agreement for CBF measurement, using the Fleiss κ analysis ($\kappa = 0.92$; 95% CI, 0.8–1.0; $P < .0001$). The median CBF variation after treatment was -43 mL/100 mg/min (IQR, -102 – 5.5 mL/100 mg/min). There

Patient characteristics^a

Characteristics	
Clinical presentation	
Male sex (%)	28 (47.5%)
Age (median) (IQR) (yr)	10.1 (7.2–13.0)
Headaches	50 (84.7%)
Seizures	15 (25.4%)
Emesis	37 (62.7%)
Focal deficit	22 (37.3%)
GCS (median) (IQR)	14 (3–15)
ICH characteristics	
Supratentorial location	41 (69.5%)
ICH volume (median) (IQR) (mL)	10.9 (0.1–58)
ICH/TBV (median) (IQR) (%)	1.2 (0.8–5.6)
IVH	8 (13.6%)
Treatment characteristics	
Total No. of treatments	105
Patients treated with unimodal treatment	38 (64.4%)
Patients treated with multimodal treatment	21 (35.6%)
No. of treatment sessions (median) (IQR)	1 (1–6)
EVT	58 (55.2%)
EVT (No. of sessions) (median) (IQR)	1.5 (1–5)
SRS	26 (24.8%)
Partial surgery	6 (5.7%)
Complete surgery	15 (14.3%)
AVM characteristics	
Brain AVM	59 (100%)
SM grade 1–2	38 (64.4%)
SM grade 3	14 (23.7%)
SM grade 4–5	7 (11.9%)
Supratentorial	49 (83%)
Deep	31 (52.5%)
Eloquent area	33 (55.9%)
Nidus size (median) (IQR) (mm)	22 (9–60)
Compact nidus	38 (64.4%)
Aneurysm (arterial/venous)	25 (42.4%)
Any deep venous drainage	30 (50.8%)

Note:—GCS, indicates Glasgow Coma Scale; ICH, intracerebral hemorrhage; TBV, total brain volume; IVH, intraventricular hemorrhage; SM, Spetzler-Martin.

^a Variables are displayed as No. (%) or median (25th to 75th quantiles).

was a higher decrease in CBF after exhaustive nidal microsurgery ($n = 13$; median, -98 mL/100 mg/min [IQR, -161 to -50]) than after EVT, SRS, or partial microsurgery ($P = .002$). There was no significant difference in CBF variations after EVT versus SRS, SRS versus partial microsurgery, or EVT versus partial microsurgery (all $P > .05$) (see Fig 2 for details). The median time interval between MR imaging examinations was 10 months (IQR, 4–20 months).

CBF Variation after SRS. Twenty-seven patients were treated with SRS, and an ASL sequence was performed before and after treatment at each SRS session. The median interval time delay between sessions of MR imaging was 26 months (IQR, 12–39.5 months). Among these patients, DSA-proved complete obliteration at last follow-up was found in 14 patients (51.9%), whereas 13 patients were still under surveillance. The mean variation in CBF values on interval MRIs was -62 (SD, 61) mL/100 mg/min in eventually healed patients, whereas it was -17 (SD, 40.1) mL/100 mg/min in patients with incomplete obliteration at last follow-up ($P = .02$). In 8 of the 27 patients treated with SRS, CBF did not decrease ($\Delta > 0$), and only 2/8 (25%) of these patients' AVMs were obliterated at the latest follow-up.

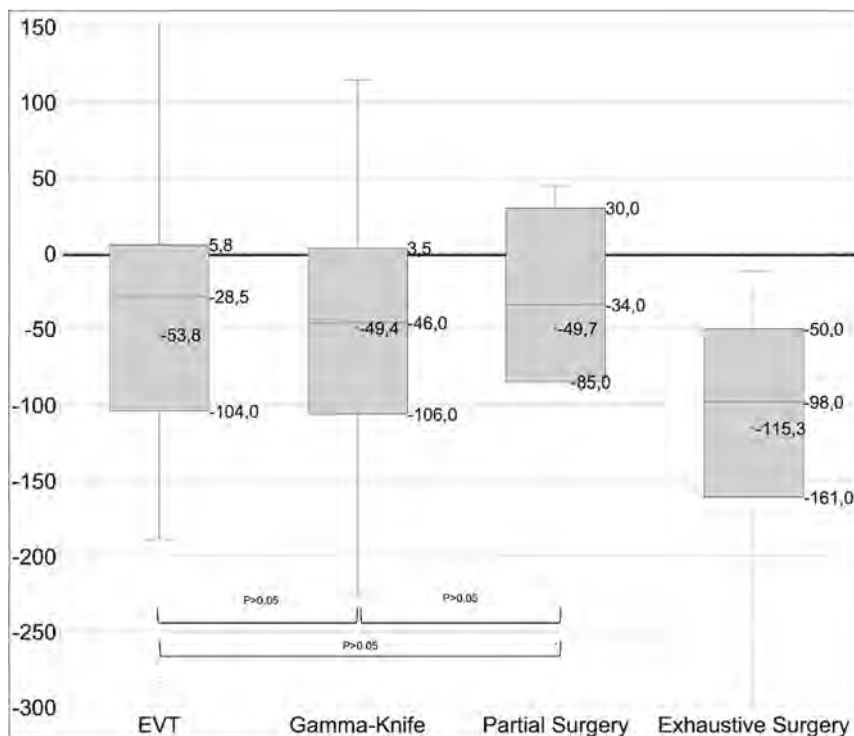


FIG 2. Boxplots of ASL variations by treatment technique per time interval.

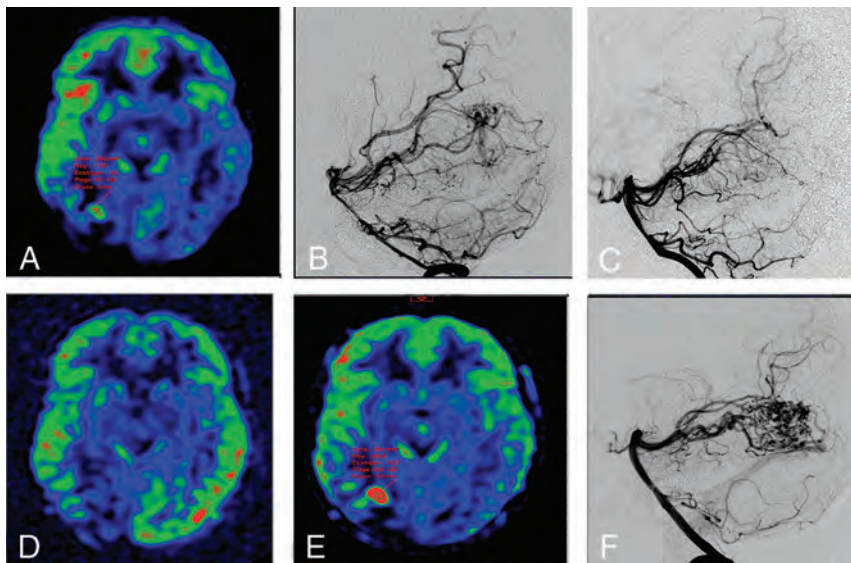


FIG 3. Example of a right occipital ruptured AVM confirmed with ASL (A) and DSA (B), completely treated with embolization 15 days after the initial diagnosis (C) and without a CBF increase, with ASL performed 4 months after the initial diagnosis (D). The 4-year ASL control revealed a focal ASL-derived CBF increase (E) suspicious for recurrence, confirmed with DSA (F).

After SRS, the mean CBF Δ for the healed children at 3 years versus the nonhealed at 3 years was, respectively, -68.3 (SD, 61.0) ($n = 4$) versus -14.5 (SD, 17.7) ($n = 2$) at 1 year after SRS ($n = 6$), and, respectively, -105.8 (SD, 66.3) versus 65.7 (SD, 150.3) at 2 years after SRS ($n = 19$). Thus, 1 year after SRS, a decrease in

CBF of $> 50\text{ mL}/100\text{ mg}/\text{min}$ was associated with a 3-fold increase in the rate of eventual obliteration after 3 years.

Follow-up after Complete Obliteration.

Among 34 patients achieving DSA-proved complete obliteration during follow-up, 4 (11.8%) children presented with a DSA recurrence at a mean delay of 21.8 [SD, 22.2] months. At the time of recurrence, the CBF increased in all patients by a mean of 89 (SD, 77) $\text{mL}/100\text{ mg}/\text{min}$, corresponding to relative CBF lesion increases of a mean of 311% (SD, 147%). See Fig 3 for an example of recurrence after treatment.

DISCUSSION

We present robust data on the role of ASL in the noninvasive follow-up of ruptured pediatric AVMs during and after treatment. Our analysis notably shows that ASL-CBF increased in all patients with DSA recurrences, with direct clinical applications in children followed up after AVM obliteration. Furthermore, we showed that 1 year after SRS, a decrease in CBF of $> 50\text{ mL}/100\text{ mg}/\text{min}$ was associated with a 3-fold increase in the rate of eventual obliteration after 3 years. In our sample, patients with eventually healed AVMs after SRS had a mean CBF decrease of $-62\text{ mL}/100\text{ mg}/\text{min}$ when it was $-17\text{ mL}/100\text{ mg}/\text{min}$ in patients with incomplete obliteration at 3 years.

These results add to the evidence of the role of noninvasive imaging in objectively delineating treatment effect in pediatric AVMs, provide additional evidence justifying intermediate MR imaging follow-up of children with obliterated AVMs, and pave the way for noninvasive biomarkers of anticipated treatment effect, especially after SRS. An additional supporting argument was the high interreader agreement for CBF measurement, suggesting the reproducibility of our findings, at least internally.

Several adult studies reported a role for ASL in AVM follow-up after treatment. Suazo et al⁷ reported a fair agreement between ASL and DSA for the

assessment of shunt reduction achieved by embolization for 8 AVMs. Other studies focusing on SRS-treated AVMs reported a promising role for ASL: first, to show and quantify differences in AVM nidus flow ratios and the associated steal phenomena between treated and untreated groups;¹⁶ and second, to detect

incomplete-versus-complete AVM obliteration.^{8–11} Altogether, these results contribute to determining the important role of ASL in AVM follow-up for patients under treatment or after obliteration, to minimize the use of DSA in the vulnerable sample of children with ruptured AVMs.

Pediatric AVMs have been shown to be dynamic lesions with vascular changes and higher rates of recurrence after complete obliteration, compared with adults.^{12,13} In addition, the susceptibility effects of the liquid embolic agents on perfusion imaging may hinder the quantitative perfusion measurements,¹⁷ justifying the need for our analysis in the subgroup of ruptured pediatric AVMs. This analysis complements a preliminary work from our group,¹⁴ in which 3 ruptured pediatric AVMs followed up after embolization alone showed a reduction in both nidus size and ASL-derived CBF values as well as 5 ruptured pediatric AVMs followed up after SRS, in which a reduction in the nidus size was observed, despite persistent elevated CBF_{nidus} values.

Despite these prior data, noninvasive AVM follow-up is an unmet need. Studies have evaluated 4D-MRA for AVM follow-up, but there are many practical drawbacks to the use of IV contrast in pediatric patients, including the need for IV access; increased scan time; children's fatigue, anxiety, and motion; and exposure to possible adverse effects of the contrast agent.^{18–23} Conversely, ASL sequences allow quantitative mapping of CBF, without contrast injection,²⁴ and are known to be relevant in detecting the presence of arteriovenous shunts by demonstrating high signal in the nidus as well as arterialized venous structures.^{14,25–27}

In line with previous studies,^{7–11,16,28} we showed that most patients had decreased CBF after treatment with SRS or embolization, yet some lesions demonstrated no CBF decrease despite interval treatment. This finding supports the concept of dynamic AVM lesions in children, considered as an evolving vasculopathy rather than a simple amorphous vascular connection, with interval increasing arterial feeding and/or shunt acceleration. It appears, therefore, that AVMs have a remodeling potential that explains the reported cases of spontaneous growth^{29,30} as well as spontaneous regression.^{31–33} Therefore, pretreatment ASL allows a radiation- and injection-free tool for treatment planning.

As previously reported, the AVM recurrence rate is higher for pediatric AVMs than for those in adults.^{12,13} In our cohort, 4 (11.8%) children presented with an angiographic recurrence with a CBF increase in all patients, by a mean of 89 (SD, 77) mL/100 mg/min. To our knowledge, we report the first preliminary data on ASL-CBF increase for the diagnosis of recurrent AVMs. We acknowledge, nonetheless, that our sample provides a limited number of recurrent AVMs and that this finding should be further supported by a larger study.

Note that at our institution, a pediatric quaternary care center and coordinating center for the French Pediatric Stroke Network, a DSA is performed in the initial AVM imaging assessment for angioarchitectural characterization and appropriate treatment. Following treatment, DSAs are performed 3 years after SRS or after the last treatment to document AVM obliteration, 3 and 5 years thereafter, and at 18 years of age, whichever comes last. Accordingly, DSA is not replaced by ASL, but ASL should be considered as a tool to facilitate the timing of follow-up DSA

studies, reduce the number of DSAs for each patient, and for the planning of additional AVM treatment.

Our study has several shortcomings, mostly inherent in its retrospective and noncontrolled design. Specifically, in our center, to optimize the SNR of the ASL sequence for AVMs detection,³⁴ we used a postlabeling delay of 1025 ms, shorter than the value typically recommended (1500 ms).³⁵ We chose this postlabeling because we have been using it since 2011, after local optimization with an excellent SNR across various cerebrovascular diseases. Second, this approach is very commonly used by experienced teams using ASL and has been validated extensively.³⁶

We also acknowledge that some patients have been lost to imaging follow-up following SRS outside our center, introducing some degree of attrition bias. Finally, these results were obtained in a sample of ruptured brain AVMs and may not be transferrable to children with initially unruptured lesions.

CONCLUSIONS

In children with ruptured AVMs, ASL allows detection of hemodynamic changes after treatment, noninvasively and without radiation exposure or contrast media administration. Our results contribute data on the role of noninvasive ASL monitoring of the response of pediatric AVMs to treatment or follow-up after obliteration. Future research may help better elucidate how ASL can assist in decisions regarding optimal timing for DSA.

Disclosure forms provided by the authors are available with the full text and PDF of this article at www.ajnr.org.

REFERENCES

1. Boulouis G, Blauwblomme T, Hak JF, et al. **Nontraumatic pediatric intracerebral hemorrhage.** *Stroke* 2019;50:3654–61 CrossRef Medline
2. Beslow LA, Licht DJ, Smith SE, et al. **Predictors of outcome in childhood intracerebral hemorrhage: a prospective consecutive cohort study.** *Stroke* 2010;41:313–18 CrossRef Medline
3. Boulouis G, Stricker S, Benichi S, et al. **Etiology of intracerebral hemorrhage in children: cohort study, systematic review, and meta-analysis.** *J Neurosurg Pediatr* 2021;27:357–63 CrossRef Medline
4. Guédon A, Blauwblomme T, Boulouis G, et al. **Predictors of outcome in patients with pediatric intracerebral hemorrhage: development and validation of a modified score.** *Radiology* 2018;286:651–58 CrossRef Medline
5. Ferriero DM, Fullerton HJ, Bernard TJ, et al; American Heart Association Stroke Council and Council on Cardiovascular and Stroke Nursing. **Management of stroke in neonates and children: a scientific statement from the American Heart Association/American Stroke Association.** *Stroke* 2019;50:e51–96 CrossRef Medline
6. Ziyeh S, Strecker R, Berlis A, et al. **Dynamic 3D MR angiography of intra- and extracranial vascular malformations at 3T: a technical note.** *AJNR Am J Neuroradiol* 2005;26:630–04 Medline
7. Suazo L, Foerster B, Fermin R, et al. **Measurement of blood flow in arteriovenous malformations before and after embolization using arterial spin-labeling.** *Interv Neuroradiol* 2012;18:42–48 CrossRef Medline
8. Amponsah K, Ellis TL, Chan MD, et al. **Retrospective analysis of imaging techniques for treatment planning and monitoring of obliteration for gamma knife treatment of cerebral arteriovenous malformation.** *Neurosurgery* 2012;71:893–900 CrossRef Medline
9. Heit JJ, Thakur NH, Iv M, et al. **Arterial-spin labeling MRI identifies residual cerebral arteriovenous malformation following stereotactic radiosurgery treatment.** *J Neuroradiol* 2020;47:13–19 CrossRef Medline
10. Kodera T, Arai Y, Arishima H, et al. **Evaluation of obliteration of arteriovenous malformations after stereotactic radiosurgery with arterial**

- spin-labeling MR imaging. *Br J Neurosurg* 2017;31:641–47 CrossRef Medline
11. Shimizu K, Kosaka N, Yamamoto T, et al. Arterial spin-labeling perfusion-weighted MRI for long-term follow-up of a cerebral arteriovenous malformation after stereotactic radiosurgery. *Acta Radiol Short Rep* 2014;3:2047981613510160 CrossRef Medline
12. Copelan A, Drocton G, Caton MT, et al; UCSF Center For Cerebrovascular Research and UCSF Pediatric Brain Center. Brain arteriovenous malformation recurrence after apparent microsurgical cure: increased risk in children who present with arteriovenous malformation rupture. *Stroke* 2020;51:2990–96 CrossRef Medline
13. Sorenson TJ, Brinjikji W, Bortolotti C, et al. Recurrent brain arteriovenous malformations (AVMs): a systematic review. *World Neurosurg* 2018;116:e856–66 CrossRef Medline
14. Blauwblomme T, Naggara O, Brunelle F, et al. Arterial spin-labeling magnetic resonance imaging: toward noninvasive diagnosis and follow-up of pediatric brain arteriovenous malformations. *J Neurosurg Pediatr* 2015;15:451–58 CrossRef Medline
15. Sporns PB, Psychogios M-N, Fullerton HJ, et al. Neuroimaging of pediatric intracerebral hemorrhage. *J Clin Med* 2020;9:1518 CrossRef Medline
16. Pollock JM, Whitlow CT, Simonds J, et al. Response of arteriovenous malformations to gamma knife therapy evaluated with pulsed arterial spin-labeling MRI perfusion. *AJR Am J Roentgenol* 2011;196:15–22 CrossRef Medline
17. Deibler AR, Pollock JM, Kraft RA, et al. Arterial spin-labeling in routine clinical practice, Part 1: technique and artifacts. *AJNR Am J Neuroradiol* 2008;29:1228–34 CrossRef Medline
18. Dillman JR, Ellis JH, Cohan RH, et al. Frequency and severity of acute allergic-like reactions to gadolinium-containing IV contrast media in children and adults. *AJR Am J Roentgenol* 2007;189:1533–38 CrossRef Medline
19. Auron A, Shao L, Warady BA. Nephrogenic fibrosing dermopathy in children. *Pediatr Nephrol* 2006;21:1307–11 CrossRef Medline
20. Foss C, Smith JK, Ortiz L, et al. Gadolinium-associated nephrogenic systemic fibrosis in a 9-year-old boy. *Pediatr Dermatol* 2009;26:579–82 CrossRef Medline
21. Hu HH, Pokorney A, Towbin RB, et al. Increased signal intensities in the dentate nucleus and globus pallidus on unenhanced T1-weighted images: evidence in children undergoing multiple gadolinium MRI exams. *Pediatr Radiol* 2016;46:1590–98 CrossRef Medline
22. Nguyen NC, Molnar TT, Cummin LG, et al. Dentate nucleus signal intensity increases following repeated gadobenate dimeglumine administrations: a retrospective analysis. *Radiology* 2020;296:122–30 CrossRef Medline
23. Flood TF, Stence NV, Maloney JA, et al. Pediatric brain: repeated exposure to linear gadolinium-based contrast material is associated with increased signal intensity at unenhanced T1-weighted MR imaging. *Radiology* 2017;282:222–28 CrossRef Medline
24. Detre JA, Rao H, Wang DJJ, et al. Applications of arterial spin-labeled MRI in the brain. *J Magn Reson Imaging* 2012;35:1026–37 CrossRef Medline
25. Wolf RL, Wang J, Detre JA, et al. Arteriovenous shunt visualization in arteriovenous malformations with arterial spin-labeling MR imaging. *AJNR Am J Neuroradiol* 2008;29:681–87 CrossRef Medline
26. Iryo Y, Hirai T, Kai Y, et al. Intracranial dural arteriovenous fistulas: evaluation with 3-T four-dimensional MR angiography using arterial spin labeling. *Radiology* 2014;271:193–99 CrossRef Medline
27. Le TT, Fischbein NJ, André JB, et al. Identification of venous signal on arterial spin labeling improves diagnosis of dural arteriovenous fistulas and small arteriovenous malformations. *AJNR Am J Neuroradiol* 2012;33:61–68 CrossRef Medline
28. Schubert T, Clark Z, Sandoval-Garcia C, et al. Non contrast, pseudo-continuous arterial spin-labeling and accelerated 3-dimensional radial acquisition intracranial 3-dimensional magnetic resonance angiography for the detection and classification of intracranial arteriovenous shunts. *Invest Radiol* 2018;53:80–86 CrossRef Medline
29. Mendelow AD, Erfurth A, Grossart K, et al. Do cerebral arteriovenous malformations increase in size? *J Neurol Neurosurg Psychiatry* 1987;50:980–87 CrossRef Medline
30. Waltimo O. The change in size of intracranial arteriovenous malformations. *J Neurol Sci* 1973;19:21–27 Medline
31. Lee SK, Vilela P, Willinsky R, et al. Spontaneous regression of cerebral arteriovenous malformations: clinical and angiographic analysis with review of the literature. *Neuroradiology* 2002;44:11–16 CrossRef Medline
32. Nukui H, Miyagi O, Tamada J, et al. Long-term follow-up study by cerebral angiography in cases with arteriovenous malformation of the brain: with special reference to spontaneous disappearance of arteriovenous malformation in cerebral angiography (author's transl) [in Japanese]. *Neurol Med Chir (Tokyo)* 1982;22:125–32 CrossRef Medline
33. Sawlani V, Handique A, Phadke RV. Spontaneous regression of cerebral AVM due to thrombosis of draining vein: angiographic and MRI demonstration. *J Neurol Sci* 2004;223:195–98 CrossRef Medline
34. Lüdemann L, Jedrzejewski G, Heidenreich J, et al. Perfusion imaging of cerebral arteriovenous malformations: a study comparing quantitative continuous arterial spin labeling and dynamic contrast-enhanced magnetic resonance imaging at 3 T. *Magn Reson Imaging* 2011;29:1157–64 CrossRef Medline
35. Alsop DC, Detre JA, Golay X, et al. Recommended implementation of arterial spin-labeled perfusion MRI for clinical applications: a consensus of the ISMRM perfusion study group and the European Consortium for ASL in Dementia. *Magn Reson Med* 2015;73:102–16 CrossRef Medline
36. Jain V, Duda J, Avants B, et al. Longitudinal reproducibility and accuracy of pseudo-continuous arterial spin-labeled perfusion MR imaging in typically developing children. *Radiology* 2012;263:527–36 CrossRef Medline

Effect of Normal Breathing on the Movement of CSF in the Spinal Subarachnoid Space

C. Gutiérrez-Montes, W. Coenen, M. Vidorreta, S. Sincomb, C. Martínez-Bazán, A.L. Sánchez, and V. Haughton



ABSTRACT

BACKGROUND AND PURPOSE: Forced respirations reportedly have an effect on CSF movement in the spinal canal. We studied respiratory-related CSF motion during normal respiration.

MATERIALS AND METHODS: Six healthy subjects breathed at their normal rate with a visual guide to ensure an unchanging rhythm. Respiratory-gated phase-contrast MR flow images were acquired at 5 selected axial planes along the spine. At each spinal level, we computed the flow rate voxelwise in the spinal canal, together with the associated stroke volume. From these data, we computed the periodic volume changes of spinal segments. A phantom was used to quantify the effect of respiration-related magnetic susceptibility changes on the velocity data measured.

RESULTS: At each level, CSF moved cephalad during inhalation and caudad during expiration. While the general pattern of fluid movement was the same in the 6 subjects, the flow rates, stroke volumes, and spine segment volume changes varied among subjects. Peak flow rates ranged from 0.60 to 1.59 mL/s in the cervical region, 0.46 to 3.17 mL/s in the thoracic region, and 0.75 to 3.64 mL/s in the lumbar region. The differences in flow rates along the canal yielded cyclic volume variations of spine segments that were largest in the lumbar spine, ranging from 0.76 to 3.07 mL among subjects. In the phantom study, flow velocities oscillated periodically during the respiratory cycle by up to 0.02 cm/s or 0.5%.

CONCLUSIONS: Respiratory-gated measurements of the CSF motion in the spinal canal showed cyclic oscillatory movements of spinal fluid correlated to the breathing pattern.

ABBREVIATION: SSAS = spinal subarachnoid space

Respirations reportedly have an effect on CSF movement in the spinal subarachnoid space (SSAS), which is also known to undergo a cardiac-driven oscillatory motion¹⁻⁴ associated with the

periodic changes in intracranial pressure, superposed on a steady motion resulting from secretion of CSF by the choroid plexus in the ventricles on the one hand and steady-streaming effects appearing as small nonzero time averages of oscillatory components on the other hand. Whereas steady secretion by the choroid plexus results in slow craniocaudal spinal fluid flow,^{5,6} commonly known as bulk flow, steady-streaming results in closed recirculating regions caused by the variation of anterior-posterior SSAS size along the spine⁷⁻⁹ or localized anatomic features such as nerve roots.¹⁰ Forced respirations have been shown to produce oscillatory motion of the CSF at a slower cycling rate than the cardiac cycle, both in the spine and the brain.¹¹⁻²⁶ Most previously published observations on spinal CSF flow during respiration have used real-time MR imaging, short acquisitions, and forced or deep breathing, coughing, or sniffing.¹¹⁻²⁴ In previous reports, the forced respiratory efforts produced both craniocaudal and caudocranial CSF movements along the entire spinal canal and especially in the lower thoracic segment. In some experiments, forced inspiration and expiration apparently were the major factors in spinal fluid flow.^{14,16,20,21,24,25} The effect

Received April 25, 2022; accepted after revision June 24.

From the Department of Mechanical and Mining Engineering (C.G.-M.), University of Jaén, Jaén, Andalucía, Spain; Grupo de Mecánica de Fluidos, Departamento de Ingeniería Térmica y de Fluidos (W.C.), Universidad Carlos III de Madrid, Madrid, Spain; Siemens Healthineers (M.V.), Madrid, Spain; Department of Mechanical and Aerospace Engineering (S.S., A.L.S.), University of California San Diego, San Diego, California; Department of Structural Mechanics and Hydraulic Engineering (C.M.-B.), University of Granada, Granada, Spain; and Department of Radiology (V.H.), School of Medicine and Public Health, University of Wisconsin-Madison, Madison, Wisconsin.

The work of S.C., V.H. and A.L.S. was supported by the National Institute of Neurological Disorders and Stroke through contract no. 1R01NS120343-01. C.G., W.C. and C.M.-B. acknowledge the support of the Spanish MICINN through the coordinated project PID2020-115961RB. C.M.B. and C.G. also acknowledge the support provided by Junta de Andalucía and European Funds through grant P18-FR-4619.

Please address correspondence to Wilfried Coenen, PhD, Departamento de Ingeniería Térmica y de Fluidos, Universidad Carlos III de Madrid, Avenida Universidad 30, 28911 Leganés, Madrid, Spain; e-mail: wcoenen@ing.uc3m.es

Indicates open access to non-subscribers at www.ajnr.org

<http://dx.doi.org/10.3174/ajnr.A7603>

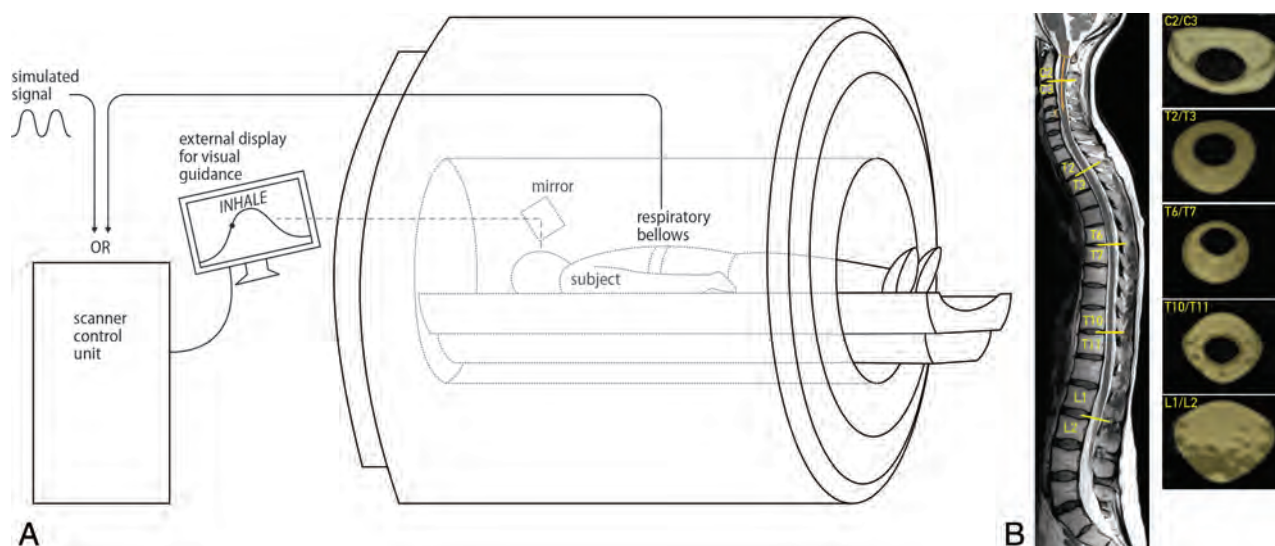


FIG 1. A, Schematic overview of the MR imaging setup. The subject, in a supine position, was instructed to breathe guided by a video on an external display. Thoracic circumference respiratory bellows were used to monitor breathing. B, High-resolution, whole-spine images were obtained using a 3-block sagittal 3D T2 SPACE sequence, and flow measurements were acquired with a 2D phase-contrast MR imaging sequence at 5 locations along the spinal canal: C2/C3, T2/T3, T6/T7, T10/T11, and L1/L2. At each level, the ROIs corresponding to the SSAS were drawn manually (yellow shaded regions). Images shown correspond to subject 3.

of normal breathing on spinal CSF flow has recently been studied,^{17,26} but only at the foramen magnum, where it was found to play a lesser role compared with cardiac-driven motion.

A detailed analysis of CSF movement along the length of the spinal canal related to normal breathing has not, to our knowledge, been published. An improved quantitative knowledge of respiratory effects on CSF flow will enhance our understanding of CSF dynamics, which is key in the characterization of nutrient movement and waste product clearance in the subarachnoid spaces and the distribution of drugs injected intrathecally.

We planned a study to quantify respiratory-related CSF motion along the length of the spinal canal during breathing at a normal rate and depth. We developed a method of maintaining a constant respiratory rhythm during flow data acquisition and used a respiratory-gated MR imaging acquisition, which achieves greater temporal and spatial resolution than the real-time MR imaging acquisition used in previous studies. We acquired flow data at multiple spinal levels to characterize, as completely as possible, the effects of normal breathing on fluid movement along the length of the spinal canal.

MATERIALS AND METHODS

Subjects

Six subjects (2 women, 4 men; age range, 27–53 years; weight range, 50–82 kg; and height range, 160–175 cm) with good health, normal pulse and respiratory rates, no spinal disorders, and no contraindications to MR imaging were enrolled for MR imaging data collection at the Mind, Brain and Behavior Research Center of the University of Granada and analysis of CSF flow. The study was approved by the institutional review board of the Universidad de Granada, and written informed consent was obtained from each subject before MR imaging. The MR images obtained in the subjects were reviewed by a neuroradiologist to exclude spinal pathologies.

Study Design

Each subject was instructed to breathe guided by a video showing a sine wave with a frequency at the subject's previously determined normal breathing rate (15–18 breaths per minute in the 6 subjects). Subjects were fitted with a thoracic circumference monitoring belt and asked to inhale and exhale normally to match the chest diameter to the sine wave, achieving inspiration and expiration of equal duration. Each subject practiced breathing to the visual guide for a period of time before imaging. For imaging, conventional T1- and T2-weighted images of the entire spine were obtained in each subject, and flow measurements were acquired at 5 locations along the spinal canal: C2/C3, T2/T3, T6/T7, T10/T11, and L1/L2 (Fig 1).

MR Imaging Measurements

All imaging was performed on a 3T Magnetom Prisma Fit MR imaging scanner (Siemens) using a 64-channel head and neck coil and a 32-channel spine coil. High-resolution, whole-spine images were obtained using a 3-block sagittal 3D T2 sampling perfection with application-optimized contrasts by using different flip angle evolution (SPACE sequence; Siemens) (Fig 1B), with the following imaging parameters: TR = 1500 ms, TE = 231 ms, bandwidth = 504 Hz/pixel, 1.4 averages, in-plane resolution = 0.8×0.8 interpolated to 0.4×0.4 mm², 64 slices per block, section thickness = 0.8 mm. CSF flow-velocity data were acquired at the 5 selected spinal locations applying a 2D phase-contrast MR imaging sequence with section orientation perpendicular to the long axis of the spinal canal. The imaging parameters included the following: flip angle = 15°, FOV = 160×160 mm², matrix = 256×205 , in-plane resolution = 0.625×0.78 reconstructed to 0.625×0.625 mm², section thickness = 10 mm. The velocity encoding was adjusted to the anticipated optimum for each subject and ranged from 3 to 15 cm/s, with TE and TR varying correspondingly between 7.71 and 9.98 and 71.22 and 89.42 ms, respectively. Between 40 and 55

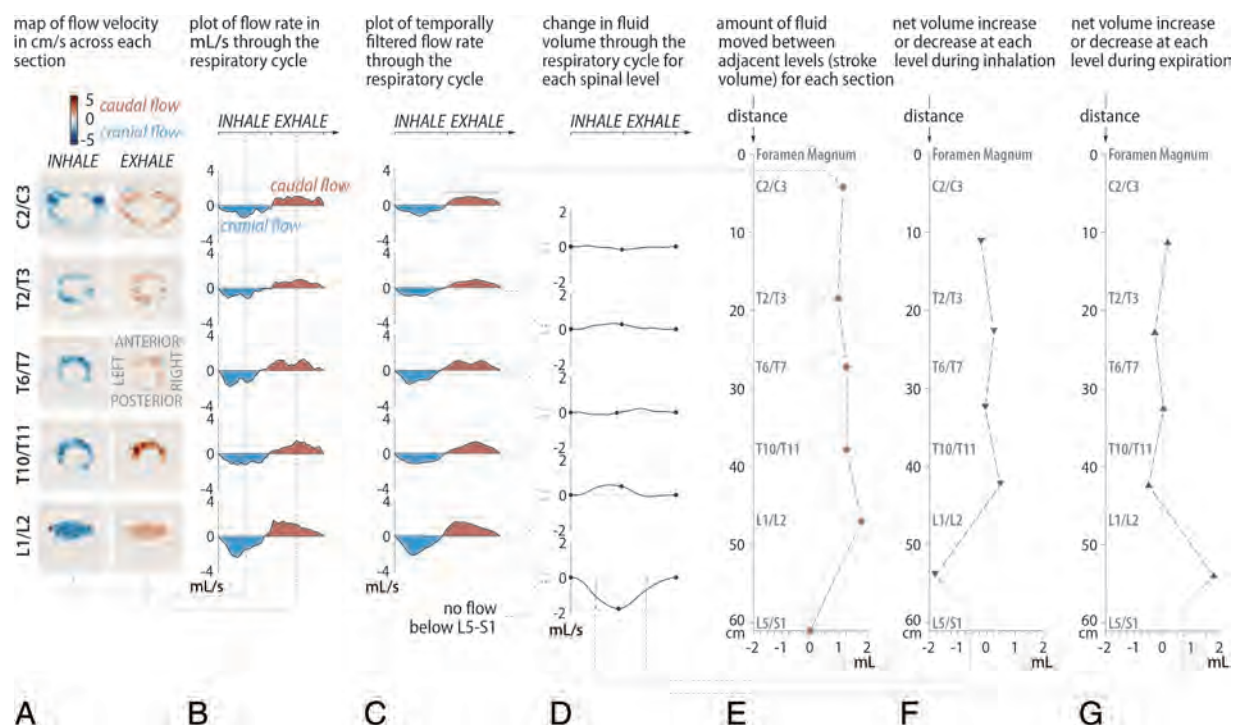


FIG 2. Results for subject 1. A, Map of flow velocity in centimeters per second across each section at mid-inhalation (*left column*) and mid-expiration (*right column*). B, Plot of the flow rate in milliliters per second across each section through the respiratory cycle. C, Plot of temporally filtered flow rate. D, Change in fluid volume through the respiratory cycle with respect to the start of inhalation for each spinal level. E, Amount of fluid moved between adjacent levels (stroke volume) for each section. F, Net volume increase or decrease at each level during inhalation. G, Net volume increase or decrease during expiration.

respiratory phases were obtained in each subject. Respiratory gating was performed by means of a retrospective protocol using an external synthetic signal with frequency equal to the breathing frequency of each subject. Scans showing velocity-aliasing artifacts were repeated or manually corrected.^{9,27}

Quantification of the Flow Rate and Spinal Canal Volume Changes Due to Respiration

An in-house-developed Matlab code (MathWorks) was used to postprocess the MR phase and magnitude measurements and to obtain the in-plane velocity distribution of velocity U in the SSAS at each spinal level (Fig 2A), the location of which has a distance x_i along the spinal canal to the foramen magnum (Fig 1B). At each level, the ROIs corresponding to the SSAS were drawn manually (Fig 1B). By numerically integrating the velocity over these ROIs, the volume flow rates across each location ($Q(x_i, t) = \int_{ROI} U dA$)

were obtained as a function of time t (Fig 2B). The results were filtered with a 5-point moving mean (Fig 2C). Stroke volume was calculated for each level by numerically integrating the flow rate over the respiratory cycle, $V_s(x) = 0.5 \int_0^T |Q(x, t)| dt$ (Fig 2E). The instantaneous change in volume of each spine segment, with respect to the start of the inhalation cycle, was computed as the integral of the difference in flow rates across the spinal levels that delimitate the segment, $\Delta V_{i \rightarrow i+1}(t) = \int [Q(x_i, t) - Q(x_{i+1}, t)] dt$ (Fig 2D). The net volume change over inhalation and exhalation (Fig 2E, -F) for each segment was calculated as $\Delta V_{i \rightarrow i+1}(t_{1/2}) - \Delta V_{i \rightarrow i+1}(0)$ and

$\Delta V_{i \rightarrow i+1}(T) - \Delta V_{i \rightarrow i+1}(t_{1/2})$, where $t_{1/2}$ corresponds to the instant in time at the end of inhalation and the start of exhalation, defined as the point where $Q(x_i, t)$ crosses zero, so that $t_{1/2} \cong T/2$.

Evaluation of Magnetic Susceptibility Artifacts in In Vivo Flow Measurements

A phantom was used to quantify the effect of magnetic susceptibility changes in the FOV induced by the thoracic motion on velocity data measured with phase-contrast MR imaging. The phantom contained a closed hydraulic circuit composed of a straight tube of constant diameter equal to 2.2 cm, a pump, and a mass flow meter. Tap water with a T1 of 2.7 seconds to simulate CSF, which has a T1 relaxation time²⁸ of about 3 seconds, was pumped through the phantom at a constant flow rate. Respiratory-gated MR imaging flow measurements were obtained of the phantom with and without a subject lying supine on the phantom. Data were acquired at 2 locations, T6/T7 and L1/L2, with the same MR imaging parameters and protocols as used for imaging the subjects.

RESULTS

MR imaging showed no evidence of spinal pathology in the 6 subjects. All subjects breathed with a sinusoidal pattern closely approximating their normal respiratory volumes. Flow measurements were obtained from MR imaging measurements successfully in all subjects and selected spinal locations. Aliasing artifacts were encountered in 2 subjects for 2 spinal levels and were corrected accordingly. We first describe the results for subject 1 in detail (Fig 2) and then compare results in the 6 subjects (Fig 3).

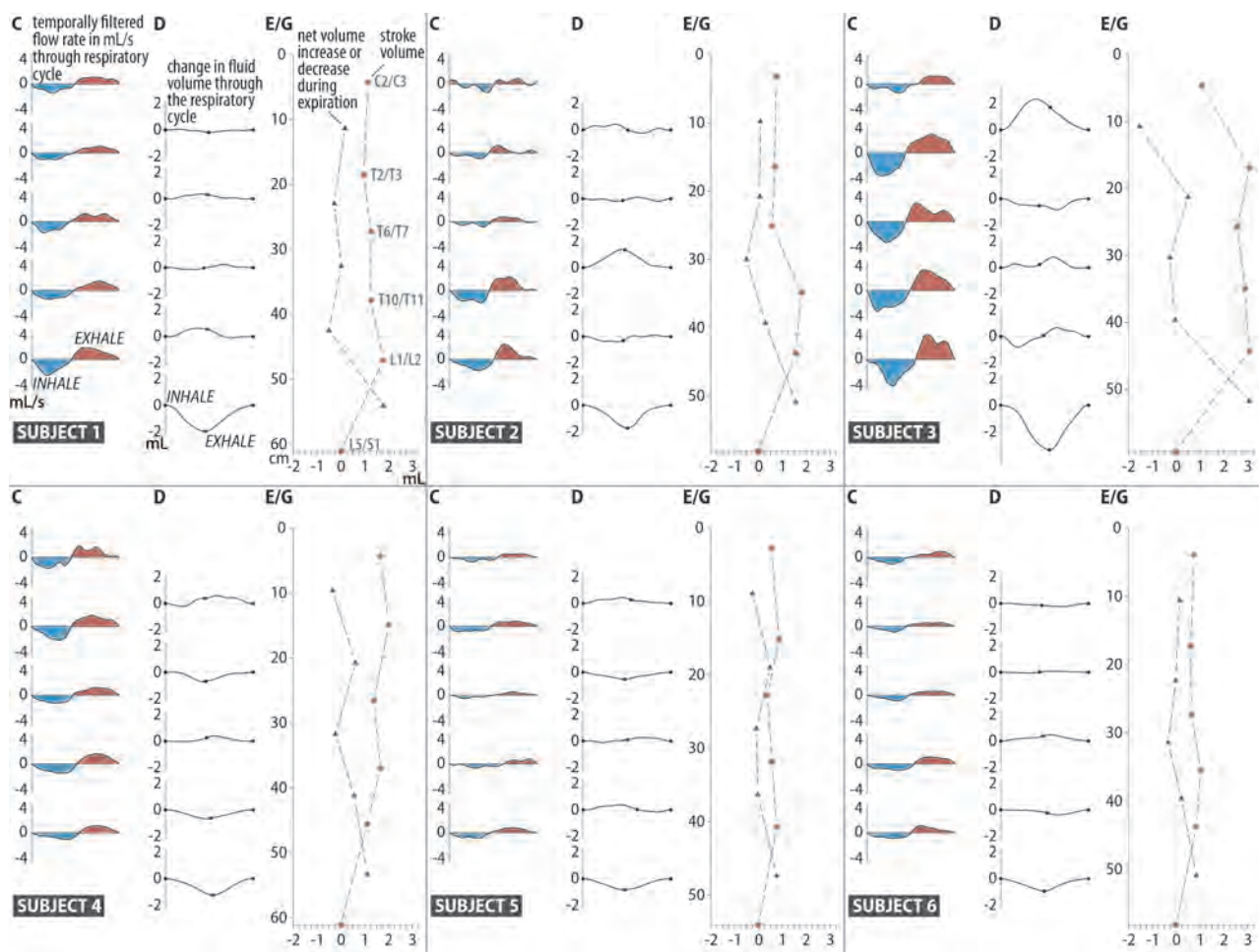


FIG 3. Selected results for subjects 1–6. C, D, E/G correspond to those in Fig 2.

In subject 1, the respiratory-gated flow was caudocranial during inhalation and craniocaudal during exhalation at all spinal levels. Velocity fields (Fig 2A) taken mid-inhalation and mid-exhalation showed that CSF flow is uniformly distributed over the cross-sectional area of the SSAS, with peak velocities ranging from 5 to 8 cm/s. The corresponding volume flow rates $Q(x_i, t)$ (Fig 2B, -C) confirmed that the directionality of the flow was in phase with inhalation and exhalation and differed in phase by 180°. Flow volume rates between inspiration and expiration differed by <10%.

The largest volume of flow rate was observed at L1/L2 (2 mL/s). The concomitant stroke volume, V_s (Fig 2E), which is a measure of the volume of CSF that passes through L1/L2 at this location, was 1.75 mL. Cranially from L1/L2, the stroke volume progressively decreased toward the foramen magnum (minimum, V_s of 1 mL). Above the L1/L2 level, the stroke volumes were <0.5 mL. Caudally from L1/L2, the stroke volume diminished to zero. The largest variation of CSF volume was found in the stretch of canal between the L1/L2 level and the caudal end of the canal. The corresponding total accumulation and depletion of CSF between the start and end of inhalation (Fig 2E) and between the start and end of exhalation (Fig 2F) were equal.

The general trends described for subject 1 are evident in all subjects (Fig 3), though large subject-to-subject variations were found. During inspiration, caudocranial CSF flow was induced, and during exhalation, craniocaudal flow. The velocity fields during inhalation were found to be comparable in magnitude with those during exhalation at all spinal levels. Correspondingly, the volume of flow rates during inhalation (Fig 3C) were similar in magnitude to those during exhalation. The variation in stroke volume (red dots in Fig 3E, -G) generally was largest in the lower lumbar region and least in the cervical region, except in 1 subject (subject 4). Peak flow rates ranged from 0.60 to 1.59 mL/s in the cervical region, 0.46 mL/s to 3.17 mL/s in the thoracic region, and 0.75 mL/s to 3.64 mL/s in the lumbar region. Differences in flow rates are correlated to differences in stroke volume and, consequently, to the increase or decrease in CSF volume. The Table summarizes the minimum, mean, and maximum observed stroke volumes and volume changes along the spinal canal. The increase or decrease in CSF volume (Fig 3D) was largest in the lumbar region.

In the phantom study of respiratory-induced artifacts in flow measurements, flow velocities measured in the phantom under a supine subject breathing typically deviated periodically during the respiratory cycle by up to 0.02 cm/s for all flow velocities tested,

Interindividual variations in stroke volume and in net volume increase during expiration at each spinal level

Section	Stroke Volume (mL)			Segment	Net Volume Increase during Expiration (mL)		
	Min	Mean	Max		Min	Mean	Max
C2/C3	0.54	0.99	1.66	C2/C3–T2/T3	–1.54	–0.29	0.17
T2/T3	0.62	1.37	3.07	T2/T3–T6/T7	–0.28	0.23	0.62
T6/T7	0.38	1.14	2.58	T6/T7–T10/T11	–0.51	–0.23	0.02
T10/T11	0.57	1.54	2.88	T10/T11–L1/L2	–0.49	0.09	0.57
L1/L2	0.76	1.52	3.07	L1/T2–L5/S1	0.76	1.52	3.07

Note:—Min indicates minimum; Max, maximum.

which ranged from 0 to 15 cm/s. The deviations did not exceed 0.5% of the mean velocities tested.

DISCUSSION

Respiratory-gated measurements of the CSF motion in the spinal canal during normal rates and volumes of respiration showed cyclic oscillatory movements of spinal fluid correlated to the breathing pattern. The stroke volume, an integral measure of how much fluid moves across a certain spinal section over the course of 1 respiratory period, was, on average, largest in the lower thoracic and upper lumbar spine, decreasing cranially up to 35% toward the foramen magnum and caudally toward the distal end, where it vanished. The concomitant net volume variation was found largest at the upper lumbar-sacral segment and considerably lower elsewhere. This finding indicates the volume variation of the subarachnoid space near the thoracolumbar junction through the respiratory cycle as the main effect of respiration. The minimum and maximum measured values of stroke volume and net volume change in the Table reveal large interindividual differences.

The results of this study agree qualitatively with those in previous studies^{12,16,17,20,21,24–26} in which spinal fluid was found to move cranially during inspiration and caudally during expiration. The effect of normal, sustained breathing was reported to induce peak velocities of approximately 1.3 cm/s at the foramen magnum,^{17,26} compared with 5 cm/s for subject 1 at C2/C3 in our results. Studies that reported the spatial distribution of respiratory-induced flow along the spinal canal mostly considered forced respiration^{12,16,20,21,24,25} or breathing maneuvers such as coughing or sniffing.²⁴ In agreement with our findings, the largest respiration-induced flow rates occurred at the upper lumbar spinal level.^{20,21} Flow rates and associated stroke volumes greater than ours were measured, consistent with the use of more forceful respiratory efforts. For example, the mean stroke volumes corresponding to forced breathing²⁰ compared with those of the present study under normal breathing are 2.4 versus 1.0 mL at C2/C3, 1.6 versus 1.1 mL at T6/T7, 6.7 versus 1.5 mL at T10/T11, and 2.0 versus 1.5 mL at L1/L2, respectively. The maximum associated net volume variation over inspiration or exhalation occurred in the caudal half of the spinal canal. For forced breathing,²⁰ the maximum was found in the segment between T6 and T10 (mean, 5.1 mL), whereas for the present work, it occurred in the lumbar segment between L1/L2 and the sacral end (mean, 1.5 mL). Previous studies have hypothesized that the nonuniform compliance of the SSAS is coupled to the extraspinal paravertebral venous plexus.^{24,25} Furthermore, forced respiratory effort induced a nonzero net CSF flow.^{20,21} On the

contrary, our data, acquired over multiple minutes of normal breathing, showed no net flow, consistent with conservation of total spinal CSF volume over the course of the experiment. We are not aware of any previously reported detailed CSF flow measurements at multiple spinal levels during normal respiration.

Respiratory-driven spinal CSF flow occurs in addition to that driven by the cardiac cycle.^{9,29–31} Induced by intracranial pressure fluctuations, the cardiac-driven flow presents a different spatial variation of flow rate and stroke volume along the spine (eg, Figs 2 and 3 in Sincomb et al³¹) with maximum values in the upper cervical region, decreasing monotonically toward the closed caudal end. Given the large subject-to-subject variations in observed respiratory-driven flow, comparisons between cardiac- and respiratory-driven flow should be conducted on a subject-to-subject basis. As an example, subjects 1 and 2 in Sincomb et al,³¹ respectively, correspond to subjects 5 and 2 of the present study. For these subjects, the ratios between respiratory- and cardiac-driven peak flow rates were, respectively, 0.1 and 0.3 at C2/C3, 0.2 and 0.4 at T6/T7, and 0.7 and 1.3 at L1 and L2, where both peak values become comparable. Nevertheless, because the respiratory cycle is approximately 3.5 times longer, the associated stroke volumes become dominant in the lower spine. In particular, the ratios between the respiratory- and cardiac-driven stroke volumes for subjects 5 and 2 are respectively 0.8 and 1.2 at C2/C3, 1.1 and 1.6 at T6/T7, and 4.9 and 7.3 at L1/L2. Future work should confirm these trends.

Our study had a small number of subjects, with an age range of 26 years. The analysis should be extended in the future to a larger number of subjects with greater anatomic variations to investigate reproducibility and determine the origin of the large interindividual differences. The influence of subject posture, which has been conjectured to influence cardiac-driven steady-streaming CSF flow,⁹ was not studied here. Furthermore, the duration of inhalation and exhalation was equal, which might not be reflective of normal breathing. The study should be extended to further evaluate the effect of different respiration modes on the CSF motion. Finally, small experimental errors might be expected from the limited accuracy of phase-contrast MR measurements of slow flow and from the section orientation not being perfectly perpendicular to the axis of the spinal canal.

This study shows that respiration affects CSF flow, especially in the lower thoracic and lumbar spine. The total pulsating motion of the CSF in the SSAS is the sum of the cardiac- and respiratory-driven components. The cardiac-driven flow exhibits near-zero velocities in the lumbar region,⁹ much smaller than those associated with the respiratory-driven flow measured here, so that respiration is the main driving mechanism in the lumbar

spine. Consequently, the respiratory cycle may be a factor in the movement of drugs and anesthetics administered intrathecally. Modeling of CSF movement and drug transport^{32,33} must take into consideration the effect of respiration.

CONCLUSIONS

Normal respiration in healthy subjects induces CSF motion in the spinal canal, which is directed caudocranially during inhalation and craniocaudally during exhalation. Compared with cardiac-driven CSF flow, respiratory-driven flow dominates in the lumbar region. Respiration constitutes, therefore, an important driving mechanism of CSF. Patient-specific analyses of cardiac-driven and respiratory-driven CSF flow and anatomic measurements in combination with complementary mathematic models can help improve the effectiveness and predictability of intrathecal drug delivery treatments in the future.

Disclosure forms provided by the authors are available with the full text and PDF of this article at www.ajnr.org.

REFERENCES

- Quigley MF, Iskandar B, Quigley MA, et al. **Cerebrospinal fluid flow in foramen magnum: temporal and spatial patterns at MR imaging in volunteers and in patients with Chiari I malformation.** *Radiology* 2004;232:229–36 CrossRef Medline
- Du Boulay GH. **Pulsatile movements in the CSF pathways.** *Br J Radiol* 1966;39:255–62 CrossRef Medline
- Du Boulay G, O'Connell J, Currie J, et al. **Further investigations on pulsatile movements in the cerebrospinal fluid pathways.** *Acta Radiol Diagn (Stockh)* 1972;13:496–523 CrossRef Medline
- Linninger AA, Tangen K, Hsu CY, et al. **Cerebrospinal fluid mechanics and its coupling to cerebrovascular dynamics.** *Annu Rev Fluid Mech* 2016;48:219–57 CrossRef
- Cserr HF. **Physiology of the choroid plexus.** *Physiol Rev* 1971;51:273–311 CrossRef Medline
- Brown PD, Davies SL, Speake T, et al. **Molecular mechanisms of cerebrospinal fluid production.** *Neuroscience* 2004;129:955–68 CrossRef Medline
- Di Chiro G. **Movement of the cerebrospinal fluid in human beings.** *Nature* 1964;204:290–91 CrossRef Medline
- Sánchez AL, Martínez-Bazán C, Gutiérrez-Montes C, et al. **On the bulk motion of the cerebrospinal fluid in the spinal canal.** *J Fluid Mech* 2018;841:203–27 CrossRef
- Coenen W, Gutiérrez-Montes C, Sincomb S, et al. **Subject-specific studies of CSF bulk flow patterns in the spinal canal: implications for the dispersion of solute particles in intrathecal drug delivery.** *AJNR Am J Neuroradiol* 2019;40:1242–49 CrossRef Medline
- Khani M, Sass LR, Xing T, et al. **Anthropomorphic model of intrathecal cerebrospinal fluid dynamics within the spinal subarachnoid space: spinal cord nerve roots increase steady-streaming.** *J Biomech Eng* 2018;140:081012 CrossRef Medline
- Bhadelia RA, Madan N, Zhao Y, et al. **Physiology-based MR imaging assessment of CSF flow at the foramen magnum with a Valsalva maneuver.** *AJNR Am J Neuroradiol* 2013;34:1857–62 CrossRef Medline
- Yamada S, Miyazaki M, Yamashita Y, et al. **Influence of respiration on cerebrospinal fluid movement using magnetic resonance spin labeling.** *Fluids Barriers CNS* 2013;10:36 CrossRef Medline
- Chen L, Beckett A, Verma A, et al. **Dynamics of respiratory and cardiac CSF motion revealed with real-time simultaneous multi-slice EPI velocity phase contrast imaging.** *Neuroimage* 2015;122:281–87 CrossRef Medline
- Dreha-Kulaczewski S, Joseph AA, Merboldt KD, et al. **Inspiration is the major regulator of human CSF flow.** *J Neurosci* 2015;35:2485–91 CrossRef Medline
- Daouk J, Bouzerar R, Baledent O. **Heart rate and respiration influence on macroscopic blood and CSF flows.** *Acta Radiol* 2017;58:977–82 CrossRef Medline
- Dreha-Kulaczewski S, Joseph AA, Merboldt KD, et al. **Identification of the upward movement of human CSF in vivo and its relation to the brain venous system.** *J Neurosci* 2017;37:2395–2402 CrossRef Medline
- Yildiz S, Thyagaraj S, Jin N, et al. **Quantifying the influence of respiration and cardiac pulsations on cerebrospinal fluid dynamics using real-time phase-contrast MRI: cardiac- and respiratory-driven CSF flow.** *J Magn Reson Imaging* 2017;46:431–39 CrossRef Medline
- Takizawa K, Matsumae M, Sunohara S, et al. **Characterization of cardiac- and respiratory-driven cerebrospinal fluid motion based on asynchronous phase-contrast magnetic resonance imaging in volunteers.** *Fluids Barriers CNS* 2017;14:25 CrossRef Medline
- Delaidelli A, Moiraghi A. **Respiration: a new mechanism for CSF circulation?** *J Neurosci* 2017;37:7076–78 CrossRef Medline
- Dreha-Kulaczewski S, Konopka M, Joseph AA, et al. **Respiration and the watershed of spinal CSF flow in humans.** *Sci Rep* 2018;8:5594 CrossRef Medline
- Aktas G, Kollmeier JM, Joseph AA, et al. **Spinal CSF flow in response to forced thoracic and abdominal respiration.** *Fluids Barriers CNS* 2019;16:10 CrossRef Medline
- Spijkerman JM, Geurts LJ, Siero JC, et al. **Phase contrast MRI measurements of net cerebrospinal fluid flow through the cerebral aqueduct are confounded by respiration: net CSF flow confounded by respiration.** *J Magn Reson Imaging* 2019;49:433–44 CrossRef Medline
- Vinje V, Ringstad G, Lindström EK, et al. **Respiratory influence on cerebrospinal fluid flow: a computational study based on long-term intracranial pressure measurements.** *Sci Rep* 2019;9:9732 CrossRef Medline
- Lloyd RA, Butler JE, Gandevia SC, et al. **Respiratory cerebrospinal fluid flow is driven by the thoracic and lumbar spinal pressures.** *J Physiol* 2020;598:5789–5805 CrossRef Medline
- Kollmeier JM, Gürbüz-Reiss L, Sahoo P, et al. **Deep breathing couples CSF and venous flow dynamics.** *Sci Rep* 2022;12:2568 CrossRef Medline
- Yildiz S, Grinstead J, Hildebrand A, et al. **Immediate impact of yogic breathing on pulsatile cerebrospinal fluid dynamics.** *Sci Rep* 2022;12:10894 CrossRef Medline
- Bioucas-Dias JM, Valadao G. **Phase unwrapping via graph cuts.** *IEEE Trans Image Process* 2007;16:698–709 CrossRef Medline
- Lu H, Nagae-Poetscher LM, Golay X, et al. **Routine clinical brain MRI sequences for use at 3.0 Tesla.** *J Magn Reson Imaging* 2005;22:13–22 CrossRef Medline
- Tangen KM, Hsu Y, Zhu DC, et al. **CNS wide simulation of flow resistance and drug transport due to spinal microanatomy.** *J Biomech* 2015;48:2144–54 CrossRef Medline
- Sass LR, Khani M, Natividad GC, et al. **A 3D subject-specific model of the spinal subarachnoid space with anatomically realistic ventral and dorsal spinal cord nerve rootlets.** *Fluids Barriers CNS* 2017;14:36 CrossRef Medline
- Sincomb S, Coenen W, Gutiérrez-Montes C, et al. **A one-dimensional model for the pulsating flow of cerebrospinal fluid in the spinal canal.** *J Fluid Mech* 2022;939:A26 CrossRef
- Lawrence JJ, Coenen W, Sánchez AL, et al. **On the dispersion of a drug delivered intrathecally in the spinal canal.** *J Fluid Mech* 2019;861:679–720 CrossRef
- Gutiérrez-Montes C, Coenen W, Lawrence JJ, et al. **Modelling and direct numerical simulation of flow and solute dispersion in the spinal subarachnoid space.** *Applied Mathematical Modelling* 2021;94:516–33 CrossRef

Celebrating 35 Years of the AJNR

September 1987 edition

Transluminal Angioplasty of the Vertebral and Basilar Artery

Randall T. Higashida,¹
Grant B. Hieshima,¹
Fong Y. Tsai,²
Van V. Halbach,¹
David Norman,¹
T. Hans Newton¹

Transluminal angioplasty of brachiocephalic vessels for atherosclerotic lesions is now being performed in selected cases. We have thus far treated 17 cases of vertebral artery stenosis and one case of basilar artery stenosis by intravascular balloon dilatation techniques. Clinical presenting symptoms included vertebral basilar insufficiency, repeated transient ischemic attacks (TIAs), and multiple strokes. We performed successful transluminal angioplasty in 16 patients with marked narrowing ($>70\%$) of the dominant vertebral artery from atherosclerosis. One patient with basilar artery stenosis with tandem atherosclerotic lesions was also treated by angioplasty techniques. Repeat angiography at 3- to 12-month intervals has revealed continued patency at the angioplasty site. Complications occurred in our one patient with basilar artery angioplasty, who suffered a brainstem infarction after treatment, and in one patient who had a TIA after bilateral vertebral artery angioplasty. Two other patients had residual vertebral stenosis but remained asymptomatic after the procedure. All other patients who had successful dilatation were asymptomatic at 8 months to 2 years (mean, 15 months) of follow-up.

These initial studies indicate that vertebral artery angioplasty may be effective for treating high-grade atherosclerotic lesions and for improving blood flow to the posterior circulation. Angioplasty of the basilar artery is technically more difficult and has a higher degree of risk because of the many perforating branches supplying the brainstem.

Percutaneous transluminal angioplasty (PTA) is being performed with increasing frequency in the innominate, subclavian, external, and internal carotid vessels [1-11]. Thus far, this technique appears to be effective for the treatment of hemodynamically significant atherosclerotic lesions. This is particularly important for vessels located in areas that are more difficult to treat surgically, such as the proximal vertebral and basilar arteries. We report our experience with transluminal angioplasty in 17 cases of hemodynamically significant atherosclerotic lesions of the vertebral artery and in one case of stenosis involving the basilar artery.

Subjects and Methods

Patients included 10 men and seven women ranging in age from 48-77 years old (mean, 62.8). Percutaneous transluminal angioplasty (PTA) of the vertebral artery was performed in 13 patients who presented clinically with symptoms of vertebral basilar insufficiency, including dizziness, diplopia, bilateral numbness, muscular fasciculations, weakness, and ataxia. Two patients presented with symptoms of multiple transient posterior circulation ischemic attacks, which included transient cortical blindness, memory disturbance, and nystagmus. Two patients presented with multiple embolic strokes and had symptoms of homonymous hemianopia, poor eye-hand coordination, visual agnosia, and vertical gaze nystagmus. All patients were managed in the acute stage of presentation by systemic heparinization or were placed on strict therapeutic doses of oral anticoagulants, including Coumadin, aspirin, and/or dipyridamole (Persantine). Only patients who failed to respond to conventional medical therapy were accepted for PTA.

In 15 patients, PTA was performed on the dominant proximal vertebral artery for atheros-



Chiari II Malformation: MR Imaging Evaluation

Samuel M. Wolpert,¹
Mary Anderson,¹
R. Michael Scott,¹
Eddie S. K. Kwiat,¹
Val M. Runge²

The purpose of this study was to explore the value of high-detail MR imaging in the diagnosis of the Chiari II malformation. Twenty-four patients with known Chiari II malformation as diagnosed by CT scanning were evaluated with cranial MR scans. Two patients also had spine scans. The sagittal-plane images were the most informative, and abnormalities of the telencephalon, diencephalon, mesencephalon, rhombencephalon, upper spinal cord, and meninges were shown extremely well. We found MR to be an easy and accurate method for demonstrating the abnormalities of the Chiari II malformation, and it is our procedure of choice.

The Chiari II malformation is a complex developmental deformity characterized by an elongated small cerebellum and brainstem with caudal displacement of the medulla, parts of the cerebellum, and pons through an enlarged foramen magnum into the cervical spinal canal [1]. A meningocele is a nearly constant accompanying feature, as is hydrocephalus. In addition, numerous other malformations of the neuraxis including polymicrogyria, subependymal heterotopias, beaked ciliolateral plate, aqueduct stenosis, diastematomyelia, diplomyelia, hydromyelia, and syringomyelia have been reported [1].

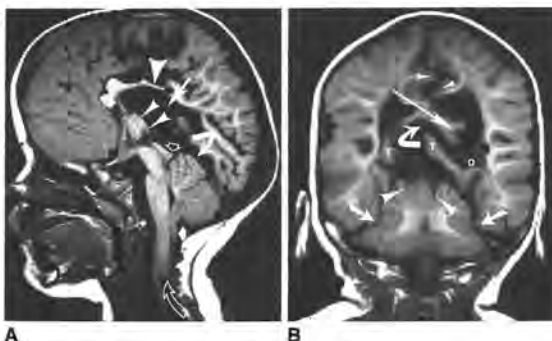
We had the opportunity to evaluate 24 patients with Chiari II malformation with high-detail MR imaging. Most abnormalities previously described as seen by CT [2-5] were also seen by MR. In this article we review these abnormalities and report on other associated features of the Chiari malformation that either have a greater frequency than has previously been reported or that have not been described before.

Subjects and Methods

Twenty-four patients with meningoceles and known Chiari II malformations as diagnosed by CT scanning were investigated with MR imaging. Three patients were less than 1 year old, five were 1-5 years old, five were 6-10 years old, and 11 were 10-20 years old. In 21 of the patients, ventricular shunts had been inserted previously; in one patient a unilateral subarachnoid-peritoneal shunt had been placed. Sagittal and axial images were obtained in all patients. The majority of the sagittal images (16) were 3 mm thick, the rest were either 4 or 5 mm thick. Eighteen patients had coronal scans (5-10 mm thick). Spin-echo techniques were used. Since the anatomy of the lesions was the prime consideration, mid T1-weighted images were obtained in all cases with a repetition time of 500, 600, or 800 msec and an echo time of 17 msec. T2-weighted images were not obtained routinely. In all patients, an attempt was made to include the upper cervical spine on the sagittal images. In addition, two patients had separate T1-weighted sagittal images of the spine, and one of the two had T2-weighted sequences as well.

Results

The results are categorized by the involvement of the different embryologic parts of the brain and are summarized in Table 1.



Received September 3, 1986; accepted after revision March 19, 1987.

Presented at the annual meeting of the American Society of Neuroradiology, San Diego, January 1986.

¹Departments of Radiology and Neurosurgery, International Neurosurgery Institute, UCSF Medical Center, 1505 Parnassus Ave., San Francisco, CA 94143. Address reprint requests to R. T. Higashida.

²University of Missouri at Kansas City, School of Medicine, Truman Medical Center, Kansas City, MO 64108.

AJNR 8:745-755, September/October 1987
0195-9582/87/060745-11\$5.00/0
© American Society of Neuroradiology

Amyloid-Related Imaging Abnormalities with Emerging Alzheimer Disease Therapeutics: Detection and Reporting Recommendations for Clinical Practice

P.M. Cogswell, J.A. Barakos, F. Barkhof, T.S. Benzinger, C.R. Jack, Jr., T.Y. Poussaint, C.A. Raji, V.K. Ramanan, and C.T. Whitlow



ABSTRACT

SUMMARY: Monoclonal antibodies are emerging disease-modifying therapies for Alzheimer disease that require brain MR imaging for eligibility assessment as well as for monitoring for amyloid-related imaging abnormalities. Amyloid-related imaging abnormalities result from treatment-related loss of vascular integrity and may occur in 2 forms. Amyloid-related imaging abnormalities with edema or effusion are transient, treatment-induced edema or sulcal effusion, identified on T2-FLAIR. Amyloid-related imaging abnormalities with hemorrhage are treatment-induced microhemorrhages or superficial siderosis identified on T2* gradient recalled-echo. As monoclonal antibodies become more widely available, treatment screening and monitoring brain MR imaging examinations may greatly increase neuroradiology practice volumes. Radiologists must become familiar with the imaging appearance of amyloid-related imaging abnormalities, how to select an appropriate imaging protocol, and report findings in clinical practice. On the basis of clinical trial literature and expert experience from clinical trial imaging, we summarize imaging findings of amyloid-related imaging abnormalities, describe potential interpretation pitfalls, and provide recommendations for a standardized imaging protocol and an amyloid-related imaging abnormalities reporting template. Standardized imaging and reporting of these findings are important because an amyloid-related imaging abnormalities severity score, derived from the imaging findings, is used along with clinical status to determine patient management and eligibility for continued monoclonal antibody dosing.

ABBREVIATIONS: A β = amyloid-beta; AD = Alzheimer disease; APP = amyloid precursor protein; ARIA = amyloid-related imaging abnormalities; ARIA-E = amyloid-related imaging abnormalities with edema or effusion; ARIA-H = amyloid-related imaging abnormalities with hemorrhage; CAA = cerebral amyloid angiopathy; CAA-RI = CAA-related inflammation; GRE = gradient recalled-echo; mAb = monoclonal antibody

As clinically defined, probable Alzheimer disease (AD) dementia is estimated to affect approximately 11% of Americans aged 65 years and older, and there is a large group of patients who may be potential candidates for emerging disease-modifying therapies.¹ Recently, monoclonal antibodies against beta-amyloid have become available (in clinical trials and early clinical practice) for the treatment of AD. These therapies require frequent brain MR imaging examinations to detect contraindications to treatment and to monitor for subclinical or symptomatic adverse

events associated with treatment, which are used to guide decisions on dose-adjustment or discontinuation.² Neuroradiologists will play an important role in diagnostic evaluations, which will include MRIs and either lumbar punctures or amyloid PET scans, and monitoring adverse events associated with treatment along with longer-term structural and functional effects of therapy, analogous to safety monitoring for progressive multifocal leukoencephalopathy in patients undergoing treatment for multiple sclerosis.^{3,4} Given the large number of AD therapeutic candidates, implementation of treatment and monitoring may greatly increase neuroradiology practice volumes. Radiologists, both neuroradiologists and generalists in private practice and academic institutions, should, therefore, be familiar with the pathophysiology of AD relevant to anti-amyloid therapy and the mechanism and appearance of amyloid-related imaging abnormalities (ARIA) that may result from treatment. In addition, knowledge of the pitfalls in interpretation of these imaging abnormalities, selection of an appropriate imaging protocol, and standardization of imaging and reporting of these findings in clinical practice are important. Use of the recommended standardized imaging protocols and reporting templates will improve ARIA detection and timely communication of

From the Departments of Radiology (P.M.C., C.R.J.) and Neurology (V.K.R.), Mayo Clinic, Rochester, Minnesota; Department of Radiology (J.A.B.), California Pacific Medical Center, San Francisco, California; Departments of Radiology (F.B.) and Nuclear Medicine (F.B.), VU University Medical Center, Amsterdam, the Netherlands; Queen Square Institute of Neurology and Centre for Medical Image Computing (F.B.), University College London, UK; Departments of Radiology (T.S.B., C.A.R.), Neurosurgery (T.S.B.), and Neurology (C.A.R.), Washington University School of Medicine, St. Louis, Missouri; Department of Radiology (T.Y.P.), Boston Children's Hospital, Boston, Massachusetts; and Departments of Radiology (C.T.W.) and Biomedical Engineering (C.T.W.), Wake Forest School of Medicine, Winston-Salem, North Carolina.

Please address correspondence to Petrice M. Cogswell, MD, PhD, Mayo Clinic, 200 First St SW, Rochester, MN 55905; e-mail: Cogswell.petrice@mayo.edu

Indicates open access to non-subscribers at www.ajnr.org

<http://dx.doi.org/10.3174/ajnr.A7586>

findings to referring providers, ensuring optimal patient care and management.

Background: Amyloid Beta, ARIA, and Cerebral Amyloid Angiopathy

Neuropathology and Pathophysiology of Alzheimer Disease and Cerebral Amyloid Angiopathy. The major proteinopathy that forms amyloid plaques is amyloid-beta ($A\beta$), specifically the 42 amino acid peptide $A\beta$ 42. Amyloid plaques are one of the 2 defining pathologic features of AD, the other being neurofibrillary tangles.⁵ $A\beta$ 42 is derived from proteolytic metabolism of amyloid precursor protein (APP). APP may be cleaved by α -secretase in a nonamyloidogenic pathway or by β -secretase in an amyloidogenic pathway to form α - or β -C terminal fragments that are subsequently cleaved by γ -secretase to form P3 and $A\beta$ peptides, respectively.⁶ Due to differential cleavage sites, $A\beta$ exists in many isoforms, but the 2 most relevant for this discussion are $A\beta$ 42 and $A\beta$ 40. Soluble $A\beta$ monomers may undergo clearance via enzymatic degradation, transport across the blood-brain barrier, or efflux out of the brain via perivascular drainage pathways, which include periarterial as well as perivenous or recently detailed glymphatic drainage pathways.^{7,8} Soluble $A\beta$ monomers may also aggregate into a range of successively larger protein complexes, oligomers, protofibrils, and mature fibrils, that can subsequently deposit in the brain as amyloid plaques (predominantly $A\beta$ 42) or in the vessel wall (predominantly $A\beta$ 40) and result in AD pathology and cerebral amyloid angiopathy (CAA), respectively.⁹ Accumulation of $A\beta$ in vessel walls may result from and further contribute to impaired $A\beta$ clearance and loss of vascular integrity. $A\beta$ is, therefore, central to the development of both AD and CAA, which often co-occur.¹⁰

Rationale for Beta-Amyloid Removal as Treatment for Alzheimer Disease. $A\beta$ removal for treatment of AD is based on the amyloid cascade hypothesis.¹¹ This model proposes that amyloid plaque deposition facilitates downstream pathophysiologic events including tau phosphorylation, neurofibrillary tangle formation, microglial activation, and eventually neurodegeneration and progressive cognitive decline.^{5,12,13} In addition, rare familial (and often young-onset) cases of AD are caused by mutations in genes with central roles in amyloid biology (presenilin 1 and 2, *PSEN1* and *PSEN2*, and *APP*), further pointing to a central early role of amyloid accumulation in the disease.¹⁴ Although tau aggregation has been shown to be more closely related to neuronal loss and cognitive decline both spatially and temporally, it is thought that amyloid plaque deposition is the key initiating step in AD pathophysiology.¹⁵⁻¹⁷ Halting β -amyloid formation or facilitating its removal is therefore expected to decrease or halt downstream pathophysiologic processes, tau phosphorylation, tau deposition, neurodegeneration, and cognitive decline. Recent clinical trials of anti-amyloid therapies have indeed demonstrated that removal of amyloid plaques from the brain can result in short-term improvement in downstream biomarkers of tauopathy and neurodegeneration, though longer-term consequences on disease biomarkers and clinical course are not fully understood.^{18,19}

Treatment Strategies and Origin of the Term ARIA. Therapeutic approaches for reducing amyloid in the brain have included inhibitors of amyloid aggregation, inhibitors of β -secretase, inhibitors of γ -secretase, and immunotherapy to remove amyloid from the brain, with immunotherapy being the most extensively employed mode of action in clinical trials.²⁰ Active and passive immunotherapy approaches have been investigated, though the use of active immunotherapy has been limited due to adverse reactions including meningoencephalitis.²¹ Clinical trials using passive immunotherapy, exogenously administered monoclonal antibodies (mAb) against $A\beta$, have been ongoing for approximately 2 decades. Bapineuzumab was the first mAb to enter clinical trials. It binds the N-terminus of $A\beta$ and clears both soluble and fibrillary $A\beta$. In early studies of bapineuzumab, monitoring MR imaging brain examinations showed edema and microhemorrhages in 3/10 participants.^{22,23} The Alzheimer's Association Research Roundtable convened a workgroup in 2010 to provide information and recommendations regarding the imaging abnormalities encountered in the anti-amyloid trials. This workgroup termed these amyloid-related imaging abnormalities as ARIA with ARIA-E for edema or effusion and ARIA-H for microhemorrhages and hemosiderosis.²⁴

Multiple monoclonal antibodies with variable targets and incidence of ARIA have since been developed and tested in clinical trials (Table 1).^{18,19,25-32} Aducanumab recently received accelerated approval by the FDA for potential clinical use in mild, symptomatic AD, based on reduction in amyloid plaque.² Other agents (donanemab, lecanemab, gantenerumab) are currently in late-phase clinical trials and will undergo similar FDA reviews.^{18,19,31} The Centers for Medicare and Medicaid Services currently proposes coverage for FDA-approved anti-amyloid mAbs in Centers for Medicare and Medicaid Services–approved randomized control trials. To date, uncertainties remain on several fronts including the presence and extent of insurance coverage, the results of an anticipated Phase IV confirmatory study required by the FDA, multiple stakeholder preparedness across a wide range of clinical practices, and other factors.

ARIA Mechanism. Amyloid deposition in vessel walls (CAA) may result in loss of vascular integrity and reduced perivascular clearance and may be related to spontaneously occurring microhemorrhages.³³ When anti-amyloid monoclonal antibody therapy is initiated, antibody-mediated breakdown of amyloid plaque and mobilization of parenchymal and vascular $A\beta$ increase the load of perivascular drainage.⁷ The overload of perivascular drainage pathways may transiently increase amyloid deposition in the arterial wall. At the same time, antibody-mediated inflammation and breakdown of amyloid also occur in the vessel wall. These processes cause further loss of vascular integrity and blood-brain barrier breakdown.³⁴ As a result, proteinaceous fluid and/or red blood cells leak into the parenchyma and/or leptomeningeal space and result in edema/effusion (ARIA-E) or microhemorrhages/superficial siderosis (ARIA-H).

ARIA versus CAA-Related Inflammation. The further loss of vascular integrity and blood-brain barrier breakdown with immunotherapy against $A\beta$ may be thought of as transient exacerbation

Table 1: Summary of anti-amyloid monoclonal antibodies in clinical trials

Monoclonal Antibody	A β Binding Site	Amyloid Target	Completed Phase III Trials	Main Results	ARIA-E Incidence ^a	ARIA-H Incidence ^a	Active Phase III Trials
Aducanumab (Salloway et al, 2022)	N-terminus conformational epitope	A β oligomers, fibrils, and plaques	EMERGE ENGAGE	Reduced decline in cognitive end points Increase in CSF A β 42 Decrease in amyloid PET SUVR and CSF p-tau	35.2% NC 20.3% NC 43.0% C	mH 19.1% 12.4% NC 22.7% C SS 14.7% 6.2% NC 19.1% C	EMBARK TRAILBLAZER-ALZ-4
Bapineuzumab (Salloway et al, 2014) ²⁸	N-terminus	A β monomers, oligomers, and fibrils	NCT00574132 NCT00575055	No effect on cognitive end points Decrease in amyloid PET SUVR and CSF p-tau in APOE ϵ 4 carriers	4.2% NC 15.3% C	–	–
Crenezumab (Guthrie et al, 2020) ²⁹	A β peptides	A β oligomers, fibrils, and plaques	CREAD CREAD 2	No effect on cognitive end points, amyloid PET or CSF p-tau Increase in CSF A β 42	0%	4.9%	–
Donanemab (Mintun et al (2021)) ¹⁸	Pyroglutamate form of A β	A β plaques	TRAILBLAZER-ALZ-2	Reduced decline cognitive end points Decrease in amyloid PET SUVR	27.5% NC 11.4% NC 44.0% C	30.5%	TRAILBLAZER-ALZ-3 TRAILBLAZER-ALZ-4
Ponezumab (Landen et al, 2017) ³⁰	C-terminus	Soluble A β 1-40	–	No effect on cognitive end points, CSF A β 42 or amyloid PET	0.7%	16.4%	–
Gantenerumab (Ostrowitzki et al, 2017) ³¹	N-terminus and central amino acids	A β oligomers, fibrils, and plaques	SCarlet RoAD Marguerite RoAD	No effect on cognitive end points or CSF A β 42 Decrease in amyloid PET SUVR and CSF p-tau	13.5% NC 11.0% NC 15.0% C	16.2% 11.0% NC 19.4% C	GRADUATE 1 GRADUATE 2 DIAN-TU
Lecanemab (Swanson et al, 2021) ¹⁹	A β protofibril	A β protofibrils		Reduced decline in cognitive end points Increase in CSF A β 42 Decrease in amyloid PET SUVR and CSF p-tau	9.9% NC 8.0% NC 14.3% C	10.7% 4.6% NC 13.1% C	CLARITY AD AHEAD 3-45
Solanezumab (Doody et al, 2014) ³²	Mid-domain	A β monomers	EXPEDITION 1 EXPEDITION 2 EXPEDITION 3 EXPEDITION PRO	No effect on cognitive end points, amyloid PET SUVR, or CSF p-tau Increase CSF A β 42	0.9%	4.9%	A4 DIAN-TU

Note:—mH indicates microhemorrhage; SS, siderosis; NC, APOE ϵ 4 noncarrier; C, APOE ϵ 4 carrier; SUVR, standardized uptake value ratio; –, none or not reported.

^a ARIA incidence reported for the highest dose in studies with variable dosing arms. ARIA incidence reported for all participants and separately for APOE ϵ 4 noncarriers and carriers when data are available.

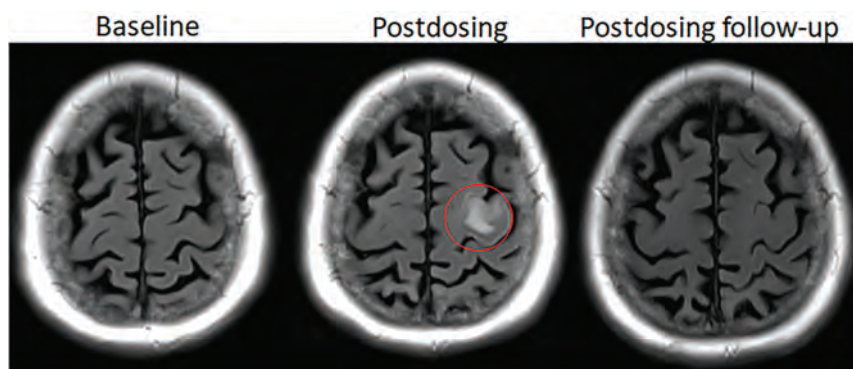


FIG 1. Dynamic and transient nature of ARIA-E. Axial T2 FLAIR images over 3 sequential time points for a patient undergoing anti-amyloid monoclonal antibody therapy. On the postdosing examination (middle, red circle), there is FLAIR hyperintensity involving the left superior frontal cortex and subcortical white matter measuring <5 cm in transverse dimension (mild ARIA-E) that is new from the baseline examination. On the 1-month postdosing follow-up examination, performed to reassess the ARIA-E, the left frontal FLAIR hyperintensity had resolved, as is typically seen and in keeping with the transient nature of ARIA-E. Images courtesy of Biogen.

of the effects of CAA, similar to CAA-related inflammation (CAA-RI). CAA-RI is a spontaneously occurring inflammatory condition that responds to steroid treatment or immunosuppression,³⁵ whereas ARIA occurs secondary to monoclonal antibody therapy and generally resolves spontaneously on interruption or discontinuation of therapy. The presence of spontaneously occurring CSF autoantibodies against A β in patients with CAA-RI suggests that CAA and CAA-RI are a natural model for ARIA.³⁶ CAA-RI and ARIA have similar imaging findings of sulcal effusion and edema involving the white and gray matter as well as microhemorrhages and siderosis and are best differentiated by whether or not the patient is undergoing anti-amyloid therapy.

ARIA Risk Factors. Risk factors for ARIA are drug exposure, *APOE-e4* allele carriership, and pretreatment microhemorrhages.^{24,27,37,38} Regarding drug exposure, the risk of ARIA was found to be greater at higher drug doses and earlier in the treatment course. It is noted that the risk for developing ARIA is reduced if patients are started at a low drug dose and progressively titrated over time to the higher final optimal treatment dose. In theory, this titration phase allows time for the cerebral vasculature to undergo the transient process of loss of structural integrity, due to amyloid removal, over a more prolonged period, thus allowing reconstitution of vascular integrity by the time the patient is titrated to higher treatment doses. As such, dose titration or dose escalation strategies have become commonplace in anti-amyloid mAb treatment studies. For example, in Phase III trials of aducanumab, the rates of ARIA were reduced with dose titration compared with nontitration. Additionally, most ARIA developed within the first 8 doses of the final target dose, during this transient phase of presumed loss of vessel wall integrity.²⁷ *APOE-e4* allele carriership remains the greatest risk factor for the development of ARIA, second only to drug dose, and is likely related to higher load of vascular amyloid and poorer vascular integrity pretreatment. In a Phase III trial of gantenerumab, ARIA-E occurred in 10.7% of homozygous *APOE-e4* carriers,

5.4% of heterozygous carriers, and 1.8% of noncarriers. Similarly, ARIA-H occurred in 32.0% of homozygous carriers compared with 19.8% in heterozygous carriers and 12.3% in noncarriers.³¹ The presence of pretreatment hemosiderin products most consistent with CAA, lobar microhemorrhages and superficial siderosis, is a serious imaging risk factor predictive of ARIA with the use of anti-amyloid mAb therapies, particularly in *APOE-e4* carriers.^{39,40} Due to the increased risk of adverse events in homozygous *APOE-e4* carriers, *APOE-e4* testing could be considered before drug initiation and could be used to help determine the frequency of safety monitoring examinations in future, updated treatment guidelines.

Additionally, in clinical trials, the incidence of ARIA has varied with the

A β binding site and targeted A β structure (Table 1). ARIA incidence was higher with mAbs that bind the N- versus C-terminus and target aggregated-versus-soluble forms of A β .

Conversely, risk factors for CAA are AD pathology and genetic factors that promote AD pathology, namely *APOE-e4*, Down syndrome, *PSEN1*, *PSEN2*, and *APP* mutations.⁴¹ Note, vessel-related risk factors for ARIA relate to amyloid deposition and as with CAA are not related to common vascular risk factors such as hypertension, hyperlipidemia, diabetes mellitus, or the severity of atherosclerosis.

ARIA-E

Imaging Appearance. The E in ARIA-E stands for edema, effusion, and exudate. A leak of proteinaceous fluid into the parenchyma results in edema, with the imaging appearance similar to that of vasogenic edema and best visualized on a T2-FLAIR sequence (Figs 1 and 2). T2-hyperintense signal occurs in the white matter, gray matter, or both. There may be associated local mass effect and gyral swelling. Findings may be differentiated from cytotoxic edema by absent diffusion restriction; intense diffusion restriction associated with an acute infarct is not a characteristic of ARIA. When the leak occurs in the leptomeningeal space, the result is a sulcal effusion or exudate, only appreciated on T2-FLAIR sequences due to T1-shortening related to proteinaceous content (Fig 3). ARIA-E may present as either parenchymal edema or sulcal effusion, or both may occur together; sulcal effusion was the most common manifestation of ARIA-E in some mAb trial analyses, and parenchymal edema, in others.^{42,43} ARIA-E most commonly affects the occipital lobes followed by the parietal, frontal, and temporal lobes and, least frequently, the cerebellum. The intensity and size of the signal abnormality are variable, from subtle small, 1- to 2-cm zones of cortico-subcortical abnormality to multifocal-to-near hemispheric signal T2-hyperintense signal alterations.^{24,42} These regions of signal abnormality generally have ill-defined margins, though they may infrequently

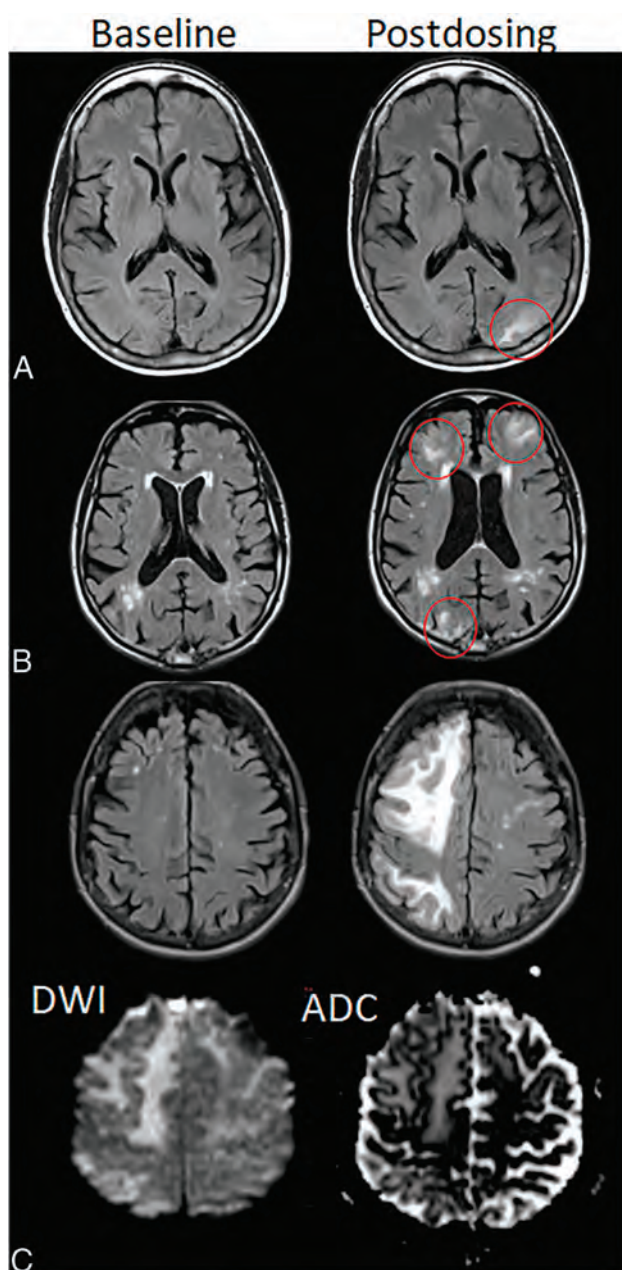


FIG 2. ARIA-E, parenchymal edema. Axial T2-FLAIR images from 3 separate patients at the time of the pretreatment baseline (*left*) and on a monitoring examination following initiation of anti-amyloid monoclonal antibody therapy (postdosing, *right*). *A*, On the postdosing examination, new T2-FLAIR hyperintense signal in the left parieto-occipital subcortical white matter with mild local mass effect and sulcal effacement measuring <5 cm the transverse dimension (mild ARIA-E, *red circle*). *B*, New multifocal, patchy T2-FLAIR hyperintense signal in the bifrontal and right occipital subcortical white matter on the postdosing examination, each region measuring <5 cm (*red circles*). A single region measuring <5 cm would be classified as mild, but >1 yields a classification of moderate ARIA-E. Multiplicity of ARIA-E involvement yields a classification of moderate, as long as each region is <10 cm in diameter. In some regions, there is involvement of the cortex, mild local mass effect, and gyral swelling. *C*, On the postdosing examination, development of extensive T2-FLAIR hyperintense signal throughout the right frontal and parietal lobes measuring >10 cm (severe ARIA-E). Associated mass effect and sulcal effacement throughout much of the right cerebral hemisphere.

have circumscribed margins and mimic a neoplastic lesion (Fig 4).

Both the edema and effusion/exudate of ARIA-E are transient and typically resolve over time upon interruption or discontinuation of anti-amyloid therapy (and have even been observed to resolve under continued dosing).⁴⁴

Interpretation Pitfalls. Imaging experience in clinical trials has provided insight into potential interpretation pitfalls in the assessment of ARIA-E. Any condition that results in T2-FLAIR hyperintensity, such as incomplete water suppression, susceptibility artifact, etc, may serve as an ARIA-E mimic (Fig 5). Shading artifacts and scanner or sequence variability may make identification and interpretation of ARIA-E-versus-artifacts difficult. Shading artifacts may occur when prescan normalization is inadvertently turned off or the patient is not centered in the receive coil, resulting in artifactually bright regions. When this occurs focally on the T2-FLAIR sequence, the artifacts may simulate ARIA-E, particularly when occurring in the occipital lobes where ARIA-E is most common. The occipital white matter signal may also vary with MR imaging scan vendor or field strength.⁴⁵ If a patient is imaged on different scanners, it may be difficult to distinguish true ARIA-E versus technical variation (Fig 5). Similarly, white matter signal may differ with scan technique, such as the use of 3D-versus-2D FLAIR.⁴⁶ CSF suppression may be suboptimal, and CSF may remain very high in signal in the presence of large susceptibility or due to inflow phenomena.⁴⁷

Other entities may simulate ARIA. Posterior reversible encephalopathy syndrome may similarly have T2-hyperintense signal involving the white and gray matter, co-occurring hemorrhage, and a predilection for the occipital lobes, though often with a more near-symmetric parasagittal distribution.⁴⁸ A subacute infarct that no longer demonstrates diffusion restriction may be difficult to differentiate from the parenchymal edema of ARIA-E in the absence of prior imaging from the acute stage or a history of focal neurologic deficit. Incomplete water suppression on FLAIR, oxygen supplementation, subarachnoid hemorrhage, and other entities that cause FLAIR hyperintense sulcal signal may mimic ARIA-E sulcal effusion.⁴⁹ Although these entities have overlapping radiographic features, when clinical history is available, they may be differentiated from ARIA by the absence of prior anti-amyloid therapy and, in some cases, the presence of clinical symptoms.

Comparison with the baseline, pretreatment T2-FLAIR study is important in ARIA-E detection. ARIA-E that is subtle or that occurs in the setting of extensive small-vessel disease, particularly in a peripheral pattern, may only be appreciated when a careful comparison is made with the baseline T2-FLAIR study. In other cases, the normal compact configuration of sulci with faint cortical/leptomeningeal hyperintensity may mimic an area of ARIA-E, when this is simply normal anatomy confirmed as present at the baseline scan. Subtraction imaging may help detect subtle ARIA-E cases.⁵⁰

Hyperintense signal on DWI (*lower left*) is confirmed to be T2 shine-through on the ADC map (*lower right*), differentiating ARIA-E from acute ischemia or other cause of cytotoxic edema. Images courtesy of Biogen and the Dominantly Inherited Alzheimer Network.

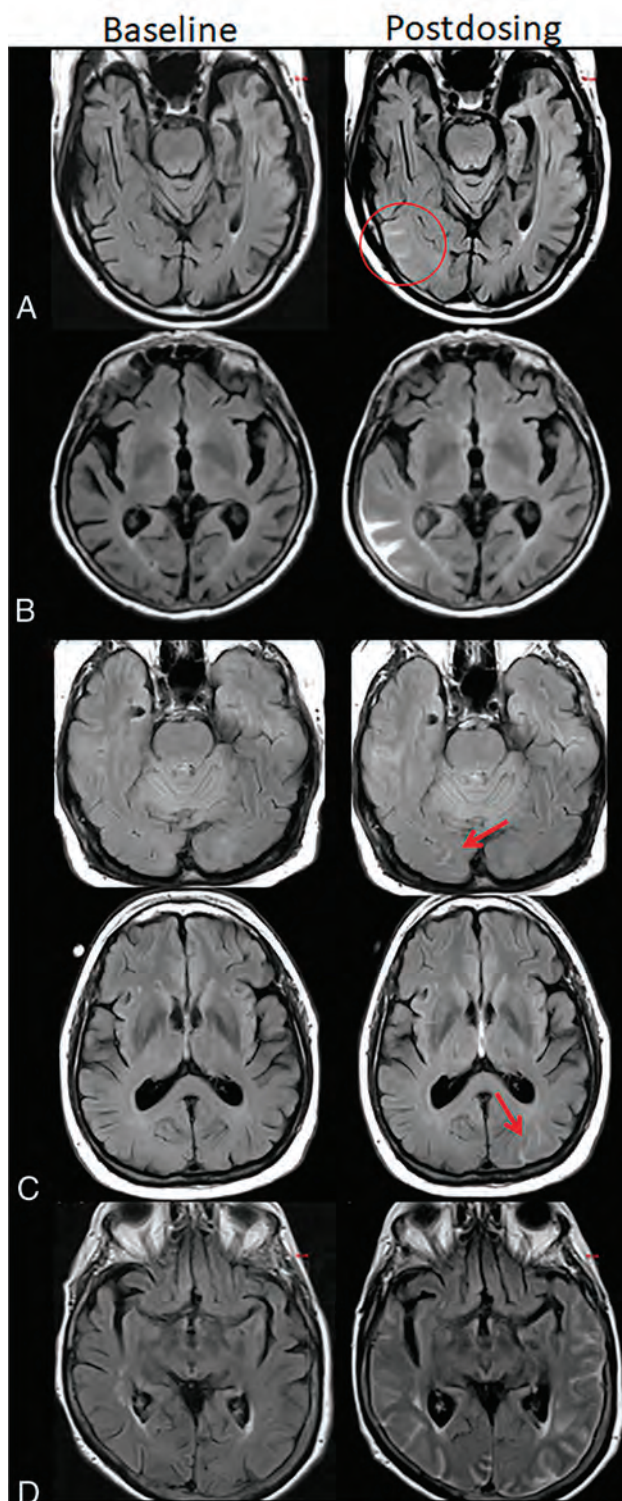


FIG 3. ARIA-E, sulcal effusion. Axial T2-FLAIR images from 4 separate patients at pretreatment baseline (*left*) and on a monitoring examination following initiation of anti-amyloid monoclonal antibody therapy (postdosing, *right*). A, Compared with the baseline examination, new sulcal T2-FLAIR hyperintense signal in the right temporal-occipital lobe measuring <5 cm in transverse dimensions (mild ARIA-E, *red circle*). B, Postdosing, new T2-FLAIR sulcal effusion involving the right posterior temporal and parietal lobes measuring 5–10 cm (moderate ARIA-E). C, Subtle multifocal, bi-occipital, sulcal effusion on the postdosing examination, each region measuring <5 cm (moderate ARIA-E,

Spontaneous Edema/Effusion versus Treatment-Emergent ARIA-E. ARIA-E is not uncommon in clinical trials of mAbs. For example, this was identified in 17% of participants in the bapineuzumab treatment arm and 35% of the aducanumab treatment arm, with incidence varying with treatment and patient-related factors described above.^{2,23} On the other hand, spontaneous, transient edema is rare and was reported in 0.05% of baseline examinations for early anti-amyloid trials and 3% of the aducanumab placebo arm.^{2,43}

Clinical Consequences. On the basis of available clinical trial data and experience, ARIA-E is most frequently detected on routine, protocol-specified, surveillance MRIs in patients who are clinically asymptomatic. When ARIA-E is symptomatic, the symptoms are most commonly nonlocalizing, such as headache or confusion, but can additionally include visual disturbances, visuospatial impairment, or praxis difficulties in view of the relative predilection for posterior involvement of ARIA-E.²⁸ Like the imaging findings, the clinical symptoms are generally expected to resolve over time with treatment pause or withdrawal. In the rare event of symptomatic ARIA-E or in cases with asymptomatic radiographically severe ARIA-E, treatment with intravenous methylprednisolone and possibly other therapies (eg, antihypertensives, anti-seizure medications) may be indicated on the basis of anecdotal reports.⁵¹

ARIA-H

Imaging Appearance. ARIA-H, hemorrhage, includes microhemorrhages and superficial siderosis. When a leakage of heme products occurs in the parenchyma, microhemorrhages develop. Microhemorrhages are punctate, rounded, and markedly hypointense foci in the brain parenchyma on T2* sequences, measuring <10 mm in diameter⁵² (Fig 6). A leak of heme products into the leptomeningeal or subpial space results in superficial siderosis, which manifests as curvilinear hypointensity along the brain surface (Fig 7). Lobar macrohemorrhage (focus of hemorrhage identifiable on T1- or T2-weighted imaging, and usually >10 mm in diameter on gradient recalled-echo [GRE]) rarely occurs with anti-amyloid agents, and when it does, it may be the result of an underlying disease process such as CAA.

ARIA-H is detected on heme-sensitive sequences, ie, T2* GRE and SWI. SWI achieves increased sensitivity for microhemorrhage detection by generating both magnitude and phase images and multiplying the magnitude image by the phase image.⁵² Sensitivity to the detection of ARIA-H is also increased by higher field strength, longer TEs, and lower readout bandwidth. Improved spatial resolution on SWI sequences compared with 2D GRE decreases partial volume effects, which may obscure microhemorrhages, but

red arrows). A single region of ARIA-E measuring <5 cm would be classified as mild, but >1 cm yields a classification of moderate. Multiplicity of ARIA-E involvement yields a classification of moderate, as long as each region is <10 cm in diameter. Identification of these subtle abnormalities requires careful comparison with prior monitoring and/or baseline examination. D, Postdosing, extensive T2-FLAIR sulcal effusion involving the bilateral temporal and occipital lobes measuring ≥ 10 cm in extent (severe ARIA-E). Images courtesy of Biogen and the Dominantly Inherited Alzheimer Network.

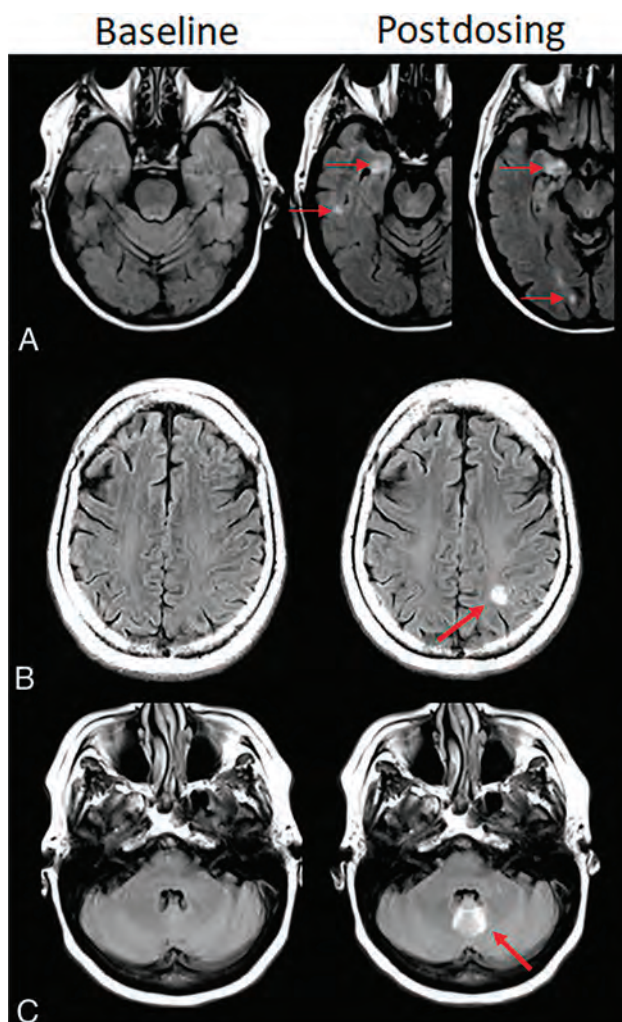


FIG 4. Atypical ARIA-E, parenchymal edema. Axial T2-FLAIR images from 3 separate patients at pretreatment baseline (*left*) and on a monitoring examination following initiation of anti-amyloid monoclonal antibody therapy (postdosing, *right*). *A*, Adjacent slices on postdosing T2-FLAIR show development of multiple nodular areas of ARIA-E (*red arrows*). This nodular presentation is less commonly encountered in contrast to the typical ARIA-E, which has an amorphous parenchymal pattern as expected for vasogenic edema. In this case, although each area of ARIA-E is small (<5 cm), the multiplicity of lesions yields a classification of moderate ARIA-E. *B*, Atypical ARIA-E as a rounded focus of T2-FLAIR hyperintense signal in the left parietal white matter (*left, red arrow*) that may be mistaken for neoplastic process and differentiated by the time course of appearance coinciding with monoclonal antibody dosing and subsequent resolution. *C*, Atypical ARIA-E in the cerebellar vermis. Postdosing, new T2-FLAIR hyperintense signal in the cerebellar vermis (*red arrow*), a less common location for ARIA-E relative to the cerebral hemispheres. Although ARIA-E has a slight predilection for the parieto-occipital lobes, similar to posterior reversible encephalopathy, any part of the brain may be affected. Images courtesy of Biogen and the Dominantly Inherited Alzheimer Network.

also results in a reduction in the SNR. The imaging sequence, sequence parameters, scanner, and field strength all affect the sensitivity for detection of microhemorrhages. As discussed below, counting the number of microhemorrhages is a key component of ARIA assessment; therefore, a standardized imaging protocol is needed.

Interpretation Pitfalls. There are both patient-related and acquisition-related interpretation pitfalls or difficulties with ARIA-H and, in particular, microhemorrhage detection (Fig 8). Blurring due to patient motion may impair detection of small microhemorrhages. Areas of prominent air-tissue susceptibility effects may induce punctate artifacts that look similar to microhemorrhages, especially near the frontal sinuses, mastoid air cells, and skull base. Susceptibility-related signal loss from physiologic mineralization in the basal ganglia may be misinterpreted as microhemorrhages and should not be incorporated into the overall microhemorrhage count. Bulk susceptibility effects that produce signal loss may preclude evaluation of the inferior temporal and anterior frontal lobes. Partial volume effects may cause a small microhemorrhage to be poorly seen or to have a variable appearance on serial examinations. Thick-section acquisitions may also make it difficult to distinguish a microhemorrhage from a vessel flow void.⁵³ A flow void should be able to be tracked across multiple contiguous slices, though a vessel image in profile may mimic microhemorrhage on a single section. T2-weighted images can be useful for comparisons, as flow voids in vessels do not have a blooming effect. Reader biases may also affect interpretation, as readers have been found to undercall possible microhemorrhages in a patient without other microhemorrhages and to overcall in patients with many.

Microhemorrhages: Spontaneous versus Treatment-Emergent versus Cerebrovascular Disease. The treatment-emergent microhemorrhages of ARIA-H have a peripheral (lobar) predilection and most commonly occur in the cortex and gray-white matter junction as well as the cerebellum, similar to where ARIA-E may occur. These microhemorrhages have the same morphologic appearance and distribution as those that occur spontaneously and characterize and define CAA. Importantly, these areas of hemosiderin deposition typically occur in different brain areas from those related to vascular risk factors, namely hypertension, which most commonly occur in the deep white matter, deep gray matter, and brainstem.^{54,55} In the current clinical trials and the aducanumab FDA label ARIA severity grading, all microhemorrhages, regardless of location and suspected etiology, were included in the count used to determine eligibility and continuation of anti-amyloid therapy.² Of note, although discrete microhemorrhages in the deep gray structures are included in the ARIA assessment, ill-defined susceptibility in the basal ganglia related to senescent change or mineralization (Fig 8) is not. In future clinical trials and clinical practice, we recommend that the inclusion of microhemorrhages in the deep gray matter and brainstem in the count used to determine treatment eligibility be reassessed, as these are most likely secondary to vascular risk factors and not related to amyloidosis. The differentiation of microhemorrhages most likely secondary to vascular risk factors from those related to amyloidosis and an increased risk of adverse events with mAbs may be particularly important as mAb use expands to clinical practice and inclusion of patient populations with higher prevalence of vascular risk factors than clinical trial populations.⁵⁶

Spontaneous microhemorrhages are relatively common in elderly persons, with a prevalence of up to 15%–30% in memory clinic and AD cohorts and a similar prevalence in baseline MR

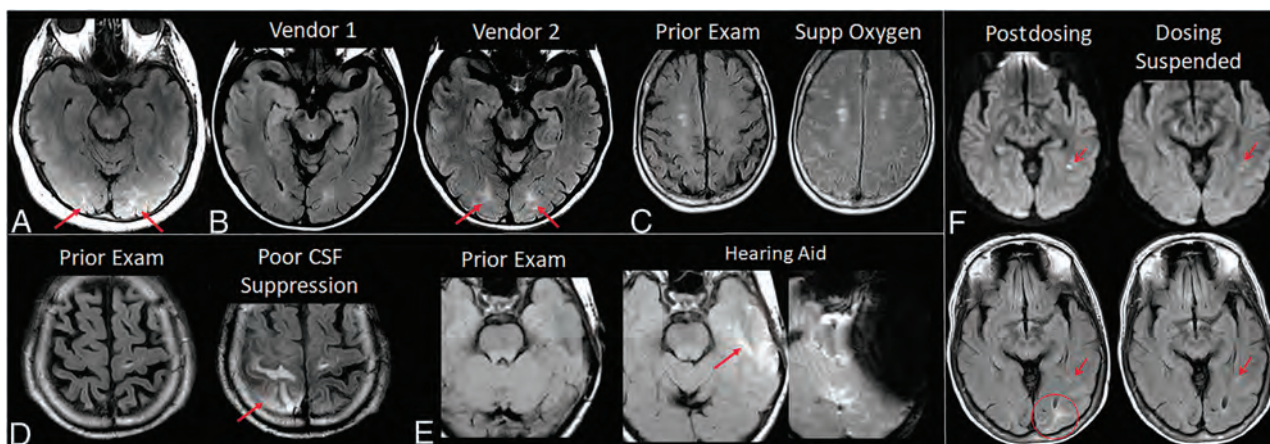


FIG 5. ARIA-E interpretation pitfalls and mimics. **A**, Shading artifacts with prescan normalize inadvertently turned off, results in T2-FLAIR hyperintense signal in the bilateral occipital white matter (red arrows) that mimics ARIA-E (edema). **B**, Axial T2-FLAIR images from 2 time points with the 2 scans performed on different vendors. T2-FLAIR hyperintense signal in the bilateral occipital white matter on vendor 2 (red arrows) appears to be new from the prior examination on vendor 1 and may be mistaken for subtle ARIA-E. The participant returned for repeat imaging on vendor 1, and the apparent abnormality was resolved (not shown). **C**, Diffuse sulcal T2-FLAIR hyperintense signal with administration of supplemental oxygen mimics ARIA-E effusion. The abnormality resolved on repeat imaging without supplemental oxygen. **D**, Poor CSF suppression results in artifactual sulcal T2-FLAIR hyperintense signal mimicking ARIA-E (red arrow) and was confirmed to be artifacts by resolution on immediate repeat imaging with optimized parameters. **E**, Susceptibility artifacts from a hearing aid results in apparent T2-FLAIR hyperintense signal (red arrow), new from the prior examination on which the patient's hearing aid was not in place. The third image in this set is the GRE scan showing the marked signal void artifacts from the hearing aid. The resulting susceptibility effect results in incomplete water suppression on T2-FLAIR, and the resulting artifacts mimic ARIA-E. **F**, Patient with left occipital subcortical T2-FLAIR hyperintense signal on the postdosing monitoring examination (mild ARIA-E, circle), which resolved on the follow-up monitoring scan. Separate subcentimeter focus of periventricular T2 signal with associated diffusion restriction (arrow, left) was consistent with an incidental acute/subacute infarct that showed expected evolution on the postdosing follow-up examination (right). Images courtesy of Biogen and the Dominantly Inherited Alzheimer Network. Supp indicates supplemental.

imaging examinations for mAb clinical trial enrollment.^{43,57,58} The prevalence of spontaneous superficial siderosis is considerably lower (prevalence 0.4% versus 12.8% for superficial siderosis versus lobar microhemorrhages in the Framingham and Rotterdam cohorts), though it may be as high as 5% in AD cohorts.^{59,60} The incidence of mAb treatment-related microhemorrhages, ARIA-H, has been variable in clinical trials, for example 4.9% in a trial of solanezumab and 30.5% for donanemab.^{18,32}

Clinical Consequences. ARIA-H is generally not associated with clinical sequelae, similar to microhemorrhages and superficial siderosis when occurring independent from anti-amyloid therapy. This is in contrast to macrohemorrhages, which are associated with brain tissue injury and potential clinical consequences. In the general community population, the presence of microhemorrhages and superficial siderosis has been shown to be associated with a slightly increased risk of stroke and macrohemorrhage.^{57,60} In clinical trials, the presence of these hemosiderin products at baseline conferred an increased risk for adverse events with the use of anti-amyloid mAb therapies.³⁹ Although data currently available from clinical trials do not support a significantly higher frequency of lobar macrohemorrhage with anti-amyloid therapy, a slightly elevated risk of lobar macrohemorrhage during treatment amid the wider population with AD may need to be taken into consideration when judging treatment candidacy amid other factors.

Co-Occurrence of ARIA-E and -H. ARIA-E and ARIA-H may be temporally or spatially associated (Fig 9), or they may be detected independently. For example, in the bapineuzumab trial, ARIA-H

occurred in approximately 50% of participants with ARIA-E though often not simultaneously and either before or after ARIA-E.³⁶

As discussed above, both ARIA-E and H share a common mechanism relating to increased vascular permeability, but MR imaging appearance depends on the composition of the leakage products. It is thought that proteinaceous fluid also leaks any time there is leakage of red blood cells or that ARIA-E occurs, to some extent, with any ARIA-H. However, isolated ARIA-H may be detected as ARIA-E is transient and resolves over the course of weeks to months, while the hemosiderin deposition of ARIA-H typically does not resolve.²⁷ In the authors' experience, the detection of isolated ARIA-H should prompt the imager to pay particular attention to the T2-FLAIR sequence in this area for subtle ARIA-E; treatment-emergent ARIA-H will often be the harbinger of subtle ARIA-E, which will only be appreciated with directed focus to this area. Note, although microhemorrhages are thought to not resolve, when incident ARIA-H is detected in the acute phase, these fresh blood-degeneration products may become less apparent on subsequent imaging, due to some degree of resorption.

In contrast, ARIA-E may occur without ARIA-H if not enough red blood cells have leaked into the extracellular or subarachnoid space or if not enough time has passed to allow heme product degradation to affect T2* signal. In summary, the recognition of ARIA-H or ARIA-E independently is likely due to the timing of imaging relative to the time of the vascular leak.

ARIA Imaging in Clinical Trials

Clinical Trial Imaging Protocols. Standardization of imaging protocols is employed in clinical imaging trials to obtain consistent

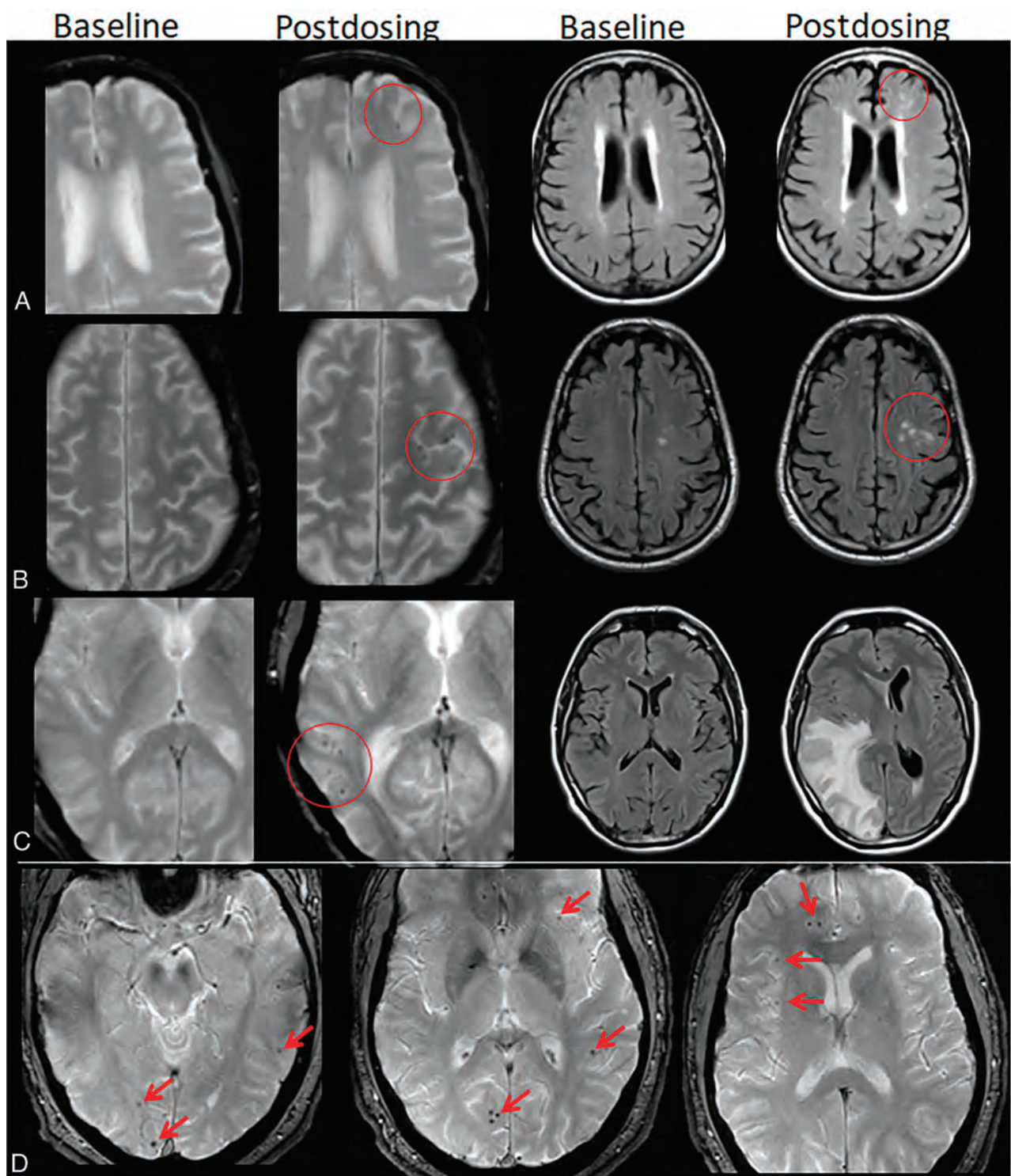


FIG 6. ARIA-H, microhemorrhage. Baseline and postdosing GRE (left, A–C) and T2-FLAIR (right, A–C) for 3 patients. A, Postdosing, few (<5) new peripheral left frontal microhemorrhages (mild ARIA-H, red circle) that occur with new patchy T2-FLAIR hyperintense signal in that region (mild ARIA-E, red circle). B, Postdosing, 5 treatment-emergent microhemorrhages (moderate ARIA, red circle) that occurred with regional mild ARIA-E edema (red circle). C, Postdosing, ≥ 10 new microhemorrhages (severe ARIA-H, red circle). Associated extensive right cerebral hemisphere T2-FLAIR hyperintense signal involving the cortex and subcortical white matter with mass effect and midline shift (severe ARIA-E). D, At least 12 treatment-emergent cerebral microhemorrhages (severe ARIA-H, red arrows) without ARIA-E. In comparison with case C, these microhemorrhages are scattered, rather than clustered. Regional distribution of microhemorrhages may vary, and both cases C and D are severe ARIA-H and would prompt discontinuation of anti-amyloid therapy per current guidelines. Images courtesy of Biogen and the Dominantly Inherited Alzheimer Network.

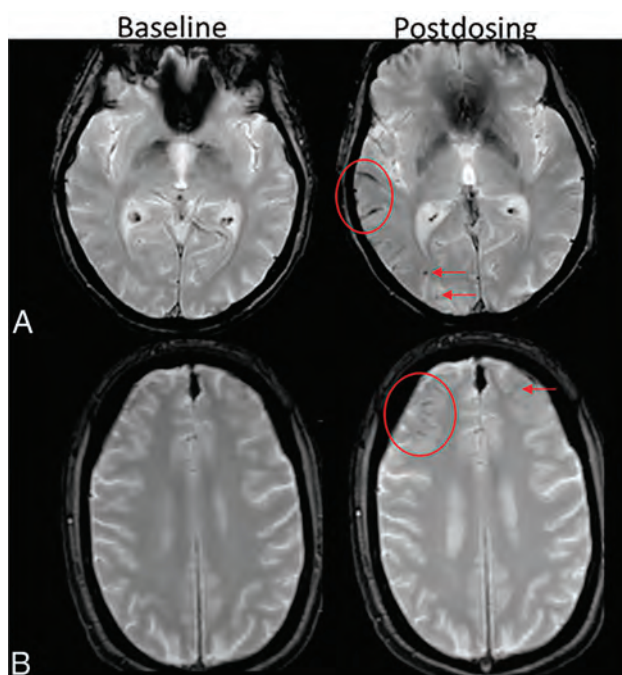


FIG 7. ARIA-H, superficial siderosis. Axial T2*-GRE imaging from 2 patients at baseline and postdosing. **A**, Postdosing, new right temporal superficial siderosis, which involves contiguous sulci when viewed over multiple slices (mild ARIA-H, siderosis, red circle). This patient also had 2 treatment-emergent microhemorrhages in the right occipital lobe (mild ARIA-H, microhemorrhage, red arrows). **B**, Two regions of treatment-emergent superficial siderosis in the right greater-than-left frontal lobes (moderate ARIA-H, red circle and arrow). Images courtesy of Biogen.

ascertainment sensitivity and performance across sites and serial participant visits. As recommended by Sperling et al,²⁴ mAb clinical trials have used axial T2-FLAIR for detection of ARIA-E and axial T2* GRE for detection of ARIA-H.

Baseline/Screening Imaging. Before therapy initiation, brain MR imaging is required to evaluate for pre-existing hemosiderin deposition associated with increased risk of adverse treatment events and provide baseline for comparison on the subsequent safety-monitoring examinations. In clinical trials, common exclusion criteria are ≥ 5 microhemorrhages or any superficial siderosis on the baseline MR imaging. The recent FDA guidance for clinical use of aducanumab lists exclusion criteria as ≥ 10 microhemorrhages, any superficial siderosis, or parenchymal hemorrhages measuring > 1 cm in the prior year.² The baseline imaging should be performed using the same MR imaging protocol as used for the subsequent safety-monitoring examinations.

ARIA Severity Grading on Monitoring Examinations. Different ARIA grading schemes have been suggested.^{42,61} However, a specific scheme was included in the recent FDA guidance for clinical use of aducanumab.² Given the FDA endorsement, this scheme is likely to become a default standard at least as a starting point. In this framework, ARIA-E, ARIA-H microhemorrhage, and ARIA-H superficial siderosis are each categorized by radiographic severity (Table 2 and Figs 2, 3, 6, and 7). ARIA-E scoring was defined as mild: 1 site of sulcal or cortical/subcortical FLAIR hyperintense signal measuring < 5 cm; moderate: 1 site measuring

5–10 cm or > 1 site each measuring < 10 cm; and severe: 1 or more sites measuring > 10 cm.

To assess ARIA-E extent, a measure is made along the single greatest dimension of the lesion. This measurement should encompass both parenchymal and sulcal T2-FLAIR hyperintensities as well as any related gyral swelling and sulcal effacement. Measuring in the plane of acquisition should be relevant in most situations. For lesions that have a greater through-plane extent, ie, craniocaudal extent, one may determine lesion size by reformatting data into another plane or estimating extent on the basis of the number of slices on which the abnormality is identified. Each lesion, which is separate and distinct (eg, separated by normal brain tissue, sulci, and gyri), should be measured separately. In other words, reporting the number of sites involved does not need to account for anatomic locations but should only rely on the presence or absence of physically separated lesions. If the lesion spans multiple contiguous brain lobes, it should still be counted as a single location. If there are lesions in both hemispheres, they should be reported as separate locations, as measurements would not cross the midline.

Microhemorrhages were scored using the cumulative number of treatment-emergent microhemorrhages: mild: ≤ 4 ; moderate: 5–9; and severe: ≥ 10 new microhemorrhages since the baseline examination. Superficial siderosis was scored as cumulative regions of treatment-emergent regions of siderosis: mild: 1; moderate: 2; severe: > 2 new areas of superficial siderosis since the baseline, pretreatment examination. As the presence of any siderosis should exclude a patient from treatment, cumulative treatment-emergent regions of siderosis should correspond with total regions of siderosis present. On the other hand, a patient may have up to 4 or 9 microhemorrhages before treatment, depending on the exclusion criteria implemented, and these would not be included in the count for ARIA-H severity grading. As with ARIA-E, the number of involved regions of superficial siderosis is important, and each involved site, region, or area is similarly defined as a physically separate region of contiguous sulcal signal abnormality.

Clinical Management Based on ARIA Findings. In deciding to continue with treatment dose and dose escalations, 2 metrics were employed in the clinical trials and are described in the aducanumab FDA label (Fig 10).² The patient had to be asymptomatic, and the following imaging criteria had to be met to continue with dosing. For asymptomatic patients, dosing was continued with mild ARIA-E and/or mild ARIA-H, but dosing was suspended in patients with moderate ARIA-E and/or moderate ARIA-H. Once dosing was suspended due to imaging findings, serial imaging was performed monthly, and dosing was resumed following the resolution of ARIA-E and stabilization of ARIA-H. If ARIA was associated with the symptoms, dosing resumed only after both the resolution of clinical symptoms and the resolution of ARIA-E and stabilization of ARIA-H. Dosing was permanently discontinued in participants with severe ARIA-H (≥ 10 treatment-emergent microhemorrhages or > 2 areas of treatment-emergent superficial siderosis) or a macrohemorrhage (> 10 mm in diameter). Real-world clinical practice guidelines may require adjustments to these protocols on the basis of further experience and depending on the extent to which the

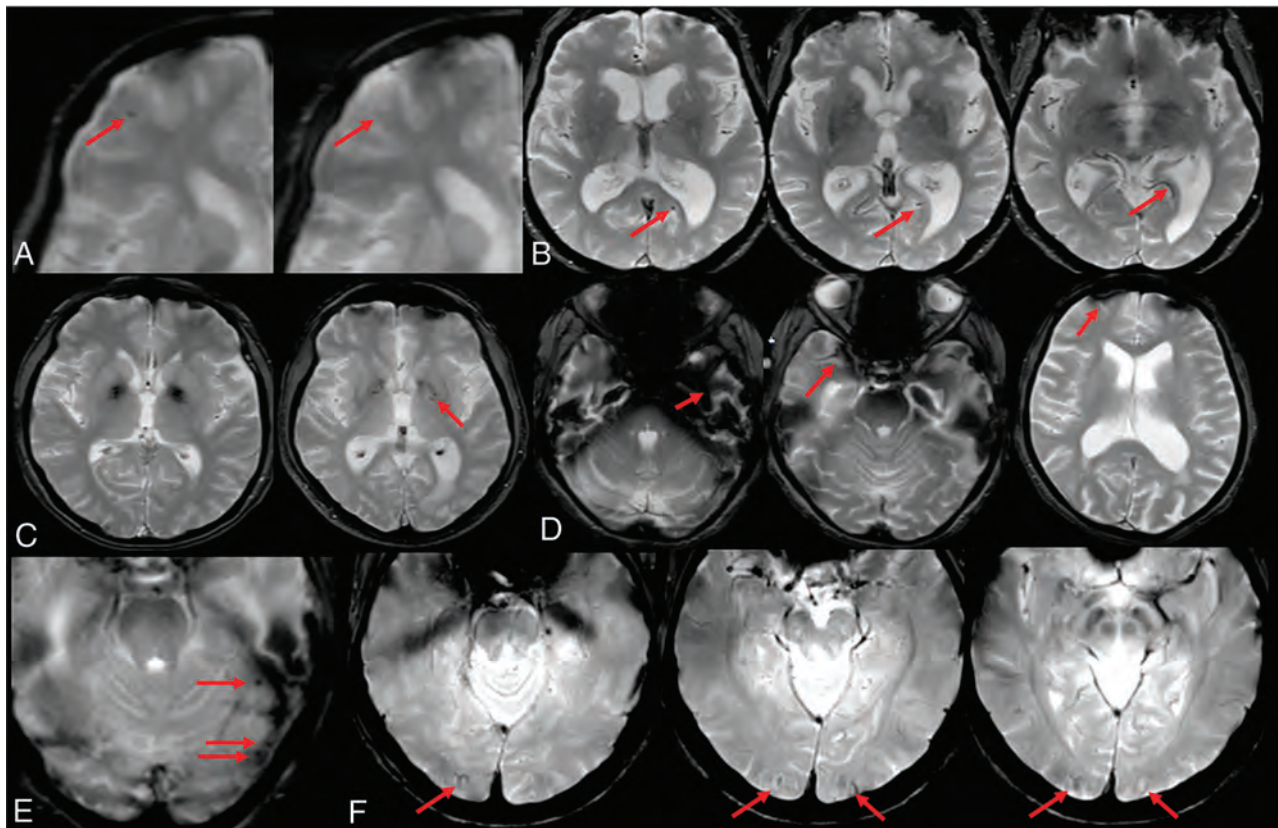


FIG 8. ARIA-H interpretation pitfalls. *A*, Motion and partial volume effects (*right*) result in poor visualization of a previously documented right frontal microhemorrhage (*left*, *red arrow*). *B*, Vessel in profile mimics a microhemorrhage on a single section (*left*, *red arrow*) but can be traced as a vessel flow void on adjacent slices (*right*, *arrow*). *C*, Deep gray mineralization is often confluent and ill-defined (*left*) and may be clearly differentiated from a microhemorrhage. However, when punctate, senescent mineralization may mimic a microhemorrhage (*right*, *arrow*). *D*, Bulk susceptibility effects preclude evaluation of the inferior temporal lobes adjacent to the mastoids and sinuses (*arrows*). *E*, Susceptibility artifacts may appear as punctate foci (*arrows*) adjacent to obvious susceptibility areas. Therefore, punctate foci of susceptibility in these regions should be interpreted with caution and in correlation with prior examinations. *F*, Phase artifacts, especially about the torcula (*red arrows*), can mimic microhemorrhages/siderosis and may be differentiated by recognition of the shape of the torcula repeating in the phase direction. Images courtesy of Biogen.

population of individuals treated with mAbs in wider practice resembles the target population in the trials.

Considerations for Neurology Practice

Developments in anti-amyloid mAbs for AD herald a potential shift in management of an exceptionally common and devastating disease. These new anti-amyloid agents are the first potentially disease-modifying agents for AD. In contrast, current mainstays of therapy for AD are not disease-modifying but, instead, are simply symptomatic and supportive in nature, predominantly related to lifestyle and environmental modifications and use of pharmacotherapies (eg, cholinesterase inhibitors), which target symptoms but do not alter the disease itself (which continues to progress). As a result, current neurology practice operations and infrastructure may need to rapidly evolve to accommodate emerging therapeutics that have very different profiles (relating to adverse effects, financial and nonfinancial costs, test and visit types, and frequencies for treatment initiation and monitoring) from existing options.

Several points of interface between neurology and radiology are relevant in this space. There is broad agreement among cognitive/behavioral neurology subspecialists that appropriate

application of anti-amyloid therapies would, at minimum, require biomarker evidence that AD is the etiology for a patient's cognitive impairment.^{62,63} As a result, sites may need to plan for increased volumes of lumbar punctures (for CSF biomarker studies) and/or amyloid PET scans as part of initial evaluations. This context could impact logistics and personnel (to ensure appropriate expertise) around fluoroscopically guided lumbar punctures and PET tracer and scanner access. Multidisciplinary input from experts at local sites could also help to inform appropriate candidacy.

In addition, given the need for regular monitoring for ARIA, practices will also benefit from anticipating an increase in MR imaging examinations to prevent delays for patients receiving treatment, including patients in whom symptoms potentially necessitate more urgent evaluation. As part of this, clinical practices will need to decide on the most appropriate timeline for scheduled safety MR imaging scans, with expert recommendations currently favoring more frequent scanning (particularly early in the course of treatment) in line with protocols from existing Phase III trials. Currently, in most clinical trials, anti-amyloid dosing occurs on a monthly basis. MR imaging is performed at baseline, and at weeks 14 and 22 as the patients are being titrated to the maximal drug

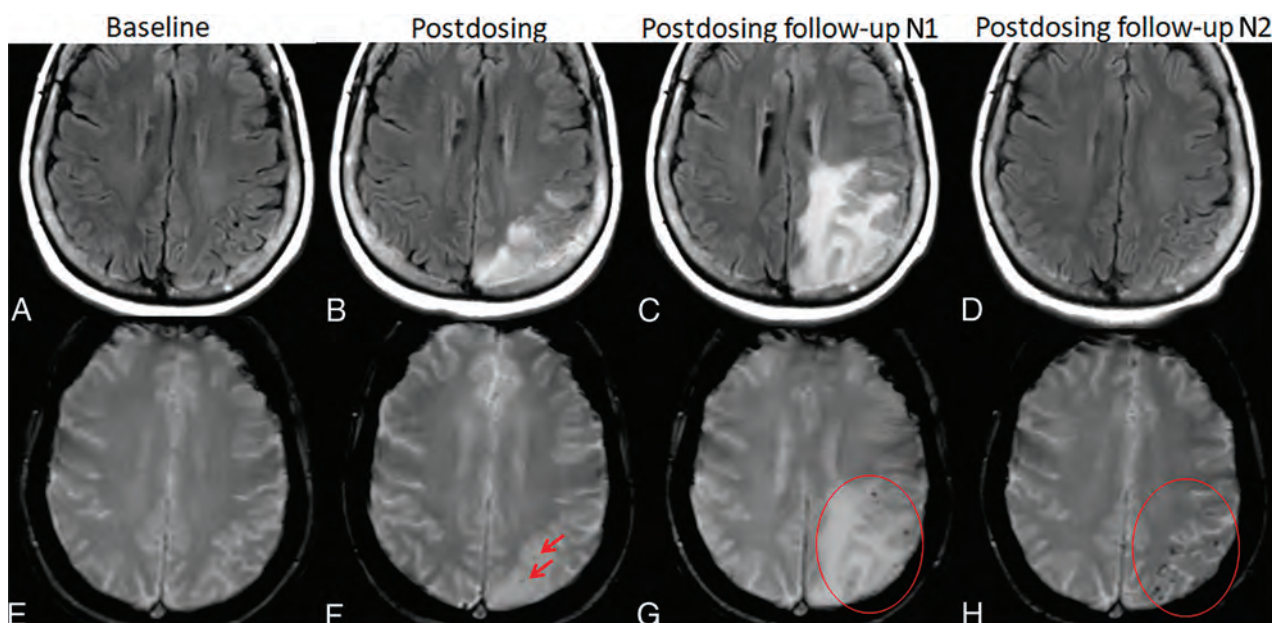


FIG 9. ARIA-E and -H. Patient on anti-amyloid therapy who developed ARIA-E (T2-FLAIR, A–D) and ARIA-H microhemorrhages (T2*-GRE, E–H). On postdosing T2-FLAIR (B), new left parietal T2-FLAIR hyperintense signal involving the cortex and subcortical white matter with associated local mass effect, consisting of sulcal effacement and gyral expansion. Despite suspension of dosing, the extent of T2-FLAIR abnormality and mass effect progressed at the postdosing follow-up No. 1 (1 month). ARIA-E resolved by postdosing follow-up No. 2 (2 months). On postdosing T2*-GRE, 2 new, treatment-emergent microhemorrhages (mild ARIA-H, F, red arrows) that increased in number over postdosing follow-up examinations with severe ARIA-H at postdosing follow-up No. 2 (H, red circle).

Table 2: ARIA severity grading^a

	Radiographic Severity		
	Mild	Moderate	Severe
ARIA-E (sulcal and/or cortical/subcortical FLAIR hyperintensity)	1 Location < 5 cm	1 Location 5–10 cm OR >1 Location each <10 cm	1 more location > 10 cm
ARIA-H (microhemorrhage)	≤4	5–9	≥10
ARIA-H (superficial siderosis)	1 Focal area	2 Focal areas	>2 Focal areas

^a ARIA is graded on the basis of treatment-emergent events. For ARIA-H, this count includes cumulative new microhemorrhages or regions of siderosis compared with the baseline, pretreatment examination.

dose. Subsequently, monitoring MR images are taken a month after receiving the maximal maintenance dose and every 3 months thereafter while patients are on this maintenance dose.

In rare cases in which hospitalization for ARIA may be required, access and education will be crucial, particularly given the subtleties of ARIA detection and distinctions with management (principally related to drug discontinuation and therapeutic steroids) in comparison with other mimics.

More broadly, it is crucial to remember that the collective clinical experience with anti-amyloid mAbs is in its relative infancy and thus far is mostly restricted to clinical trial populations, which may not fully reflect real world practice within the broader population having symptomatic AD. In addition, there are ongoing trials testing an anti-amyloid mAb in asymptomatic individuals with intermediate (A3 trial) and elevated (A45 trial) brain amyloid loads,⁶⁴ and results from these trials may further influence the timing and target population for therapy. As such,

neurology and radiology providers will benefit from being collaborative and nimble over the coming period.

ARIA Imaging in Clinical Practice

Role of the Radiologist in Clinical Management. Detailed description and quantification of ARIA findings will be used in guiding patient therapeutic dosing, and changes over time must be accurately assessed. To obtain accurate longitudinal assessment of findings, standardized methods are needed for image acquisition and reporting. The minimum sequences and reporting guidelines should be standardized within an institution or practice and ideally across institutions. To promote such efforts, recommendations for an imaging protocol and reporting template are provided below.

Recommendations for Clinical Imaging Protocol

Minimal Required Sequences. The minimal recommended sequences for ARIA ascertainment are T2-FLAIR, T2* GRE, and DWI

Clinical symptom severity	ARIA-E severity			ARIA-H severity		
	Mild	Moderate	Severe	Mild	Moderate	Severe
Asymptomatic	C	S	S	C	S	D
Mild	S	S	S	S	S	D
Moderate	S	S	S	S	S	D
Severe	S	S	S	S	S	D
Serious (other)	S	S	S	S	S	D
Serious	D	D	D	D	D	D

FIG 10. Patient management based on ARIA severity and clinical symptoms. ARIA-H management rules are the same for each severity of microhemorrhages and superficial siderosis. C (green) indicates continue dosing at current dose and schedule; S (yellow), suspend dosing; resume dosing at same dose once ARIA-E resolved or ARIA-H stable and clinical symptoms resolve; D (red), discontinue dosing; Serious (other), medical event unrelated to anti-amyloid therapy.

Table 3: Recommended imaging sequences for baseline imaging and ARIA monitoring examinations based on clinical trial experience and current guidelines^a

	Minimal	Recommended	Notes
Field strength	1.5T	3T	Use of a consistent field strength for serial imaging of a given patient is important; imaging may be performed at 1.5T if a patient is not a candidate for imaging at 3T or 3T scanners are not available at a site
ARIA-E detection	2D-FLAIR	2D- or 3D-FLAIR	Either 2D or 3D is acceptable, whichever can be performed with consistent quality and optimal CSF suppression
ARIA-H detection	T2*-GRE	T2*-GRE (\pm SWI)	Recommendations for enrollment and dose suspension are based on T2*-GRE detection of blood products; SWI may also be performed for confirmation and may be of value to gather data going forward
Infarct assessment	DWI	DWI	DWI required to differentiate ARIA from acute/subacute infarct and identification of incidental infarcts

^a Additional optional sequences may be added per individual site preference.

(Table 3). T2-FLAIR imaging is necessary for detection of ARIA-E. In clinical trials, 2D axial T2-FLAIR imaging was performed. Over the past decade, 3D FLAIR imaging has become more widely employed and has some advantages relative to 2D FLAIR, including improved CSF suppression and increased sensitivity for parenchymal edema.^{47,65} Therefore, 3D FLAIR may be preferred if it can be performed routinely with high quality and in a standardized fashion. However, if that is not feasible in your practice at the current time, 2D FLAIR should be performed. In summary, T2 FLAIR imaging is required for ARIA-E detection and should be performed using whichever technique is reliable, reproducible, and works for your practice.

T2* sequences are required for ARIA-H assessment, and in clinical trials, the GRE sequence was used. SWI may provide improved sensitivity for microhemorrhage detection⁵² but is less widely available and has more variability among MR image vendors compared with the GRE sequence. Also, current rules for dose-adjustment are based on 2D-GRE data. In other words, the

increased sensitivity of SWI in the detection of microhemorrhages may cause a patient to enter the category of dose suspension due to too many microhemorrhages detected, whereas on the basis of the GRE scan, the lower microhemorrhage count would allow for continued treatment. Therefore, 2D axial GRE is recommended for ARIA-H assessment in clinical practice and should use parameters similar to those employed in clinical trials (non-EPI technique: 3T TE, \sim 20 ms; maximum section thickness, 4 mm; acquisition time, \sim 4–5 minutes).

Whenever a new signal abnormality is noted on a monitoring MR imaging study, the DWI sequence plays an important role in helping to differentiate ARIA-E from potential cytotoxic edema as may be noted with an incidental acute-to-subacute infarct. As such, it is recommended that a standard clinical axial 2D trace DWI sequence be included as routine protocol.

Standardized versions of these 3 sequences are required at the enrollment (pretreatment screening/baseline) examination and each treatment monitoring examination. In regard to ARIA-E,

standardized imaging will allow the detection of subtle T2-FLAIR changes by comparison with baseline. In regard to ARIA-H, baseline imaging is essential for patient selection to exclude those patients with pre-existing siderosis or too many microhemorrhages, for whom there is a higher rate of adverse events. As such, baseline imaging is critical to ensure proper patient selection, image interpretation, and patient management.

Considerations for Additional Optional Sequences, Enrollment, and Monitoring Protocols. Additional sequences may be performed at individual sites on the basis of their standard protocols and procedures, interests, and available scan time, and these additional sequences could be tailored to separate enrollment and monitoring protocols. For example, in many practices, MPRAGE and volumetric analyses are performed on all MR imaging scans for the evaluation of dementia, and the enrollment MR imaging scan would fall under this category. However, such volumetric assessment is not needed for safety monitoring during treatment. Therefore, the MPRAGE sequence could be included in a dedicated enrollment protocol. T2 TSE/FSE may be included to help resolve ambiguous T2* findings, such as differentiating a microhemorrhage from a vessel flow void. SWI could be added (but not replace GRE) to either the enrollment or monitoring protocols if there is interest in more sensitive microhemorrhage detection or academic comparison with GRE. Postcontrast imaging is not recommended unless there is a diagnostic dilemma or incidental finding requiring further evaluation.

Importance of Consistent Serial Imaging: Field Strength and Vendor. In addition to a standardized imaging protocol, patients would also ideally be imaged on the same field strength and vendor on sequential visits due to scanner-related differences (see “ARIA-E” “Interpretation Pitfalls”). As with recent clinical trials, we recommend that imaging be performed at 3T rather than 1.5T due to improved SNR with higher field strengths, which may allow improved detection of small microhemorrhages and subtle ARIA-E.^{53,65} However, if 3T imaging is not available or the patient is not a candidate for 3T imaging (eg, devices), imaging may be performed on 1.5T. Whichever field strength and vendor is used for imaging a patient, effort should be made to be consistent from scan to scan whenever possible. Patients may be encouraged to visit a consistent imaging facility for their monitoring scans. Within an institution, AD therapeutic imaging could be triaged to a certain group of scanners as scheduling allows.

Need for Routine MR Imaging: Consideration for AD Therapeutic Enrollment. Patient factors that would preclude routine MR imaging should be considered at the time of enrollment. Patients with MR imaging–unsafe devices or other MR imaging contraindication (eg, metallic foreign body in the eye) would not be able to be imaged. Patients with MR imaging–conditional devices requiring scanning at specific institutions and imaging slots for which scanning may be monitored by an MR imaging physicist may be ineligible. Additionally, patients with claustrophobia, unable to undergo MR imaging without anesthesia, may be considered ineligible for treatment.

Online Resources. If in the future, vendor-specific protocols are made available for ARIA monitoring, these will be posted on the American Society of Neuroradiology website. As additional mAbs obtain FDA approval and guidelines are modified, the recommended imaging sequences and protocols may evolve.

Recommendations for Reporting/Communication

Clinical History. Relevant clinical history should be available at the time of image review and include the drug the patient is receiving, drug dose, duration of treatment, date of last dose, and whether the patient has experienced previous episodes of ARIA.

Reporting of Baseline/Enrollment MR Imaging Examination. The number and location of existing microhemorrhages and superficial siderosis must be tabulated on the baseline examination. In line with exclusion criteria, microhemorrhage number should be summarized as 0–4, 5–9, and ≥ 10 and superficial siderosis as present or absent. Any significant incidental and acute findings, such as acute or chronic infarctions, also should be documented in the report narrative.⁶²

Reporting of Monitoring MR Imaging Examinations. The radiology report must allow the patient to be given an ARIA severity score for each ARIA-E, ARIA-H microhemorrhage, and ARIA-H superficial siderosis, which will be used along with the clinical symptom score to determine continued dosing. The quantitative nature of the ARIA severity scoring lends itself to a templated report including the following sections. ARIA-E must be noted as absent or present. If present, the location and maximal transverse diameter of each noncontiguous, involved site must be reported. When following a patient with ARIA-E at the prior time point, one must describe interval change and resolution. For microhemorrhages, the number and location of prior and new microhemorrhages must be reported, and the number of cumulative treatment-emergent microhemorrhages may be reported in relevant categories of 0–4, 5–9, and ≥ 10 . The description of superficial siderosis should include the number and location of each prior and new noncontiguous site. Incidental and acute findings such as acute or interval (nonacute) infarct should be included in the report narrative.

Considerations for ARIA Reporting. As the presence of ARIA-E and siderosis, the number of microhemorrhages, and changes over time directly determine patient management, radiologists must carefully consider their level of diagnostic uncertainty and level of sensitivity versus specificity for ARIA detection. In clinical trial interpretations, the practice at some central reading sites is that each finding is marked as possible or definite and only definite findings are counted toward ARIA severity scoring and exclusion or dosing-discontinuation criteria. Possible findings may include a subtle abnormality (small, faint possible microhemorrhage or subtle increased extent of occipital white matter hyperintensity) or be related to image acquisition (motion-degraded examination, poor CSF suppression, or change in imaging technique). While only definite findings are counted toward ARIA severity scoring, participants may be asked to return for repeat imaging in the case of possible ARIA-E, as its presence would affect continued drug dosing. Although exact cut-points for microhemorrhages are used

in severity scoring, the presence of a possible microhemorrhage is less likely to affect the treatment course.

In clinical ARIA reporting, we recommend that only definite microhemorrhages be included in the quantitative ARIA template; possible microhemorrhages should be described in the report narrative as a pointer to direct the next radiologist interpreting a scan for this patient. For ARIA-E, we recommend both definite and possible ARIA-E (parenchymal edema or effusion) be included in the templated report. Finally, we recommend including whether the image quality is adequate for ARIA assessment or inadequate, such as due to motion or poor CSF suppression, requiring the patient to return for repeat imaging.

Recommended Reporting Template. A recommended reporting template is posted on the American Society of Neuroradiology website at <https://www.asnr.org/alzheimers-webinar-series/>. As with the imaging protocol, the recommended reporting template may evolve and will be updated as guidelines are modified on the basis of growing experience in clinical trials and clinical practice.

Communication with Referring Physicians. Use of the recommended ARIA reporting template will allow clear communication of relevant ARIA findings that will, in part, determine eligibility for treatment and further drug dosing. All ARIA reports should be generated in a timely manner, as each dosing session is typically preceded by imaging and dose administration is dependent on a satisfactory radiographic report. Findings of severe ARIA should be communicated in an urgent manner as they may affect dosing and patient management.

CONCLUSIONS

The emerging monoclonal antibody therapies for AD require both baseline pretreatment brain MR imaging as well as frequent monitoring MR imaging examinations for the detection of potential subclinical adverse events that may require dose adjustment. As these therapies begin to be implemented in clinical practice, treatment enrollment and monitoring brain MR imaging examinations may greatly increase neuroradiology practice volumes and will introduce a new imaging entity, ARIA, requiring awareness by all radiologists. ARIA-E is transient, treatment-induced edema or sulcal effusion, identified on T2-FLAIR that must be differentiated from an acute infarct or other entities causing hyperintense T2 signal. ARIA-H is treatment-induced microhemorrhages or superficial siderosis identified on T2* GRE, qualitatively similar to spontaneous hemosiderin deposition in CAA. Use of the recommended standardized imaging protocols and reporting templates will improve ARIA detection and timely communication of findings to referring providers, ensuring optimal patient care and management.

ACKNOWLEDGMENTS

We thank Biogen and the Dominantly Inherited Alzheimer Network for images and the American Society of Neuroradiology for support in development of this manuscript.

REFERENCES

1. Rajan KB, Weuve J, Barnes LL, et al. **Population estimate of people with clinical Alzheimer's disease and mild cognitive impairment in the United States (2020-2060).** *Alzheimers Dement* 2021;17:1966-75 CrossRef Medline
2. ADUHELM® (aducanumab-avwa) is FDA Approved for Healthcare Professionals. <https://biogen.com/us/aduhelm-pi.pdf>. Accessed June 7, 2021
3. Honce JM, Nagae L, Nyberg E. **Neuroimaging of natalizumab complications in multiple sclerosis: PML and other associated entities.** *Mult Scler Int* 2015;2015:e80925 CrossRef Medline
4. Wattjes MP, Vennegoor A, Steenwijk MD, et al. **MRI pattern in asymptomatic natalizumab-associated PML.** *J Neurol Neurosurg Psychiatry* 2015;86:793-98 CrossRef Medline
5. Jack CR, Bennett DA, Blennow K, et al. **NIA-AA Research Framework: toward a biological definition of Alzheimer's disease.** *Alzheimers Dement* 2018;14:535-62 CrossRef Medline
6. Chen G, Xu T, Yan Y, et al. **Amyloid beta: structure, biology and structure-based therapeutic development.** *Acta Pharmacol Sin* 2017;38:1205-35 CrossRef Medline
7. Greenberg SM, Bacskai BJ, Hernandez-Guillamon M, et al. **Cerebral amyloid angiopathy and Alzheimer disease: one peptide, two pathways.** *Nat Rev Neurol* 2020;16:30-42 CrossRef Medline
8. Tarasoff-Conway JM, Carare RO, Osorio RS, et al. **Clearance systems in the brain-implications for Alzheimer disease.** *Nat Rev Neurol* 2015;11:457-70 CrossRef Medline
9. Miller DL, Papayannopoulos IA, Styles J, et al. **Peptide compositions of the cerebrovascular and senile plaque core amyloid deposits of Alzheimer's disease.** *Arch Biochem Biophys* 1993;301:41-52 CrossRef Medline
10. Corriveau RA, Bosetti F, Emr M, et al. **The Science of Vascular Contributions to Cognitive Impairment and Dementia (VCID): a framework for advancing research priorities in the cerebrovascular biology of cognitive decline.** *Cell Mol Neurobiol* 2016;36:281-88 CrossRef Medline
11. Karran E, Mercken M, Strooper BD. **The amyloid cascade hypothesis for Alzheimer's disease: an appraisal for the development of therapeutics.** *Nat Rev Drug Discov* 2011;10:698-712 CrossRef Medline
12. Jack CR, Knopman DS, Jagust WJ, et al. **Hypothetical model of dynamic biomarkers of the Alzheimer's pathological cascade.** *Lancet Neurol* 2010;9:119-28 CrossRef Medline
13. Jack CR, Knopman DS, Jagust WJ, et al. **Tracking pathophysiological processes in Alzheimer's disease: an updated hypothetical model of dynamic biomarkers.** *Lancet Neurol* 2013;12:207-16 CrossRef Medline
14. Tanzi RE. **The genetics of Alzheimer disease.** *Cold Spring Harb Perspect Med* 2012;2:a006296 CrossRef
15. Brier MR, Gordon B, Friedrichsen K, et al. **Tau and A β imaging, CSF measures, and cognition in Alzheimer's disease.** *Sci Transl Med* 2016;8:338ra66 CrossRef Medline
16. Johnson KA, Schultz A, Betensky RA, et al. **Tau positron emission tomographic imaging in aging and early Alzheimer disease.** *Ann Neurol* 2016;79:110-19 CrossRef Medline
17. Jack CR, Therneau TM, Weigand SD, et al. **Prevalence of biologically vs clinically defined Alzheimer spectrum entities using the National Institute on Aging-Alzheimer's Association Research Framework.** *JAMA Neurol* 2019;76:1174 CrossRef Medline
18. Mintun MA, Lo AC, Duggan Evans C, et al. **Donanemab in early Alzheimer's disease.** *N Engl J Med* 2021;384:1691-704 CrossRef Medline
19. Swanson CJ, Zhang Y, Dhadda S, et al. **A randomized, double-blind, phase 2b proof-of-concept clinical trial in early Alzheimer's disease with lecanemab, an anti-A β protofibril antibody.** *Alzheimers Res Ther* 2021;13:80 CrossRef Medline
20. Davies P, Koppel J. **Mechanism-based treatments for Alzheimer's disease.** *Dialogues Clin Neurosci* 2009;11:159-69 CrossRef Medline

21. Gilman S, Koller M, Black RS, et al; for the AN1792(QS-21)-201 Study Team. **Clinical effects of Abeta immunization (AN1792) in patients with AD in an interrupted trial.** *Neurology* 2005;64:1553–62 CrossRef Medline
22. Salloway S, Sperling R, Gilman S, et al; Bapineuzumab 201 Clinical Trial Investigators. **A phase 2 multiple ascending dose trial of bapineuzumab in mild to moderate Alzheimer disease.** *Neurology* 2009;73:2061–70 CrossRef Medline
23. Black RS, Sperling RA, Safirstein B, et al. **A single ascending dose study of bapineuzumab in patients with Alzheimer disease.** *Alzheimer Dis Assoc Disord* 2010;24:198–203 CrossRef Medline
24. Sperling RA, Jack CR, Black SE, et al. **Amyloid Related Imaging Abnormalities (ARIA) in amyloid modifying therapeutic trials: recommendations from the Alzheimer's Association Research Roundtable Workgroup.** *Alzheimers Dement* 2011;7:367–85 CrossRef Medline
25. Cummings J, Lee G, Zhong K, et al. **Alzheimer's disease drug development pipeline: 2021.** *Alzheimers Dement (N Y)* 2021;7:7:e12179 CrossRef Medline
26. van Dyck CH. **Anti-Amyloid- β monoclonal antibodies for Alzheimer's disease: pitfalls and promise.** *Biol Psychiatry* 2018;83:311–19 CrossRef Medline
27. Salloway S, Chalkias S, Barkhof F, et al. **Amyloid-related imaging abnormalities in 2 Phase 3 studies evaluating aducanumab in patients with early Alzheimer disease.** *JAMA Neurol* 2022;79:13–21 CrossRef Medline
28. Salloway S, Sperling R, Fox NC, et al; Bapineuzumab 301 and 302 Clinical Trial Investigators. **Two Phase 3 trials of bapineuzumab in mild-to-moderate Alzheimer's disease.** *N Engl J Med* 2014;370:322–33 CrossRef Medline
29. Guthrie H, Honig LS, Lin H, et al. **Safety, tolerability, and pharmacokinetics of crenezumab in patients with mild-to-moderate Alzheimer's disease treated with escalating doses for up to 133 weeks.** *J Alzheimers Dis* 2020;76:967–79 CrossRef Medline
30. Landen JW, Cohen S, Billing CB, et al. **Multiple-dose ponzemumab for mild-to-moderate Alzheimer's disease: safety and efficacy.** *Alzheimers Dement (N Y)* 2017;3:339–47 CrossRef Medline
31. Ostrowitzki S, Lasser RA, Dorflinger E, et al; SCarlet RoAD Investigators. **A Phase III randomized trial of gantenerumab in prodromal Alzheimer's disease.** *Alzheimers Res Ther* 2017;9:95 CrossRef Medline
32. Doody RS, Thomas RG, Farlow M, et al; Solanezumab Study Group. **Phase 3 trials of solanezumab for mild-to-moderate Alzheimer's disease.** *N Engl J Med* 2014;370:311–21 CrossRef Medline
33. Kim SH, Ahn JH, Yang H, et al. **Cerebral amyloid angiopathy aggravates perivascular clearance impairment in an Alzheimer's disease mouse model.** *Acta Neuropathol Commun* 2020;8:181 CrossRef Medline
34. Zago W, Schroeter S, Guido T, et al. **Vascular alterations in PDAPP mice after anti-A β immunotherapy: implications for amyloid-related imaging abnormalities.** *Alzheimers Dement* 2013;9:S105–15 CrossRef Medline
35. Antolini L, DiFrancesco JC, Zedde M, et al. **Spontaneous ARIA-like events in cerebral amyloid angiopathy-related inflammation: a multicenter prospective longitudinal cohort study.** *Neurology* 2021;97:e1809–22 CrossRef Medline
36. Eng JA, Frosch MP, Choi K, et al. **Clinical manifestations of cerebral amyloid angiopathy-related inflammation.** *Ann Neurol* 2004;55:250–56 CrossRef Medline
37. Bohrmann B, Baumann K, Benz J, et al. **Gantenerumab: a novel human anti-A β antibody demonstrates sustained cerebral amyloid- β binding and elicits cell-mediated removal of human amyloid- β .** *J Alzheimers Dis* 2012;28:49–69 CrossRef Medline
38. Sevigny J, Chiao P, Bussière T, et al. **The antibody aducanumab reduces A β plaques in Alzheimer's disease.** *Nature* 2016;537:50–56 CrossRef Medline
39. Brashear HR, Ketter N, Bogert J, et al. **Clinical evaluation of amyloid-related imaging abnormalities in bapineuzumab Phase III studies.** *J Alzheimers Dis* 2018;66:1409–24 CrossRef Medline
40. Barakos J, Purcell D, Suh J, et al. **Detection and management of amyloid-related imaging abnormalities in patients with Alzheimer's disease treated with anti-amyloid beta therapy.** *J Prev Alzheimers Dis* 2022;9:211–20 CrossRef Medline
41. Yamada M. **Cerebral amyloid angiopathy and gene polymorphisms.** *J Neurol Sci* 2004;226:41–44 CrossRef Medline
42. Barakos J, Sperling R, Salloway S, et al. **MR imaging features of amyloid-related imaging abnormalities.** *AJNR Am J Neuroradiol* 2013;34:1958–65 CrossRef Medline
43. Carlson C, Siemers E, Hake A, et al. **Amyloid-related imaging abnormalities from trials of solanezumab for Alzheimer's disease.** *Alzheimers Dement (Amst)* 2016;2:75–85 CrossRef Medline
44. Sperling R, Salloway S, Brooks DJ, et al. **Amyloid-related imaging abnormalities in patients with Alzheimer's disease treated with bapineuzumab: a retrospective analysis.** *Lancet Neurol* 2012;11:241–49 CrossRef Medline
45. Neema M, Guss ZD, Stankiewicz JM, et al. **Normal findings on brain fluid-attenuated inversion recovery MR images at 3T.** *AJNR Am J Neuroradiol* 2009;30:911–16 CrossRef Medline
46. Kakeda S, Korogi Y, Hiai Y, et al. **Pitfalls of 3D FLAIR brain imaging: a prospective comparison with 2D FLAIR.** *Acad Radiol* 2012;19:1225–32 CrossRef Medline
47. Kallmes DF, Hui FK, Mugler JP. **Suppression of cerebrospinal fluid and blood flow artifacts in FLAIR MR imaging with a single-slab three-dimensional pulse sequence: initial experience.** *Radiology* 2001;221:251–55 CrossRef Medline
48. Bartynski WS. **Posterior reversible encephalopathy syndrome, Part 1: fundamental imaging and clinical features.** *AJNR Am J Neuroradiol* 2008;29:1036–42 CrossRef Medline
49. Stuckey SL, Goh TD, Heffernan T, et al. **Hyperintensity in the subarachnoid space on FLAIR MRI.** *AJR Am J Roentgenol* 2007;189:913–21 CrossRef Medline
50. Moraal B, Wattjes MP, Geurts JJG, et al. **Improved detection of active multiple sclerosis lesions: 3D subtraction imaging.** *Radiology* 2010;255:154–63 CrossRef Medline
51. VandeVrede L, Gibbs DM, Koestler M, et al. **Symptomatic amyloid-related imaging abnormalities in an APOE $\epsilon 4/\epsilon 4$ patient treated with aducanumab.** *Alzheimers Dement (Amst)* 2020;12:e12101 CrossRef Medline
52. Haller S, Haacke EM, Thurnher MM, et al. **Susceptibility-weighted imaging: technical essentials and clinical neurologic applications.** *Radiology* 2021;299:3–26 CrossRef Medline
53. Nandigam RK, Viswanathan A, Delgado P, et al. **MR imaging detection of cerebral microbleeds: effect of susceptibility-weighted imaging, section thickness, and field strength.** *AJNR Am J Neuroradiol* 2009;30:338–43 CrossRef Medline
54. Haller S, Vernooij MW, Kuijper JP, et al. **Cerebral microbleeds: imaging and clinical significance.** *Radiology* 2018;287:11–28 CrossRef Medline
55. Viswanathan A, Chabriat H. **Cerebral microhemorrhage.** *Stroke* 2006;37:550–55 CrossRef Medline
56. Koenig LN, McCue LM, Grant E, et al. **Lack of association between acute stroke, post-stroke dementia, race, and β -amyloid status.** *Neuroimage Clin* 2021;29:102553 CrossRef Medline
57. Cordonnier C, van der Flier WM, Sluiter JD, et al. **Prevalence and severity of microbleeds in a memory clinic setting.** *Neurology* 2006;66:1356–60 CrossRef Medline
58. Siemers ER, Sundell KL, Carlson C, et al. **Phase 3 solanezumab trials: secondary outcomes in mild Alzheimer's disease patients.** *Alzheimers Dement* 2016;12:110–20 CrossRef Medline
59. Zonneveld HI, Goos JD, Wattjes MP, et al. **Prevalence of cortical superficial siderosis in a memory clinic population.** *Neurology* 2014;82:698–704 CrossRef Medline

60. Shoamanesh A, Akoudad S, Himali JJ, et al. **Cortical superficial siderosis in the general population: the Framingham Heart and Rotterdam studies.** *Int J Stroke* 2021;16:798–808 CrossRef Medline
61. Barkhof F, Daams M, Scheltens P, et al. **An MRI rating scale for amyloid-related imaging abnormalities with edema or effusion.** *AJNR Am J Neuroradiol* 2013;34:1550–55 CrossRef Medline
62. Cummings J, Aisen P, Apostolova LG, et al. **Aducanumab: appropriate use recommendations.** *J Prev Alzheimers Dis* 2021;8:398–410 CrossRef Medline
63. Cummings J, Rabinovici GD, Atri A, et al. **Aducanumab: appropriate use recommendations update.** *J Prev Alzheimers Dis* 2022;9:221–30 CrossRef Medline
64. Aisen PS, Cummings J, Doody R, et al. **The future of anti-amyloid trials.** *J Prev Alzheimers Dis* 2020;7:146–51 CrossRef Medline
65. Wattjes MP, Lutterbey GG, Harzheim M, et al. **Higher sensitivity in the detection of inflammatory brain lesions in patients with clinically isolated syndromes suggestive of multiple sclerosis using high field MRI: an intraindividual comparison of 1.5 T with 3.0 T.** *Eur Radiol* 2006;16:2067–73 CrossRef Medline

Regarding “Brain Perfusion Alterations on 3D Pseudocontinuous Arterial Spin-Labeling MR Imaging in Patients with Autoimmune Encephalitis: A Case Series and Literature Review”

We read with interest the article by Li et al, “Brain Perfusion Alterations on 3D Pseudocontinuous Arterial Spin-Labeling MR Imaging in Patients with Autoimmune Encephalitis: A Case Series and Literature Review,” recently published in the *American Journal of Neuroradiology*. In this retrospective case series, the authors found that all patients with autoimmune encephalitis (AE) had increased CBF in the inflammatory area.¹ Indeed, arterial spin-labeling (ASL) is critical in the diagnosis of AE and may serve as early evidence preceding conventional abnormal findings on MR imaging and laboratory diagnosis. Sachs et al² found cerebral hyperperfusion in anti-N-methyl-D-aspartate (NMDAR) encephalitis. Vallabhaneni et al³ demonstrated increased CBF and CBV in the left parieto-occipital gray matter on CT perfusion. Sarria-Estrada et al⁴ revealed ASL hyperperfusion overlapping the involved lesions, but they also found increased perfusion and increased metabolism on [¹⁸F] FDG-PET/CT and SPECT in paraneoplastic autoimmune encephalitis.

As mentioned above,⁴ we have also encountered several cases of AE with hypoperfusion or without any visible changes on ASL perfusion in clinical practice. We retrospectively reviewed image data from 30 consecutive patients with AE in the most recent 2 years including major constituents of AE-covered anti-NMDAR (11 patients), anti-leucine-rich glioma inactivated-1 (5 patients), anti-G-protein coupled receptor for gamma-aminobutyric acid receptor (4 patients), anti-myelin oligodendrocyte glycoprotein antibody associated encephalitis (3 patients), anti-contactin-associated protein-like 2 antibody-associated disease (3 patients), Hashimoto encephalopathy (2 patients), anti-glutamic acid decarboxylase-65 AE (1 patient), and anti-CV2 AE (1 patient). All MR imaging of our patients was also performed on a 3T MR imaging scanner (Discovery 750; GE Healthcare) with a 3D ASL sequence. Seven patients had visible infected lesions with increased perfusion on ASL, 5 patients showed asymmetric changes across brain regions without intracranial lesions on T2 FLAIR, and 2 patients presented with decreased perfusion with visible infected focus, while the rest

of the patients presented with normal perfusion without intracranial lesions.

Comparing the findings of Li et al,¹ we wondered why our hospitalized patients with AE failed to show a high proportion of hyperperfusion changes on ASL. We reviewed the published CBF studies evaluated using 3D ASL perfusion imaging in patients with AE and found that brain MR imaging revealed no morphologic abnormalities in patients with anti-NMDAR AE, but 3D ASL perfusion imaging showed reduced CBF in the special brain regions, including the left frontal and temporal regions and the right cerebellum.⁵ Li et al⁶ also found hyperintensities in the bilateral hippocampus on MR imaging for patients with anti-LGI 1 AE, but no abnormal perfusion/metabolism on ASL and [¹⁸F] FDG-PET/CT.

Different from the higher CBF in patients with herpes simplex encephalitis at the acute stage,⁷ AE is one of the emergent causes of subacute changes caused by antibodies. CSF analysis and MR imaging could reveal inflammatory changes. However, less than half of the cases of AE showed any abnormal findings on brain MR imaging,³ which is also consistent with our findings. ASL hyperperfusion of the affected brain regions in AE may be due to either a seizure-related outcome or active inflammation of the brain involved. Kumar et al⁸ found MR imaging changes (9 patients included) in Rasmussen encephalitis on conventional MR imaging (without atrophy), corresponding to regional hyperperfusion in 7 patients on ASL, and they also found ASL hypoperfusion in 2 patients, who had respective volume loss on MR imaging.⁸ Most cogently, 5 patients showed a concordance between ASL hyperperfusion and the clinical ictal onset zone.

Another very interesting finding was that several cases with ASL hyperperfusion were concordant with the interictal epileptiform discharges (7 patients) and the electroencephalogram ictal onset zone (6 patients).⁸ This finding can be confirmed in the other studies as well. Despite normal MR imaging findings, reversible mixed perfusion on iodine 123 (¹²³I-IMP) SPECT was found in patients with anti-alpha-amino-3-hydroxy-5-methyl-4-isoxazolepropionic acid (AMPA) receptor encephalitis and anti-gamma-aminobutyric

<http://dx.doi.org/10.3174/ajnr.A7563>

acid B (GABAB) receptor encephalitis,^{9,10} in which the first SPECT revealed hypoperfusion of the limbic system and cerebellum. These areas often contain high levels of GABAB receptors. Meanwhile, hyperperfusion in the motor strip and left temporal lobe was consistent with some of the patients' symptoms, like seizures. In view of our cases, some patients with hyperperfusion may be in status epilepticus or an acute stage of the disease, while normal perfusion or hypoperfusion may be due to their invisible abnormal findings on brain MR imaging or subclinical and chronic phases. Of course, susceptibility artifacts are unavoidable and should be excluded in cases with misrepresentation of brain MR imaging. Our findings need to be confirmed by a larger sample size and electrophysiology in the future.


In conclusion, 3D pseudocontinuous arterial spin-labeling may have added value in the early diagnosis and assessment of the therapeutic effects in AE. ASL not only presented hyperperfusion changes, but also showed no perfusion changes or hypoperfusion at different stages of the disease.


Disclosure forms provided by the authors are available with the full text and PDF of this article at www.ajnr.org.

REFERENCES

1. Li R, Jin S, Wang Y, et al. **Brain perfusion alterations on 3D pseudo-continuous arterial spin-labeling MR imaging in patients with autoimmune encephalitis: a case series and literature review.** *AJNR Am J Neuroradiol* 2022;43:701–06 CrossRef Medline
2. Sachs JR, Zapadka ME, Popli GS, et al. **Arterial spin labeling perfusion imaging demonstrates cerebral hyperperfusion in anti-NMDAR encephalitis.** *Radiol Case Rep* 2017;12:833–87 CrossRef Medline
3. Vallabhaneni D, Naveed MA, Mangla R, et al. **Perfusion imaging in autoimmune encephalitis.** *Case Rep Radiol* 2018;2018:3538645 CrossRef Medline
4. Sarria-Estrada S, Toledo M, Lorenzo-Bosquet C, et al. **Neuroimaging in status epilepticus secondary to paraneoplastic autoimmune encephalitis.** *Clin Radiol* 2014;69:795–803 CrossRef Medline
5. Watanabe Y, Sano F, Fukao T, et al. **Arterial spin labeling perfusion imaging in an infant with anti-N-methyl-D-aspartate receptor encephalitis: a case report.** *Brain Dev* 2022;44:405–09 CrossRef Medline
6. Li X, Yuan J, Liu L, Hu W. **Antibody-LGI 1 autoimmune encephalitis manifesting as rapidly progressive dementia and hyponatremia: a case report and literature review.** *BMC Neurol* 2019;19(1):19 CrossRef Medline
7. Li R, Shi PA, Liu TF, et al. **Role of 3D pseudocontinuous arterial spin-labeling perfusion in the diagnosis and follow-up in patients with herpes simplex encephalitis.** *AJNR Am J Neuroradiol* 2019;40:1901–07 CrossRef Medline
8. Kumar S, Nagesh CP, Thomas B, et al. **Arterial spin-labeling hyperperfusion in Rasmussen's encephalitis: is it due to focal brain inflammation or a postictal phenomenon?** *J Neuroradiol* 2018;45:6–14 CrossRef Medline
9. Fukumoto T, Miyamoto R, Fujita K, et al. **Reversible mixed perfusion on (123)I-IMP SPECT in anti-AMPA receptor encephalitis: a case report.** *J Neurol Sci* 2021;421:117306 CrossRef Medline
10. Ohta K, Seki M, Dalmau J, et al. **Perfusion IMP-SPECT shows reversible abnormalities in GABA(B) receptor antibody associated encephalitis with normal MRI.** *Brain Behav* 2011;1:70–72 CrossRef Medline

 X. Zhang

 D. Zheng

 Q. Huang

Department of Radiology
Nanjing Brain Hospital, Nanjing Medical University
Jiangning District, Nanjing, China

REPLY:

We appreciate the comments by Dr Zhang and colleagues on “Brain Perfusion Alterations on 3D Pseudocontinuous Arterial Spin-Labeling MR Imaging in Patients with Autoimmune Encephalitis: A Case Series and Literature Review” and thank the Editor for giving us the opportunity to reply to the comments. The application of arterial spin-labeling (ASL) for the assessment of autoimmune encephalitis (AE), a heterogeneous group of newly identified disorders, has seldom been described previously, and we agree that AE may have different abnormal perfusion patterns on 3D pseudocontinuous arterial spin-labeling (pCASL).

First, the authors mentioned the proportion of hyperperfusion alterations on ASL in their hospitalized patients with AE, which may be related to the types of AE included. AE subtypes that predominantly involve the white matter are less likely to cause hyperperfusion compared with autoimmune limbic encephalitis. In our study, the cases mainly included autoimmune limbic encephalitis and anti-N-methyl-D-aspartate receptor (NMDAR) encephalitis, not, as the author mentioned in the letter, AE subtypes that predominantly involve the white matter, such as anti-myelin oligodendrocyte glycoprotein antibody-associated encephalitis and Hashimoto encephalopathy, and usually present with a clinical profile and MR imaging features clearly different from those of autoimmune limbic encephalitis.¹

Second, 2 main abnormal metabolic patterns (mixed hyper-/hypometabolic and neurodegenerative-like) on PET/CT have been reported,² and different “paradigms” of encephalitis (mainly limbic versus NMDAR) may have different PET/CT findings.³ Studies have shown that metabolic patterns on PET/CT, to a certain extent, are associated with different autoantibody subtypes,⁴ implying that different pathophysiologic mechanisms may exist. We admit that the brain perfusion patterns may be associated with different autoantibody subtypes, which is an impetus for further studies revealing the correlation between perfusion and metabolism in AE subtypes.

Third, perfusion alterations for AE are also linked to the staging of disease, which usually presents with hyperperfusion during the acute and subacute periods and hypoperfusion in the chronic phase, though the division of the staging is controversial in clinical practice. Meanwhile, treatment may also affect the perfusion changes.^{5,6}

Finally, the authors mentioned the mechanisms leading to the perfusion alteration for AE. The exact pathophysiologic mechanism remains to be elucidated, and possible reasons include an

inflammatory process due to an antigen-antibody-mediated immune response and the loss of vascular autoregulatory mechanisms due to autonomic instability, and so forth. In addition, many subtypes of AE are frequently accompanied by seizures, which can also affect CBF. In our study, the patients who had clinical seizures were imaged during the interictal phase, but this effect cannot be completely excluded theoretically.

In summary, we admit that the sample size was small and the type of patients with AE was limited in our study. However, we believe that 3D pCASL may have added value in the early diagnosis and assessment of therapeutic effects in AE. Because perfusion alterations may be associated with multiple factors, such as autoantibody subtypes, the staging of disease, and whether the disease is accompanied by seizures, large cohort and longitudinal studies are needed to elucidate the contribution of 3D pCASL in the scenarios discussed above.

REFERENCES

1. Graus F, Titulaer MJ, Balu R, et al. **A clinical approach to diagnosis of autoimmune encephalitis.** *Lancet Neurol* 2016;15:391–404 CrossRef Medline
2. Fisher RE, Patel NR, Lai EC, et al. **Two different 18F-FDG brain PET metabolic patterns in autoimmune limbic encephalitis.** *Clin Nucl Med* 2012;37:e213–18 CrossRef Medline
3. Dinoto A, Cheli M, Ajcović M, et al. **ASL MRI and 18F-FDG-PET in autoimmune limbic encephalitis: clues from two paradigmatic cases.** *Neurol Sci* 2021;42:3423–25 CrossRef Medline
4. Baumgartner A, Rauer S, Mader I, et al. **Cerebral FDG-PET and MRI findings in autoimmune limbic encephalitis: correlation with autoantibody types.** *J Neurol* 2013;260:2744–53 CrossRef Medline
5. Sachs JR, Zapadka ME, Popli GS, et al. **Arterial spin labeling perfusion imaging demonstrates cerebral hyperperfusion in anti-NMDAR encephalitis.** *Radiol Case Rep* 2017;12:833–87 CrossRef Medline
6. Li R, Jin S, Wang Y, et al. **Brain perfusion alterations on 3D pseudocontinuous arterial spin-labeling MR imaging in patients with autoimmune encephalitis: a case series and literature review.** *AJNR Am J Neuroradiol* 2022;43:701–06 CrossRef Medline

© R. Li

Department of Medical Imaging
Tianjin Huanhu Hospital
Tianjin, China

Department of Radiology

The First Medical Center of PLA General Hospital
Beijing, China

© L. Ma

Department of Radiology
The First Medical Center of PLA General Hospital
Beijing, China

<http://dx.doi.org/10.3174/ajnr.A7621>